



# ASTRONOMY AND ASTROPHYSICS LIBRARY

---

**Series Editors:**

I. Appenzeller, Heidelberg, Germany  
G. Börner, Garching, Germany  
M. Harwit, Washington, DC, USA  
R. Kippenhahn, Göttingen, Germany  
J. Lequeux, Paris, France  
P.A. Strittmatter, Tucson, AZ, USA  
V. Trimble, College Park, MD, and Irvine, CA, USA

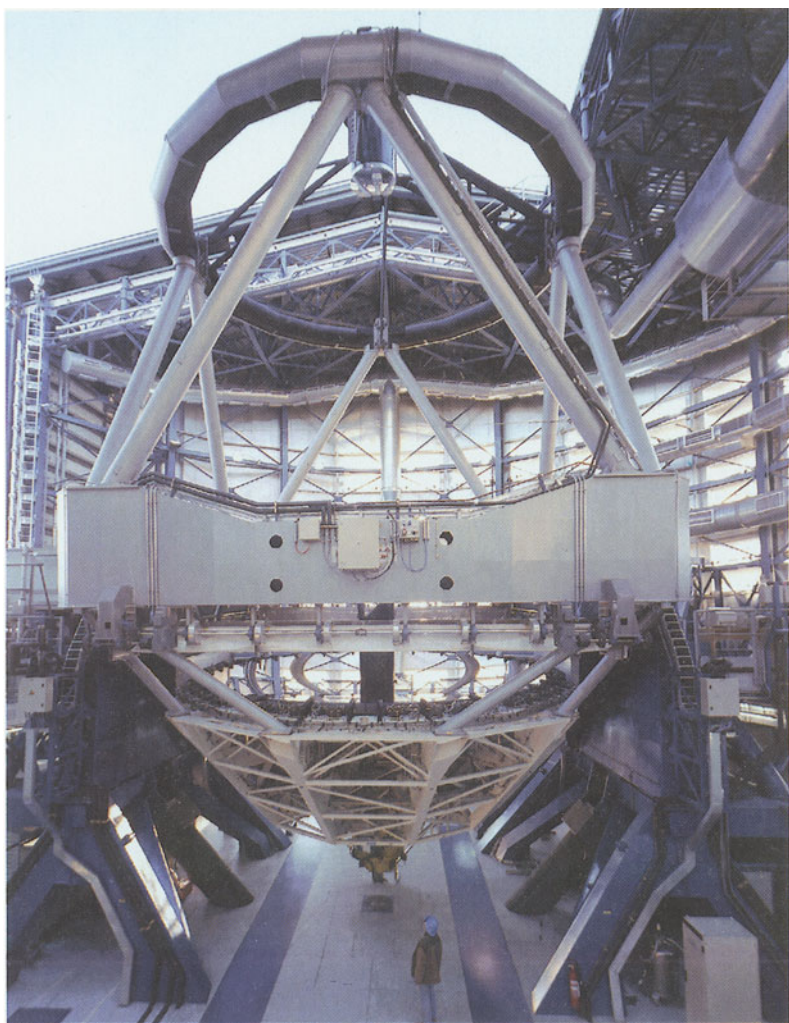
**Physics and Astronomy**



ONLINE LIBRARY

<http://www.springer.de/phys/>

Springer-Verlag Berlin Heidelberg GmbH



For legend see front matter page IV

R. N. Wilson

# Reflecting Telescope Optics II

Manufacture, Testing, Alignment,  
Modern Techniques

With 240 Figures and 39 Tables



Springer

Raymond N. Wilson

Waaler Str. 29

85296 Rohrbach/Ilm

GERMANY

---

**Cover picture:**

The two 10 m Keck telescopes at the observatory on Mauna Kea, Hawaii. On the left Keck II, on the right Keck I. At the time of completion of the text of this book (December 1997), these were not only the largest unit telescopes in the world, but also the only very large telescopes using new technology which were already in operation. (Photograph courtesy of the W.M. Keck Observatory, through J. Nelson and A. Perala. The high-resolution copy used was kindly provided by Richard J. Wainscoat, who holds the copyright).

**Legend to frontispiece:**

*The ESO VLT:* Unit Telescope No. 2 (Kueyen), photographed in March 2000 by Hans-Hermann Heyer, ESO.

*Photo upper left:* A 3-colour composite photo of the Crab Nebula (Messier 1) taken with the VLT Unit Telescope No. 2 and the FORS-2 instrument on 10 November, 1999. Distance about 6000 light-years. Exposures 1–5 min with seeing (FWHM) 0.65–0.80 arcsec.

*Photo upper right:* A 3-colour composite photo of the Spiral Galaxy NGC 2997 taken with the VLT Unit Telescope No. 1 (Antu) and the FORS-1 instrument on 5 March, 1999. Distance about 55 million light-years. Exposures 3–5 min. With a best star image quality of 0.25 arcsec (FWHM) in the near-infrared band (the other bands gave 0.35 and 0.34 arcsec FWHM), this is probably still the highest-resolution photo ever taken with a large ground-based telescope. Formatting of the photos by Ed Janssen, ESO. All photos and information courtesy of ESO.

---

Library of Congress Cataloging-in-Publication Data applied for.

Die Deutsche Bibliothek – Cip Einheitsaufnahme

**Wilson, Raymond N.:** Reflecting telescope optics / R.N. Wilson. – Berlin; Heidelberg; New York; Barcelona; Hong Kong; London; Milan; Paris; Singapore; Tokyo: Springer (Astronomy and astrophysics library)  
2. Manufacture, testing, alignment, modern techniques: with 39 tables. – 1999 ISBN 3-540-60356-5

Corrected Second Printing 2001

This work is subject to copyright. All rights are reserved, whether the whole or part of the material is concerned, specifically the rights of translation, reprinting, reuse of illustrations, recitation, broadcasting, reproduction on microfilm or in any other way, and storage in data banks. Duplication of this publication or parts thereof is permitted only under the provisions of the German Copyright Law of September 9, 1965, in its current version, and permission for use must always be obtained from Springer-Verlag. Violations are liable for prosecution under the German Copyright Law.

ISBN 978-3-642-08223-8      ISBN 978-3-662-08488-5 (eBook)

DOI 10.1007/978-3-662-08488-5

<http://www.springer.de>

© Springer-Verlag Berlin Heidelberg 1999

Originally published by Springer-Verlag Berlin Heidelberg New York in 1999.

Softcover reprint of the hardcover 1st edition 1999

The use of general descriptive names, registered names, trademarks, etc. in this publication does not imply, even in the absence of a specific statement, that such names are exempt from the relevant protective laws and regulations and therefore free for general use.

Typesetting: Data conversion by A. Leinz, Karlsruhe

Cover design: *design & production* GmbH, Heidelberg

Printed on acid-free paper    SPIN: 10882789    55/3111 – 5 4 3 2 1

To  
**Gerhard Schwesinger**

born 1913 in Krappitz, Upper Silesia,  
who developed the first complete Fourier theory  
for the support of primary mirrors of telescopes  
and thereby also stimulated my thinking on  
active optics, culminating in the ESO NTT

To  
**The NTT Team**

at ESO, Garching, who developed the telescope;  
to all the consultants and industrial groups  
who contributed to its manufacture; and to  
the team at ESO, La Silla, who have ensured  
correct maintenance and operation

## General Preface (Preface to Volume I)

The development of telescope optics is a fascinating story. Until this century, the optical theory of reflecting telescopes was essentially limited to the Cartesian treatment of axial imagery. In 1905, Karl Schwarzschild initiated a revolution by applying third order (Seidel) theory to the field imagery of 2-mirror telescopes. Since then, the whole gamut of possible telescope systems has been invented, analysed and, in many cases, tried out in practice.

Over all its history, the optical development of the telescope has also depended on *technical* inventions, above all in mirror materials, glasses, support systems and means of achieving high reflectivity. Over the last 30 years, developments have been particularly spectacular, above all in manufacture and test techniques and generally in enhancing the image quality available.

When I started this work in 1988 there was little literature in book form available on telescope optics. Two of the best were in German: "Die Fernrohre und Entfernungsmesser" by König-Köhler (1959) and the monograph on "Teleskope" by K. Bahner in "Handbuch der Physik", Vol. XXIX, which appeared in 1967. A major part of this latter work was devoted to a condensed, but excellent exposition of the theory of telescope optics. Inevitably, more modern technical developments which have since assumed great importance could not be included; furthermore, the fact that it was written in German has reduced its impact and dissemination to a limited section of the interested community.

In 1987, "Astronomical Optics" by D. J. Schroeder appeared. Harland Epps kindly drew my attention to this excellent book in 1988 and I reflected then whether scope for a further work on the subject still existed. I finally concluded that it did: Schroeder's book covers a much wider field, since "astronomical" optics includes the broad subject of astronomical instruments, whereas my intention was (and remains) only the comprehensive coverage of the optics of the *reflecting* telescope, in the broadest interpretation of that term. Furthermore, Schroeder's work emerged more from the university orbit and includes much basic optical theory addressed to graduate students who need, and can profit from, the whole physics background.

The aim of the present book is different from Schroeder's. It is addressed primarily to specialists in the field, both in the astronomical community itself and in the industries concerned, although I hope it may also be useful to students. Consequently, subjects such as practical alignment and test techniques,

## VIII General Preface (Preface to Volume I)

as well as maintenance aspects, occupy a significant part. Nevertheless, there are inevitably major overlap areas with both Bahner's and Schroeder's books which the informed reader will recognise. This overlap, involving repetitions in a somewhat different context, is unavoidable for a complete presentation.

Bahner's book included sections on achromatic objectives for refracting telescopes, astrographic objectives and oculars. No such material is included in this book. The refractor as such and the optical design of oculars are only of historical interest in large telescope optics and are only mentioned in this context. Of course, refracting *elements* still play an important role in wide-field telescopes, field correctors and focal reducers, and these are dealt with in Chapters 3 and 4. In general, mirrors supply the optical power while refracting elements have only the subordinate but important role of improving the imagery.

I favour the morphological approach with a strong emphasis on the historical background of the subject. In this sense, Chapter 5 is to be seen as essential background for understanding the current situation in telescope optics. For the background of the general theory of optical aberrations and diffraction, the reader is referred to specialist books in the field of optics. Only the essential consequences of Gaussian optics, third order theory and diffraction theory are given: the emphasis is on a complete treatment of the *application* to reflecting telescope optics.

At the suggestion of the publisher, the work has been split into two volumes. The first volume deals with the historical development (but there is no claim to completeness as a history of telescope optics - that would be a separate work) and the theory of reflecting telescope optics, including that of the refracting corrector elements. The second volume deals with technical aspects and modern developments in general. Although there is considerable cross-referencing between the volumes, the split is a logical one, since each volume has its own entity.

Every attempt has been made to give complete references to the international literature. It is hoped that the work will be useful, apart from its own content, as a "source book" of the subject.

While I was writing the book, three further works on the subject were published: "Telescope Optics" by Rutten and van Venrooij (1988), "Astrooptik" by Laux (1993) and "Reflective Optics" by Korsch (1991). The first two are primarily destined for amateurs, but have equally great value for professionals. As with the works of Bahner and Schroeder, there is considerable overlap with my material and I have referred to them liberally in my text. I only became aware of Korsch's work when my own text was finished, but again there is inevitably considerable overlap of treatment. However, not only the content and aim of these five works, all admirable, are very different, but also their styles. In this sense, I feel confirmed in my own enterprise.

Chapter 3 of Vol. I, dealing with the aberration theory of reflecting telescopes, is the longest and certainly one of the most important in the whole work. It is in this area that there is the greatest overlap with the above

books. However, an illustration of the major, and legitimate, differences in presentation is the data given on the optical quality of systems discussed. Spot-diagrams are the commonest way of representing the quality according to geometrical optics. Rutten-van Venrooij and Laux give virtually complete spot-diagram analyses of the systems they discuss, a very valuable feature. To keep Vol. I within reasonable bounds, I have preferred to limit myself to chosen examples, intended to illustrate with spot-diagrams the key points of the development. Some of these are taken from the literature; but most of those in Chapter 3 (and a few in Chapter 4) have been optimized by Bernard Delabre of ESO from starting systems I set up from the basic theory, or with minor modifications emerging from the calculations. I am deeply grateful for this major contribution to the work.

I owe a great debt of gratitude to many specialist members of the astronomical community and associated industrial concerns, particularly Carl Zeiss (Oberkochen) and REOSC (Paris), who have generously supplied information. This debt extends, too, to many ESO colleagues. Above all, I am grateful to the ESO management for supporting the project and for extensive help in establishing the final text. In the detailed work, I wish to thank specifically, as well as Bernard Delabre mentioned above, Marion Beelen, Samantha Milligan, Baxter Aitken (who has not only played a major role in the text-processing but also kindly read through the entire work), Ed Janssen (who drew and formatted the figures) and Hans-Hermann Heyer for much hard work and enthusiastic support. My gratitude is also due to Richard West for general encouragement and support. Finally, I thank the publisher, Springer-Verlag, for excellent cooperation, and, last but by no means least, my wife Anne, for much help with the text and, above all, for patience throughout the whole task.

D-85296 Rohrbach  
January 1996

Ray N. Wilson

## Preface to Volume II

The aim and style of Vol. II follows exactly the intentions expressed in the preface to Vol. I, above. The general approach is, therefore, again historical and morphological, although the subjects of Vol. II are, in general, more recent than much of the theory of Vol. I. Most of the developments described are a product of the last 50 years – many of them, indeed, of the last 20 years. Nevertheless, the history of the developments discussed often goes back a long way: in Chap. 4 there is a reference to W. Herschel in 1800, in Chap. 3 to S. D. Poisson in 1829. It is my hope that the two volumes together include the most complete bibliography of reflecting telescope optics that exists. Chapter 1 of Vol. II, dealing with manufacture and test technology, has 166 numbered references; Chap. 3, dealing with modern technical solutions for reflecting telescopes in general and the longest in the book, has 260 numbered references. So Vol. II will hopefully also serve as a source book.

One important consequence of the fact that the bulk of the material of Vol. II is, in its nature, modern or ultra-modern, is that the exposition given is bound to date fairly rapidly in those areas where development is most intensive. Such a key area is, of course, *adaptive optics*, the correction of atmospheric seeing dealt with in Chap. 5. Depending on the material involved, the cut-off date for new developments in this book lies between about 1993 and February 1998 at the latest. So developments after 1993 are only partially covered and effectively not at all after 1997.

Since no developments occurring in 1998 could be included in the text, it follows that there is no reference to the remarkable “First Light” results of the ESO VLT UT1, the first telescope with an 8 m monolithic primary to be completed. The image quality (raw) published at “First Light” was remarkable enough, with best star images having a FWHM equal to 0.43 arcsec or even 0.38 arcsec. However, on 6 June 1998 this was bettered by star images of the globular cluster M55 with a FWHM of 0.27 arcsec! Such remarkable results, expected to be achieved only about 3 years later, are a complete vindication both of the thin-meniscus active technology of the telescope and of the excellent site of Paranal in Chile. It is clear that the age of very large telescopes based on new technology, initiated with dramatic success by the two Keck 10 m telescopes completed in 1992 and 1996 respectively, will in the next few years be represented by about a dozen or more superb individual instruments using different technologies and all with apertures between

6 $\frac{1}{2}$  m and 10 m, some of which are intended for linked operation in the interferometric mode. A marvellous astronomical prospect for the new millenium indeed! It is my hope that I have done justice in this book to all these projects and the remarkable technologies driving them.

It was my intention to include specific chapters on solar telescopes, X-ray telescopes using near-grazing incidence, and interferometry with telescopes. Subsequently, I abandoned coverage of these fields for the following reasons. Solar telescopes have very different requirements from those of normal astronomical telescopes, and refracting telescopes, which are not treated in this work, still play a significant role. Similarly, X-ray telescopes have very special technical requirements, though the close link to the Mersenne telescope was indicated in Vol. I. Furthermore, these systems have been admirably dealt with by Korsch in his "Reflective Optics" (Academic Press, 1991). The interferometric requirements for telescopes have been treated briefly in Chap. 5; but I concluded that a treatment in depth of interferometry with telescopes would require a whole book in its own right, even if my own expertise in this field were adequate, which is not the case.

I owe a vast debt of gratitude to a wide circle of friends and colleagues in the astronomical community and the "big optics" community associated with it. Specific acknowledgments are given at the beginning of Chap. 1 in the areas of manufacture and testing of optical surfaces. The other chapters, above all Chap. 3, are so wide-ranging that it would be impossible to express adequate acknowledgment in this preface to the many sources of generous help and advice. I hope, therefore, it will suffice here if I thank globally all those who have helped with information or figure material. I believe the credits in the text, references and, above all, the figures are the best way to express my deep gratitude.

Specifically, I wish here to thank the management of ESO for their continued encouragement and support of the whole project, above all for the major work of the preparation of the figures. This was organised through the kind help of Richard West and executed, as for Vol. I, by Ed Janssen. He has again done a wonderful job in a key area and I express here my grateful thanks to him. My thanks are also due to Hannes Heyer for his assistance on the photographic side. On the technical side, many colleagues have given valuable information, particularly Philippe Dierickx, Lothar Noethe, Martin Cullum, Paul Giordano, Bernard Delabre and Francis Franz. The original text processing was done by Marion Beelen, Samantha Milligan and Baxter Aitken, to whom I express my gratitude for an enormous task. Ingrid Weber has given valuable secretarial help in many ways. Finally, the ESO library has been a central factor in the fundamentally important area of literature: my grateful thanks are due to Uta Grothkopf and Angelika Treumann for their efficient and friendly service.

As with Vol. I, the collaboration with Springer-Verlag has been excellent in all respects. I express here my grateful thanks to Prof. W. Beiglböck and his staff for the help and understanding they have constantly given me; also for

financial support in preparation of the revised and corrected manuscript. The latter text-processing work has been carried out with admirable efficiency and cooperation by Mr. Adam Leinz, to whom I also express my grateful thanks.

When Vol. II appears, about the end of 1998, the whole project will have covered a period of exactly ten years, perhaps 6–7 years full-time equivalent. My wife, Anne, has not only given me much valuable help in checking the style and correctness of the text, but also borne with my obsession with the task with great patience and understanding, for which I owe her a great debt of gratitude.

D-85296 Rohrbach  
June 1998

Ray N. Wilson

# Contents

<b>1.</b>	<b>Manufacture and test procedures . . . . .</b>	<b>1</b>
1.1	Introduction and acknowledgements . . . . .	1
1.2	Grinding, polishing and figuring technology . . . . .	1
1.2.1	Background of optical surface working . . . . .	1
1.2.2	Lapping techniques . . . . .	2
1.3	Test technology . . . . .	46
1.3.1	General aspects of test technology development . . . . .	46
1.3.2	Interferometers . . . . .	46
1.3.3	Test procedures other than interferometry . . . . .	74
1.3.4	Null (compensation) systems . . . . .	76
1.3.5	Test systems for Cassegrain secondary mirrors . . . . .	86
1.3.6	Test methods for large flats . . . . .	101
<b>2.</b>	<b>Sensitivities, alignment of telescopes and test procedures in function . . . . .</b>	<b>105</b>
2.1	Sensitivities . . . . .	105
2.1.1	Decentering errors . . . . .	105
2.1.2	Despace errors . . . . .	109
2.2	Alignment and adjustment of telescopes . . . . .	111
2.2.1	General theoretical principles of telescope alignment . .	111
2.2.2	General set-up situation and definition of the aims of alignment . . . . .	122
2.2.3	Alignment at the prime focus of telescopes with field corrector . . . . .	130
2.2.4	Alignment of Schmidt telescopes . . . . .	130
2.2.5	Field correctors at the Cassegrain focus . . . . .	131
2.3	Test methods and image analysis of telescopes in function . .	131
2.3.1	Classical qualitative methods . . . . .	131
2.3.2	“Pupil plates”: geometrical assessments of defocused star images . . . . .	133
2.3.3	Hartmann-based techniques . . . . .	144
2.3.4	Curvature sensing: the Roddier test . . . . .	161
2.3.5	Other methods of testing the optical quality of telescopes in function . . . . .	166

<b>3. Modern telescope developments:</b>	
<b>pupil segmentation and techniques to reduce mass . . . . .</b>	<b>169</b>
3.1 Evolution and revolution in telescope optics . . . . .	169
3.2 Examples of modern projects using the technologies of Table 3.3 . . . . .	175
3.2.1 Direct segmentation with a filled aperture . . . . .	175
3.2.2 Separate telescopes with monolithic primaries on a single mount (MMT-type indirect segmentation) .	186
3.2.3 Other large telescope projects using lightweighted monolithic blanks . . . . .	192
3.2.4 Projects with thin-meniscus flexible primaries, controlled actively, or of stiff composites . . . . .	199
3.3 Blank production for new technology telescopes . . . . .	216
3.3.1 General considerations and physical properties . .	216
3.3.2 Glass ceramic blank production . . . . .	223
3.3.3 Fused quartz (silica) blank production . . . . .	225
3.3.4 Modern blank production with BSC (borosilicate) glass (Pyrex) . . . . .	227
3.3.5 Modern blank production in metal . . . . .	231
3.3.6 Compacted powder, sintered or vapour-deposited materials for blanks . . . . .	238
3.3.7 Lightweight composite materials for blanks . . . .	240
3.3.8 Liquid mirror telescopes (Hg) . . . . .	240
3.4 Mirror support systems in modern telescopes . . . . .	242
3.4.1 The basic laws of axial supports for mirrors . . . .	242
3.4.2 Modern work on the theory of mirror supports: axial support solutions . . . . .	253
3.4.3 Lateral (radial) supports for mirrors . . . . .	259
3.4.4 Mirror handling . . . . .	272
3.5 Active optics control systems . . . . .	274
3.5.1 Introduction and definitions . . . . .	274
3.5.2 The principles of the ESO active optics system, as developed for the 3.5 m NTT . . . . .	279
3.5.3 Operational results for the ESO 3.5 m NTT and conclusions from its performance . . . . .	291
3.5.4 Extension of the active optics system to the ESO 8 m VLT . . . . .	298
3.5.5 Other active optics developments in current projects .	304
3.5.6 Conclusions on the current state of development and future potential of active optics in telescopes . .	313
3.6 Local environmental aspects of telescopes . . . . .	314
3.6.1 Definition of "local air" and its importance . . . .	314
3.6.2 Recent evolution in telescope enclosures and "local air" error measurements in functioning telescopes . . . . .	318

3.6.3	Other recent investigations by laboratory experiment or theory: mirror seeing . . . . .	327
3.6.4	Further work on “dome seeing” in general . . . . .	338
3.6.5	General conclusions on local air seeing and enclosures .	343
3.7	Optical data of the major ground-based telescope projects using new technology . . . . .	345
4.	<b>Image quality specification and optical efficiency criteria . . . . .</b>	349
4.1	Classical specification criteria: geometrical angular or wavefront aberration . . . . .	349
4.2	Specifications for modern ground-based telescope projects . .	353
4.3	Optical efficiency criteria . . . . .	367
5.	<b>Atmospheric optics, adaptive optics, telescope quality for interferometry . . . . .</b>	373
5.1	Atmospheric optics . . . . .	373
5.1.1	Atmospheric refraction and atmospheric dispersion . .	374
5.1.2	Atmospheric turbulence (“seeing”) . . . . .	376
5.2	Adaptive optics . . . . .	396
5.2.1	Definitions and aims: active and adaptive optics . . .	396
5.2.2	The principles of adaptive optics . . . . .	398
5.2.3	Practical systems for adaptive optics in astronomical telescopes . . . . .	403
5.2.4	Limitations of the isoplanatic patch: artificial reference sources . . . . .	409
5.2.5	Adaptive optics for the ESO VLT and experimental correction results (COME-ON and COME-ON PLUS systems) . . . . .	413
5.2.6	Adaptive optics using laser reference sources for military purposes applicable to astronomy . . . . .	416
5.3	Site selection in height . . . . .	418
5.4	High resolution imaging apart from adaptive optics . . .	420
5.4.1	Michelson interferometry . . . . .	420
5.4.2	Speckle interferometry . . . . .	421
6.	<b>Mirror Reflecting Coats: Production and Cleaning . . . . .</b>	423
6.1	Introduction: evolution to the current situation . . . . .	423
6.2	Modern perspectives for reflecting coatings . . . . .	430
6.2.1	Multi-coat enhancement of reflecting coats . . . . .	430
6.2.2	Silver reflecting coat with single protecting coat and other recent developments . . . . .	434
6.2.3	Cleaning and maintenance of reflecting coats . . . . .	442
6.2.4	Summary . . . . .	448

<b>7. Adapters and beam combination aspects, baffles</b> . . . . .	449
<b>7.1 Adapters</b> . . . . .	449
7.1.1 Background of adapter development . . . . .	449
7.1.2 The adapter for the ESO 3.5 m NTT (Nasmyth focus) .	450
7.1.3 The adapters for the VLT 8 m unit telescopes . . . . .	456
7.1.4 Beam combination aspects . . . . .	458
7.1.5 Mountings and field rotation . . . . .	459
<b>7.2 Baffles</b> . . . . .	459
<b>8. Maintenance and operation of telescope optics</b> . . . . .	469
<b>8.1 Ground-based telescopes</b> . . . . .	469
<b>8.2 Space telescopes</b> . . . . .	474
<b>Appendix: Mathematical symbols</b> . . . . .	475
<b>References</b> . . . . .	477
<b>List of figures</b> . . . . .	499
<b>List of tables</b> . . . . .	515
<b>Name index</b> . . . . .	519
<b>Subject index</b> . . . . .	525

# 1. Manufacture and test procedures

## 1.1 Introduction and acknowledgements

Optical manufacture and testing is a vast subject which can only be dealt with as a review in the current chapter. Apart from many literature sources, I am particularly grateful for the generous information given during visits to the workshops of REOSC in Paris, Carl Zeiss in Oberkochen and Horst Kaufmann in Crailsheim. The former are two of the world's major producers of large astronomical optics, the latter an example of an excellent small workshop capable of producing mirrors up to 1 m diameter. Information by post has also been generously supplied by R.E. Parks in Tucson, G. Lemaître in Marseilles, R. Angel in Tucson, Litton ITEK in Lexington, Eastman Kodak in Rochester, the Keck 10 m telescope development team and T. Korhonen in Turku. Much of this chapter reflects the technologies practised by these sources. Sincere thanks are also due to ESO, in particular to Philippe Dierickx, for valuable information concerning the production of the optics for the VLT.

## 1.2 Grinding, polishing and figuring technology

### 1.2.1 Background of optical surface working

The principle of rubbing the optical surface with a tool and abrasive is as old as the spectacle lens. The simple geometrical fact that this automatically tends to produce a spherical surface because of constant curvature in all tool positions still has fundamental importance in the bulk of manufacturing processes.

The initial preparation of the rough form of mirror blanks is performed today with great efficiency by diamond milling machines. The conventional optical work can then avoid removal of large quantities of glass by coarse grinding and can proceed effectively to fine grinding with silicon carbide (Carborundum) and smoothing with aluminium oxide (Aloxite). Classically, fullsize cast iron tools, turned to the required radius, are used, but for very large mirrors such procedures with fullsize tools may no longer be practicable.

Polishing for high quality surfaces is still performed by pitch laps covering the tools – the same material as was used by Newton for the first reflector in

1668. Rouge (iron oxide), used as polishing abrasive till about 1950, has now been displaced by cerium oxide (Cerox) except for special processes.

Classical working methods are well described in older books, for example Dévé [1.1] or Twyman [1.2]. For the case of astronomical optics, an excellent account is given by Maksutov [1.3]. It has long been agreed that the grinding process with *glass surfaces* consists of conchoidal fracturing [1.2] [1.4] [1.5] under pressure. The polishing process, on the other hand, has been a matter of debate between three main theories, the *mechanical*, the *chemical* and the *flow* theories. The mechanical theory sees the essential process as a slow removal of glass material through fine abrasive in association with the pitch surface and water. The chemical theory assumes chemical effects in which water and the polishing abrasive play a complex role including recrystallisation. The flow theory assumes local flow effects from intensive local heating. Each of these theories has protagonists with valid arguments in their support [1.2] [1.3] [1.5]. A review was given by Götz [1.6] in which it was concluded that all three can play a significant role, the relative importance depending strongly on the numerous physical parameters involved. That mechanical removal takes place is widely accepted and is the basis of figuring operations. The fact that a high level of polish can be achieved with diamond [1.7], with which chemical reactions are assumed to be absent, supports the view that the mechanical process can be so fine that the residual roughness can be reduced to the order of a few nm. Conventional polishing of glass gives a surface structure better than 0.5 nm, the highest quality being about 0.05 nm [1.7]. Since the classical value for the radius of an atom, defined from scattering effects, is about 0.1 nm (1 Å), such a quality of polish implies a perfect surface within the limits of the structure of the material. A polishing quality of 0.5 nm is also achieved with metal surfaces such as the Canigen (nickel) coating on aluminium mirrors. A modern analysis of polish has been given by Izumitani [1.7] [1.8].

### 1.2.2 Lapping techniques

The fundamental law governing the removal of material by an optical lapping process is Preston's Law [1.9] [1.10]

$$U = Apv , \quad (1.1)$$

where  $U$  is the wear per unit time,  $A$  is a constant depending on the physical parameters of the process (Preston constant),  $p$  is the pressure of the tool on the workpiece surface and  $v$  is the relative velocity of the tool to the workpiece. The integral wear over a surface per unit time is then

$$\sum U = A \int_{-x}^{+x} \int_{-y}^{+y} p(x, y)v(x, y) dx dy \quad (1.2)$$

The larger the area of the tool, the more area elements  $dx dy$  can be worked in parallel and the more efficient the operation. For a given area element  $dx dy$  the total wear in time  $t$  is

$$\int_0^t U(x, y) dt = \int_0^t Ap(t)v(t) dt \quad (1.3)$$

which expresses the possibilities of influencing the figure by varying the parameters  $p$ ,  $v$  and  $t$ . The possibilities are then:

- For a tool of fixed area to vary the effective time  $t$  by directing the movements of the tool.
- To vary the effective time  $t$  by varying the area of the tool.
- To vary the pressure  $p$  exerted by the tool at different points.
- To vary the relative velocity  $v$  applied by the tool at different points.

In practice, this leads to the control possibilities [1.7] given in Table 1.1.

Small workshops [1.11] (or in general for optical elements  $\leq 1\text{ m}$ ) will mainly use 1.a), 2 and 3.a) [1.12] [1.13], with effectively fullsize tools, but all possibilities are exploited for large sizes involving steep aspherics. Which methods are used will depend on the preferences and experience of the manufacturer.

An important aspect for larger sizes is the *support* of the workpiece, above all for mirrors, because deflection errors enter directly with a factor 2 into the wavefront aberration of the mirror. Lens surfaces are far less critical ( $4\times$ ) in this respect. For smaller sizes, a mirror is usually stiff enough with a classical aspect ratio of 6–8 to be supported on compressed, elastic pads. For a mirror of 700 mm, Kaufmann [1.11] used 12 foam rubber supports, each about 25 mm thick, when supporting the mirror. For classically rigid mirrors, such supports have been used for larger mirrors with plane backs.

More sophisticated supports for large sizes of more flexible mirrors will have to resist and compensate the pressure of polishing tools. For fullsize tools, the supports may be modifications of the two basic mirror support systems due to Grubb and Lassell (Chap. 5 of RTO I) whose use in classical telescopes is described by Maksutov [1.3]. We shall refer again to these basic supports in Chap. 3.

We shall now consider the main modern developments in lapping techniques on the basis of Table 1.1.

**1.2.2.1 Computer controlled polishing: CCP.** As in virtually all other aspects of optics technology, modern computers have played an essential role in figuring and test technology. Some of the first systematic attempts to apply computer controlled polishing to telescope mirror figuring were reported by Brown [1.14] concerning work at Grubb-Parsons. Brown emphasized the dilemma which thereafter forced progress: rigid, fullsize tools not only tend to produce the spherical form but also ensure rotational symmetry; but they are difficult to apply to steep aspherics unless made more flexible or given very limited amplitude of movement. He gave preliminary results for computer control using fullsize tools whereby the computer program controlled the movement and the area and shape of the polishing surface (2. in Table 1.1).

**Table 1.1.** Figuring control possibilities resulting from Preston's Law

- |   |
|---|
| 1. Full aperture tools (diameter limit 4–5 m)                               |
| a) Stiff  |
| b) Flexible (allowing variable pressure)                                    |
| c) Driven (stressed laps)   |
| d) Stress polishing (stressed workpiece – fabrication “active optics”)      |
| 2. Full aperture pattern tools (e.g. “petal” laps, variable area and shape) |
| 3. Sub-aperture tools   |
| a) Variable dwell time (movement control)                                   |
| b) Variable pressure  |
| c) Variable size (area)   |
| 4. Membrane tools (combining all the above features)                        |

At that time (1970), the reference test data had to be derived by scanning photographic interferograms; today the existence of CCD cameras with direct readout (see § 1.3) makes the feedback loop to the polishing process far more rapid and convenient.

Perkin-Elmer (now Hughes Danbury) in the U.S.A. also started an ambitious and systematic program of Computer Controlled Polishing (CCP) in the early 1970s. The test input was based on the scanning of interferograms by a high speed digitized microdensitometer giving a phase map of the errors [1.15]. The basic technique was the computer control of *sub-aperture* tools (3. in Table 1.1) because of the advantages analysed by Lysyannyi [1.16]. These advantages are the ability to adapt to aspheric surfaces if the tool is relatively small and free to tilt; the ability to operate rapidly on high spatial frequency errors, and the relative insensitivity to workpiece distortion through pressure since the removal of material is local. The disadvantage of small tools is the loss of natural control of rotational symmetry: this must be established by the computer control. In a classic paper, Jones [1.17] established the principles of such a CCP system. The machine had a small rotating tool assembly which travelled over the workpiece surface along a predetermined path. This path and the velocity along the path were controlled by a small computer. The tool size could be varied (3.c) in Table 1.1), but for a given choice the controlled parameter was the polishing *time* at a given point (“dwell time”) (3.a) in Table 1.1), the pressure being held constant. Figure 1.1 shows the CCP head unit. *x* and *y* servo-drives controlled the velocity of the polishing tool carriage along the beam and the latter’s velocity along two support rails. The entire polishing tool could be rotated by a hydraulic servo motor. Careful experiments were performed to determine the optimum movement configuration shown in Fig. 1.2. An epicyclic configuration was the best. The head was mounted on a plate and a motor and drive system used to move the plate in a small circle. While the head travelled in a 3.8 cm diameter circle, it also rotated at higher speed causing the two 3.5 cm diameter polishing

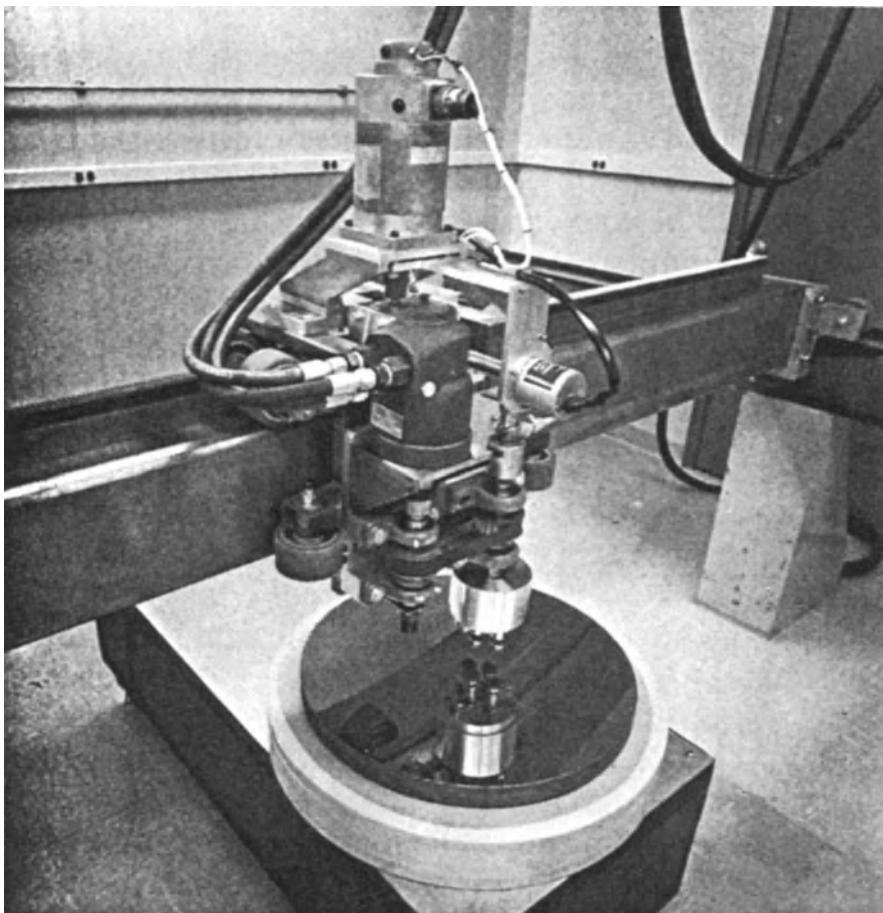
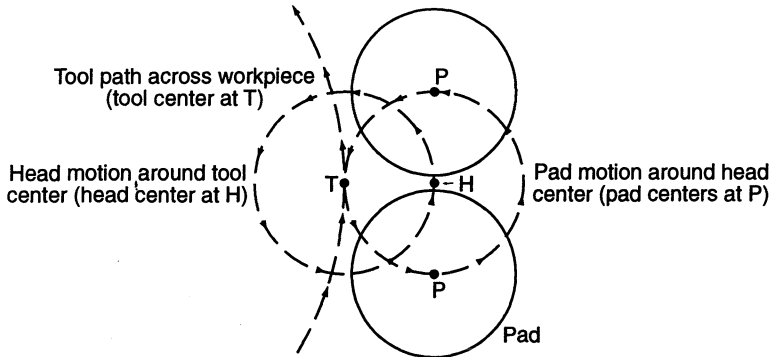


Fig. 1.1. Perkin-Elmer CCP head unit (Jones [1.17])

pads, separated by 3.8 cm, to rotate about the point  $H$  midway between their centers.

Jones [1.17] cites three impressive first results. A 38 cm diameter Cervit mirror was polished flat in 4 hours with the CCP, the quality being improved from  $0.22 \lambda$  rms to  $0.012 \lambda$  rms ( $\lambda = 633$  nm). A lightweighted beryllium mirror,  $81 \times 83$  cm, was polished flat in 65 hours from  $0.40 \lambda$  rms to  $0.05 \lambda$  rms. An aspheric corrector plate was taken with 99 hours polishing time from  $1.56 \lambda$  rms to  $0.17 \lambda$  rms, surpassing the figure goal of  $0.20 \lambda$  rms. Further details and progress with the CCP were given by Jones [1.18] [1.19]. A flexible 1.5 m ULE mirror with 9 cm thickness and hyperbolic form was polished from  $1.35 \lambda$  rms to  $0.074 \lambda$  rms, most of the residual error being in the edge zone. This was improved by special work. A further example is a 1.8 m diameter lightweight ULE f/1.5 spherical mirror. The starting figure had  $0.161 \lambda$  rms



**Fig. 1.2.** Epicyclic tool configurations for Perkin-Elmer CCP (Jones [1.17])

error (Fig. 1.3 (a)). The computer provided the prediction surface shown in Fig. 1.3 (b) with  $0.091 \lambda$  rms for the first CCP run, which consisted of six passes over the mirror along an annular spiral path taking 23 hours. This gave the result of Fig. 1.3 (c) with  $0.084 \lambda$  rms, 10 % better than the improvement predicted. The accuracy of the prediction from Fig. 1.3 (b) and (c) is impressive. Table 1.2 shows the further progress in three further cycles taking 49 hours, giving finally  $0.039 \lambda$  rms. The lower rate of convergence at the end was due to the figure measuring error of  $0.028 \lambda$  rms. The initial and final interferograms are shown in Fig. 1.4.

**Table 1.2.** Progress in figuring a 1.8 m lightweighted spherical f/1.5 mirror with the Perkin-Elmer CCP (Jones [1.19])

Cycle	Polishing time (hours)	Predicted rms wavefront error in $\lambda$ ( $\lambda = 633$ nm)	Actual rms error in $\lambda$
Initial state	—	—	0.161
1	23	0.091	0.084
2	15	0.054	0.060
3	17	0.030	0.050
4	17	0.020	0.039

Although this demonstration was performed on a spherical mirror, the result represented a milestone in the figuring of large astronomical mirrors, since the actual form of the surface is of little consequence with the small tools used. The limitation of convergence was effectively determined by the test procedures. Since these have further improved since 1980, Jones effectively proved that the problem of automatic figure control for astronomical mirrors was solved, apart from minimal edge effects and limitations of speed of polishing dictated by the tool size. CCP was used for polishing the primary of the Hubble Space Telescope (HST) to very high measured figure quality,

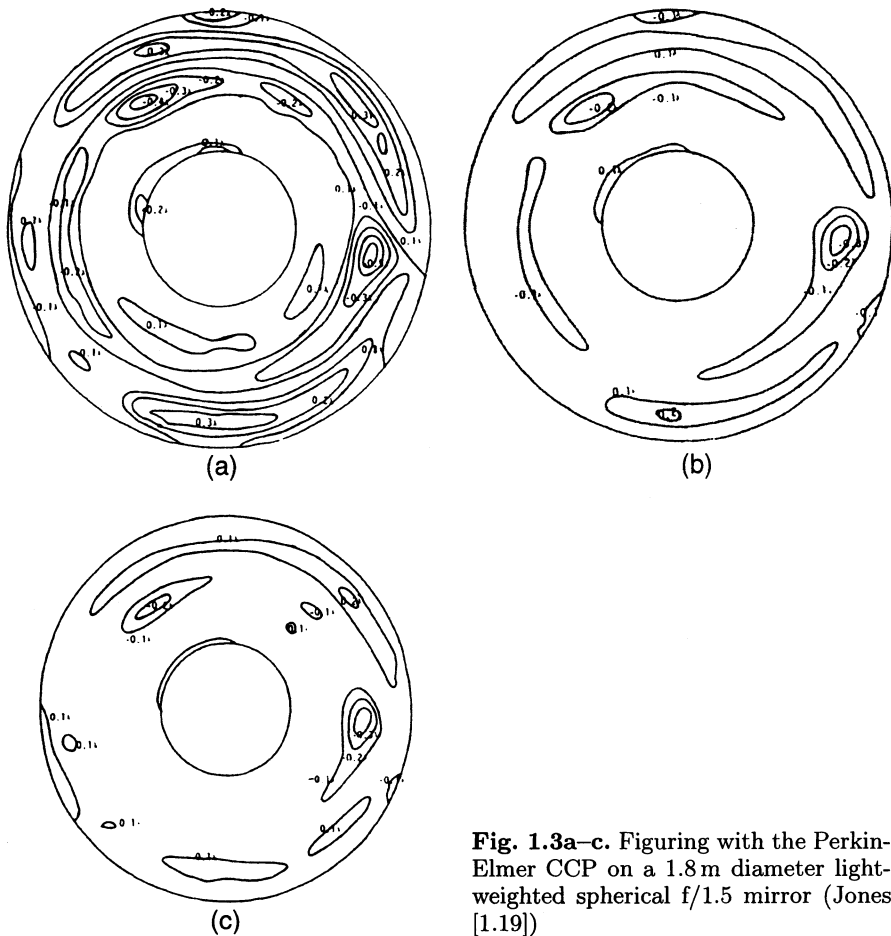


**Fig. 1.3a–c.** Figuring with the Perkin-Elmer CCP on a 1.8 m diameter light-weighted spherical f/1.5 mirror (Jones [1.19])

as reported by Facey et al. [1.20]. Of course, this could take no account of the systematic error of the test procedure subsequently revealed in the HST primary.

A further paper by Jones [1.21] was dedicated to the problem of the application of CCP to *segment* production for segmented large mirrors with specific reference to the Keck telescope [1.22] (Chap. 3). Jones points out the advantages of CCP for segments, which, in the normal case of aspheric primaries, have no axis of symmetry, are hexagonal rather than circular and must have accurate figures to the very edge, an extremely difficult requirement. A CCP experiment was performed on an existing spherical mirror, cut to form a 60° segment of a 0.91 m diameter mirror with 30 % linear obscuration. The segment was extremely steep with f/0.66. For convenience in testing, the surface figured was a sphere, but the figuring technology would have been the same for an off-axis aspheric. The aim was a best effort surface in a limited time. In general, the same principles were used as in the previous CCP experiments,

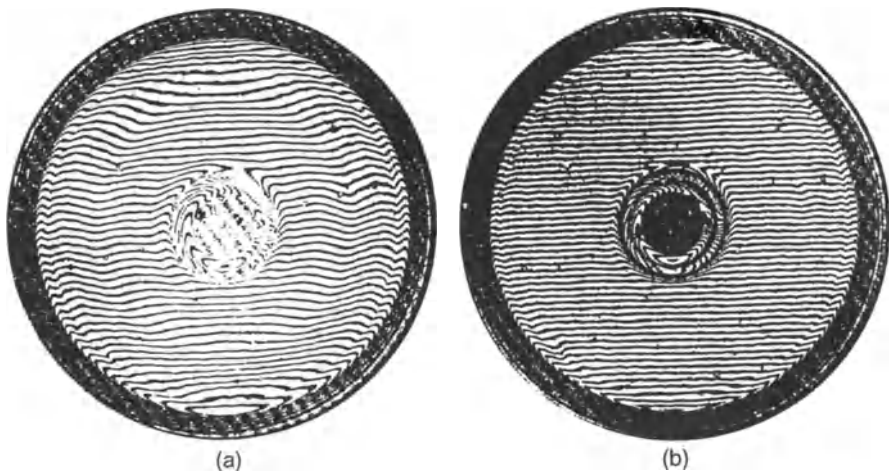


**Fig. 1.4.** Interferograms of a 1.8 m lightweighted spherical f/1.5 mirror, (a) initially, (b) after 72 hours of polishing with the Perkin-Elmer CCP (Jones [1.19])

but the extreme requirements for the edge required a special "overhang" technique, giving greater pressure on the edge zone compared with the constant pressure used elsewhere. Initially, the surface was too high along most of the cut edges. The initial error was fairly low,  $0.042 \lambda$  rms. The CCP was used for 5 iterative cycles, using a raster movement over the workpiece, the total time being less than 4 hours. The resulting figure (Fig. 1.5) was  $0.012 \lambda$  rms ( $\lambda = 633 \text{ nm}$ ). This demonstration proved that the CCP technology with small tools was a powerful rival to the "stress polishing" technique finally preferred for the segment manufacture of the Keck telescope [1.23]. This is the technique 1.d) of Table 1.1 which will be further discussed below.

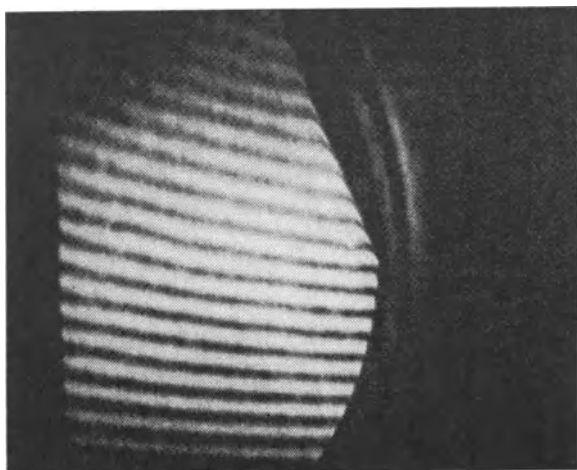


**Fig. 1.5.** Segment improved using the Perkin-Elmer CCP (Jones [1.21]). The figure shows virtually no deviation at the edge

CCP has been developed and applied in recent years by all the major manufacturers of large telescope optics. Jones further developed his earlier CCP work at ITEK into a powerful and universal system – see below.

REOSC in France developed such a system (CCST-Computer Controlled Surfacing Technique) about 1985 and has since applied it to the manufacture of the ESO VLT 8.2 m primary mirrors [1.24] [1.25] [1.26]. The method is applied to both aspheric grinding and polishing, since for large, modern primaries with steep aperture ratios it is no longer reasonable to do aspherizing solely by polishing. The technique is essentially identical except that ceramic tiled tools are used in grinding and pitch tiles in polishing. The smallest tools have a diameter about one eighth of the full diameter. The CCST is a “dwell time” control of such small tools, using constant pressure and constant relative surface velocity to ensure optimum surface “cleanness” (quality of polish). REOSC combines CCST figuring with the use of large-size flexible tools (in the VLT case 5 m diameter) to achieve surface smoothing. These are effectively of type 2. in Table 1.1, with a patterned tool surface shape. Their flexibility enables, too, the use of variable pressure in the group 1.b) of Table 1.1. Figure 1.6 shows a CCST head able to work mirrors up to 2 m. An example of the use is a 60 cm test mirror which was taken from an initial  $0.53 \lambda$  rms by seven polishing runs to  $0.11 \lambda$  rms and a further seven to  $0.05 \lambda$  rms (Fig. 1.7). This left a slight edge error due to a defect in the test



**Fig. 1.6.** Computer Controlled Surfacing Technique (CCST) at REOSC [1.25] for mirrors up to 2 m diameter

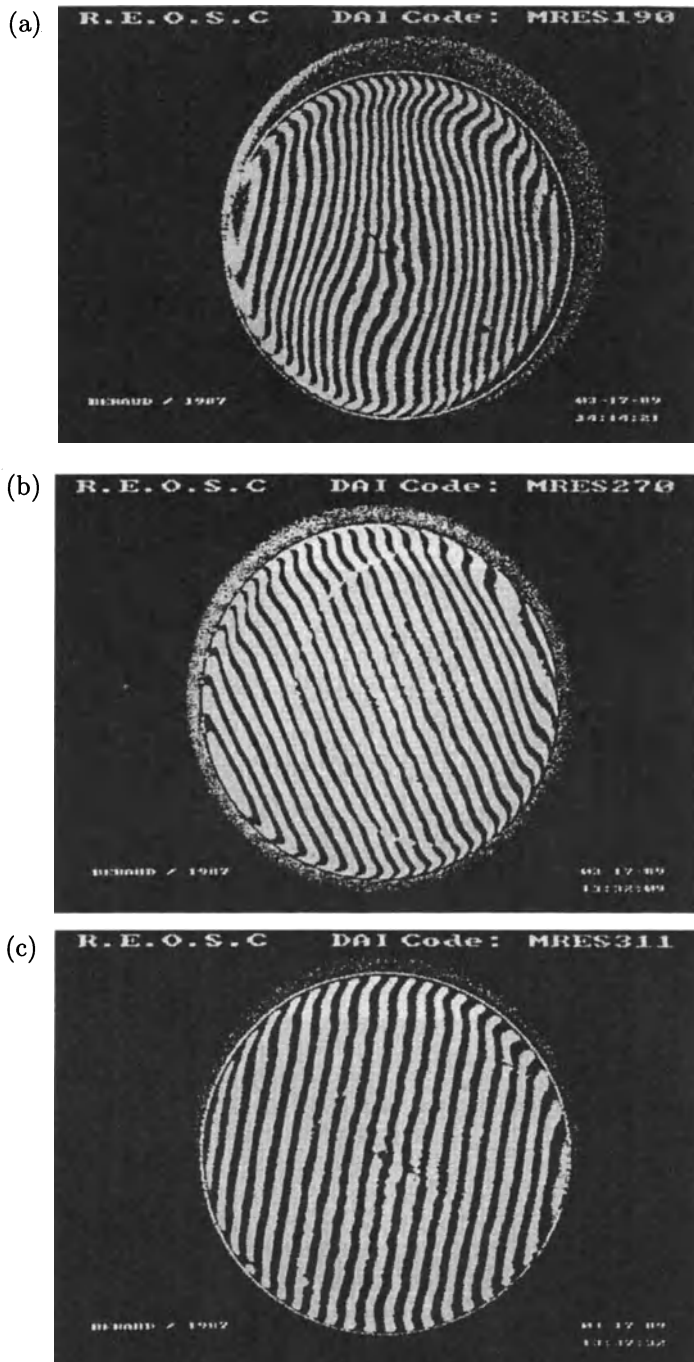


**Fig. 1.7.** CCST at REOSC [1.25] with a 60 cm test mirror. (a) The initial state, (b) after 7 polishing runs, (c) after a further 7 polishing runs

program which did not have enough sampling points for the wavefront at the edge. Such edge errors can now be avoided. The limit of correction is set simply by the noise of the wavefront measurement and can be pushed to the order of  $0.01 \lambda$  rms with modern interferometric techniques. REOSC also use computer control with large patterned (petal) laps, but the precision of prediction of material removal was not then considered as accurate as that with the small sub-aperture tools.

In connection with their study for the 8.2 m VLT primaries [1.27], Carl Zeiss of Oberkochen have also perfected a CCP system capable of going to the limits of noise in the wavefront measurement. A detailed analysis was made of the merits of generating aspherics by both grinding and polishing by:

- 1) Larger-size petal laps used with a short stroke and reduced rotational speed of the tool.
- 2) Larger-size petal laps used with a fixed azimuth relationship to the mirror to attack non-rotationally symmetrical errors.
- 3) Sub-aperture tools using CCP as above.

Figure 1.8 shows a typical petal tool for 1). Such a system has the advantages that the entire mirror is machined at once and that non-rotationally symmetrical errors are largely reduced and can be further suppressed by technique 2). However, this and short strokes can produce ripple. The sub-aperture tool method 3) has been fully tested with CCP. Zeiss not only uses *dwell-time* as the controlling parameter, but also *variable pressure* (3.b) as well as 3.a) in Table 1.1). This gives very powerful control. At that time (1985), Carl Zeiss tended to prefer the sub-aperture CCP method which has since been further refined. In addition, the powerful *membrane method* [1.27] [1.28] – see below – has been perfected and offers all advantages. According to Beckstette [1.7],

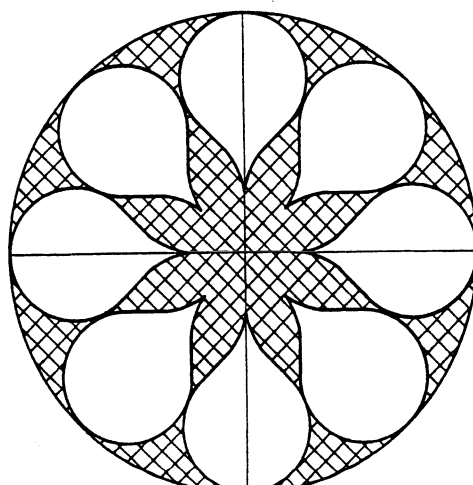


**Fig. 1.8.** Petal tool for aspherizing by grinding or polishing considered by Carl Zeiss [1.27] for the ESO VLT 8.2 m primaries

Carl Zeiss have used CCP with small sub-aperture tools and *pressure control* for the working of the Galileo 3.5 m primary (the Italian version of the NTT). The same technology was also used for the optics of the SOFIA space project [1.28]. Many small tools were used and the smoothing of residual edge errors was achieved with the *membrane polisher* – see below – which was also applied as a correction for Galileo. Spherical mirrors of 30 cm diameter have also been polished routinely by CCP using 1 cm tools at Carl Zeiss, Jena, to a quality of  $0.1 \lambda$  ptv. For mirrors of 3.5 m diameter, the final polishing stage to optimum figure is best achieved by CCP with a small, rigid tool using *pressure* rather than dwell-time control [1.7]. The time required is < 200 hours.

The earlier work of R.A. Jones described above has been further developed by him and associates at Litton ITEK [1.29] [1.30] [1.31]. The system is named Computer Controlled Optical Surfacing (CCOS) and has been developed not only to produce aspheric surfaces of high precision, both axisymmetric and off-axis segments, but also to accelerate and automate the whole production process so that high volume production is possible. The major advances were made after 1986, with a number of new processes based on a deeper understanding of the physics and mechanics of glass processing. The most spectacular results have been achieved with thin (solid or lightweight) face plates, on- or off-axis, for active or semi-active systems, and lightweight thick mirrors predominantly on-axis for passive systems. For such elements, polishing pressure in conventional polishing operations would produce print-through of the structure or support, so new techniques were essential. CCOS can solve these problems and is quite general in application to any aspheric surface irrespective of rotational symmetry. The principle is a feedback system, similar to that described above, using an orbital tool motion. Figure 1.9 shows the basic CCOS cycle. An improved algorithm (“Proportional Option”) for the dwell-time function (Fig. 1.10) gave dramatic improvement in convergence.

A computer regulates 6 robot motions: three positional, two tilt, one tool orientation. At that time (Dec. 1991), Litton ITEK had 9 CCOS units. During grinding, a non-rotating orbiting tool is moved over the workpiece, the orbit amplitude being fixed in advance. The pad surface must adapt to the curvature change. It is rigid and cannot flex because it must smooth ripples, so it must *wear* to shape. This is why a fixed angular orientation is required to

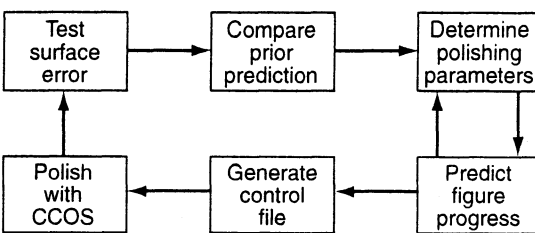


**Fig. 1.9.** Operations for a CCOS cycle (Litton ITEK [1.31])

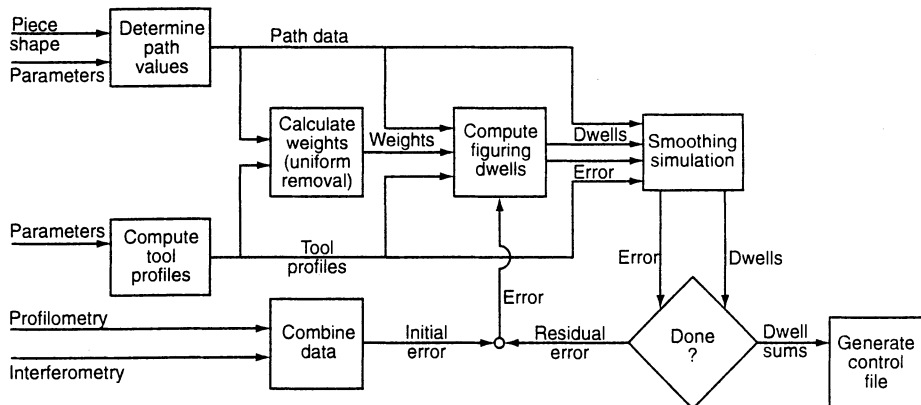


**Fig. 1.10.** A block diagram showing key components of the “proportional option” CCOS algorithm (Litton ITEK [1.31])

the optical axis. The work path must be optimized to minimize the required pad shape change.

In polishing, the pitch must flow to adapt to the surface change. Low spatial frequencies are corrected by “figuring”, high spatial frequencies by “pad smoothing”. In “figuring”, the spatial frequency is lower than the pad size, in “pad smoothing” it is higher [1.29]. Figure 1.11 shows a CCOS machine capable of handling 4 m workpieces.

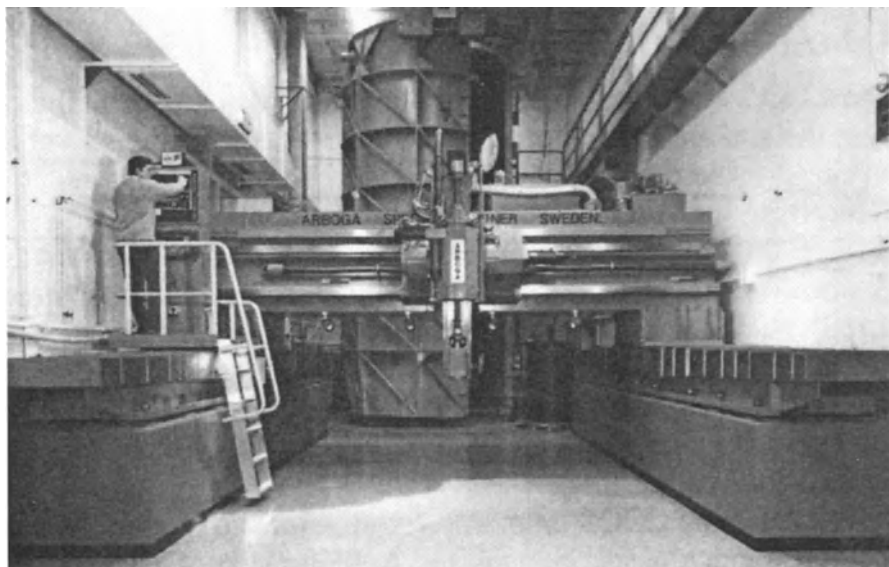


**Fig. 1.11.** Arboga NC unit usable for CCOS and machining operations (Litton ITEK [1.31])

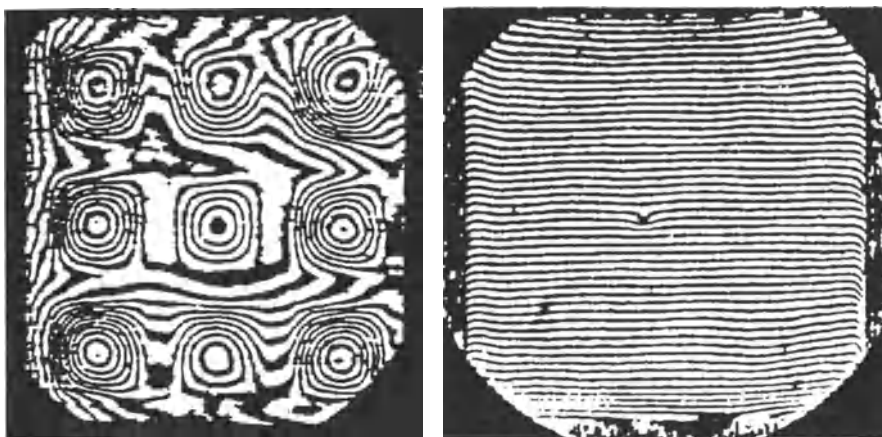


**Fig. 1.12.** Interferograms for a lightweight test piece after conventional and vacuum induced force surfacing (Litton ITEK [1.31])

CCOS technology is based on small-size tools. Tool loading can produce printthrough in lightweighted blanks, so a vacuum system was developed to apply tool pressure without loading. Figure 1.12 shows the striking difference in the resulting interferogram if this vacuum system is combined with *microgrinding*.

*Microgrinding* is another important development [1.30] [1.31]. Classical fine grinding used abrasives of about  $10\text{ }\mu\text{m}$  leaving a similar sub-surface damage depth for removal by polishing. Because material removal is some 50 times slower in polishing than grinding, polishing time was a major part of the total manufacturing schedule. Microgrinding uses  $1\text{--}3\text{ }\mu\text{m}$  diamond abrasives with composite metal (e.g. brass) or ceramic lapping tools. A surface form accuracy of  $0.1\text{ }\mu\text{m}$  can be achieved with microgrinding and CCOS. The polishing process is left with the task of removal of a  $1\text{--}2\text{ }\mu\text{m}$  damage layer and minimal figuring to produce the final figure accuracy of about  $0.02\text{ }\mu\text{m rms}$ .

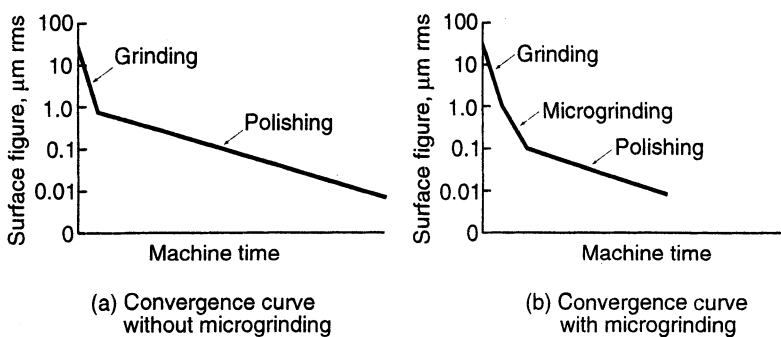
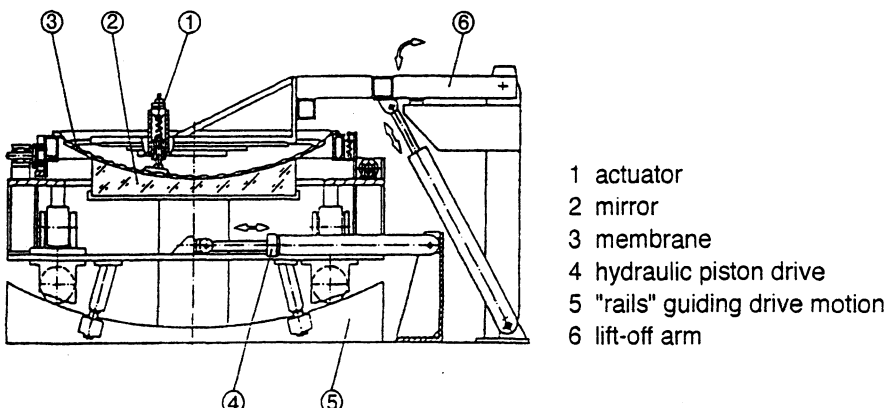


**Fig. 1.13a, b.** Gain in total machine time using microgrinding with CCOS (Litton ITEK [1.30])

Microgrinding also produces a semi-specular surface suitable for interferometric testing. Figure 1.13 shows the gain in machine time. For large aspheric optics, the CCOS fabrication times were reduced from about 40 to 10 weeks over three years. A further factor of two was expected. Examples were given of both off-axis aspheric segments and centered aspheric mirrors.

A recent review of CCOS techniques and other modern techniques is given by Jones [1.32].

**1.2.2.2 Membrane and strip tools.** This elegant technique (4. in Table 1.1) has been developed at Carl Zeiss, Oberkochen, and is described by Heynacher [1.33] and by Beckstette and Heynacher [1.10]. The membrane method makes direct use of Preston's Law – Eq. (1.1) – by separating the two operating parameters: relative velocity  $v$  and the pressure  $p$ . Figure 1.14 shows the principle of membrane polishing. The tool consists of two major parts: a fairly thin membrane which carries the polishing pitch and performs the relative motion between tool and workpiece and a set of actuators at the tool's rear (upper) side which apply the necessary pressure for material removal. This pressure is dynamically controlled by a computer. The complete membrane tool works, in principle, like an arrangement of many small tools working in parallel with the CCP technique. However, the amount of material removed by each sub-tool is controlled by the *pressure* applied through the actuator instead of the dwell-time approach of normal CCP or its variants. The membrane must be designed to be flexible enough to accommodate the desired variations in curvature of the aspheric surface, but stiff enough to provide adequate smoothing of the printthrough effect of the actuators. In the basic form of the technique, the membrane will be more-or-less full-size. For a 4 m diameter mirror, the membrane might be up to 20 cm thick. Possible materials are aluminium or plastics. It should be noted that the geometry of the actuators is fixed relative to the workpiece: the membrane



Membrane tool polishing machine

Fig. 1.14. The principle of membrane polishing (Carl Zeiss [1.10] [1.33])

moves between them. This has the important advantage that the abrasive effect can be directed specifically at any point, with appropriate smoothing by the membrane. The membrane technique combines all the advantages of other methods:

- The tool can directly remove errors with high and medium spatial frequencies. The highest spatial frequency which can be attacked is only limited by the actuator size.
- The tool does not rely on its own shape or adaptation to the mirror shape to remove low spatial frequency errors. This reduces mirror support problems during the process and deals with the problem of tool adjustment to variations in curvature of the aspheric by appropriate membrane flexibility.
- As the tool covers (either in 2 dimensions or – see below – in 1 dimension) the whole workpiece surface, it can apply bending moments at the edges of the “subtools” which prevent the inherent edge problem of small tools with CCP [1.21] and also the production of ripples.
- The large tool area gives high material volume removal.
- The removal function can be changed without any tool preparation, since the pressure parameter is used. Test data, suitably modified, are fed straight to the computer for the next iteration.
- A “self-teaching mode” can accommodate physical parameters such as hardness of material, support or structure printthrough.
- With small tool CCP work, a “hole” in the wavefront is serious because the whole surface must be lowered to the same level. The membrane tool is much more efficient, since the whole surface is worked.
- The membrane tool can be used for off-axis segments just as well as for axisymmetric surfaces.

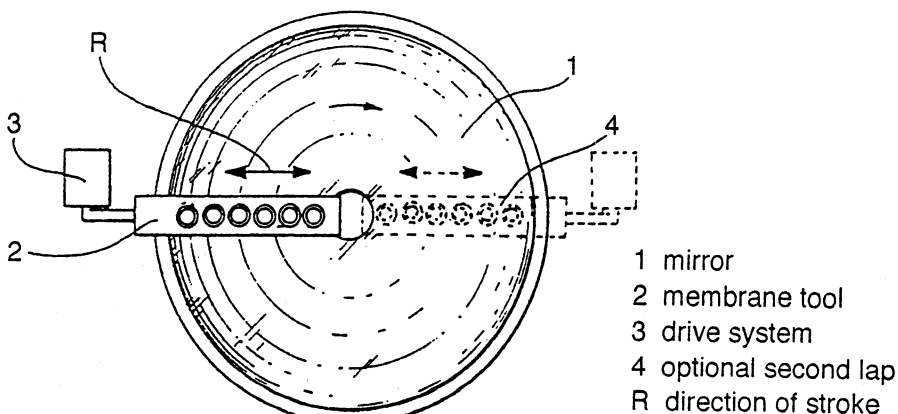


**Fig. 1.15.** Rectangular (strip) membrane tool for working axisymmetrical surfaces, e.g. primary mirrors (Carl Zeiss [1.10])

The membrane principle has been modified for the production of large axisymmetrical prime mirrors as shown in Fig. 1.15, using a rectangular (strip) membrane. The relative motion between tool and workpiece is performed by rotating the mirror and giving a radial stroke to the tool. For primaries with a relatively big central obstruction, the rectangular tool automatically compensates the increased relative velocity with zone radius by reduced relative polishing area: such a tool gives nearly uniform material removal with uniform pressure distribution. Since the rectangular membrane has only small radial shifts, its flexibility can be much lower than that necessary if it rotated freely. This is an important advantage in reducing edge and ripple problems.

Figure 1.16 shows a lapping process of the 3.5 m ESO NTT f/2.2 primary using two rectangular membrane tools. At that time (1986), the pressure variation technique was not fully operational, so aspherization was done by lapping from the sphere using area compensated tools of basic rectangular shape. The pitch surface for each step was computer controlled. Since there was no relative motion other than mirror rotation between tool and mirror surface, the pitch-trim was critical for avoiding high frequency ripple. This was controlled with great success, particularly because of the rectangular tool shape. About 200 µm of aspherization was produced; also further fine correction.

Non-rotational errors were removed by CCP with two medium- to small-size, circular tools, whose polishing pressure was controlled as discussed in § 1.2.2.1 above.

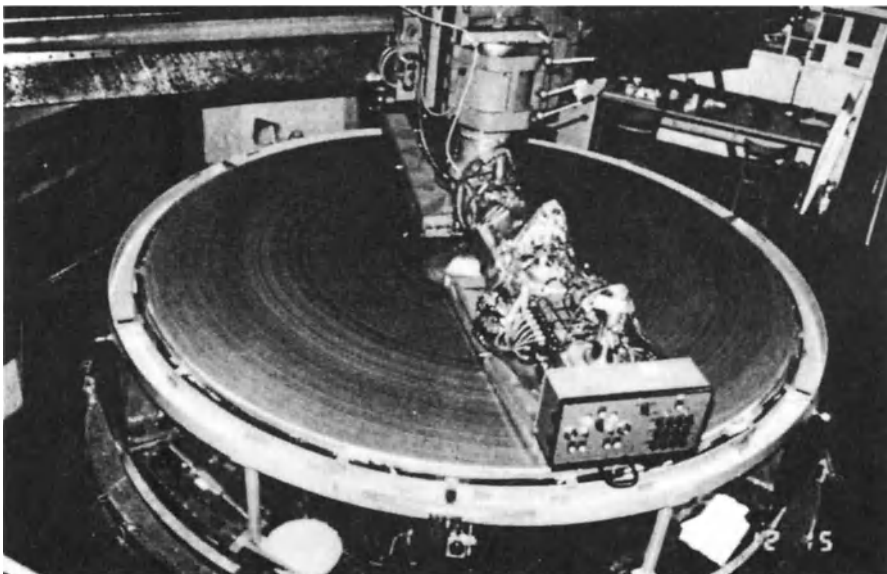


**Fig. 1.16.** Lapping of the ESO NTT 3.5 m primary (f/2.2) with two rectangular tools at Carl Zeiss in 1986 [1.10] [1.34]

These two techniques gave the remarkably smooth surface corresponding to an "Intrinsic Quality", after low spatial frequency term removal, of  $d_{80} = 0.095 \text{ arcsec}$  or a wavefront error of 13.5 nm rms. No hand figuring was required (see Chap. 3).

The efficiency of material removal in aspherizing is of central importance as aspherics get steeper, since the deviation from the best fitting sphere to the aspheric increases with the inverse cube of the f/no and linearly with the diameter. This is evident from the second (third order) term of Eq. (3.11) of RTO I. For the 3.5 m, f/2.2 NTT primary, the deviation is 210  $\mu\text{m}$ ; for 8 m, f/1.8 VLT primaries 890  $\mu\text{m}$ ; for an 8 m, f/1.0 primary 5200  $\mu\text{m}$  [1.10]!

Computer controlled figuring using a type of *strip tool* has been proposed and applied by Korhonen and Lappalainen [1.35] [1.36]. As with the Carl Zeiss membrane polisher, the parameter controlling the rate of polishing removal is *pressure* rather than dwell-time. The tool consists of subtools which are equipped with computer controlled force actuators. The turntable and stroke mechanism are equipped with position encoders, the local polishing pressure then being adapted to the requirements at that position. The force actuators are electromagnetic, the response time being only limited by the rise time of the current in the coil. Therefore a virtually continuous variation of polishing force is possible. A force response accuracy of 1 % can be achieved. Actuators are available which are suitable for large mirrors, or for lightweight or thin components where low surface pressures are applied.

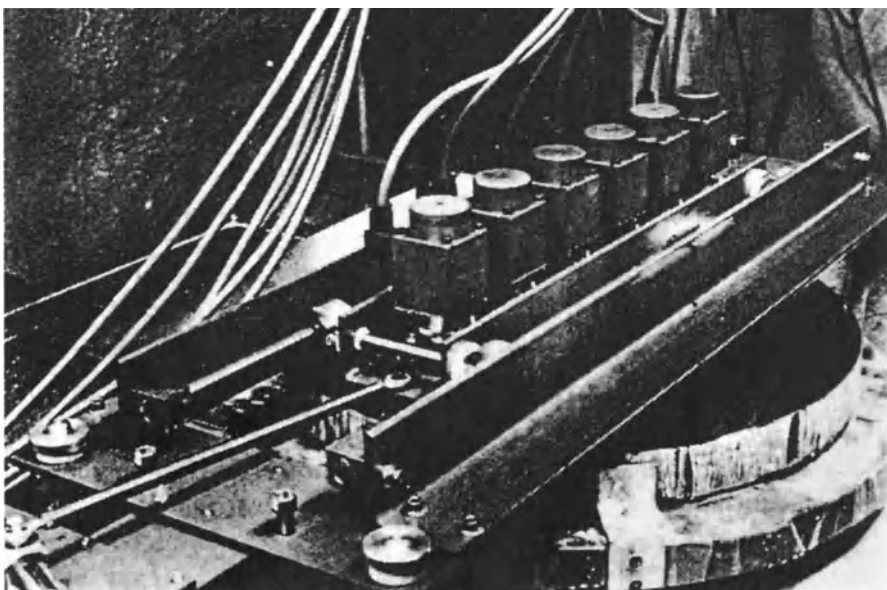


Fig. 1.17. Computer controlled figuring of a 60 cm test mirror (Korhonen and Lappalainen [1.35])

Figure 1.17 shows a linear tool with six actuators applied to the figuring of a 60 cm test mirror. The actuator response time is < 0.01 s. Because the force distribution can be controlled within about 1 %, the quantitative control of the figuring procedure depends mainly on other parameters, e.g. pitch quality, polishing compound and water mixture. At that time, clear results were not available but a predictability of 90 % was hoped for, a big advance on classical methods. The necessary stroke length is small, but the rigid subtools smooth out high spatial frequency errors. It would be possible to increase the tool width in azimuth to improve azimuthal smoothing, working with 2 or more actuators in parallel if required.

**1.2.2.3 Stressed laps.** This technique, corresponding to 1.c) of Table 1.1, has been proposed and developed by Angel et al. The basis was laid down by Angel and Parks [1.37] and by Angel [1.38]. The specific aim was to solve the problems associated with the production of very steep aspheric primaries, working at f/1.0. If the tool shape adapts to the desired shape of the surface at the local point of contact, then the situation is no different from working a sphere with a similar sized tool. This overcomes one of the main problems of CCP unless very small tools are used. But larger tools give better smoothing. For a local point of contact at distance  $y$  from the aspheric axis of a primary mirror of radius of curvature  $r$ , the distance  $z_L$  between its local surface and a spherical reference surface touching at point  $y$  is given by [1.37]

$$z_L \simeq \frac{b_s y^2 r_L^2 (2 + \cos 2\theta)}{4r^3} + \frac{b_s y r_L^3 \cos \theta}{2r^3} + \frac{b_s r_L^4}{8r^3}, \quad (1.4)$$

where  $r_L$  is measured from the contact point  $y$ ,  $\theta$  from the direction of the radius vector from the aspheric axis and  $b_s$  is the Schwarzschild constant. Omitting terms in tilt and piston, this leads to three terms [1.37] in focus (curvature), astigmatism and coma. A similar analysis was given for the analogous problem of stress polishing, for which the workpiece is stressed, by Lubliner and Nelson [1.39]. Angel discussed the generation of these terms by spring-loaded laps and demonstrated that they could be very effectively produced. For figuring an 8 m, f/1.0 paraboloid, he envisaged an active stressed lap of 2 m diameter (giving good smoothing) needing a bending of about 2 mm pvt as it is translated and rotated over the 8 m surface. The cycling stress period would be a few seconds, the forces being updated about every millisecond. After fine grinding with IR testing at 10  $\mu\text{m}$ , the same active lap would be faced with pitch for polishing. For distortion of fairly stiff steel tools, forces up to 1000 kg were envisaged. If necessary, smaller tools of 1 m or 0.5 m diameter would be used for finishing.

Further developments were given by Martin, Angel and Cheng [1.40]. The first application of actively controlled stressed-lap polishing was the 1.8 m, f/1.0 primary of the Vatican telescope, the stressed lap having a diameter of 0.60 m. The maximum lap distortions at the edge of the mirror are given, from modified equations following [1.39], as

$$\begin{aligned}
 (\delta z_L)_{20} &= -853 \mu\text{m} && \text{(focus)} \\
 (\delta z_L)_{22} &= -363 \mu\text{m} && \text{(astigmatism)} \\
 (\delta z_L)_{31} &= -224 \mu\text{m} && \text{(coma)}
 \end{aligned}$$

Moments were applied through a set of lever arms attached to the edge of the lap by means of electro-mechanical actuators mounted at the top of the lever arms and tensing wires in the required modal fashion. The Stressed-Lap Polishing Machine is shown in Fig. 1.18. A microcomputer controls the translation of the lap and the rotation of the lap and the mirror. Positions are sensed by encoders, and speeds of all three motors are updated about 20 times a second. A cycle of polishing strokes is determined by computer simulation to establish a desired removal function. A separate microcomputer controls the shape of the lap.

A further demonstration was given by Wizinowich and Angel [1.41] using a *full-size stressed lap*. The origins of this approach go back to Brown [1.42], who used a *passively* deformed full-size rigid tool to aspherize the primary of the 4.2 m WHT. The limitation of such a passive deformation proportional to  $\rho^4$ , where  $\rho$  is the zonal radius, to give the required asphericity as third order spherical aberration, is that an excentric position (overhang) of the tool due to the polishing stroke produces a mismatch which is, to a first approximation, the differential of the function, i.e. third order coma. The concept of the active full-size stressed lap is to correct this mismatch by a comatic deformation of the lap actively adjusted to the overhang (Fig. 1.19). The resultant figure of Fig. 1.19 (c) is a Schmidt plate surface. For normal primary mirrors with  $b_s < 0$ , the aspherization has the wrong sign, so this procedure would have to be reversed; but it is directly applicable to steep convex hyperbolic secondaries. An important advantage of the method is that, once the desired shape is attained, continued polishing produces uniform wear and does not change it. Polishing time is therefore uncritical in contrast to work with rigid laps. The authors give results of a successful demonstration on a 20 cm diameter pyrex blank of 3.4 cm thickness. The Schmidt plate form produced by grinding corresponded to a pure fourth order profile difference term of about 30  $\mu\text{m}$ , very close to the prediction. After polishing, the residual departure from the desired fourth power figuring due to higher order terms was 60 nm rms.

This experiment gave further confidence in the use of stressed sub-diameter laps for fast primaries.

The successful completion of the Vatican (Lennon) 1.8 m, f/1.0 primary was documented by the Progress Report of the Steward Observatory Mirror Lab [1.43]. Figure 1.20 shows the final interferogram. It was said at that time to be the fastest and most aspheric telescope mirror ever made: indeed, its asphericity is about  $5\frac{1}{2}$  times higher than that of the 3.5 m, f/2.2 NTT primary. It has a borosilicate, honeycomb blank made by the S.O. Mirror Laboratory. The wavefront error is 17 nm rms, a remarkable achievement for such a steep aspheric function. The figure quality was taken from 440 nm rms to the final

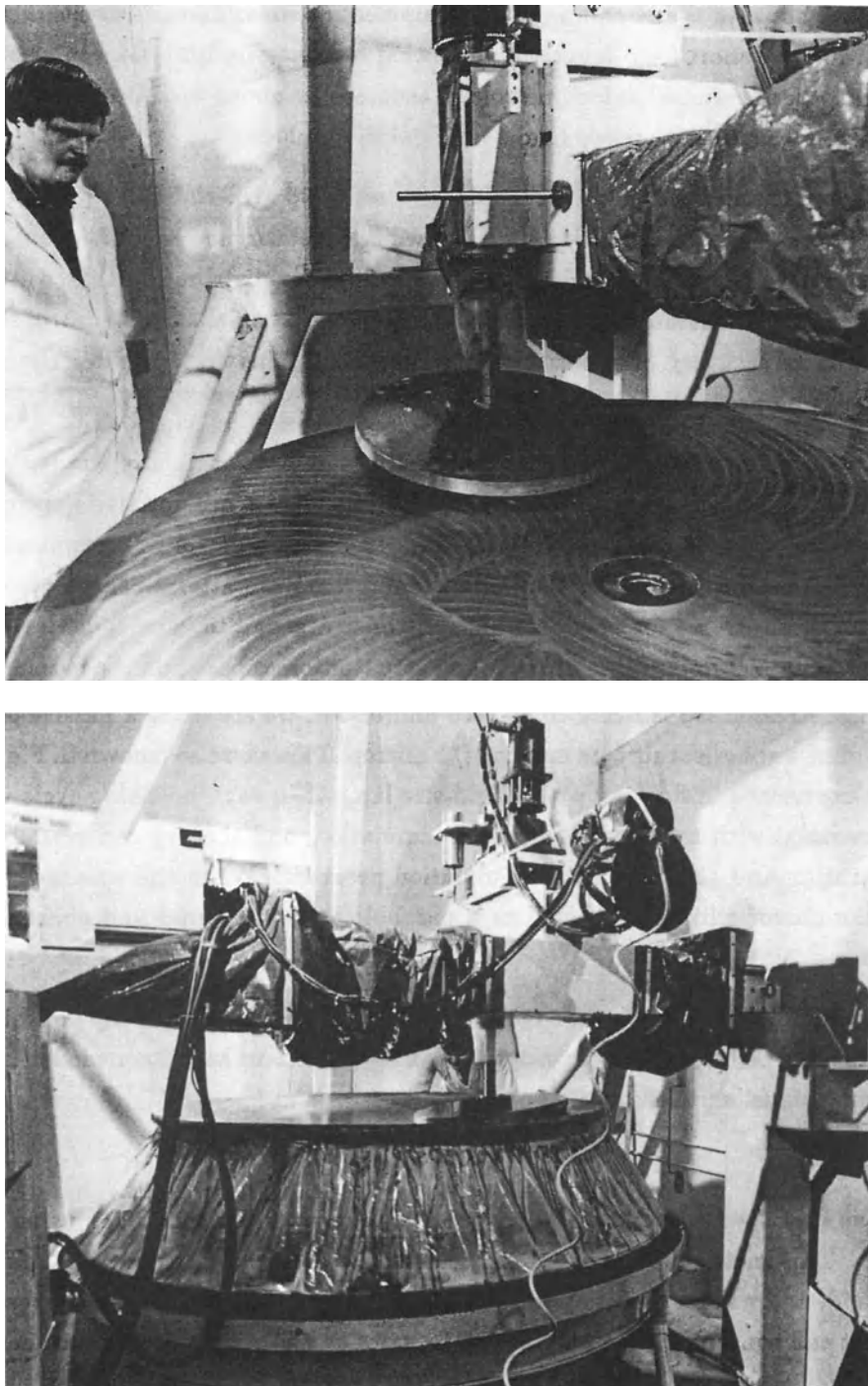


**Fig. 1.18.** Stressed-Lap Polishing Machine at Steward Obs. Mirror Lab (Martin et al. [1.40])

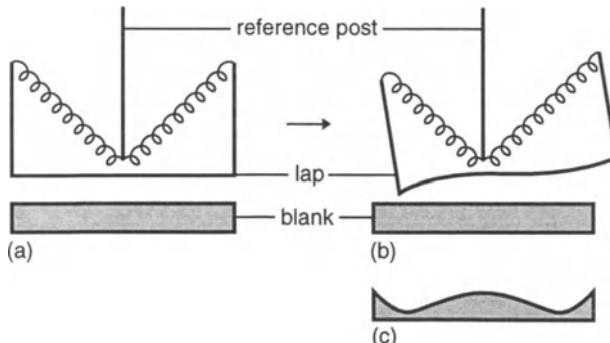


**Fig. 1.19.** Schematic demonstration of avoiding lap mismatch through overhang by stressing a full-size lap with a coma term as well as spherical aberration. (a) Lap centered over workpiece, (b) decentered with supplementary comatic distortion, (c) the generated aspheric surface (Wizinowich and Angel [1.41])



**Fig. 1.20.** Final interferogram of the Vatican (Lennon) 1.8 m, f/1.0 primary produced by stressed-lap technology (Steward Obs. Mirror Lab [1.43])

17 nm rms in only 8 months. The encircled energy (including diffraction) has  $(d_{80})_{diffr.} = 0.28$  arcsec. According to Beckers [1.44], the final interferogram was achieved after some additional hand retouching following the stressed-lap polishing.

Another success reported was the completion of the Phillips Lab 3.5 m, f/1.5 primary with a final wavefront error of 20 nm rms and an encircled energy  $(d_{80})_{diffr.} = 0.17$  arcsec. The stiffness of the honeycomb blank enabled the simple support of 16 triangular "load spreaders" and 4 two-point "load-spreaders" to be used, together with 20 additional single point attachments. In the operating telescope cell, these will connect to programmable force ac-

tutors for active control. For polishing they rested on glycerine-filled pads, interconnected to distribute forces in correct proportion. This simple passive support, together with 3 radial single-point restraints, proved entirely adequate, also for avoiding astigmatism.

**1.2.2.4 Stress polishing (stressed workpiece).** The concept of “stress polishing” (deforming the workpiece by stresses, working it spherical, then releasing the stresses to form the required aspheric shape) was first formulated and systematically applied by Schmidt [1.45] to the manufacture of a corrector plate for his newly invented Schmidt telescope. The method has been much applied to the manufacture of smaller Schmidt plates of amateur sizes and is well described by Wenske [1.46]. A solid steel plate is turned off to leave a rim about 3 mm wide with a diameter exactly that of the plate, the depth being about 2 mm. The rim must be carefully turned flat and fine ground. Up to 250 mm diameter, the glass plate has a thickness of 6–7 mm at maximum and must be carefully worked as a plane-parallel optical plate. The plate is carefully sealed on the steel rim with thick vacuum grease, then the thin chamber is pumped out to cause the plate to assume a concave upper surface. Schmidt showed that this led to an axisymmetrical deformation involving the terms  $\rho^2$  and  $\rho^4$ , where  $\rho$  is the plate radius from its center. The sag of the plate is measured with a spherometer. Wenske gives the proof from an empirical formula that the sag of the plate must be set at

$$z_{pl} = \frac{1.065}{(n - 1)} \frac{\rho_m^4}{r^3} , \quad (1.5)$$

where  $z_{pl}$  is the sag,  $\rho_m$  is the semi-diameter of the corrector plate in the Schmidt telescope,  $r$  the radius of curvature of its mirror and  $n$  the refractive index of the plate. The required bending can be achieved without excessive strain for  $f/nos \geq f/2$ . For steeper cameras, either the plate must be thinner, causing polishing problems, or both plate sides must be aspherized. The optimum Schmidt plate form is given if the constrained, concave plate is ground and polished with a convex spherical tool whose sag is given by

$$z_t = \frac{0.940}{(n - 1)} \frac{\rho_m^4}{r^3} \quad (1.6)$$

If correctly carried out, this should lead to the profile form

$$\delta z_{pl} = \frac{3\rho_m^2}{8(n - 1)r^3} \rho^2 - \frac{1}{4(n - 1)r^3} \rho^4 , \quad (1.7)$$

the optimum form from geometrical optics without taking account of diffraction – see the discussion in § 3.6.2.2 of RTO I and Eq. (3.242) therein, which is identical with (1.7) for a profile parameter  $k_{pl}$  of 1.5.

A definitive analysis of Schmidt plate manufacture by such elastic means has been given by Lemaître [1.47]. In the above Schmidt-type arrangement with the plate supported at its edge with an underpressure difference  $q$  giving a constant load, the deformation is given to the third order term by

$$z_{Elas} = \frac{3(1-\nu^2)}{16} \frac{q}{E} \left(\frac{\rho_m}{t}\right)^3 \left[ 2 \left(\frac{3+\nu}{1+\nu}\right) \bar{\rho}^2 - \bar{\rho}^4 \right] \rho_m , \quad (1.8)$$

where  $\bar{\rho} = \rho/\rho_m$ ,  $t$  is the thickness,  $E$  Young's modulus and  $\nu$  the Poisson ratio of the glass. Now, if the sagged surface is ground and polished spherical with a convex tool of radius of curvature  $r_t$ , then setting  $\omega = \rho_m/2r_t$ , the resulting sphere is

$$z_S = \omega(\bar{\rho}^2 + \omega^2\bar{\rho}^4)\rho_m \quad (1.9)$$

Releasing the underpressure, the top surface will assume the desired profile  $z_{Sch}$  if

$$z_{Sch} - z_{Elas} + z_S = 0 \quad (1.10)$$

From Eq. (3.242) of RTO I, setting the plate parameter  $k_{pl} = 1.5$ , we have

$$z_{Sch} = \frac{\rho_m}{256(n-1)N^3} \left( \frac{3}{2} \bar{\rho}^2 - \bar{\rho}^4 \right) \quad (1.11)$$

Equation (1.10) then leads to the following third-degree equation

$$1024 \left( \frac{3+\nu}{1+\nu} \right) \omega^3 + 512\omega - \frac{(9+\nu)}{(1+\nu)(n-1)} \frac{1}{N^3} = 0 \quad (1.12)$$

This equation always has a unique and positive real root which is  $\ll 1$  since  $N^2 \geq 2$  for all but extremely steep Schmidt telescopes. It follows with  $0 < \nu < 0.5$  that the term in  $\omega^3$  is negligible. This is simply the equivalent of the statement that the term in  $\bar{\rho}^4$  for the sphere is negligible compared with the  $\bar{\rho}^4$  term from the elastic deformation.

Since  $r = 8\omega N r_t$ , the radius of the spherical tool  $r_t$  can be expressed as a function of the radius  $r$  of the Schmidt mirror, giving from (1.12)

$$r_t = \frac{64(1+\nu)(n-1)}{(9+\nu)} N^2 r \quad (1.13)$$

For a typical case with  $\nu = 0.2$  and  $n = 1.5$ , then  $r_t = 4.174 N^2 r$ .

Knowing  $\omega$ , we can deduce the plate thickness  $t$  from (1.8) as

$$t = \left[ \frac{3}{4}(1-\nu^2)(n-1) \frac{q}{E} \right]^{1/3} r \quad (1.14)$$

Equations (1.13) and (1.14) completely define the manufacturing conditions. For highly aspheric plates, a maximum  $q$  representing a full vacuum under the plate is desirable. A typical borosilicate crown ruptures at  $N = 1.75$  if only one face is figured; at  $N = 1.40$  if both faces are figured. This is in agreement with Wenske's conclusions for amateur Schmidt telescopes.

The above classical method produces, in principle, an aspheric plate of the required form over its whole surface. If one accepts an unusable zone at the edge, one can find a configuration of load and support that results in plates with twice the asphericity possible with the classical method. This method, proposed by Lemaître [1.47], is shown in Fig. 1.21. It also has the advantage

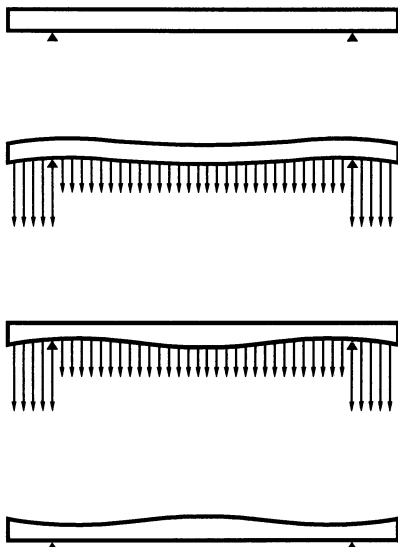


**Fig. 1.21.** Principle of the dioptric elasticity method of stress polishing for the production of Schmidt plates proposed by Lemaître [1.47]

of requiring only a flat tool, not a spherical one depending on Eq. (1.13). The disk of radius  $\rho_2$  is supported on a metal ring of radius  $\rho_1$ . A load  $p_1$  is exerted on the inner zone and a load  $p_2$  on the outer zone. The deformed disk is ground and polished flat under these loads.

The basic equation is the Lagrange differential equation for small deformations  $z$  of a thin plate of constant thickness  $t$

$$D_r \nabla^2 (\nabla^2 z) - p = 0 , \quad (1.15)$$

where  $D_r$  is the rigidity constant

$$D_r = \frac{Et^3}{12(1-\nu^2)} , \quad (1.16)$$

and  $p$  is the load on the plate. With a circular plate, the Laplacian operator  $\nabla^2$  in polar coordinates can be used:

$$\nabla^2 = \frac{\partial^2}{\partial \rho^2} + \frac{1}{\rho} \frac{\partial}{\partial \rho} \quad (1.17)$$

In an elegant reduction, Lemaître shows that there are an infinite number of solutions in terms of the normalized parameter pairs of radius ( $\rho_2/\rho_1$ ) and pressure ( $p_2/p_1$ ) which satisfy the “Kerber condition” (Schmidt plate parameter  $k_{pl} = 1.5$ ) for zone 1 of Fig. 1.21, inside the support ring. If the surface is worked flat as shown, the right profile is obtained *whatever thickness is used*; the same apparatus can be used with different plate thicknesses to compensate Schmidt mirrors of different curvatures. However, it remains prudent to adapt the final mirror to the finished plate. From a reasonable range of parameter pairs giving Kerber profiles, Lemaître establishes a rupture limit of  $f/1.40$  for a normal borosilicate glass if one face is figured;  $f/1.10$  if both sides

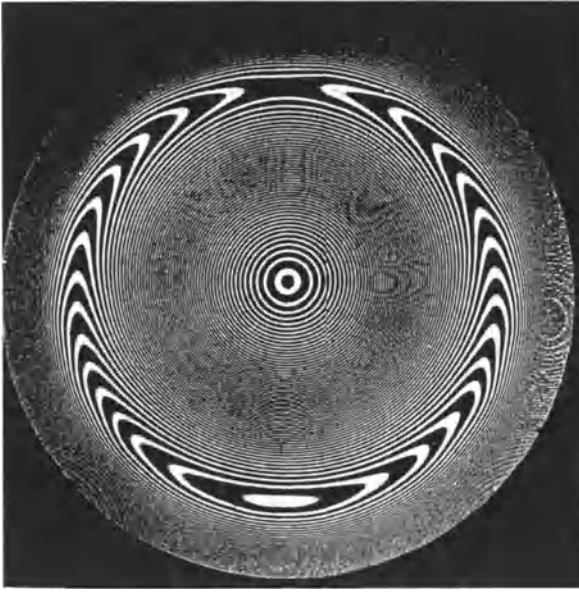


**Fig. 1.22.** Fringes of equal thickness of a plate made by the dioptric elastic (stress polishing) method (Lemaître [1.47])

are figured. In quartz, f/1.0 plates have been made, representing the limit for classical optical materials.

Figure 1.22 shows Fizeau fringes of a small plate manufactured as above. One fringe represents a deformation of the refracted wavefront of  $\lambda(n - 1)/2n \simeq \lambda/6$  for a refractive index  $n \simeq 1.5$ .

The great attraction of stress polishing, as shown in Fig. 1.22, is the inherent *smoothness* (freedom from high spatial frequency errors) of the technique, a common virtue of all *active optics* procedures, whether performed at the tool, the workpiece before manufacture, or the workpiece after manufacture.

Stress polishing was applied by Lemaître to many smaller elements over 15 years [1.48]. A summary in the global framework of active optics is given in a more recent paper [1.49]. He considers very large mirrors with a thickness in agreement with an axial support density under gravity to give an acceptable sag between supports. The total amplitude of flexure for an infinite plate of thickness  $t$  supported on a triangular mesh of points separated by  $a$ , where the supports have diameter  $b$ , is given by

$$z_0 = \frac{3}{64}(1 - \nu^2) \frac{\delta_r g a^4}{E t^2} \left[ 1 - \frac{b^2}{a^2} + \frac{b^2}{a^2} \ln \frac{b^2}{a^2} \right] , \quad (1.18)$$

where  $\delta_r$  is the relative density,  $\nu$  the Poisson ratio,  $g$  the acceleration due to gravity and  $E$  Young's modulus. For typical values of  $b/a \leq 0.1$ , the term in the bracket  $\geq 0.94$  and can usually be set  $\simeq 1$ . The support density in the triangular arrangement is  $n_d = 2/\sqrt{3} a^2$ , giving from (1.18)

$$z_0 n_d^2 t^2 \simeq \frac{(1 - \nu^2) \delta_r g}{16 E} = \text{constant} \quad (1.19)$$

for a given material. For glasses and aluminium, the physical parameters are similar with  $\nu \simeq 0.25$ ,  $\delta_r \simeq 2.5 \times 10^3 \text{ kg m}^{-3}$ ,  $E \simeq 8 \times 10^{10} \text{ Pa}$ ,  $g \simeq 10 \text{ m s}^{-2}$ , giving

$$z_0 n_d^2 t^2 \simeq 1.8 \times 10^6 \text{ m}^{-1} \quad (1.20)$$

Lemaître then considers the stressed polishing situation for mirror thicknesses  $t$  giving a reasonable support density. The basic form is the constant thickness distribution (CTD), but he also considers vase type forms with variable thickness distribution (VTD), as shown in Fig. 1.23. In the CTD class, the mirror is subjected to a tangential couple as shown; in the VTD class, different loadings can be combined with different VTD. Examples are given of distortion in the modes of astigmatism, coma and spherical aberration. The latter, symmetrical mode can be seen as analogous to the problem of Schmidt plates, discussed above, which was successfully applied to the 0.62 m corrector for the OHP Schmidt telescope. For intermediate size mirrors, Lemaître has mainly considered applications to Cassegrain secondary mirrors (including active in-situ form variation potential) or plane mirrors such as reflecting Schmidt plates. The author suggested to him in 1989 that one of the best applications with CTD would be the production of aspheric primary mirrors by spherical polishing under stress, *combined with active control in the telescope to relax the low spatial frequency manufacturing tolerances* (see § 3.5.5.1). This exploits in an optimum way the potential of active optics both before and after manufacture. It was hoped (March 1992) to fabricate a test mirror suitable for the primary of a 1.8 m RC telescope in this way. With active

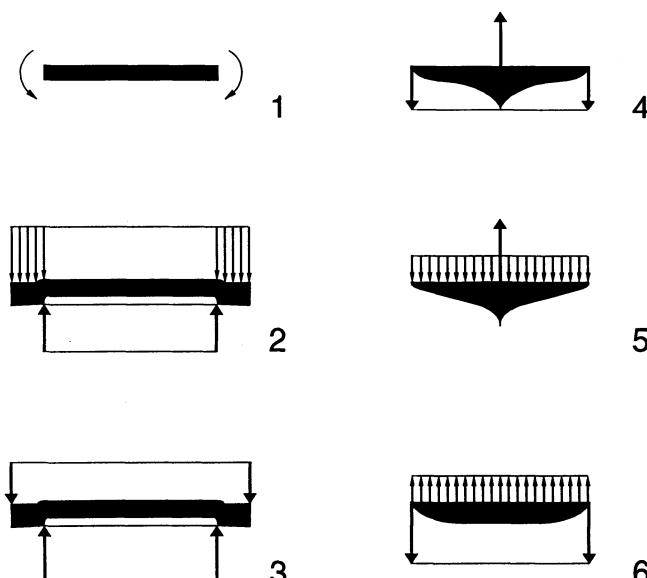


**Fig. 1.23.** Mirror forms for stressed polishing with constant thickness distribution (CTD) and variable thickness distributions (VTD) (Lemaître [1.49])

optics control, the material for such a mirror is uncritical: it could be glass ceramic, aluminium or stainless steel. In stainless steel, the cheapest option, the thickness for stress polishing would be about 45 mm, giving an aspect ratio of 40. Unfortunately, up to the time of writing (March 1997), it has not been possible to pursue this project.

The most dramatic application of stress polishing so far has been for the off-axis segments of the segmented *10 m primary of the Keck telescope*. Previous work had been concerned with axisymmetrical deformation or deformations in certain low spatial frequency aberration modes [1.48]. Lubliner and Nelson [1.39] performed the first general theoretical analysis of strain deformation for the production of non-axisymmetric mirrors, in particular off-axis segments of a large paraboloid. They considered the general case of the difference  $w$  normal to the surface between a local sphere in contact with some off-axis point of the paraboloid and the corresponding local segment of the paraboloid. If the function  $w$  is expressed in similar terms as those used for active optics control (Chap. 3) in the NTT, we have

$$w = \left. \begin{aligned} & \alpha_{20}\rho^2 + \alpha_{22}\rho^2 \cos 2\phi + \alpha_{31}\rho^3 \cos \phi + \alpha_{33}\rho^3 \cos 3\phi \\ & + \alpha_{40}\rho^4 + \alpha_{42}\rho^4 \cos 2\phi + \dots \end{aligned} \right\} , \quad (1.21)$$

where  $\rho$  and  $\phi$  are the normalized radius and azimuth about the axis of the local sphere. Let the vertex radius of curvature of the paraboloid be  $r_0$ , the semi-diameter of the off-axis plate be  $a$ , the radius of curvature of the sphere  $r_s$ , and the slope of the paraboloid at the off-axis point  $\varepsilon = \rho_p/r_0$ , then Lubliner and Nelson give the coefficients of (1.21) as:

$$\left. \begin{aligned} \alpha_{20} &= \frac{a^2}{2r_0} \left( \frac{r_0}{r_s} - 1 + \varepsilon^2 + \frac{9}{8}\varepsilon^4 + \frac{5}{4}\varepsilon^6 + \dots \right) && \text{(defocus)} \\ \alpha_{22} &= \frac{a^2}{4r_0} \varepsilon^2 \left( 1 - \frac{3}{2}\varepsilon^2 + \frac{15}{8}\varepsilon^4 + \dots \right) && \text{(astigmatism)} \\ \alpha_{31} &= \frac{a^3}{2r_0^2} \varepsilon \left( 1 - \frac{11}{4}\varepsilon^2 + \frac{21}{4}\varepsilon^4 + \dots \right) && \text{(coma)} \\ \alpha_{33} &= -\frac{a^3}{8r_0^2} \varepsilon^3 \left( 1 - 3\varepsilon^2 + 6\varepsilon^4 + \dots \right) && \text{(triangular)} \\ \alpha_{40} &= \frac{a^4}{8r_0^3} \left[ \left( \frac{r_0}{r_s} \right)^3 - 3\varepsilon^2(1 - 4\varepsilon^2 + \dots) \right] && \text{(spherical} \\ & \qquad \qquad \qquad \text{aberration)} \\ \alpha_{42} &= -\frac{a^4}{4r_0^3} \varepsilon^2(1 - 5\varepsilon^2 + \dots) && \text{(fifth order} \\ & \qquad \qquad \qquad \text{astigmatism)} \end{aligned} \right\} \quad (1.22)$$

The principal term in each coefficient  $\alpha_{mn}$  is of the order  $(a^m/r_0^{m-1})\varepsilon^n$ . Since both  $a$  and  $\rho_p$  are small compared with  $r_0$ , it follows that the largest of the neglected terms of Eq. (1.21) have high orders of  $a/r_0$  and  $\varepsilon$ . For  $a < 1$  m,  $r_0 = 40$  m (f/2.0 paraboloid) and  $\rho_p \leq 5$  m, the neglected terms are  $\leq \sim 1$  nm.

The sphere radius may be chosen to minimize the rms value of  $w$  in (1.21). Lubliner and Nelson give as a close approximation

$$r_s = r_{s0} \left( 1 + \frac{a^2}{4r_{s0}^2} \right) , \quad (1.23)$$

where  $r_{s0} = 2r_0/(\cos \theta + \cos^3 \theta)$ , in which  $\theta$  is the semi-aperture angle of the paraboloid at the off-axis point.

The relative importance of the various coefficients in practice is shown in Fig. 1.24. As would be expected, the coma  $\alpha_{31}$  and astigmatism  $\alpha_{22}$  terms are completely dominant.

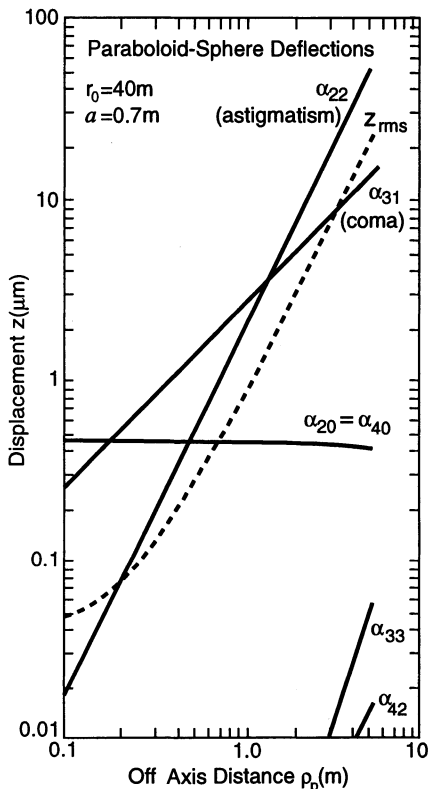


**Fig. 1.24.** Coefficients describing deflections needed to transform a sphere into an off-axis parabola (segments with  $a = 0.7\text{ m}$ ,  $r_0 = 40\text{ m}$ ). Best fitting sphere assumed. (Lubliner and Nelson [1.39])

The plate bending theory is based on Eqs. (1.15)–(1.17) for thin plates. The desired deflection expressed by Eq. (1.21) may be produced by a combination of bending moments and shearing forces around the edge and uniform transverse loading. For the loading required, a more accurate theory for moderately thick plates was used.

Stress analysis could be performed for the maximum allowable stress on the basis of thin plate theory, leading to an equation for the largest off-axis distance  $\rho_{p\max}$  that may be achieved without exceeding the allowable stress.

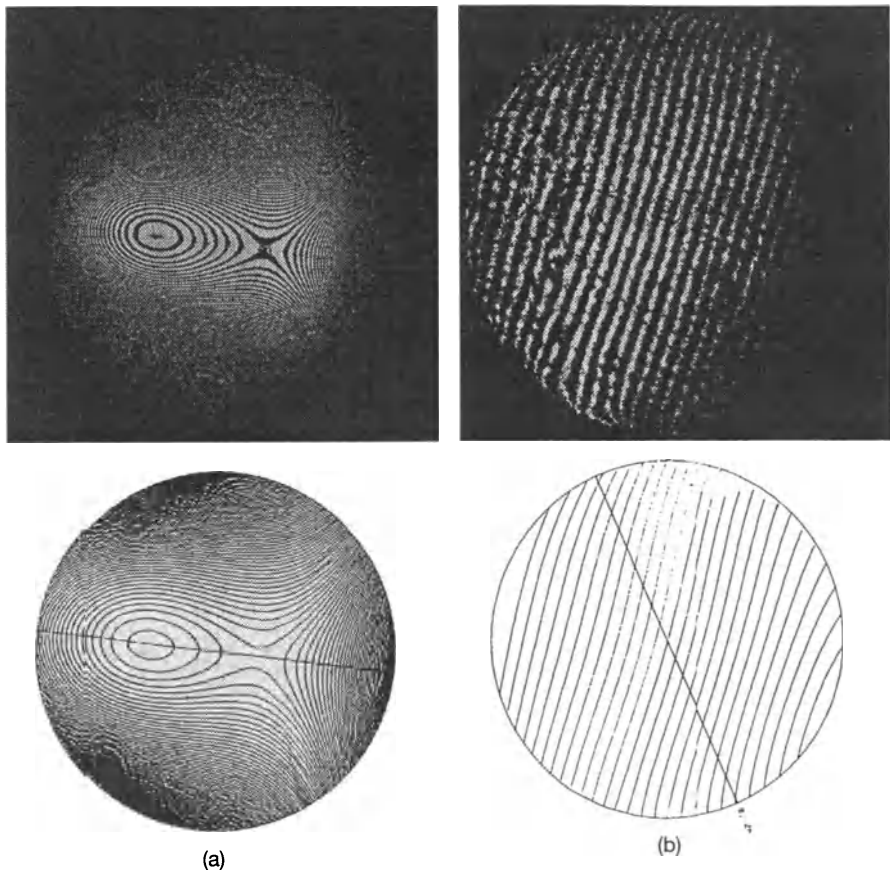


**Fig. 1.25.** Reconstructed interferograms of stress polishing on a 36 cm circular, off-axis segment of a paraboloid. (a) Original spherical mirror under stress before polishing ( $9.9 \mu\text{m rms}$ ); (b) Final result relative to the paraboloid with best fit position ( $0.03 \mu\text{m rms}$ ). The lower contour plots were generated from a fourth-order fit. (Nelson et al. [1.50])

The technique was applied first [1.50] to a circular blank, 36 cm in diameter and with an aspect ratio of 14. Two iterations were performed with the remarkable result that a  $9.9 \mu\text{m rms}$  deflection from the polished sphere was produced with an error from the desired surface of only  $0.03 \mu\text{m}$ . The maximum forces applied were about  $-20 \text{ kg}$ , the maximum couples about  $250 \text{ kg cm}$ . Figure 1.25 shows the reconstructed interferogram of the original spherical mirror under stress before polishing ( $9.9 \mu\text{m rms}$ ) (a) and the final result relative to the desired parabola with the mirror in the best fit position ( $0.03 \mu\text{m rms}$ ) (b).

If it were possible to fill the aperture with *circular* segments, the evidence above implies that stress polishing provides an admirable solution for getting a smooth, correct figure right to the edge. Experiments at KPNO [1.51]

[1.52] also confirmed successful stress polishing with circular segments. However, problems were reported as soon as cutting to the final hexagonal shape was carried out [1.53]. The segment size had been increased from 1.4 m to 1.8 m with thickness 7.5 cm. Also the primary paraboloid was steeper with  $f/1.75$ . Cutting *after* polishing was preferred because it was considered much more favourable for getting high quality to within a few mm of the segment edge. As reported previously, achieving a quality of about 40 nm rms by stress polishing the *circular* blanks (Zerodur) could be reliably achieved; but cutting to produce the hexagon introduced warping of about 500 nm rms, over ten times the error of the circular segments. The warping was mainly in the *defocus* mode, with a little coma and astigmatism. It was thought to be due to two possible sources: release of residual stress from the casting, and stress due to the subsurface damage of the ground back. However, it was felt that a residual unpredictable warping was inevitable to a level that would not be acceptable. The best solution was considered to be permanent active optics correction in the telescope using a “warping harness” based on springs attached to the whiffle tree supports [1.54].

Production techniques at ITEK for the segments were reported further in 1988 [1.55]. The manufacturing steps were:

*Convex Side Polish → Stressed Mirror Polishing →  
Cutting and Boring → Support Mounting → Final Figuring*

The error budget was < 40 nm rms on the figure and < 0.3 mm on the radius. The figure quality from stressed polishing was < 150 nm. Final figuring was being tackled by computer controlled optical surfacing (CCOS – see above) and by a “warping harness”. With the latter, an FE prediction showed that the  $d_{80}$  value could be reduced from 0.84 arcsec after cutting to 0.27 arcsec by warping, close to the specification of 0.24 arcsec. Modelling was done with a NASTRAN beam model [1.56].

Further details of the manufacture of the segments at ITEK were given by Mast and Nelson in 1990 [1.57]. The desired surface is now expressed in Zernike polynomials, which modifies Eq. (1.21) to

$$w = C_{20}[2\rho^2 - 1] + C_{22}[\rho^2 \cos 2\phi] + C_{31}[(3\rho^3 - 2\rho) \cos \phi] \\ + C_{33}[\rho^3 \cos 3\phi] + C_{40}[6\rho^4 - 6\rho^2 + 1] + C_{42}[(4\rho^4 - 3\rho^2) \cos 2\phi] \quad \{ \quad (1.24)$$

From the symmetry of the hexagonal geometry, 5 types of segment are required. Table 1.3 gives the desired coefficients in microns for the extreme inner and extreme outer types, the other segment type values lying on monotonic functions between these extreme values. The difficulty consists in generating the dominant defocus ( $C_{20}$ ), astigmatism ( $C_{22}$ ) and coma ( $C_{31}$ ) terms as discussed above. The total error budget for the telescope gives  $d_{80} = 0.42$  arcsec; for the primary 0.34 arcsec, and for the segment figuring 0.24 arcsec. The cutting produces errors which are predominantly axi-symmetrical. In one case, these were  $\delta C_{20} = 1.470 \mu\text{m}$ ,  $\delta C_{40} = -0.253 \mu\text{m}$ ,

**Table 1.3.** Desired Zernike coefficients (microns) for extreme inner and outer segments (Mast and Nelson [1.57])

Segment	$C_{20}$	$C_{22}$	$C_{31}$	$C_{33}$	$C_{40}$	$C_{42}$
Inner	5774.221	-11.481	-4.410	0.007	0.001	0.002
Outer	5684.125	-100.910	-12.669	0.170	0.015	0.016

$\delta C_{60} = 0.043 \mu\text{m}$ ,  $\delta C_{80} = -0.083 \mu\text{m}$ . The corresponding surface error was  $0.794 \mu\text{m rms}$  with  $d_{80} = 3.94 \text{ arcsec}$ , a large value. However, the variation from segment to segment was fairly modest, but by no means negligible. The fabrication experience at ITEK was *summed up* as follows:

Using stress polishing, a polished asphere ( $C_{22} \sim 50 \mu\text{m}$ ,  $C_{31} \sim 10 \mu\text{m}$ ) was produced in about 6 weeks to within ca.  $250 \text{ nm rms}$  of the desired surface. Further convergence to the desired quality of  $20\text{--}40 \text{ nm rms}$  was slower and costly. In addition, errors in predictions of warping from cutting residual stress release were typically  $200 \text{ nm rms}$  and sometimes  $1000 \text{ nm rms}$ . The strategy adopted was:

- Use “adjustable optics” (i.e. dc active optics in the terminology of this book) to optimize the figure using a 30 spring warping harness.
- Stop polishing when
  - The polished surface error is  $< 250 \text{ nm rms}$
  - The predicted surface meets the final goals where the prediction includes
    - The predicted improvement by positioning the hexagon cut
    - The predicted warping from cutting
    - The predicted improvement by the warping harness.

Table 1.4 reproduces results quoted for six segments before and after correction with the warping harness. The rms target was given as about  $0.020\text{--}0.040 \mu\text{m rms}$  and was largely met, but the discrepancy was higher than the  $d_{80}$  target of  $0.24 \text{ arcsec}$ , with an average value of  $0.52 \text{ arcsec}$ .

**Table 1.4.** Segment quality before and after final correction with the warping harness for six segments (Mast and Nelson [1.57])

Segment	Error rms ( $\mu\text{m}$ )		Error $d_{80}$ (arcsec)	
	Before	After	Before	After
SN 005	0.61	0.040	2.83	0.62
SN 006	0.28	0.026	1.55	0.47
SN 007	0.26	0.025	1.69	0.47
SN 008	0.21	0.032	1.41	0.56
SN 009	0.72	0.054	3.89	0.63
SN 018	0.11	0.019	0.80	0.34
Target				0.24

After this publication, the Keck telescope celebrated “first light” with nine segments in place and it was stated that about half the segments were in operation in Feb. 1992. The performance was limited by the quality of the individual segments, not by their relative adjustment [1.58]. The conclusions will be discussed further in Chap. 3. At that time, it appeared that stress polishing could be highly successful with circular elements, either axisymmetric or off-axis, but that the problems with non-circular segments were not fully solved. Subsequently, they were effectively solved by the technique of ion beam figuring, discussed in the next section.

**1.2.2.5 Ion beam figuring (IBF).** The effectiveness of this technique was first demonstrated by Wilson, Reicher and McNeill in 1988 [1.59]. It was, above all, developed by the Eastman Kodak Company who set up a practical figuring facility in operation since about 1990. This admirable work has been widely reported in company brochures and publications [1.60] [1.61] [1.62] [1.63] [1.64] [1.65]. Ion beam figuring (IBF) is a perfect complement to computer controlled small tool polishing. An ion beam “tool” is unaffected by workpiece influences (such as local surface fit and edge effects). The accuracy achievable is limited only by the accuracy of the test data for virtually any optical form. IBF functions by sputtering material from the workpiece, at the atomic level, by means of a momentum transfer from a directed ion beam which physically bombards the surface.

The Eastman Kodak facility was designed for workpieces up to maximum dimensions of  $2.5 \times 2.5 \times 0.6$  m mounted in a high-vacuum chamber. The ion source directs a beam upwards on to the workpiece, positioned face down. It is a Kaufman broad-beam ion source producing a well-controlled, collimated beam of argon ions. This generates the neutral-ion-beam removal function for material removal. Beam removal function distributions ranging from 5 to 15 cm in diameter have been demonstrated [1.64]. The translation system of the ion source has three linear and two angular degrees of freedom, enabling fine figuring control over a very broad spatial frequency band. It follows that this technique is ideal for correcting edge or printthrough (quilting) errors left over from conventional techniques in massive or lightweighted blanks.

There can be no doubt that IBF is one of the most important technical developments in optical manufacture that have emerged in the last few decades.

Figure 1.26 shows schematically Kodak’s ion figuring system [1.60]. By analogy with computer-controlled small tool technology, the IBF process is a “dwell time” process, material removal being proportional to the dwell time and therefore accurately predictable. The beam removal function is highly symmetrical and near-Gaussian in form. In an investigation of thermal effects [1.61], sharp temperature changes of nearly  $30^\circ\text{C}$  were recorded as the ion beam scanned back and forth near the sensor location. The maximum temperatures detected on the front face of a  $20\text{ cm} \times 20\text{ cm}$  lightweighted workpiece were  $100\text{--}120^\circ\text{C}$  and  $65^\circ\text{C}$  on the back face. No adverse effects

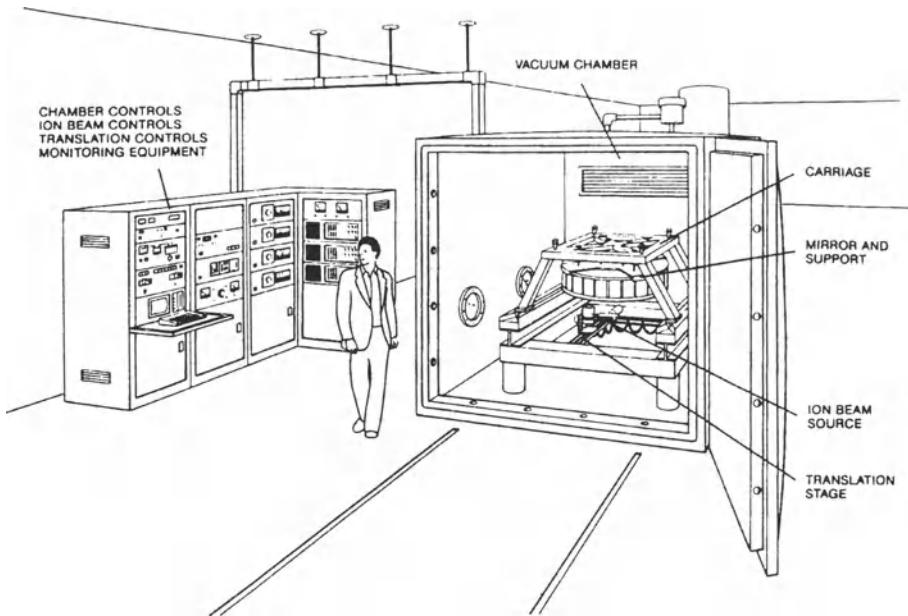


**Fig. 1.26.** Schematic of Kodak's ion figuring system [1.60]

were observed from ion beam heating, which supports the general conclusion that workpiece heating is not a problem if care is taken in critical cases.

An impressive example quoted in a Kodak brochure [1.65] was the correction of a 1.3 m ULE frit-bonded, ultra-lightweight, off-axis primary segment by the ion figuring process. The surface figure error of the segment following conventional polishing was  $5.02 \lambda_{\text{ptv}}$  ( $0.62 \lambda_{\text{rms}}$ ) with  $\lambda = 632.8 \text{ nm}$ . This was corrected to  $0.17 \lambda_{\text{ptv}}$  ( $0.015 \lambda_{\text{rms}}$ ) in *four iterations*. Such IBF processing can give up to 1000 % improvement in surface figure per iteration, whereas conventional polishing techniques were found to lead to improvements of 110–130 % per correction cycle. Another interesting example, the successful correction of printthrough (quilting), is given by Allen and Romig [1.61] with interferograms before and after correction.

Undoubtedly one of the most important and striking successes of IBF so far reported has been the correction of off-axis, aspheric segments for the Keck 10 m telescope primary [1.62] [1.64]. The case reported in detail [1.62] concerned segment SN 009. The diameter of such segments is 1.8 m. The stress polishing production process, followed by cutting to the hexagon, had left in this case an error of  $3.13 \mu\text{m}_{\text{ptv}}$  ( $0.726 \mu\text{m}_{\text{rms}}$ ), too large to be adequately corrected by a 30-lever warping harness. The predominant term of the error was defocus. The IBF correction process comprised 2 iterations. For each iteration, the measured error was modelled by an 8th order (45 term) Zernike fit which supplied the basis for the movements of the ion beam head. The first iteration required 14 days, the second 6 days. The surface figures involved

**Table 1.5.** Summary of the IBF correction results at Kodak on the Keck primary segment SN 009 [1.62]

State	Surface error ( $\mu\text{m}$ )	
	ptv	rms
Initial	3.13	0.726
First iteration	1.08	0.252
Second iteration	0.51	0.090

are shown in 3D models in the paper and are summarised in Table 1.5. The optical surface figure of segment SN 009 was improved in these two IBF iterations to yield a predicted 50 % encircled energy within 0.25 arcsec, which was comparable to many of the other Keck telescope segments.

This successful result with such a Keck primary segment firmly established the merits of IBF as a fundamental tool for off-axis segment production.

A similar highly successful operation was the correction of an off-axis, aspheric petal in four iterations [1.63] – see Fig. 1.29 below.

Figure 1.27 shows an interior view of Kodak's Ion Figuring Chamber in preparation for the IBF of a 1.3 m workpiece. Figure 1.28 shows the IBF processing of one of the Keck primary mirror segments. Figure 1.29 shows

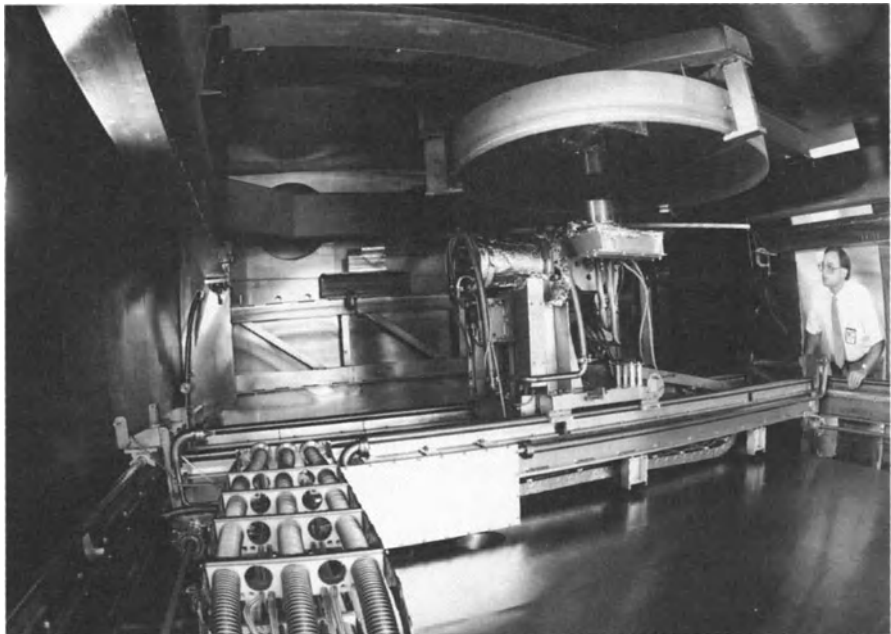


**Fig. 1.27.** An interior view of Kodak's Ion Figuring Chamber showing preparation for the IBF of a 1.3 m workpiece (courtesy T.J. Wilson and the Eastman Kodak Company)

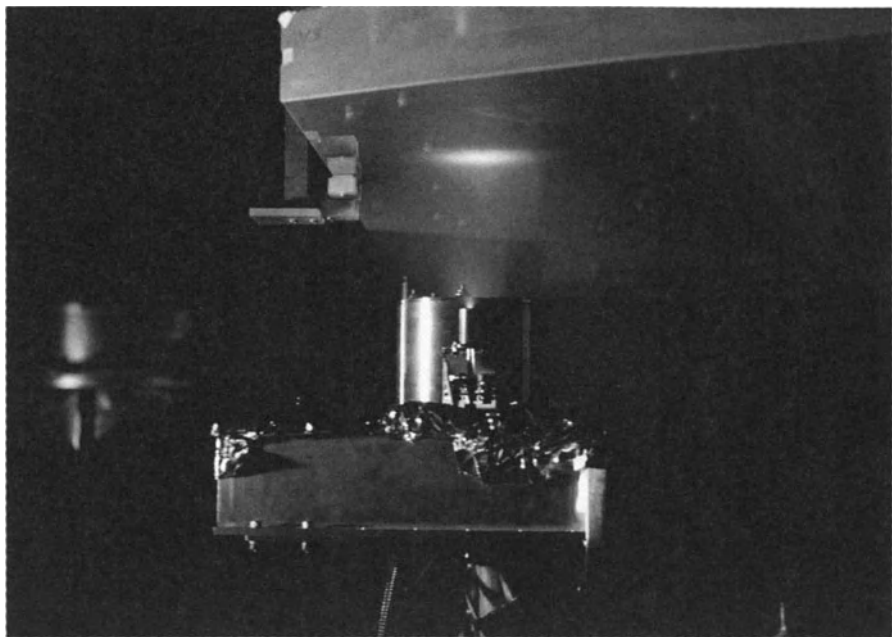


**Fig. 1.28.** Ion Beam Figuring at Kodak of one of the Keck primary mirror segments (courtesy T.J. Wilson and the Eastman Kodak Company)

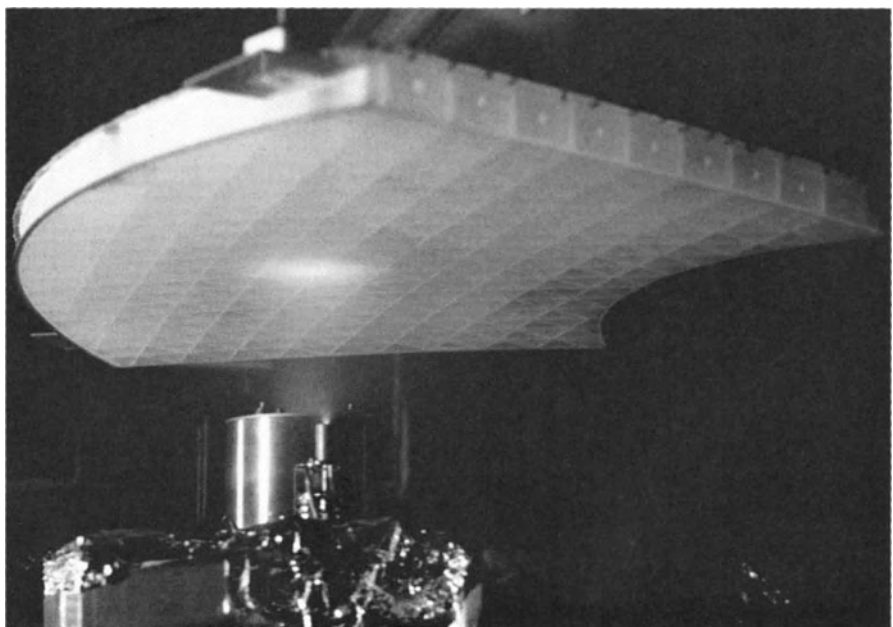


**Fig. 1.29.** Ion Beam Figuring at Kodak of an off-axis, aspheric petal to a surface figure better than  $0.01 \mu\text{m}$  rms in four iterations (courtesy T.J. Wilson and the Eastman Kodak Company)

the IBF processing of the off-axis, aspheric petal (referred to above) figured with IBF to better than  $0.01\text{ }\mu\text{m rms}$  in four iterations, giving an improvement of over 400 %.

**1.2.2.6 Figuring techniques in combination with active optics giving tolerance relaxation.** Reference has been made above to various forms of active control by flexing laps or workpieces. If a general system of image optimization is to be used, as described in Chap. 3 under the term “Active Optics”, then important relaxation of low spatial frequency manufacturing tolerances becomes possible. Because of the close association with ESO in connection with the 1 m test mirror for the NTT, the 3.5 m NTT optics and the contract for the 8 m primaries of the VLT, the firms REOSC in Paris and Carl Zeiss in Oberkochen have acquired special experience in this approach. An account was given above of the CCP (Computer Controlled Polishing) methods used. We will now consider other aspects of this technology in connection with large and very large mirrors. It is recalled that the VLT primaries are menisci with a diameter of 8.2 m and a thickness of 0.175 m (aspect ratio = 47).

#### REOSC technology for 8 m primary mirrors [1.25] [1.26]

a) **Support concept for the VLT primaries.** The support must provide correct compensation of gravity effects *and* of polishing tool pressure in view of the aspect ratio of 47. During testing, the support must provide for easy centering and must enable the low spatial frequency terms, which are afterwards to be corrected actively (see Chap. 3), to be corrected during figuring to prevent “fringe swamping”, i.e. masking of high spatial frequency errors by low spatial frequency terms which are unimportant if active optics is available [1.66]. This enables full advantage to be taken of the low frequency tolerance relaxation which is one of the two principal aims of active optics. The support used by REOSC has the same geometry as that in the final telescope with 150 individual supports, all of which can be controlled to give the desired force. Pneumatic actuators are used – see Fig. 1.30. The support operates in two different regimes: for polishing and for testing. The piston shaft is free during testing to avoid application of spurious forces; during polishing, a linear bearing applies constraint to stop mirror movement and each actuator is isolated from the others to provide a pre-calibrated force.

The active control of the support also effectively provides for a “stress polishing” facility for controlling low spatial frequency terms with large size tools. The force control accuracy is 2–3 N because of friction, though load cells can measure to 1 N. The support is based on 3 sectors, as in the finished telescope.



**Fig. 1.30.** Pneumatic support for the figuring of the VLT 8.2 m primaries (courtesy REOSC, Works photo)



**Fig. 1.31.** Newly built (April 1992) optical production facility of REOSC for the ESO VLT 8.2 m primary mirrors (courtesy REOSC, Works photo)

**b) Figuring concept for the VLT primaries.** REOSC analysed the relative merits of diamond milling and grinding to achieve the basic spherical surface or required form. The maximum sag difference of the hyperboloid to the best sphere for figuring is 2.3 mm at the edge, giving a mass of glass (Zerodur) to be removed of about 150 kg. They concluded that a milling operation is not significantly faster than grinding and that grinding is safer. The pneumatic (air-bag) support is well adapted to grinding and polishing, but too flexible for fast milling. Above all, vibration during milling could be a breakage risk for the mirror.

The newly built optical production facility for the 8.2 m VLT blanks (Fig. 1.31) contains a large Computer Controlled Milling Machine (CCMM) with final accuracy of about  $100\text{ }\mu\text{m}$  (see Fig. 1.32); but this will only be used to machine the support system, to locate the actuator and special pad positions accurately and to machine the grinding and polishing tools.

Spherical grinding is performed with the maximum stiff tool size considered feasible, with 4–5 m diameter. A starting spherical surface is still considered the best guarantee of avoiding high spatial frequency and non-axisymmetric errors. Both local errors such as “hills” and low spatial frequency errors can be corrected by the active force control (stress grinding). Aspheric grinding is performed with smaller tools of 1–2 m diameter under computer control (CCST discussed in § 1.2.2.1). The surface form is smoothed with a 4–5 m flexible tool. It should be remembered that the active optics concept puts great weight on reduction of high spatial frequencies to achieve the “Intrinsic Quality”, the essential feature of the active optics specification. For smoothing (fine grinding) of the surface roughness, REOSC also uses a 5 m flexible tool with a ceramic tiled surface. This has a “petal-lap” form to achieve equal wear on the aspheric surface.

The techniques for polishing are similar to those for aspheric grinding, the basic methods being CCST and a large (5 m) flexible tool of “petal lap” form to smooth the figure. The ceramic tiles used for grinding are replaced by pitch tiles. Figure 1.33 shows the type of lapping surface proposed. The dashed curve is an “equal wear” petal-lap form, while the full-line shows a possible modification to attack a high zone and neighbouring low zone. Another approach envisaged [1.26] was a sector of about  $45^\circ$  form on a 4 m flexible tool of calculated flexibility, operated with variable local pressure. The polishing with CCST was discussed in § 1.2.2.1.

The REOSC test methods are discussed in § 1.3.

**c) Results for the ESO VLT 8.2 m primary mirrors.** Up till March 1997 REOSC had completed three of the four VLT primaries [1.67] [1.68]. The whole figuring and testing procedure has effectively gone according to plan without any significant problems – a remarkable achievement if one considers that these are by far the largest monolithic telescope mirrors ever manufactured. REOSC is, at this time, also figuring the two similar-sized mirrors for the Gemini project.

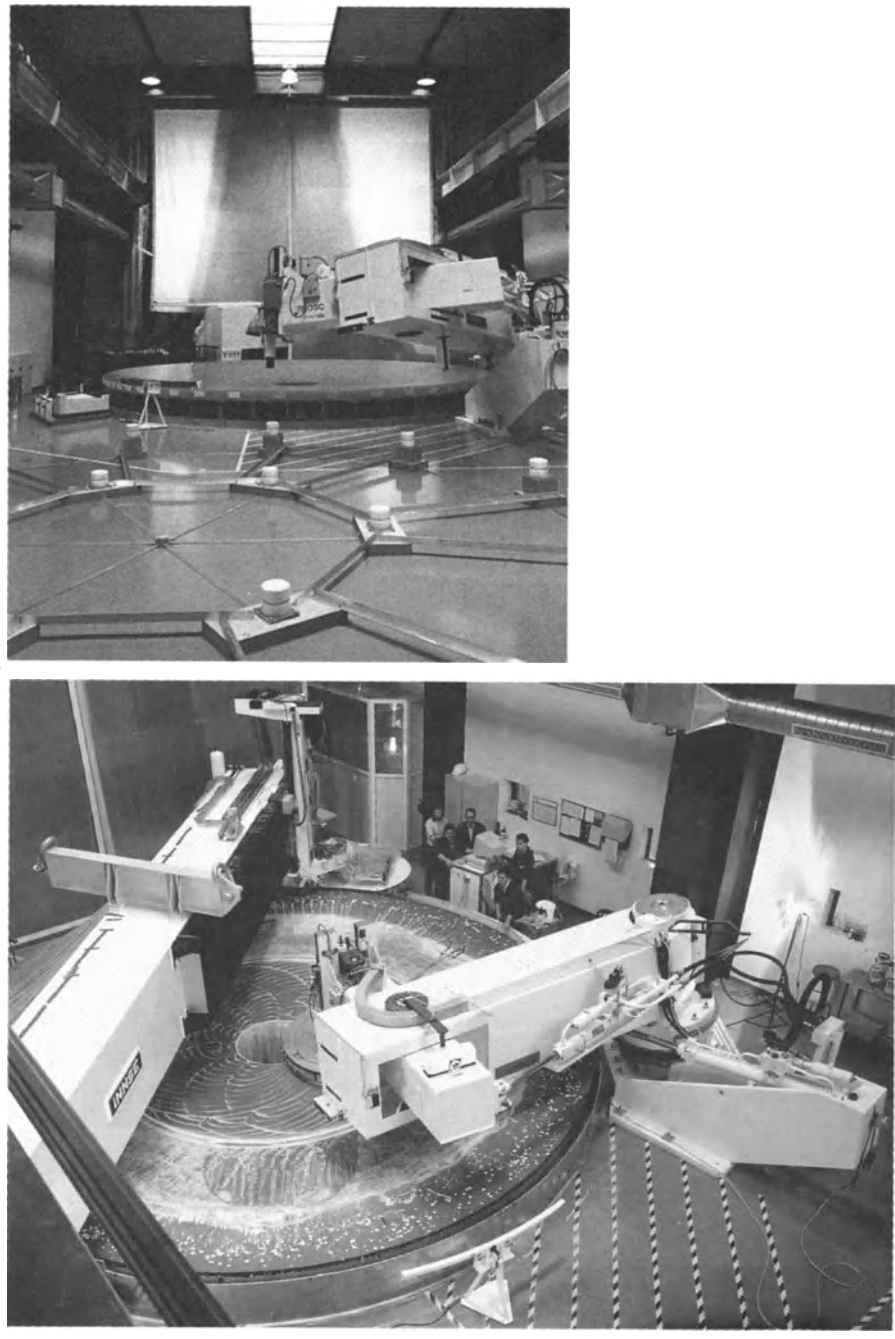


**Fig. 1.32.** (a) The Computer Controlled Milling Machine (CCMM) installed at REOSC with one of the 8.2 m VLT primary mirror blanks mounted on the turntable. The relative thinness of the blank (175 mm, AR = 47) is noteworthy. (Courtesy REOSC, Works photo). (b) Another view during the grinding operation

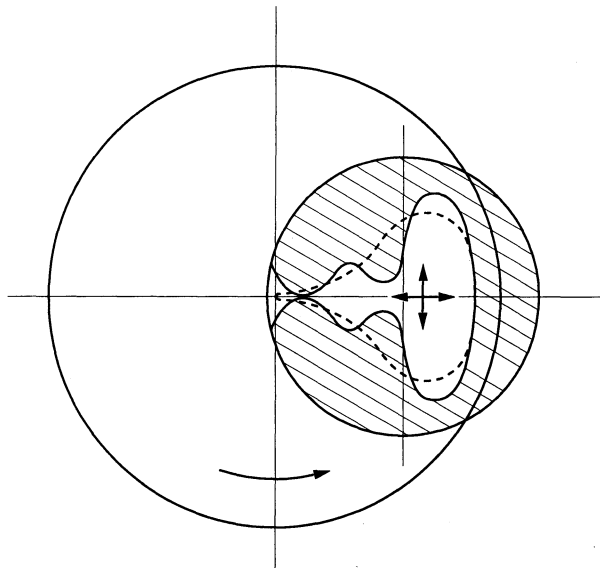


**Fig. 1.33.** “Equal wear” petal-lap polishing form with possible modification (full lines) for zonal work on the ESO 8.2 m primaries at REOSC [1.25]

Figure 1.34 shows a test operation being performed on one of the VLT primaries. The production of the 8.2 m mirrors has become such a matter of routine that REOSC can now complete them at a rate of one every 8–10 months [1.68]. Dierickx et al. [1.67] give an excellent account of the practical results. Table 1.6 gives a summary of the final values for the first two VLT primaries. We see that the figure quality corresponding to the active mode (Intrinsic Quality with active correction of those low frequency terms to be corrected in the telescope) is markedly better from the CIR values than the specification. Since the convergence was still excellent, further improvement could readily have been achieved. However, Dierickx has shown from a simulated star field, for seeing 0.4 arcsec at  $\lambda = 500$  nm, that there is no detectable difference between a perfect telescope and the quality shown in Table 1.6 for primary #1 [1.67]. Figure 1.35 shows the final interferogram of primary #2 in the active mode (Intrinsic Quality). Primary #3 has a quality at least as good as primary #2 [1.68].

It may be concluded that the art of figuring and testing monolithic primaries, even of the largest sizes that can be cast and handled, has now reached such an advanced stage that, in combination with active optics, the degradation of optical quality due to manufacture can be made negligible even for the best conceivable ground-based atmospheric seeing. Indeed, primary #1 is diffraction limited at the  $H_{\alpha}$  wavelength in the red and the other two are even better.

Of course, for future telescopes of the largest sizes, monolithic primaries will be superseded by *segmented* primaries. REOSC considers that *ion beam figuring* is essential for the efficient figuring of high quality segments and has set up a practical facility which is now routinely available for all such cases.

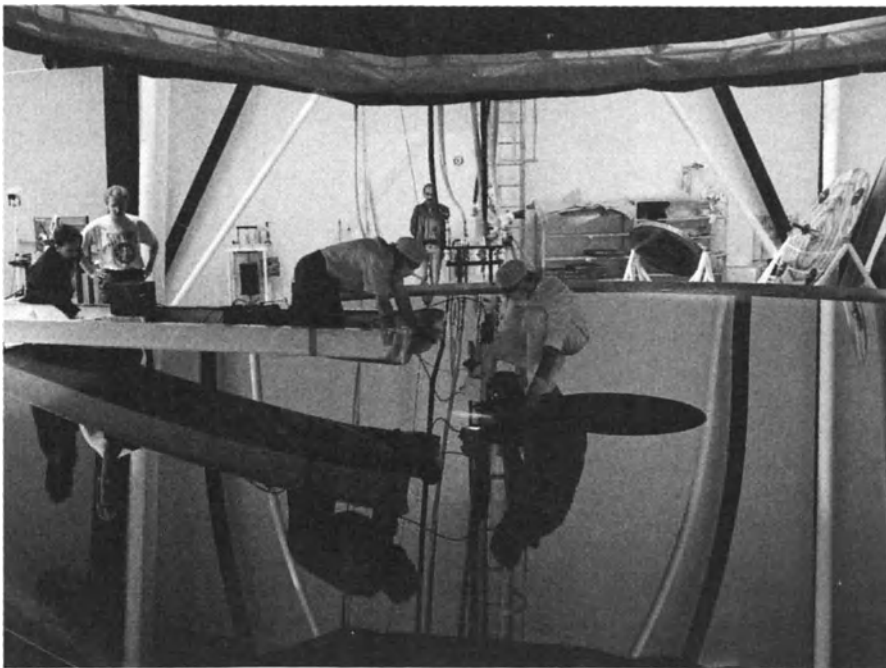


**Fig. 1.34.** A test operation being performed on one of the VLT primaries (courtesy REOSC, Works photo)

**Table 1.6.** Summary of the results for the first two ESO VLT 8.2 m primaries (Dierickx et al. [1.67])

Property	Specification	Result VLT Primary #1	Result VLT Primary #2
Radius of curvature (mm)	$28\ 800 \pm 100$	28 762.9	28 764.9
Conic constant (passive mode)	-1.004616	-1.004457	-1.005089
Active forces applied (N)	$\leq \pm 120$	-83 + 52	$\pm 80$
RMS Wavefront (active mode) (nm)	N/A	43	38
RMS Slope (active mode) (arcsec)	N/A	0.055	0.055
Strehl Ratio at $\lambda = 500$ nm	$\geq 0.25$	0.714	0.791
CIR ( $\lambda = 500$ nm, $r_0 = 500$ mm*)	$\geq 0.820$	0.854	0.884
Microroughness (Å)	N/A	15–20	8–11

\* Corresponds to atmospheric seeing of 0.20 arcsec

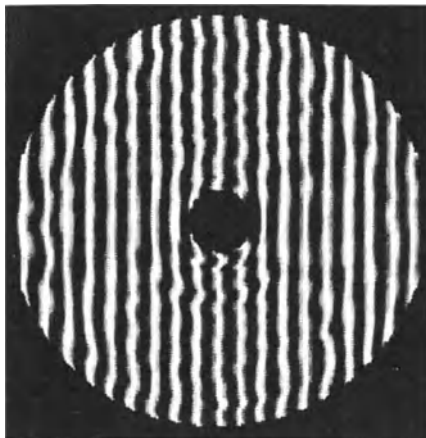


**Fig. 1.35.** Synthetic interferogram of the finished VLT primary #2 in the active mode (Intrinsic Quality) (Dierickx et al. [1.67])

### Carl Zeiss (Oberkochen) technology for 8 m and smaller mirrors

a) **Support concept.** A detailed analysis of the necessary support for an 8 m meniscus with thickness 200 mm was performed in 1985 [1.27] for the VLT proposal. For thin meniscus technology using active optics, the support system is considered of central importance. There were three cases defined for analysis:

- The dead weight axially supported
- Polishing pressure in axial direction
- Frictional forces due to polishing

Both FE and analytical methods were used. A general treatment is given by Cheng and Humphries [1.69] and an analytical treatment, above all for the NTT, by Schwesinger [1.70]. A proposed solution had 328 support pads and gave, for the axial deadweight, a wavefront error of 18.6 nm rms. For active optics simulations or control, an adequate proportion or all of these supports would require force adjustment possibilities. The influence of polishing pressure for the calculated case is shown in Fig. 1.36. The support was adequate for reasonable polishing pressure at  $AR \leq 40$ , but not at  $AR = 80$ .

Since 1985, Carl Zeiss has made further major advances, also in connection with manufacture with the strip tool. The support principle remains the same, but with a continuous back support surface and radial relaxation. It has been possible to work to high quality for a space project a mirror of 4 m diameter with thickness only 10 mm – an aspect ratio of 400! With a working support of this principle, the manufacture of primary mirrors such as those of the 8 m VLT telescopes with an aspect ratio of 46 would cause no problems at all from the support point of view [1.7].

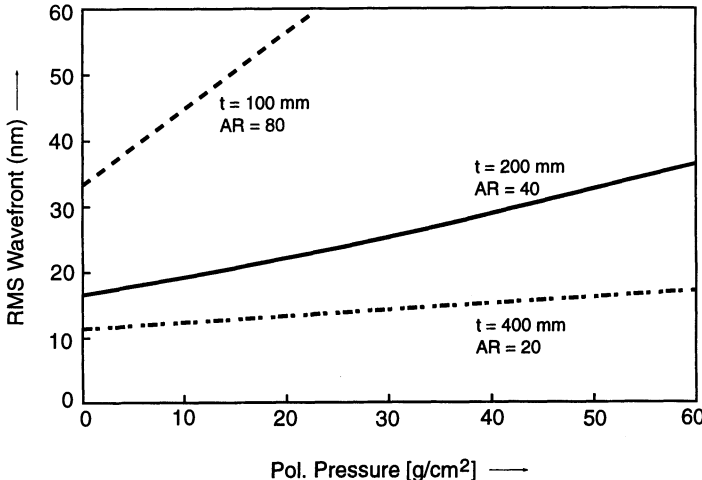


Fig. 1.36. Wavefront aberration (rms) generated by polishing pressure for 8 m mirrors with aspect ratios 20, 40 and 80 (Carl Zeiss [1.27])

**b) Figuring concept.** The figuring concept is documented in [1.10] [1.27] [1.28] and [1.71]. The projects to which advanced technology has been applied are, above all, the 3.5 m NTT, the 3.5 m Galileo telescope based on the NTT and the 2.7 m SOFIA primary. This latter had a thickness of 60 mm (AR = 45) and an f/ratio of f/1.2 [1.28]. The technology used in such extreme cases was the CCP technique with *pressure control* discussed in § 1.2.2.1 using small tools combined with a figure smoothing operation with the *membrane tool* of § 1.2.2.2. This was also used for the NTT and the Galileo optics and, above all, corrects the edge zone errors of CCP. Ion beam polishing avoids edge zone problems and is a useful touching-up technique in certain cases. Material removal  $\leq 1 \mu\text{m}$  can be achieved without serious surface roughness problems ( $< 5 \text{ nm}$ ). In general, Carl Zeiss commences from the sphere with f/nos  $\geq$  ca. 1.8.

Lap surface modification is also used (petal-laps) for figure smoothing and can be computer controlled to some extent (in a differential sense), but it is more difficult to apply the Preston theory than with small tools. The strip (rectangular) tool of the membrane or strip polisher is also modified in its polishing surface to handle axisymmetrical errors. The basic methods for producing steep primaries are [1.28] [1.7]:

- Generation of the asphere by diamond wheel grinding
- A lapping (grinding) process using 2–3 carborundum grades with relatively large tools to remove large errors, preferably using the strip tool
- A similar process for figuring (polishing) and fine correction, the relatively stiff tool preventing ripple production

Aspheric lapping by grinding is applied if the normal interferogram has more fringes than one can handle (fringe swamping). In practice, today, this means

asphericities of  $>$  ca.  $10\text{ }\mu\text{m}$ , although conventional polishing techniques can handle asphericities up to  $50\text{ }\mu\text{m}$ . Then IR testing is applied. This sets the test limit for lapping to about  $1\text{ }\mu\text{m}$  which must be corrected by polishing. Material removal by lapping (grinding) is at least 10 times as efficient as polishing. Polishing removes about

$$0.03\text{ }\mu\text{m}/\text{hour/kilopascal} \ ,$$

whereby a pressure of 3–5 kilopascal is normal. Membrane polishing requires a special membrane for each mirror and had only been extensively used up to 1992 on the SOFIA mirror.

Fine figuring at the very end is usually done with stiff sub-aperture tools using *pressure control*. Such a final stage may require up to 200 hours, but this may be improved by a factor of 3. Typically, near the end, 5 min polishing time may be followed by 40 min cleaning and 1–2 h testing! The active optics relaxation of low spatial frequency terms, above all astigmatism, is a big help in retouching of high spatial frequency errors.

The NTT 3.5 m, f/2.2 primary had an Intrinsic Quality (IQ) of  $d_{80} = 0.096\text{ arcsec}$  or  $W = 27\text{ nm rms}$  [1.72] [1.71]. The equivalent results for the similar Galileo primary were  $d_{80} = 0.07\text{ arcsec}$  and  $W = 16\text{ nm rms}$  [1.73]. Figure 1.37 shows an interferogram of the final figure, (a) without active correction with only piston, tilt, focus and coma removed, and (b) with active correction (intrinsic quality). The latter was probably the highest quality large optical surface manufactured up to that time (1992). However, it was by no means the steepest, having a relative aperture f/2.2.

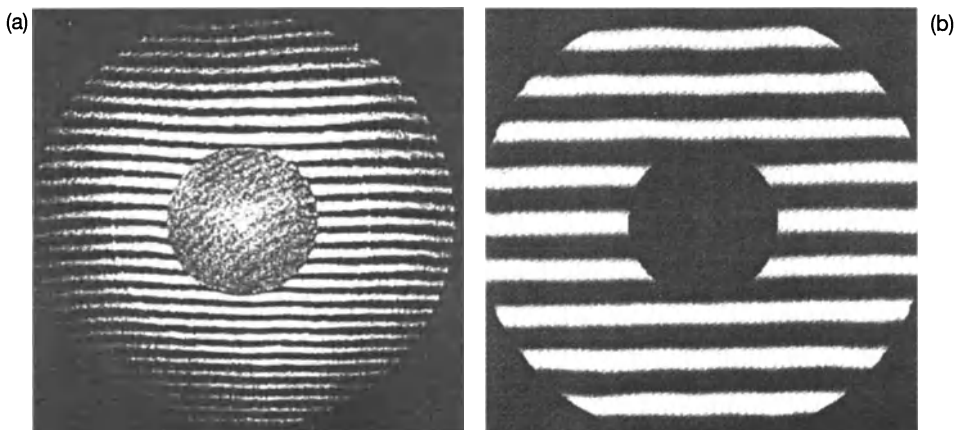


**Fig. 1.37.** Interferogram of the final figure of the 3.5 m, f/2.2 primary of the Galileo telescope: (a) before active correction, (b) after active correction (Carl Zeiss [1.73])

## 1.3 Test technology

### 1.3.1 General aspects of test technology development

In Chap. 2 we shall consider a number of test technologies suitable for testing finished telescopes *in function*. The situation is quite different from that obtaining in an optical workshop, although a number of procedures are used in both. The most important difference is that a functioning telescope cannot be tested by an interferometer using an artificial reference source, which rules out the most effective forms of interferometry used in the workshop for large optics.

Although interferometry in its simplest form (Newton's rings) goes back to the origins of the reflecting telescope, its application to the manufacture of telescope optics is only a recent development. It should be remembered that the primary of the Palomar 200-inch telescope was tested with the Foucault knife-edge technique made quantitative by using masks to measure the differences of radius of curvature of different zones, and by Hartmann tests in the final stages. No interferometric technique was available for large optics at that time. The breakthrough occurred with the introduction of the LUPI (Laser-Unequal-Path-Interferometer) form of the Twyman and Green interferometer made possible by lasers. But Hartmann methods and other tests could still rival interferometry because of problems of vibration, air turbulence and evaluation techniques. These problems have now all been effectively solved by the application of modern detectors (particularly CCDs) and computers. Thus, the dominance of interferometry in modern testing of large optics is far more pronounced than it was 20–30 years ago.

### 1.3.2 Interferometers

The best practical review of basic interferometer forms and their use is given by Malacara [1.74]. Here, we can only briefly deal with the essential characteristics and applications.

**1.3.2.1 Interferometers for smaller elements.** The commonest forms are the Fizeau and Haidinger interferometers, invaluable test equipment for workshops making high quality elements up to about 300 mm. As an example, the workshop of H. Kaufmann in Crailsheim, producing optics up to 1 m diameter, has both a vertical and horizontal Fizeau interferometer of aperture 250 mm as well as a smaller (100 mm) Haidinger interferometer.

The *Fizeau interferometer* (Fig. 1.38) is closely related to the simplest Newton interferometer [1.74]. The Newton interferometer consists of an extended monochromatic source, a beam divider and two surfaces virtually in contact producing Newton's fringes (sphere against flat) or parallel fringes (two flats with thin air-wedge between them or two mating spheres as in test plate pairs). For two flats with a narrow air-wedge between them, the optical path difference in double pass leading to dark fringes is given by

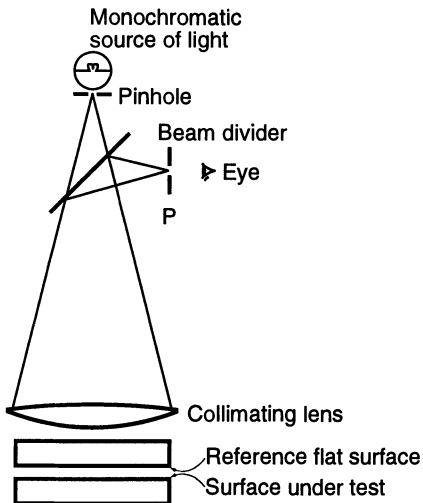


**Fig. 1.38.** Schematic arrangement of a Fizeau interferometer using a lens collimator (after Malacara [1.74])

$$2\alpha y = 2t = m\lambda \quad , \quad (1.25)$$

where  $\alpha$  is the wedge angle,  $y$  is the distance from the intersection line of the planes,  $t$  the separation and  $m$  an integer. Dark fringes result from the phase change at the air-glass surface. The only difference, physically, in the Fizeau compared with the Newton form, is that the air gap is much larger so that the order of the fringes  $m$  is much higher. This makes the practical work simpler by avoiding surface contact, but requires a collimated system with a pinhole source. The Newton arrangement with an appreciable source size falsifies the fringe pattern if  $m$  is large because Eq. (1.25) becomes, with oblique vision at angle  $\theta$ ,

$$2t \left( \frac{1}{\cos \theta} - \tan \theta \sin \theta \right) = 2t \cos \theta = m\lambda \quad (1.26)$$

In the Newton form,  $m \leq 10$ . For a precision  $\lambda/20$ , we require  $1 - \cos \theta \leq 0.005$  or  $\theta \leq 0.1$  rad, a source size of less than about  $10^\circ$ . If the gap is about 5 mm in the Fizeau form, then  $m \sim 20\,000$  and the source must be about 50 times smaller, in practice a pinhole with a monochromatic source and collimator.

The Fizeau interferometer can be used without a collimator for testing spherically curved surfaces of similar radii (Fig. 1.39). The reference surface can be either the concave or convex surface. Alternatively, the two faces of a meniscus can be tested if near to concentricity, but the order  $m$  may be very high.

The Newton and Fizeau interferometers give fringes of equal thickness measuring directly the variations in an air (or glass) space. In the *Haidinger interferometer*, the thickness of the air (or glass) space is uniform and the source is of large angular size (Fig. 1.40). This gives circular fringes of equal inclination, formed at infinity. These are governed by Eq. (1.26) and are the exact equivalent of the basic circular fringes observed with a Michelson in-

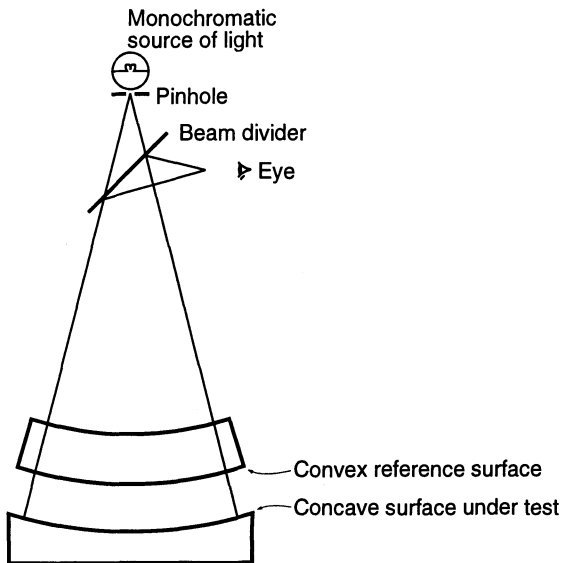


**Fig. 1.39.** Fizeau interferometer without collimator for curved surfaces (after Malacara [1.74])

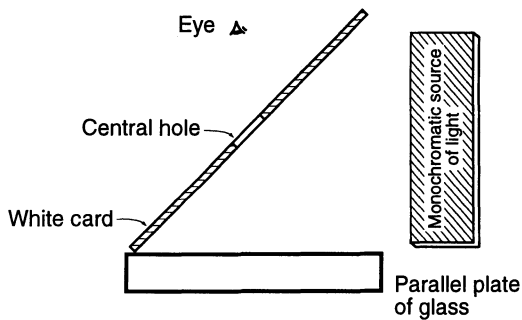


**Fig. 1.40.** Simple arrangement for seeing Haidinger fringes with a quasi-parallel glass plate (after Malacara [1.74])

terferometer [1.75]. The Haidinger fringes can be better seen if  $m$  is large by focusing them by a lens. This is effectively the same as a Fizeau interferometer except that the pinhole is replaced by a hole giving a large angular size of the source. Alternatively, the fringes can be viewed with a small telescope. Kaufmann [1.11] can detect angle errors down to 0.01 arcsec with his Haidinger interferometer.

Except for the form of Fig. 1.39, all such interferometers using collimators are limited in test diameter by the collimator.

**1.3.2.2 The classical Twyman-Green interferometer.** The Twyman-Green interferometer [1.74] is derived from the original Michelson interferometer [1.75] in exactly the same way that a Fizeau is related to the basic Haidinger interferometer. Its original form [1.76] was for testing prisms and microscope objectives, later [1.77] also camera objectives. A detailed account of classical applications is given in [1.2]. The original form is shown in

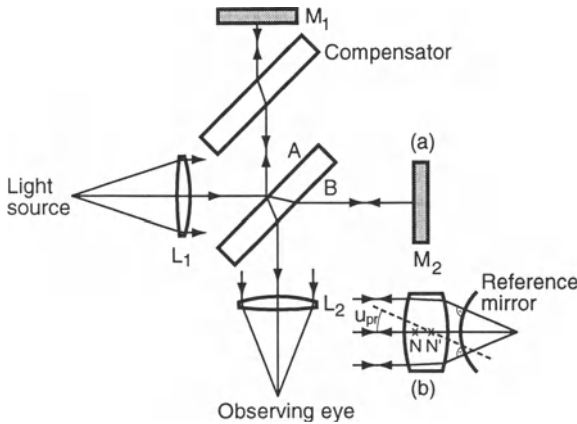


**Fig. 1.41.** The basic form (equal path) of a Twyman-Green interferometer: (a) testing a plane mirror, (b) camera objective test arrangement

Fig. 1.41. The camera-lens testing version (b) is normally combined with a “nodal-slide” arrangement, whereby the field performance at field angle  $u_{pr}$  is tested by rotating about the second nodal point  $N'$  and axially moving the convex reference mirror to compensate for the flat field. As with the modification of Fig. 1.39 for the Fizeau interferometer without a collimator, there is an equivalent Twyman-Green form whereby the plane mirrors are replaced by identical concave mirrors (Fig. 1.42 (a)). Twyman [1.74] [1.78] suggested this form would be suitable for testing large mirrors or lenses, as no collimator was required; but Michelson [1.74] [1.79] had correctly pointed out that the lack of sufficiently coherent light sources at the time meant that the optical paths of the two arms would have to be substantially equal, i.e. the reference concave mirror would have to be effectively as large as the test mirror. The form of Fig. 1.42 (a) is usually called a Williams interferometer because Burch [1.80] attributed it [1.74] to Williams.

The coherence requirements (size - spatial coherence) and monochromaticity (temporal coherence) of the light source were analysed by Hansen [1.81] and are summarised by Malacara [1.74].

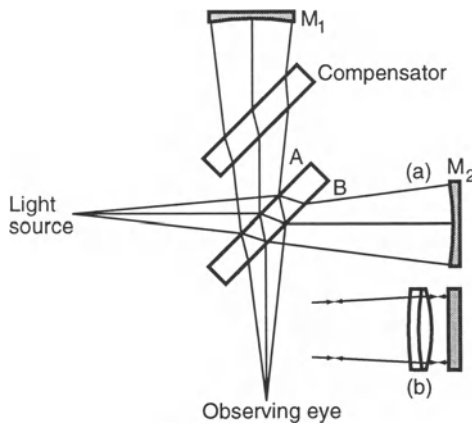


**Fig. 1.42a, b.** Twyman-Green interferometer without a collimator (Williams type) (after Malacara [1.74])

Concerning *spatial coherence*, an interferometer is “uncompensated” if it has more glass in one arm than the other. The maximum source size has then an elliptical form and a Michelson interferometer gives elliptical fringes. For the case of a glass plate of thickness  $t_{n'}$  normal to the axis of the beam, the mirror should be shifted for a quasi-monochromatic light source by

$$t_0 = t_{n'} \left( 1 - \frac{1}{n'} \right) , \quad (1.27)$$

where  $n'$  is the refractive index. This implies that the virtual images of the mirrors at the end of each arm are at the same place when the interferometer is compensated for the finite size of the source. The fringes are then localised near the mirrors and the viewing system must be focused on them.

Concerning *temporal coherence*, if there is an uncompensated plate thickness  $t_{n'}$  in the interferometer, then for an axial ray through a plate normal to the axis, the change of optical path with wavelength is

$$\Delta(\text{OPD}) = 2t_{n'} \left( \frac{dn'}{d\lambda} \right) \Delta\lambda \quad (1.28)$$

Using the Rayleigh limit  $\Delta(\text{OPD}) \leq \lambda/4$  as the criterion for fringe visibility, this gives

$$\Delta\lambda \leq \frac{\lambda}{8t_{n'}(dn'/d\lambda)} \quad (1.29)$$

For non-compensation,  $\Delta\lambda$  will be small, whereas white light can be used for an exactly compensated interferometer, as was classically the case with the Michelson interferometer.

If the arms are very unequal – as in the Laser Unequal Path Interferometer (LUPI) below – then we have as in Eq. (1.25)

$$(\text{OPD})_0 = 2t_0 = m\lambda \quad (1.30)$$

From the Rayleigh criterion, the order  $m$  should not change between  $\lambda$  and  $(\lambda - \Delta\lambda)$  by more than  $\frac{1}{4}$ , giving

$$m\lambda = (m + \frac{1}{4})(\lambda - \Delta\lambda) , \quad (1.31)$$

where  $\Delta\lambda$  is the permissible bandwidth for fringe visibility. Equations (1.30) and (1.31) reduce to the good approximation

$$\Delta\lambda \leq \lambda^2/8t_0 , \quad (1.32)$$

the requirement for good fringe visibility. This condition proves Michelson’s assertion [1.79] that the testing of large optics with the Twyman-Green interferometer of the Williams type (Fig. 1.42(a)) before the invention of the laser was not feasible. However, if the Williams interferometer is modified as shown in Fig. 1.42(b), whereby one concave mirror is replaced by a collimator lens and a flat of the same size, as (according to Burch [1.80]) was proposed by Williams, the problem of the size of the second concave mirror is

solved. According to Malacara [1.74], this was also proposed by R.E. Hopkins in conjunction with a laser source. Without this, the arms must still meet the condition of (1.32) for equality, which remains a major problem for large concave mirrors. In an inverted scheme with the concave mirror as reference and the objective as the test object, complete small telescopes have been successfully tested without a laser source [1.74] [1.82]. However, such devices have now been replaced by the LUPI.

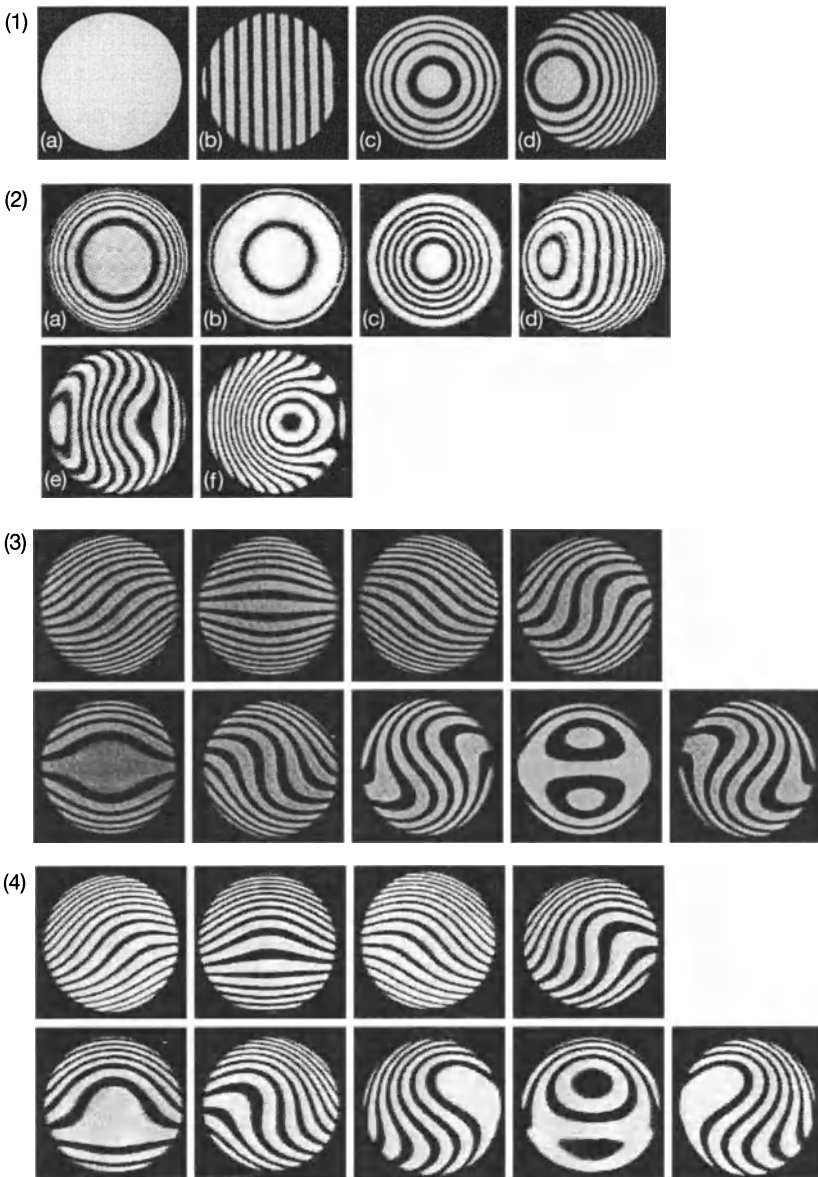
In two classic papers, Kingslake [1.83] [1.84] analysed the interferogram patterns for the first order (tilt and defocus) and third order (spherical aberration, coma and astigmatism) aberrations. The corresponding interferograms, both individually and in various combinations, are reproduced by Malacara [1.74]. Since these interferograms give the basic forms encountered in all practical cases, they are reproduced in Fig. 1.43. For details of the aberration coefficients involved, the reader is referred to Malacara [1.74].

**1.3.2.3 The Laser Unequal Path Interferometer (LUPI).** The development of gas lasers was the fundamental requirement for the practical application of the extreme unequal paths in a Twyman-Green interferometer, which are necessary if the reference beam is to be made small and compact compared with large test optics. In the earlier development, single mode lasers with very high spectral purity were very expensive and had very low power outputs. So multimode lasers were used for which good fringe contrast could only be obtained near certain evenly spaced OPD positions [1.74] [1.85]. If the length of the laser having several longitudinal modes is  $L$ , then the  $(OPD)_0$  on the axis to give good fringe contrast must be

$$(OPD)_0 = 2t_0 \simeq M \cdot 2L , \quad (1.33)$$

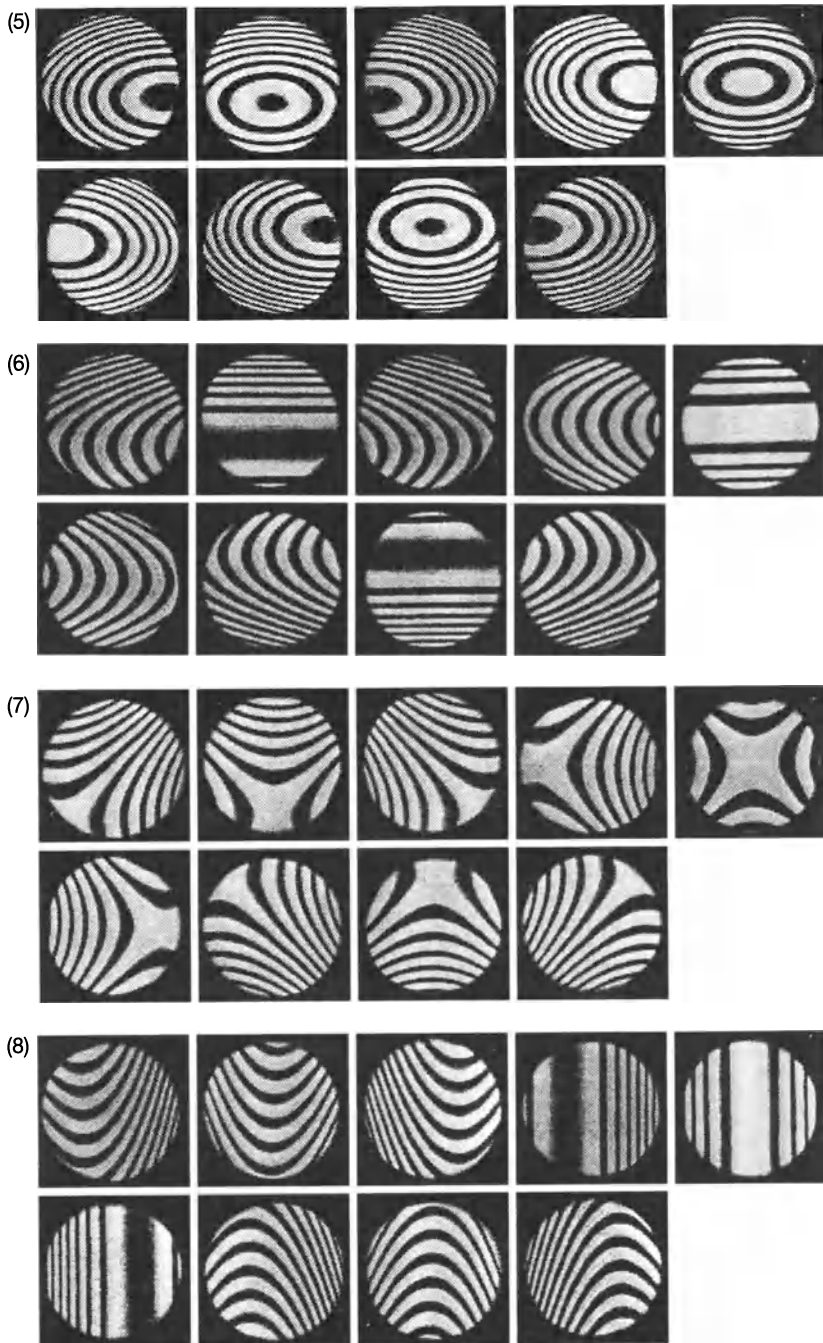
where  $M$  is a digit. However, stabilized single mode lasers are now available at a reasonable price: they enable LUPI interferometry over any OPD required by modern large optics without any loss of fringe contrast.

A modern, versatile form of LUPI was designed by Houston et al. [1.74] [1.86], shown schematically in Fig. 1.44. The beam expander expands the parallel laser beam to the beam size of the interferometer. Slight aberration here is uncritical as it is present in both interferometer arms. The beamsplitter operates at the Brewster angle and has a small wedge angle to avoid reflections from the front face. The beam diverger produces a divergent beam with negligible spherical aberration at an f/no able to cover the steepest concave spherical mirrors to be tested (Fig. 1.44(a)). Aspheric test mirrors require a supplementary compensation or null system, whose function it is to produce an aberrated wavefront at the position of the test mirror of the same shape as the aspheric form required (Fig. 1.44(b)). This means that all aperture rays will meet this surface normally (see § 1.3.4) and the perfect aspheric will yield a perfect test interferogram as for a spherical mirror tested without a null system, i.e. a perfect autocollimation test if the test mirror has the desired shape.



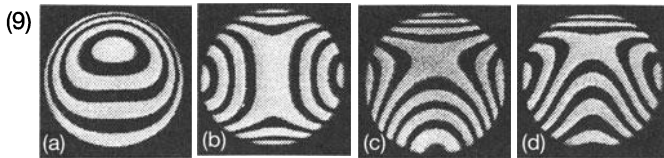
**Fig. 1.43 (1–9).** Interference patterns for standard aberrations (after Malacara [1.74] and Kingslake [1.83] [1.84]):

- (1) Perfect lens: (a) No tilt or defocus, (b) With tilt, (c) With defocus, (d) With tilt and defocus.
- (2) Interferograms showing spherical aberration (*without tilt*): (a) Paraxial focus, (b) Medium focus, (c) Marginal focus. (*With tilt*), same foci (d), (e), (f).
- (3) Coma at the paraxial focus. The central figure has no tilt, the others are with tilt contributions for the directions shown.
- (4) Coma plus a small defocus contribution. The central figure has no tilt, the others are with tilt contributions for the directions shown.
- (5–9) see next pages

**Fig. 1.43.** (continued)

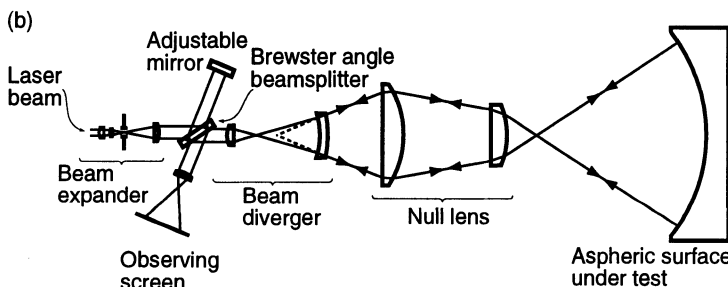
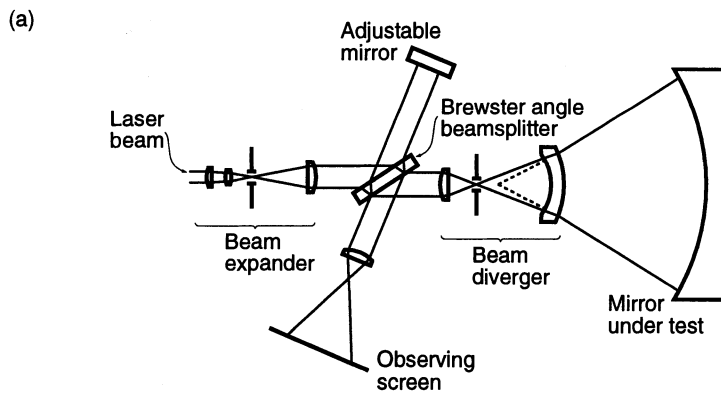
(5)(6)(7)(8) Astigmatism at different foci, the central figure with no tilt, the others with tilt contributions for the directions shown: (5) Petzval focus; (6) Sagittal focus; (7) Best focus; (8) Tangential focus.

(9) see next page

**Fig. 1.43.** (continued)

- (9) Combined aberrations: (a) Spherical aberration with coma, (b) Spherical aberration with astigmatism, (c) Coma with astigmatism, (d) Spherical aberration with coma and astigmatism.

The fringe focusing lens must focus the exit pupil of the system on to the detector. Earlier, this was a photographic plate, now an electronic detector (normally a CCD camera) is an essential part of a modern LUPI. Where is the “pupil”? If the test mirror is perfect in the sense that all incident rays strike it exactly normally and return along their incident paths, then the system has zero field and the term “pupil” is meaningless. However, as soon as the interferogram contains error information, the reflected rays leave the test mirror as though it is the pupil, returning through the system with slightly different paths. For small aberrations, the law of isoplanatism of optical systems ensures that the aberrations measured are not significantly

**Fig. 1.44a, b.** Basic version of LUPI designed by Houston et al. [1.74] [1.86]

falsified by the path change. The fringe pattern then measures the OPD between the wavefront incident on the test mirror and its actual surface. Therefore, the fringe focusing lens must focus the image of the test mirror, as transferred back through the null system and beam diverger optics, on to the detector with the correct size. Since the beams are already recombined, the quality of this lens is uncritical. The critical element is the null system (§ 1.3.4). In principle, this can be combined with the diverger optics – see below.

The other major advance in the application of the Twyman-Green interferometer, following the unequal path development due to lasers, was the computer analysis of interferograms. This was already done using scanning procedures of photographic records, but the real revolution has taken place with on-line CCD cameras enabling direct read-out of the fringe coordinates. An important new area of technology has developed (see § 1.3.2.4) for deducing the *phase map* of the wavefront with high accuracy and convenience. The data points are fitted by a least squares procedure to a defined polynomial. If classical Hamilton terms (see Chap. 3 of RTO I) are used, they are not general orthogonal functions unless identical to Zernike terms without central obstruction [1.87] (§ 3.10 of RTO I). The procedure is satisfactory for a few terms but leads to an ill-conditioned matrix if many terms are used: this reflects the situation where non-orthogonal terms of different orders balance each other giving high individual coefficients with large errors. This situation is not limited to interferometric analysis: it also occurs with other measures, such as Hartmann-based tests.

Orthogonal polynomials such as those of Zernike (or natural vibration modes – see Chap. 3) convert the matrix into a diagonal one and remove the problem of ill-conditioning. Very effective software packages are available, such as the FAST system [1.88], giving not only polynomial analysis from a CCD-camera scan, but also point spread functions with diffraction, MTF data and Strehl Intensity Ratios. Even a small workshop such as Kaufmann [1.11] has been working with such a system since 1986. Typically it may be used for testing telescope primary paraboloids or complete Cassegrain telescopes in autocollimation with double pass (Fig. 1.45), though the same set-up can be used for other forms of image analysis such as the Foucault knife edge or direct observation of the image of a point source, as shown here. The plane mirror is in the foreground, testing a complete Cassegrain telescope from its Nasmyth focus.

The test of aspheric primaries alone by the standard method at their center of curvature, as in Fig. 1.44, normally requires a null system for large or steep mirrors. This method is in single pass and does not require a reflecting coat on the mirror, which is essential for double pass as in Fig. 1.45. Kaufmann [1.11] performs such tests in single pass in a LUPI of Williams form (Fig. 1.42), avoiding null systems by doing measurements of the shifts of the centers of curvature of different zones. This is the equivalent of the Foucault measurements using zonal masks as practised by amateurs [1.89].

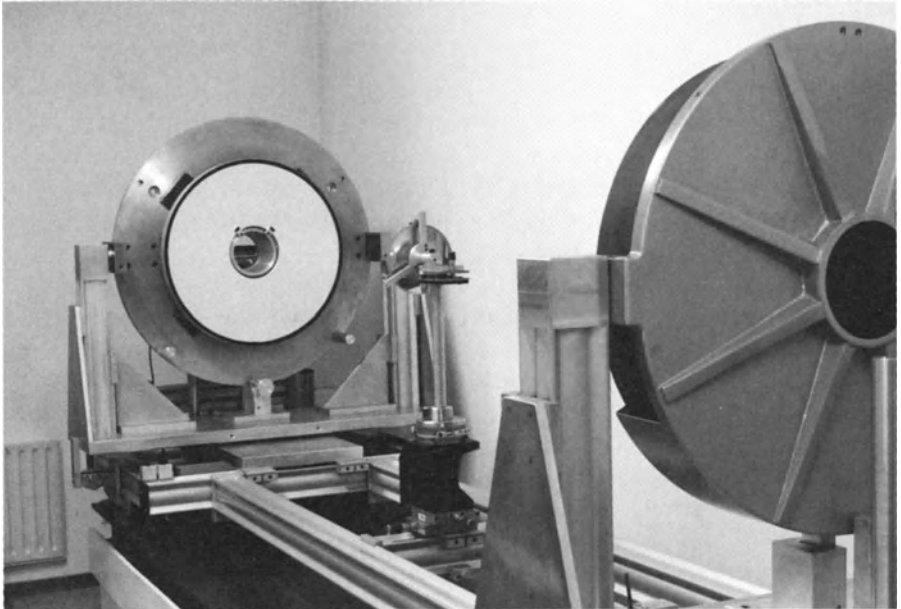


**Fig. 1.45.** Set-up for testing parabolic telescope primaries with double-pass in autocollimation against a plane mirror (courtesy H. Kaufmann [1.11])

and for the 200-inch Palomar primary. However, Kaufmann adjusts the tilt in his Williams-type Twyman-Green to match that of any given point on his test mirror and adjusts the focus to get a minimum number of circular interference fringes at that point. This gives a measure of zonal radius of curvature differences of higher precision and greater simplicity of operation than such measures with the Foucault knife-edge. This method is essentially similar to that proposed by Liu et al. [1.90].

**1.3.2.4 Modern phase shift and fringe scanning interferometry.** The earlier evolution of fringe scanning interferometry in general is excellently treated by Bruning [1.91], the pioneer of phase shift methods [1.92]. Previously, till the late 1960s, double-beam interferograms were recorded photographically and judged visually or measured by hand. Such photographs contained all the errors due to air turbulence, vibrations and interferometer errors. Reduction of these by averaging a number of photographs was a laborious and inefficient process, often of doubtful validity for high accuracy and always requiring much operator experience and judgement. *Passive* fringe scanning techniques for photographic interferograms were described by Jones and Kadakia in 1968 [1.93]. Non-linear response of the photographic process falsifies the information between fringes, so it was necessary to use many tilt fringes over the interferogram. Although the automatic evaluation was

a great advance, the fundamental problems of air turbulence and vibration were not resolved.

One way of getting round the interpolation problem between fringes is to introduce a known *temporal* phase shift. Real-time electronic detectors were essential to this development, earlier with TV detectors, later with solid state detectors as an array. Modern systems normally use CCD cameras. The intensity of the fringe pattern is detected over each point of this fixed grid and the reference path length changed in a systematic manner to change the phase at each recording point. According to the definitions given by Wyant [1.94], an interferometer using a constant continuous phase difference rate in time is termed a *heterodyne* or *phase shifting interferometer*, while an interferometer using phase shifts in discrete steps is a *phase stepping interferometer*. Phase shifts may be generated by direct movements of the reference mirror or by polarisation techniques. Various techniques exist [1.94] for extracting the phase, some of which we will consider below. Since the heterodyning approach essentially solves the interpolation problem, it is no longer necessary to introduce tilt fringes into the interferogram, thereby relaxing the isoplanatism requirements of the interferometer.

Such *temporal heterodyning* is not the only possible approach. Before considering the temporal heterodyne approach in more detail, it is instructive to see how phase information can be extracted from a *single interferogram*.

An elegant system for direct phase detection in the case of a *hologram* was given in 1972 by Ichioka and Inuiya [1.95]. The spatial spectrum of the hologram distributed in the spatial frequency domain as a central triangular signal with two symmetrical sidebands around the reference spatial frequency  $\pm k \sin \theta$ . The hologram was transformed into time-sequential signals by a video system so that the distribution of the dispersed spectrum in the spatial domain was transformed into the temporal one. The phase  $\phi$  of the hologram was extracted from the electrical signal in the temporal domain by eliminating the unwanted spectral components through an electric filter, the demodulating circuit, and the computing circuit. The hologram arising from the complex amplitude  $A(x, y)$  of the object and  $B$  of the reference was transformed by a vidicon tube into the electrical signal

$$I(t) = A^2(t) + B^2 + 2A(t)B \cos[\omega t - \phi(t)] , \quad (1.34)$$

where  $\omega = k \sin \theta$ . The first two terms consist of the bias and very low frequency components which were removed by the filter. The carrier frequency was then removed by multiplying the third term of (1.34) by  $\cos \omega t$  and  $\sin \omega t$ . If this process is carried out for the complete Eq. (1.34), it gives

$$\left. \begin{aligned} C_R(t) &= I(t) \cos \omega t \\ &= [A^2(t) + B^2] \cos \omega t + A(t)B \cos[2\omega t - \phi(t)] \\ &\quad + A(t)B \cos \phi(t) \\ S_I(t) &= I(t) \sin \omega t \\ &= [A^2(t) + B^2] \sin \omega t + A(t)B \sin[2\omega t - \phi(t)] \\ &\quad + A(t)B \sin \phi(t) \end{aligned} \right\} \quad (1.35)$$

The spectra of these signals are shown schematically in Fig. 1.46. The spectrum containing the desired information of amplitude  $A$  and phase  $\phi$  is dispersed as the sideband around the zero spectrum. The first two unwanted terms in (1.35) are eliminated through the appropriate low pass filter, leaving only the third terms. These are then

$$\left. \begin{aligned} C_R(t) &= A(t)B \cos \phi(t) \\ S_I(t) &= A(t)B \sin \phi(t) \end{aligned} \right\}, \quad (1.36)$$

giving the desired amplitude and phase as

$$\left. \begin{aligned} A^2(t) &= C_R^2(t) + S_I^2(t) \\ \phi(t) &= \arctan[S_I(t)/C_R(t)] \end{aligned} \right\} \quad (1.37)$$

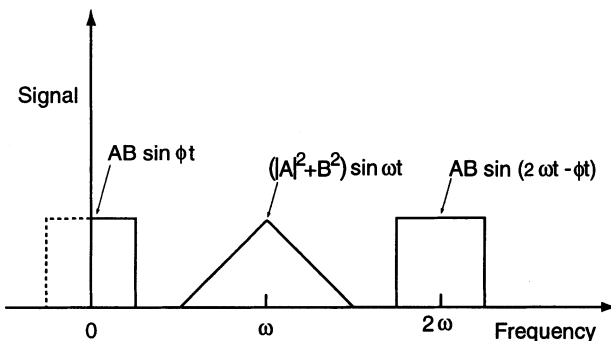


**Fig. 1.46.** Phase and amplitude extraction in the direct phase detecting system of Ichioka and Inuiya [1.95]. The spectrum of the signal  $S(t)$  or  $C(t)$  is shown

The system described displayed the phase map scaled linearly over the phase, modulo  $2\pi$ , as a video intensity distribution, enabling real-time analogue observation of the wavefront.

The above system, although extremely elegant, gives the wavefront in analogue intensity pattern form. In general, a digital output and analysis is an essential feature of high accuracy wavefront analysis. A general Fourier formulation of the problem of phase extraction from a *single interferogram* was given by Takeda et al. in 1982 [1.96]. Tilt is introduced to produce normal non-contour fringes. Since this formulation is general and physically instructive, we will summarise it here using the Takeda notation. The fringe pattern has the form

$$g(x, y) = a(x, y) + b(x, y) \cos[2\pi f_0 x + \phi(x, y)] , \quad (1.38)$$

where the phase  $\phi(x, y)$  is required and  $a(x, y)$  and  $b(x, y)$  are unwanted irradiance variations arising from unequal transmission or non-uniform reflections in the interferometer.  $b(x, y)$  is a measure of the fringe visibility. In general, these vary slowly compared with the variation due to the rapid spatial modulation introduced by the tilt carrier frequency  $f_0$ . Conventionally, the phase was obtained by setting the tilt frequency  $f_0$  to zero, giving contour fringes. The weaknesses are that the sign cannot be determined (confusion of "hills" and "valleys"); that the sensitivity is limited to  $2\pi$  (otherwise there are no fringes); and accuracy is affected by the variations  $a(x, y)$  and  $b(x, y)$ . These are the problems solved by temporal heterodyne techniques [1.91] [1.92] but they require precision phase-shifting hardware. Takeda et al. propose instead a general Fourier solution.

They assume an array detector with sufficient spatial resolution, particularly in the  $x$  direction perpendicular to the fringes, to satisfy the sampling theorem. Equation (1.38) is re-written as

$$g(x, y) = a(x, y) + c(x, y) \exp(2\pi i f_0 x) + c^*(x, y) \exp(-2\pi i f_0 x) , \quad (1.39)$$

where

$$c(x, y) = \frac{1}{2}b(x, y) \exp[i\phi(x, y)] \quad (1.40)$$

and  $c^*$  is the complex conjugate. Equation (1.39) is now Fourier transformed with respect to  $x$  by a fast transform (FFT) giving

$$G(f, y) = A(f, y) + C(f - f_0, y) + C^*(f + f_0, y) , \quad (1.41)$$

where  $f$  is the spatial frequency in the  $x$  direction. Since the spatial variations of  $a(x, y)$ ,  $b(x, y)$  and  $\phi(x, y)$  are slow compared with  $f_0$ , the Fourier spectra in (1.41) are separated by the carrier frequency  $f_0$ , as shown schematically in Fig. 1.47. We make use of one of the two sidebands, say  $C(f - f_0, y)$ , and translate it by  $f_0$  on the frequency axis to the origin to obtain  $C(f, y)$ . Again using the FFT, the inverse Fourier transform is calculated from  $C(f, y)$  with respect to  $f$  to obtain  $c(x, y)$ , given by (1.40). The complex logarithm gives

$$\log[c(x, y)] = \log \left[ \left( \frac{1}{2} \right) b(x, y) \right] + i\phi(x, y) , \quad (1.42)$$

in which the imaginary part gives the desired phase completely separated from the unwanted amplitude variation  $b(x, y)$  in the real part by using a filter centered at  $f_0$ . The carrier frequency  $f_0$  is then removed by shifting to the origin. The phase  $\phi$  is given from the real (Re) and imaginary (Im) parts of  $c(x, y)$  by

$$\phi(x, y) = \arctan [Re\{c(x, y)\}/Im\{c(x, y)\}] \quad (1.43)$$

Takeda et al. give a procedure for overcoming the limitation of modulo  $2\pi$  and determining a uniquely defined phase function. Such a procedure is termed *phase tracking* or *phase unwrapping* and various algorithms have been proposed [1.97].

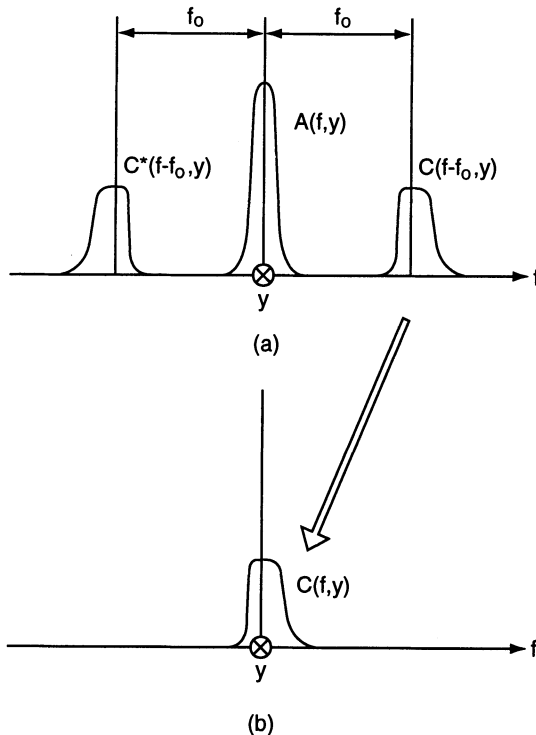


**Fig. 1.47a, b.** Separated Fourier spectra of a non-contour (i.e. tilted) type of fringe pattern. The  $y$ -axis is perpendicular to the paper. (After Takeda et al. [1.96])

The work of Takeda et al. was followed up by a notable paper by Mertz [1.98]. He pointed out that the Fourier transform calculation technique, though elegant and effective, was very slow for practical work and also unnecessary. The introduction of a tilt frequency  $f_0$  is simply *spatial heterodyning*. The tilt was set to give about 3 pixels per fringe in a TV video signal. Three separate signal channels each sense one phase of a three-phase stroboscope or moiré. This functions as a three-sample convolution filter having complex coefficients. The complex convolution is for the three adjacent samples A, B, C of the image

$$Z = A \exp(-2\pi i/3) + B \exp(0i) + C \exp(+2\pi i/3) , \quad (1.44)$$

whose real or cosine part is

$$C_R = (-1/2)A + B + (-1/2)C \quad (1.45)$$

and whose imaginary or sine part is

$$S_I = (-\sqrt{3}/2)A + (+\sqrt{3}/2)C \quad (1.46)$$

Then, as in Eq. (1.37), the phase including tilt is given simply by

$$\phi = -\arctan(S_I/C_R) \quad (1.47)$$

Mertz indicates the circuitry required to perform this convolution and shows practical results. This work showed that *spatial heterodyning* with 3 steps of

$2\pi/3$  can give all the information required to extract the phase in real time. With 3 pixels/fringe, the phase with tilt removed is

$$\phi = -\arctan(S_I/C_R) - 2\pi m/3 , \quad (1.48)$$

where  $m = 1, 2, 3$  is the pixel sampling at  $-2\pi/3, 0, +2\pi/3$ .

The Mertz method is called *sinusoidal fitting* by Macy [1.99], who compares its accuracy with that achieved by the FFT method of Takeda et al. above. He shows that the accuracy of sinusoidal fitting is less good because it allows negative spatial frequencies which are blocked by the Fourier transform function filter. The effects of negative frequencies can be removed by smoothing with a suitable filter function.

Womack [1.100] further developed the technique for deriving the phase from a single interferogram using spatial heterodyning with high tilt. Following Takeda et al. from Eq. (1.38), the fringe pattern in a general 2-dimensional formulation was given by

$$\left. \begin{aligned} g(x, y) &= a(x, y) + b(x, y) \cos 2\pi \phi(x, y) \\ g_R(x, y) &= \cos 2\pi \phi_R(x, y) \end{aligned} \right\} , \quad (1.49)$$

where  $\phi(x, y)$  and  $\phi_R(x, y)$  represent the unknown phase error and the known reference (spatial heterodyne) deviation respectively. The heterodyne product combination gave

$$\left. \begin{aligned} g(x, y)g_R(x, y) &= a \cos 2\pi \phi_R(x, y) \\ &+ \frac{b}{2} \cos 2\pi [\phi(x, y) + \phi_R(x, y)] \\ &+ \frac{b}{2} \cos 2\pi [\phi(x, y) - \phi_R(x, y)] \end{aligned} \right\} \quad (1.50)$$

If the difference between  $\phi(x, y)$  and  $\phi_R(x, y)$  is small, the third term represents a low spatial frequency term that can be, at least partially, separated out by low pass filtering. In the spatial domain, this filtering was achieved by convolving the product function  $g(x, y)g_R(x, y)$  with a window function  $h(x, y)$ . Assuming perfect isolation of the difference term, the difference of phase is given by

$$\phi(x, y) - \phi_R(x, y) = \frac{1}{2\pi} \arctan \frac{M_2(x, y)}{M_1(x, y)} , \quad (1.51)$$

where  $M_1$  and  $M_2$  are the third term of Eq. (1.50) and the same term with  $\sin 2\pi$  substituted for  $\cos 2\pi$  respectively,  $M_2$  corresponding to the same convolution for a reference spatially shifted by  $\pi/2$ .

In practice, this technique requires a window several periods wide, which implies a high tilt fringe density so that the spatial phase shift is negligible compared with the total pupil size. A rectangular window leads to serious side lobes: a much better filter is the Hamming function of the form  $h(x) = k_1 + k_2 \cos 2\pi x/x_0$ . The primary advantage of this so-called quadrature multiplicative moiré algorithm (QMM) is that the modulo  $\pi$  transitions

are widely spaced so that the measurements can be several fringes apart without causing difficulties in removing the transitions (unwrapping). A high accuracy was claimed, comparable with temporal heterodyne methods. However, with the microcomputer used, the time for the phase computation over a grid sampling of  $128 \times 64$  points and a least squares fit of tilt and focus was about 15 minutes. This calculation time was probably the weak point of the procedure.

All techniques for extracting phase data from a single interferogram using high tilt as a spatial reference are essentially based on the Takeda et al. approach in some form or other. Nugent [1.101] has analysed the errors arising from incorrect shifting of the sidelobe (i.e. an error in the definition of the spatial heterodyne frequency  $f_0$ ) and from non-linearity in the detector. He proposes algorithms for correcting these.

Before we proceed to further optimizations of such phase retrieval methods based on a single interferogram with spatial heterodyning using tilt, it is useful to return to the other approach of *temporal* heterodyning which was effectively introduced by Bruning et al. [1.91] [1.92], since the formulation and algorithms are closely related. The basic equations are given in many sources, for example by Bruning [1.91] [1.92], Wyant [1.94] [1.102], Grievenkamp [1.103] and Kinnstaetter et al. [1.104]. We start from the basic interferogram intensity equation (1.38) expressed in the form

$$I(x, y, l) = I_0(x, y) [1 + V(x, y) \cos \{\phi(x, y) - l\}] \quad , \quad (1.52)$$

where  $I_0$  is the mean intensity,  $V$  the fringe visibility,  $\phi$  the desired phase and  $l$  is a *temporally* variable reference phase. The data required for heterodyne interferometry are a series of interferograms recorded with different phase shifts  $l$ . In the heterodyne definition of Wyant [1.94],  $l$  varies linearly over a range  $\Delta l$  covering many periods and a sample interferogram  $i$  integrates the effect giving

$$I_i(x, y) = \frac{1}{\Delta l} \int_{l_i - \Delta l/2}^{l_i + \Delta l/2} I(x, y, l) dl \quad (1.53)$$

The phase shift at the center of each integration is  $l_i$  and the factor  $\Delta l$  is a normalization so that the integrated signal in each interferogram is independent of  $\Delta l$ . Equation (1.53) corresponds to the *integrating bucket* method first given by Wyant [1.102]. If the signal is read out continuously, this would give an infinite number of buckets. But if the signal is read out over a short time when the phase changes by  $\pi/2$ , a three bucket detection can be performed: from 0 to  $\pi/2$ , from  $\pi/2$  to  $\pi$  and from  $\pi$  to  $3\pi/2$  [1.94]. In the limit when  $\Delta l \rightarrow 0$ , the method reduces to the more common *phase stepping* technique of phase shifting interferometry (PSI), whereby the phase is held constant over the integration period, giving from (1.52)

$$I_i(x, y) = I_0 + I_0 V \cos(\phi - l_i) \quad (1.54)$$

The processing system in PSI is achieved by a correlation process in which Eq. (1.54) is multiplied by the functions  $\cos l_i$  and  $\sin l_i$  respectively of the

carrier frequency, giving

$$\left. \begin{aligned} I_i \cos l_i &= I_0 \cos l_i + \frac{1}{2} I_0 V [\cos \phi + \cos(\phi - 2l_i)] \\ I_i \sin l_i &= I_0 \sin l_i + \frac{1}{2} I_0 V [\sin \phi - \sin(\phi - 2l_i)] \end{aligned} \right\} \quad (1.55)$$

If the sum is taken of  $m$  such measurements over one or several complete cycles, it follows from the averaging and the orthogonality of the sine and cosine functions that the variable terms in  $l_i$  on the right-hand side of (1.55) vanish. This method is equivalent to synchronous detection techniques in communication theory [1.94]. We then have

$$\left. \begin{aligned} 2 \sum_{i=1}^m I_i \cos l_i &= m I_0 V \cos \phi \\ 2 \sum_{i=1}^m I_i \sin l_i &= m I_0 V \sin \phi \\ \sum_{i=1}^m I_i &= m I_0 \end{aligned} \right\}, \quad (1.56)$$

from which we calculate the phase as

$$\phi = \arctan \left[ \frac{\sum_{i=1}^m I_i \sin l_i}{\sum_{i=1}^m I_i \cos l_i} \right] \quad (1.57)$$

One of the commonest phase stepping techniques is to shift the phase  $l_i$  from zero in steps of  $\pi/2$ . This gives directly from (1.54) a set of 4 equations enabling the phase  $\phi$  to be determined:

$$\left. \begin{aligned} I_1(x, y) &= I_0 + I_0 V \cos \phi(x, y) \\ I_2(x, y) &= I_0 - I_0 V \sin \phi(x, y) \\ I_3(x, y) &= I_0 - I_0 V \cos \phi(x, y) \\ I_4(x, y) &= I_0 + I_0 V \sin \phi(x, y) \end{aligned} \right\} \quad (1.58)$$

The phase, modulo  $2\pi$ , is then given by

$$\phi(x, y) = \arctan \left[ \frac{I_4(x, y) - I_2(x, y)}{I_1(x, y) - I_3(x, y)} \right] \quad (1.59)$$

It follows from Eq. (1.54) with its three unknowns  $I_0$ ,  $V$  and  $\phi$  that *three* equations (measurements) are, in principle, sufficient to determine the phase. Introducing a constant bias of  $\pi/4$ , which has no effect but simplifies the equations [1.94], the values  $l_i$  are then  $\pi/4$ ,  $3\pi/4$ ,  $5\pi/4$ . This leads to

$$\phi(x, y) = \arctan \left[ \frac{I_3(x, y) - I_2(x, y)}{I_1(x, y) - I_2(x, y)} \right] \quad (1.60)$$

It is easily shown [1.94] that the 3-bucket detection system leads to an identical result.

The pioneer work of Bruning et al. [1.92] aimed to remove the following problems of static fringe analysis:

- Non-linearity effects of detectors, particularly photographic emulsions
- The need to introduce a spatial heterodyne frequency, i.e. tilt fringes
- The problems of atmospheric turbulence and vibration
- Difficulties of calibration of interferometer errors
- The lengthy and cumbersome operations of previous static analysis

The processing took 1–2 minutes over a 1024-element photodiode array and gave a real-time presentation. Excellent reproducibility was claimed giving  $\lambda/100$  accuracy.

The above system required collection of several data frames followed by digital processing, the phase changes being produced by a piezo-electrically-driven reference mirror. Massie et al. [1.105] aimed to improve the speed of real-time phase extraction by producing phase shifts by polarisation techniques using Bragg cells. The 3-signal method was exploited by Frantz et al. [1.106]. Massie's system was further developed [1.107] to give a serial data acquisition rate of 50 microsecond/point, a spatial resolution of 500 points/line and a phase accuracy of  $\lambda/100$ .

An important analysis of error sources in these techniques was given by Schwider et al. [1.108]. Suppose such sources lead to an error  $\Delta\phi$  between the measured phase  $\phi'$  and the true phase  $\phi$ . From (1.57) we have

$$\tan \phi' = \frac{\sum_{i=1}^m I'_i \sin l_i}{\sum_{i=1}^m I'_i \cos l_i} = \frac{N}{D} , \quad (1.61)$$

where  $N$  and  $D$  simply refer to the numerator and denominator of the measured functions of the tangent. Then, from

$$\Delta\phi = \phi' - \phi \quad (1.62)$$

and (1.61) we have

$$\Delta\phi = \arctan\left(\frac{N}{D}\right) - \arctan(\tan \phi),$$

which reduces to

$$\Delta\phi = \arctan\left[\frac{N \cos \phi - D \sin \phi}{D \cos \phi + N \sin \phi}\right] \quad (1.63)$$

Suppose the reference phase  $l_i$  has an error  $\varepsilon_i$ . If  $\varepsilon$  is small, one can set  $\cos \varepsilon = 1$  and  $\sin \varepsilon = \varepsilon$ . Using the orthogonality relations of the sine and cosine functions, Schwider et al. derive the following expression:

$$\Delta\phi = \arctan\left[\frac{\sum_{i=1}^m \varepsilon_i - C \cos 2\phi - S \sin 2\phi}{m - C \sin 2\phi + S \cos 2\phi}\right] , \quad (1.64)$$

in which

$$\left. \begin{aligned} C &= \sum_{i=1}^m \varepsilon_i \cos 2l_i \\ S &= \sum_{i=1}^m \varepsilon_i \sin 2l_i \end{aligned} \right\} \quad (1.65)$$

This is an important relation showing that only terms in  $\sin 2l_i$ ,  $\cos 2l_i$ ,  $\cos 2\phi$  and  $\sin 2\phi$  occur, apart from the linear term with mean value

$$\frac{1}{m} \sum_{i=1}^m \varepsilon_i$$

However, constant contributions independent of  $x, y$  are eliminated by the least squares reduction algorithm, so phase disturbances stem only from the  $\phi$ -dependent terms. They show that the simple 4-step algorithm of (1.59), having the merit of being very fast, is sensitive to such reference phase errors. Schwider et al. give modified algorithms for reducing this sensitivity and that due to other errors. They achieved repeatabilities in experiments to better than  $\lambda/200$ . One of their techniques is to use multiple sampling with  $m > 4$ .

Grievenkamp [1.103] gives an algorithm similar to Wyant's 3-bucket algorithm mentioned above yielding improved accuracy and permitting unequal spacing of the phase steps and a range greater than  $2\pi$  with 3 or more steps.

Hariharan et al. [1.109] propose an error-compensating algorithm using 5 measurements, improving on a self-calibrating 4-measurement algorithm due to Cheng and Wyant [1.110]. The 5-measurement algorithm gives the phase as

$$\phi = \arctan \left[ \frac{2(I_2 - I_4)}{2I_3 - I_5 - I_1} \right] \quad (1.66)$$

Kinnstaetter et al. [1.104] developed a technique whereby the errors can be displayed in an analogue way with Lissajous figures, enabling direct interpretation of the nature and amount of the errors.

A general Fourier description of digital phase-measuring interferometry, interpreting the heterodyning as a filtering process in the frequency domain, is given by Freischlad and Koliopoulos [1.111]. They derive phase error functions in terms of a phase shift error  $\varepsilon$  for six cases:

- Case 1: 4 samples with  $\pi/2$  steps
- Case 2: 4 samples with  $\pi/2$  steps, but with a constant phase shift compared with case 1
- Case 3: 3 samples with  $\pi/2$  steps
- Case 4: 3 samples with  $\pi/2$  steps, but with a constant phase shift compared with case 3
- Case 5: 3 samples with  $2\pi/3$  steps
- Case 6: 5 samples with  $\pi/2$  steps

They show that case 6 using 5 samples at  $\pi/2$  steps [1.108] [1.109] gives the lowest errors resulting from systematic effects such as a phase shift error  $\varepsilon$  or from harmonic effects. An improved 4 sample algorithm is also given. They point out that filter functions with weighted samples can reduce the higher order spectral content of the filter functions, thus improving the phase measuring accuracy. For random errors, the advantage of case 6 is less clear.

The aim of all this work in phase shifting interferometry (PSI) from its introduction in 1974 [1.92] onwards was to improve two aspects: the phase measuring precision by better algorithms and the speed of the processing to get genuinely real-time measurements. This latter is also fundamental to absolute accuracy because of the advantage in averaging out vibration and air turbulence.

The ultimate solution for the application of temporal heterodyning (PSI) to *large optics* would appear to be at the time of writing (1992) the *Simultaneous Phase Shift Interferometer* (SPSI) of Koliopoulos [1.112]. The PSI systems discussed above can give accuracies better than  $\lambda/100$  routinely, but are still limited in large optics by vibration and air turbulence. Vibrations reduce fringe contrast and produce rapid phase jumps. Air turbulence effects can only be reduced by averaging: the more random the effects, the better will be this reduction. Air stirring is therefore helpful to reduce systematic effects such as astigmatism.

Vibration can be much reduced by damping systems, but a system which can accept a certain amount of vibration has huge technical advantages. Twyman-Green interferometers are sensitive to both path-length (piston) and tilt errors. Common path interferometers such as shearing, scatterplate or point diffraction (Smartt) interferometers are much less sensitive to piston change but are still sensitive to tilt.

PSI methods must all read out intensity data over a solid state detector array with high sampling. If several measures (3, 4, 5) are made with corresponding phase shifts *in a sequential mode*, the processing time is inevitably correspondingly greater. This limits the real-time averaging possibilities because the phase shifts are falsified over the exposures. The obvious solution is *parallel channel* phase shift interferometry using polarising methods, as proposed by Massie et al. [1.105] [1.107] and later by Smythe and Moore [1.113] in a 4-channel system. The phase shifted information is available simultaneously for all channels.

The preferred algorithm uses 4 channels because of the hardware convenience. It is the improved algorithm referred to above [1.111], whereby the phase at each digitized pixel location is calculated by

$$\phi(x, y) = \arctan \left[ \frac{I_1 + I_2 - I_3 - I_4}{-I_1 + I_2 + I_3 - I_4} \right] \quad (1.67)$$

This phase algorithm minimizes phase errors due to small intensity variations between the channels by correlating with a sampled sinusoidal reference function. The four intensities are digitized simultaneously with four separate digitizers.

Figure 1.48 shows the layout of the SPSI system. The major features are:

- 4 simultaneous phase-shifted interferograms are created
- 4 electronically-shuttered CCD cameras freeze the fringe motion
- 10 mWatt He-Ne laser allows very short exposure times

- Polarisation-based Twyman-Green (LUPI) interferometer
- Afocal imaging system
- Cameras aligned to sub-pixel tolerances
- Interferometer wavefront accuracy  $< \lambda/15$  over 10 mm aperture
- Wavefront measurement accuracy is better than  $\lambda/50$  ptv for a single measurement
- Adjustable fringe contrast without changing the reflectivity of the reference mirror

The four phase-shifted interferograms are generated by polarisation splitting and amplitude separation in a dielectric coated beamsplitter (BS) of Fig. 1.48. The 4 phase shifts of the two arms are 0,  $\pi$  and  $\pi/2$ ,  $3\pi/2$  respectively.

Parallel read-out of the 4 channels is not in itself sufficient to overcome severe vibration effects. This also requires extremely short exposure times, otherwise fringe contrast is not adequate. The electronic shuttering and powerful laser permit exposure times down to  $10^{-4}$  second. The polarisation phase-shift system is very stable requiring minimal calibration. Standard CCD cameras with format  $384 \times 242$  pixels are used. The PC calculates the phase map with software commercially available from the firm Phase Shift Technology. Phase maps containing 40 000 points can be calculated within 10 seconds; Seidel aberration coefficients with tilt and focus subtraction require a further 6 seconds. With a special interface, the phase map can be calculated modulo  $2\pi$  in real time, offering data at 0.017 s rates. A reference back-up system

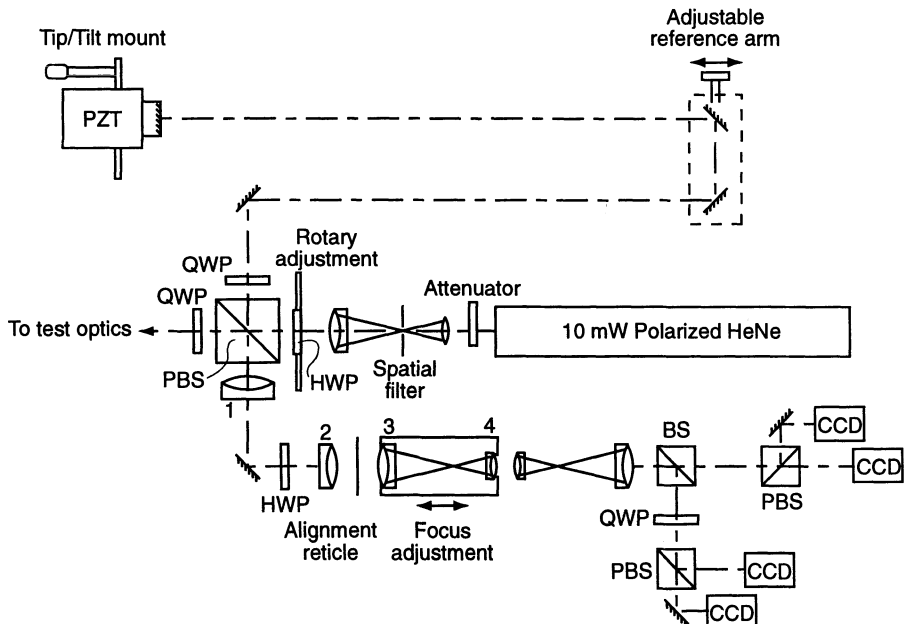


**Fig. 1.48.** Layout of the Simultaneous Phase Shift Interferometer (SPSI). From Koliopoulos [1.112]

using one channel allows operation in a conventional PSI mode by moving the reference mirror with a piezoelectric transducer.

The parallel detection system has the disadvantage that the automatic removal of detector characteristics with a *single* detector is lost. The biggest problem arises from optical coherent noise differences in the different channels due to dust, surface and coating errors and interference and scattering effects in the CCDs. Without care to reduce these errors, they may amount to  $\lambda/20$  ptv. *Such phase disturbances must be reduced by careful cleaning and good quality coating of the optics.* There are also spatially independent error sources due to the channel splitting mechanism. Alignment of the system is performed using the Lissajous figures technique of Kinnstaetter et al. [1.104].

Repeatability in a test case gave phase maps within  $\lambda/1000$  rms over a  $6\sigma$  range. The ptv variation was about  $\lambda/100$ .

Unquestionably, this SPSI system represents one of the most powerful test tools available for large optics, above all because the total exposure time for the 4 interferograms can be as short as  $10^{-4}$  sec. It is also a particularly effective test tool for measurement in air-flow (wind tunnel) applications.

We return now to the latest advances in the alternative technique of phase measuring interferometry, that using a *a single interferogram and spatial heterodyning by a large tilt*, following the pioneer work described above by Ichioka and Inuiya [1.95], Takeda et al. [1.96] and Mertz [1.98]. This line of development has profited in parallel from the algorithm development and error analysis in PSI.

The most sophisticated equipment of this type is the *DIRECT 100* system, developed at Carl Zeiss, Oberkochen, by Küchel et al. [1.114]. Küchel points out that, until the development of modern phase measurement techniques, optical manufacture was the only branch of manufacture where the measurement accuracy was of the same order as the tolerances. This was the essential barrier to improved manufacture and is the reason why a precision of  $\lambda/100$  has brought a revolution in manufacturing efficiency. Conventional PSI could achieve this accuracy on a small scale; but it was too slow to cope with the vibration and air turbulence problems of large optics. Only the very fast SPSI variant of temporal phase shifting developed by Kolopoulos can cope with these.

*DIRECT 100* (DMI) is an extremely fast system using spatial phase shifting by tilt for measurements on a single interferogram. "Fringes" can be displayed in real time, but they are no longer the physical intensity fringes: they are a calculated fringe pattern from the phase map measured. They can be manipulated as desired. The wavelength can be chosen at will, or a pre-defined wavefront can be subtracted. Because of the rapidity of short exposure times of the order of 20 milliseconds and a phase unwrapping time of 40 ms, a genuine real-time presentation is possible. A certain level of vibration becomes an advantage, as it provides a sort of temporal heterodyne overlay which improves the averaging. The main features are:

- Real-time wavefront calculation and display
- Real-time display of wavefront gradients
- Real-time wavefront averaging
- Real-time correction of systematic residual errors of the instrument
- Insensitivity to vibrations
- Built-in “electronic hologram”
- Modular concept of the instrument
- Broad-band optics and 2 lasers
- Spatial resolution  $480 \times 480$  points
- Automated testing sequences available (testing robot)
- Capability of averaging 1000 wavefronts in 1 minute (cycle time 60 ms) gives reproducibility better than  $\lambda/200$ , even with poor turbulence conditions
- Because of the short exposure time (20 ms), fast phenomena such as the wavefront from a pulsed laser can be recorded

The application to the testing of large optics is shown in Fig. 1.49. This total system includes the possibility of active vibration stabilization in 3 dimensions. This stabilization had more significance before the introduction of the DMI system. It is only necessary to avoid high vibration frequencies which would seriously reduce the fringe visibility over an exposure time of 20 ms.

The evaluation is based on the spatially heterodyned fringe pattern of Eq. (1.38) or Eq. (1.53). Following Küchel [1.116] [1.117], we will write this in the form

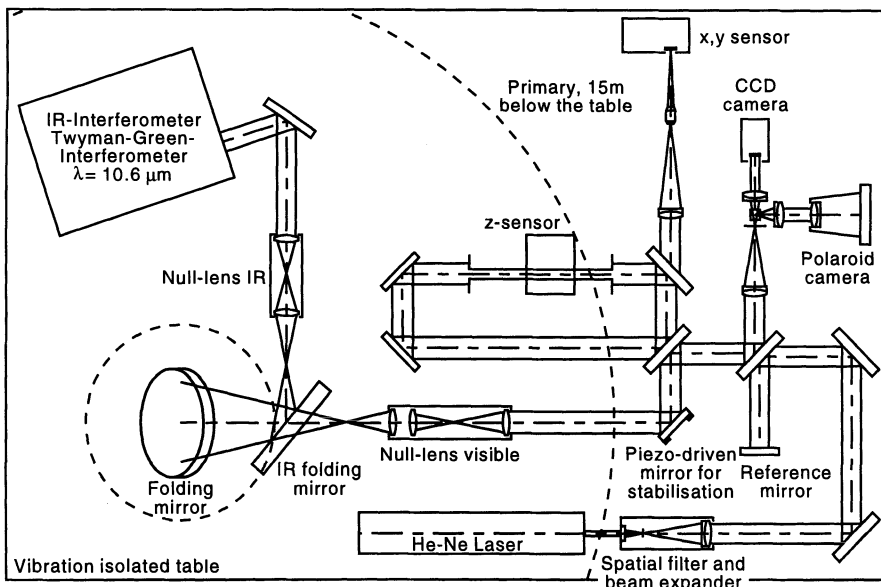


**Fig. 1.49.** Schematic of the test set-up at Carl Zeiss, Oberkochen, for large optics, including active vibration stabilization (from Küchel and Heynacher [1.115])

$$I(P) = A + B \cos(\phi + P) , \quad (1.68)$$

with  $\phi$  the phase to be measured which modulates the tilt carrier wave  $P$ . This can formally be either spatial or temporal. The constant function  $A$  includes ghost reflections from null systems, above all of the Offner type (see § 1.3.4) giving sharp reflection zones, which are objectionable even if they can, in principle, be calibrated out. This effect (see Fig. 1.50 (a)) can be largely removed by using 2 interferograms instead of one, where the second has a phase shift  $\delta$  of about  $\pi$  compared with the first. Then from (1.68), with fringes perpendicular to the  $x$ -direction:

$$\begin{aligned} \Delta I(x) &= I_b(x) - I_a(x) \\ &= 2B(x) \sin(\delta/2) \cos[\phi(x) + P(x) + \delta/2 + \pi/2] \end{aligned} \quad (1.69)$$

The phase constants  $(\delta + \pi)/2$  are in the argument of the cosine function and have no effect on  $\phi$ . Since the modulation  $B(x)$  of the interferogram is only a slow and small variation of  $x$ ,  $\Delta I(x)$  is almost a pure cosine function with a period  $x_0$ , where  $P(x) = 2\pi x/x_0$ , which can be demodulated very accurately. The processing steps are shown in Fig. 1.50.

We will now consider the algorithm which is discussed by Küchel [1.117] and is a major feature of the success of the DMI system.

The phase modulated signal is measured at 5 different phase values  $P_m$  with  $m = 1 - 5$  giving 5 equations of the form

$$I_m = A + B \cos P_m \cos \phi - B \sin P_m \sin \phi \quad (1.70)$$

These 5 equations can be evaluated in 3 groups of three equations using  $I_1, I_2, I_3; I_2, I_3, I_4; I_3, I_4, I_5$  to give the phase  $\phi$  in terms of  $P_m$  in the form  $\phi_n$  with  $n = 1 \dots 3$ :

$$\phi_n = \arctan \left[ \frac{I_n(\cos P_{n+1} - \cos P_{n+2}) + I_{n+1}(\cos P_{n+2} - \cos P_n) + I_{n+2}(\cos P_n - \cos P_{n+1})}{I_n(\sin P_{n+1} - \sin P_{n+2}) + I_{n+1}(\sin P_{n+2} - \sin P_n) + I_{n+2}(\sin P_n - \sin P_{n+1})} \right] \quad (1.71)$$

If the measurements were error-free, the 3 values of  $\phi_n$  would be identical. If, for example, an error  $\varepsilon_2$  is introduced into the nominal value of  $P_2$  in the equation for  $\phi_1$  of (1.71), then, if  $\varepsilon \ll \pi/2$ ,

$$\phi_1^* = \frac{N_1^*}{D_1^*} = \frac{\sin \phi^*}{\cos \phi^*} = \frac{N_1 - \varepsilon_2 \sin P_2(I_1 - I_3)}{D_1 + \varepsilon_2 \cos P_2(I_1 - I_3)} \quad (1.72)$$

This is the same error function as that given by Schwider et al. [1.108] in Eqs. (1.63) to (1.65), since it reduces to the form

$$\tan \phi_1^* - \tan \phi_1 \simeq -\tan \phi_1 \left( \frac{\Delta D_1}{D_1} + \frac{\Delta N_1}{N_1} \right) , \quad (1.73)$$

where  $\Delta D_1 = \varepsilon_2 \cos P_2(I_1 - I_3)$  and  $\Delta N_1 = \varepsilon_2 \sin P_2(I_1 - I_3)$ . In the Küchel algorithm, the individual values  $\phi_n$  are not calculated. Instead he calculates a mean phase value  $\phi$  from

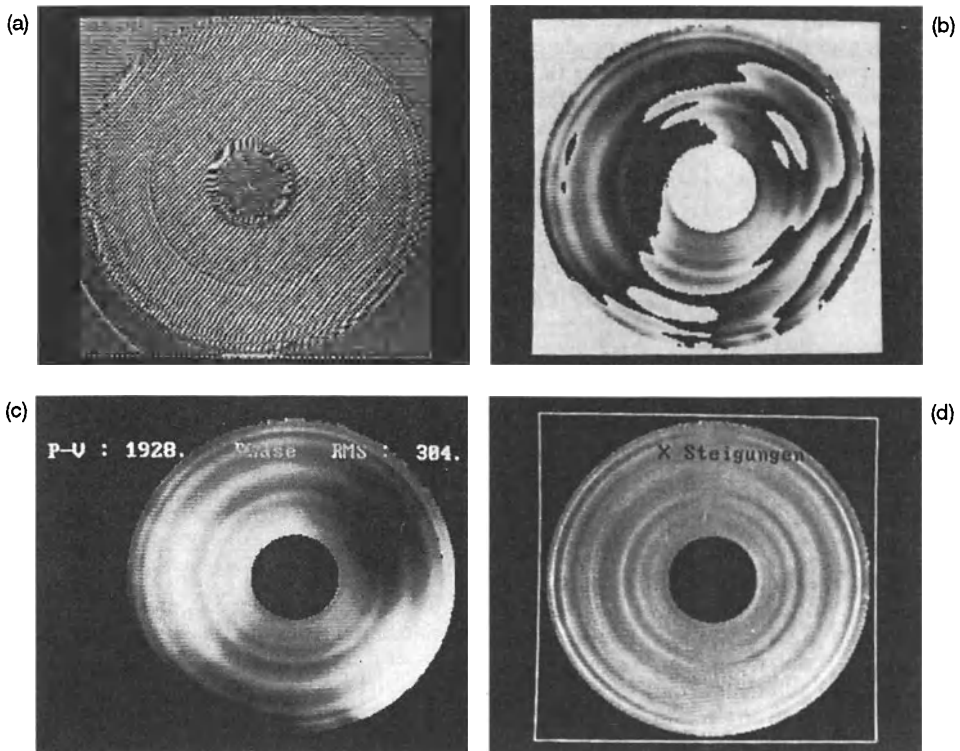


**Fig. 1.50.** Interferogram evaluation with the Carl Zeiss DMI method. (a) Typical interferogram showing ring ghost reflection from the Offner-type null system. (b) Phase map modulo  $2\pi$ . (c) Unwrapped phase map, showing astigmatism. (d) Phase gradients in the  $x$ -direction. (From Küchel [1.116])

$$\phi = \arctan \left( \frac{N}{D} \right) = \arctan \left[ \frac{\alpha_1 N_1 + \alpha_2 N_2 + \alpha_3 N_3}{\alpha_1 D_1 + \alpha_2 D_2 + \alpha_3 D_3} \right] , \quad (1.74)$$

in which each individual numerator  $N$  and denominator  $D$  is multiplied by a factor  $\alpha_n$ , which has no effect on the individual phase values. The effect of these weighting factors is to change the metric and hence the slope of the error function so that 3 zero points are obtained by a suitable choice of the  $\alpha_n$ . The procedure is the equivalent of achieving achromatism by eliminating the linear tilt of the chromatic function, which is also equivalent to changing the metric of the focal length of the system for one colour to match that of the other. If, instead of 5 phase shift values,  $m$  are taken, then in general there are  $m - 2$  zero points. The algorithm is therefore very insensitive to phase shift errors.

The geometry of the pixels of the detector determines the spatial phase shift. This is shown in Fig. 1.51, where a window of nine pixels scans fringes placed at  $45^\circ$  to the pixel pattern as shown. This gives 5 phase shifts over the window with pixel numbers as follows:  $64 = -\pi$ ;  $54, 63 = -\pi/2$ ;

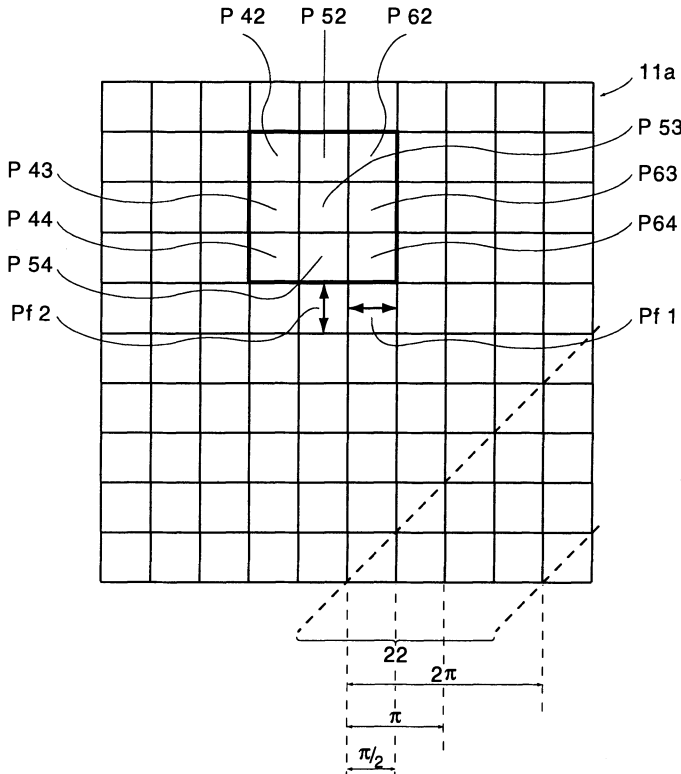


**Fig. 1.51.** The Carl Zeiss DMI system: fringe scanning with tilt fringes at  $45^\circ$  to the pixel raster (after Küchel [1.117])

$44, 53, 62 = 0; 43, 52 = +\pi/2; 42 = +\pi$ . The basic pixel step is  $\pi/2$ , giving a high fringe density and spatial resolution for a  $480 \times 480$  pixel CCD camera.

Figure 1.52 shows the complete DMI system in function. Averaging is possible over a maximum of 65 000 phase maps (1 hour). Statistical air turbulence is deliberately introduced by a fan, so that not only vibration but also air turbulence is completely averaged out.

The spatial heterodyning system appears to have reached its culmination in the Carl Zeiss DMI system. It appears to have two advantages over the ultimate temporal heterodyning method of Koliopoulos with the parallel reading SPSI system described above, namely a single detector and a single interferogram for the basic information. A disadvantage is that the high tilt places more demands on the interferogram optics, but this is a soluble problem.

The firm REOSC, Paris, has developed an evaluation system also based on the measurement of a *single* interferogram with a *single* detector using spatial rather than temporal heterodyning [1.118]. This system, which is called



**Fig. 1.52.** The Carl Zeiss DMI system in function. Reproduced from a Carl Zeiss brochure "Laser Interferometer DIRECT 100" (1991) (courtesy Carl Zeiss)

FLIP (FLow Interferogram Processing), uses a new algorithm for processing the information in each interferogram and was developed for the testing of the four VLT primary mirrors of 8.2 m diameter for ESO. The elimination of vibration and air turbulence effects requires the averaging of several thousand interferograms. With a sampling of  $256 \times 256$ , the system must be capable of analysing an interferogram in less than 1 second, the exposure time being of the order of a millisecond. Fourier transform methods were considered but found to be too slow and too sensitive to errors. Temporal phase shifting in conventional form was found to be too slow to overcome high frequency vibrations. FLIP overcomes these problems by its speed and by an algorithm dealing with the measurements on each pixel of the interferogram. This avoids boundary effects and permits parallel processing – hence the *FL* in the acronym FLIP. FLIP also has the following important characteristics: it does not need a separate "unwrapping" calculation in order to calculate the phase map; a theoretical error of phase calculated by FLIP is a function of tilt and piston, and this error is completely removed by averaging if the tilt and piston errors are random, as provoked by vibration. The accuracy was tested by simulated known errors, such as spherical aberration, a sharp zone with a triangular intensity function, and high frequency ripple of very low amplitude originating from the VLT primary axial supports, on to which errors were superimposed errors due to non-uniformity of illumination by the laser and of reflectivity of the mirror. It was initially also tested in practice

with great success in the manufacture of two 1.7 m aluminium mirrors and was then introduced as the general test system for precision optics. It uses commercial, modest cost, electronic systems to achieve the required speed. The system appears to have completely fulfilled the stringent requirements for the fabrication of the VLT 8.2 m primaries.

**1.3.2.5 IR interferometry.** It has been mentioned above that modern, steep mirrors are so highly aspheric that they cannot be aspherized by polishing alone. The efficiency of grinding (lapping) arising from the Preston constant (see above) is about 10 times higher. Although, earlier, more was removed by polishing, the rational limit today is about 10  $\mu\text{m}$ . In comparison, the f/2.2 NTT primary required removal of about 200  $\mu\text{m}$  relative to the best-fitting sphere. Systematic aspherizing by lapping requires an accurate test method. One such successful method is a LUPI interferometer using an IR source, as used at Carl Zeiss, Oberkochen. A CO<sub>2</sub> laser supplied by WYKO is used, with  $\lambda = 10.6 \mu\text{m}$ . At this wavelength, the lapped surface is optically “smooth”. Of course, null systems are also used (see Fig. 1.49). The lapping process can be taken to within about 1  $\mu\text{m}$  of the final surface, minimizing polishing.

**1.3.2.6 Other interferometers in the workshop for large optics.** In Chap. 2, other interferometers are considered from the point of view of functional tests of telescopes using natural stars, for which the Twyman-Green form cannot be applied. In the workshop, such forms had some advantages over the Twyman-Green form. However, the LUPI form of the Twyman-Green, using modern fringe measuring techniques as outlined in § 1.3.2.4, is so accurate, rapid and powerful that the earlier disadvantages no longer exist. Of course, such evaluation techniques can also be applied to transverse wave-shearing interferometers or point diffraction interferometers, but there is no evident advantage over LUPI. The reader is referred to Malacara [1.74] for further information.

### 1.3.3 Test procedures other than interferometry

The primary of the Palomar 5 m telescope was mainly tested by the *Foucault knife-edge test* using zonal masking (see Chap. 5 of RTO I). The knife-edge test remains unbeaten in sensitivity, but has been limited in practice by the difficulty of obtaining *quantitative* results. Its quantitative automation requires accurate photometry which is much more difficult than the phase measurement of fringe scanning interferometry. This classical method dates from the time before null systems – see § 1.3.4 – were introduced. These now play an essential role in the professional manufacture of large optics. However, smaller workshops may wish to avoid their use, for cost and technical reasons. The interferometric zonal method of Liu et al. [1.90], referred to in § 1.3.2.3, is a modern alternative to Foucault zonal testing.

The complication of photometric evaluation limiting the Foucault test also applies to the *Roddier curvature sensing* method, discussed in Chap. 2. This technique, which has become very effective for testing functional telescopes, is unlikely to rival interferometry in the workshop.

*Hartmann testing* (see Chap. 2) was a major rival to interferometry until fringe scanning methods were introduced, because it was much less sensitive to vibration. It can be used for testing at the center of curvature of a concave aspheric mirror in two modes: with or without a null (compensation) system. Compared with fringe scanning interferometry, classical Hartmann testing with a large screen in combination with null systems must be considered an old-fashioned technology. However, modern variants, such as Shack-Hartmann, can be applied in a similar test set-up to that used for LUPI interferometry. In principle, it could be automated in a similar way to fringe scanning methods, but is unlikely to rival the accuracy and convenience of the fringe scanning systems described above. It retains its interest for a completely independent cross-check for acceptance tests and was used in this way for the primary of the NTT.

Of more interest today is the use of a Hartmann test *without* a null system as an independent check on the null systems. This technique has been successfully applied by REOSC. It has sufficient accuracy that agreement on the value of the spherical aberration (the critical aberration for null systems – see § 1.3.4) within about 30 nm ptv has been obtained [1.25]. The center of gravity of the Hartmann spots of a cross-arm screen can be measured to about 10 µm. The method is particularly useful for determining the Schwarzschild aspheric constant  $b_s$  [1.119] if the radius is accurately known, e.g. from spherometry – see below.

Apart from the use of IR LUPI interferometry for testing aspherics generated by grinding, REOSC also successfully apply *bar spherometers* [1.25]. For the VLT 8.2 m primaries, REOSC used bar spherometers with a length of 1.64 m. The measuring accuracy is 0.1 µm rms. The total accuracy of a profile determination is about 1 µm for low frequency errors, the measurements being performed by shifting the spherometer about half its length. The spherometer is calibrated against a suitable spherical mirror, so only small differences require to be measured. The complete measurement of a net of points can be made in about 30 min thanks to the automated positioning of the spherometer by the carriage of a milling machine. Because several diameters are measured, astigmatism can also be detected within the global accuracy of the system [1.120]. Curved bar spherometers – three points on a circle instead of a straight line – are also used [1.25]. Spherometers give both the radius of curvature and the aspheric constant.

For the VLT, REOSC [1.120] uses the bar spherometer system above all during rough grinding of the aspheric. During fine grinding, IR interferometry is preferred, since it gives a higher accuracy of about 500 nm ptv. Testing during polishing is entirely with the FLIP fringe scanning interferometry system, as described above.

The enormous potential of mechanical measuring systems has been emphasized by Miller [1.121] in connection with the manufacture of the secondary for the Keck 10 m telescope. A 2-coordinate *profilometer* was used, with a read-out accuracy of 25 nm. For a whole measurement, an accuracy of  $\lambda/10$  (50 nm) was attained. According to Miller, if the beam of the carriage is replaced by a reference flat, an accuracy of 10 nm would be attainable. Such profilometers may have an important role to play in future optical testing.

### 1.3.4 Null (compensation) systems

Figures 1.44 and 1.49 show schematically the use of null, or compensation, systems in the test arm of a LUPI interferometer for testing aspheric concave mirrors at their center of curvature without spherical aberration. A parabolic primary can be tested without spherical aberration from its focus against a flat mirror in autocollimation without a null system, but this is limited to primaries no larger than an available test flat. Large, high quality plane mirrors are extremely difficult to make and test and are correspondingly expensive. Very few test flats larger than 1 m diameter exist.

If, in Fig. 1.44, the null system is omitted, the situation of Fig. 1.53 obtains. The so-called diverger  $D$  of the interferometer is a high quality optical system producing a convergent beam with negligible spherical aberration over the relative aperture required to cover the test mirror. A spherical test mirror then gives a zero aberration test system without a null system. An aspheric (hyperbolic) mirror  $M$ , placed such that rays strike its edge zone normally, returns these along their own paths to  $O$ ; but the zones nearer the axis are steeper and reflect the rays to an axial point  $O'$  nearer to  $M$  than is the point  $O$ . They therefore converge in the interferometer and show strong zonal spherical aberration for a strongly aspheric mirror. Furthermore, they traverse the diverger  $D$  and the interferometer with different paths from those of the incident beam. In general, the diverger  $D$  will not be free from aberration for a non-parallel beam and will add a further error to the final detected aberration. The purpose of the null system is to introduce aberration which accurately compensates the theoretical aberration of the desired

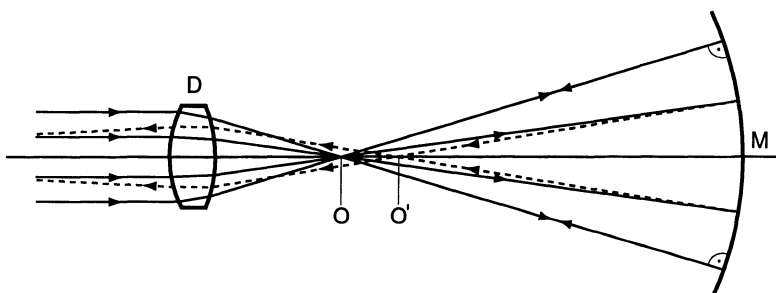


**Fig. 1.53.** Effect of testing a strongly aspheric concave mirror at its center of curvature without a null system

mirror. Then all rays will strike the mirror, having the correct aspheric form and being correctly placed, normally: all rays return exactly along their own paths giving an aberration-free image exactly as with a spherical mirror tested without a null system. Figure 1.54 shows schematically the two ways this can be achieved. In Fig. 1.54 (a), a normal aberration-free diverger  $D$  is used followed by a null system  $N$  which produces the large longitudinal spherical aberration  $O' O''$  corresponding to the theoretical radius difference of the required aspheric. In Fig. 1.54 (b), the functions of diverger  $D$  and null system  $N$  are combined.

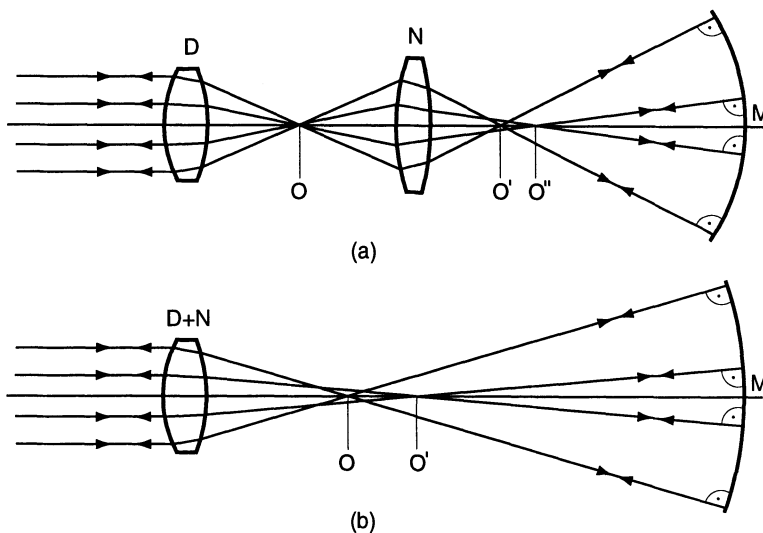


**Fig. 1.54.** Two ways of building a null system into a LUPI interferometer: (a) using an aberration-free diverger and a separate null system, (b) a combined diverger-null system

The function of the null system can also be understood as a system producing a highly aberrated wavefront. This aspheric wavefront, at the correct position  $M$  defined by the curvature of the required mirror, must be physically materialized on the front surface of the mirror blank.

An excellent review of the development of null testing is given by Offner [1.122]. The technique was apparently invented by the great French optician Couder [1.123] in 1927, who used a roughly afocal, 2-lens compensator for testing a 30 cm f/5 paraboloid with the Foucault test (Fig. 1.55). The significance of this invention was not generally recognised at the time. Burch proposed a compensator using a spherical mirror [1.124] and then a single planoconvex lens compensator in double pass for paraboloids of modest relative aperture ( $f/8$ ) [1.125]. According to Offner [1.122], a compensator was also in use during the manufacture of the Palomar 5 m  $f/3.3$  primary, as computed by Ross [1.126], who designed the PF field correctors for that telescope

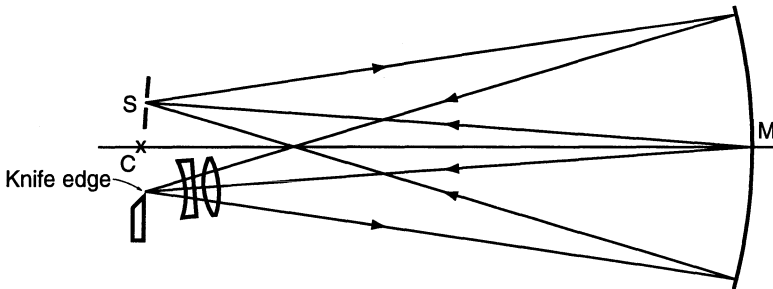


**Fig. 1.55.** Roughly afocal, 2-lens compensator used by Couder [1.123] in single pass for testing a paraboloid with the Foucault test (after Offner [1.122])

– see Chap. 4 of RTO I. The Ross solution, unlike that of Couder, was in double pass on the mirror axis, the modern solution. The lens had a diameter of 25 cm but, for the large  $f/3.3$  paraboloid of the Palomar telescope, still had too much zonal error. This was compensated by a weak aspheric plate (Fig. 1.56). In modern null systems, it is a rule that no aspheric surface is acceptable, since its manufacture poses similar problems to those of the test piece.

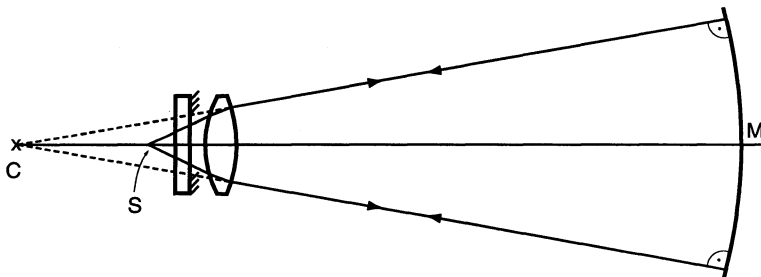


**Fig. 1.56.** Double-pass lens compensator design by Ross [1.126] for testing the 5 m,  $f/3.3$  Palomar primary (after Offner [1.122])

Compensation testing only became general following the work of Dall [1.127] [1.128]. He re-invented the scheme of Couder, but using a single plano-convex (non-afocal) lens with plane face towards the mirror. Dall pointed out that the aberration introduced by the lens could be increased or reduced by moving it towards or away from the mirror: with a single lens, paraboloids of different focal lengths or apertures could be tested. Figure 1.57 shows the Dall magnification parameter  $m = s'/s$  [1.122]. If  $n$  is the refractive index,  $f_p$  is the focal length of the parabola and  $f_l$  that of the lens, Offner gives the relation for balancing the aberration of the parabola at its center of curvature as

$$\frac{f'_p}{f'_l} = \frac{1}{4}(m-1)^2 \left[ \frac{n^2(m-1)^2}{(n-1)^2} + \frac{(3n+1)(m-1)}{(n-1)} + \frac{3n+2}{n} \right] \quad (1.75)$$

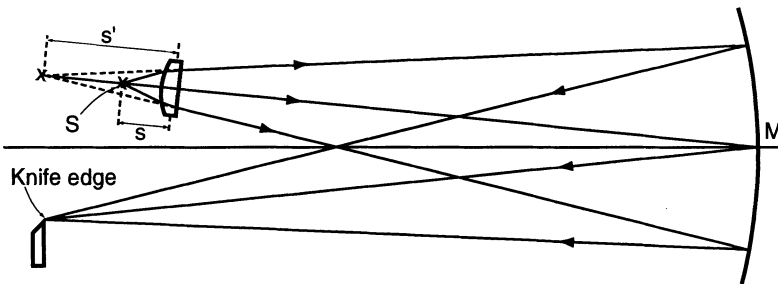


**Fig. 1.57.** Single-pass plano-convex lens compensator due to Dall [1.122] [1.127] [1.128]

This formula is derived from the general formula for the third order spherical aberration of a thin lens in terms of its “shape” and “magnification” factors [1.129] and was used in another special case in Eq. (4.52) of RTO I. Dall found the compensation was adequate if the ratio of Eq. (1.75) lies between 5 and 20. This system has since been widely used both by amateurs and professionals. Offner [1.122] quotes the following example. For a paraboloid of 0.6 m aperture with f/5 we have  $f'_p = 3$  m. Taking  $n = 1.52$  and setting  $m = 2$  arbitrarily gives  $f'_p/f'_l = 5.888$ , within the limits set by Dall for adequate compensation of zonal error. Then  $f'_l = 0.5095$  m, giving from the basic lens formula (Eq. 2.8 in RTO I)

$$1 - m = \frac{s'}{f'} \quad (1.76)$$

with  $m = 2$  the value  $s' = -f' = -0.5095$  m and hence  $s = -0.25475$  m. The zonal wavefront error is  $0.048 \lambda_{\text{rms}}$  for  $\lambda = 632.8$  nm. Dall [1.128] gives a curve for the calculation, assuming  $n = 1.52$ .

For large professional optics, special null systems are calculated and made according to the requirements of the mirrors to be tested. The set-up shown in Fig. 1.54(a) has advantages over the Couder or Dall arrangement in that the intermediate image enables more positive power to be used in the null system  $N$ . The positive power gives spherical aberration of the right sign to compensate aspheric mirrors with a Schwarzschild constant  $b_s < 0$ , i.e. normal cases of elliptical, parabolic or hyperbolic primaries. However, steep mirrors of large sizes would require very large lenses if the zonal error is to be reasonable. This is normally not practicable, although the set-up (a) is more flexible than (b) in that the diameter can be chosen at will. The normal solution is to compensate the zonal error (fifth or higher order spherical aberration) by a further lens or lenses. If the lenses are fairly close together near the maximum beam diameter, then “compact” null systems with 2 or 3 lenses, rather like the Couder system except that there is considerable positive power, can give excellent compensation [1.130]. If one lens is near the aberrated intermediate image  $O''$  in Fig. 1.54(a), then the null system is of the *Offner* type [1.131]. The latter type, which we consider below, gives a

beautifully flexible control of zonal error, but has the disadvantage of being much more sensitive to stray light (see Fig. 1.50 (a)). With compact systems, the zonal error control is more difficult and often requires more lenses. The set-up of Fig. 1.54 (b) is normally compact but, by increasing its length, can also be given the Offner form. Its principal limitation is that the diameter is set by that of the interferometer beam. Since, for a given focal length, the third order spherical aberration (wavefront) of a lens is proportional to the fourth power of its diameter, this is a very important parameter in the design of null systems.

Figure 1.54 (a) reveals two fundamentally important aspects of null system technology. Equation (1.75) shows that the aberration introduced for a given shape and power of the null system is a strong function of its magnification  $m$ . This is true whatever the design of the null system, since it is, by its nature, working well away from its minimum aberration conditions. If, then, the paraxial magnification  $m = NO''/NO$  in Fig. 1.54 (a) is slightly varied, there is an appreciable variation in the aberration produced. If, therefore, the null system  $N$  is set up with the wrong separation  $DN$ , then  $NO$  will also be wrong,  $m$  will be wrong and the wrong mirror will be produced: normally an undetectable systematic error. Such an error, if small, will only produce an error in the third order spherical aberration, but this leads directly to a systematic error in the Schwarzschild aspheric constant  $b_s$  of the test mirror. Such errors are, unfortunately, very common and have caused many tragedies in telescope history. The primary of the ESO 3.5 m NTT had such an error due to a spacing error of 1.8 mm which caused an aberration  $W \simeq 3000$  nm [1.132]. Fortunately, in this case, the test tolerances had been laid out with the active nature of the telescope in view and the error could be completely corrected by the active optics system – see Chap. 3. The most tragic case with the most disastrous consequences was the Hubble Space Telescope, where a systematic error of 1.3 mm in a reflecting Offner-type null system produced an error of  $W \simeq 4350$  nm which could not be corrected [1.133] [1.134] – see Chap. 3.

Internal errors of compact null systems, whether they be errors of radii, separations or refractive index, will also produce systematic third order spherical aberration errors. The manufacture is therefore very critical, with extreme tolerances, and correspondingly expensive. Normally, no test method for the complete system is available: they are made to absolute tolerances. However, workers at the Steward Observatory Mirror Lab. have recently published a technique for the independent testing of null systems which appears to represent a major advance in the subject – see the end of this section.

Since the wavefront generated by  $N$  in Fig. 1.54 (a) is aspheric, the distance  $NM$  is also critical, since an aspheric wave changes its form as it is propagated further into space. Only a spherical wavefront maintains its form independent of its radius. The distance  $NM$  must be maintained within tight tolerances so that the wavefront which is realised physically on the surface of the mirror at that point has the correct paraxial radius and the correct lon-

itudinal spherical aberration  $O'O''$ . An error in the distance  $NM$  exceeding the tolerance will also lead to an error in third order spherical aberration, i.e. in  $b_s$ .

These dangers and the accompanying problems of manufacture and set-up are the price paid for the huge advantage of null testing: it is an analogue means of disposing of excessive numbers of circular fringes, whose presence inevitably reduces the accuracy of the measurement.

The *Offner compensator*, proposed by Offner in 1963 [1.131] [1.122] is, in various forms, the most powerful – and probably the most widely used at professional level – null system yet devised. Offner started from the principle that the ideal compensator, though completely impracticable, would be a lens as large as the test mirror and in contact with it. Since, in practice, a much smaller lens must be used, he imaged this lens on to the test mirror with a field lens as shown in Fig. 1.58. Offner points out [1.135] that Shupmann first used a field lens in this way to control secondary spectrum for his medial telescopes – see Fig. 3.70 of RTO I. However, the field lens concept assumes there is a field: with zero aberration, the field of a null system is effectively zero by definition and remains very small for practical amounts of aberration. There is therefore no need to apply the field lens principle accurately, which would also put unnecessary restrictions on the form of the lens  $N$ . Also, the “field lens”  $F$  does not have to be fixed at the paraxial intermediate image. The real power and function of the Offner system comes from the following concept (Fig. 1.59): the lens  $N$  must achieve the necessary third order longitudinal spherical aberration corresponding to the normals of the aspheric, while the “field lens” is simply an additional lens placed in or near the caustic of the highly aberrated image enabling a sensitive control of higher order (zonal) spherical aberration without much influence on the third order aberration. The marginal rays focus at  $O'$  and are only weakly influenced by the lens  $F$ , while the zonal rays focusing at  $O''$  are strongly influenced so that  $O'O''$  can be adjusted accurately to the separation of the normals to the required mirror. The control of the third and fifth orders is thereby largely decoupled giving more or less a diagonal solution matrix. “Compact” systems, consisting of two or more lenses at  $N$  are much less favourable in this respect.

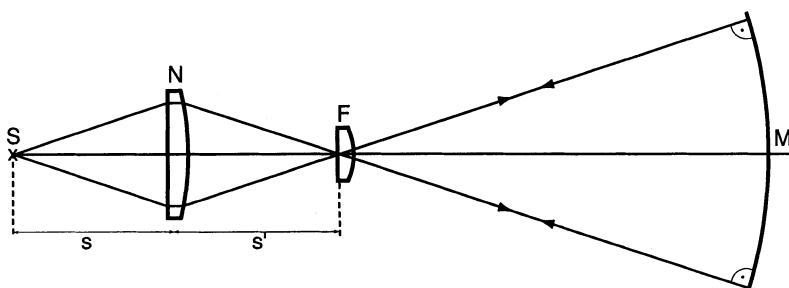


**Fig. 1.58.** Original principle of the Offner compensator using a field lens [1.131] [1.122]

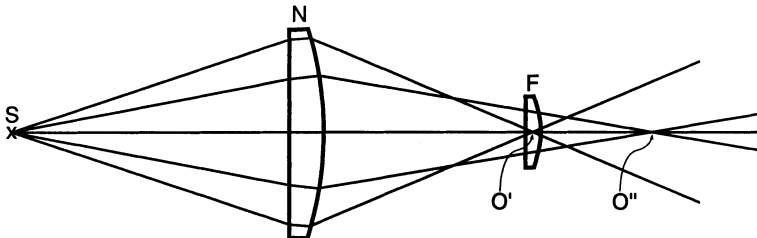


**Fig. 1.59.** Effective function of a refracting Offner compensator, in which the “field lens” controls the higher order spherical aberration

Offner [1.122] gives the following relation to define the plano-convex lens  $N$ :

$$-\frac{b_s r}{f_l} = (1 - m)^2 \left[ \frac{n^2(1 - m)^2}{(n - 1)^2} + \frac{(3n + 1)m(1 - m)}{(n - 1)} + \frac{(3n + 2)m^2}{n} \right] \quad (1.77)$$

In this formula,  $b_s$  is the Schwarzschild constant for the mirror of paraxial radius  $r$ ,  $f_l$  is the focal length of the lens  $N$ ,  $n$  the refractive index and  $m = s'/s$  the magnification defined by the sign convention  $m < 0$ . Apart from this change in the sign convention and the generalisation to any conicoid with  $b_s < 0$ , Eq. (1.77) is essentially the same as (1.75) and assumes no effect from the lens  $F$  on the third order aberration. Offner gives the example of a 1 m, f/4 paraboloid as test mirror. Using a lens  $N$  of diameter 1/20 of that of the mirror and  $m = -\frac{2}{3}$ , the lens produces a residual zonal error of 0.23λ rms at  $\lambda = 632.8$  nm. This is reduced to 0.0003 λ by a suitable field lens of about twice the focal length of  $N$ . In general, such systems are a trivial design operation with any normal optical design program. A convenient way of assessing the compensation quality is to use such a program to calculate the angular error from the normals at the mirror surface of the incident rays. The surface giving zero angular errors is the surface the manufacturer will be attempting to make.

It should be noted that the exact 1:1 reflective imagery of all such compensation systems means that the third order field coma is zero: it is therefore uncritical if the source  $S$  is not exactly on the axis.

The principles of “compact” or Offner compensators can be applied to *reflecting elements*. This was recognised and applied by Burch [1.124] using aberration generated by a spherical concave mirror with  $m \neq -1$ . Such an Offner reflecting compensator is shown in Fig. 1.60. The ratio of the diameters  $D_T$  of the test conicoid with Schwarzschild constant  $b_s$  to that  $D_N$  of the spherical null mirror  $N$  is given [1.122] by

$$\frac{D_T}{D_N} = \frac{(m^2 - 1)^2}{4b_s(m - 1)} , \quad (1.78)$$

with  $m = s'/s$  as before. This ratio for paraboloids ( $b_s = -1$ ) is 4.0 for  $m = -3$  and 24.0 for  $m = -5$ . High aberration requires a large value of  $|m|$ .

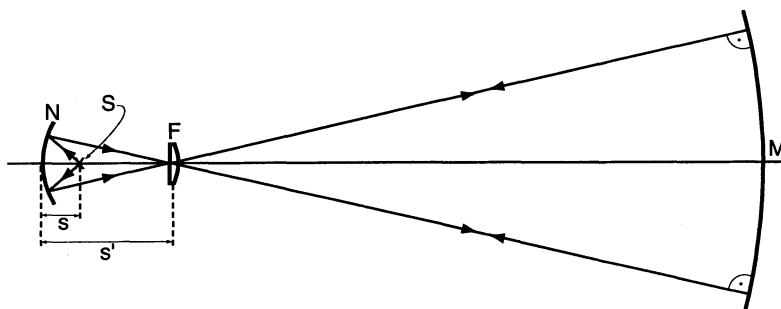


Fig. 1.60. Single mirror Offner-type compensator [1.122]

This, in turn, reduces the relative aperture of the beam. So steep, highly aspheric test mirrors require larger or steeper compensating mirrors  $N$ .

A further development of the reflecting type is the *2-mirror Offner compensator* shown in Fig. 1.61. This is a Gregory-type two-mirror system with intermediate image, where both mirrors contribute to the aberration. It has the advantage of compactness and gives a more accessible source  $S$  than the single-mirror type of Fig. 1.60. The obscuration ratio of the mirrors  $N_1$  and  $N_2$  must not exceed that of the test mirror  $M$ . The complete theory is given by Offner [1.122]. Such systems can give a very high degree of compensation for fairly modest diameters. In an example quoted by Offner, a 3 m,  $f/1.5$  paraboloid was compensated by a system with  $D_{N_1} = 14.82$  cm and  $D_{N_2} = 27.22$  cm. With an appropriate field lens  $F$ , the residual wavefront error was only  $0.009 \lambda$  rms at  $\lambda = 632.8$  nm. Better accuracy of compensation would require larger mirrors.

Such a 2-mirror Offner compensator may be considered as the ultimate in null system technology. However, the problems of manufacture and, above all, adjustment to correct position remain. For the primary of the Hubble Space Telescope (HST), a simpler refracting Offner compensator was used together with such a 2-mirror Offner compensator for final exact compensa-

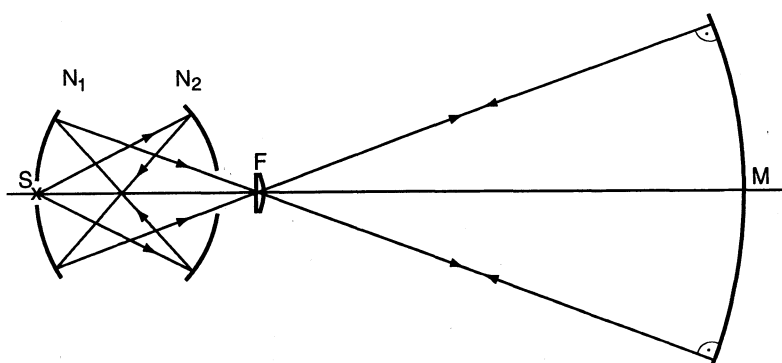


Fig. 1.61. 2-mirror Offner compensator [1.122]

tion. Unfortunately, the 2-mirror system had a systematic axial positioning error of about 1.3 mm while the simpler refracting one was correct [1.136] [1.134] [1.133]. The former was taken to be correct, which led to the spherical aberration error – see Chap. 3.

Various systems for auto-compensation exist, whereby the optical arrangement itself produces zero aberration without an additional null system. Most of these are concerned with the testing of secondary mirrors and will be dealt with in the next section.

For high quality large optics production, null systems are an essential aspect of the test technology. *Carl Zeiss* uses a series of null systems during the generation of the required aspheric, working with IR interferometry. The lenses are made of Germanium or BaF<sub>2</sub> [1.115]. Seven such systems were used for the NTT. This was followed by the null system for visible interferometry, a refractive Offner system.

REOSC proposed [1.26] 2-lens Offner-type IR compensators, using ZnS lenses, for the manufacture of the 8.2 m, f/1.8 primaries of the VLT. It was considered best at this stage to have simple, reliable compensators and accept an error of  $\lambda/32$  for  $\lambda = 10 \mu\text{m}$ . For the visible interferometry, they used refracting Offner-type systems consisting of 2 lenses (residual aberration  $0.1 \lambda$  for  $\lambda = 632.8 \text{ nm}$ ) and 3 lenses (residual aberration  $0.01 \lambda$ ). The lens diameters were of the order of 220 to 240 mm. A 2-mirror Offner-type compensator with mirrors of 400 and 600 mm diameter was also considered. This gives very high performance but, in agreement with ESO, it was decided that the refractive compensators were simpler and more reliable. As we saw in § 1.3.2.4, a small known systematic error in the interferometer system can easily be removed during the fringe scanning processing operation, and higher order compensation errors can be calculated with very high accuracy. This problem is simpler than removing asymmetric interferometer errors by calculation, though this can also be done [1.137]. A good way of eliminating the danger of positioning errors leading to third order spherical aberration is to use *two* independent null systems of different design and mount. If there is disagreement in the aberration produced, the source of the discrepancy *must* be found. The *active optics concept* of the VLT relaxes positioning tolerances – see Chap. 3.

It should be mentioned that the correction of zonal spherical aberration can be produced by means other than a lens. A synthetic hologram is one way of achieving this [1.138]. The third order aberration is produced by a single lens. A single lens is excellent at producing considerable aberration, but rather inflexible in its distribution over different orders. A hologram can only produce limited aberration, but the order is irrelevant. So the properties of the lens and hologram are complementary. However, in practice, the method has been rarely applied, mainly because of problems of stray light and its effects on fringe contrast. However, the Offner-type field lens may also have ghost image problems even if carefully coated (Fig. 1.50 (a)).

Finally, we return to the important issue of an independent test of null systems. The significance of this has been emphasized above. Apart from the HST case, by far the most dramatic and costly example of the terrible consequences of errors in null systems, there have been many other cases of “matching error” in ground-based telescopes resulting from such errors.

A solution to this problem seems now to be available, thanks to pioneer work at the Steward Observatory Mirror Lab. by Burge, Martin et al. [1.139] [1.140]. The key to the method is a small *computer-generated hologram* (CGH) which mimics the function of the theoretical primary (or test) mirror. This technique was specifically developed for the testing of the 6.5 m, f/1.25 primary for the MMT conversion. Figure 1.62 shows the optical arrangement for testing the null system. The hologram (CGH), consisting of a set of reflective rings on flat glass, is placed at the position of the paraxial center of curvature of the primary mirror in the normal test set-up. It is designed and made, independently of the null system, to match the wavefront that would propagate to coincide with, and be realised on, the surface of the primary mirror. The hologram is measured exactly as is the primary mirror, aligning the interferometer and null system simply by translating and tilting them as a rigid body to eliminate power, tilt and coma. Any wavefront error obtained in this measurement would represent an error either in the hologram or in the null system: such an error must be completely clarified and corrected before final testing can proceed. Initially, the visible null system *did*, in fact, reveal a spherical aberration wavefront error of  $1.9 \mu\text{m}$ . The ensuing investigation showed that the error was indeed in the null system, due to a wrong interpretation of the refractive index of the melt glass for the large lens. Without the holographic test, this error would have been worked into the primary mirror. After the necessary correction, the aberration measured in the hologram test was smaller than the accuracy of the wavefront measurement in the interferometer set-up, giving complete proof of the correctness of the null system finally used.

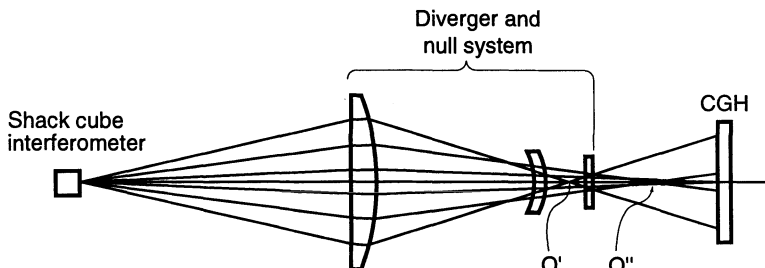


**Fig. 1.62.** Technique for independently testing a null system. A computer-generated hologram (CGH), placed at the paraxial center of curvature, mimics the function of the primary (or test) mirror. (After Martin et al. [1.139])

### 1.3.5 Test systems for Cassegrain secondary mirrors

**1.3.5.1 The problem of testing convex mirrors.** In Chaps. 2 and 3 of RTO I we considered the advantages of the Cassegrain form of reflecting telescope, above all because of its strong telephoto effect and resulting compact form compared with its focal length. In comparison, the Gregory form is little used except for solar telescopes where the length is usually less critical, the aperture relatively modest and an intermediate solar image is very useful for absorbing the heat. But this great advantage of the Cassegrain form over the Gregory for normal telescopes has its price: the *convex* secondary. A *concave* mirror on its own can form a real image at its focus in autocollimation; at its center of curvature with a magnification of  $-1$ ; or at some other magnification in the range  $0 > m > -\infty$ . Only if the source is inside the focus is there no real image. A *convex* mirror on its own, on the other hand, cannot form a real image of a real object source. This means that the imprint of its errors on a reflected wavefront cannot be investigated with a real image *without supplementary optics*. The technology of testing secondaries is therefore essentially the technology of producing a real image from an optical system including the secondary in a way where the errors of the secondary can be separated from those of the other components.

Of course, *mechanical* tests are equally possible on convex as well as concave mirrors. The fabrication of the 10 m Keck telescope secondary referred to above [1.121] using a precision profilometer may have great significance for the future. Here, we shall limit ourselves to the normal optical tests. The real image produced can be analysed by any of the methods discussed above, normally today by interferometry.

**1.3.5.2 Review of optical test methods for convex secondaries.** A general review of methods in use at the time (1974) was given by the author [1.141]. The methods were classified according to two criteria:

- A1** The system gives a real image with autocompensation of the spherical aberration without a null system
- A2** The system produces a real image with spherical aberration which must normally be compensated by a null system
- B1** The whole pupil (test surface) is covered *instantaneously* by the test
- B1\*** The B1 characteristic only applies to the area of the secondary covered by the functional *axial* beam, not the supplementary field annulus required for a telescope whose pupil is at the primary
- B2** The whole pupil can only be determined by the integration of time-dependent observations

Here, we shall follow this scheme with comments on each method, only briefly if the method has low current interest. An excellent general review of most methods has also been given by Parks and Shao [1.142]. Many methods use a combination of primary and secondary, either in their functional or in another

geometry. Information on the secondary is then given by subtracting known errors of the primary from those of the total system.

#### M1 Functional test with natural stars (A1, B1)

This is the oldest method and one still used by amateurs. The great problem for professional telescopes is that the secondary must be made on site. Seeing must be eliminated by a Hartmann-based or other method using adequate integration. The method is too inefficient for normal professional use.

#### M2 Autocollimation or equivalent in functional geometry with unchanged ray-path

##### M2.1 Full-size plane mirror (A1, B1\*)

The ideal method for small telescopes if the necessary flat exists. It requires coated surfaces because of the double pass. Small workshops [1.11] often find chemical silvering the most practical way of getting reflectivity: the coating quality is not critical. The aberration of the primary must be known. The double pass gives good sensitivity.

Theoretically, mercury pool flats can be used in a vertical set-up, but the technology is difficult.

##### M2.2 Double telescope (A1, B1\*)

Two identical telescopes are set up opposite each other, the one (already tested) serving as a collimator for the other, otherwise only the total error is obtained. The method is most interesting for series production of smaller telescopes, one serving as collimator for the others.

##### M2.3 Reduced size plane mirror (A1, B2)

This method is often used [1.11]. Extrapolation and integration of results is reasonable up to diameters about 50 % more than that of the flat. Beyond that, extrapolation becomes dangerous since third order spherical aberration varies as wavefront aberration with the fourth power of the aperture.

##### M2.4 Pentaprism or double pentaprism (A1, B2)

This test is of great importance as a supplementary test to other B1 tests. It provides a reliable and direct measure of *spherical aberration* only and, as such, is an excellent check against systematic errors of null systems. In my view [1.133], this was the test that was missing in the manufacture of the Hubble Space Telescope: it would have revealed the error at relatively low cost with great reliability.

The method was invented by Wetthauer and Brodhun in 1920 [1.143] and is shown in Fig. 1.63. The Cassegrain telescope is set up in its functional geometry with a pinhole source at its designated Cassegrain focus. This projects a plane wavefront above the telescope. Instead of

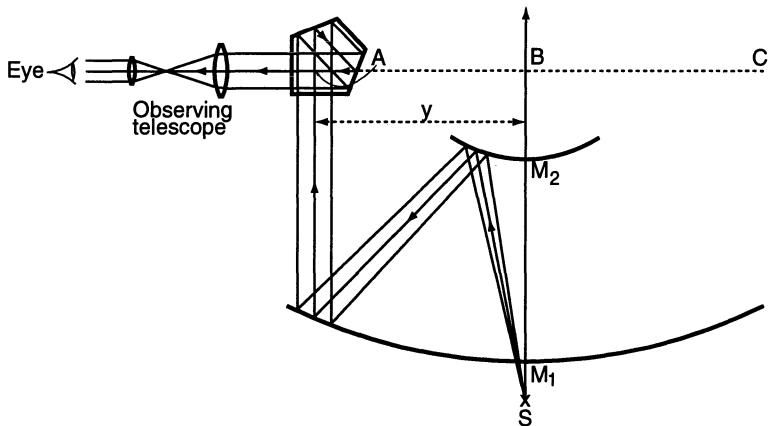


**Fig. 1.63.** The pentaprism test for spherical aberration (schematic) [1.146] [1.141]

an autocollimation flat, a sub-aperture is intercepted by a pentaprism  $A$  which can be moved over a diameter of the aperture on a rail. The pentaprism deflects the sub-aperture beam about  $90^\circ$  into a small telescope (originally) or a camera capable of automatically detecting very small image shifts in a more modern form. The pentaprism has the property that *the deflection angle in the plane of the diagram* is unaffected by slight rotations about an axis perpendicular to this plane, which are inevitable when it is moved across the aperture. In other words, the pentaprism is like a  $45^\circ$  mirror with a perfect constancy of its angle as it moves over the diameter. The vertical positions of the image in the small telescope measure the slope errors of the plane wavefront integrated over the sub-apertures. In the horizontal plane, the pentaprism is like a plane mirror and is simply adjusted by rotation about  $AC$  to maintain the image in the central plane. The third order spherical aberration can be extracted as the function of  $y^3$  for the angular aberration. A term in  $y^2$  is due to decentering coma and is eliminated in the reduction. It has been claimed that information on astigmatism can also be obtained by measuring across different diameters, but there is doubt concerning the validity of the reference sphere. In any event, the test is completely justified for spherical aberration alone. It was used in the United States in 1939 to test Schmidt cameras for spectrographs [1.144] and again in 1969 [1.145]. But the most systematic use has been by REOSC in Paris [1.146], who have applied it systematically for over 20 years in the double pentaprism modification. For this reason, this manufacturer has avoided "matching error" between the aspherics of primary and secondary, which has plagued so many telescopes because of errors in null systems. It has also been applied systematically by Korhonen [1.36], both for the 2.5 m Nordic

telescope and for the 1.2 m telescopes for the Geneva Observatory and the University of Louvain. Korhonen applies the pentaprism test not only to the *combined system*, but also to the *primaries alone*. For parabolic primaries, this is a perfect null test in autocollimation. For lightly hyperbolic RC primaries, the small residual spherical aberration is measured directly, giving an excellent measure of the aspheric constant.

A sensitivity of about 1/4 arcsec can be achieved, but 0.1 arcsec is difficult because of the resolution of the sub-apertures and the sampling over the diameter, except for very large telescopes. However, the precision attained is ample to detect *systematic* errors, such as those that occurred with the Hubble Space Telescope. Other B1 methods of test will provide the *high accuracy* measure of spherical aberration.

The positioning tolerances in the pentaprism test are very relaxed and this is another great advantage of the method. There are only two positional requirements: the position of the source  $S$  behind the pole of the primary and the separation of  $M_1$  and  $M_2$ . The position of  $S$  can easily be set up to the nominal Cassegrain image position within about 1 mm, an error giving negligible spherical aberration in all practical telescopes. This will ensure freedom from spherical aberration. If the distance  $M_1M_2$  is incorrect, the radius of  $M_1$  or  $M_2$  (or both) is wrong. But this will not lead to spherical aberration, since the pentaprism test will lead to a compensating aspheric form on the secondary. It will, however, lead to a departure from the nominal telescope form, e.g. from a strict RC telescope. However, the tolerance on  $M_1M_2$  is relatively generous in such cases, so the establishment of the necessary value is quite easy.

#### **M2.5** Mach-Zehnder (A1, B2), Prism Band (A1, B1\*), Zenith mirror (A1, B2) methods

These methods [1.141] were proposed at Carl Zeiss but not tried in practice. They may or may not have useful advantages compared with the pentaprism method. The zenith mirror method (small plane mirrors suspended from pendulums) has since been proposed and investigated by Hu [1.147]. In spite of its elegance, it is difficult to see an advantage over the pentaprism method. It is certainly far more sensitive to vibration.

#### **M3** Tests with an artificial source in functional or quasi-functional geometry and with or without focal shift (A1 or A2, B1)

Tests with an artificial star at a considerable distance are very old. Herschel established the rule that the change of spherical aberration is negligible if the source is at least 40 focal lengths away. The horizontal ray paths are then very long, usually prohibitive because of air turbulence. If the source is nearer, the image position is shifted and

may not be accessible in the finished telescope, but possible in the workshop. The test length can be reduced by a folding mirror [1.141].

- M4** Autocollimation tests using the primary and secondary mirrors in non-functional geometry and ray path

**M4.1** Double reflection at the primary (A2, B1)

This method [1.141] [1.130], which has not, to my knowledge, been applied in practice, is shown in Fig. 1.64. The autocollimation is based on a double reflection at both primary and secondary, the second reflection at the primary being normal and the reflections at the secondary therefore being at the same height, giving clear information on the

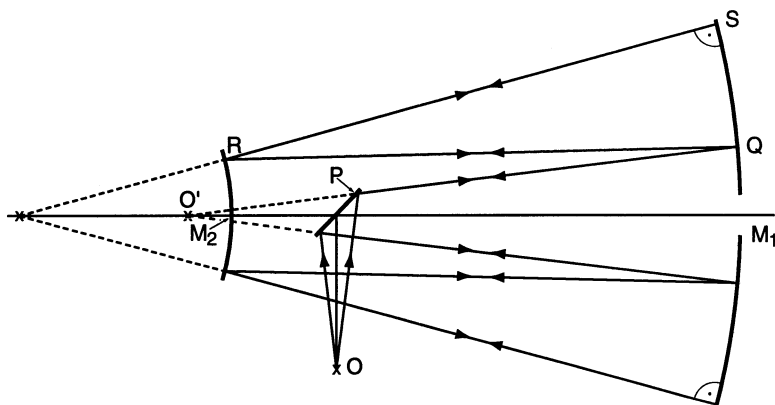
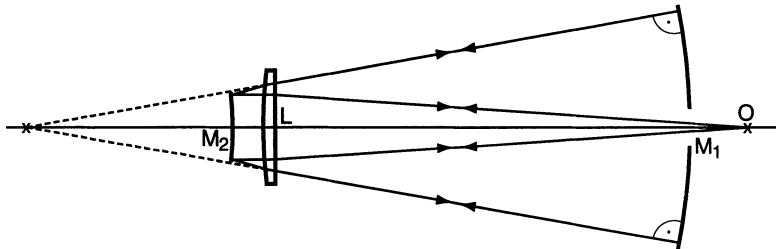


Fig. 1.64. Test method using double reflection at primary [1.141] [1.130]

secondary in double pass. The separation of the mirrors must be sufficiently small to cover the secondary with the beam, but is about twice the normal separation. This separation determines the heights  $Q$  and  $P$  and, with them, the obstruction relative to  $Q$  of the primary mirror hole and of the plane mirror  $P$  at the secondary. A compensator is required (A2). If the obstruction factors are too unfavourable, an auxiliary spherical mirror can be used for the reflexion at  $Q$ , which relaxes the geometrical constraints. The double pass at both mirrors will normally require reflecting coatings on *both*, but these can be of indifferent quality. This means that the secondary could be *chemically silvered*, a rapid and simple process.

- M4.2** As in M4.1 but with refracting optics in front of the secondary (A2, B1)

Instead of the double reflection at the primary, the beam is deflected by a weak convex lens, as large as the secondary, into the normal Cassegrain image position [1.141]. Figure 1.65 shows the arrangement. The effective power of the lens is doubled by the double pass. The



**Fig. 1.65.** Autocollimation test against the primary using a weak convex lens in front of the secondary

lens must have high glass homogeneity as well as good surface figure. In practice, a lens of the order of  $f/10$  is sufficient. Its aberration is immaterial if a compensator is used (A2), but it tends to compensate the aberration of the mirror system anyway (quasi A1). If a test plane mirror of the same size is available, the lens quality can be tested against it independently in autocollimation.

#### M4.3 Lytle test (A2, B1)

This test was proposed by Lytle [1.148] and has been used at REOSC for supplementary tests of the secondaries of the ESO 3.6 m telescope [1.141] [1.149]. The purpose was to supplement the pentaprism test (M2.4 above), which had B2 classification, by a B1 method to reveal the high spatial frequency quality of the surface. Instead of normal incidence on the primary as in M4.1 and M4.2, the Lytle method (Fig. 1.66) uses normal incidence on the *secondary*. The mirror separation is greater than in M4.1, about  $2\frac{1}{2}$  times the normal separation in a typical case. The source  $O$  is compensated by the null system  $N$  and imaged via the  $45^\circ$  plane mirror at  $O'$ , which is inside the cen-

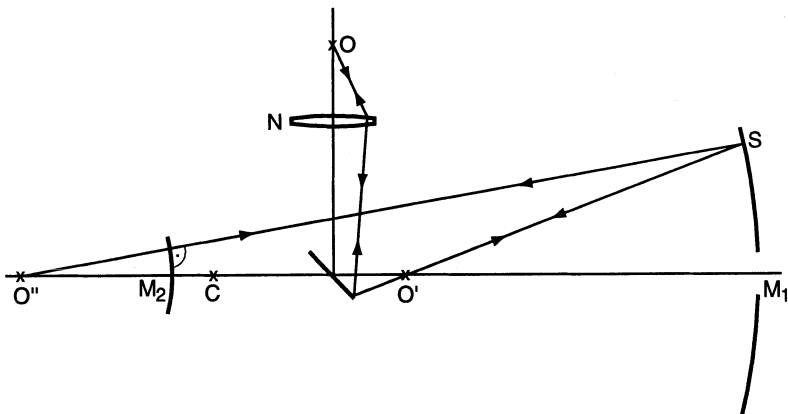


**Fig. 1.66.** The Lytle test [1.148] [1.141] [1.149]

ter of curvature  $C$  of the primary. The primary reflects the beam to the secondary which is placed to reflect the beam normally with its center of curvature at  $O''$ . The Lytle test does not have the obstruction problems of M4.1, but has a longer beam path. The total beam path for the 3.6 m tests was about 80 m. The null system has to correct considerable aberration, since the primary over-compensates the spherical aberration of the secondary. The residual overcorrection has the favourable sign for the lens compensator.

- M5 Test methods of the secondary alone without the primary and without large auxiliary optics

#### M5.1 Refraction through the mirror as a Cartesian lens (A1, B1)

This method (Fig. 1.67) is based on the work of Descartes who showed [1.150] that aberration-free refraction at a glass-air surface requires a hyperbolic form. The Cartesian refraction requires (see Eqs. (3.10) and (3.93) of RTO I) the condition

$$\frac{n'}{n} = \varepsilon = (-b_s)^{1/2} = \frac{m - 1}{m + 1}, \quad (1.79)$$

where  $n'$ ,  $n$  are the refractive indices of the glass and air,  $\varepsilon$  is the excentricity and  $b_s$  the Schwarzschild constant, and  $m$  the magnification (negative) of the hyperbola *in reflection* from focus to focus. This latter is the same as the secondary magnification  $m_2$  for a *classical* Cassegrain telescope, but *not* for other forms such as the RC. With  $n'/n = 1.51$ , Eq. (1.79) gives  $m = -4.92$ . This is a very normal magnification for modern classical Cassegrain telescopes, making the method above all interesting for smaller and amateur telescopes. Exploiting the extreme range of normally available glasses,  $m$  values between about  $-4$  and  $-5.4$  can be achieved. Of course, high homogeneity of the glass is required. A collimator of the mirror diameter can be used, but a better method is usually to apply autocollimation by reflection from the plane back (Fig. 1.67(b)). A high quality plane

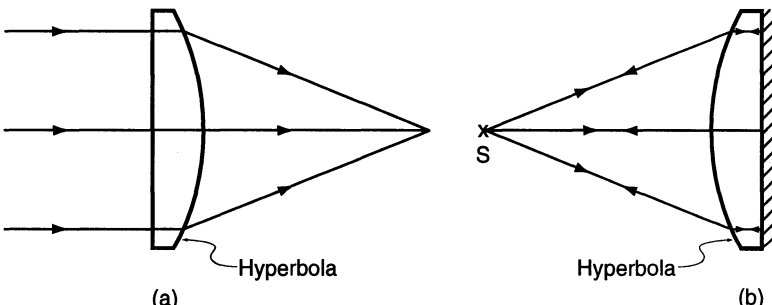


**Fig. 1.67a, b.** Test by a refraction through the secondary as a plano-convex Cartesian lens [1.141] [1.142]

back surface is then required: the sensitivity to errors of the plane back surface as a mirror is twice that of the refracting surface in double pass for  $n'/n = 1.5$ .

Parks and Shao [1.142] give a modification, which is not quite auto-compensating, by increasing the source distance somewhat and using a very shallow concave spherical back surface, which is much easier to test. For the Keck 10 m telescope secondary, this would give an error of spherical aberration of  $0.07 \mu\text{m ptv}$ .

The test has been proposed independently by various workers but its advantage for amateurs was first pointed out by Norman [1.151].

### M5.2 Test by reflection through the back surface (A1 or A2, B1)

This method overcomes the fundamental problem of the convex mirror surface by treating it as a concave mirror from behind. The test can be used in the general sense as an A2 test with a null system, with any desired back surface of high quality and any refractive index. Of course, high homogeneity is always required.

An excellent form of this test was given by Schmadel [1.152], giving a true A1 (autocompensating) method for the third order spherical aberration (Fig. 1.68). The autocompensation of the third order spherical aberration is achieved by the only free parameter, the spherical radius of the back surface. Unfortunately, the compensation requires a *convex* back surface, making it more difficult to test than a concave surface. However, for smaller mirrors, it can be tested by a concave proof plate. Schmadel gives an elegant iterative procedure. The calculation with an optical design program is trivial. For a 20-inch telescope, he gives an example for  $m_2 = -3$  using Schott BK7 glass. The radius of the hyperbolic surface is 2067 mm, the thickness of the mirror 30 mm. The required convex radius is given as 3734.5 mm. The residual zonal error is  $< \lambda/50$ . The test is suitable for values of  $m_2$  between about -2 and -4.

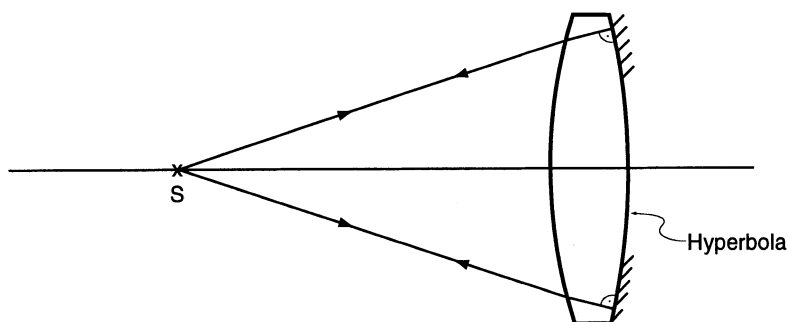


**Fig. 1.68.** Test by reflection through the back surface due to Schmadel [1.152]

Similar proposals were made later by Meinel and Meinel [1.153], also discussed by Parks and Shao [1.142]. They considered the possibilities for the Keck 10 m telescope secondary. The Keck telescope has  $m_2 = -15/1.75 = -8.57$  for the Cassegrain secondary, a high value compared with most Cassegrain telescopes. The Meinels set up a system similar to that of Schmadel with a convex back giving quasi-compensation with a residual error of  $0.8 \lambda_{\text{rms}}$  [1.142]. The radii were 4731 mm for the mirror and 63705 mm for the spherical convex back. The Meinels investigated a number of cases with a convex, plane and concave back spherical surface. They also introduced a further correction parameter: different conjugates instead of simple autocollimation with normal reflection from the hyperboloid. In the Keck case, using separate conjugates and a moderately *concave* back, they produced a solution for the Keck secondary giving a wavefront error of only  $0.06 \mu\text{m rms}$  [1.142].

For smaller amateur telescopes, the technique of Schmadel and the Meinels is one of the most powerful and practical available. It is also used by professional workshops [1.11]. For larger telescopes, the homogeneity of the glass is the main problem. It is possible to calibrate this and separate it out from the surface errors [1.142]. The method has the major advantage over M5.1 (in the autocollimation form) that the M5.2 method is twice as sensitive to errors in the hyperbolic surface as in the back surface, whereas with M5.1 the situation is the reverse.

It is instructive to recall that the secondary of the Keck telescope was finally tested largely by a *mechanical* method [1.121] – see above.

## M6 Test methods of the secondary alone without the primary, but using large auxiliary optics

### M6.1 Hindle sphere (A1, B1)

The Hindle test [1.154] [1.155] is geometrically the most elegant way of testing convex hyperboloids. The principle of the test (Fig. 1.69) makes direct use of the focal properties of the hyperboloid as conjugate, aberration-free points. In a *classical* Cassegrain telescope, the foci of the secondary hyperboloid are also the primary and secondary image positions. This is *not* true in an RC telescope; but the secondary is still to high accuracy a hyperboloid, but with higher excentricity – see Chap. 3 of RTO I. A point source at the (secondary) focus  $O$  forms a virtual image at the conjugate focus  $O'$ . The Hindle sphere is a spherical mirror centered on  $O'$ , giving autocollimation. If the Hindle sphere is in the same plane as the primary, since its center of curvature is at the prime focus  $O'$ , it is clear that the Hindle sphere is twice as steep as the primary and, for the same vertex position, has the same diameter. In practice, it can be made somewhat smaller as the system

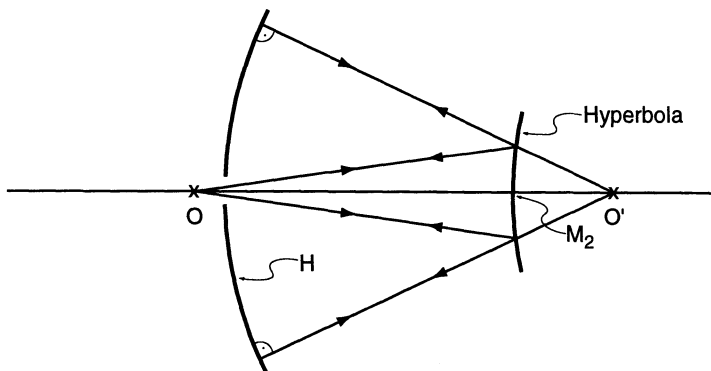


**Fig. 1.69.** The Hindle sphere test for secondaries [1.154] [1.155]

does not have to transmit any significant field and the image position  $O$  can be made more favourable. For an RC telescope, the geometry must be changed so that the distances  $OM_2$  and  $M_2O'$  correspond to the eccentricity  $\varepsilon = (-b_s)^{1/2}$  for the value of  $b_{s2}$  given by Eq. (3.109) of RTO I. For the Cassegrain secondary of the ESO 3.6 m quasi-RC telescope, for example, a Hindle sphere would need a diameter of about 2.3 m with a relative aperture about  $f/1.2$ , i.e.  $f/2.4$  at its center of curvature. This is steeper than for a classical Cassegrain because  $|b_{s2}|$  is higher.

Such a steep, large diameter sphere is a formidable object to make and support. This is the limitation of the Hindle test, in practice.

For a parabolic secondary, the point  $O$  is at infinity and the beam from the secondary is parallel: a supplementary collimator is required to form a real image [1.122].

#### M6.2 Inverse Hindle arrangement for a concave hyperboloid: the Silvertooth test (A1, B1)

Silvertooth [1.156] pointed out that the Hindle geometry can be applied to *concave* hyperboloids. This test is assuming increasing importance, because its geometry (Fig. 1.70) is more favourable than the original Hindle geometry and also because a *concave* negative (or matrix) of a convex hyperbolic secondary can be used to test a series of identical secondaries. There is also the possibility of producing such mirrors by replication from a concave master [1.157]. In the Silvertooth geometry the distance  $OM_2^*$  is the short conjugate and  $M_2^*O'$  the long conjugate, the reverse of the situation in the Hindle test. The relative aperture of the Silvertooth sphere  $St$  is therefore modest and its diameter does not greatly exceed the diameter of the secondary itself. The test set-up is correspondingly compact.

The Silvertooth test was used by the Rayleigh Optical Corporation to manufacture a negative test plate for the 48-inch RC telescope of

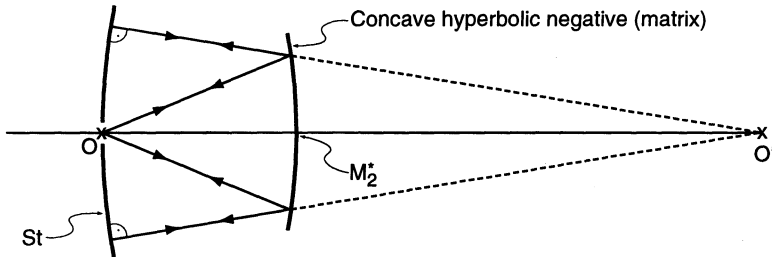


**Fig. 1.70.** The inverse Hindle test for concave hyperboloids: the Silvertooth test [1.156]

the Smithsonian Astrophysical Observatory [1.158]. The two convex mirrors were made by a test plate procedure in a Fizeau arrangement dealt with in M6.4.

This is one of the best test techniques even for a single convex hyperboloid. For more than one convex mirror, it becomes even more attractive. Such a case is the ESO VLT [1.159], where 4 identical secondaries are required for the 4 unit telescopes. The manufacturer, REOSC, has produced a hyperbolic concave negative (matrix) for the secondaries and tests the convex secondaries, produced by normal aspherizing techniques, against this concave master by the interferometric “test-plate” arrangement of M6.4 below. The concave matrix was *not*, in fact, tested by the Silvertooth test, but by the more conventional method of autocollimation at the center of curvature, using a refracting Offner-type null system (see also § 1.3.5.3 below). Unless a suitable spherical mirror is available for the inverse Hindle (Silvertooth) sphere, the Offner null system is probably cheaper and gives also flexible control of the zonal (fifth order) aberration. The VLT secondaries have beryllium blanks, requiring cutting after figuring. Should the cutting lead to unacceptable figure change, a fall-back solution remains the *replication* of the secondaries from the concave master [1.157].

### M6.3 The transmission meniscus Hindle sphere (A1 or A2, B1)

According to Offner [1.122] this test was devised by Simpson et al. in 1974 [1.160], but the test was in use at Grubb-Parsons for routine testing before this [1.141] and was successfully used for the secondaries of the 3.9 m AAT. The arrangement is shown in Fig. 1.71. The excessive size of the Hindle sphere of Fig. 1.69 is reduced by moving the sphere almost into contact with the secondary. The sphere becomes a meniscus which transmits the beam twice. The system is therefore not strictly an A1 classification as the meniscus introduces aberration. However, the back surface can be designed, taking account of the thickness, to remove the third order spherical aberration. According to

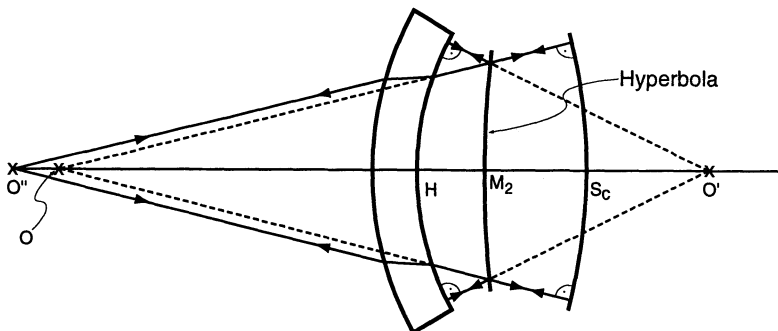


Fig. 1.71. The transmission meniscus Hindle sphere [1.141] [1.122] [1.160]

Offner [1.122], the zonal error is negligible: he quotes a residual wavefront error of  $0.0016 \lambda$  for  $\lambda = 632.8 \text{ nm}$ . The front, concave surface of the meniscus is the Hindle sphere which is given a 50 % reflecting coat.

This is an excellent test which permits a certain range of secondary parameters. Its weakness is the high homogeneity requirement of the meniscus, a difficult element for large secondaries. In fact, it is possible to calibrate directly the wavefront errors due to lack of homogeneity. The test mirror  $M_2$  is removed and replaced by a concave calibration sphere  $S_C$ . If  $S_C$  is perfect, the wavefront errors observed in autocollimation at  $O''$  give *exactly* the total wavefront error, from all sources, introduced by the meniscus in double pass in its test function. With the phase measurement techniques discussed in § 1.3.2.4 above, this error phase map can be stored and subtracted from the test results. For high level products with a production schedule that can profit from the investment in transmission Hindle spheres, the method is an excellent one.

#### M6.4 Interference test with a concave negative (matrix)

This was referred to in M6.2 in connection with the Silvertooth test for testing concave hyperbolic negatives. Such negatives can also be tested at their centers of curvature like primary mirrors using null systems. This method for testing secondaries has been used routinely and very successfully for many years by Carl Zeiss, Oberkochen (Fig. 1.72). Some workshops, to save work on the negative and because they are using the pentaprism test for the basic profile of the secondary, use a *spherical* negative; but this gives many circular fringes and reduced test sensitivity over the aperture. The set-up of Fig. 1.72 (a) supposes that the secondary mirror is capable of transmitting the beam. This is the case with modern high quality Zerodur; also, of course, with quartz. It should be emphasized that the homogeneity requirements are quite different from test set-ups like Fig. 1.71, where the optical

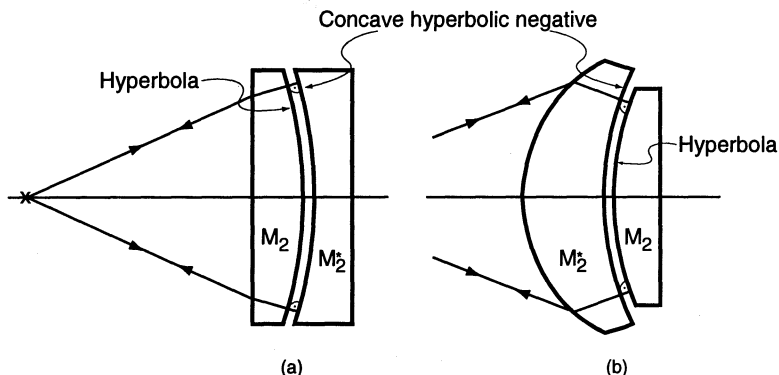


**Fig. 1.72a, b.** Matrix interference test for secondaries as used at Carl Zeiss [1.141]

path length affects the phase directly. This is not the case in the interference test of Fig. 1.72, since localised (Haidinger) fringes are formed in a 1 mm gap. The optics to the left of the gap simply has to transfer these fringes without significant distortion. If the material of  $M_2$  is not suitable for transmission, the scheme of Fig. 1.72 (b) can be used: the transmission is through the matrix  $M_2^*$  with a strongly convex back surface or with an additional collimator to converge the beam.

#### M6.5 Auxiliary lens in front of the secondary (A2, B1)

This method (Fig. 1.73) is a more extreme form of M4.2 (Fig. 1.65). The lens now has to overcome the convex nature of the secondary alone. High homogeneity and a high quality convex (spherical) surface are required for the lens. Unfortunately, such a plano-convex lens produces undercorrected spherical aberration of the same sign as the hyperbolic test mirror, which is difficult to correct by (null) refracting optics. However, a concave mirror compensator such as that shown in Fig. 1.60 is capable of such compensation. But this method remains very far from autocompensation. One advantage is that it could be used with a wide variety of secondaries if a variable compensator is

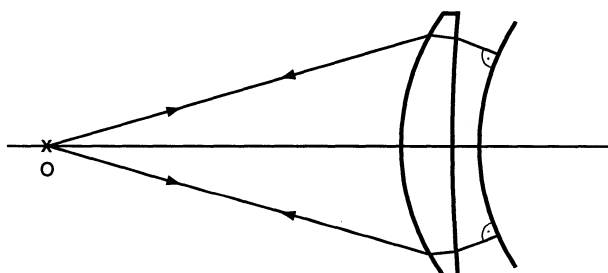


**Fig. 1.73.** Auxiliary convex lens in front of the secondary [1.141]

available. The aberration of the lens alone can be calibrated by a spherical convex mirror.

A variant of this test would use an aspheric (hyperbolic) compensating surface on the lens which could be tested through its back surface as a concave mirror in autocollimation.

#### M6.6 Richardson test (A2, B1)

This method, proposed by Richardson [1.141] [1.161], resembles the Lytle test (M4.3) in its basic approach, but replaces the primary as the element producing the real image by an auxiliary concave mirror  $M_A$  (Fig. 1.74). In fact, this test in its basic form was proposed in 1954 by Maksutov [1.3] (page 201), who also pointed out that it could be an A1 autocompensating test if the convex mirror were an oblate spheroid rather than the opposite form, the hyperboloid. The concave mirror can be placed closer to the secondary and is correspondingly smaller. Its radius of curvature can be chosen to optimize the geometry. The mirror  $M_A$  is working at a magnification very different from unity, unlike the primary in the Lytle test, and is spherical. It therefore produces *undercorrected* spherical aberration, as does the secondary. If the mirror  $N$  produced a corrected image of the source  $O$  at  $O'$ , the image re-formed at  $O'$  by reflection at  $M_A$  (twice) and  $M_2$  would be strongly *undercorrected*, hence also that at  $O$ . Since this is unfavourable for a lens compensator, Richardson proposed a *hyperbolic* mirror compensator at  $N$ . Since this is concave, it can be tested at its center of curvature by a lens compensator.

The problem of compensation, solved by using an aspheric, is a definite weakness of the Richardson test. It was used for the secondaries of the 3.6 m CFHT, installed at Hawaii. A significant matching error of the aspheric constants of the secondary relative to the primary

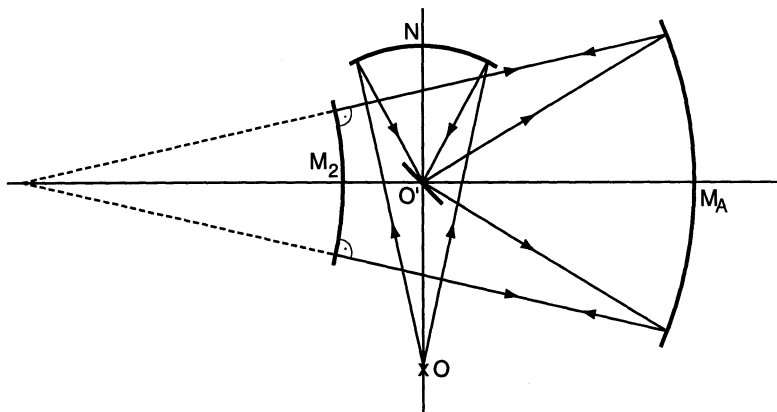


Fig. 1.74. Richardson test [1.141] [1.161]

resulted. This was subsequently corrected by a permanent bending of the secondary (dc active bending). This general problem is considered in § 1.3.5.3 below.

**1.3.5.3 Conclusions on optical test methods for secondaries.** All the methods above which use the secondary in combination with the primary or with other large optical elements in an A2 mode (i.e. requiring correction of spherical aberration by a null system) are incapable of giving reliable information on spherical aberration because the positioning tolerances of the null systems are impossible to meet in the long beam paths involved. This situation applies to all M4 methods and M6.6 (Richardson test). A1 mode methods such as the Hindle sphere are better because of autocompensation. But one should remember that errors of positioning the source, or radius errors on the Hindle sphere or  $M_2$  will also lead to spherical aberration. In fact, this is true of any set-up, but the shorter and simpler the beam path, the less the danger.

The A2 methods M4 and M6.6 are only suitable as supplements to the pentaprism test M2.4, which is unquestionably the best method for ensuring freedom from spherical aberration (matching error). These tests may be a useful solution for a final acceptance test revealing the full aperture (B1 mode).

For *amateurs* or professional workshops making smaller telescopes, the tests in the M5 group are probably the most practical, particularly those of Schmadel and the Meinel's (M5.2).

For large telescopes, the most practical and reliable methods with the B1 characteristic (test of the whole pupil at once) are probably those in the M6 group, particularly:

- M6.2: The Silvertooth test for concave hyperbolic negatives (matrices)
- M6.3: The transmission meniscus Hindle sphere
- M6.4: The interference test using a concave matrix, produced by M6.2 or by conventional null systems

These are all likely to lead to matching error, unless extreme care in positioning is taken, particularly if null systems are used. For this reason, it is highly desirable to add

- M2.4: The pentaprism test ,

above all for classical “passive” telescopes. For active telescopes, matching is less critical if sufficient dynamic range is available to allow substantial correction of spherical aberration – see Chap. 3.

For the VLT, REOSC analysed the test procedures for the secondaries [1.162] (see M6.2 above) and concluded that the technique M6.4, producing the concave matrix by a conventional null system, was the most favourable, particularly as 4 identical secondaries were required. A naked (uncompensated) Hartmann test of a hyperbolic concave negative (matrix) of the secondary, tested as in M6.4, can be a satisfactory substitute for the pentaprism test, as REOSC technology for the VLT has demonstrated.

### 1.3.6 Test methods for large flats

Smaller flats can be tested by test plates or against a high quality collimator, i.e. an inverse telescope, but collimators larger than 0.5 m are rare in optical workshops. The definitive solution to this problem was given by Common in 1888 [1.163]. The method was re-invented by Ritchey in 1904 [1.164] [1.165] and has been widely used since then. The method is very simple (Fig. 1.75) and is well described by Maksutov [1.3] (page 196) or in Malacara [1.74] (page 274). A high quality reference spherical mirror  $M$  is tested at its center of curvature alone, and then after a double-pass reflection at the plane mirror under test. The double pass gives doubled sensitivity for the test of the flat, a further advantage of the method. The incidence angle  $i$  can be made anything convenient for the size of the flat and reference sphere available. But, if the value of  $i$  is chosen to be the same as in its final function, for example 45° for a Nasmyth plane mirror in a Cassegrain telescope, then the method also gives the correct absolute value of astigmatism due to a slight curvature of the flat. This is a very important advantage, since astigmatism is extremely sensitive to small errors of curvature at large angles of incidence. This property has been used in an inverse process to measure very long radii [1.3] [1.166].

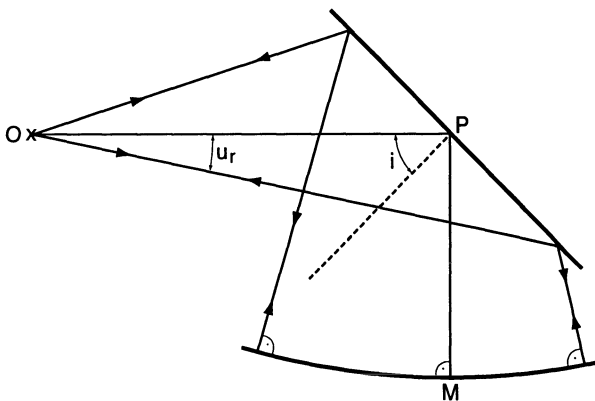


Fig. 1.75. The Common-Ritchey test for plane mirrors [1.163] [1.164] [1.165]

The astigmatic difference along the axis  $OP$  due to a very long radius  $r_P$  of the plane mirror can easily be derived as follows. Without limitation of the field angle, the astigmatic fields of a spherical concave mirror of radius  $r$ , imaging a parallel beam, lie on a circle of radius  $r/2$  ( $t$ -image) and on straight line ( $s$ -image) as shown in Fig. 1.76. The astigmatic difference  $(\Delta_{ast})_P$  is then given, from the geometry of the circle, by

$$(\Delta_{ast})_P = \frac{r_P}{2} \left( \frac{1}{\cos i} - \cos i \right) \quad (1.80)$$

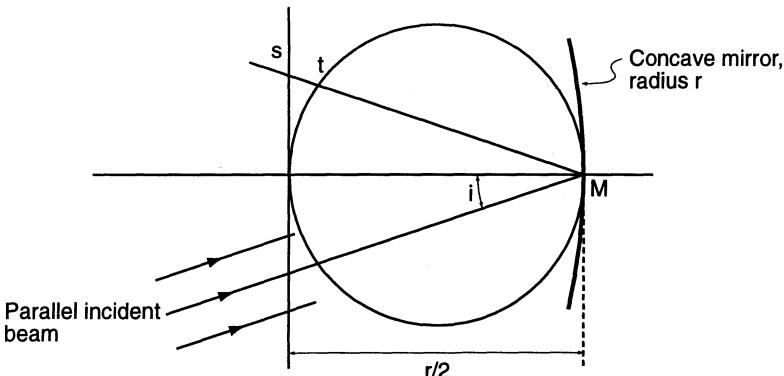


Fig. 1.76. Astigmatism due to a concave mirror imaging a parallel beam

In the Common-Ritchey set-up, the corresponding wavefront aberration for a single pass is imposed on that of the spherical reference mirror which has a semi-aperture angle  $u_r$ , (Fig. 1.75). Now from Eq. (3.205) of RTO I, the astigmatic difference is a function of the wavefront aberration expressed by  $S_{III}$  and  $1/u^2$ . For the image formed by the concave reference mirror, therefore,  $(\Delta_{ast})_P$  must be multiplied by

$$\left(\frac{u_P}{u_r}\right)^2 = \left(\frac{p}{r_P/2}\right)^2 , \quad (1.81)$$

with  $OP = p$ , giving

$$(\Delta_{ast})_r = \frac{2p^2}{r_P} \left( \frac{1}{\cos i} - \cos i \right) \quad (1.82)$$

for the observed astigmatism for a single passage. In double pass we have

$$(\Delta_{ast})_{2r} = 2(\Delta_{ast})_r = \frac{4p^2}{r_P} \left( \frac{1}{\cos i} - \cos i \right) = \frac{4p^2 \sin^2 i}{r_P \cos i} \quad (1.83)$$

The corresponding sagitta  $z$  of the quasi-plane surface can be derived from its diameter  $D$  and its radius of curvature  $r_P$  from (1.83) and  $z = D^2/8r_P$  as

$$z = \frac{D^2(\Delta_{ast})_{2r}}{32p^2} \left( \frac{\cos i}{\sin^2 i} \right) \quad (1.84)$$

A feeling for the great sensitivity of curvature in generating astigmatism can be obtained by taking a typical case and setting the astigmatic effect produced at the Rayleigh limit with  $W = \lambda/4$ . From Eq. (3.204) of RTO I we have

$$(\overline{W}_{III})_{GF} = \frac{1}{2} \left( \frac{y}{y_m} \right)^2 S_{III} = \frac{1}{2} S_{III} , \quad (1.85)$$

for the edge of the pupil with  $y = y_m$ , as the total wavefront aberration for astigmatism alone in the Gaussian plane in the absence of field curvature  $S_{IV}$ . Now from (3.206) of RTO I

$$I'_m I'_t \equiv \frac{1}{2} \Delta_{ast} = \frac{1}{2} \left( \frac{f'}{y_1} \right)^2 S_{III} , \quad (1.86)$$

giving from (1.85)

$$\Delta_{ast} = \left( \frac{f'}{y_1} \right)^2 S_{III} = \left( \frac{f'}{2y_1} \right)^2 8(\bar{W}_{III})_{GF} \quad (1.87)$$

Setting  $(\bar{W}_{III})_{GF} = \lambda/4$  for the diffraction limit gives

$$\Delta_{ast} = \left( \frac{f'}{2y_1} \right)^2 2\lambda \quad (1.88)$$

From (1.82), this gives for  $(r_P)_{\lambda/4}$  in single pass

$$(r_P)_{\lambda/4} = \frac{2p^2}{(f'/2y_1)^2 2\lambda} \left( \frac{1}{\cos i} - \cos i \right)$$

But the distance  $p$  in this formula is the same as the effective focal length  $f'$  of the image forming beam, giving with  $D = 2y_1$ ,

$$(r_P)_{\lambda/4} = \frac{D^2}{\lambda} \left( \frac{1}{\cos i} - \cos i \right) = \frac{D^2}{\lambda} \sin i \tan i \quad (1.89)$$

If the reference mirror has  $D_r = 1000$  mm and the projected diameter of the flat is  $D = 700$  mm for a typical large coudé mirror working with  $i = 45^\circ$  and with  $\lambda = 500$  nm, Eq. (1.89) gives

$$(r_P)_{\lambda/4} = 693 \text{ km!}$$

On axis,  $(r_P) = 0$  if  $i = 0$ , since curvature produces no astigmatism on axis.

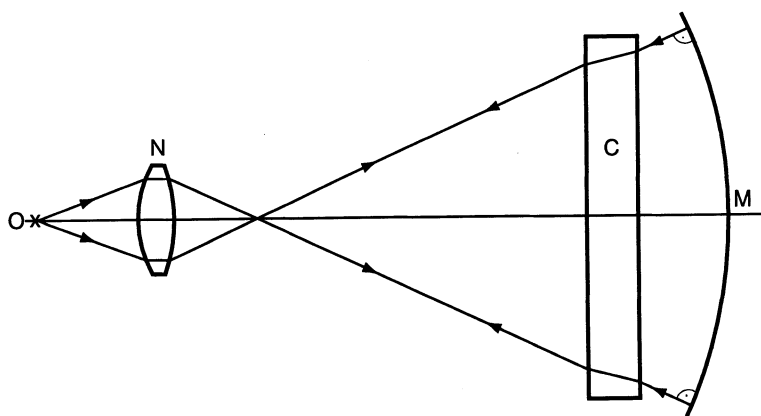


**Fig. 1.77.** General arrangement for testing afocal or quasi-afocal correctors in autocollimation against a spherical concave reference mirror

The image at  $O$  of Fig. 1.75 can be examined by any of the methods given in this chapter. Normally, interferometry will be used, allowing simple deduction of the error in the reference mirror. Of course, it is perfectly legitimate to compensate the curvature astigmatism of a plane mirror by figuring into the surface the same amount of astigmatism of opposite sign: but this compensation is only strictly correct for a predetermined and fixed value of  $i$  and requires correct orientation of the mirror.

It should be mentioned that an auxiliary concave reference mirror is a powerful general tool in testing astronomical optics apart from its use with plane mirrors. For example, afocal or quasi-afocal correcting systems, such as field correctors  $C$  can be placed in front of such a concave reference mirror  $M$  and tested in autocollimation using appropriate null systems  $N$ . Figure 1.77 shows the general arrangement for such tests.

## 2. Sensitivities, alignment of telescopes and test procedures in function

### 2.1 Sensitivities

In Chap. 3 of RTO I we gave the essential formulae for optical errors that arise in telescopes through maladjustments. In a 2-mirror telescope, such errors fall into two classes: decentering errors and axial despace errors. It is useful to recall here the relevant results from RTO I, bearing in mind that the notation is identical and is defined in Appendix A therein.

#### 2.1.1 Decentering errors

Expressed in arcsec, Eqs. (3.363) and (3.364) in RTO I give the tangential coma (see Fig. 3.18 in RTO I) resulting from a *lateral (shear) decenter*  $\delta$  (uniform over the field) as

$$\left[ (\delta u'_p)_{Comat} \right]_\delta = -\frac{3}{32} \frac{(m_2 + 1)^2}{N^2} \left[ (m_2 - 1) - (m_2 + 1)b_{s2} \right] \frac{\delta}{f'} (206\,265) \text{ arcsec} \quad (2.1)$$

for the general case of a 2-mirror telescope, and

$$\left[ (\delta u'_p)_{Comat} \right]_{\delta, Aplan} = -\frac{3}{16} \frac{m_2}{N^2} \left[ (m_2^2 - 1) + \frac{1}{1 - R_A} \right] \frac{\delta}{f'} (206\,265) \text{ arcsec} \quad (2.2)$$

in the case of an aplanatic, normally RC, telescope. In (2.2) the first term in the square bracket corresponds to the classical telescope, the second term is the RC supplement.

As a typical case of a modern telescope we will take the ESO New Technology Telescope (NTT) with  $m_2 = -5$ ,  $N = 11$ ,  $f' = 38500$  mm,  $R_A = 0.229$ , giving

$$\left[ (\delta u'_p)_{Comat} \right]_{\delta, NTT} = 1.050 \delta_{(mm)} \text{ arcsec} , \quad (2.3)$$

the RC supplement being only about 5 %, typically insignificant. Equation (2.3) shows that  $\delta = 1$  mm decenter in this 3.5 m telescope generates about one arcsec of decentering coma. This sensitivity dominates the situation in “passive” telescopes and its control is the most important feature of “active” control.

The other decentering sensitivity comes from a rotation of the secondary about its pole. From RTO I, Eq. (3.376), we have

$$\left[ (\delta u'_p)_{Coma_t} \right]_{2,rot} = -\frac{3}{16} \frac{R_A(m_2^2 - 1)}{N^2} (u_{pr2})_{arcsec} \text{arcsec} , \quad (2.4)$$

where  $u_{pr2}$  is the rotation of the secondary in arcsec. Since the derivation of this formula places the stop by definition at the secondary, this decentering coma is independent of the form of the mirror. For the NTT this gives

$$\left[ (\delta u'_p)_{Coma_t} \right]_{2,rot,NTT} = -0.00852 (u_{pr2})_{arcsec} \text{arcsec} , \quad (2.5)$$

or 1 arcsec of coma for  $u_{pr2} = 117.4$  arcsec. This is relatively insensitive.

The balance of these two decentering errors is of great importance for the alignment and maintenance procedures.

In § 3.7.2.1 of RTO I it was emphasized that third order *decentering coma* is by far the most important decentering aberration. It was also pointed out that this dominance of coma compared with astigmatism arises because of the *linear* field dependence of coma, implicit in the derivation of Eqs. (2.1) and (2.2), compared with the *quadratic* dependence of astigmatism. For most “normal” (i.e. “passive”) telescopes, it will be entirely sufficient to limit the consideration of decentering aberrations to coma alone. However, for modern “active” telescopes of effectively diffraction-limited quality in excellent sites capable of the exploitation of this extreme quality, *decentering astigmatism* may become significant. The better the field correction of the telescope, the more critical such astigmatism will become: this may already be true for aplanatic telescopes and will certainly be even more so for more complex forms giving anastigmatism.

It was shown in RTO I how the decentering sensitivity formula for coma of Eq. (2.1) could readily be deduced from the *general recursion formulae* given in § 3.6.5.2. The equivalent formula for astigmatism can be derived in a similar way as follows. From Fig. 3.97 and p. 259 of RTO I, we can take over for the telecentric principal ray

$$y_{pr2} = +\delta ,$$

the lateral decenter, and

$$\bar{A}_2 = \frac{y_{pr2}}{r_2}$$

$$(HE)_2 = \frac{y_{pr2}}{y_2}$$

Applying the recursion formulae (3.336) to the aperture ray gives

$$y_2 = y_1 \left( 1 - \frac{2d_1}{r_1} \right) = y_1 R_A$$

from (2.72) of RTO I, and

$$\Delta \left( \frac{u}{n} \right)_2 = (\mu_2 + 1) \left( -2 \frac{y_1}{r_1} \right)$$

$$\mu_2 = \frac{1}{r_2} (r_1 - 2d_1 - r_2)$$

$$\tau_2 = 2b_{s2} \frac{y_2^4}{r_2^3}$$

Then, from (3.20) of RTO I,

$$(S_{III})_2 = -y_2 \left( \frac{y_{pr2}}{r_2} \right)^2 (\mu_2 + 1) \left( -\frac{2y_1}{r_1} \right) + \left( \frac{y_{pr2}}{y_2} \right)^2 2b_{s2} \frac{y_2^4}{r_2^3} \quad (2.6)$$

From (2.72) and (2.90) of RTO I

$$r_1 = r_2 \frac{1}{R_A} \left( \frac{m_2 + 1}{m_2} \right) ,$$

so that with

$$y_1 = \frac{y_2}{R_A}$$

$$\mu_2 + 1 = \frac{m_2 + 1}{m_2} ,$$

Eq. (2.6) reduces at once to the simple form

$$(S_{III})_2 = 2 \frac{y_2^2}{r_2} (1 + b_{s2}) \left( \frac{\delta}{r_2} \right)^2 \quad (2.7)$$

or

$$(S_{III})_2 = 2 \frac{y_1^2 R_A^2}{r_2} (1 + b_{s2}) \left( \frac{\delta}{r_2} \right)^2 \quad (2.8)$$

The factor  $(\delta/r_2)^2$  arises from the basic dependence of third order astigmatism on the square of the field.

These equations reveal an interesting property. If the secondary has a parabolic form ( $b_{s2} = -1$ ), then the astigmatism due to pure lateral decenter is zero since the spherical and aspheric terms compensate each other. This result can also be interpreted from an elegant geometrical property of the paraboloid: sections through it parallel to its axis are always the same as the generating parabola itself [2.1]. This means that the vertex curvature of such parallel sections of (a paraboloidal)  $M_2$  in Fig. (3.97) of RTO I is always the same. This is operative for the *sagittal* beam. But the off-axis curvature in the *tangential* section is less than the vertex curvature. It is given by the well-known general formula for the radius of curvature (*normal* to the surface) of any point of a function, in our case of a parabola defined by  $z = y^2/2r$  according to Eq. (3.2) of RTO I, as

$$\rho_t = \frac{\left[ 1 + \left( \frac{dz}{dy} \right)^2 \right]^{3/2}}{\frac{d^2 z}{dy^2}} , \quad (2.9)$$

from which we have  $dz/dy = y/r$  and  $d^2z/dy^2 = 1/r$ . Now  $y = \delta$ , the lateral decenter, giving to the third order

$$\rho_t = r \left( 1 + \frac{3}{2} \frac{\delta^2}{r^2} \right) \quad (2.10)$$

From the cosine obliquity effect of the curvature in the sagittal section, bearing in mind that the basic radius of curvature  $r$  of the section parallel to the axis must be *divided* by the cosine of the angle to the normal because of the transfer from a “small circle” section to a “great circle” section [2.2], we have the *normal* sagittal radius of curvature

$$\rho_s = r \left( 1 + \frac{1}{2} \frac{\delta^2}{r^2} \right) \quad (2.11)$$

Application of Eqs. (3.88) and (3.206) of RTO I, ignoring  $S_{IV}$  and setting  $s_{pr1} = 0$ , lead to astigmatic focus shifts for a beam on the centered surface at equivalent field angle  $\delta/r$  of

$$I'_{pr} I'_s = -\frac{1}{4} r \frac{\delta^2}{r^2} \quad (2.12)$$

for the sagittal beam and

$$I'_{pr} I'_t = -\frac{3}{4} r \frac{\delta^2}{r^2} \quad (2.13)$$

for the tangential beam. Since, for a parallel beam, the focal length is  $\rho/2$ , the positive supplements to the radius of curvature of Eqs. (2.10) and (2.11) above exactly compensate the astigmatic contributions of Eqs. (2.13) and (2.12) respectively.

Of course, the above treatment assumes that *parallel* beams are falling on a *parabolic* primary or secondary. But this is implicit in the assumption of a parabola for the secondary, because such a 2-mirror telescope must have a parallel *emergent* beam (i.e. must be afocal) for spherical aberration correction. Thus the above treatment with  $b_{s2} = -1$  refers to a *Mersenne afocal telescope* either of Cassegrain or Gregory form, which has, to the third order, zero sensitivity to pure decentering astigmatism.

From Eq. (3.208) of RTO I, Eq. (2.8) above gives the angular length of the astigmatic line for pure decenter as

$$(\text{Ast}_{line})_{\delta,gen} = -4 \frac{y_1}{r_2} R_A^2 (1 + b_{s2}) \left( \frac{\delta}{r_2} \right)^2 (206 265) \text{ arcsec} \quad (2.14)$$

for the general case. For an aplanatic telescope, a more convenient form in terms of fundamental parameters is

$$\begin{aligned} & (\text{Ast}_{line})_{\delta,Aplan} \\ &= -\frac{m_2(m_2+1)}{NR_A} \left[ 1 - \frac{1}{2(1-R_A)(m_2+1)} \right] \left( \frac{\delta}{f'} \right)^2 (206 265) \text{ arcsec}, \end{aligned} \quad (2.15)$$

in which the second term in the square bracket represents the supplement of the aplanatic telescope compared to the classical telescope with a parabolic primary, for which the square bracket term is unity.

Equations (2.14) and (2.15) were recently given by Wilson and Delabre [2.3] in a general treatment of the theory of telescope alignment, illustrated by the NTT. It was shown for that telescope that the very large decenter value of  $\delta = 10$  mm gives only about 1/8 arcsec for the astigmatic line from Eq. (2.15), whereas the tangential coma from Eq. (2.2) has the enormous value of about 10.5 arcsec! This reveals the clear dominance of coma as the fundamental error induced by lateral decenter. In the NTT, the very small astigmatism value is also the result of its relatively high secondary magnification  $m_2 = -5$ . This becomes evident if we set  $f' = m_2 f'_1$  and  $N = m_2 N_1$  in (2.15). A high value of  $m_2$  implies the telescope is approaching the limit case of the Mersenne afocal form, for which (2.15) also gives zero astigmatism.

### 2.1.2 Despace errors

In the set-up of 2-mirror telescopes, the free parameter is the separation  $d_1$  between the two mirrors, controlled by the focus movement of the secondary. The differential effect  $dd_1$  on the other parameters (see Fig. 2.12 in RTO I) is from RTO I, Eqs. (3.394) to (3.399),

$$dL = m_2^2 dd_1 \quad (2.16)$$

$$db = (m_2^2 + 1) dd_1 \quad (2.17)$$

$$dm_2 = \frac{m_2^2(m_2 + 1)}{L} dd_1 \quad (2.18)$$

$$df' = \left( \frac{f'}{f'_1 - f'_2 - d_1} \right) dd_1 \quad (2.19)$$

These are changes affecting the *Gaussian (first order)* geometry of the telescope. But a change in mirror separation  $d_1$  also affects the *third order* aberrations. Because of the convergence of the aberration function, only two of these are of significance: the effect on the spherical aberration and field coma. The latter is only significant in aplanatic systems, such as the RC telescope, for which the field coma is nominally corrected.

The change in *third order spherical aberration in arcsec* due to the differential  $dd_1$  is from RTO I, Eq. (3.409),

$$\begin{aligned} d(\delta u'_p)_{BF,S_I} = & -\frac{1}{32N_1^3} \left[ \left( \frac{m_2^2 - 1}{m_2^2} \right) - \left( \frac{m_2 + 1}{m_2} \right)^3 \right. \\ & \times \left. \left\{ \left( \frac{m_2 - 1}{m_2 + 1} \right)^2 + b_{s2} \right\} \right] \frac{dd_1}{f'_1} (206\,265) \text{ arcsec} \end{aligned} \quad (2.20)$$

in the *general case*, where  $N_1$  and  $f'_1$  refer to the primary mirror and the angular aberration refers to the “best focus” combination with defocus. For

the *RC case*, we have from RTO I, Eq. (3.407), and  $d_1 = \frac{f'_1}{m_2}(1 - R_A)$  from RTO I, Eq. (2.72),

$$[d(\delta u'_p)_{BF}]_{Aplan} = -\frac{1}{32N_1^3 m_2^2} \left[ (m_2^2 - 1) + \left( \frac{2}{1 - R_A} \right) \right] \frac{dd_1}{f'_1} 206\,265 \text{ arcsec} \quad (2.21)$$

Again, the first term in the square bracket is for the classical telescope, the second term the RC supplement. The NTT values give from (2.21)

$$[d(\delta u'_p)_{BF}]_{Aplan, NTT} = 0.0836 dd_1 \text{ arcsec} \quad (2.22)$$

Therefore, a change  $dd_1 = 1 \text{ mm}$  produces from (2.17) a shift of the final image in the NTT of 26 mm and a spherical aberration at best focus of 0.0836 arcsec.

Finally, the change in *third order tangential field coma in arcsec* due to the differential change  $dd_1$  is given from RTO I, Eqs. (3.415) and (3.198),

$$[d(\delta u'_p)_{Coma_t}]_{Field} = \frac{3}{8N_1^2} \frac{1}{R_A} \left[ \left( \frac{4R_A - 3}{m_2^3} \right) \xi + (1 - R_A) \left( \frac{m_2^2 - 1}{m_2^2} \right) - \frac{m_2 + 1}{m_2^2} \right] u_{pr1} \frac{dd_1}{f'_1} (206\,265) \text{ arcsec} , \quad (2.23)$$

where  $u_{pr1}$  is the semi-field angle in rad, for the general case, in which

$$\xi = \frac{(m_2 + 1)^3}{4} \left[ \left( \frac{m_2 - 1}{m_2 + 1} \right)^2 + b_{s2} \right]$$

from RTO I, Eq. (3.41). For the RC telescope, (2.23) gives with RTO I, Eqs. (3.108) and (3.420),

$$[d(\delta u'_p)_{Coma_t}]_{Field, Aplan} = \frac{3}{8N_1^2} \frac{1}{m_2^2 R_A} \left[ - \left( \frac{4R_A - 3}{2(1 - R_A)} \right) + (1 - R_A)(m_2^2 - 1) - (m_2 + 1) \right] u_{pr1} \frac{dd_1}{f'_1} (206\,265) \text{ arcsec} , \quad (2.24)$$

with the semi-field angle  $u_{pr1}$  expressed in rad. The last two terms in the square bracket express the result for a classical telescope, the first term the RC supplement. The parameters of the NTT give in (2.24) with  $u_{pr1} = 15 \text{ arcmin}$

$$[d(\delta u'_p)_{Coma_t}]_{Field, NTT} = 0.0377 dd_1 (\text{mm}) \text{ arcsec} \quad (2.25)$$

Therefore, a change of  $dd_1 = 1 \text{ mm}$ , producing an image shift of 26 mm in the NTT, generates 0.0377 arcsec of field coma, varying linearly with the field, at the semi-field of 15 arcmin.

## 2.2 Alignment and adjustment of telescopes

### 2.2.1 General theoretical principles of telescope alignment

Although we shall also consider the cases of prime focus telescopes and Schmidt telescopes below, the 2-mirror Cassegrain geometry has firmly become the standard tool for modern astronomical research. The alignment of classical or aplanatic (RC) Cassegrain telescopes is therefore by far the most important aspect of modern telescope alignment in general. With minor modifications, the same principles apply to Gregory telescopes.

The sensitivities discussed in § 2.1 confirm the well-known fact that the principal decentering aberration is *coma*. This will remain true in any practical telescope form. The alignment must therefore have as its first aim the reduction of decentering coma to acceptable values. With the dramatic improvements in optical quality arising from manufacturing technology, optimum sites, thermal control and active optics (i.e. active maintenance), the demands on alignment quality have correspondingly increased.

A “perfectly centered telescope” is an abstraction, a mathematical limit case of no practical meaning. Residual errors will always be present, but should be small enough to meet the image specification tolerances discussed in Chap. 4 below. In general, one can say that the errors due to misalignment should be small compared with the total image error of the perfectly centered telescope, including, of course, atmospheric seeing.

It must be emphasized that the *aspheric* surfaces of normal 2-mirror telescopes, particularly in their steep modern forms giving short systems, complicate the alignment compared with, say, a lens system containing only *spherical* surfaces. The latter have *no axis*: decenter is only a matter of tilt of the surface relative to some reference “axis”. But aspheric surfaces have a genuine unique axis of revolution. As we have seen in § 3.7 of RTO I, there are therefore *two* coma decentering effects of the secondary relative to the primary as expressed by Eqs. (2.1) and (2.4) above, lateral decenter of the aspheric axis and rotation about the pole. Thus a compensation of the two coma effects is possible. For the small decenter effects acceptable in practice, the third order formulae given above are extremely accurate. Such a coma – free system due to such compensation is called a “coma-free Schiefspiegler” (CFS), following the proposals of Kutter (see Fig. 3.93 of RTO I). Now, to third order accuracy, the decentering coma is a *constant* vector over the field, whereas field coma, in a telescope for which it is not corrected, grows linearly with the field and is therefore a radial vector growing linearly with the distance from the field center, as shown in Fig. 2.1. In this example, the field and decentering vectors cancel at the field point A, so this becomes the new field center free from coma instead of the point O. However, the combined coma in the field is still a symmetrical function about A. It follows that, if OA is small compared with the field radius and the point A is brought to the mechanical field center of the telescope by a small pointing change, *the*

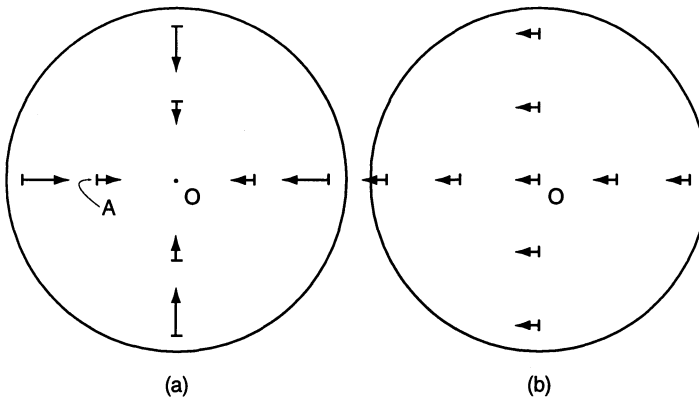


**Fig. 2.1.** Combination of (a) field coma, growing linearly with the field radius, and (b) decentering coma, constant over the field

*observer is completely unaware that decentering coma is present.* Of course, this statement is only true for small errors adequately defined by the third order approximation and where the decentering astigmatism remains negligible. The case of Fig. 2.1 corresponds to that of a *classical* Cassegrain telescope with a parabolic primary. An *aplanatic* (RC) telescope has no field coma to the third order, so there is no field point of compensation of the decentering coma which therefore appears in full over the whole field. Clearly, then, correction of decentering coma is more critical for an aplanatic telescope.

The coma-free Schießspiegler (CFS) is therefore the practical basis of telescope alignment and relaxes the theoretical abstraction of a perfectly centered system. Figures 2.2(a) and 2.2(b) show the situations of “pure” lateral decenter and the coma-free Schießspiegler respectively. The former is the situation corresponding to the coma of (2.1) and the astigmatism of (2.14). In Fig. 2.2(b) the line  $M_1M_2$  joining the poles of the mirrors is considered to be the nominal “optical axis” of the telescope (OPT) which will also be the definition of the “tube axis”. The fundamental parameter of the CFS is the quantity  $\delta$ , the relative lateral displacement of the aspheric axes. An incident principal ray is drawn to  $M_1$  (assumed to be the pupil) with the angle  $u_{pr1}$  such that the reflected ray passes through  $M_2$ . For CFS coma compensation, the secondary must be rotated in the sense shown through the angle *rot* so that the reflected ray is deflected further from the axial image point  $O$  to the image point  $I'_S$ . This image point  $I'_S$  is then the effective center point of the CFS field and is brought to the mechanical field center by a small pointing change of the telescope, whose precise significance will be treated below.

In § 3.7.1 of RTO I, the condition for coma compensation in the CFS was given as

$$\frac{u_{pr2}}{u_{pr1}} = -\frac{r_1 r_2^2}{(r_1 - 2d_1)^2(r_1 - 2d_1 - 2r_2)} \quad (2.26)$$

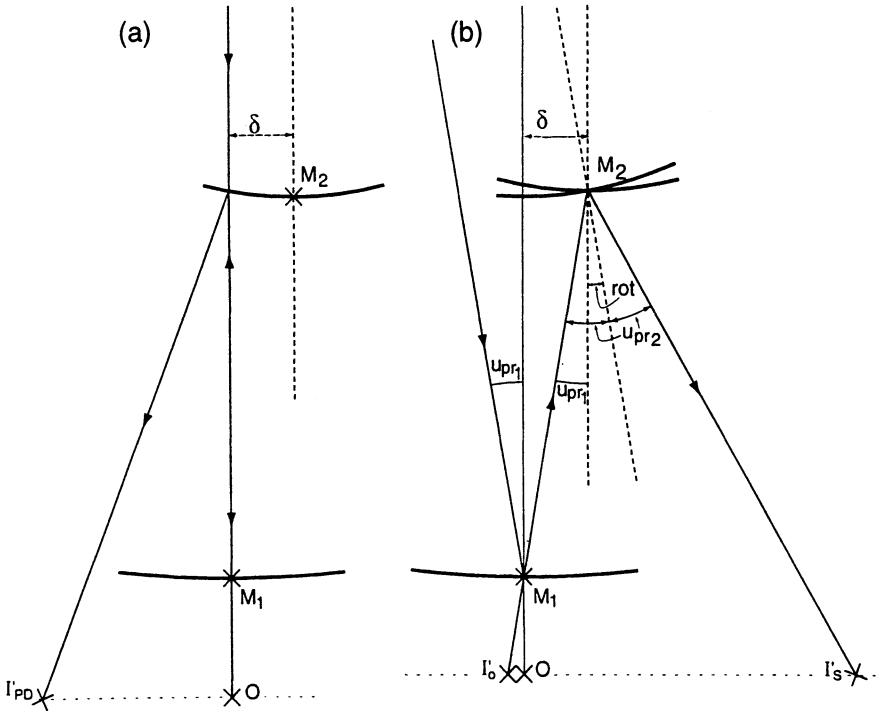


Fig. 2.2. (a) ‘‘Pure’’ lateral decenter, (b) Coma-free Schiefspiegler (CFS) (after Wilson and Delabre [2.3])

If this relation, defining the CFS, is entered into the formulae for the astigmatism contributions given by Eqs. (3.349) and (3.350) in RTO I for the primary and the secondary, then the astigmatism in the ‘‘axial’’ point \$I'\_S\$ of the CFS is [2.3]

$$(Ast_{line})_{\delta,S} = -\frac{m_2}{N} \left[ 1 - \frac{r_1 r_2^3}{(r_1 - 2d_1)^2 (r_1 - 2d_1 - 2r_2)^2} \right] \left( \frac{\delta}{d_1} \right)^2 (206\,265) \text{ arcsec} , \quad (2.27)$$

where the first term 1 in the square bracket represents the contribution of the primary and the second term that of the secondary.

Ray tracing confirms that Eq. (2.27) is extremely accurate in practice. For the 3.5 m NTT with \$m\_2 = -5\$, \$N = 11\$, \$r\_1 = -15\,400\$ mm, \$r\_2 = -4416.7\$ mm, \$d\_1 = -5933.3\$ mm (see Fig. 3.4 (b) in RTO I for the complete data of the NTT), and a value \$\delta = 2.5\$ mm, Eq. (2.27) gives

$$(Ast_{line})_{2.5\,mm,S} = -0.046\,330 \text{ arcsec} ,$$

a normally negligible value even for the best telescopes and sites. However, the value grows with \$\delta^2\$, so that for \$\delta = 10\$ mm we have \$(Ast\_{line})\_{10\,mm,S} = -0.74127\$ arcsec, an unacceptable value. This reveals the fundamental question concerning the elimination of decentering coma with a CFS: *how large*

*may the determinant parameter  $\delta$  be before other errors, notably astigmatism, become too large [2.3]?*

Two aspects of Eq. (2.27) must be emphasized. Firstly, *it is independent of the asphericity of the secondary*. This is because the “axial” beam shown in Fig. 2.2(b) strikes both mirrors “centrally”, i.e. the coma and astigmatism introduced by  $M_2$  are independent of stop position and are solely dependent on the rotation of  $M_2$  relative to the incident “axial” beam. Secondly, *it is formally only valid for the region near the CFS “axis”*: the astigmatic effects further out in the field require more detailed analysis.

Bhatia, in a ray-tracing analysis based on NTT optical geometry, has suggested [2.4] that, for such telescopes, the zero-coma condition is a necessary but not sufficient condition and that separate degrees of freedom of  $M_2$  (translation and rotation) must be used to correct both decentering coma and astigmatism. However, he assumed a CFS with  $\delta > 5$  mm, an unsatisfactory state of basic adjustment and far worse than that actually established for the NTT at initial set-up, which was about  $\delta \leq 2.5$  mm [2.3]. Here we must bear in mind the astigmatism dependence on  $\delta^2$  of Eq. (2.27).

The general nature of the decentering aberration function was analysed in a fundamental paper by Shack and Thompson [2.5]. They point out that, when the elements of a system are decentered laterally or rotationally, the aberration field contributions *from each surface* essentially remain rotationally symmetrical about some point in the field. Because of the unique axis of aspheric surfaces, the shift of the effective field center for such a surface will be different for its spherical and aspheric components. For each effect alone, the symmetrical nature of the aberration to its shifted field center is largely maintained, but the *combination* of the different effects produces a more complex field dependence. Because of the basic dependence on the square of the field, the general case of decentering astigmatism is more complex than that of coma. Shack and Thompson show that the general form is *binodal*, i.e. the astigmatism still grows roughly with the square of the field, but about *two* zero points (nodes), disposed along the field axis in the direction of the decenter and with a separation linearly dependent on  $\delta$ . Figure 2.3 shows the nature of this function. Three limit cases are important: zero separation of the nodes corresponds to normal astigmatism varying with the *square* of the field but with shifted field center; one node stationary and the other at infinity gives a *linear* field dependence; both nodes at infinity with stationary center of symmetry gives a *constant* astigmatism over the field.

Shack and Thompson give the vector analysis in terms of Seidel aberration coefficients as constants in the equations for the decentered systems. The same basic approach has recently been further refined in an excellent paper by McLeod [2.6]. Extending formulations by Schroeder [2.7], McLeod gives an expression for the two astigmatic components of a decentered system. Let the field height in Fig. 2.5 of RTO I be expressed in angular measure  $\theta = \eta'/f'$  and let the CFS rotation angle *rot* of  $M_2$  in Fig. 2.2(b) be termed  $\alpha \equiv \text{rot}$ , whereby the tilted axis of  $M_2$  with angle  $\alpha$  will cut the  $M_1$  axis at

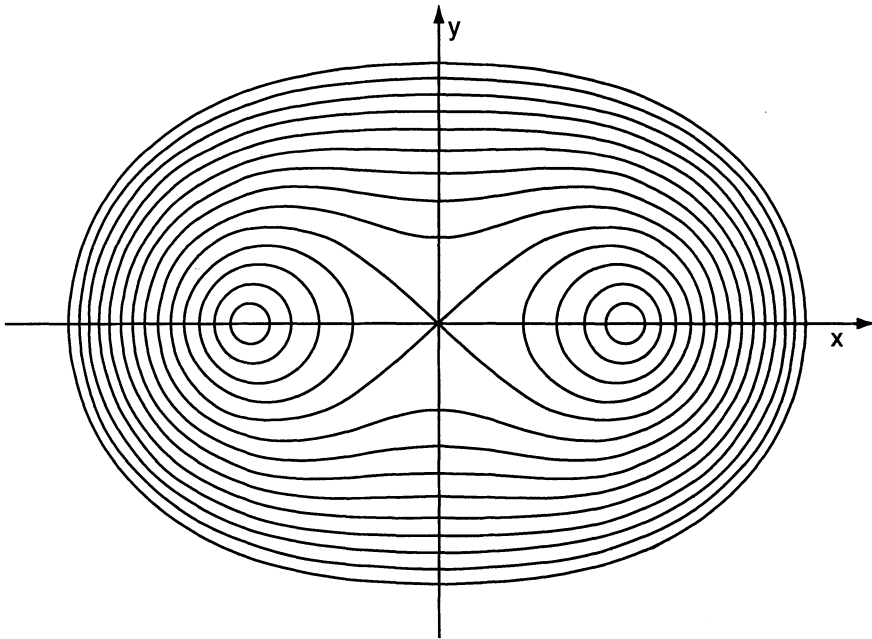


**Fig. 2.3.** Nature of the *binodal* decentering astigmatism function (after Shack and Thompson [2.5])

the “coma-free point” – see § 3.7.2.3 of RTO I. Then the astigmatism terms, as wavefront aberration resolved in  $x, y$  directions relative to some vector direction of the tilt, are given by McLeod as

$$\left. \begin{aligned} (W_{ast})_{\cos 2\phi} &= B_0(\theta_x^2 - \theta_y^2) + B_1(\theta_x \alpha_x - \theta_y \alpha_y) + B_2(\alpha_x^2 - \alpha_y^2) \\ (W_{ast})_{\sin 2\phi} &= 2B_0\theta_x\theta_y + B_1(\theta_x \alpha_y + \theta_y \alpha_x) + 2B_2(\alpha_x \alpha_y) \end{aligned} \right\}, \quad (2.28)$$

whereby  $\phi$  is the azimuth angle in the pupil defined in § 3.2.1 of RTO I. Equations (2.28) give the binodal field astigmatism shown in Fig. 2.3. Shack and Thompson point out that the contours of this function are *ovals of Cassini*, whereby the magnitude of the astigmatism for any field point is proportional to the product of the distances from the two nodes.

If we define the  $x$ -direction of Eqs. (2.28) to be the same as the decenter section, i.e. the same as the  $x$ -direction of Fig. 2.3, then  $\alpha_y$  in (2.28) is zero and the function along the  $x$ -axis field direction is given by

$$(W_{ast})_{\cos 2\phi, x} = B_0\theta_x^2 + B_1\theta_x \alpha_x + B_2\alpha_x^2 \quad (2.29)$$

For the nodes, this function must be zero, giving nodal field positions  $(\theta_x)_N$  for a given decenter  $\alpha_x$

$$(\theta_x)_N = \frac{\alpha_x}{2B_0} \left[ -B_1 \pm (B_1^2 - 4B_0B_2)^{1/2} \right] \quad (2.30)$$

The shift of the field center, halfway between the nodes, is then

$$(\theta_x)_{\Delta\eta_A} = -\frac{B_1}{2B_0}\alpha_x , \quad (2.31)$$

while the field distance from this center to the nodes is

$$(\theta_x)_{\Delta\eta_N} = \pm\frac{\alpha_x}{2B_0}(B_1^2 - 4B_0B_2)^{1/2} \quad (2.32)$$

If  $|B_0|$  and  $|B_1|$  are similar and  $|B_2|$  is negligible in comparison, then

$$(\theta_x)_{\Delta\eta_N} \simeq \pm(\theta_x)_{\Delta\eta_A} \quad (2.33)$$

and *one of the nodes will lie near the  $M_1$  axis, the field center of the centered telescope*. We shall see below that this approximates to the normal telescope case.

McLeod gives expressions for  $B_0, B_1, B_2$  in the notation of Schroeder [2.7]. In the notation of RTO I they can be written

$$\left. \begin{aligned} B_0 &= (A_0)_1\rho_1^2 - (A_0)_2\rho_2^2 \\ B_1 &= -\left[2(A_0)_2 + (s_{pr2} + z_{CFP})(A_1)_2\right]\rho_2^2 \\ B_2 &= -\left[(A_0)_2 + (s_{pr2} + z_{CFP})(A_1)_2 + (s_{pr2} + z_{CFP})^2(A_2)_2\right]\rho_2^2 \end{aligned} \right\} , \quad (2.34)$$

in which

$$\left. \begin{aligned} A_0 &= \frac{(s_{pr})^2}{2r} \left[ \frac{b_s}{r^2} + \left( \frac{1}{s_{pr}} - \frac{1}{r} \right)^2 \right] \\ A_1 &= \frac{s_{pr}}{r^2} \left[ \frac{1}{s_{pr}} - \frac{(b_s + 1)}{r} \right] \\ A_2 &= \frac{b_s + 1}{2r^3} \end{aligned} \right\} \quad (2.35)$$

In these equations,  $\rho$  represents the ray height in the pupil,  $s_{pr}$  the pupil distance from the surface 1 or 2,  $r$  the radius of curvature,  $z_{CFP}$  the distance from the coma-free point to  $M_2$  (taken as *positive* to give a positive  $\alpha$  with positive  $\delta$ ),  $b_s$  the Schwarzschild constant. With the normal case of the stop at the primary,  $s_{pr1} = 0$  and  $s_{pr2} = -d_1$ , a positive quantity. Table 2.1 gives the necessary data for the evaluation in the case of the ESO 3.5 m NTT. For this telescope, the coefficients of (2.34) are

$$\left. \begin{aligned} B_0 &= -24.3679 \mu\text{m deg}^{-2} \\ B_1 &= +30.0717 \mu\text{m deg}^{-2} \\ B_2 &= + 0.17675 \mu\text{m deg}^{-2} \end{aligned} \right\} , \quad (2.36)$$

the units  $\mu\text{m deg}^{-2}$  being the same as those given by McLeod for the example of the Mt. Hopkins 1.2 m RC telescope, the angular field being given in

**Table 2.1.** Parameters for the evaluation of Eqs. (2.34) and (2.35) in the case of the ESO 3.5 m NTT

Mirror	$r$ (mm)	$b_s$	$s_{pr}$ (mm)	$z_{CFS}$ (mm)	$\rho$ (mm)
$M_1$	-15400	-1.023822	0	-	+1750.0
$M_2$	-4416.7	-2.452784	+5933.3	+1676.1	+401.52

degrees. Since this telescope has a roughly similar Cassegrain geometry to that of the NTT, the relative values of the three coefficients are also roughly similar. We see that  $|B_0|$  and  $|B_1|$  are indeed similar and that  $|B_2|$  is very much smaller, as in the Mt. Hopkins case. Equation (2.33) is therefore applicable to such telescopes, i.e. one of the nodes remains roughly at the  $M_1$  axis. For the NTT, the linear shift of the astigmatic field center is, from (2.31) with  $\delta = 2.5$  mm and  $f' = 38\,500$  mm,

$$\Delta\eta_A = f'(\theta_x)\Delta\eta_A = +35.432 \text{ mm} \quad (2.37)$$

from the  $M_1$  axis. Now, for comparison, the shift of the coma-free “axis” point  $I'_s$  of the CFS of Fig. 2.2(b) is [2.3]

$$\Delta\eta_{CFS} = +32.57 \text{ mm} \quad (2.38)$$

These two values are similar. It is important to consider whether this is always the case or whether it is due to the specific geometry of the NTT. In fact, it can easily be shown to a rough approximation that

$$\Delta\eta_{CFS} \approx +2\alpha_x L , \quad (2.39)$$

if in Fig. 2.2(b)  $u_{pr1} \ll 2u_{pr2}$ , as is the case, and  $L$  is the back focal distance  $M_2 I'_0$ . Similarly, if we apply the rough approximation from (2.36) that  $B_1 \approx -B_0$ , then from (2.31)

$$\Delta\eta_A \approx +\frac{1}{2}\alpha_x f' \quad (2.40)$$

Now  $L = R_A f'$  from (2.72) of RTO I, where  $R_A = 0.22944$  is the axial obstruction ratio of the NTT. We see from Eqs. (2.39) and (2.40) that

$$\Delta\eta_A \approx \Delta\eta_{CFS} \quad (2.41)$$

if the telescope has an axial obstruction ratio  $R_A \approx 0.25$ . That of the NTT is quite near to this value which is indeed typical for modern Cassegrain telescopes. Lower values of  $R_A$  will give values of  $\Delta\eta_{CFS}$  less than  $\Delta\eta_A$ .

For Cassegrain telescopes of normal geometry as with the NTT, therefore, the astigmatic field center shift will be similar to the shift of the CFS “axis”  $I'_s$  and one of the nodes will be quite near the  $M_1$  axis, since  $B_2$  will always be relatively small for normal geometries. These are important geometrical properties of the field aberrations of the decentered system.

A further theoretical property of importance is the condition for which the nodal separation becomes zero, i.e. the case of a pure shift of field center. This is given by Eq. (2.30) if the second term becomes zero, so that

$$B_1^2 - 4B_0B_2 = 0$$

or

$$B_2 = \frac{B_1^2}{4B_0} \quad (2.42)$$

Since  $B_0$  is always negative in practice, this requires that  $B_2$  also be *negative*. It would be satisfied by the relative values  $B_0 = -1$ ,  $B_1 = \pm 2$ ,  $B_2 = -1$ , as is also evident by substituting in the basic astigmatism equation (2.29). However, as mentioned above, such a large negative value of  $B_2$  is impossible with normal optical geometries of Cassegrain telescopes, *i.e.* with fairly large values of  $|m_2|$  and normal positions of the final image. As we have seen, the normal case is that  $B_1^2 \gg 4B_0B_2$  with  $B_2$  of the wrong sign (positive) for compensation, giving a nodal separation slightly greater than twice the field center shift  $\Delta\eta_A$ . The binodal astigmatic field function is, therefore, the normal case for practical telescopes with decentering.

The first term in  $B_0$  of Eqs. (2.28) and (2.29) is simply the normal quadratic field astigmatism of the centered telescope. This is also given explicitly by the first of McLeod's equations (2.34) as the wavefront aberration of the tangential astigmatism per (unit field)<sup>2</sup>. In fact, it gives an identical result to that of Eqs. (3.61) and (3.202) in RTO I for the field astigmatism. However, proving the equivalence of the formulae requires considerable transformation: it is more readily shown from the fundamental terms of the recursion formulae (§ 3.6.5.2 of RTO I) for the primary and secondary mirrors to give the equivalent of  $(A_0)_1$  and  $(A_0)_2$  in McLeod's formulation.

The property mentioned above of the ovals of Cassini of Fig. 2.3, that the astigmatism at any field point is proportional to the product of its distances from the nodes, leads to an important general conclusion. In the  $x$ -section of decenter corresponding to Eq. (2.29) the astigmatism at an edge field point distant  $x_E$  from the point of field symmetry is simply

$$\text{Ast} \propto (x_E - \Delta x)(x_E + \Delta x) = x_E^2 - \Delta_x^2, \quad (2.43)$$

where  $\pm\Delta x$  is the distance of the nodes from the central symmetry point. Clearly, if  $\Delta x \ll x_E$ , the relative error will be small compared with the simple assumption of a normal quadratic law applied to a shifted field center at the field symmetry point. This assumption was made in the set-up of the NTT, in which the image analyser normally measures the astigmatism at the field edge and a correction is made for an effective (measured) field center shift. The limits of the validity of this assumption have been discussed by Wilson and Delabre [2.3]. On the basis of the measured field center shift of about 20 mm, they concluded that the effective lateral decenter  $\delta_{eff}$  of the CFS set up with the initial alignment was

$$\delta_{eff} \leq 2.6 \text{ mm} \quad (2.44)$$

and that the assumption of a simple field center shift introduced negligible astigmatism errors, even at the edge of the field. They concluded that, *provided the value of  $\delta_{eff}$  of the CFS set up is sufficiently small*, the coma-free

condition is a sufficient as well as a necessary condition for the alignment of "normal" telescopes, whereas Bhatia's opposite conclusions [2.4] were based on  $\delta_{eff}$  values of the CFS which were too large, i.e. the basic alignment procedure assumed was not adequate, bearing in mind that the effect on astigmatism is proportional to  $\delta^2$ . Classical Cassegrain telescopes are the least critical, RC (aplanatic) telescopes more so (particularly if they are actively controlled). The most critical will be wide-field *anastigmatic* telescopes, for which the whole field is used for observation.

McLeod [2.6] suggests correcting the residual CFS error  $\delta_{eff}$  by measurements in the astigmatic field and a least-squares process to deduce  $\delta_{eff}$ . This is an elegant approach and a similar procedure is now (end of 1996) being applied to the NTT: a mapping of the astigmatic field to determine the positions of the field center and the nodes. The value of  $\delta_{eff}$  can then be directly determined from the equations above. Although the assumption of a simple field center shift in the NTT was adequate at the time of set-up, it would make no sense today since the field can readily be mapped and the nodal separations, even with  $\delta \leq 2.6$  mm, are by no means as negligible as was assumed at the time.

Finally, it is instructive to tabulate some of the astigmatism values in the  $x$ -section of Fig. 2.3 given by Eq. (2.29) for a value  $\delta = 2.5$  mm in the NTT. Expressing the corresponding decenter angle  $\alpha_x$  in degrees, we have  $\alpha_x = +0.085458^\circ$ . Table 2.2 gives the astigmatism as  $(Ast_{line})_{cos2\phi,x}$  in arcsec. The sign of the total aberration has been reversed from that of McLeod's equations above to give agreement with the sign convention of Table 3.3 of RTO I. The last value, for the centered system, originates from the  $B_0$  term of Eq. (2.29). If this value is modified by a simple field center shift  $\Delta\eta_A = +35.432$  mm, then the astigmatism  $(Ast_{line})$  errors for the edge field points  $\pm 168.0$  mm of the decentered system are about  $+0.065$  arcsec. These

**Table 2.2.** Astigmatism values for the decentered NTT ( $\delta = 2.5$  mm) for various field points and in comparison with the centered system

$\delta$ (mm)	Field point	Field height from $M_1$ (mm)	$(Ast_{line})_{cos2\phi,x}$ (arcsec)
2.5	$M_1$ axis	0	-0.0012171
	L.H. node	-0.336	0
	R.H. node	+71.200	0
	Center of ast.field ( $\Delta\eta_A$ )	+35.432	-0.065106
	CFS "axis" ( $\Delta\eta_{CFS}$ )	+32.57	-0.064689
	L.H. field edge	-168.0	+2.040906
	R.H. field edge	+168.0	+0.829217
0	Centered system field edge	$\pm 168.0$	+1.436278

errors are about 30 % higher than those determined from ray tracing [2.3]. Similarly, the tabular values in the central field region between the nodes are about 30 % higher than ray trace values. In general, third order formulae involving the asphericity as defined by  $b_s$  tend to give astigmatism results which are somewhat too large when the astigmatism values are very small. This is true of the McLeod formulae and also for Eq. (2.8) giving astigmatism from simple lateral decenter. By contrast, Eq. (2.27) giving the astigmatism at the “axial” point of a CFS remains remarkably accurate even for very small values, because it does *not* involve the asphericity. For the point  $\Delta\eta_{CFS} = +32.57$  mm it gives the accurate value  $-0.046330$  arcsec compared with the value  $-0.064689$  arcsec of Table 2.2.

Apart from the decentering effects on the astigmatic field, there is another effect arising from the coma-free Schießspiegler (CFS) which may become significant in the total telescope system. This is the inevitable lateral decenter of the *exit pupil*, which leads to a *collimation error* and *an inclination of the exit beam to the mechanical telescope axis*. The former can be corrected by pointing software, but the latter is an inevitable consequence of the CFS solution with a finite  $\delta$ -value. Both the above errors will increase *linearly* with  $\delta$ . The practical consequence of the beam inclination is the lateral shift of the transferred pupil of an instrument mounted axially to the telescope. The origin of these errors is treated in detail by Wilson and Delabre [2.3] and is shown in Fig. 2.4, which demonstrates the consequence of the pointing correction in the CFS to bring the “axial” image back from  $I'_S$  to  $I'_0$  on the projected axis  $M_2M_1$  of the CFS. Instead of a principal ray on the  $M_1$  axis giving the central field point  $O$  for the centered telescope, the CFS pointing correction requires a principal ray ( $Pr$ )<sub>P</sub> incident on  $M_1$  which passes, after reflection at the secondary, through  $I'_0$  on the CFS axis. The apparent beam inclination to the CFS axis  $M_2M_1I'_0$  is then  $\gamma$ , while the collimation error is  $\beta$ . It is shown in the paper that the theory gives  $\gamma = 2.026$  arcmin in the NTT with  $\delta = 2.5$  mm, no measured value being available as the effect had not disturbed the observations in any way. In practice, with typical spectrographs, the *pupil aberration* is normally several times larger than the above value of  $\gamma$  and is the limiting factor in pupil imagery on to gratings. Only in the thermal IR or for interferometric use of telescopes is the angle  $\gamma$  likely to be more critical, particularly for interferometry at visual wavelengths.

We may conclude, therefore, that the field astigmatism effects will set the practical limit to the coma-free Schießspiegler error  $\delta$  acceptable in normal telescopes and that this limit is about 2.5 mm with NTT geometry and the relatively stringent conditions of active optics with image analysis at the field edge. We have seen above that Cassegrain telescopes with a modern geometry will normally have McLeod constants in Eq. (2.29) of  $B_1 \approx -B_0$  and  $B_2 \ll B_1$ . From (2.31) and (2.32) it follows that the potentially dangerous linear decentering astigmatic effects are effectively proportional to  $(B_1/B_0)\alpha_x$ . Since the axial linear distances in such Cassegrain telescopes will be, to a crude approximation, proportional to the focal length of the primary, and

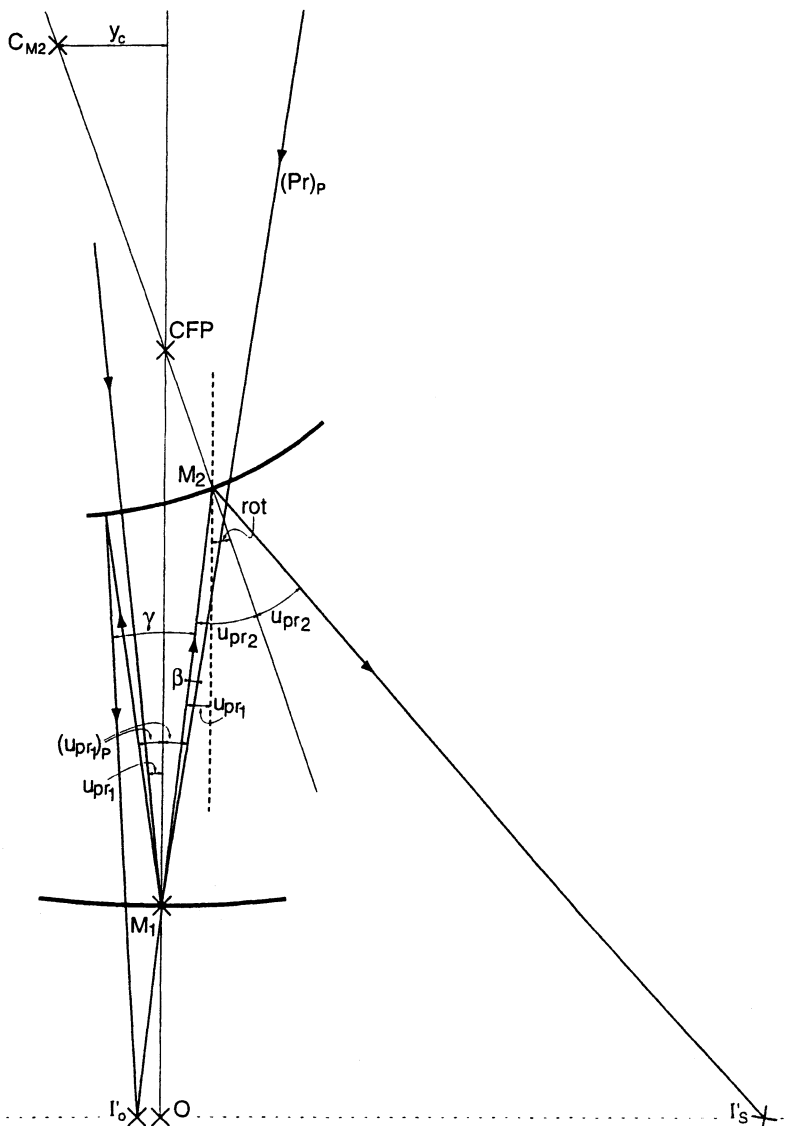


**Fig. 2.4.** Pointing correction necessitated by the coma-free Schiefspiegler (CFS) (after Wilson and Delabre [2.3])

since  $\alpha_x = \delta/z_{CFS}$  it follows that the acceptable  $\delta$ -value in such telescopes, from the astigmatic viewpoint with similar quality criteria, will be roughly proportional to the primary f/no  $N_1$ . A limit value  $\delta \leq 2.5$  mm for the NTT with  $N_1 = 2.2$  can thus be a rough guide for most modern telescopes.

In this section, we have now established that the coma-free Schiefspiegler (CFS) remains the basis of the alignment of 2-mirror telescopes and that the field astigmatism effects will limit the acceptable basic decenter  $\delta$  of the CFS.

In the next section, the practical procedure for establishing such a CFS is considered.

### **2.2.2 General set-up situation and definition of the aims of alignment**

We shall confine ourselves in this section to *Cassegrain* telescopes, either in normal geometry or with additional Nasmyth or coudé plane mirrors, since the vast majority of modern professional telescopes are of this form. The procedures described are equally valid, with obvious modifications, for Gregory telescopes.

The optical manufacturer should have delivered the optical elements with tolerances in agreement with the optical specification. The prime mirror normally has a central hole. For the normal case of an aspheric primary it has a unique aspheric axis, but this can only approximately be physically defined by a cross or marking. Such a marking is often requested on a convex secondary. Such definitions are made on the assumption of mirrors always mounted in the same position on the turntable of the figuring machine and axisymmetrical effects of the polishing process. According to information from Carl Zeiss, the geometrical center of the finished cylindrical block will agree with the aspheric axis within one mm for a 3.5 m primary of about  $f/3$ . Such a precision is quite adequate for a rational set-up operation.

The basic aims of the set-up and alignment operation can be defined as follows (Fig. 2.5):

- a) The mechanical axis supporting the telescope tube (declination axis for an equatorial, altitude axis for an Alt-Az) is optically defined as the *t-axis*.
- b) A line is defined perpendicular to the *t-axis* which cuts this *t-axis* and passes through the nominal center of the prime mirror ( $M_1$ ) cell. This point may, in practice, be defined as the mechanical center of a rotator attached to the PM cell. This line is *defined* as the mechanical axis of the telescope tube and as the effective “optical axis” (OPT).
- c) The secondary mirror ( $M_2$ ) is centered with its cell on OPT and its center set perpendicular to OPT.
- d)  $M_1$  is mounted in its cell, preferably with a mechanical centering precision to the cell fixation within  $D/5000$ , where  $D$  is the diameter of  $M_1$ . If this precision cannot be realised, however, it may not be serious for the function of the telescope if the following procedure is correctly adhered to and the theory of § 2.2.1 is carefully applied.
- e) A natural star near the zenith is then observed at the nominal Cassegrain focus, i.e. at a point on, or very near, the axis OPT and focused with  $M_2$  at the predefined distance behind the pole of the primary (b in Fig. 2.12 of RTO I).
- f) The coma (i.e. *decentering coma*, since we are observing on axis) is measured by an image analyser or equivalent device. *The  $M_1$  cell is then tilted*

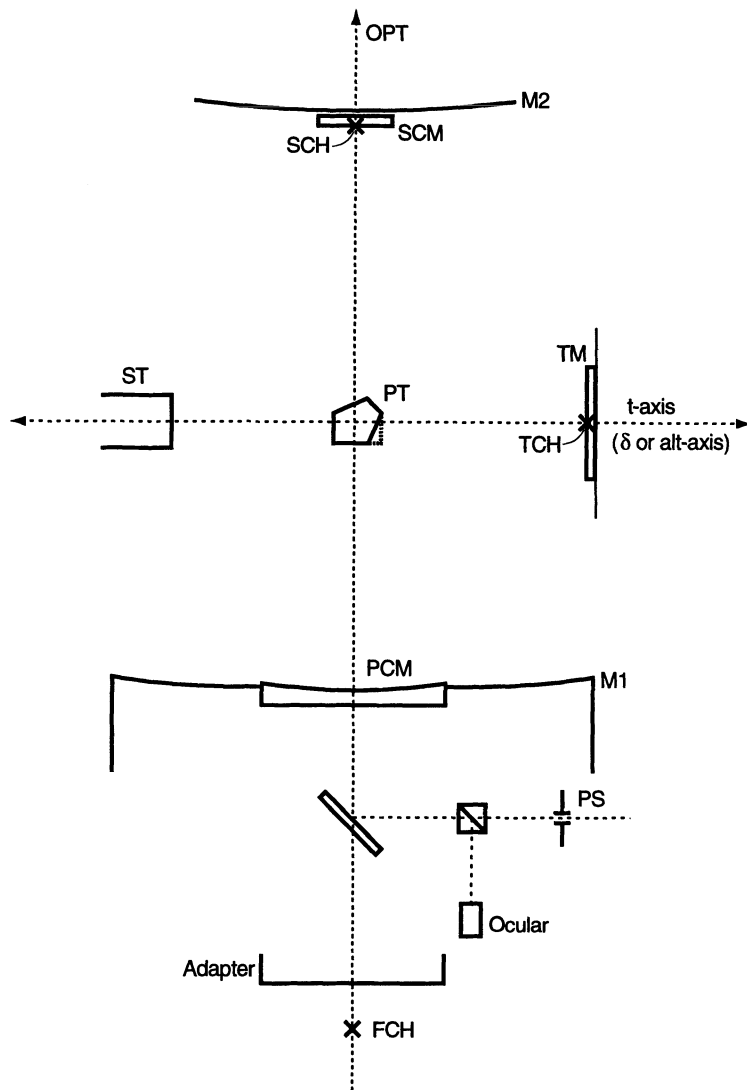


Fig. 2.5. Alignment of a Cassegrain telescope

appropriately to correct this decentering coma, or  $M_1$  is tilted on its fixed points. The tilt required can be calculated from Eqs. (2.1), (2.2) and (2.4) or with the aid of an optical design program. The directions required are dealt with in § 2.3.

- g) General *image analysis* at the field center. Apart from the *residual coma* not corrected by  $f$ ), the *spherical aberration* and *astigmatism* are important at this stage. Bearing in mind that such errors can also be generated in the local air surrounding the telescope and that such errors may be stable over several hours, a fixed residual and non-negligible spherical

aberration at the correct axial image point will imply a systematic figuring error by the manufacturer. An erroneous axial position will give aberration according to Eq. (2.20). A non-negligible astigmatism *may* imply a manufacturing error, but a more likely culprit at this stage is an error somewhere in the mirror support systems.

Step f) is fundamental to the concept of practical alignment of 2-mirror telescopes, since it is the procedure which sets up the coma-free Schießspiegler (CFS) discussed in detail in § 2.2.1 above and shown in Figs. 2.2(b) and 2.4. The effective  $\delta$ -value of this CFS,  $\delta_{eff}$ , will be the resulting vector error of all the lateral centering errors in the alignment procedure, including all alignment setting errors and the basic errors of the aspheric mirror axes to their mechanical centers. The precision of the alignment settings must take account of the final acceptable value of  $\delta_{eff}$ , depending on the nature of the telescope as discussed in § 2.2.1.

We now return to the steps a)–g) above and consider how they can be achieved in detail. This detailed procedure was used by J. Andersen, F. Franzia and R. Wilson on the 1.54 m Danish telescope, an equatorially mounted RC, at the La Silla Observatory in 1978, but would be applicable to any Cassegrain telescope. One essential tool is a standard *sighting telescope* (ST) of the sort supplied by a number of firms (e.g. Möller in Germany, Taylor-Hobson in England, Kollmorgen in the U.S.). The ST must be of the focusable sort, from about 2 m to infinity in the case of this 1.54 m telescope. Using a Möller ST with  $f = 300$  mm and aperture 50 mm, the focus shift is about 50 mm. The procedures require observations of plane mirrors in autocollimation, by which an illuminated graticule is projected and returned by the mirror, and of cross-hairs or targets in the set-up system. Depending on the precision of the basic mechanical mounting, a preliminary adjustment with a laser can be very useful. In aligning a plane mirror perpendicular to the sighting axis of an ST, the maximum angular error acceptable in order to get light back into the ST is  $\frac{1}{4}D/s$  rad, where  $D$  is the aperture of the ST and  $s$  the distance of the mirror. A relatively large aperture  $D$  is therefore a great help, particularly for long distances in coudé telescopes. But the larger barrel makes the adjustment of the reticle in the ST on its mechanical axis more critical for the focusing movement. A preliminary laser adjustment relaxes the requirements in angular field and therefore  $D$ . The change in effective sighting direction with focus movement should be only a fraction of 1 arcmin, preferably  $\leq 10$  arcsec. It is possible to test and adjust an ST in this respect, but investment in high quality equipment saves much work and time.

Another essential tool (see Fig. 2.5) is a *pentaprism* (PT) with an aperture comparable with that of the ST. A pentaprism has the property (Fig. 2.6) of deflecting a beam through  $90^\circ$  as shown. A well-made PT will produce a deflection of  $90^\circ$  with an error of a few arcsec, at most. The essential property, however, is not so much this high deflection accuracy (5 arcsec accuracy would be ample for our purposes) but the property of *maintaining exactly the same*

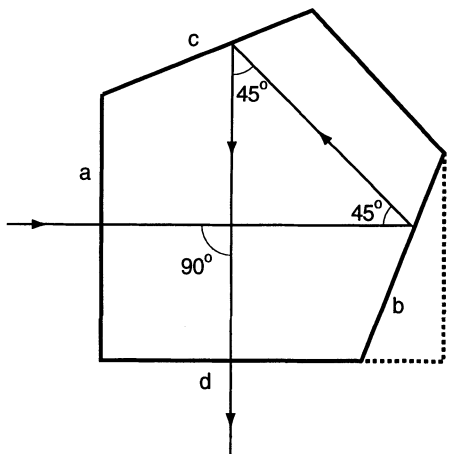


**Fig. 2.6.** The function of the pentaprism, an essential tool in telescope alignment

deflection when the PT is rotated appreciably about an axis perpendicular to the plane of Fig. 2.6. The deflection in this section is then independent of adjustment errors of the PT. This is its essential advantage over a plane mirror at  $45^\circ$ . In the planes at right angles (rotation axes in the plane of Fig. 2.6) the PT behaves on rotation like a plane mirror. Sometimes, the PT is supplied with a wedge prism so that straight-through vision is possible, a useful feature. Face *b* is then aluminized to give about 50 % reflectivity.

For this telescope, the following requirements were specified to the manufacturer (see Fig. 2.5):

- The inclination of the optical axis of the flat secondary collimation mirror (SCM) and the optical axis of  $M_2$  should be  $\leq 0.5$  arcmin. The manufacturer estimated 0.1 arcmin.
- The centering of the secondary cross-hair (SCH) should be within a radius of 0.5 mm from the optical axis of  $M_2$ . The manufacturer estimated 0.1 mm.

All adjustments should be made with an error appreciably less than 1 arcmin.  $M_1$  and  $M_2$  should already be aluminized. The telescope tube is set roughly vertical.

## Alignment procedure (see Fig. 2.5)

### Step (a)

1. Set up the *target mirror* (TM) on the  $\delta$ -axis ( $t$ -axis) of the telescope.
2. Set up the *sighting telescope* (ST) on the platform opposite the TM.
3. Using the TM in autocollimation with the ST, align the TM perpendicular to the  $\delta$ -axis ( $t$ -axis) by rotation of the telescope in  $\delta$ . When circular image movement is effectively eliminated by adjustment of the

TM, *incline* the ST until the center of the residual circle of movement is centered in the ST. The axis of the ST is now *parallel to, but not necessarily coincident with*, the  $\delta$ -axis.

4. Focus the ST on the *target cross-hair* (TCH). Center the TCH on the  $\delta$ -axis by rotation of the telescope in  $\delta$  by translating TM as necessary.
5. *Translate* the ST to center the residual circle of movement of the TCH on its axis. *This brings the axis of the ST into coincidence with the  $\delta$ -axis.*
6. Check and correct steps 3, 4 and 5 as required. In this case, 3 iterations were sufficient to achieve the following results:

Lateral error of TCH to ST and $\delta$ -axis	$\leq$ 0.08 mm
Error of alignment of ST axis to TM-normal	$\leq$ 0.05 arcmin
Error of squaring of TM to $\delta$ -axis	$\leq$ 0.1 arcmin

### Step (b)

7. Mount a *pentaprism* (PT) in front of the ST at the intersection of the  $\delta$ -axis and the mechanical axis of the telescope tube. The PT is roughly centered to the ST axis by focusing on its face, and face *a* (Fig. 2.6) is squared on to the ST axis by autocollimation from this face. Neither direction is critical but the horizontal direction should be within about 1 arcmin.
8. Mount a *focus cross-hair* (FCH) mechanically centered in the adapter unit and in the plane of the telescope focus.
9. Align the FCH, as viewed via the PT, on the axis of the ST by moving the PT parallel to the axis of the ST. *The sighting line via the PT is now a line perpendicular to the  $\delta$ -axis which cuts it and goes through the FCH.* In this case, the error of adjustment of FCH was  $\leq$  0.4 mm.
10. This telescope was provided with a collimation check system consisting of the SCM plane mirror and the primary collimation mirror (PCM), an annular spherical mirror rigidly fixed to the edge of the central hole of the primary and with a radius of curvature half that of the primary, the 45° plane mirror which can be switched into the beam and the unit containing a collimator, which can be switched into the beam, a beam splitter, *pinhole source* (PS) and ocular. This system works in autocollimation and detects rotational or lateral shifts of  $M_1$  or  $M_2$ . In passive telescopes it can be a very useful feature, in active telescopes it would normally be superfluous. The collimator enables  $M_2$  to be squared on by autocollimation with PS from SCM. Otherwise, the pinhole PS is viewed directly in autocollimation via  $M_2$  and PCM to check the squaring on of  $M_1$ . However, since this latter process uses only the central part of  $M_2$ , which is effectively spherical, and the PCM, which is effectively a Hindle sphere (see Chap. 1), this autocollimation check cannot distinguish between translation and tilt errors.

Switch in the  $45^\circ$  mirror and observe the PS in the ST. Align the PS on the axis of the ST by adjusting the  $45^\circ$  mirror. In this case, the adjustment was already correct within 0.15 mm.

11. Replace the FCH by a plane mirror mounted parallel to the telescope plateholder. Using autocollimation in the ST, measure the squaring error of this mirror (corresponding to plateholder tilt) to the sighting line. If the error exceeds 2 arcmin, adjust the adapter (or  $M_1$  cell at the flexion bars or tube attachments) and repeat the procedure from 7 onwards. In this case, no adjustment was needed as the tilt error was only 1.2 arcmin.
12. The PT is rotated  $180^\circ$  about the telescope tube axis. The ancillary  $22\frac{1}{2}^\circ$ -prism on the PT is now essential for viewing with the ST through the PT towards the TM. As in 7, the PT is adjusted roughly in height and is squared on to the ST axis by autocollimation from the prism face directed towards the ST.
13. Via the  $45^\circ$  mirror, the PT, the TM and back through the PT, the illuminated PS is viewed in the ST. It is then centered:
  - By rotation of the PT about the ST sighting line to get correction in the N-S direction (horizontal error).
  - By moving the PT in the E-W direction (along the axis of the ST) to correct the E-W error (vertical error). Alternatively, the PT is moved up or down along the telescope tube axis, which achieves the same effect.

Once this centering is achieved, the PT must not be disturbed before the next operations are completed.

14. Remove the ST from the platform and mount it in the adapter.
15. View the TM via the PT in autocollimation. Center the image by the ST *tilt screws*. The ST axis is now *parallel* to the telescope tube axis.
16. View the TCH via the PT and center it by the ST *translation movements*. The ST is now coincident with the defined sighting line and tube axis in both E-W and N-S directions. *The ST axis thereby defines OPT, the effective telescope axis.*
17. Recheck 15 and 16 and iterate if necessary. In this case, the precision obtained without iteration was:
  - Autocollimation  $\leq 0.05$  arcmin
  - Alignment on TCH  $\leq 0.03$  mm

Remove the PT to allow sighting on  $M_2$  with the ST.

**Step (c)**

18. Focus on the SCH of  $M_2$  and center  $M_2$ <sup>1</sup> by lateral movement of its centering screws (if these are absent, the spiders must be adjusted). In this case, the E-W error was corrected to  $\leq 0.07$  mm. This is the direction normally defined as “collimation error”. The N-S correction is assessed with the telescope in the nominal zenith position. It is much less critical since it can be corrected at once by a small change in the initialisation of  $\delta$  and an appropriate tilt of the primary (see 22). In this case, the centering range did not permit full correction and about 1.3 mm error was left. It was not considered necessary to correct this at the spiders.  *$M_2$  is now centered on OPT to the required precision.*
19. Viewing through the telescope collimator and ocular, adjust (by inclining  $M_2$ ) the SCM in autocollimation until the image PS' of PS is centered on PS. *This sets  $M_2$  perpendicular to OPT.* (If the telescope has no collimation system with PS, the same procedure is done with the ST. A cross-check can be performed to confirm 13). Check with ST that the centering of SCH has not been disturbed and readjust  $M_2$  by translation if necessary. In this case, no readjustment was necessary. The residual error of inclination of  $M_2$  was  $\leq 4$  arcsec.

**Step (d)**

20. Adjust the inclination of  $M_1$ , using the PCM in autocollimation from the ocular, by adjusting the *fixed points* of the  $M_1$  axial support. This adjustment is, above all, useful to test the autocollimation system provided with this telescope. Otherwise it is replaced by 22 below. Note that the placeholder was squared on to OPT by 11 above by adjusting *the whole cell at the flexion bars*. This should not be disturbed for this reason, also the ST would be disturbed from its adjustment with its axis on OPT.

---

<sup>1</sup> The original procedure foresaw the lateral centering of  $M_2$  by, instead of 12, rotating the PT about the  $\delta$ -axis and viewing SCH through the ST while it was still mounted on the platform. This procedure was abandoned for two reasons:

- Before and after rotation of the PT, the height centering of its aperture must be performed to a much better accuracy than the centering precision required for  $M_2$ ; since in the E-W direction, a height centering error  $x$  introduces an error  $2x$  in the centering of  $M_2$ . While this height centering is possible, it is not easy. The procedure adopted, by contrast, is completely uncritical regarding height centering.
- The original procedure gives no control over the N-S adjustment of  $M_2$  unless the PT can be turned 180° with high precision. The procedure adopted, by contrast, gives equal precision in E-W and N-S and is uncritical regarding the rotation of the PT.

The uncritical positioning of the PT is possible in the adopted procedure because the PT is *adjusted* to the sighting line while the ST is on the platform and is left *undisturbed* while the ST is transferred to the adapter and its sighting line reset.

This is why  $M_1$  is inclined here with its *fixed points*, independently of its cell and adapter.

21. Test the *Serrurier function* of the telescope tube by measuring the variation of lateral and angular decentering of  $M_2$  for zenith distances between  $0^\circ$  and  $70^\circ$ . This can be done with high reliability by observing SCH, and SCM in autocollimation, with the ST. Clock measurements can also measure the lateral movement of  $M_2$  relative to the top unit. But there is no substitute for the ST measurements which give the complete error: clock measurements help in understanding the Serrurier behaviour. In this case, they showed lateral movements  $< 0.1$  mm whereas the ST measurements gave 0.7 mm. Further investigations observing cross-wires over the Serrurier struts of the tube and across the centerpiece of the telescope tube proved that the ST deflections were almost entirely caused by flexure at the image plane of the telescope, i.e. in the ST mount itself. Eliminating this gave a total Serrurier lateral decentering sag of 0.13 mm, including the sag of  $M_2$  in its cell of 0.1 mm, an excellent value.

### Steps (e) and (f)

22. The final centering as a *coma-free Schiefspiegler* is done on a *natural star* near the zenith. This requires *image analysis* of some sort for the nominal image point behind the primary, a subject dealt with in the section below. At this stage, all we need is the coefficient of third order (Seidel) coma, the sensitivity of the telescope to lateral decenter from Eqs. (2.1) or (2.2) above and the corresponding means of correcting this by *tilting the primary on its fixed points about its pole*. This translates the intersection point of its aspheric axis at  $M_2$  with the long lever arm of the separation  $M_1M_2$ . The correction is thus very sensitive. There is also a small angular change which produces a normally negligible change of the strictly lateral decentering coma. In this case, a coma of only 0.30 arcsec was measured with variations for zenith distances to  $45^\circ$  in S, N, E, W directions  $\leq 0.25$  arcsec. The coma in the zenith was reduced to 0.1 arcsec by changing the fixed point heights by a maximum of 41  $\mu\text{m}$ .

### Step (g)

The image analysis was performed on this telescope in 1978 using so-called “pupil plates”, a simple, classical technique discussed in § 2.3. At that time, it was done photographically but, today, it can be performed with a CCD detector. More sophisticated techniques (§ 2.3) can determine the coma and other coefficients with high accuracy. A problem always requiring great care is the direction of the coma point in the physical coordinate system of the telescope: this is also discussed in the next section.

The above alignment procedure has been given for a typical Cassegrain telescope. Depending on the nature of the telescope, various modifications are possible and reasonable, but the basic principles will remain. For an *active* telescope, like the ESO NTT, the basic procedures are discussed in Chap. 3 but are influenced by the active concept.

### 2.2.3 Alignment at the prime focus of telescopes with field corrector

At the *prime focus*, at which a *field corrector* is used, the axis of the field corrector plays an equivalent role in the *lateral* centering tolerances to that of  $M_2$  in the Cassegrain focus. However, there is an important and fundamental difference: there is no equivalent of a coma-free Schießspiegler because the corrector has normally very little total optical power and is relatively insensitive to tilt. So if decentering coma is present, the corrector must be translated to correct it. The decentering coma involved is approximately the field coma of the primary induced by the field angle  $u_{pr1}$  of Fig. 2.2(b), whereby the point  $M_2$  corresponds to the center of the corrector. For a parabolic primary, or in general if the stop is at the primary, this coma is given by Eq. (5.4) of RTO I as

$$(\delta u'_p)_{Comat} = -\frac{3}{16} \frac{1}{N_1^2} (u_{pr1})_{arcsec} \text{arcsec} \quad (2.45)$$

Hence a measurement of the coma value enables  $u_{pr1}$  to be calculated from (2.45) and, from this and the separation, the lateral decenter  $\delta_{corr}$  of the corrector.

The theory of prime focus correctors was given in Chap. 4 of RTO I. If the corrector is also correcting spherical aberration (e.g. for an RC telescope), then this correction will be sensitive to the axial position of the corrector. So a measurement of both coma and spherical aberration should normally be made to give optimum adjustment both laterally and axially.

### 2.2.4 Alignment of Schmidt telescopes

The theory of the Schmidt telescope was given in § 3.6.2 of RTO I. It was pointed out in § 3.6.2.5 that the Schmidt form is uncritical for set-up tolerances of the optical elements except for lateral decenter of the corrector plate. The sensitivity to decentering coma is readily derived as follows.

The axis of the Schmidt telescope is solely (and weakly) defined by the aspheric axis of the corrector plate. The spherical mirror has no axis and must simply be set up *normally* to the plate axis. A tilt error  $u_{pr1}$  of the mirror about its pole to this plate axis introduces a field coma of the mirror proportional to  $u_{pr1}$  as though the stop were at the primary. For the real stop at the plate, the tilt error of the mirror is then, to the third order, identical for all the real principal rays. The consequence of the tilt decenter of the

mirror to the plate axis is therefore uniform decentering coma over the field as in a decentered Cassegrain telescope. Since the decentering coma originates at the spherical mirror as though it were at the stop, Eq. (2.45) gives its value also in this case of a Schmidt telescope. Now, referred to the mirror “axis” (i.e. its normal at the intersection point of the plate axis), the plate is laterally decentered by  $\delta_{Schm}$  and rotated through the angle  $u_{pr1}$ . However, this small plate rotation is completely insensitive since it only produces a small asymmetry in the nominal field center. The equivalent lateral decenter of the corrector plate is then simply

$$\delta_{Schm} = 2f'_1(u_{pr1})_{rad} \quad (2.46)$$

If we define a fixed tolerance for the decentering coma  $(\delta u'_p)_{Comat}$ , then the combination of (2.45) and (2.46) gives

$$\delta_{Schm} = -\frac{32}{3}N_1^2 f'_1 [(\delta u'_p)_{Comat}]_{rad} \quad (2.47)$$

Setting the decentering coma limit at  $1 \text{ arcsec} = 1/206\,265 \text{ rad}$  gives for the 1 m ESO Schmidt telescope with  $N_1 = -3.0$  and  $f'_1 = -3000 \text{ mm}$  the typical tolerance

$$(\delta_{Schm})_{ESO} = 1.40 \text{ mm arcsec}^{-1} \quad (2.48)$$

of decentering coma. Alternatively, one can express the tolerance for 1 arcsec of decentering coma directly from (2.45) as a tilt of the primary by  $u_{pr1} = 48 \text{ arcsec}$ .

Since no Schießspiegler compensation is possible by tilt of the corrector plate, it follows that the Schmidt telescope is, in this sense, more sensitive to decenter than a Cassegrain telescope with a primary having the same f/no  $N_1$ .

### 2.2.5 Field correctors at the Cassegrain focus

These are very simple to mount because the tolerances are much more generous than for PF correctors. The effect on spherical aberration is very small because of the small axial beam width. Centering tolerances are generous and will become more so, the weaker the definition of the optical axis.

## 2.3 Test methods and image analysis of telescopes in function

### 2.3.1 Classical qualitative methods

Qualitative (subjective) testing of the image quality of telescopes is as old as the invention of the telescope itself. The classical method is to observe the image of a star with an eyepiece, either in focus or, better, somewhat defocused. For small telescopes, this remains a powerful and useful procedure.

Above all, for telescopes whose aperture does not greatly exceed the Fried parameter (see Chap. 5), the telescope quality should be diffraction limited, so that diffraction rings may be visible in the defocused image. A detailed account is given in an old work by H.D. Taylor [2.8], partly reproduced by Ingalls [2.9]. With large modern telescopes great care must be taken in forming judgements on image quality because of the magnification problem illustrated by the Ramsden disk (Figs. 1.8 and 2.8 in RTO I), i.e. the exit pupil of the visual telescope. According to Eq. (2.45) in RTO I, the magnification is equal to the beam compression ratio, the ratio of the diameters of the entrance and exit pupils. As discussed in Chap. 2 of RTO I, if the star image appears bright to the eye, the eye pupil will shrink down to about 1 mm diameter and will diaphragm down a 3.5 m telescope if the magnification is less than about 3500, a value incompatible with normal atmospheric “seeing”. For this reason alone, visual judgements of the image quality of large telescopes with oculars are subjective at best and completely misleading and over-optimistic at worst.

This does not mean that assessment of the defocused image is of no interest: quite the contrary, as will be illustrated below. It means simply that the eye as detector *via an ocular* is quite inadequate, even qualitatively, for large telescopes.

A better visual method is the Foucault knife-edge method [2.10], referred to in Chap. 5 of RTO I as the first really scientific method of testing telescope optics. This method remains the most sensitive ever invented and is still widely used in workshops as a qualitative test (see Chap. 1) and by amateurs [2.9]. The limitation in its use in a functioning telescope is the atmospheric seeing and the inability of the eye to integrate. However, the instantaneous perception of the eye with the Foucault test can be very revealing concerning the effects of atmospheric seeing and of local air turbulence. If the fixed telescope errors are required, eliminating the atmospheric seeing is possible by integration over a period of 30 s *for good seeing*, or 60 s or more for indifferent or poor seeing, and recording the “Foucaultgram” photographically or on an electronic detector (CCD). All that is required is an objective in the beam after it has passed the knife-edge, which images the exit pupil of the telescope on the photographic plate or detector. Figure 2.7 shows the result for a typical case, the MPIA 2.2 m telescope II, after set-up at ESO La Silla. The shadow distribution gives excellent *qualitative* information of the wavefront. If the knife-edge penetrates from the left, dark areas correspond to wavefront slopes with normals inclined to the left and obscured by the knife. The problem has always been to interpret the photometric information. Proposals have been made to quantify this [2.11] [2.12], but have classically met with little success because of the difficulties of photometric analysis using photographic plates with non-linear intensity response.

An excellent analysis of the possibilities of obtaining quantitative information from the Foucault method with a more modern detector (a quad cell) is given by Goad et al. [2.13]. They overcome the problem of the directional

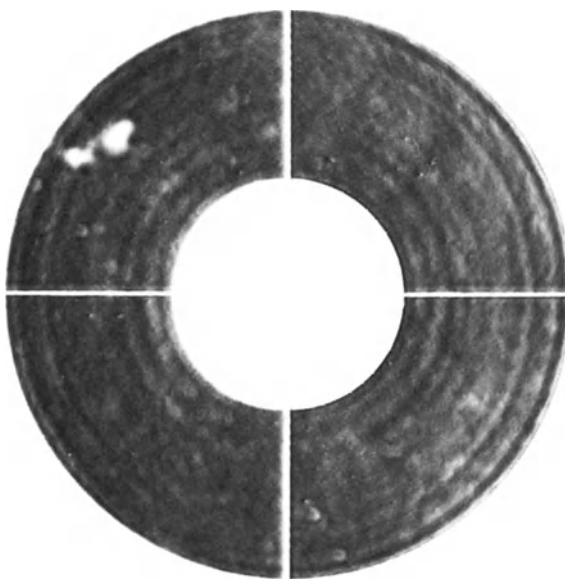


**Fig. 2.7.** Foucaultgram of the MPIA 2.2 m telescope II after set-up at La Silla in 1983. This picture was obtained on a  $6 \times 6$  cm photographic plate with 1 m exposure

sensitivity of the Foucault knife-edge, favouring the axis perpendicular to the knife, by rotating it. Nevertheless, they show there is still a sensitivity loss of  $\sqrt{2}$  averaged over a rotation cycle. Furthermore, half the light is obstructed compared with the Hartmann based sensors discussed below, giving a loss of a factor of 2 in the error in position arising from photon noise. In spite of these defects, the Foucault method may still have interest as a quantitative photometric test, probably with CCD detectors, because of the enhanced photometric differences compared with the curvature sensing method discussed below.

### 2.3.2 “Pupil plates”: geometrical assessments of defocused star images

Above, we have referred to the time-honoured technique of assessing telescope image quality by observing the defocused image of a star with an ocular. The basic limitations of such visual assessments (diaphragming effect of the eye pupil and lack of integration) can be overcome by recording the defocused image on a photographic plate or modern electronic detectors such as a CCD. The magnitude of the star observed must be such that the integration time is at least 30 s (at least 60 s with indifferent seeing) for the detector and defocused image size chosen. A detailed analysis of such procedures was introduced in 1980 at the ESO La Silla observatory [2.14] and was successfully used for many years. It has now been largely supplanted by measurements with the ANTARES image analysis system using a CCD detector, but the analogue presentation of such “pupil plates” still represents an important

complementary test easily performed with a CCD. The size of the defocused image is not critical, but the defocus must be well outside the “caustic” so that the ordering of a raster of “rays” from the pupil is reproduced in the defocused image. Within the caustic, this ordering is lost: physically, this means that the Fourier transform process from pupil to image (see Chap. 3 of RTO I) must be incomplete. Both pupil and image (transform) information is then available, which explains the power of the method compared with investigation of the focused image, for which the pupil information is lost unless recoverable by complex Fourier transform techniques. These properties, together with time integration to eliminate atmospheric seeing, enable a precision of detection at least 5 times better than the external seeing. Exactly the same principles apply to all Hartmann-based procedures – see below – except that the precision in the best procedures is at least 10 times better than the normal seeing limit.

Failure to integrate out the seeing (i.e. less than 30 s although 15 s may be sufficient with excellent seeing) inevitably leads to erroneous results, as the instantaneous atmospheric function for the frequency concerned is superimposed on the fixed telescope aberrations. Such measures may be interesting for measurements in the “adaptive optics” bandpass (see Chap. 5) but are useless and dangerous for normal telescope testing.

With good seeing, the defocused image sizes given in Table 2.3 have been proven empirically to be reasonable. Although these are not critical, it is disadvantageous to expand the image more than necessary, since this wastes light and reduces the relative distortions due to aberrations of the “pupil plate” obtained. This term was introduced because the defocused image shows the *pupil* in a form distorted by aberrations. Of course, it is not a direct photograph of the pupil, which would give no information since the Fourier transform has not begun. With CCD detectors, even relatively coarse pixels will give ample sampling, since the pixel size is normally determined for the *focused* image.

Unless spherical aberration is to be determined, it is sufficient, in principle, to take a single plate on one side of the focus; but plates at both sides are always desirable to give a cross-check and better accuracy. In this case,

**Table 2.3.** Defocused image sizes for “pupil plates” for telescopes of sizes about 1.5 to 3 m [2.14]

Relative aperture	Defocused image diameter with good seeing (mm)	Defocused image diameter with poor seeing (mm)
f/3	1–1.5	2–2.5
f/8	2–2.5	3–4
f/15	3	4
f/30	4	5–6

the sizes should be similar if photographic plates are used to give a similar intensity distribution from the same star: linear detectors are less critical.

The aberrations and defects one aims to detect and measure with pupil plates are the three basic third order terms (spherical aberration, decentering coma and support-induced astigmatism), all uniform over the field and therefore only requiring measurements at the field center; higher order errors such as ripple, zones, turned edges (up or down), and “dents” or protuberances at the edge of the pupil due to excessive pressure, e.g. screws used in primitive edge supports of secondaries. The latter are also uniform over the field. Figure 2.8 shows the pupil plate appearance due to the third order aberrations. The appearance of “geometrical adjustment error” means the following. It may happen that the secondary is not well centered in the

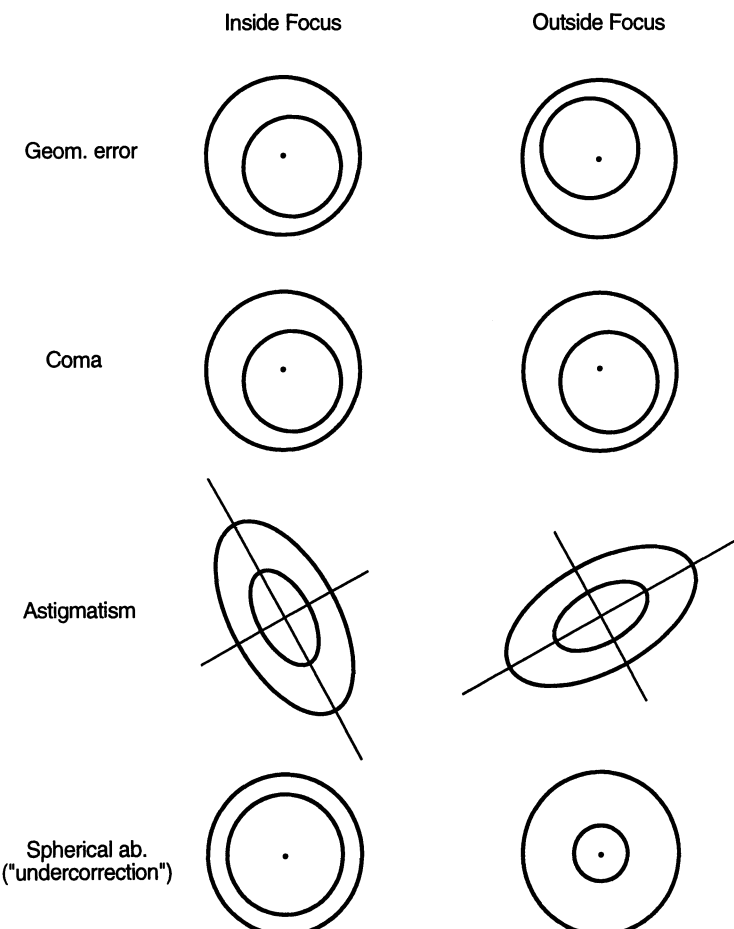


**Fig. 2.8.** Appearance of “pupil plates” showing geometrical adjustment error and the three basic third order aberrations [2.14]

telescope tube. If the primary is slightly inclined, the coma may well be excellently compensated giving a coma-free Schieffspiegler, as discussed above in § 2.2. If a beam corresponding to the field center is investigated, the projection of the secondary may not be at the center of the entrance pupil. For a pupil plate on one side only of the focus, this effect cannot be distinguished from coma. However, it inverts on the other side of the focus *whereas coma remains unchanged*. Therefore, if plates are taken on both sides of the focus, the mean value of the displacement of the obstruction gives the coma, the geometrical effect being eliminated. Essentially, the information comes from the fact that the obstructed aperture of the telescope behaves like a special Hartmann screen with two bits of information, the outer and inner aperture circles. Bearing in mind the aperture dependence of the transverse aberrations (astigmatism with  $y$ , coma with  $y^2$ , spherical aberration with  $y^3$ ), it is possible to deduce the amounts of aberration present. In the coma case, if the central obstruction were negligibly small, the displacement of its center relative to the outer pupil is *the same as the transverse size of the coma patch of Fig. 3.18 in RTO I*. This stays constant as the defocus increases, so that the relative eccentricity for a given coma patch decreases linearly with the size of the defocused image. This is the reason the latter should not be increased more than necessary.

### Measurement of the coma vector

The quantities  $a$ ,  $b$ ,  $c$ ,  $d$  in Fig. 2.9 are measured from a photographic plate with a measuring machine or from the CCD readout. A reading step of  $1 \mu\text{m}$  is desirable. The lateral coma vector  $L_c$  is given by

$$L_c = \left[ \left( \frac{a-b}{2} \right)^2 + \left( \frac{c-d}{2} \right)^2 \right]^{1/2} \mu\text{m} , \quad (2.49)$$

while the direction of the coma point (towards the thin edge of the annulus) is given by

$$\theta = \arctan \left( \frac{c-d}{a-b} \right) \quad (2.50)$$

The *inverse scale* of the telescope, defined by (2.103) in RTO I, is  $\bar{S} \mu\text{m}/\text{arcsec}$ . Then, ignoring obstruction, the full coma vector is  $L_c/\bar{S} \text{ arcsec}$ . In practice, we are normally concerned with a finite central obstruction factor  $\varepsilon$ , usually about  $1/3$ . The resulting correction factor is small and easily calculated from the geometry of the coma patch, as shown in Fig. 2.10. Referring back to Figs. 3.17 and 3.18 of RTO I, the upper and lower marginal rays, when defocused, form the points on the outer circle of Fig. 2.9 lying in the symmetry line of the coma point. For the focused image, they both pass through the extreme circle point 1 of the coma patch in Fig. 3.18 of RTO I, i.e. the point  $o$  in Fig. 2.10. Similarly, the center of the inner circle of Fig. 2.9 corresponds

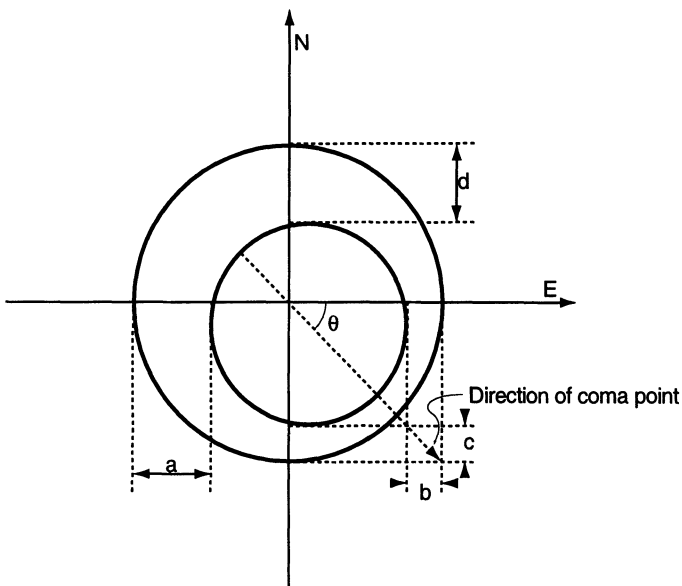


Fig. 2.9. Evaluation of the coma vector from a pupil plate [2.14]

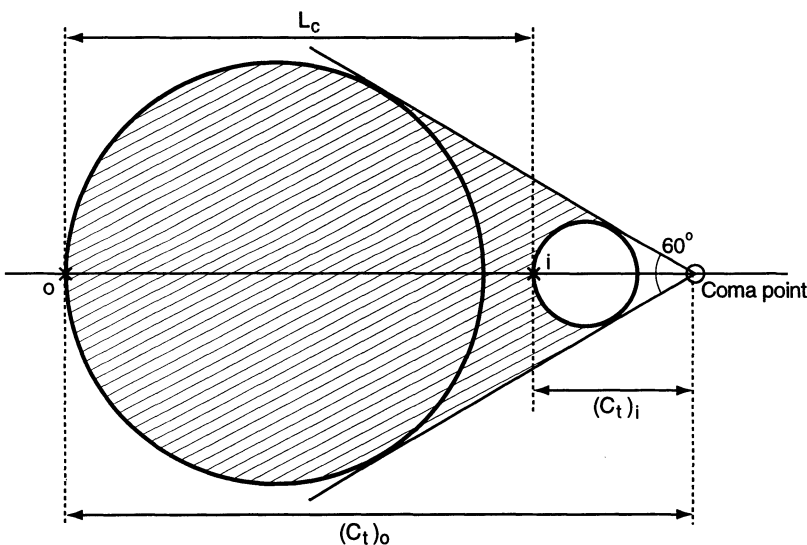


Fig. 2.10. Geometry of the coma patch with central obstruction [2.14]

to the point  $i$  of Fig. 2.10. Now it was shown that the ray coordinates of Figs. 3.18 of RTO I or 2.10 lie on circles of diameter  $(1/u')S_{II}(y/y_m)^2$  whose centers are shifted by the same amount from the principal ray intersection point. This diameter can be written

$$D_c = \frac{f'}{y} S_{II} \left( \frac{y}{y_m} \right)^2 = \frac{f'}{y_m} \frac{y_m}{y} S_{II} \left( \frac{y}{y_m} \right)^2 = \frac{f'}{y_m} S_{II} \left( \frac{y}{y_m} \right) , \quad (2.51)$$

which shows that the diameters and shifts of the circles from the principal ray are linear functions of the aperture, as must be the case if they fit into the 60° triangle. The significance of the measured quantity  $L_c$  is then as shown in Fig. 2.10. We have for the general case with obstruction factor  $\varepsilon$

$$(Coma_t)_{arcsec} \approx \frac{L_c}{S} \left( \frac{1}{1 - \varepsilon} \right) \quad (2.52)$$

This result corresponds to the full length of the coma patch, i.e. 100 % geometrical energy. In practice, the precision obtained is rarely better than about 0.25 arcsec because of distortions of the outer and inner circles of Fig. 2.9. The coma patch itself distorts the circles unless its size is small compared with the defocused patch. More serious, in practice, are often the local distortions arising from supports or dome seeing effects. Nevertheless, pupil plates are a powerful and simple way of maintaining good centering if more sophisticated means, such as Shack-Hartmann, are not available. The obstruction ratio may be deduced from the pupil plate itself, as the ratio of the circle diameters in Fig. 2.9, *provided the ratio is not seriously affected by spherical aberration – see below*. For most Cassegrain and coudé telescopes, the value of  $\varepsilon$  varies between about 0.3 and 0.15.

Pupil plates have an advantage over other methods for correcting decentering coma in that the direction of the coma point can be identified from Fig. 2.9 and Eq. (2.50) in a direct analogue way if the directions of the pupil plates are identified in  $\alpha$  and  $\delta$  for an equatorially mounted telescope. There are five means, in principle, for the correction, once the coma point direction is known in the physical coordinates of a Cassegrain telescope:

- a) *Raise* the primary mirror cell on the side *towards* the coma point (rotation of primary)
- b) *Raise* the primary mirror on its fixed points on the side *towards* the coma point (rotation of primary)
- c) *Translate* the primary mirror *in the opposite direction* from the coma point
- d) *Translate* the secondary mirror *in the same direction* as the coma point
- e) *Lower* the secondary on the side *towards* the coma point (rotation of the secondary about its vertex).

Of these, c) is rarely practicable. If sensitive movement is available, d) is the best. a) and b) are over-sensitive, because of the long lever arm of the point where the axis of the primary cuts the secondary, but are often the only means available. e) is often available but too insensitive, leading to big pointing changes. The amounts of movement required can be deduced at once from Eqs. (2.1), (2.2) and (2.4).

It should be noted that the calculation of aberrations from pupil plates is strictly related to their *original size*. If an enlargement of a factor of two

is made from the original, the coma (or any other aberration) deduced will also be doubled.

### Measurement of the astigmatism vector

It is best to judge the astigmatism solely from the external pupil shape, since the obstruction aperture is much less sensitive. This is the case because the transverse effect (length of the astigmatic lines) diminishes linearly with aperture. This follows from Eqs. (3.205) and (3.208) of RTO I for the diameter of the astigmatic circle at mean focus

$$\begin{aligned} (\delta u'_p)_{ast,m} &= -\frac{1}{y} S_{III} \left( \frac{y}{y_m} \right)^2 = -\frac{1}{y_m} \left( \frac{y_m}{y} \right) S_{III} \left( \frac{y}{y_m} \right)^2 \\ &= -\frac{S_{III}}{y_m} \left( \frac{y}{y_m} \right) \text{ rad} \end{aligned} \quad (2.53)$$

In absolute terms, therefore, detection of ellipticity of the central obstruction is  $\varepsilon$  times less sensitive.

In principle, measurement of astigmatism requires measurements of the outer pupil across 4 diameters at  $45^\circ$ , but if the position of the major and minor axes can be judged visually (usually the case if the astigmatism has any significance), it is sufficient to measure in the estimated directions of the axes (Fig. 2.11). The diameter of the astigmatic circle at best mean focus is

$$\phi_{ast} = \frac{(a - b)}{2} \mu\text{m}$$

and the length of the astigmatic lines is  $2\phi_{ast}$ . With the inverse scale of the telescope as  $\bar{S} \mu\text{m}/\text{arcsec}$

$$(\phi_{ast})_{\text{arcsec}} = \frac{\phi_{ast}}{\bar{S}} \text{ arcsec} \quad (2.54)$$

Since the central obstruction is not used, no correction for it is necessary. Note that the pupil plate procedure will always reveal astigmatism if it is present. By contrast, the focused image *may* reveal astigmatic lines one way or the other; but if the chosen focus happens to be at the mean focus between

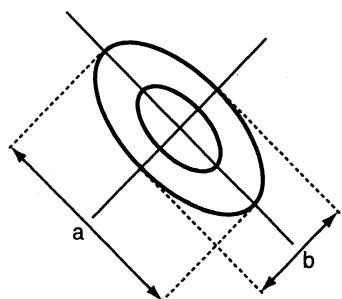


**Fig. 2.11.** Measurement of astigmatism from pupil plates [2.14]

the astigmatic lines, a circular image results which cannot be distinguished from spherical aberration or seeing.

As with coma, astigmatism *can* be measured from a single focus plate on one side of the focus; but better precision is obtained by a second measurement on the other side of the focus, thereby rotating the major axis 90°. If this rotation is not found, the error is *not* astigmatism: almost certainly it is a *guiding error*. Confusion here is very common.

### Measurements of spherical aberration

Unlike coma and astigmatism, spherical aberration can only be detected and measured with reasonable accuracy if pupil plates are taken on both sides of the focus to give the relative size of the central obstruction in each case. The plates should be exposed with the same star, the same exposure times and the same image diameters within about 20 %. If these conditions are not respected, the differences of densities (with photographic plates) can seriously falsify the results. Furthermore, the presence of a turned-down or turned-up edge either at the exterior of the pupil or at the obstruction can give wrong values. For these reasons, the evaluation of spherical aberration is less reliable than that of coma and astigmatism.

The measurement of the diameters of the obstruction and outer pupil diameters of the pupil plates on each side of the focus lead to a difference  $\Delta D$  of the central obstruction, normalized to the outer diameter, of

$$\Delta D = D_I - D_E \left( \frac{d_I}{d_E} \right) , \quad (2.55)$$

where  $D_I$  and  $D_E$  are the obstruction diameters of the intrafocal and extrafocal plates respectively and  $d_I$  and  $d_E$  the corresponding outer diameters. The change in true obstruction ratio  $\phi$  is then given by

$$\phi = \frac{\Delta D}{2f'} (206\,265) \text{ arcsec} \quad (2.56)$$

The formula for the coefficient of third order spherical aberration is then deduced from Fig. 2.12 as follows.  $D_I$  and  $D_E$  are the recorded normalized obstruction (hole) diameters and  $\phi$  is clearly half the difference. Let  $(du'_H)_{GF}$  be the angular aberration corresponding to the aperture of the hole in the Gaussian focus. Then

$$\phi = (du'_H)_{GF} \left( \frac{ds'_M - ds'_H}{ds'_H} \right) , \quad (2.57)$$

where  $ds'_M$  and  $ds'_H$  are the longitudinal aberrations of the outer (marginal) rays and those corresponding to the hole. From (3.184) and (3.187) of RTO I

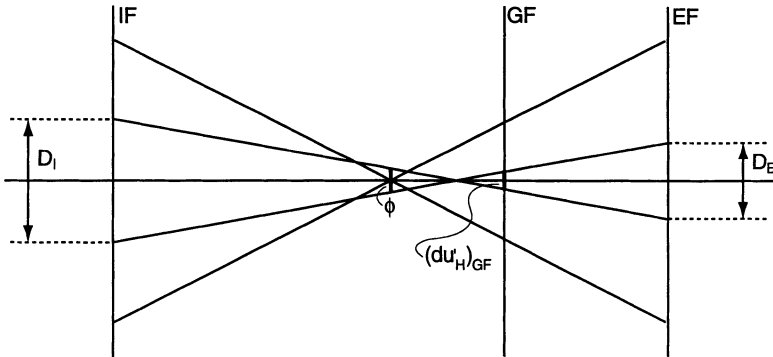


**Fig. 2.12.** Deduction of the third order spherical aberration coefficient from the relative obstruction ratio of intra- and extrafocal pupil plates [2.14]

$$\left. \begin{aligned} ds'_M &= \left( \frac{f'}{y_M} \right)^2 \frac{1}{2} S_I \\ ds'_H &= \left( \frac{f'}{y_M} \right)^2 \frac{1}{2} S_I \left( \frac{y_H}{y_M} \right)^2 \end{aligned} \right\} \quad (2.58)$$

Hence

$$\frac{ds'_M - ds'_H}{ds'_H} = \frac{1 - \varepsilon^2}{\varepsilon^2} , \quad (2.59)$$

where  $\varepsilon$  is the obstruction factor  $y_H/y_M$ . Similarly, from (3.184) and (3.190) of RTO I,

$$(du'_H)_{GF} = \frac{1}{y_M} S_I \left( \frac{y_H}{y_M} \right)^3 = \frac{1}{y_M} S_I \varepsilon^3 \text{ rad} \quad (2.60)$$

We wish to derive the angular spherical aberration *at best focus* (disk of least confusion) for the full aperture  $y_M$ . From (3.184) and (3.190) of RTO I, this is given by

$$(du'_M)_{BF} = \frac{1}{y_M} \frac{1}{4} S_I \text{ rad} \quad (2.61)$$

From (2.57), (2.59) and (2.60)

$$\phi = \frac{1}{y_M} S_I \varepsilon (1 - \varepsilon^2) , \quad (2.62)$$

giving with (2.61)

$$(du'_M)_{BF} = \frac{\phi}{4\varepsilon(1 - \varepsilon^2)} \text{ rad} , \quad (2.63)$$

and, finally, from (2.56)

$$(du'_M)_{BF} = \frac{1}{8\varepsilon(1-\varepsilon^2)} \frac{\Delta D}{f'} (206\,265) \text{ arcsec} \quad (2.64)$$

for the spherical aberration (100% energy) of the full unobstructed aperture. For an obstruction factor  $\varepsilon = \frac{1}{3}$ , (2.64) gives

$$(du'_M)_{BF} = \frac{27}{64} \frac{\Delta D}{f'} (206\,265) \text{ arcsec}$$

Note that the sign of the spherical aberration is revealed with great certainty by pupil plates. From Fig. 2.12, “undercorrection” (marginal rays focusing short) gives a larger obstruction at the intrafocal position.

As an example, Fig. 2.13 shows pupil plates taken in 1978 at the set-up of the 1.54 m Danish telescope at La Silla, discussed above in connection with alignment procedures. Because of pressure from the observing schedule, no pupil plates were taken on the other side of the focus although the large size of the apparent obstruction indicated the existence of spherical aberration. This was later confirmed and corrected by an outward shift of the final image.

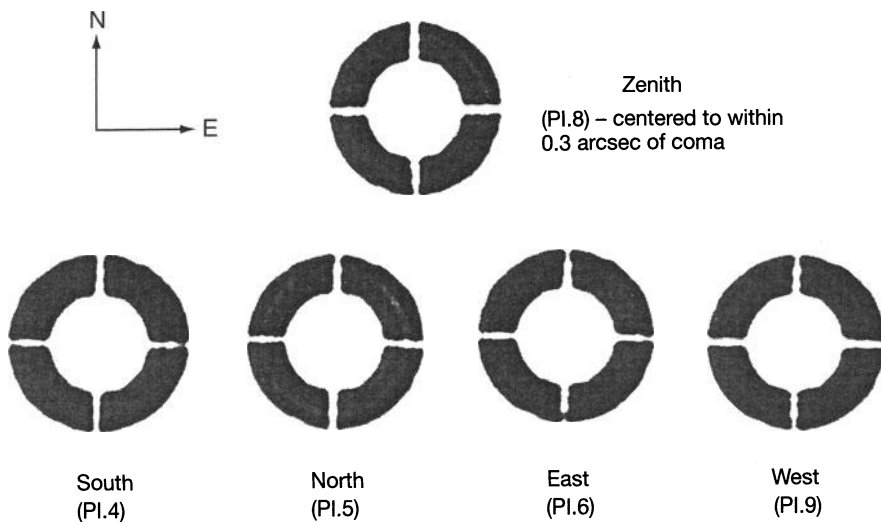


**Fig. 2.13.** Typical pupil plates, taken on one side of the focus with the 1.54 m Danish telescope at La Silla for the final centering. The negligible coma change on inclining the telescope showed the excellent mechanical centering stability of this telescope. Original image plate diameter ca. 2.5 mm

### Irregular and high spatial frequency defects from pupil plates

Apart from the above third order aberrations, pupil plates are an excellent method for revealing higher order and irregular defects. However, the angular spread cannot usually be calculated. One should look out for the following defects:

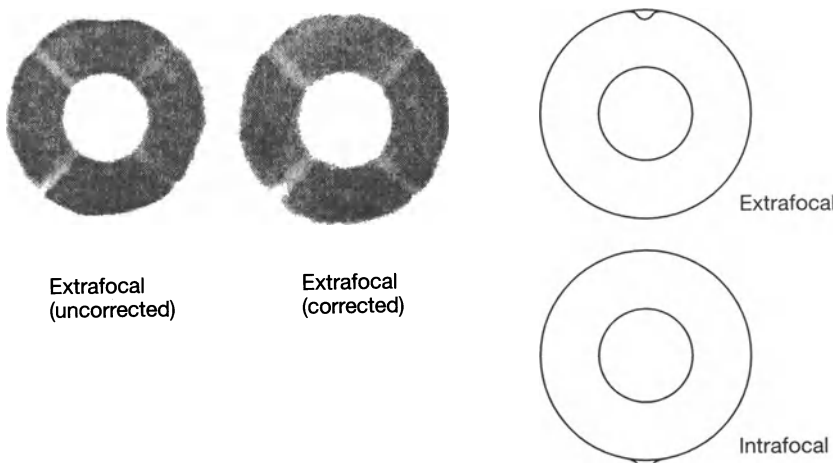


**Fig. 2.14.** Extrafocal pupil plates taken in 1980 for the ESO 1 m telescope at La Silla showing (*left*) a “dent” at the top due to screw pressure on the edge of the secondary and (*right*) its correction by relaxing the pressure. The two figures at the right show schematically such an effect both extra- and intrafocally. The original pupil plate diameter was 3.5 mm

- a) Dents or bumps in the outer pupil (or, more rarely, at the central hole). These are often caused by poor quality lateral supports of the secondary – see Fig. 2.14. Concentrated local heat sources are another common cause. The wavefront slopes are high giving image flares. Such defects are very serious.
- b) Dents or bumps at spider ends. These may be due to strain on the secondary cell from the spider, but a more common cause is thermal effects on the local air near the spider due to its thermal mass and radiation cooling of the metal. The larger the telescope, the more likely such effects will be.
- c) A triangular distortion of the pupil without noticeable bumps or dents. This is almost certainly due to over- or underloading of the axial fixed points of the primary; or possibly the lateral fixed points of primary or secondary. In principle, the coefficient of the triangular aberration can be calculated but, in practice, the clear triangular effect is too small to be measurable.
- d) Concentric zones. Most telescopes show some zones. Very common is turned-down or turned-up edge. A turned-down edge leads to a more diffuse edge of lower intensity in the intrafocal pupil plate.

Such irregular errors, as with coma and astigmatism, lead to defects in the image which are readily noticed by astronomers. Spherical aberration is much less evident, as it is confused with external seeing because of its axial symmetry. Correct measures of spherical aberration are therefore most important. The same is true of concentric zones.

Because of sampling limitations in Hartmann-based procedures, pupil plates provide in a direct analogue fashion important information on high spatial frequency errors which might otherwise be overlooked or misunderstood.

### 2.3.3 Hartmann-based techniques

**2.3.3.1 The classical Hartmann test.** The Hartmann test was invented by J. Hartmann in 1904 [2.15] and applied to the 80 cm Potsdam refractor. It represented the first truly scientific method of analysing image quality in operational telescopes in that it supplied direct *quantitative* results. In modified forms, it remains today the basis of most accurate measures of telescope image quality. In its original form, the Hartmann test was used to measure only axisymmetrical error, essentially spherical aberration but also zones if the sampling was high enough. The principle and basic theory of this original approach (Fig. 2.15) is well described by Bahner [2.16]. The test is shown for convenience with the Hartmann screen  $H$  placed before an objective, but the principle is identical if it is placed before a reflecting telescope, in front of the prime focus or Cassegrain secondary. The screen has holes which isolate sub-apertures of mean height  $y$  from the axis, the classical hole diameter recommendation being 0.2 to 0.5 % of the focal length. Photographic plates are placed at  $I_1$  and  $I_2$  well outside the caustic of the image. Measuring axial intercepts from an arbitrary point, we have on the assumption that the rays intersect in the meridian plane

$$\frac{s'_y - s'_1}{s'_2 - s'_y} = \frac{e_1}{e_2},$$

where  $e_1$  and  $e_2$  are the separations of the “Hartmann spots” recorded on the photographic plates. This gives

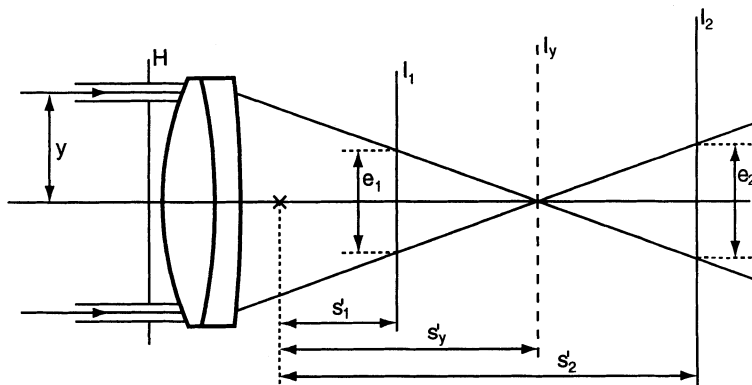


**Fig. 2.15.** Geometry of the classical axisymmetrical Hartmann test (after Bahner [2.16])

$$s'_y = s'_1 + \left( \frac{e_1}{e_1 + e_2} \right) (s'_2 - s'_1) , \quad (2.65)$$

where  $s'_2 - s'_1$  is the distance between the two measuring planes. The variations  $\Delta s'_y$  as a function of  $y$  give the desired information regarding spherical aberration and – provided the sampling of the Hartmann screen is high enough – axisymmetrical zones. In § 3.3 in RTO I, reference was made to the general equations of Nijboer expressing the Fourier transform from wavefront aberration to transverse ray intercepts. For the axisymmetrical case, the derivation is very simple [2.17] and can be expressed for angular aberrations which are small compared with the semi-aperture angle  $u'$  for a system in air as

$$W' = \int_0^{u'_m} \Delta s'_y \sin u' du' , \quad (2.66)$$

in which  $\Delta s'_y$  is the difference in longitudinal aberration referred to a desired mean value of  $s'_y$  corresponding to the wavefront reference sphere (see Fig. 3.1 of RTO I). For modest relative apertures, such as those of Cassegrain telescope foci, we can set  $\sin u' = u' = \tan u' = y/f'$  in (2.66). Then  $du' = dy/f'$  and (2.66) becomes

$$W' \simeq \frac{1}{f'^2} \int_0^{y_m} \Delta s'_y y dy \quad (2.67)$$

For very steep prime foci, the nature of this approximation, similar to that made in § 3.10.1 of RTO I for basic Fraunhofer diffraction theory, must be borne in mind.

Hartmann and his successors made use of the so-called “Technical Constant”  $T$ , introduced by Lehmann (2.18), to define the geometrical optical quality of a telescope:

$$T = \frac{2 \times 10^5}{f'^2} \frac{\sum y^2 |s'_y - s'_m|}{\sum y} \quad (2.68)$$

In this definition, the angular aberrations of the Hartmann radial zones are weighted by  $y$  corresponding to their areas and the factor  $2 \times 10^5/f'$  normalizes the angular error radius of the criterion roughly to arcsec. With the fairly low sampling traditionally used, identifying the optimum focus plane with  $s'_m$  posed problems. High quality optics was classically defined as having  $T \sim 0.2$  or less.

The evaluation in classical terms of the axisymmetrical case, but also extended to astigmatism, is treated in detail by Danjon and Couder [2.19]. A technical constant based on the axisymmetric case, such as that of Lehmann, is only of academic interest today. The modern equivalent is based on a 2-dimensional analysis leading to an rms wavefront error and corresponding rms angular error or percentage energy concentration error – see below and Chap. 4. This generalisation was first proposed by Kingslake [2.20] [2.16] and requires treating each “ray”, as defined by a Hartmann screen hole, individually. For a given choice of image plane in the axial direction  $z$ , the intersection

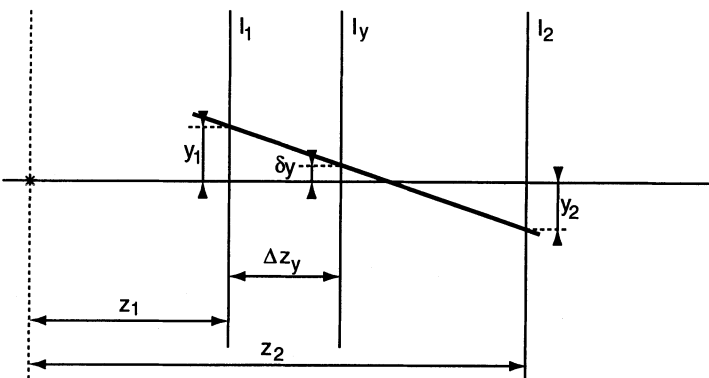


**Fig. 2.16.** The generalised Hartmann test for individual rays measured in 2 dimensions (after Bahner [2.16])

points of each ray are determined in the  $x, y$  coordinates, as shown in Fig. 2.16 for  $y$ . Then

$$\delta y = \frac{\Delta z_y}{(z_2 - z_1)}(y_2 - y_1) + y_1 \quad (2.69)$$

If measurements are made in the two planes  $I_1$  and  $I_2$ , errors in spacing of the holes in the Hartmann screen are automatically eliminated. However, two sets of measurements are required. If the Hartmann screen is made with the necessary precision of hole spacing, then it provides itself a reference plane and one measurement in  $I_1$  or  $I_2$  is sufficient. Beck and Fehlkamm [2.21] [2.16] proposed a rectangular, equal-step grid of holes, giving the important advantage that each ray has equal photometric weight in the total geometrical optical image. This is the most commonly used arrangement today in all Hartmann-based procedures, although concentric rings are also sometimes used. The rectangular grid also gives optimum sampling of all pupil zones. The generalisation of Hartmann testing was a logical development in parallel with the concept of *spot-diagrams*, introduced by Herzberger in 1956 [2.22] (see § 3.2.5.3 in RTO I), in optical design. Both these developments were only made possible with the introduction of modern computers.

The first generalised, 2-dimensional analysis of a modern telescope was performed in 1960 by Mayall and Vasilevskis on the 3 m *Lick primary* [2.23], using natural stars. The Hartmann screen did not use a rectangular grid: the holes were on spirals intersecting radial arms with a fixed azimuthal angular step. Analysis was first done radially, in classical Hartmann manner, and then tangentially to measure astigmatism and azimuthal irregularities. Plates were taken both intra- and extrafocally, but a cross check was done from the accurate Hartmann screen which had an estimated error of positioning of hole centers  $\leq 0.4$  mm. With this screen accuracy, one plate position was, in principle, sufficient. For a perfect paraboloid, account must be taken of field coma (collimation error of the incident beam), since the definition of the field

center is not necessarily on the axis of the paraboloid. The radial distance  $\rho$  of a spot from the pattern center on an extrafocal plate is then

$$\rho \simeq \Delta z_p \frac{\rho_s}{f'} \left[ 1 + \left( \frac{\rho_s}{2f'} \right)^2 \right] , \quad (2.70)$$

with  $\rho_s$  the height of a hole from the Hartmann screen center and the second term being a consequence of the coma patch geometry of Eq. (3.194) of RTO I. After conversion to rectangular coordinates, radial and tangential measurements of each hole gave two equations with six unknowns: 2 for the collimation error (position of paraboloid axis), 2 for the correction of lateral centering in the measuring machine, 1 for orientation error affecting the tangential measurement, and 1 for scaling error. These were evaluated from a least squares solution from all the holes. The residues in radial and tangential directions gave the inclinations of the pupil elements defined by the holes and integration along radii and round zones led to the contour map shown in Fig. 2.17. Depending on how many holes are used, the technical constant  $T$  derived from the generalised formula

$$T = 2 \times 10^5 \frac{\sum \rho \delta}{f' \sum \rho} , \quad (2.71)$$

where  $\rho$  is the radial distance of the spot from the pattern center and  $\delta$  the vector error, is given as 0.10 to 0.12 for axisymmetrical errors only and 0.16 to

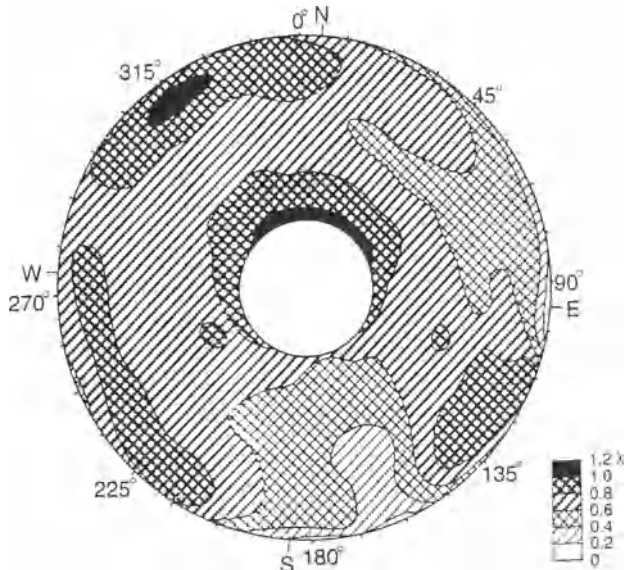


**Fig. 2.17.** Contour map at intervals of  $0.2\lambda$ , showing the surface of the 3 m Lick primary after correction of astigmatism on 3 January 1959 ( $\lambda = 500$  nm) (after Bahner [2.16])

0.17 for both radial and tangential (full) errors. In more modern terms, 76 % of the geometrical optical energy was concentrated in 0.34 arcsec diameter for the radial error alone; 56 % for both radial and tangential errors. The equivalent figures for 0.68 arcsec diameter were 98 % and 95 % respectively, implying by interpolation *about 80 % energy within 0.48 arcsec ( $d_{80}$ ) for the total error of the primary.*

This careful test analysis introduced the modern era of telescope testing and set the framework for the manufacturing specifications of the Bowen class of 3.5–4 m telescopes initiated during the 1960s. Surprisingly, however, there was relatively little systematic follow-up in the United States on functioning telescopes of the pioneer work of Mayall and Vasilevskis, although workshop test technology was making steady progress.

Very complete Hartmann testing was performed in 1976 [2.24] on the *ESO 3.6 m primary*, in combination with the Gascoigne plate correctors of this quasi-RC primary. A Hartmann screen was used with a square grid pattern as proposed by Beck and Fehlkamm. This was manufactured with care so that Hartmann plates were exposed in only one, extrafocal plane. There were about 286 holes sampling the annular aperture of the primary. The wavefront calculation was done by integration in the  $x$  and  $y$  directions using the trapezoidal rule. An important feature was a polynomial analysis, whereby polynomial terms were subtracted successively by a least squares process. The essential purpose of this was to investigate the importance of residual errors of various types in the telescope; but an important subsidiary aim was to lay the basis for a future *active* telescope. The polynomial used at that time was, apart from minor modifications, the same as that used later in the NTT, which was as follows:

$$\begin{aligned}
 W' = & k_{00} && \text{integration constant} \\
 & + k_{11}\rho \cos(\phi + \theta_{11}) && \text{wavefront tilt} \\
 & + k_{02}\rho^2 && \text{defocus} \\
 & + k_{13}\rho^3 \cos(\phi + \theta_{13}) && \text{decentering coma} \\
 & + k_{04}\rho^4 && \text{third order spherical aberration} \\
 & + k_{06}\rho^6 && \text{fifth order spherical aberration} \\
 & + k_{22}\rho^2 \cos(2\phi + \theta_{22}) && \text{third order astigmatism} \\
 & + k_{33}\rho^3 \cos(3\phi + \theta_{33}) && \text{"triangular" coma} \\
 & + k_{44}\rho^4 \cos(4\phi + \theta_{44}) && \text{"quadratic" astigmatism}
 \end{aligned} \quad \left. \right\} \quad (2.72)$$

The first two terms must be removed in any Hartmann analysis, and defocus is also normally removed. The last two terms were applied because “triangular” error is a natural consequence of over- or underloading axial fixed points, and a “quadratic” error with 4 symmetry axes had been detected on another telescope. The effective powers of  $\cos \phi$  and  $\rho$  in these terms are in agreement with the rules of the Hamilton Characteristic Function or the Zernike polynomials given in Tables 3.1 and 3.23 of RTO I. However, the azimuthal effect  $\cos n\phi$  is, in practice, completely dominant in a least squares fit because of

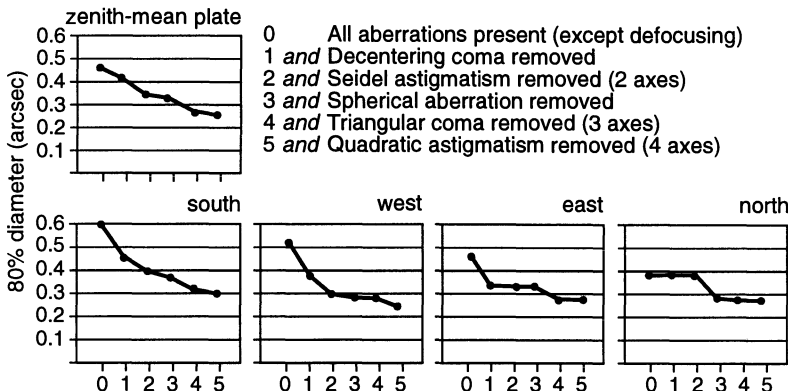


**Fig. 2.18.** Hartmann tests of the ESO 3.6 m telescope after set-up in 1976 at the prime focus with the Gascoigne plate correctors showing the effect of theoretical removal of the polynomial terms indicated (after Franz et al. [2.24])

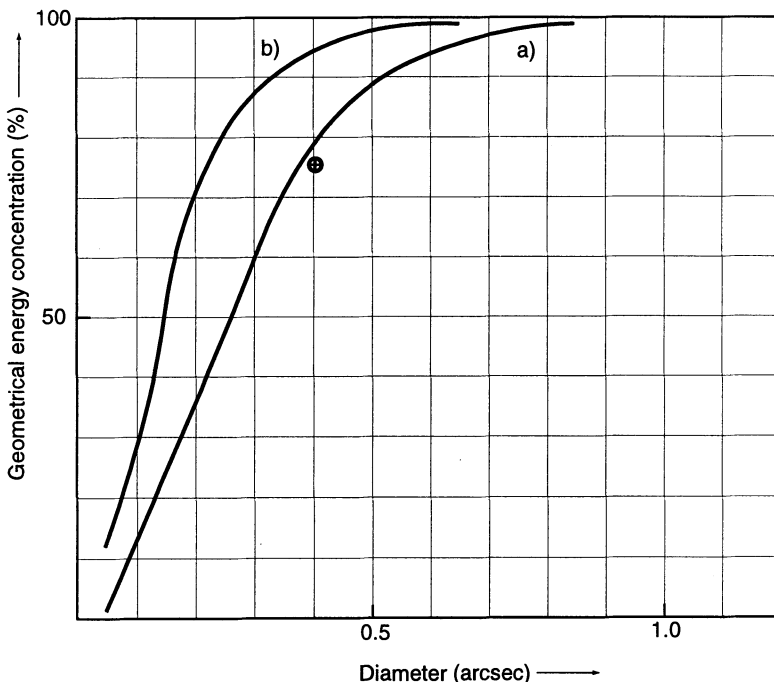
orthogonality, and powers  $\rho^m$  with  $m$  other than 3 or 4 give virtually identical coefficients in the cases of triangular and quadratic error respectively.

The result of the averaged Hartmann plates for zenith distances roughly  $0^\circ$  and about  $50^\circ$  in the south, west, east and north directions is shown in Fig. 2.18. This was a purely *mathematical* operation and there was no means of correcting any of the terms shown except decentering coma off-line by translating the Gascoigne plate. The mean zenith plate showed that the diameter containing 80 % of the geometrical energy  $d_{80}$  was about 0.41 arcsec if coma was removed. This showed that the specification of  $d_{75} \leq 0.40$  arcsec for the primary alone had been easily met, since the measured  $d_{80}$  values included the errors of the Gascoigne plate, itself a difficult technical object. The average right-hand point of the five graphs in Fig. 2.18 gives

$$(d_{80})_{IQ} \simeq 0.27 \text{ arcsec}$$

for the so-called *Intrinsic Quality (IQ)* of this telescope, a term that was defined from these tests as that quality resulting after removal of those terms which can vary in operation. This is fundamental to the concept of *Active Optics* (see Chap. 3). For a passive telescope of this period, this value of the IQ showed exceptionally smooth surfaces in the optics. The assessment of the actual image quality was limited by problems of inferior dome seeing at the time of telescope set-up. These were analysed in some detail in the report [2.24]. Figure 2.19 shows the result considered most reliable for the zenith image quality (primary combined with the “red” Gascoigne plate).

The polynomial analysis enabled a much clearer impression of the “dome seeing” effects to be obtained. Variations of spherical aberration revealed strong “chimney effects” when the naked primary was tested without the Gascoigne plate. These were markedly improved by the sealing effect of the air column by adding the Gascoigne plate. After this, the most serious variations



- a) Decentering coma only removed
- b) All polynomial terms removed
- ⊕ ESO-REOSC contract

**Fig. 2.19.** Geometrical energy concentration of the image at best focus near zenith of the ESO 3.6 m telescope with the “red” Gascoigne plate and 10 mm filter glass. The specification required 75 % geometrical energy concentration within 0.4 arcsec for the primary alone. (After Franz et al. [2.24])

were in astigmatism. The stability of the telescope for decentering coma was also investigated for “top unit” changes.

The classical Hartmann test, using a full-size screen placed above the secondary (or outside the prime focus) of a large telescope must be considered today an old-fashioned procedure, since the “transferred pupil” techniques treated in the next section are capable of measurements at least as accurate and at higher sampling using a small instrument mounted at the focus. Nevertheless, for smaller telescopes without access to modern detectors, the classical Hartmann, linked to a PC for the evaluation, remains a fully valid test procedure.

**2.3.3.2 Hartmann test procedures using a “transferred pupil”: the Shack-Hartmann test.** The concept of a transfer of the exit pupil of a telescope to an element of an instrument, for example the grating of a spectrograph, has been standard practice for a long time. Suggestions for a Hartmann-type test using such a transferred pupil have been made many

times, but always met with the objection that the optics imaging the pupil would introduce unknown supplementary errors. Such a proposal was made in 1971 by Platt and Shack [2.25]. In a more complete form [2.26], this has become the most widely used test for modern telescopes. In this basic form, originally used with photographic plates, such a Shack-Hartmann (S-H) test device was built at ESO about 1979 and has been used for testing a large number of telescopes, both at the ESO observatory and elsewhere. More recently, a very versatile version, applicable to a range of  $f$ /numbers from about  $f/3$  to  $f/50$ , has been constructed at ESO under the name "ANTARES", with a CCD detector and complete software package. The image analyser for the application of active optics to the New Technology Telescope is also of the S-H type.

Figure 2.20 shows the original form developed at ESO for photographic plates with an additional system for alternative use with a CCD detector [2.27]. A (reference) pinhole source (1) is conjugate with the axial telescope image (9) via a beamsplitter (2) of high quality. The reference source is transferred by the beamsplitter to the collimator (3) (often called a Fabry lens from its analogue use in instruments) which forms the image of the exit pupil of the telescope in the plane (4). This plane contains the Hartmann-type screen; in the S-H device, it is a rectangular raster of square lenslets following the proposal of Shack. Each lenslet forms a sub-aperture of the transferred pupil and focuses the parallel beam of its sub-aperture on the photographic plate (5) to form a spot of light. For use with a CCD, a field lens (6) and objective (7) (schematic) transfer the plane (5) to the CCD (8) with appropriate reduction.

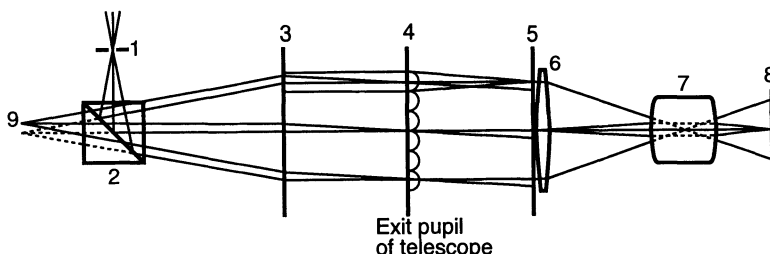


**Fig. 2.20.** Construction (schematic) of basic Shack-Hartmann telescope test device for use with photographic plates or CCD detector (after Wilson et al. [2.27])

In the basic ESO test device, the S-H screen (4) is a square raster of  $40 \times 40$  lenslets,  $1 \times 1$  mm square with a focal length about 160 mm. The lenslets are therefore extremely weak with sagittae of the order of  $2 \mu\text{m}$  for a refractive index of 1.5.

The telescope image of a suitable star (9) sends a similar beam into the system. It is slightly displaced from the axis to give a separation of the set of spots produced. Figure 2.21, reproduced from [2.27], shows an actual S-H

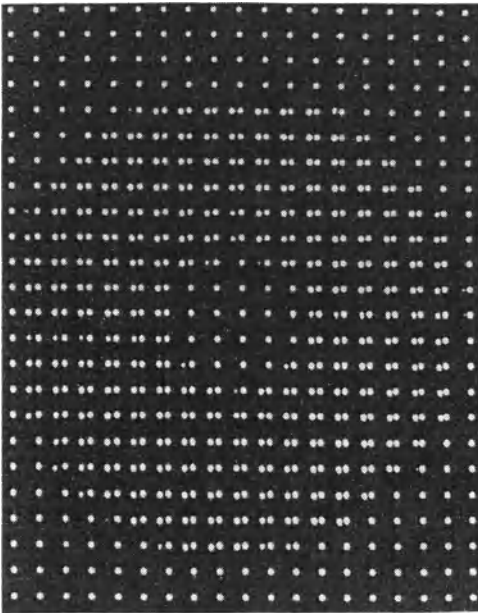


**Fig. 2.21.** Typical S-H test plate exposed at the MPIA 2.2 m telescope II in 1983. The raster corresponding to the telescope image shows the form of the pupil of the telescope. The general raster comes from the reference source. (After Wilson et al. [2.27])

plate produced during the set-up and test of the MPIA 2.2 m telescope II at La Silla in 1983. The offset of the reference should not be more than one third of the raster step to avoid confusion of related points.

The information on the S-H plate is a direct measure of the local wavefront tilt corresponding to each spot. The lateral aberration of a given sub-aperture in the telescope image plane (9) in Fig. 2.20 is transferred through the system to the recording plane (5) with the factor  $f'_c/f'_s$ , where  $f'_c$  is the focal length of the collimator (3) and  $f'_s$  that of the Shack lenslets (4). For an existing Shack raster,  $f'_c$  must be chosen to give adequate sampling over the pupil. The original master rasters offer a maximum sampling, in practice, of about  $36^2$  points over the unobstructed square or about 900 points over a circular, typically obstructed, telescope aperture. This is enormous compared with the sampling of conventional Hartmann tests. In practice, sampling of the order of 300–400 points is ample for high-quality telescope optics with acceptable high spatial frequency content in the wavefront error.

The procurement of suitable S-H lenslet rasters is not a trivial technical problem. Shack [2.26] made his original masters by forming cylindrical lenses in a milling machine and crossing copies of two such masters at right-angles. The lenslets are so weak that the difference between crossed cylinders and axially symmetrical lenslets is below the diffraction limit. Another process which has been employed is by pressing spherical balls into a resin, but this tends to give errors of overlap at the edges between the square lenslets. In our experience, the most successful technique has been *laser etching*, a procedure developed by Gale and Knop [2.28] at the RCA Laboratories in Zurich, now

the Paul Scherrer Institute. Such negative metal masters can be copied to produce positive copies in resin by standard techniques used, for example, for holographic gratings. Excellent copies have been made for ESO and many other institutes by the firm Jobin-Yvon in Paris.

Apart from the S-H raster, the components of an S-H test device are quite simple. The collimator is uncritical and a simple doublet is sufficient unless the telescope has a very high relative aperture (in prime focus). Only the beamsplitter is critical since, after it, *all elements are traversed by both reference and telescope beams*. In fact, the most important aspect of the reference spot grid is the effect of errors in the Shack raster itself. However, all such errors are essentially stable. We shall see below that, with more modern versions based solely on CCD detectors, the provision of the reference wavefront becomes simpler. The size of the reference source is uncritical: it should preferably be comparable with the best seeing disk, say 50 µm in a telescope like the NTT with a scale of 187 µm/arcsec.

In the original S-H concept of Fig. 2.20, intended primarily for photographic plates, it is essential that the condition of *isoplanatism* be maintained for the aberrations over the small angular shift of the reference source to the telescope image. This is no problem for the conventional optical elements, but the Shack raster may contain high spatial frequency errors whose Fourier transform could give problems of lack of isoplanatism even over small angles. However, with the angular shift of the order of that shown in Fig. 2.21, no such problem has been found with available raster screens.

The S-H raster screen is, in a sense, less fundamental for Hartmann-based methods using a transferred pupil than the provision of a reference beam: this was the essential step. It is quite possible to use a small Hartmann screen with conventional holes instead of the S-H lenslet raster. Such a test device was constructed and successfully used by Bahner and Loibl [2.29]. Nevertheless, the lenticular raster screen proposed by Shack has the following important advantages:

- Higher sampling. The contiguous disposition of the lenslets together with the spot concentration offers a level of pupil sampling which is impossible with a classical Hartmann screen containing simple holes. As indicated above, sampling up to 900 points is quite feasible with available screens.
- On photographic plates, the spot-pair arrangement over the pupil shown in Fig. 2.21 removes all problems such as emulsion distortion or measuring machine error over a significant range, since only differential measurements over the small vector distances of the spot-pairs are required. The information on aberrations comes from the variations in the individual vector differences of the spot-pairs. With modern CCD detectors, used as discussed below, this advantage is less significant.
- There is a gain of about  $3.5^m$ – $5^m$  ( $25\times$ – $100\times$ ) in light efficiency due to the spot concentration (spot diameters 100–200 µm instead of 1 mm). Since the light of the telescope image is spread over a diameter up to 35 mm, this

advantage is important. With III-aF plates used to test the ESO 3.6 m telescope, stars of  $8^m$ - $9^m$  were used; at the NTT with a CCD, the limit is about  $14^m$ . We shall see that this advantage is particularly important for the active control of telescopes using available guide stars for image analysis (see Chap. 3).

According to Fig. 2.20, the S-H screen is placed at the transferred exit pupil of the telescope. In practice, this is very uncritical because only the *axial* image of the telescope needs to be tested. (Tests in the field are unnecessary because the field aberrations are essentially stable functions which will never vary: they will always be effectively those given by the nominal optical design of the telescope. The variations found in the axial image will simply be vectorially superimposed on the field aberrations as shown in Fig. 2.1). The effective field used by the telescope beam is therefore the maximum seeing disk, plus errors of centering the star on the reference cross or guiding errors over the integration period of the order of 30–60 s. This field is so small that the position of the pupil is anyway weakly defined. It can easily be shown that the only practical effect of even considerable pupil position error is a small loss of sampling.

The S-H test device is therefore a simple, robust device with generous manufacturing tolerances.

The image analysis is performed in a similar way to that given above for classical Hartmann testing, the standard test polynomial being of the general form

$$W' = k_{nm} \rho^m \cos(n\phi + \theta_{nm}) , \quad (2.73)$$

shown in Eqs. (2.72). Apart from the fifth order spherical aberration included there, two other fifth order terms are sometimes included:

$$\left. \begin{aligned} &k_{24} \rho^4 \cos(2\phi + \theta_{24}) - \text{fifth order astigmatism} \\ &k_{15} \rho^5 \cos(\phi + \theta_{15}) - \text{fifth order coma} \end{aligned} \right\} \quad (2.74)$$

In order to see the importance of different low frequency terms, it is instructive to remove the terms individually. This process is illustrated in Table 2.4 for the *MPIA 2.2 m telescope II*, tested in October 1983 after set-up. Column 2 shows the  $d_{80}$  quality (diameter containing 80 % of the geometrical optical energy) actually measured for this excellent passive telescope, including residual decentering coma. The mean values were 0.47 arcsec and 0.62 arcsec near the zenith and at  $Z \sim 45^\circ N$  respectively. With coma removed (Column 3 – the true quality of the telescope), the values were 0.42 arcsec and 0.60 arcsec. Columns 4–9 show the effect of removal of coma  $C$  and one of the other terms  $S$ ,  $A$ ,  $\Delta$ ,  $\square$ , or pairs of terms. Finally, Column 10 shows the  $d_{80}$  value after removal of all five basic terms – the *Intrinsic Quality* (IQ). The IQ of this telescope (not realisable because of its passive nature) is  $(d_{80})_{IQ} = 0.35$  arcsec. The results showed that the aberrations near the zenith were all small, only  $S$  and  $A$  having detectable effect. At  $Z \sim 45^\circ N$ ,

**Table 2.4.** Shack-Hartmann test results of the MPIA 2.2 m telescope II (RC focus) at La Silla in October 1983 (after erection and centering). All results are in arcsec and are the mean diameters corresponding to 80% geometrical energy obtained from 4 S-H plates. (From Wilson et al. [2.27])

1	2	3	4	5	6	7	8	9	10
<i>Basis</i>	Telescope performance incl. decentering coma $C$ (arcsec)	Minus $C$ $\equiv$ Telescope actual geom. opt. quality	Minus $C+S$	Minus $C+A$	Minus $C+\Delta$	Minus $C+\square$	Minus $C+S+A$	Minus $C+S+A+\Delta$	Minus $C+S+A+\Delta+\square$ $\equiv$ Telescope intrinsic geom. opt. quality
ZENITH									
Bad SHACK spots removed	0.490	0.431	0.398	0.399	0.424	0.431	0.371	0.370	0.368
Bad + doubtful spots removed	0.446	0.401	0.370	0.370	0.396	0.398	0.337	0.332	0.330
Mean	0.47	0.42							0.35
ZENITH DISTANCE ca. 45° N									
Bad SHACK spots removed	0.628	0.610	0.560	0.490	0.603	0.601	0.434	0.427	0.411
Bad + doubtful spots removed	0.604	0.592	0.538	0.464	0.586	0.583	0.416	0.408	0.393
Mean	0.62	0.60							0.40
<i>Key</i> $C$ = 3rd order coma, $S$ = 3rd order spherical aberration, $A$ = 3rd order astigmatism, $\Delta$ = "triangular coma" (trifoil), $\square$ = "quadratic astigmatism" (quadrifoil)									

the astigmatism  $A$  was the principal reason for decline in quality, also to a lesser extent spherical aberration  $S$ . According to Bahner ([2.27]-discussion), the increase of astigmatism at large  $Z$  was not found for the equivalent 2.2 m telescope I at Calar Alto. It *may* therefore have been in the local air. This illustrates the value of such tests. More measurements would have been necessary to clear up this point.

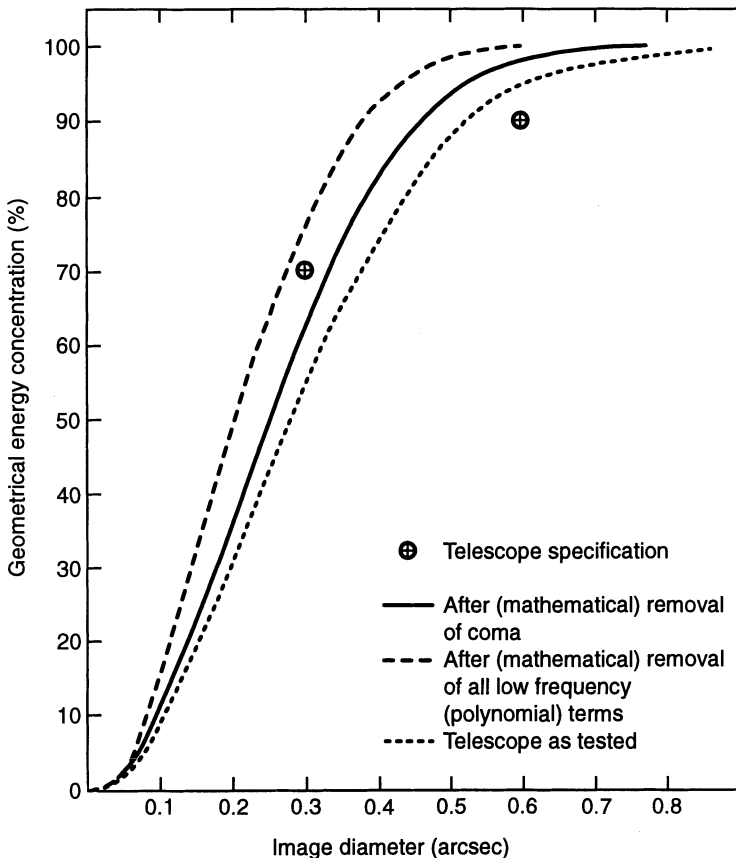


**Fig. 2.22.** Image profile of the MPIA 2.2 m telescope II after set-up in October 1983 as given by the test S-H plate taken near the zenith, in comparison with the specification (from Wilson et al. [2.27])

Figure 2.22 shows the image profile deduced from the best S-H plate near zenith, compared with the specification. The result with coma removed was well inside the specification for  $d_{90}$  but slightly outside it for  $d_{70}$ . It should be emphasized that this is an excellent result for a passive telescope of this size manufactured in the 1970s.

If inadequate sampling is performed, the high spatial frequency errors will be progressively underestimated, giving an over-favourable value for the IQ above all, but also for the measured telescope quality with all errors present. The effect of reduction in sampling in the above case was given in [2.27].

The scheme shown in Fig. 2.20 was essentially laid out for photographic plates, the CCD being added later. Modern S-H test devices will use CCDs only, with all the advantages of linear response, high efficiency and, above all, immediate display of the results. This is yet a further example of the revolution of CCDs in astronomy. Of course, care must be taken that pixel

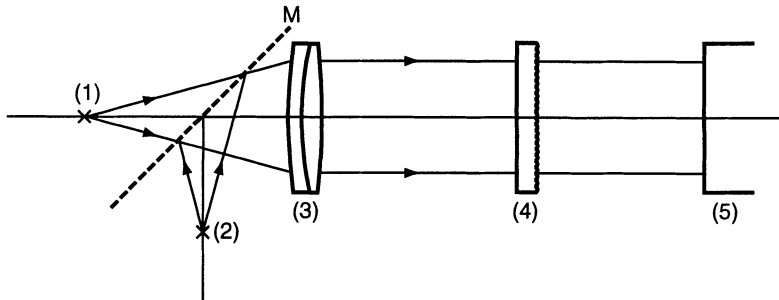


**Fig. 2.23.** Simplified S-H test arrangement as intended for the 8 m unit telescopes of the ESO VLT [2.30]

sampling is adequate with the CCD: this will be discussed further in Chap. 3 in connection with active control and the NTT. For the 8 m unit telescopes of the ESO VLT, there is no reduction from the transferred pupil to the CCD (Fig. 2.23) [2.30]. Instead of a beamsplitter, the reference source (2) can be switched in or out as required by a switching mirror  $M$ . The S-H raster (4) consists of lenslets of only 0.5 mm square and feeds the CCD (5) directly. The maximum beam size is then 10 mm diameter with a sampling over the unobstructed square of 400. The CCD has  $578 \times 592$  pixels of  $19 \mu\text{m}$  diameter.

Although it cannot rival a test device with a CCD for *on-line* use, a Shack-Hartmann tester using photographic plates may still be very useful for *off-line* work if a measuring machine is available. Such a device was the so-called ANTARES I, designed and built at ESO about 1978 for off-line testing of the telescopes at the La Silla observatory [2.31]. This is shown in Fig. 2.24. The square Shack raster had  $40 \times 40$  lenslets of  $1 \times 1$  mm, giving a maximum pupil sampling of about 1000 with normal central obstruction of a circular pupil. This was far higher than the normal sampling of classical Hartmann screens. Such a device, systematically applied, can lead to dramatic improvement in practical telescope quality.

For the active NTT, a built-in on-line S-H test device was essential to the whole concept and the fact that CCDs were becoming readily available for astronomical use was a fundamental technical advantage. The NTT image analyser was essentially the same as the scheme of Fig. 2.20. In parallel, a general purpose *off-line* S-H test device was developed in 1987, using a CCD detector, under the name of ANTARES II. The optical concept, due to B. Delabre and F. Franza [2.31], enables the testing of telescopes from about  $f/3$  to  $f/50$ . By switching elements symmetrically with a double revolver system, this wide range of  $f/\text{nos}$  is made possible without changing the optical path length. Figure 2.25 shows the optical scheme in the case of an  $f/11$  telescope output beam. The compact transfer system reduces the S-H spot image given by the  $40 \times 40$  mm lenslet raster by a factor of about 2.9 times to match the CCD. The accompanying software package and output is effectively identical with that of the NTT which is discussed in detail in Chap. 3. The output

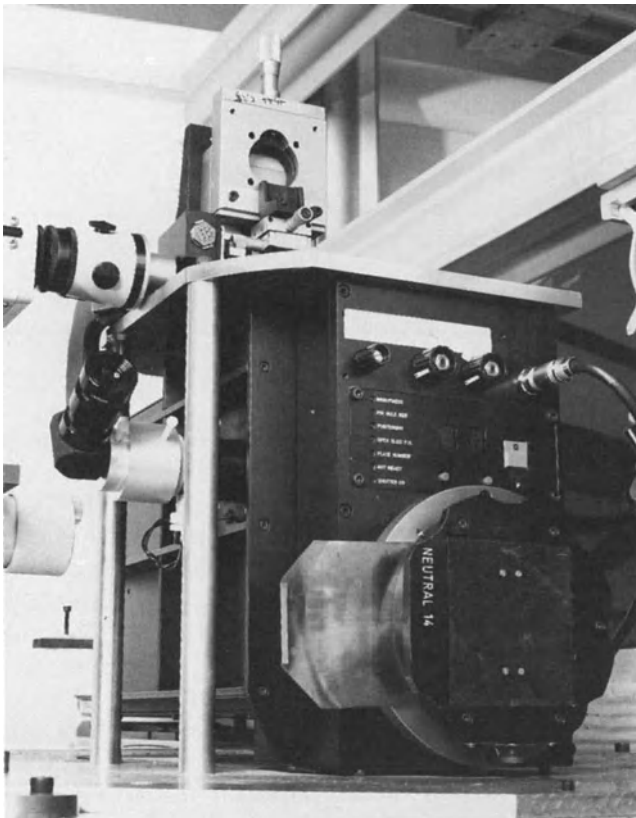


**Fig. 2.24.** The ESO off-line S-H test device ANTARES I, constructed in 1978 for use with photographic plates [2.31]

data give not only complete information on the low spatial frequency terms but also global information on the high spatial frequency terms. The value of the latter and its variations give an excellent measure of the condition of the local air ("dome seeing"). It is quite common to find telescopes whose optical quality is completely limited by these local air conditions.

Software packages for S-H image analysis (or by any other method) can be subject to error. The best way of testing their correctness is to use decentering coma and despace spherical aberration from Eqs. (2.1), (2.4) and (2.20) to give known theoretical *changes* in these aberrations which are then measured directly. The defocus and wavefront tilt coefficients of Eqs. (2.72) may also be used, calibrated by Eqs. (3.211) and (3.212) of RTO I.

**2.3.3.3 Interferometric modification of the Hartmann test.** An elegant interferometric modification of the Hartmann test has been proposed by Korhonen [2.32] [2.33] [2.34] and applied with success to the 2.5 m Nordic Op-

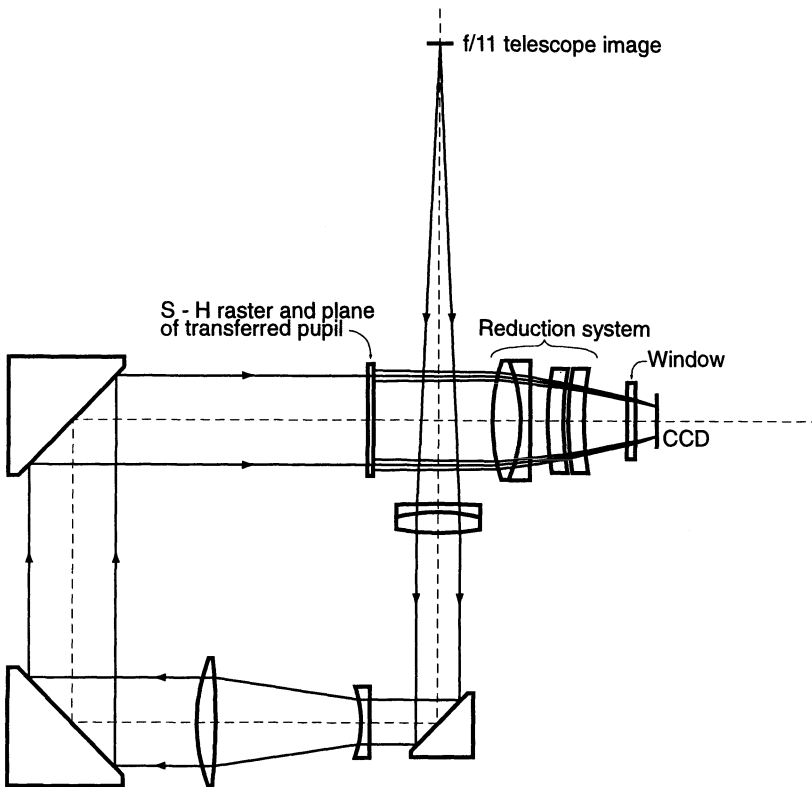


**Fig. 2.25.** Optical layout of the ESO general purpose off-line test device ANTARES II (1987), for use with a CCD detector. The figure shows the (switchable) optics for an f/11 telescope output beam [2.31]

tical Telescope (NOT), both during optics fabrication and in the functioning telescope [2.35].

The technique is based on the following principle. Suppose a Hartmann plate is exposed in the classical way, well outside the caustic of the image, to give the pattern of a group of spots as shown in Fig. 2.26(a). If the plate is exposed much nearer the image so that the spots are partially overlapping and interfering, the appearance of Fig. 2.26(b) is produced. There are strong primary interference maxima such as *A* and weaker secondary maxima. The maximum *A* is formed by the four spots 1, 2, 3, 4 in the same way as interference in two cross slit pairs. The center of the interference maximum is, of course, at that point where the optical paths are equal. The measured positions of the primary maxima are reduced for the nominal focal plane exactly as for classical Hartmann measurements. To obtain a good interferogram, the correct distance  $s_I$  of the photographic plate from the focus is

$$s_I = \lambda \left( \frac{f'}{\Delta y_H} \right) , \quad (2.75)$$

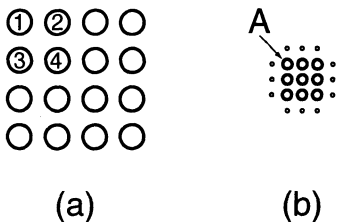


**Fig. 2.26.** (a) Group of spots produced by a Hartmann plate in the classical way. (b) Interference effect produced by the same group of spots if the plate is exposed much nearer the image giving partial overlap and interference between spots. (After Korhonen [2.32])

where  $\lambda$  is the test wavelength,  $f'$  the focal length and  $\Delta y_H$  the hole spacing of the Hartmann screen. A hole diameter  $d_H$  about 1/3 to 1/2 of  $\Delta y_H$  has proved successful.

Korhonen adduces the advantage of the interferometric method over classical Hartmann from the relative size of the spots in Fig. 2.26(a) and (b). Diffraction gives a minimum diameter of the Hartmann spots, from (3.447) of RTO I, as

$$\phi_H = 2.44\lambda/d_H \text{ rad} , \quad (2.76)$$

while the diameter from the interference effect is

$$\phi_I = \lambda/\Delta y_H \text{ rad} \quad (2.77)$$

In a typical Hartmann screen  $\Delta y_H/d_H \geq 3$ . Using the same screen, this implies

$$\phi_H/\phi_I \geq 7.3 \quad (2.78)$$

Accepting the classical rule of photographic astrometry that the precision of measurement of the centroid of a round image is about 1 % of its diameter, Korhonen claims higher accuracy for the interferometric method on the basis of (2.78). The sampling can also be higher than in classical Hartmann.

The Shack-Hartmann modification is more efficient and accurate than classical Hartmann in that the S-H spot sizes are smaller than the sub-apertures formed by the lenslets. But Korhonen considers there is still a gain of a factor of about 2.5 with the interferometric method over the S-H technique [2.35] assuming equal sampling and perfect lenslets. In the form of the test device used in 1991 on the NOT, a small Hartmann screen is used in the transferred pupil, containing 792 holes. The interference spots are less than 1 arcsec diameter, giving a centroiding precision of the order of 0.01 arcsec, recorded on a CCD with 15  $\mu\text{m}$  pixels.

According to measurements with the Korhonen interferometric test device [2.35], the NOT has exceptional quality for a passive telescope at the Cassegrain focus,  $d_{80} \simeq 0.35$  arcsec after removal of coma alone. The IQ is given as  $(d_{80})_{IQ} = 0.196$  arcsec. It was intended to activate the telescope to achieve this IQ (see Chap. 3), a perfectly feasible aim since the aspect ratio of the primary mirror is 16.8, more extreme than the NTT (15).

Korhonen and Haarala also point out [2.34] the attractions of their interferometric test for *segmented* mirrors, since “piston” errors of the wave-

front can also be detected, not just slope errors as with the S-H technique. This advantage has been recognised for the case of the segmented 10 m Keck telescope. For the hexagonal geometry of the Keck primary, Korhonen and Haarala propose a triangular system of Hartmann screen holes. Phase errors in the corner of three adjacent segments are measured with a 3-hole system.

### 2.3.4 Curvature sensing: the Roddier test

In § 2.3.2 “pupil plates” were discussed as a generalisation of time-honoured techniques of assessing image quality by examining intra- and extrafocal images. It was shown how the three basic low spatial frequency aberration coefficients (spherical aberration, coma and astigmatism) can be derived from the appearance of the obstructed pupil of a telescope. The information comes from the pupil considered as a primitive sort of Hartmann screen containing the following information: the  $x$  and  $y$  displacements of the center of the obstruction circle relative to that of the outer pupil, their degree of ellipticity and their relative size in the intra- and extrafocal positions. Apart from these low spatial frequency errors, pupil plates can show irregularities in the average circular shape at both outer and inner pupil boundaries as well as marked photometric variations, above all from zones and ripple. An extreme example is shown in Fig. 2.27, pupil plates exposed in 1979 for the old 50 cm ESO telescope at La Silla [2.36]. This telescope was only used for photometry with a normal minimum diaphragm of 10 arcsec, so the image quality is uncritical. If it were used for direct imaging, the loss of quality due to the high zonal slopes would be very serious.

Beckers and Williams [2.37] were also concerned in 1979 with zonal appearances in out-of-focus images at the MMT, though in this case the effect was much less serious. They point out that the photometric intensity dif-

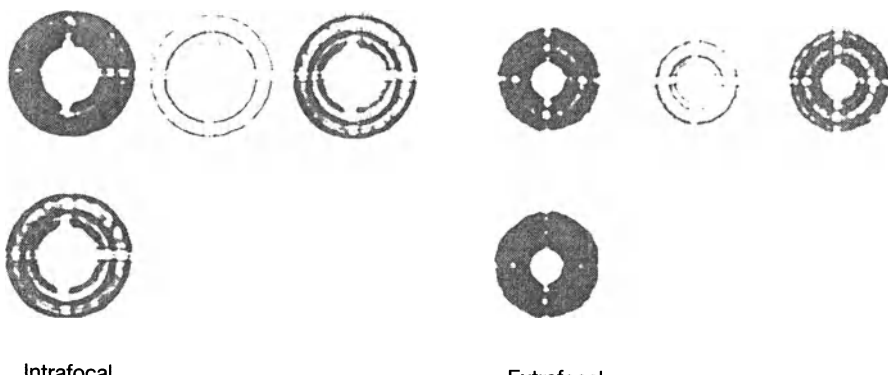


**Fig. 2.27.** Pupil plates showing strong “ripple” taken in 1979 at the ESO 50 cm telescope. The plates were taken with various exposures to reveal the zones, at the left intrafocally, at the right extrafocally. Original plate diameters 3.5 mm (*left*) and 2.8 mm (*right*). At this stage, the telescope still had 1.3 arcsec of decentering coma

ferences revealing the zones are a measure of the local curvature (second derivative) of the wavefront and that photometric sensing could give the information required to calculate the wavefront. They attempted this with a CID camera but failed because of lack of sensitivity. Interferograms had revealed that the zonal wavefront errors on the primary were only about  $0.1 \lambda$  though they were clearly revealed in the polaroid photographs (pupil plates).

The photometric approach was taken up later by Roddier et al. [2.38]–[2.43]. In these and other papers, the theory of curvature sensing is analysed in complete form. The earlier work [2.38] was more specifically concerned with the application of wavefront sensors to *adaptive optics* (see Chap. 5), whereas [2.41] and [2.42] are concerned with the general application to the testing of telescope images.

Instead of measuring the local slopes  $\partial W'/\partial x$  and  $\partial W'/\partial y$  of the wavefront function  $W'(x, y)$ , Roddier et al. aim to measure the local curvatures  $c(x, y)$  expressed by the Laplace operator

$$c(x, y) = \frac{\partial^2 W'}{\partial x^2} + \frac{\partial^2 W'}{\partial y^2} = \nabla^2 W' \quad (2.79)$$

The basis of the method [2.41] is to measure the illumination  $I_1$  in a plane  $P_1$  at a distance  $s$  before the focal plane  $O'$  (Fig. 2.28) and  $I_2$  at the same distance  $s$  after the focal plane. The upper figure shows the image space.  $P'$  is the “pupil” in the simplified sense of an equivalent telescope where the pupil is at the principal plane, at a distance  $f'$  from  $O'$ . Theoretically, to ensure complete symmetry, a field lens at  $O'$  with a focal length  $f'/2$  should re-image the exit pupil  $EP'$  at a distance  $f'$  beyond  $O'$ ; but, in practice, since  $s \ll f'$  this field lens can be omitted. The lower figure shows the object space. The image space defocus planes  $P_1$  and  $P_2$  can be projected back into the object space in an analogue way to that shown in Fig. 4.2 and Eq. (4.2) of RTO I for the position of a virtual corrector plate in object space for the equivalent of a primary at  $P'$ . This gives the symmetrical spacing of  $I_1$  and  $I_2$  about  $P'$  at a distance  $\pm \Delta z$ . A local wavefront curvature error produces an excess illumination in one plane and a lack of illumination at the other. Then the difference  $\Delta I = I_1 - I_2$  provides a measure of the local wavefront curvature or Laplace operator of the wavefront surface. If  $s \ll f'$ , then according to geometrical optics with  $\rho^2 = x^2 + y^2$  defining the vector pupil position of the sub-aperture

$$\frac{\Delta I}{I}(\rho) = 2 \frac{\lambda f'^2}{s \rho_m^2} \nabla^2 W'(\rho) , \quad (2.80)$$

where  $W'$  is expressed in units of wavelength  $\lambda$ ,  $\rho_m$  is the pupil radius and  $I = (I_1 + I_2)/2$  is the average illumination. The authors point out that the method is fairly insensitive to non-uniformities of the intensity distribution in the pupil plane, since they produce a similar effect in both planes  $P_1$  and  $P_2$  which cancels out in the normalized difference. Radial tilts at the pupil edge produce local shifts at the beam cross-sections. In deducing the difference

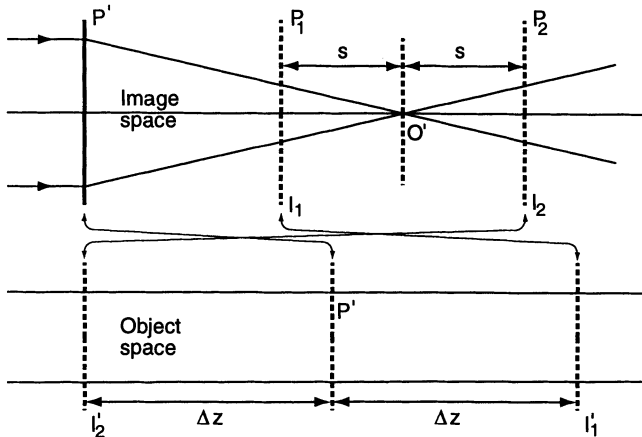


**Fig. 2.28.** Curvature measurement following Roddier et al. [2.41] for testing telescopes

$\Delta I$ , such shifts produce a narrow but strong edge signal proportional to the radial tilt. Their general reconstruction method computes the wavefront from its Laplace operator by solving the Poisson equation following the boundary conditions with the edge tilt according to the Neumann potential function [2.43].

If one is concerned with adaptive optics, the integration times will be short and depend on the correction frequency intended; for testing of telescopes, on the other hand, integration over the time ( $\sim 30$  s) necessary to integrate out the external atmosphere will be required, exactly as with Shack-Hartmann or any other method. If the integrated seeing disk has the diameter  $(\delta u')_s$  rad, then the linear blurring effect of pupil-plate information is  $\simeq (\delta u')_s f'$ . This blurring effect must be small compared with the minimum size  $\delta \rho$  of the wavefront errors we wish to measure. The minimum size of the pupil plates is then given by

$$(\delta u')_s f' \ll \delta \rho \frac{s}{f'} \quad (2.81)$$

With  $D = 2\rho_m$ , the pupil diameter, it follows that the maximum number of sampling points across the diameter is

$$\frac{D}{\delta \rho} = \frac{D_s}{(\delta u')_s f'^2} \quad (2.82)$$

Increasing  $s$  increases linearly the number of sampling points in the reconstructed wavefront but decreases  $\Delta I$ , i.e. the sensitivity to small amplitude wavefront errors. The maximum sampling is therefore a compromise determined by the sensitivity of photometric detection. Equation (2.80) for the geometrical optics case is valid if (2.81) holds.

Roddier and Roddier [2.42] [2.43] give the generalised form of (2.80) to include the wavefront slope effect at the edge of the pupil as

$$\frac{I_1 - I_2}{I_1 + I_2} = \frac{f'(f' - s)}{s} \left[ \frac{\partial W'}{\partial \tilde{n}} \delta_c - P_t \nabla^2 W' \right] , \quad (2.83)$$

where  $\delta_c$  is an impulse (Dirac) distribution around the pupil edge,  $\tilde{n}$  is a unit vector perpendicular to the edge and  $P_t$  is the pupil transmission function normally assumed to be 1 inside the pupil and zero outside it.

The method was tested in practice in 1989 at the prime focus of the University of Hawaii 88-inch telescope [2.41]. This was an uncorrected RC prime focus giving a large amount of systematic “overcorrected” spherical aberration, confirmed by the appearance of the “pupil plates” with a relatively larger central obstruction in the extrafocal plate (the opposite of the case shown in Fig. 2.12). The spherical aberration coefficient was estimated first by the equivalent of (2.64) from the obstruction *geometry* as  $-10.9 \mu\text{m}$ . It was then deduced *photometrically* using a CCD camera and the Poisson algorithm to give a final estimate of  $-11.0 \pm 0.1 \mu\text{m}$ , in excellent agreement with the geometrical estimate. This work was then extended to a reconstruction of the mirror wavefront after removal of the spherical aberration term. Fig. 2.29 shows a contour plot of the wavefront after removal of the remaining low frequency terms: tilt, defocus, coma, astigmatism. Zernike polynomials were fitted, the largest values being coma and astigmatism, as one would expect. Since the Laplace operator is zero for astigmatism, the value is obtained only from the edge (slope) terms.

According to Roddier [2.43] the main disadvantage of curvature sensing is error propagation in the wavefront reconstruction algorithm. It is also weak on astigmatism since the total curvature information from the Laplace operator is zero. The authors claim the following advantages:

- a) The sensitivity is comparable to that of the Shack-Hartmann technique.
- b) No additional optics is required (throughput advantage).
- c) No calibration with a reference source is required.

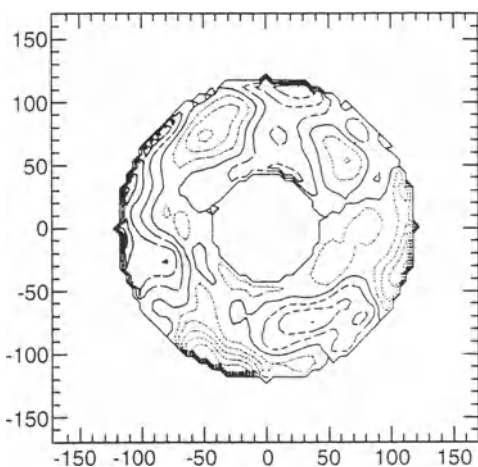


**Fig. 2.29.** Contour plot of the reconstructed wavefront from curvature sensing of the primary of the 88-inch University of Hawaii telescope in April 1989 after removal of low spatial frequency terms. Increment  $0.025 \mu\text{m}$ , dotted line positive, dashed line negative. (From Roddier et al. [2.41])

There is still (end of 1996) relatively little *published* test information available on different telescopes with the Shack-Hartmann or curvature sensing techniques. A large amount of data is available from S-H tests (many thousands alone at the NTT) and experience has shown that the sensitivity and accuracy with modern CCDs is ample for all purposes. In practice, the limitation in measuring precision is set by *dome seeing*, not by inherent limitations in the S-H technique. However, apart from the results achieved at set-up of the NTT [2.44], this data has not been published. Some comparative tests with Shack-Hartmann (using the ESO ANTARES test device) and with curvature sensing have been made at the Cerro Tololo 4 m telescope [2.45], but this was too limited a basis for serious comparison of the two methods. Roddier and Roddier [2.46] and Roddier et al. [2.47] have published more extensive data with curvature sensing on a number of telescopes, including a comparison of the two methods at the NTT. Such test data analyses are of fundamental importance to the development and optimization of modern optical telescopes: it is to be hoped that corresponding publications on the results of systematic Shack-Hartmann testing will also appear. The results quoted in [2.46] for the NTT indicate good general agreement in the basic aberration coefficients derived from curvature sensing and S-H measurements. It remains to be seen whether curvature sensing will displace the S-H device. If good master raster screens are available (as is the case), procurement of such screens is no problem. Otherwise, S-H test devices are simple and robust. Furthermore, the reduction algorithm is simple and direct and measurement in *one* image plane is sufficient, an important time-saving advantage for on-line, active control. The current evidence is that both methods are excellent for accurate testing of functional optical quality and it is a matter of individual preference and experience which method is chosen.

Roddier et al. [2.41] mention the interesting proposal by Behr [2.48] to measure decentering coma by photometric measurements in a device intended for centering telescopes. Such a device was built in ESO and tested by Franzia and Wilson [2.49] in 1980 at the Danish 1.54 m telescope at La Silla. The principle was elegant, making use of the theoretical linear reduction in intensity in the direction of the coma axis in a pupil plate (Fig. 2.9). The out-of-focus image was scanned by a rotating diaphragm with a small excentric hole. In the presence of coma, this scan should produce a sinusoidal intensity function with maxima and minima in the direction of the coma axis. We found that the device gave clear indications for coma coefficients down to about 1 arcsec, below which the results became completely random. This remained the case even if the rotation period was much longer than the atmospheric integration time used (60 s). The reason was clearly the fundamental weakness that the scanning aperture was fairly small and that an integration time of the order of 30 s would be required *before the scanning hole moves a significant fraction of its own diameter*. With the small hole used, this would have required a rotation period of over an hour. So, in fact, the device was simply measuring the random local atmospheric variations of coma over the

moving sub-aperture, superimposed on the fixed telescope effect. Since the seeing was indifferent at the time, the random atmospheric coma contributions were completely dominant. The problem could have been alleviated by using a much bigger diaphragm hole, but this would have lowered the sensitivity of detection of the sinusoidal function. Hence, it was concluded that the photometric scanning principle, though elegant in theory, had a fundamental weakness in practice. Instead, geometrical assessment of pupil plates was used as discussed in § 2.3.2. The Roddier curvature sensing technique does not suffer from the weakness of the Behr scanning technique since the whole pupil is registered in one integration.

### **2.3.5 Other methods of testing the optical quality of telescopes in function**

In the excellent analysis of Goad et al. [2.13], Hartmann-based wavefront sensors were compared not only with rotating Foucault knife-edge devices referred to above in § 2.3.1 but also to radial grating interferometers [2.50] [2.51] [2.52]. Their analysis shows that such interferometers are slightly less efficient than rotating knife modulators, themselves a factor 2.33 times less efficient than imaging Hartmann devices. They concluded that the Shack-Hartmann principle was the most favourable of these three possibilities for an adaptive optics sensor at that time, before curvature sensing was advanced as a potential candidate.

Any interferometer which does not require a separate reference source is a potential candidate for testing telescopes in function. This rules out all variants of Twyman and Green interferometers (see Chap. 1), but leaves the possibility of various forms of interferometer which produce interference in some way only from the test wavefront coming from a star. They must be capable of operating with a reasonably broad spectral bandpass. Two obvious candidates are:

- The wave-shearing interferometer – Bates [2.53].
- The point-diffraction interferometer – Smartt [2.54].

According to Goad et al. [2.13], the Smartt interferometer has a too low efficiency to be competitive in the testing of functional telescopes. It can be used with a polychromatic source but, in its nature, involves considerable light loss.

In the wave-shearing interferometer, the wavefront is sheared laterally against itself. This device is technically simple [2.55] and was used with great success by Brown at Grubb-Parsons [2.56] (see Chap. 1) for the production of telescope optics, and has the advantage of being very insensitive to vibration. The fringes produced correspond essentially to the first derivative of the wavefront aberration. The obvious limitation is the wavelength dependence of the fringe pattern which severely limits the bandpass available and lowers the efficiency. Little attempt seems to have been made to test telescopes this

way and it seems most unlikely it can rival the light efficiency of Hartmann-based, curvature sensing or rotating knife techniques.

It seems that interference is better exploited in combination with a Hartmann-type procedure, as developed by Korhonen – see § 2.3.3.3. Such possibilities are further analysed by Roddier and Roddier [2.42]. They propose the interferometric analogy of interferometric Hartmann as a phase retrieval system which extends the wavefront reconstruction from defocused images into the diffraction regime. This was applied to images from the Hubble Space Telescope.

Another old and well-tried test procedure which may be susceptible to modernisation with linear detectors and computer analysis is the *Ronchi test*. The origins of the Ronchi test go back to 1923 [2.57], but the modern form dates from 1958 [2.58] [2.59] and uses a fine grating (Ronchi grating) with a step of the order of  $10^{-2}$  mm placed in front of the image. If an aberrated wavefront passes through the grating, then overlapping of the diffracted orders produces distorted interference fringes which are straight and equidistant if no aberration is present. Deviations in the fringes are a measure of the aberrations.

### 3. Modern telescope developments: pupil segmentation and techniques to reduce mass

#### 3.1 Evolution and revolution in telescope optics

In Chap. 5 of RTO I an account was given of the *evolution* of the reflecting telescope from the optical point of view from Lord Rosse, about 1830, up to about 1980. From about this time, the evolution of telescope optics, which had retained certain essential features ever since Galileo's telescopes in 1610, was supplanted by a *revolution*. A summary of this process was recently given by the author [3.1].

Up to about 1980, telescopes retained the following basic characteristics:

- A nominally *rigid* and monolithic primary element (objective or mirror)
- A nominally *rigid* or (following the Palomar 5 m telescope) a passively compensating structure holding the optical elements
- A generally “*passive*” nature, whereby adjustments could only be made by off-line interventions

Within this global framework, the evolution of telescope optics was above all represented by the physical appearance of the telescope. Figure 3.1 shows seven major telescopes corresponding to the state of the art at the time – see Table 3.1. Their appearance depends essentially on the f/nos of their primaries. This evolution is shown graphically in Fig. 3.2.

The systematic reduction after 1800 occurred over a period of 200 years because of progress in figuring and testing techniques. Apart from a period of

**Table 3.1.** Evolution of primary f/no in reflecting telescopes

Telescope	Date of completion	Primary f/no
W. Herschel 48-inch	1789	f/10
Melbourne (Grubb) 48-inch	1869	f/7.5
Mt. Wilson (Ritchey) 60-inch	1908	f/5.0
ESO 3.6 m	1976	f/3.0
ESO NTT 3.5 m	1989	f/2.2
ESO VLT 4 × 8 m	1998 ...	f/1.8
Columbus (now called LBT) 2 × 8 m	2001 ...	f/1.14

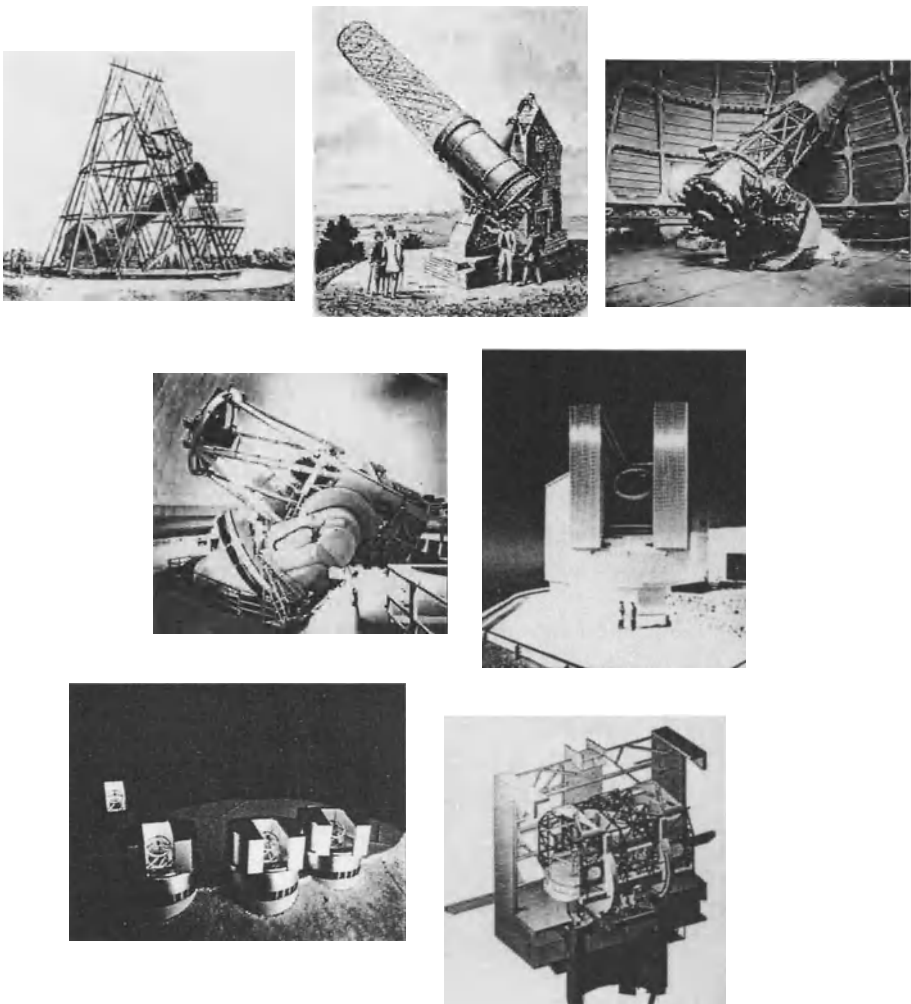


**Fig. 3.1.** The evolution of primary  $f/\text{no}$  in reflecting telescopes and its effect on their appearance. From top to bottom and left to right as in Table 3.1 [3.1]

stagnation around 1940-1960, the fall in  $f/\text{no}$  has been an essentially monotonic function reaching the two values shown of about  $f/1.5$  and  $f/1.0$  for the year 2000. Will this development go further? Opinions differ where the useful limit lies. The aspheric figuring required for a given Schwarzschild constant increases with the inverse cube of the  $f/\text{no}$ , while the space and mechanical stability gains diminish rapidly at extreme values. At  $f/0.25$  a spherical primary has an edge zone parallel to the axis. Beyond that it becomes theoretically impossible to obey the sine condition unless, with an aspheric primary, the final  $f/\text{no}$  is increased, as in the Cassegrain form. Probably Galileo would not have recognised the last three telescopes of Fig. 3.1 as telescopes at all,

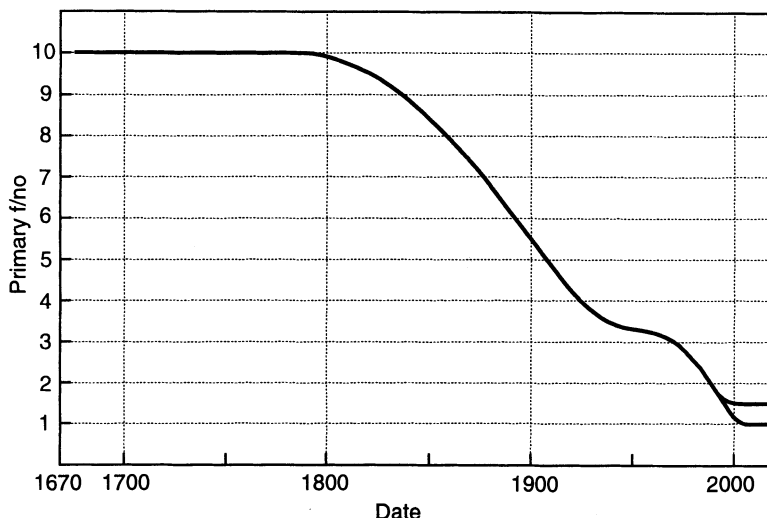


Fig. 3.2. The evolution of primary f/no in reflecting telescopes as a function of time [3.1]

certainly not the last two. The first four telescopes followed the traditional evolution; the last three form part of the modern revolution.

Of course, not only optics has contributed to these evolutionary and revolutionary processes: also mechanics. Furthermore, without modern electronics and computers, no revolution would have been possible. Figure 3.3 shows the important effect, also on telescope optics, of the switch from the conventional equatorial mount to the alt-az mount, the commonest form for modern large telescopes. After 130 years of domination by the equatorial mount, two-axis tracking made possible by computers and modern electronics has allowed

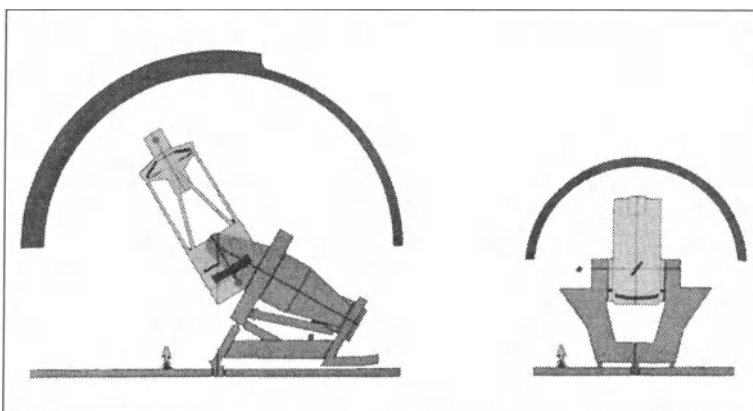


Fig. 3.3. “Sweep circles”, determining the enclosure size, for the ESO 3.6 m equatorial and the NTT 3.5 m alt-az telescopes [3.1]

this reversion to the oldest form of telescope mount. The significance for telescope *optics* is the further huge reduction in the volume of the enclosed air. Figure 3.3 indicates that the alt-az mount is as significant for air volume reduction as the tube shortening due to reduced primary f/nos. However, this viewpoint is disputed by some authorities. For example, E.H. Richardson (private communication 1996) doubts whether the gain is significant compared with the technical complication of the field rotation induced.

The main driver for the telescope revolution was the ancient and fundamental parameter *cost*. For the conventional telescope, Rule [3.2] pointed out that the cost was a function of the *weight* of the telescope, which depends on the diameter. He established the basic weight-cost law for conventional telescopes

$$\text{Cost} \propto D^{2.4} , \quad (3.1)$$

where  $D$  is the telescope diameter. The weight of the mechanics dominates the total weight but depends on the weight of the *primary* which multiplies through the whole system of cell, tube and mount. This thinking was extended in detailed analyses by Meinel [3.3] [3.4] [3.5]. In [3.3] he concludes the power law of (3.1) should be 2.63 for conventional optical telescopes prior to 1975 and 2.94 for radio telescopes. At that time, a 25 m NGT (New Generation Telescope) was under discussion. Using a 2.7 power law, Meinel [3.4] predicted a cost for a conventional telescope of 25 m aperture as  $\$ 2 \times 10^9$  (1978)! Such costs were completely unrealistic for ground-based astronomy and forced new thinking. In 1982 [3.5], Meinel confirmed a power law of about 2.6, applicable not only to conventional telescopes, but also modern conceptions with reduced weight as well as to blanks themselves. For a 15 m telescope, he concluded that the total costs (\$ 1980) in three technical versions would be as shown in Table 3.2. At that time, the MMT (Multi-Mirror-Telescope) with 4.4 m equivalent aperture, was the only non-conventional telescope in function (1979) – see below. Further sophistication of cost scaling laws has been proposed by Humphries et al. [3.6].

New thinking was also forced by flexure (support) and thermal problems of primary mirrors. The flexure problem under gravity of a mirror is expressed by the Couder Law [3.7]

$$W = k \frac{D^4}{t^2} = k \left( \frac{D}{t} \right)^2 D^2 = k A^2 D^2 , \quad (3.2)$$

**Table 3.2.** Cost estimates by Meinel [3.5] showing the advantage of modern over conventional technology

Telescope type (15 m)	Cost (million \$ 1980)
Conventional (equatorial) f/2.75	1092.5
Quasi-conventional (alt-az) f/2.75	630.9
MMT (6-telescopes f/1.0)	186.1

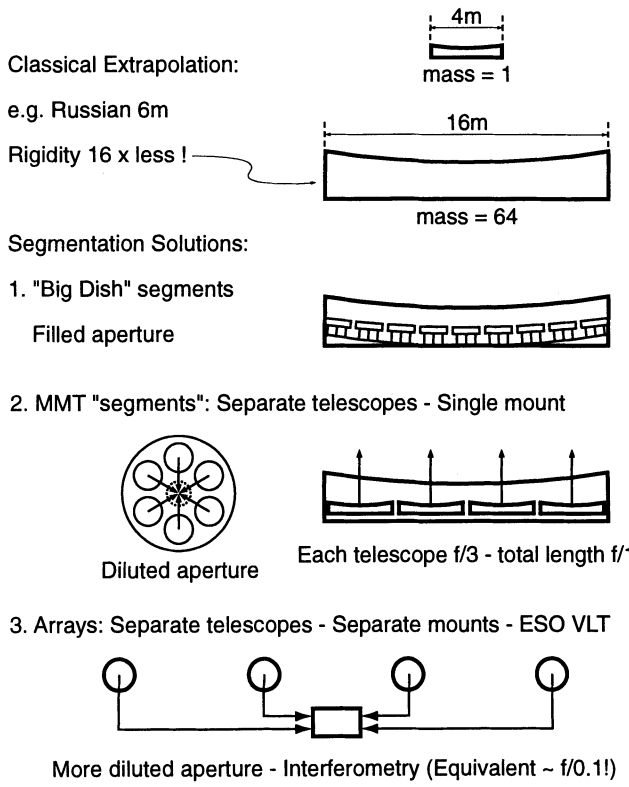


**Fig. 3.4.** The flexure-mass problem of classical mirror blanks and the solution through *segmentation* [3.1]

where  $W$  is the flexure,  $D$  the diameter,  $t$  the thickness of the (cylindrical) mirror,  $A$  the “Aspect Ratio”  $D/t$  and  $k$  a constant including the modulus of elasticity and relative density of the material. Figure 3.4 shows the consequences of the Couder Law (which we will consider in depth below in connection with active supports) for the classical extrapolation of a mirror blank: a 4 m blank extrapolated, with the same aspect ratio  $A$ , to  $D = 16$  m has a mass 64 times as great, but the flexure  $W$  is nevertheless 16 times greater! If the slope of the wavefront  $dW/dy$  is taken as a measure of the effect of flexure (see Chap. 4), the 16 m blank is still 4 times more flexible. The support problem for extrapolation of conventional telescopes is therefore as intractable as the mass problem. The Russian 6 m blank would already have exceeded the reasonable extrapolation limit in an equatorially mounted telescope. This telescope also reveals a further problem of classical extrapolation: the *thermal problems* resulting from the thermal capacity which follows the mass law. If the material of the blank has significant thermal expansion, such as borosilicate glass (Pyrex), the high thermal capacity leads to expansion problems in a conventional telescope. If a quasi-zero expansion

material is used, such as glass ceramic or ULE quartz, the thermal capacity may still cause problems of *mirror seeing* through its thermal interaction with the ambient air and high thermal inertia. The key word in the solution to these problems and essentially the hinge of the revolution of modern telescope optics is *segmentation*. This can be either *direct* or *indirect*, as shown in Fig. 3.4. The weight gain from direct segmentation (“big-dish” segments) is obvious: the area is that of  $n$  segments but the thickness remains that of a single segment  $t_s$ . The flexure is also formally that of a single segment, but there is an additional adjustment and phase-holding problem which is far from trivial – see below. *Indirect* segmentation has exactly the same effect in achieving weight gain but produces a *dilute aperture* compared with the *filled aperture* of direct segmentation. Two basic solutions of indirect segmentation are possible: separate telescopes on a single mount (the MMT-type solution), or separate telescopes on independent mounts (the “array” type solution). In both cases, the beams can be combined, with or without phase, or both. Clearly from Fig. 3.4, the aperture dilution may be relatively modest for the MMT-type but is very high for the array type. However, the array type, if combination with phase is achieved, allows the possibility of interferometry over baselines an order of magnitude greater than the apertures, giving enormous spatial resolution. The aperture dilution is then the technical problem of sampling in the u-v plane well-known in radio astronomy.

The number of segments  $n$  in direct segmentation is a technical compromise, but  $n$  is usually a fairly large number (e.g.  $n = 36$  for the Keck 10 m telescope – see below). However, one proposal for the German 12 m DGT has a small value of  $n$ , using direct segmentation. With indirect segmentation, proposals have been made for arrays with many telescopes (e.g. an early proposal for the ESO VLT with  $n = 16$  for 16 telescopes of 4 m aperture constituting a 16 m in combination). However, most indirect segmentation proposals are for a low value of  $n$  of the order of 2 to 6, usually as low as possible to give the largest unit telescopes achievable with *monolithic* primaries (e.g. ESO VLT  $4 \times 8$  m, Columbus (LBT)  $2 \times 8$  m, Gemini  $2 \times 8$  m). In principle, of course, a combination of direct and indirect segmentation is possible: direct segmentation with  $n_d$  segments of  $n_i$  unit telescopes combined in an MMT or array type assembly. The beam combination of indirect segmentation always requires further reflections, causing additional efficiency losses unless super high reflectivity coatings are used.

For the normal indirect segmentation solution with a small value of  $n$  giving the largest monolithic unit telescope primaries possible, the weight and flexure problems require new technological approaches apart from the indirect segmentation: the mass of the “segments” (primaries) is reduced either by *lightweighting structures* or by using *thin, flexible blanks* whose form is directly controlled by active optics. The three key technologies for reducing weight and solving the flexure and thermal problems are shown in Table 3.3. These three technologies are the basis of the revolution in modern telescope optics.

**Table 3.3.** The three key technologies which form the basis of the revolution in modern telescope optics (weight reduction, control of flexure and thermal problems)

<i>1. Segmentation:</i>	Direct or indirect
<i>2. Lightweighted blanks:</i>	For large “segments” (monolithic mirrors) with or without active optics control
<i>3. Thin, flexible blanks:</i>	For large “segments” (monolithic mirrors) with active optics control

Hybrid solutions exist, for example separated circular segments of a spherical or aspheric primary in a diluted aperture big-dish arrangement. An example of this is the French TEMOS project. In some form or combination, all modern projects for very large telescopes fall into the essential scheme of Table 3.3. This includes fixed or semi-fixed telescope designs by which the earth’s rotation produces the field change and a large segmented primary is used – see below.

For movable telescopes, the optical design basis remains the Cassegrain telescope, either in classical or RC forms. More advanced forms are well known, such as the designs using 3 or 4 powered mirrors discussed in detail in § 3.6.5 of RTO I, which give better performance with bigger fields. But their use has remained limited by the failure to improve on simple evaporated aluminium reflecting coats (invented in 1932!) for *large* optics. This is now the most backward area of modern telescope optics: a revolution is urgently needed and may be impending as a result of the admirable development program of the Gemini project recently reported (1997) by Mountain, Gillett and Kurz [3.8]. This work on protected silver coatings promises to be one of the major technical advances in telescope technology of this century – see also Chap. 6. Dielectric multi-coats may also provide a viable solution, but their application still seems to be limited in practice to a maximum diameter of about 2 m.

## 3.2 Examples of modern projects using the technologies of Table 3.3

### 3.2.1 Direct segmentation with a filled aperture

Pioneer work took place in Italy (Bologna) in the 1950s with the work of G. Horn-d’Arturo and in Finland of Y. Väisälä [3.9]. In fact, Horn-d’Arturo was inspired by the work of Lord Rosse [3.10] [3.11], who was the first to attempt to make a segmented mirror in 1828. He made a 6-inch mirror consisting of a central disk, axially adjustable, surrounded by a ring  $1\frac{1}{2}$  inches wide. The whole mirror was then polished spherical and the central disk moved backwards to achieve best coincidence of the images from the disk and ring segments. Rosse thereby reduced the spherical aberration by 50 %.

Inspired by this idea, Horn-d'Arturo made a fixed tessellated primary consisting of 60 spherical segments of trapezoidal shape and giving a full aperture of about 1.04 m at f/10. Each segment was adjustable in depth and tilt to produce an optimum common focus. A small field was tracked over a limited time by moving a plate holder in the prime focus plane. The earth's rotation provided access to a strip of sky.

The Horn-d'Arturo concept was taken up for the *Next Generation Telescope (NGT)* project of Kitt Peak and elaborated in a more sophisticated form (the “*Rotating Shoe*”) above all by Mertz [3.12] [3.13]. It was discussed in comparison with other concepts by Barr [3.14], from whose paper Fig. 3.5 has been reproduced. In this concept, a fixed tessellated primary of strip form is scanned by a two-mirror secondary arrangement [3.12] rotating round an altitude axis, along which a third mirror sends the beam to the equivalent of a Nasmyth focus. Since the primary is *spherical*, the optical form of the telescope is of the Gregory or Cassegrain “*spherical primary*” type (see § 3.2.6.3(d) of RTO I) and suffers from massive field coma. The 2-mirror secondary arrangement is designed to correct both spherical aberration and field coma and achieves, in the form shown [3.14], a reasonable correction over 5 arcmin field diameter. The whole arrangement rotates round an azimuth axis.

The NGT became the NNTT (National New Technology Telescope) project and has still not been realised. At a later stage an MMT-type concept was favoured over the “*Rotating Shoe*” concept. The original goal was a 25 m (1000 inch) aperture which would have required a 100 m long strip primary [3.14]. Apart from the small field resulting from the spherical primary, the fact that the secondary scans different points of the primary during an observation can cause serious problems because of variable reflectivity and IR background radiation.

For these reasons, and because indirect segmentation can lead to total equivalent apertures of 15 m or more with more conventionally mounted movable primaries with active control, the “*Rotating Shoe*” has not been further pursued for very large telescopes. However, the system of Horn-d'Arturo, with the addition of an azimuth rotation and a fixed 30° tilt from the vertical to give access to a ring of sky (“*Optical Arecibo*” design), has been taken over for the 8 m Penn State Spectroscopic Survey Telescope (PSSST) of Ramsey et al. [3.15] [3.16], using a spherical primary. A 2-mirror, prime focus corrector corrects for spherical aberration and coma for a 1 arcmin diameter field, sufficient for the spectroscopic survey telescope intended. A focal plane tracking arrangement can track objects up to 1 hour. The primary consists of 85 identical 1 m diameter circular segments of spherical form (Fig. 3.6), each with 13 m focal length. It should be noted that this is a quasi-filled aperture solution, since the segments of the primary are circular. This avoids the cutting problems of hexagonal segments and the gaps are not serious for a telescope not intended for IR use. The image quality design goal is given as 1 arcsec [3.16]. The cost estimate in 1988 was \$ 6 million.

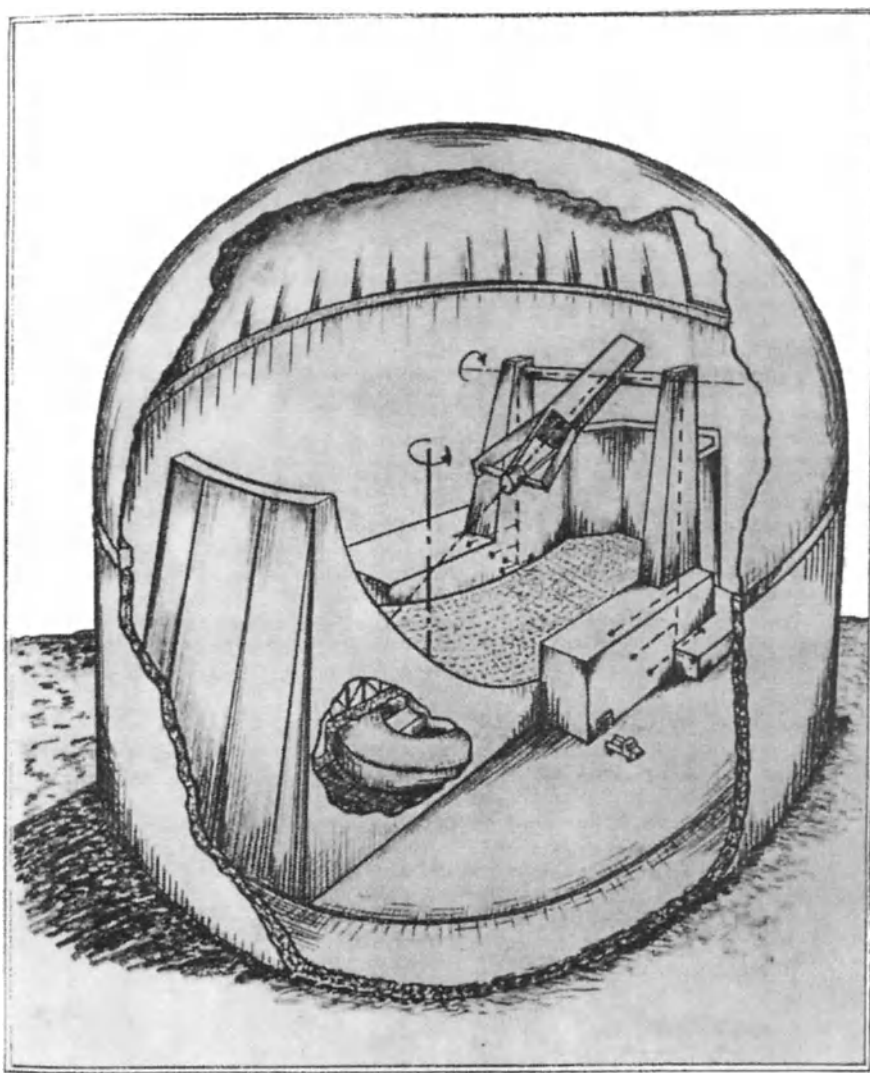


**Fig. 3.5.** The “Rotating Shoe” concept for a large telescope due to Mertz [3.12]. Figure reproduced from Barr [3.14] as a proposal for the NGT

Through the involvement of another institute (the University of Texas), the PSSST was renamed by 1988 simply the SST [3.15] and was further elaborated and discussed by Ray in 1992 [3.17], the error budget giving at the end of 1991 a total system image of 0.66 arcsec for 50 % encircled energy. Further developments were reported in 1996 by Sebring and Ramsey [3.18]. The universities of Stanford, Munich and Göttingen had joined the project which is now called the Hobby-Eberly Telescope (HET). The HET has an 11 m primary of spherical form with an aperture of 9.5 m and contains 91

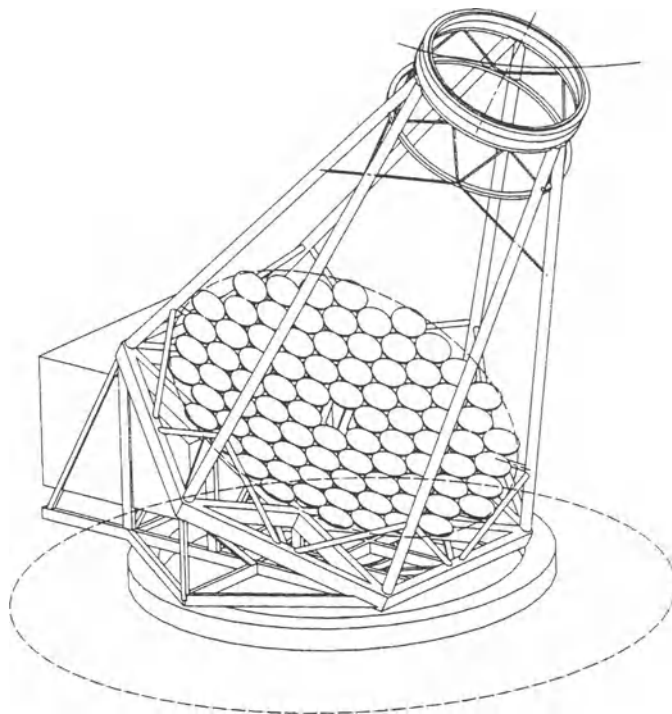


**Fig. 3.6.** The 8 m Penn State Spectroscopic Survey Telescope (PSSST) project with an “Optical Arecibo” concept using a stationary, inclined, tessellated primary with azimuth rotation (from Ramsey et al. [3.15])

*hexagonal* segments. Completion was expected in 1997 at a total cost of \$ 13.5 million. The image quality intended is quoted as 0.6 arcsec.

A further extension of the same basic concept is also reported by Bash et al. [3.19]. They propose its application to the ELT (Extremely Large Telescope) with an aperture of 25 m, utilizing a 33 m spherical primary array. This paper also gives an example of the type of corrector proposed, similar to that for the HET. Figure 3.7 reproduces this design, containing four powered, aspheric mirrors. Mirrors  $M_2$ ,  $M_3$  and  $M_4$  are conic sections, while  $M_5$  has higher order deformations from the conic. Over a 4 arcmin field, a quality of 0.5 arcsec (50 % encircled energy) is quoted for this system. Such correctors are bound to be relatively complex, even for such small angular fields, because of the huge spherical aberration of the 25 m spherical primary (ca. f/1.6) and the modest size of the corrector in comparison. For the ELT, the corrector shown in Fig. 3.7 is of the order of 4 m in diameter, less than 1/6 of the primary aperture of 25 m. But the movable corrector is still comparable in size with a classical 4 m telescope. The discrepancy in size compared with the primary aperture inevitably impairs the field correction. It is interesting to compare the ELT corrector with the optical design

of conventionally mounted 4-mirror telescopes based on a spherical primary (§ 3.6.5.3 of RTO I). In particular, the design for the 25 m Nordic Telescope, using a third mirror somewhat, but not much, larger than the ELT corrector achieves, according to Ardeberg et al., with 3 aspheric mirrors in addition to the spherical primary, a very good image quality (0.10 arcsec) over a field of more than 20 arcmin [3.20] [3.21]. The pupil position can be optimized in both conventional systems of this sort and in the ELT corrector. But the pupil position shown in Fig. 3.7, not far from the focus of the primary, inevitably leads to a major increase of diameter of the primary over its aperture, even for modest fields.

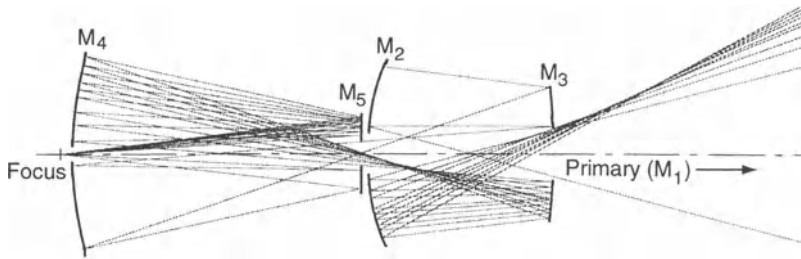


**Fig. 3.7.** A corrector design for the ELT similar to that for the HET. Mirrors  $M_2$ ,  $M_3$  and  $M_4$  are conic sections, while  $M_5$  has higher order departures from the conic (after Bash et al. [3.19])

The cost estimate of the ELT is \$ 200 million. The constant angle of the primary relative to gravity is claimed as a major opto-mechanical advantage compared with conventional telescope mounts.

The extent to which “stationary”, segmented primary concepts, with their mechanical advantage of a “gravity constant” primary, can rival current generally movable designs will also depend on the success of the latter in active figure control of directly segmented primaries and monoliths and the efficiency (and cost) of beam combination in indirect segmentation solutions.

The project for which direct segmentation has been applied in the most sophisticated form is the *Keck I 10 m telescope*, commissioned in 1993 when it became the largest functioning telescope in the world [3.22]. An account of the most important aspect of the optics of this telescope, the manufacturing techniques for the primary segments using stress polishing and ion beam polishing, was given in § 1.2.2.4 and § 1.2.2.5 above. Figure 3.8(a) shows the arrangement of the 36 hexagonal segments, made of glass ceramic “Zerodur” from Schott, of the f/1.75 lightly hyperbolic RC primary of 9.9 m aperture across the sides of the total hexagon. The side of the unit segment is 0.9 m or 1.8 m across its corners, the thickness being 7.5 cm giving an aspect ratio of 24. The segment manufacture [3.23] proved to be the most difficult aspect of the manufacture of the Keck telescope. It is much more difficult than the manufacture of a monolith for the following reasons:

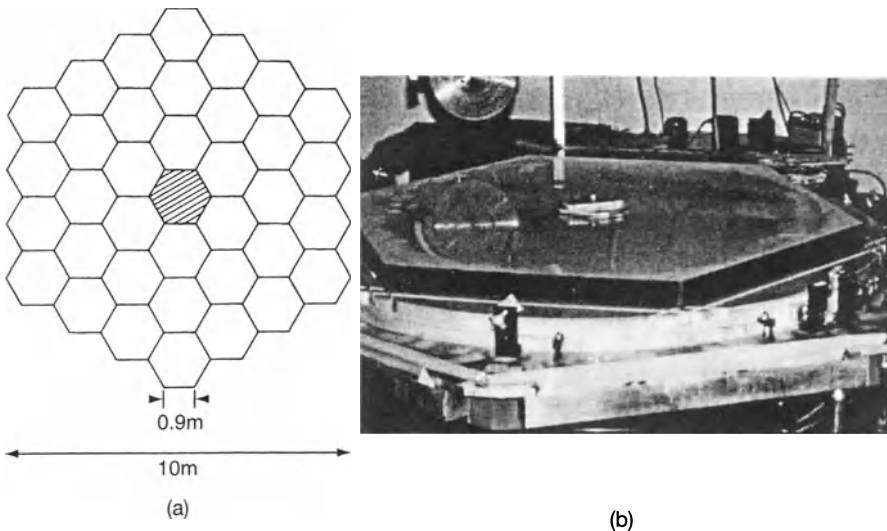


**Fig. 3.8.** Hexagonal segments (36) forming the primary mirror of the 10 m Keck telescope. (a) The complete mirror, (b) an individual segment during manufacture (figures kindly supplied by the Keck project)

- The strongly aspheric primary means that the segments are unsymmetric, the asymmetry growing with the distance from the axis, giving 5 different sorts of segment. This poses not only a manufacturing problem (see § 1.2.2.4) but also a test problem.
- The segments must have high quality right to the edge, a hard requirement which rarely obtains for monolithic mirrors, for which a manufacturing “run-out” is normally possible.
- The segments must have the same radius of curvature to a very tight tolerance. Normally, the focal length of a telescope with a monolithic mirror is relatively uncritical, although this may no longer be true for the beam combination of solutions using indirect segmentation.
- Finally, the hexagonal form arising from the packing law of nature required cutting after figuring. The stress relief proved a major problem finally solved by ion beam polishing to optimize the figure.

The cell and associated mechanics and controls for phasing the segments are extremely complex. Figure 3.9 shows this complexity.

The design of the Keck project started at the beginning of 1977. When operation started in 1993, it had taken 16 years from inception to completion, by no means an excessive time for such an ambitious concept, both in size and technical nature. The engineering phase started in 1985, implying only 8 years for realisation [3.24]. Every telescope conference since 1977 [3.25] has contained accounts of the progress of the project. It should be remembered that many aspects were laid down much earlier than for more recent projects.

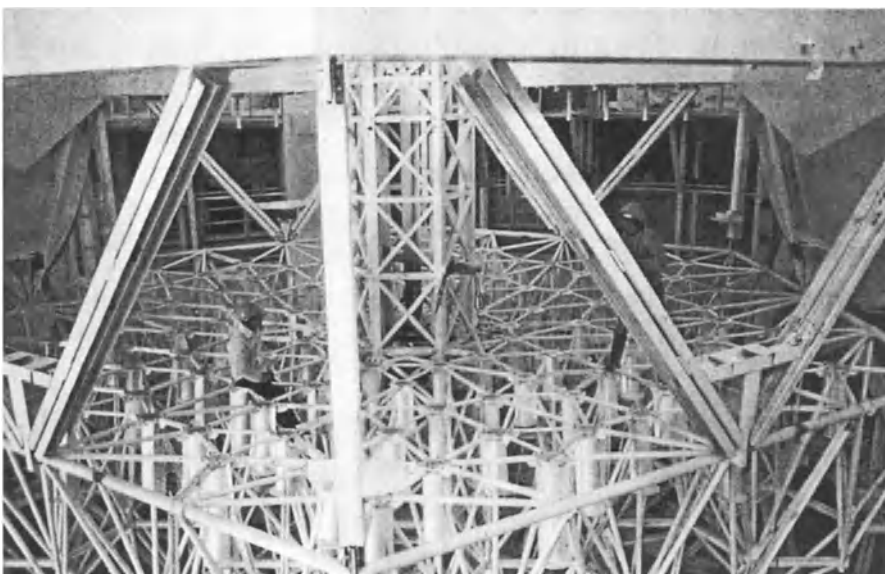


**Fig. 3.9.** The Keck 10 m telescope: the prime mirror cell and associated mechanics (figure courtesy of the Keck project)

The optical concept and realisation is above all the achievement of J. Nelson. An excellent account of the essential features was given in 1985 [3.26]. Figure 3.10 shows a model of the mechanical structure of the Keck telescope [3.23]. As far as the optics is concerned, the most complex part apart from segment production is the active position and tilt control. A complete account of this system is given in § 5 of ref. [3.26]. We shall discuss this aspect of the Keck telescope in § 3.5 on active optics control.

The last segment of the primary was inserted in April 1992 [3.24]. The PF (f/1.75) is not intended for astronomical use. The Cassegrain/Nasmyth foci have f/15, the IR Cassegrain f/25. The secondary mirror has been successfully completed [3.27] (see also § 1.3.3 on the test procedures used and results). The complete optical error budget is given in refs. [3.23] [3.24] – see also § 4.2. The latest information [3.24] gives the total optical budget as  $d_{80} = 0.42$  arcsec, of which 0.24 arcsec is budgeted for segment figuring. Using the warping harness to correct low frequency terms (see § 1.2.2.4), an average segment value of 0.44 arcsec was achieved, well outside the specification. Ion beam retouching at Kodak improved this average to 0.25 arcsec, near the specification [3.28]. The active control system seems very reliable and successful, the reliability being limited early on by the computer system (4 failures in 6 months – board replacement about 1 hour). Further details of the final work on the segment manufacture and optical quality and alignment are given by Mast and Nelson [3.28]. Dome seeing and thermal conditions appear to be favourable [3.24], but no clear quantitative evidence was then available.

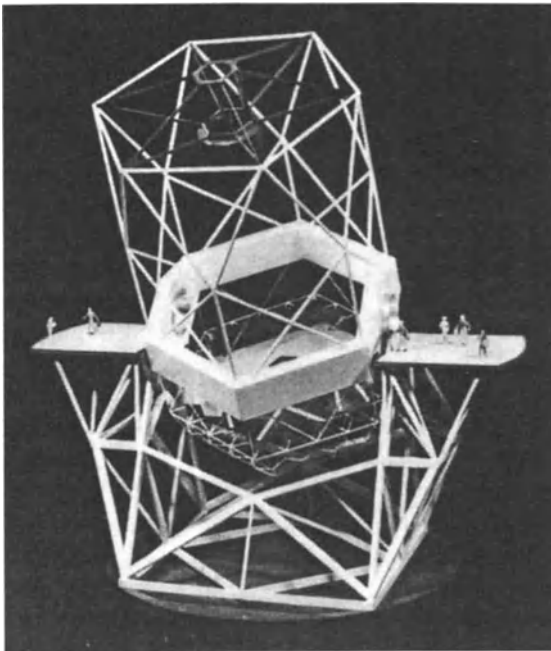


**Fig. 3.10.** The space frame structure of the Keck 10 m telescope [3.23]

The financial budget was largely held except for the primary segment fabrication. For the telescope itself (Keck I), the 1996 (actual) budget estimate is given by Smith [3.29] as \$ 93.5 million. A second Keck II telescope [3.29] was funded in 1990 with \$ 93.3 million, the project beginning in January 1991. The time planned for construction until operation was 69 months. This schedule was held and observing started in October 1996, a remarkable achievement. The actual budget in 1996 was only \$ 77.7 million, markedly more favourable than the cost projection. A number of factors contributed to this saving: technically, the most important was the reduction of segment figuring costs due to the development of ion beam figuring.

The total optical specification of  $d_{80} \leq 0.42$  arcsec of Keck I is relatively modest compared with more recent projects (see Chap. 4). But, at the time of its specification, above all bearing in mind its novel segment technology, it was a valid and even ambitious choice for such a large project. An excellent account of the technical function of Keck I over the first 2 years of operation from 1994 to 1996 has been given by Gillingham [3.22]. Figure 3.11 reproduces his analysis of the measured image quality (FWHM arcsec at 650 nm). In the best cases, when the segments of the primary were “restacked” and the secondary mirror realigned, the image quality was little inferior to the mean segment image, e.g. in January 1995 when the best segment image was FWHM 0.35 arcsec. Of course, such results implied exceptionally good atmospheric seeing. Gillingham concludes that the routine optical quality,

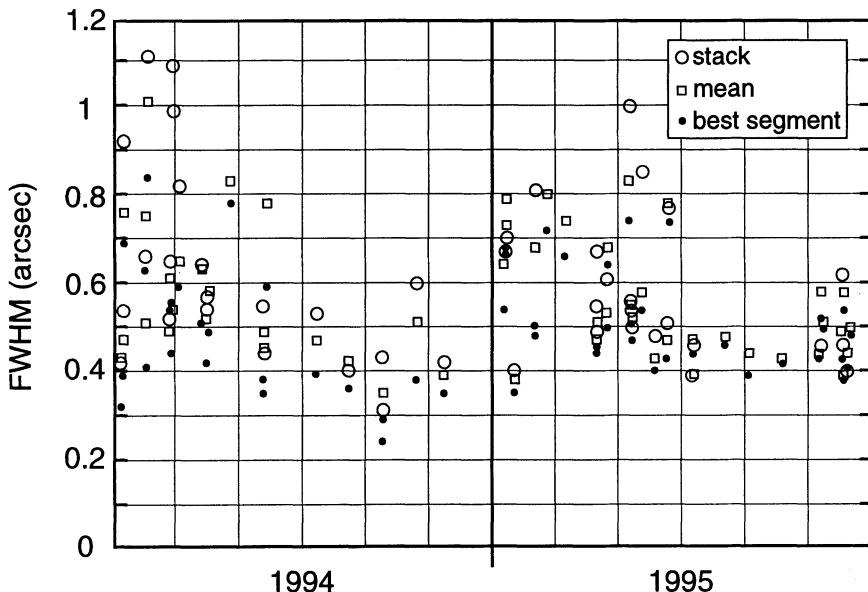


**Fig. 3.11.** Star image sizes (FWHM arcsec) for segments and for a full aperture ( $\lambda = 650$  nm). “Best” refers to the smallest of the averages for individual segments, “mean” is the average for all segments, “stack” is the combined image for all 36 segments. (After Gillingham [3.22])

although very good, still falls short of the potential of the site/telescope combination. It is hoped to improve telescope adjustment and to minimize local seeing degradation.

It is already clear from the results obtained that Keck I (Fig. 3.12) represents a milestone in the history of the telescope and astronomy and a remarkable technical and organisational achievement. Its sheer size, combined with excellent optical quality at one of the best (if not *the* best) sites on Mauna Kea, Hawaii, makes it unrivalled by other ground-based telescopes until the new generation of the 8 m-class telescopes comes into operation.

In 1988 Hügenell [3.30] published a proposal for a 20 m telescope (“Zentralachsenspiegel” or ZAS, i.e. “Central axis reflector”) of segmented primary optical concept, in principle identical to that of the Keck 10 m telescope. Extreme claims were made concerning novel manufacturing techniques and other technical features, but these were not supported by theoretical or experimental evidence or by any references. Concerning the mounting and adjustment of the 366 segments, it was stated that the principles of the Keck telescope would be taken over. The primary f/no was given as f/1.5 and the focal lengths for Cassegrain/coudé and Nasmyth foci correspond to a secondary magnification  $m_2$  of 2.33 and 2.17 respectively. Such values would give high central obstruction and require an extreme RC solution to give a reasonable field. However, there was no comment on the optical design.

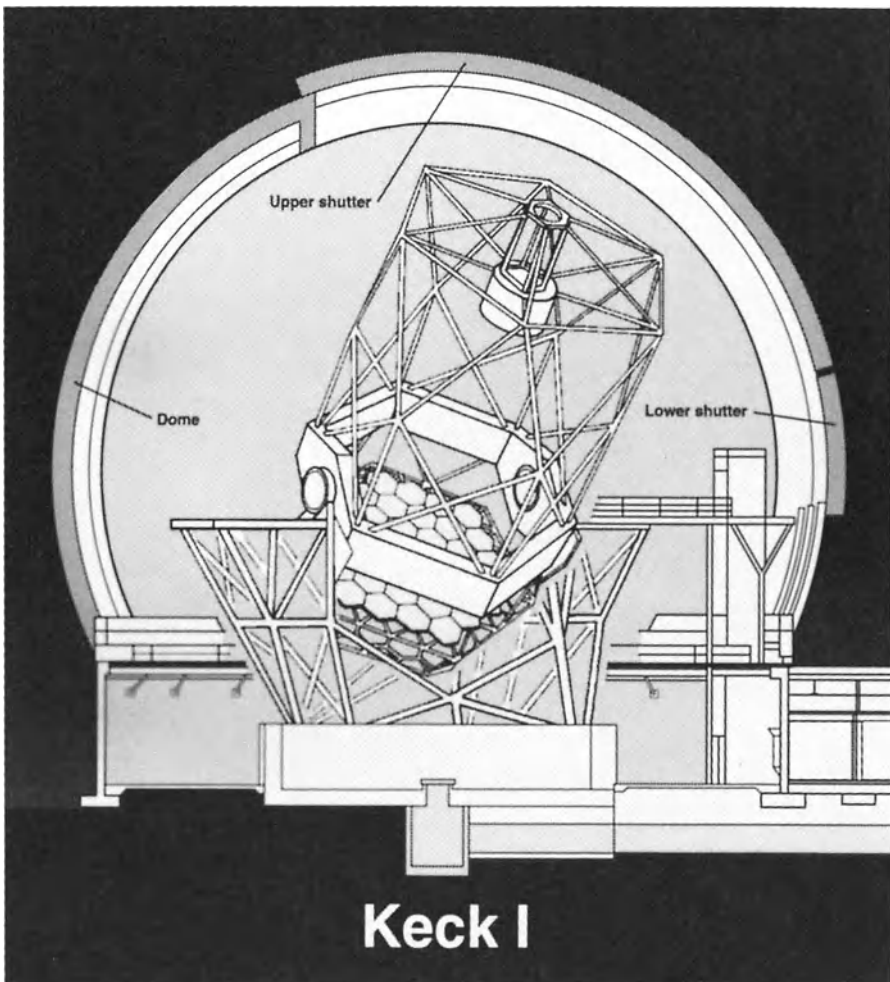


**Fig. 3.12.** Drawing of the 10 m Keck I telescope in its dome. See also the photograph on the cover of this book. (Courtesy W.M. Keck Observatory, through J. Nelson and A. Peralta)

The only comment on the optical quality specification is that “focal point tolerances of 10 nm” are achievable on the Keck basis.

A project in which primary mirror segmentation of a different sort is proposed, with only a small number of segments, is the DGT (German Large Telescope) for which an aperture of 12 m was planned [3.31]. A two half-mirror segmentation scheme was considered impracticable, but two other schemes were considered feasible (Fig. 3.13). The principal argument for limiting the number of segments is the IR background. The segmentation scheme (b) is essentially the same as one of the proposals for the NGT [3.14] due to Aikens et al. for use in large unit telescopes for MMT or array-type solutions for

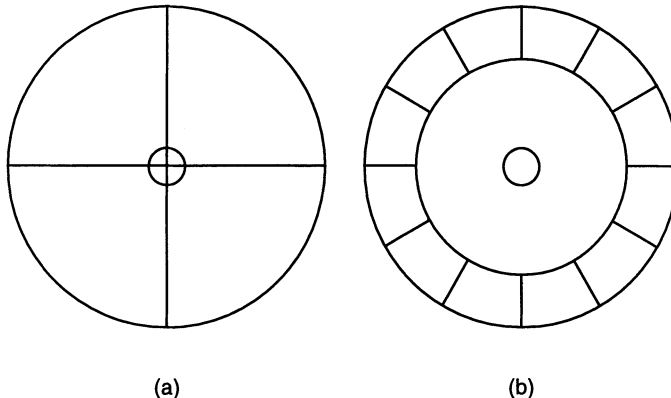


**Fig. 3.13a, b.** Proposed segmentation schemes for the DGT primary mirror (after Appenzeller [3.31])

indirect segmentation. The attraction of the scheme (b) is that the central element could be the largest monolith available with existing technology: in 1992 about 8 m. Aikens et al. [3.32] proposed a passively-supported central element with an open-loop active system adjusting the outer segments to it. This was essentially the solution adopted for the Keck 10 m telescope. Appenzeller proposed supporting the central monolith actively in the same way as the ESO NTT and VLT (see § 3.5). A further discussion on the feasibility of manufacture of such a segmented 12 m primary is given by Appenzeller et al. [3.33].

The most ambitious concept using direct segmentation of the primary was proposed by Ardeberg et al. [3.34] for a 25 m *spherical* primary, working at f/0.8 (Nordic extremely large telescope). We referred to a later version of this concept, using 4 powered mirrors, above. The optical design of such 4-mirror telescopes is discussed in § 3.6.5.3 of RTO I. In the 1992 version of the Nordic concept, the convex  $M_2$  was extremely aspheric (oblate spheroid), the concave  $M_3$  mildly aspheric and the concave  $M_4$  (also segmented) highly aspheric.  $M_1$  and  $M_4$  consisted of 141 segments. This design solution only gave a field of about 40 arcsec of good correction with a primary of f/0.8. The later concept in 1996 [3.20] [3.21] relaxes the primary to f/0.96 and has an improved design with more normal hyperbolic (to third order) forms for  $M_2$ ,  $M_3$  and  $M_4$ . The well-corrected field is now over 20 arcmin.  $M_1$  and  $M_4$  retain the number of 141 segments proposed earlier. The pupil  $M_1$  is imaged on to  $M_4$  and these two segmented mirrors are actively controlled. The segment production for the *spherical* segments of the primary (segments 2 m wide) is considered straightforward and amenable to mass production. Figure 3.14 shows the optical layout and the segmentation of the primary [3.20].

Other large segmented projects under discussion are a Russian 10 m telescope [3.35] and a Spanish 10 m telescope [3.36].

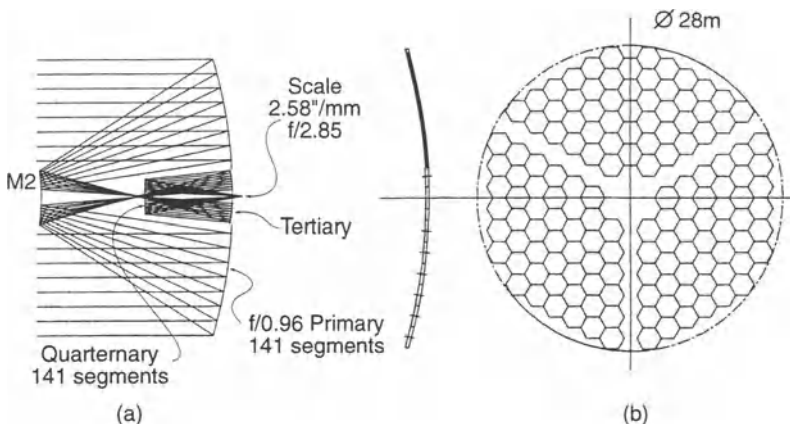


**Fig. 3.14.** Optical layout (a) and primary mirror segmentation (b) for the Nordic 25 m telescope concept [3.20]

### 3.2.2 Separate telescopes with monolithic primaries on a single mount (MMT-type indirect segmentation)

The progenitor of all such designs was the original Multi-Mirror-Telescope (MMT) which was inaugurated in 1979. It was not only epoch-making in being the first major telescope to depart from the classical optical monolith conception, but also used an alt-az mount in a revolutionary square building which rotated synchronously with the telescope (Fig. 3.15). The six 1.8 m unit telescopes working at f/2.7 were arranged around a 0.75 m central guide telescope and the 6 images were combined in a central collecting unit. The equivalent aperture was 4.4 m.

Soon after its completion, a review of the performance and technical aspects of the MMT was given by Beckers and Williams [3.37]. An account of the image optimization and stabilization was given by Reed [3.38]. The beam combination and stabilization arrangement is shown in Figs. 3.16 and 3.17, taken from Reed's paper. The system envisaged utilised a laser-generated marginal ray measurement technique to give simultaneous alignment and focus information for each of the 6 telescopes. This was intended to control the position of each image relative to the other 5 images. Figure 3.16 shows a pair of telescopes. On the left-hand telescope is shown the light path through the telescope to a 6-faced beam combiner. The right-hand telescope shows the optical path of the laser beams for aligning the telescopes.

The individual telescopes did not have very high quality, about 0.6 to 0.7 arcsec [3.39]. Nevertheless, Beckers and Williams [3.37] reported that it was possible to use pairs of the 6 telescopes at optical and IR ( $5\text{ }\mu\text{m}$ ) wavelengths in a coherent way so as to cause interference, giving a resolution corresponding to a 7 m telescope. This was only possible at one point of the field because of the tilts of the 6 image planes – see Fig. 3.16. My under-

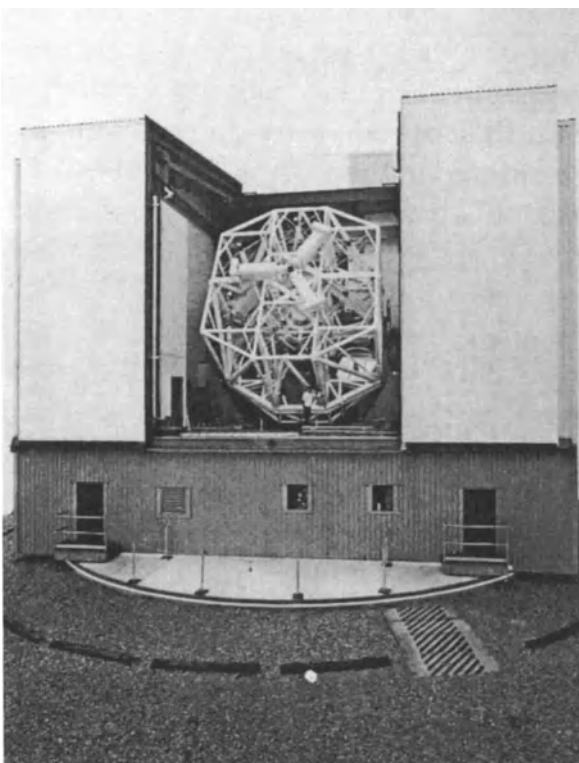


**Fig. 3.15.** The 4.4 m equivalent MMT with its synchronously rotating building

standing is that the complex open-loop laser active alignment system was later abandoned in favour of the much simpler and more direct closed-loop active approach of correction for the individual images of a star. We shall return to this matter in § 3.5.

Notable as it was as the first large telescope using indirect segmentation, it is my view that the most important optical advance of the MMT was not the telescope itself but its *enclosure* (Fig. 3.15). This represented a radical break from the large and expensive dome of conventional telescopes and exploited logically the symmetry advantages of the alt-az mount. The MMT enclosure was the progenitor of the ESO NTT building and others: it initiated the “natural ventilation” concept.

An excellent and complete account of the MMT in all its aspects was given by Beckers et al. in 1981 [3.40]. In spite of its potential, the decision was taken in 1987 to abandon the MMT concept because of its diluted aperture and replace the six telescopes by a single primary of lightweight construction. To have the same tube length, this 6.5 m monolithic primary must work at about  $f/1.25$ . An account of this conversion was given by Chaffee [3.41]. Two secondaries of  $f/5.27$  and  $f/15$  were intended. First light was planned for late 1994. A more recent account of this project is given by West et al.

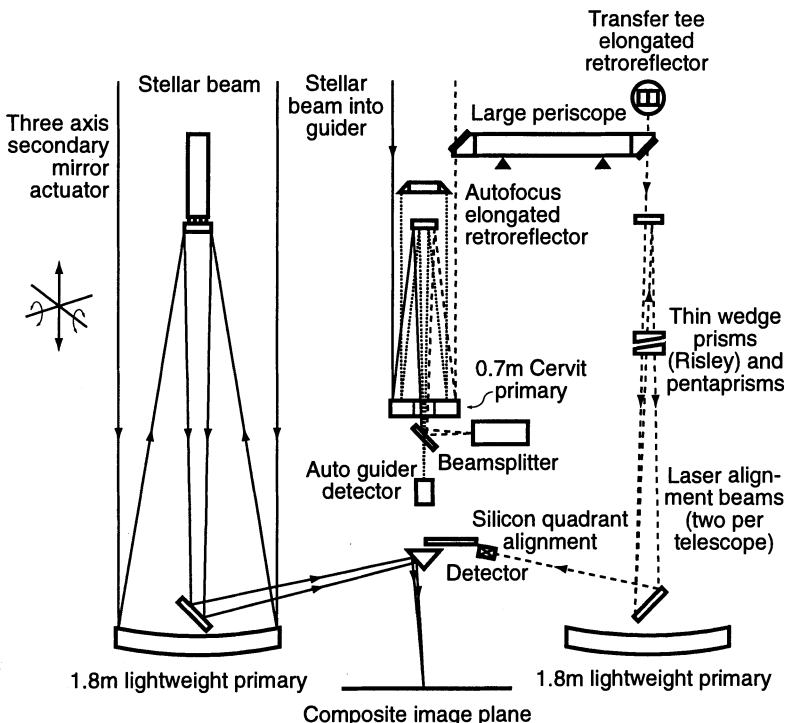


**Fig. 3.16.** MMT: Alignment system optical paths (from Reed [3.38])

[3.42]. The conversion to a monolithic primary more than doubles the light-gathering power and enables, by suitable design, an increase of the angular field of view by a factor of 15. Three secondaries give five observing foci: a)  $f/9$  with a field of 13 arcmin, b)  $f/5.25$  with a field of 5 arcmin, c)  $f/5.4$  with a field of 60 arcmin, d)  $f/15$  (fixed/chopping) with a field of 20 arcmin, e)  $f/15$  (fully adaptive). The large field of view at  $f/5.4$  is made possible by a refractive corrector designed by Epps. Minor modifications to the building were necessary, but the total conversion budget is only \$20 million. First light is now planned for 1998.

In spite of its abandonment for quite rational astronomical and technical reasons, the basic concept of indirect segmentation in this way remains perfectly valid. However, its normal application will be to diluted apertures *larger* than feasible monolithic primaries. For the original MMT, this was no longer the case.

An interesting MMT-type variant was the TEMOS concept of Baranne and Lemaître [3.43] [3.44], discussed in § 3.2.6.3 (d) and § 3.6.5.3 of RTO I. The primaries of the unit telescopes are then round segments of a much larger *spherical* primary and use a common secondary. As illustrated in RTO I, the addition of two more powered mirrors gives excellent compact solutions with large well-corrected fields. However, this form of “dilute” segmentation

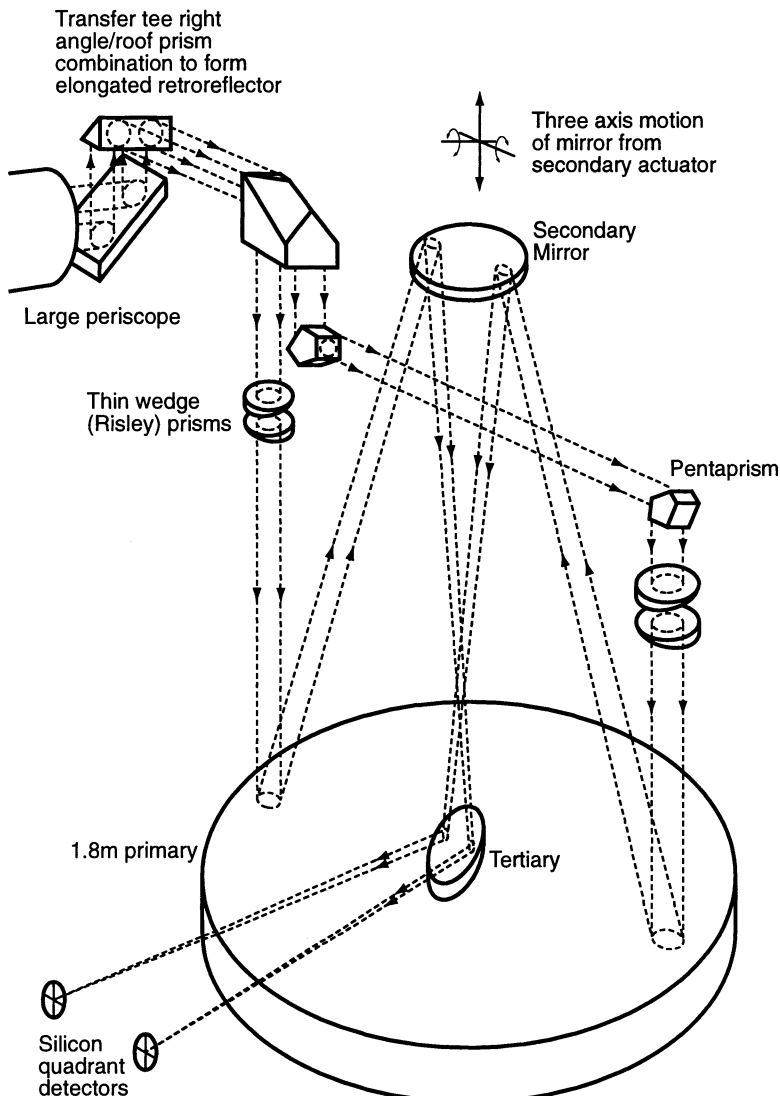
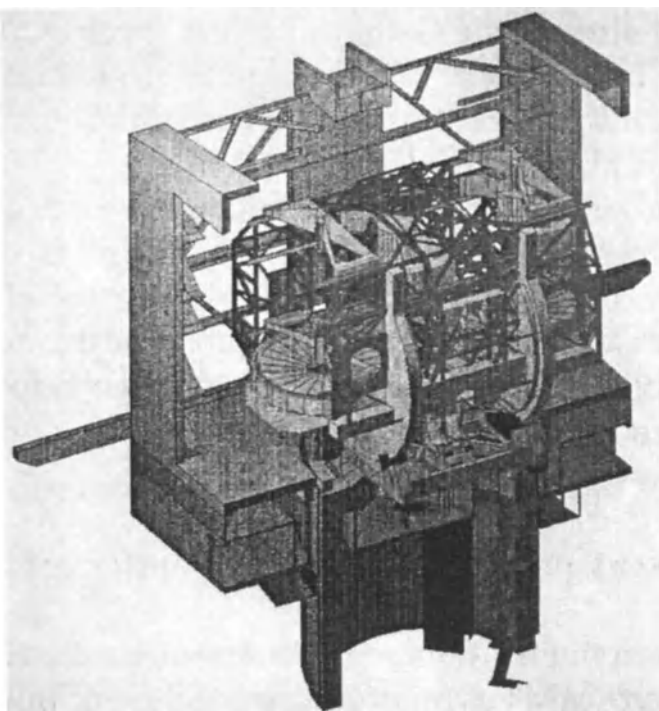


Fig. 3.17. MMT: Laser alignment beam optical paths (from Reed [3.38])

would have to compete with the more efficient “direct” segmentation using hexagonal segments, such as that of Ardeberg et al. [3.20] discussed above.

The largest MMT-type project is *Columbus*, recently renamed the *Large Binocular Telescope* (LBT), with two 8 m-class telescopes on a single mount (Fig. 3.18). The initial Columbus proposals (1985) were described by Strittmatter in 1988 [3.45]. The 8 m primaries were very steep ( $f/1.2$ ) lightweighted monoliths. A cost-performance analysis validated the MMT-type choice with 2 telescopes. With co-phasing, the maximum angular resolution, assuming progress in adaptive optics, was planned to correspond to a 22 m baseline.



**Fig. 3.18.** The Columbus project: 2 × 8 m MMT-type (recently renamed the Large Binocular Telescope (LBT))

An update report was given by Salinari in 1992 [3.46]. The clear aperture had been increased to 8.4 m, steepening the primaries to f/1.142. The image quality goal was 0.22 arcsec FWHM, the specification being in terms of  $r_0$ , the Fried parameter (see Chaps. 4 and 5). A notable optical feature was that aluminizing (and prime mirror cleaning) was to be performed *on the telescope without dismounting the primary*. The enclosure concept was a further extreme development from the MMT concept: it was open at the top, front, back and sides. Overpressure at the top forces the wind downwards to give optimum ventilation. The projected budget in 1989 was \$ 60 million.

A recent account of this (renamed) Large Binocular Telescope (LBT) project was given in 1996 by Hill [3.47]. The previously defined (parabolic) primaries and budget are retained. The baseline optical configuration of the LBT includes wide-field Cassegrain secondaries with optical foci above the primaries to provide a corrected 60 arcmin field at f/4, using 3-element refractive correctors. Undersize Gregory secondaries for an f/15 IR focus can be combined with folded beams in a joint interferometric focus. The Gregory secondaries are intended to give maximum flexibility for adaptive optics. Some instruments can also use the f/15 Gregory foci directly behind the primaries. Figure 3.19 gives a 3-D impression of the geometry of the LBT.

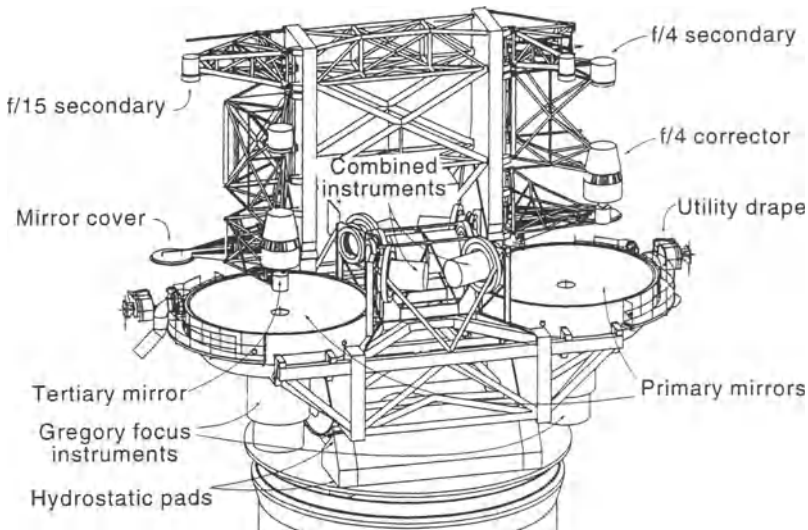


**Fig. 3.19.** The latest Large Binocular Telescope (LBT) design. Drawing by ADS Italia [3.47]

First light with a single optical train is scheduled for the year 2001. Binocular operation should start one or two years later.

A project which is a hybrid between an MMT concept and a directly segmented strip mirror concept such as the “Rotating Shoe” above, is a recent Chinese proposal for a spectroscopic survey telescope [3.48]. A strip-form primary has an aperture 4 m wide and 12.4 m long and is of spherical form. It is scanned by 4 tracking frames which scan different parts of the mirror, as the secondary unit does in the “Rotating Shoe”, so that the 12.4 m strip mirror is the equivalent of four 4 m telescopes, all mounted on a single horizontal axis in E-W direction. The directly segmented primary consists of 94 spherical mirrors of circular form, each of 0.75 m diameter. A field of  $3.58^\circ \times 3.58^\circ$  is achieved by four  $1\text{ m} \times 1\text{ m}$  plates on the tracking frame performing the tracking motion, each having about 600 fibres and 20 mm diameter correctors.

An elegant further development for wide field spectroscopic observation, under the project name LAMOST, has been published by Wang et al. [3.49]. It is essentially a fixed Schmidt telescope with a coelostat feed, this feed being combined with a *reflecting* Schmidt plate corrector. The clear aperture is 4 m which, as the authors point out, will make it easily the largest Schmidt telescope in the world. Both the spherical mirror and the reflecting Schmidt plate are built up of 37 and 24 hexagonal segments respectively. The spherical mirror works at  $f/5$  and the system has a field of  $5^\circ$  diameter. Figure 3.20 shows an overview of LAMOST.

The reflecting corrector plate has an alt-az mount and the spherical mirror axis is inclined at  $25^\circ$  to the horizontal. The observable sky area is defined by  $-10^\circ \leq \delta \leq +90^\circ$  and objects can be tracked for 1.5 hours as they pass

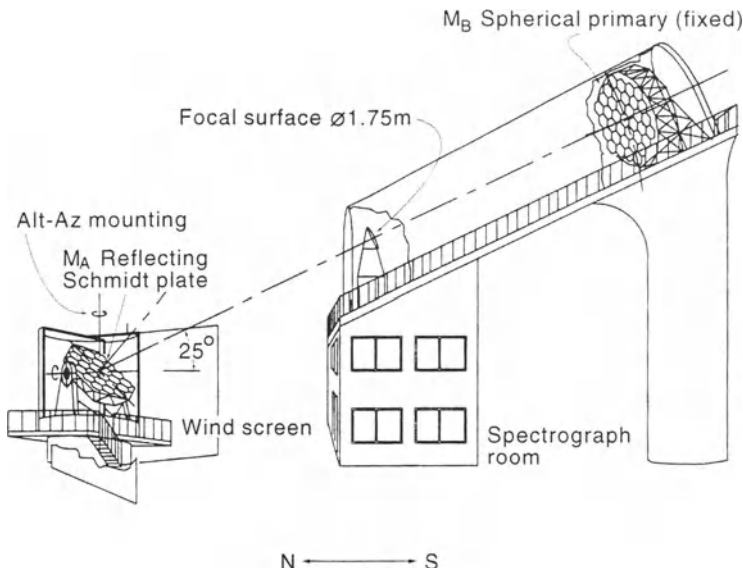


**Fig. 3.20.** Overview of the Chinese LAMOST telescope [3.49]

through the meridian. Because of the variable inclination (cosine effect) to the system axis, the corrector shape must also be variable. The authors give the formula for the depth correction in terms of the corrector coordinates and the incidence angle of the field center point. It is proposed to achieve this variable correction by active optics control. The simulated image quality (spot-diagrams) in the field is best in the region  $-10^\circ \leq \delta \leq 0^\circ$  (well within 1 arcsec) and deteriorates at large  $\delta$ -values (about 2 arcsec at the field edge for  $\delta = +60^\circ$ ).

### 3.2.3 Other large telescope projects using lightweighted monolithic blanks

Apart from the 6.5 m f/1.25 lightweighted blank for the MMT-upgrade and the two 8.4 m, f/1.14 blanks for the LBT (Columbus) (see § 3.2.2 above), the lightweighted blank production shop of Angel [3.50] [3.51] received an order for a further 6.5 m blank for the *Magellan project* of the Carnegie Institute to be set up near their site Las Campanas in Chile [3.52]. Notable optical features of this design are a support system with designed-in damping at high frequencies, an important issue we shall return to in § 3.5, and an enclosure concept with ventilation openings near the base, a concept very successfully pioneered by the 2.5 m Nordic Optical Telescope (NOT). The budget was given as \$31.4 million without instrumentation and the completion date as (hopefully) 1997. The project is technically closely linked to the MMT-upgrade. A more recent account is given by Johns [3.53]. The optical configuration has some common features (e.g. use of Gregory as well

as Cassegrain secondaries) with the LBT. Commissioning of Magellan 1 is scheduled for 1998.

An account of lightweighted blank production at the Mirror Lab. facility developed by J.R.P. Angel at the University of Arizona is given in § 3.3.4 below.

Another possible candidate for two 8 m lightweighted blanks was the *Gemini 2 × 8 m project*. A decision on whether to choose lightweighted blanks from Angel or thin meniscus blanks from Schott or Corning (see § 3.2.4) was scheduled to be taken about June 1992 [3.54]. Further details of the project were given by Osmer [3.55]. The decision finally taken on the primary blanks was in favour of the *thin meniscus* solution, as in the ESO VLT and Japanese Subaru projects. The dimensions of the Gemini primaries are given Huang [3.56] as 8.1 m diameter and 200 mm thick. Thin meniscus blank production is treated in § 3.3.2 and § 3.3.3. The project is international with the financial participations US = 50%; UK = 25%; Canada = 15%; Chile, Argentina, Brazil = 10%. One telescope is intended for Mauna Kea (Hawaii), the other for Cerro Pachon (Chile), so all-sky coverage is available. Low IR emissivity is a high priority, 2–4% background. The 8 m primaries will work at f/1.8 with a central hole of 1.2 m. A wide-field focus station at f/6 is planned for  $\lambda = 0.3\text{--}2.2 \mu\text{m}$  and an IR focus at f/16 with a 3.5 arcmin field for  $\lambda = 1\text{--}30 \mu\text{m}$ . The telescope image quality goal is 0.25 arcsec FWHM. For Gemini 1, “first light” is scheduled for 1998, for Gemini 2 for 2000. Since the decision to use thin menisci for the primaries, the Gemini project now belongs in type in § 3.2.4: but it is treated here for comparison of its general characteristics with the other large American projects. A recent report was given by Mountain et al. [3.8]. Apart from the pioneer work on silver coatings referred to in § 3.1 above, the Gemini project is also notable for some of the most advanced concepts on image quality and wind-buffetting [3.56] and thermal control, aspects dealt with in § 3.6 below.

Although not a modern telescope from the point of view of the epoch of its conception and manufacture, the 2.4 m *Hubble Space Telescope* (HST) must logically be included in this section, because of the highly lightweighted nature of its primary. A general account of the HST project was given by O’Dell [3.57]. The optical system was defined as a conventional RC with f/24 and a primary of f/2.3. The material of the primary blank is Corning ULE quartz (see below and § 3.3.3).

In the summer of 1990, about two months after launch, came the revelation that the image quality was degraded by a large amount of third order spherical aberration arising from “matching error”. The possible correction of this error in terms of the general theory of aspheric plates was dealt with in § 3.4 of RTO I, while its origins in null-systems error were discussed in § 1.3.4 and § 1.3.5. It is difficult now to recapture the euphoric atmosphere leading up to, and accompanying the launch of the HST after delays of 7 years beyond the original launch date and an overrun of its original cost estimate by a factor of 4 or 5, the official cost figure at the time (1990) being \$ 1600 million

[3.58]. A typical comment of many, on the eve of launch, was: “Stated briefly, Space Telescope allows astronomers to see the universe with some 10 times finer resolution and with 50 times greater sensitivity” [3.59]. This sentence shows the danger of using the present tense about characteristics which can only be proven in the future. It is the very common confusion in all optical telescope history between a *specification* (an intention, an aim, a hope) and a proven, quantitatively measured *performance result*.

In fact, an immense amount of careful and admirable technical work went into the HST optics. An excellent account of the specification and performance expectations was given by Schroeder [3.60]. The nominal optical parameters as an RC telescope are [3.60] [3.61]:

$$\begin{aligned} D_1 &= 2400 \text{ mm} & r_1 &= 11040 \text{ mm (f/2.300)} & b_{s_1} &= -1.0022985 \\ D_2 &= 310 \text{ mm} & r_2 &= 1358 \text{ mm} & b_{s_2} &= -1.49686 \\ m_2 &= -10.435 & b &= 1500.1 \text{ mm (see Fig. 2.12 of RTO I)} \\ f' &= 57601.2 \text{ mm (f/24.000)} \end{aligned}$$

From an optical design point of view, the HST is therefore a conventional Ritchey-Chrétien design, except that the secondary magnification  $m_2$  is higher than is usual in a ground-based telescope for a focus used for direct imaging. The new technology aspect of the optics was the extreme lightweighted “egg-crate” primary (Fig. 3.21) made in fused quartz (ULE) by Corning. This had the virtue of being extremely rigid for its weight, but this advantage turned sour later when the mirror was found to be much too stiff to be corrected actively: in other words, the dynamic range was inadequate to correct the large spherical aberration (see § 3.5).

The basic quality specification of the HST as given by Schroeder [3.60] was a wavefront error  $\leq \lambda/21$  rms at  $\lambda = 633$  nm combined with an rms pointing error  $\leq 0.007$  arcsec. Schroeder gives the predicted point spread functions (PSF) for  $\lambda = 1000, 633, 450$  and  $350$  nm. He also gives the predicted optical transfer functions in various forms, encircled energies as well as the Strehl Intensity Ratio and FWHM as functions of wavelength. These latter two functions are reproduced in Fig. 3.22. This shows that the Strehl Ratio was predicted to be about 0.8, the normal diffraction limit, for the test wavelength  $\lambda = 633$  nm. The corresponding FWHM hardly exceeds that of a perfect telescope and is about 0.055 arcsec for that wavelength and about 0.046 arcsec for  $\lambda = 500$  nm. Such a value, if it had been achieved without background smearing due to the spherical aberration, would have been about seven times better than the “First Light” images of the groundbased NTT (FWHM = 0.33 arcsec – see § 3.2.4 below) and would have justified the sentence quoted above from Chaisson and Villard [3.59].

Schroeder [3.60] also gives the predicted encircled energy concentrations for various wavelengths, corresponding to the same quality specification as that for Fig. 3.22. These are shown in Fig. 3.23, reproduced from Schroeder. Note that  $\alpha$  in his notation is the *radius* of the PSF in arcsec, but it is *not* equal to half the image diameters, such as  $d_{80}$  for the diameter containing

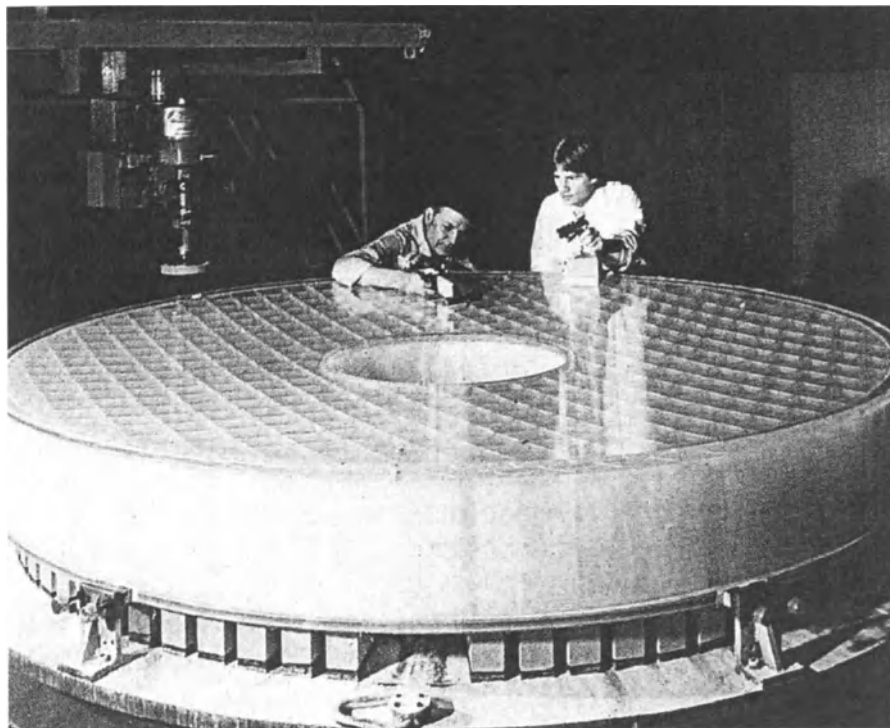


**Fig. 3.21.** The Hubble Space Telescope (HST): the primary mirror during polishing. The fine “egg-crate” structure of the fused quartz blank is clearly visible. Reproduced from Hecht [3.62]

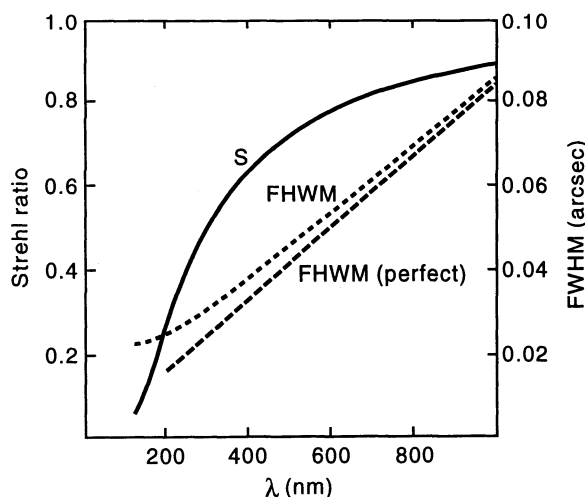


**Fig. 3.22.** The Hubble Space Telescope (HST): predicted Strehl Intensity Ratio and FWHM corresponding to the specification  $W \leq \lambda/21$  rms at  $\lambda = 633$  nm and rms pointing error  $\leq 0.007$  arcsec (reproduced from Schroeder [3.60])

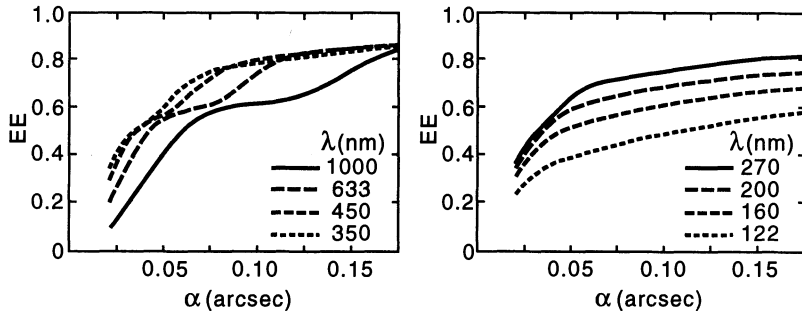


**Fig. 3.23.** The Hubble Space Telescope (HST): predicted encircled energy concentrations in two wavelength bands for the same quality specification as in Fig. 3.22. Note that  $\alpha$  is the *radius* of the PSF in the Schroeder notation. (Reproduced from Schroeder [3.60])

80 % of the geometrical energy, more usually quoted for ground-based telescopes. This is because diffraction must be taken into account for the HST, since it had a diffraction-limited quality specification. The asymptotic trend of the curves for  $\lambda = 633, 450$  and  $350$  nm to the value 0.8 corresponds simply to flattening of the equivalent function for a perfect telescope due to the first diffraction minimum (see Fig. 3.104 of RTO I).

Apart from the plethora of popular and semi-popular articles on the spherical aberration error of the HST, it was carefully measured and analysed by a major effort of the astronomical and NASA community concerned. According to the report of the Allen Committee [3.61] [3.63] [3.64] appointed to investigate the origin of the error, it can be explained both in amount and sign by an axial spacing error of about +1.3 mm in the separation of the second mirror  $N_2$  and the field lens  $F$  (see Fig. 1.61) of the reflecting Offner-type compensator used to test the primary, which was revealed by the Committee's investigations. A cross-check with a simpler refracting Offner compensator was performed, which in fact revealed the discrepancy. However, the results of the reflecting compensator (which was more accurate for higher order compensation) were taken to be correct and the cross-check discrepancy was ignored. It has been stated – and I believe this is a truism – that this was the most costly error in the entire history of optics!

The nature, amount and significance of the spherical aberration error and all known possibilities of correction or compensation were analysed in detail by the HST Strategy Panel [3.65]. A summary of the conclusions was given in the ST-ECF Newsletter [3.66]. It was concluded that the measured spherical aberration can be fully explained by the error on the primary. The magnitude of the measured error in the Cassegrain focus of the HST was known to 10 % or better and corresponded to a longitudinal spherical aberration of about 40 mm. The equivalent wavefront aberration (see § 3.3.1 of RTO I) was 4350 nm ptv and the angular aberration corresponding to 100 % of the geometrical energy at the Gaussian (paraxial) focus was 5.98 arcsec diameter

or 1.50 arcsec diameter at best focus ( $d_{100}$ ). The change of the Schwarzschild constant of the primary from its nominal value  $b_{s1,RC} = -1.002299$  to the actual value  $b_{s1,A} = -1.01359$  producing the above error amounts to an error in aspherizing from the sphere of 1.13%: a large error. The analysis of correction possibilities in terms of aspheric plates was dealt with briefly in § 3.4 of RTO I and is given in refs. [3.65] [3.66]. There are three basic reasons why the correction of the spherical aberration of the HST in orbit was difficult:

- The enormous wavelength bandpass extending into the far UV. This severely limits the choice of refracting materials available and gives chromatic problems, thus favouring a reflecting solution.
- The high magnification  $m_2$  of the secondary in the HST (-10.435). This complicates the correction due to the field aberrations introduced.
- Assuming the spherical aberration is virtually entirely induced by an error in the primary (pupil), this has advantages in that no field coma is produced in the uncorrected state; but it is unfavourable for most correction solutions because the plane of the primary is not accessible.

The conclusion of the Strategy Panel was that the best solution, taking full account of the logistic problems in orbit, was COSTAR (Corrective Optics Space Telescope Axial Replacement) [3.65] [3.66]. The COSTAR solution does not attempt a general correction of the HST field: it supplies a corrector on the axis of each instrument, which much simplifies the field correction requirements. Because of the chromatic problems of refracting elements, a two-mirror corrector solution proposed by Bottema [3.65] was adopted, shown schematically in Fig. 3.24. One instrument was abandoned (the High Speed Photometer – HSP) and replaced by COSTAR, a deployable “tree” of 2-mirror correctors for the instruments FOS, GHRS and the f/96 and f/48 optical trains of the FOC. The direct imaging camera WFPC II included a correction in its own optical system. The production schedule of COSTAR was tight for an intended launch at the end of 1993. A delay beyond mid-1994 would have involved a review of the whole instrument programme.

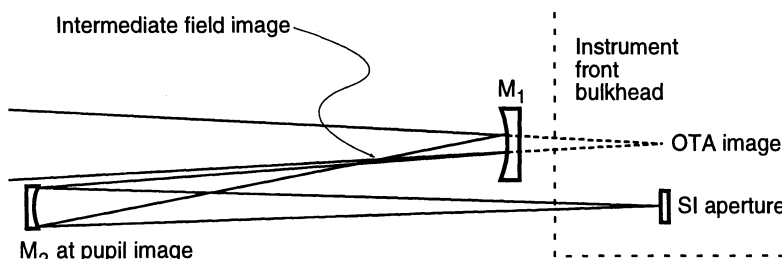


**Fig. 3.24.** The Hubble Space Telescope (HST): COSTAR solution for the correction of the spherical aberration error (from Benvenuti and Wilson [3.66])

Meanwhile, without correction, high resolution work was still possible by eliminating the “wings” of the spherical aberration PSF [3.61] by image processing. The nominal FWHM (Fig. 3.22) was largely retained because of the steepness of the spherical aberration function, but the amount of light contained in this core image was only about 15 %: in other words, at high resolution the HST was reduced from a 2.4 m telescope to an effective aperture of about 0.93 m. Allowing for losses, it was predicted that COSTAR would restore the effective aperture of the HST for high resolution from 15 % to over 80 % (and possibly over 90 %) of its real aperture. If this could be achieved, the HST might yet restore its tarnished public image and justify its high cost by spectacular astronomical discoveries.

The repair mission, including the “optical repair” of the spherical aberration error by the replacement of the Wide Field Planetary Camera WFPC I by WFPC II and the insertion of COSTAR for the other instruments, was performed in December 1993 with total success. Already in January 1994 it was clear that the specified optical quality had effectively been restored, though

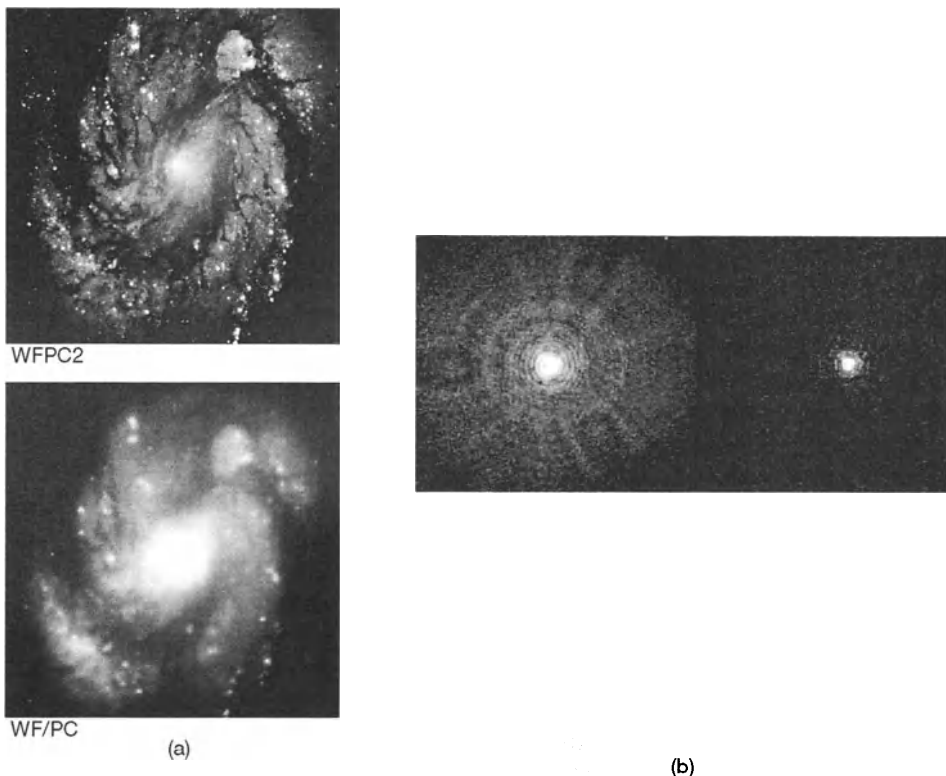


**Fig. 3.25.** Images before and after the repair mission of the HST: (a) The galaxy M 100 with WFPC II compared with WFPC I; (b) A highly magnified star image with the FOC before and after the addition of COSTAR. (Courtesy Fischer and Duerbeck [3.67])

the addition of the two COSTAR mirrors inevitably absorbs some light. An excellent account of the whole story, with superb photographs, is given by Fischer and Duerbeck [3.67]. Figure 3.25, reproduced from that work, shows the dramatic improvement in image quality. Figure 3.25(a) compares the images of the galaxy M 100 recorded with WFPC II compared with WFPC I; while Fig. 3.25(b) shows a highly magnified star image taken with the FOC before and after the addition of COSTAR.

In the last  $3\frac{1}{2}$  years since the successful repair mission, the HST has been converted from a public debacle to a public and astronomical triumph. Epoch-making results have emerged making the HST, together with the ground-based 10 m Keck telescope for spectroscopy, the most powerful astronomical tools in existence (1997).

### **3.2.4 Projects with thin-meniscus flexible primaries, controlled actively, or of stiff composites**

This is the third of the three key technologies of Table 3.3 for achieving very large telescopes using indirect segmentation (Fig. 3.4). As we saw above, direct segmentation normally uses segments which are sufficiently small to be considered as rigid mirrors with negligible flexure if carefully supported: the active control is then limited to the relative height and tilt of the segments. With large monolith primaries forming large indirect “segments”, general active optics control is essential if weight reduction is to be achieved by using thin, solid blanks. An example of such indirect segmentation, where the size of the monolithic telescopes is pushed to the currently accepted limit, is the *ESO VLT* ( $4 \times 8$  m telescopes in an array, using thin meniscus primaries). The other projects with unit telescopes of similar size are *Gemini* ( $2 \times 8$  m separate telescopes – the decision on whether to use thin meniscus or lightweighted primary blanks was taken in favour of thin menisci in 1992 – see § 3.2.3 above) and the Japanese *Subaru* (JNLT) consisting of  $1 \times 8.2$  m with a thin meniscus primary. As with lightweighting technology, thin meniscus technology is fully applicable up to the maximum diameter currently considered practicable (about 8 m) for monolithic telescopes before segmentation in some form becomes essential. Thin meniscus technology shares with lightweighting technology the advantage over direct segmentation solutions that the IR background is inherently better.

Active optics control will be dealt with in detail in § 3.5. As we shall see, various aspects of active control existed in other projects conceived in the 1970s, notably the MMT and the Keck 10 m telescopes. But the first fully active telescope, optimizing the image quality in a consistent scheme from manufacture to its operational function, was the ESO 3.5 m *New Technology Telescope (NTT)*, which had “First Light” in 1989.

The NTT, an alt-az mounted telescope, envisaged originally three areas of technological innovation concerned with the optics or optical quality:

- A complete scheme of active optics control of the image quality
- A rotating building based on the concept of the MMT building, but modified to give improved natural ventilation
- A metal (aluminium) primary mirror, as well as a conventional one in glass ceramic (Zerodur from Schott), to profit from the high thermal conductivity

The first aspect (active optics) will be dealt with in detail in § 3.5, the second in § 3.6. The third, to be discussed in § 3.3, was finally abandoned in the NTT purely for organisational and financial reasons: in 1984–1985 we were completely confident that the competitive manufacture of the aluminium blank was technically feasible and that the optical working presented no special problems. Valid offers for all aspects of the work were available. The great attraction of an aluminium blank in the NTT was that any form deformation through “warping”, previously fatal in conventional “passive” telescopes, could be easily corrected by active optics (§ 3.5). Because the density and other mechanical properties are quite similar to those of glass, the support system for the glass mirror could have been taken over unchanged except for minor adjustment for the total weight.

From the point of view of optical design, the NTT is a 3.5 m RC telescope with an  $f/2.2$  primary (considered quite steep at the time of its layout in 1981) with two identical Nasmyth foci of  $f/11$  ( $m_2 = -5.0$ ). To simplify the tube structure and reduce weight and length, prime, Cassegrain and coudé foci were rejected. The primary would have been made thinner (aspect ratio  $A = 18$ ) from the active optics concept; but the management of ESO insisted (understandably in an unproven new concept) that the NTT should have conventional optical quality (like the ESO 3.6 m telescope) also in the *passive* mode, without active correction. This dictated the limit of  $A = 15$ , which would be thicker than necessary today. A general description of the NTT is given by Tarenghi and Wilson [3.68]. The budget of DM 24 million, provided by the entry of Italy and Switzerland into ESO in 1982, was not fully used. This was much less than half the cost of the conventional ESO 3.6 m telescope of similar size, although the optical quality of the NTT is far higher (see § 3.5 and Chap. 4).

Because of the modal system of active correction, certain manufacturing tolerances, e.g. astigmatism and spherical aberration, could be relaxed. The manufacturer (Carl Zeiss, Oberkochen) could then concentrate on the high spatial frequency smoothness of the optical surfaces to achieve the specification assuming active correction in function, i.e. the “Intrinsic Quality” (IQ), as it was termed in this active optics system [3.69]. In the case of the (for current technology) only moderately thin NTT primary with an aspect ratio  $A = 15$ , it is only necessary to correct six aberration modes. Of these, two (defocus and decentering coma) are corrected by axial and lateral movements of the secondary; the other four by deforming the primary according to a simple algorithm by force variations of the active, astatic-lever type support. If

these are corrected to zero, the IQ is obtained. The specification for the IQ of the NTT (total optics train of three mirrors) was

$$(IQ)_{spec} \equiv (d_{80})_{spec} \leq 0.15 \text{ arcsec}$$

and the value attained by the manufacturers was even better

$$(IQ)_{fab} \equiv (d_{80})_{fab} = 0.125 \text{ arcsec} ,$$

$d_{80}$  being the diameter of the 80 % geometrical energy concentration. The equivalent  $(d_{80})_{fab}$  value for the primary mirror alone was 0.096 arcsec, corresponding to a wavefront error of 25.4 nm rms [3.68]. This was a remarkable achievement of optical manufacture at the time (1988), which has since even been exceeded for the “Galileo” project (see below). However, it should be mentioned that a systematic matching error with  $W \simeq 3000$  nm ptv, similar in origin and amount to that of the HST, was present in the primary of the NTT [3.70]. However, the relatively flexible primary permitted full correction of the error by the active optics system whose dynamic range had been designed to cope with such possible manufacturing errors (see § 3.5).

Figure 3.26 shows the primary mirror of the NTT, after acceptance at Carl Zeiss while still under the test tower. After erection at the La Silla observatory in Chile and the set-up and first application of the active optics correction system, the “First Light” results (accompanied by the good fortune of excellent external seeing and ventilation conditions) gave first images with an FWHM of 0.33 arcsec, considered at that time to be the best images ever formally recorded in ground-based astronomy. This was achieved in spite of the fact that integration times were limited to a maximum of 10 s because of tracking limitations and lack of field rotation compensation, and that the zenith distances were limited to about 25° because the active optics could not be operated on-line during these first observations, only in a pre-calibrated mode.

The NTT in its rotating building is shown in Fig. 3.27. Although it is not clear from this photograph, the slit of the building can effectively be fully opened at the top, the front and the back, permitting improved ventilation compared with the MMT. Figure 3.28 gives a view of the underside of the primary mirror cell, showing the 4-ring axial support geometry of the 78 supports (75 active plus 3 fixed points). Further details are given in § 3.5.

Detailed analysis of the optical performance of the NTT is given in refs. [3.70] and [3.72] and in § 3.5. The general conclusion was that the actively-controlled telescope defects can be reduced to  $(d_{80})_{tel} \leq 0.1$  arcsec, but that the limitations of the *local air* (“dome seeing”), in spite of the excellent ventilation properties of the building, are such that

$$(d_{80})_{tot} \simeq 0.20 \text{ arcsec}$$

probably represents the present practical limit of the total system, where  $(d_{80})_{tot}$  implies all error sources except atmospheric seeing and residual tracking errors. Maintenance constantly to this limit, or possibly even better,



**Fig. 3.26.** The ESO NTT: the primary mirror (full diameter 3.58 m) mounted on its final support in its cell which is placed on the manufacturing table at Carl Zeiss for test in the test tower [3.68] [3.71]

should become even more reliable through systematic use of correlations with temperature and wind sensors and the introduction of a fairly fast correction cycle (ca. 10 minutes) which is still being automated in the NTT. Such a fully automatic cycle is necessary to complete the active optics concept [3.73]. At present, the most difficult mode to control is defocus, because the mechanical focusing system is not really capable of fine focus movements while maintaining a tracking quality  $< 0.1$  arcsec. The NTT optical quality really requires a tracking quality  $\leq 0.05$  arcsec. The Galileo project (see below) will have an improved system.

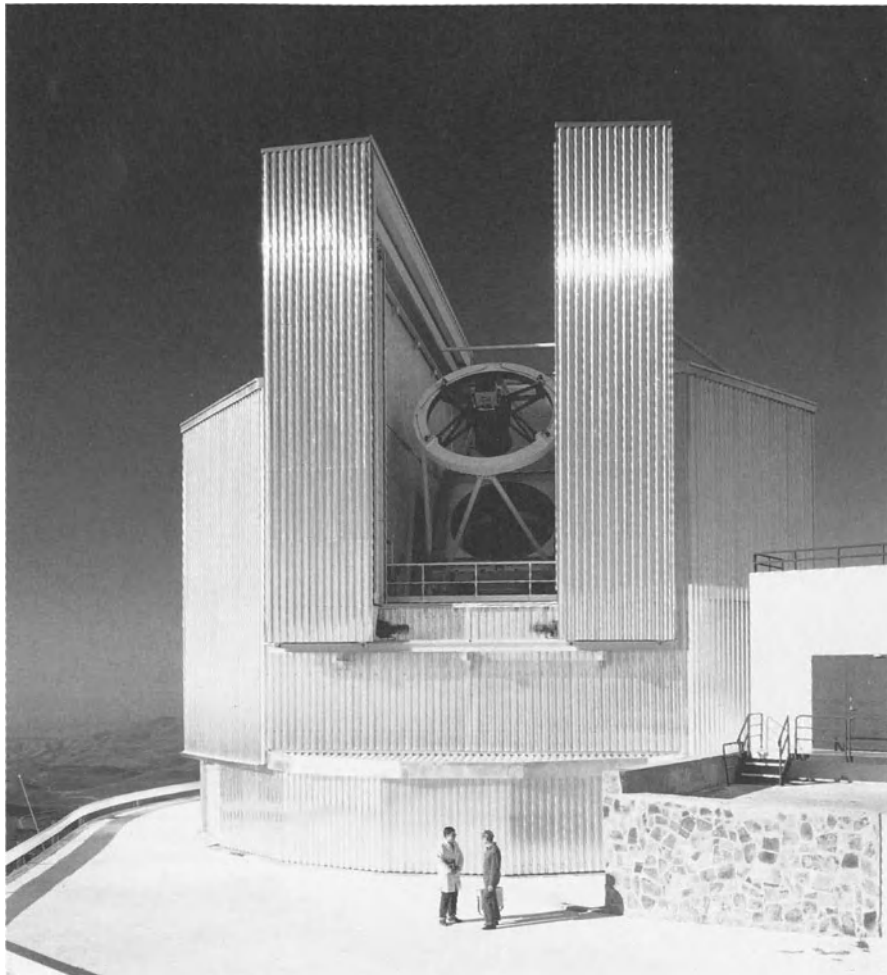


**Fig. 3.27.** The ESO 3.5 m NTT in its rotating building at La Silla, Chile [3.70]

A review of the effective optical quality of the NTT in 1991 (2 years after “First Light”) compared with the best conventional telescopes at the same observatory is given in ref. [3.73]. We shall return to the general question of the optical quality and efficiency of modern telescopes in Chap. 4.

It should be mentioned that the “brain” of the NTT and the essential element of the control loop is the *image analyser* which measures not only the coefficients of the errors to be corrected, but also gives high and low spatial and temporal information on the errors introduced by the *local air*. *Combined with the temperature and wind sensors and an external seeing monitor, the image analyser gives complete information on all the sources of degradation of the optical image.* Details of the Shack-Hartmann image analyser are given

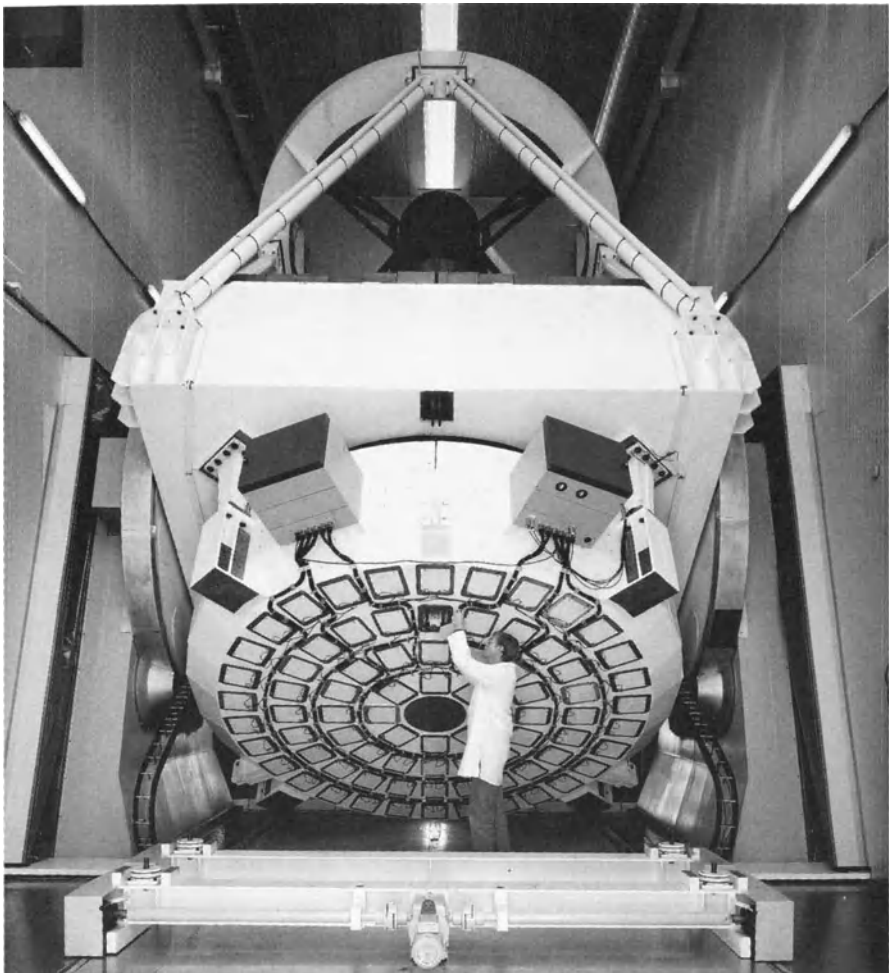


**Fig. 3.28.** The ESO 3.5 m NTT showing a view of the underside of the primary mirror cell with the 4-ring axial support geometry of the 78 supports, which are in the recesses under the covers shown [3.70]

in § 3.5 and ref. [3.72]. The fact that such devices can today be considered as routine tools is due in no small measure to the availability of CCD detectors, which have revolutionised telescopes not only as observational detectors but also for technical purposes.

Following the success of the NTT, many enquiries and tentative projects for emulating its concept emerged, but few of them have yet been funded. One such, which entered its commissioning phase at the beginning of 1997 [3.74], is the Italian “*Galileo*” (TNG) telescope. This is essentially based on the NTT, but has profited from certain important improvements carried out in the NTT as well as some very significant modifications. The most important

of these are an improved focusing system for the secondary  $M_2$  and a high frequency guiding system using the Nasmyth mirror  $M_3$ . General accounts of the telescope and its optics manufacture are given by Barbieri et al. and Knohl et al. [3.75] [3.76] [3.77] [3.78] [3.79]. The Intrinsic Quality (IQ) of the Galileo telescope primary exceeds even the remarkable value of the NTT (see above), being  $(d_{80})_{fab} = 0.07 \text{ arcsec}$  corresponding to a wavefront error of 16 nm rms. Interferograms of the final figure of this 3.5 m primary are shown in Fig. 1.37 above. In its actively-corrected form (Intrinsic Quality), this is probably one of the highest quality large optical surfaces yet produced and is a remarkable proof of the progress in polishing and test techniques in the last decade. Such an IQ is so good, it will be difficult to exploit it fully in the telescope, even with an optimal active optics system at an extremely good site (La Palma in the Canary Islands).

The largest telescope project currently underway is the ESO *VLT* ( $4 \times 8 \text{ m}$ , giving formally a 16 m equivalent aperture at the combined focus). A review of the VLT concept was given in 1988 by Enard [3.80] and this is still essentially valid from the point of view of the *optics*, though not of the enclosures or general layout. Later information was given by Beckers and Tarenghi [3.81] and by Enard [3.82]. Recent accounts of a number of aspects were given at the telescope conference in Landskrona in 1996, on the optical manufacturing side above all by Dierickx et al. [3.83], already referred to and discussed in Chap. 1 above.

Although earlier studies had been performed from 1976 onwards, and these had eliminated a “big dish” concept and an “array” concept of  $16 \times 4 \text{ m}$  telescopes in favour of an “array” concept of  $4 \times 8 \text{ m}$  telescopes (Fig. 3.4), the formal study phase of this latter concept only began in 1982. The project on this basis was approved and funded in December 1987. The first unit telescope is scheduled for completion and “First Light” in 1998.

The optical concept follows the NTT as a thin meniscus active telescope. However, the NTT has a primary with  $D = 3.58 \text{ m}$  and an aspect ratio  $A = 15$  in Eq. (3.2), whereas for the VLT  $D = 8.2 \text{ m}$  and  $A = 46.9$  for a thickness  $t = 175 \text{ mm}$  [3.83]. According to (3.2), the VLT primaries (also of Schott “Zerodur” like the NTT) are therefore over *fifty times* as flexible as the NTT primary. The optical design basis of the VLT is also a strict RC telescope, the primaries being somewhat steeper with  $f/1.8$ . Unlike the NTT, the pupil unit telescopes is at the *secondary*, for IR reasons. There are two Nasmyth foci, as in the NTT, with  $f/15$  ( $m_2 = -8.333$ ) and a Cassegrain with  $f/13.79$ . The system is optimized to the RC form for the *Nasmyth foci*; for the Cassegrain, the change of spherical aberration due to the significant change in axial image position is compensated actively by bending the primary. The active optics system is discussed in more detail in § 3.5. The axial support has 150 individual supports. The beam combination is via the coudé focus ( $f/32$ ) of the individual telescopes (Fig. 3.29) followed by the incoherent or coherent combination train shown schematically in Fig. 3.30. The incoherent combination does not require equal path lengths and will be mainly used for

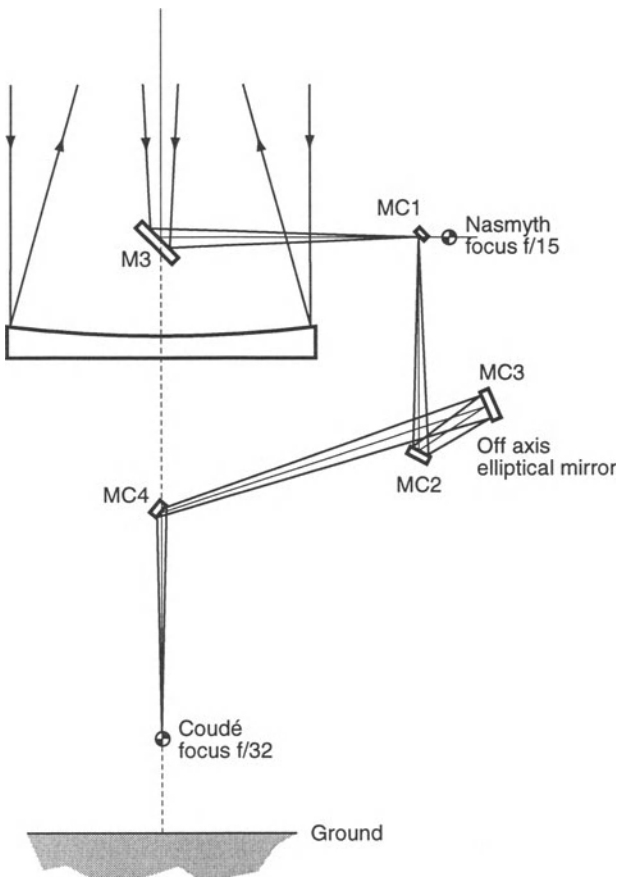


**Fig. 3.29.** The ESO 4 × 8 m VLT: Nasmyth and coudé foci of the individual telescopes (after Enard [3.80])

spectroscopy in the visible and IR. The mirrors of the optical trains for the coudé and combined foci will have high efficiency coatings of 99 % or more. On one Nasmyth side, the train is optimized for the blue, on the other side for the red.

The coherent (interferometric) combination was one of the basic reasons for the choice of indirect segmentation using an array (Fig. 3.4). The VLT concept assumed that four smaller, auxiliary telescopes would be part of the VLT complex so that experience could be gained with smaller apertures. Auxiliary (movable) telescopes with an aperture of 1.8 m were envisaged [3.81]. They may be upgraded to 2 m [3.84]. The 8 m telescopes are fixed. Plans in 1992 [3.81] envisaged a disposition of the 4 large fixed telescopes at the site on Cerro Paranal in Chile as shown in Fig. 3.31, which also shows the possible stations for the auxiliary telescopes. A postponement of the work on the interferometric mode (VLTI) in 1993 delayed the project. However, work is

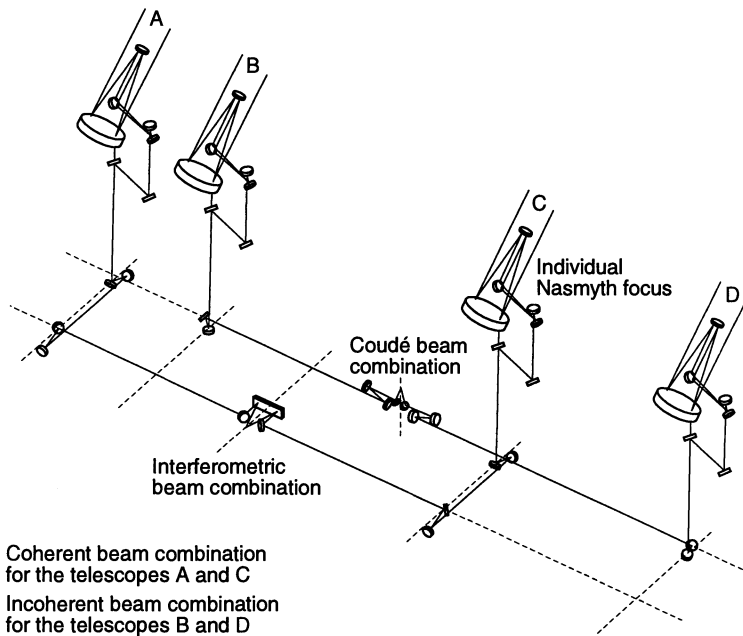


**Fig. 3.30.** The ESO 4 × 8 m VLT: principle of the beam combination showing the incoherent combined focus as well as the interferometric combination (after Enard [3.80])

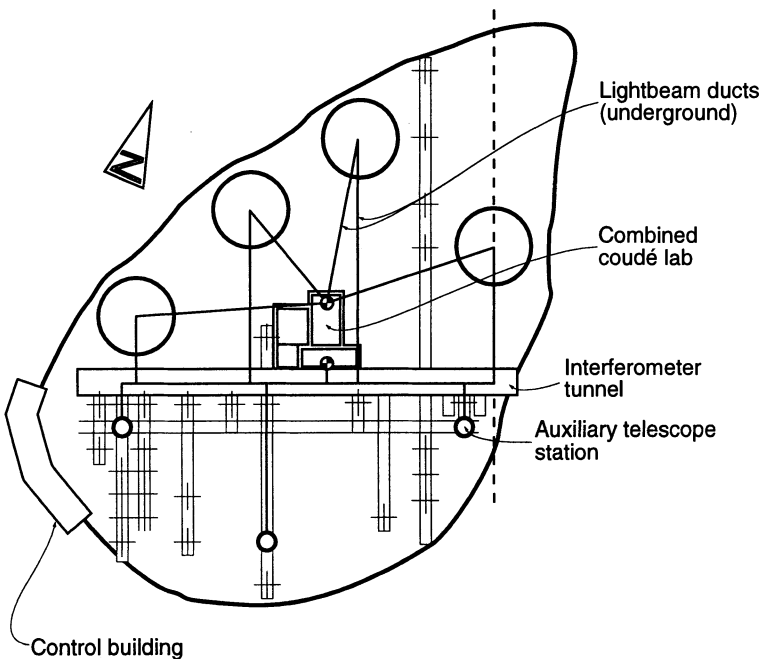


**Fig. 3.31.** The ESO 4 × 8 m VLT: layout proposed (summer 1992) for the 4 telescopes on Cerro Paranal, Chile. The small circles mark the possible stations for the auxiliary telescopes. (After Beckers and Tarenghi [3.81])

now proceeding and it is hoped to achieve first interferometric fringes with two of the 8 m telescopes around the year 2000, and routine operation with the auxiliary telescopes from 2003 onwards [3.84].

The VLT enclosure (building) concept has been through a number of phases with very different solutions [3.85]. Because of its influence on the "local air", the enclosure has indeed become a central (and very complex) element in the telescope optics. The final building version is shown in Fig. 3.32 [3.86].

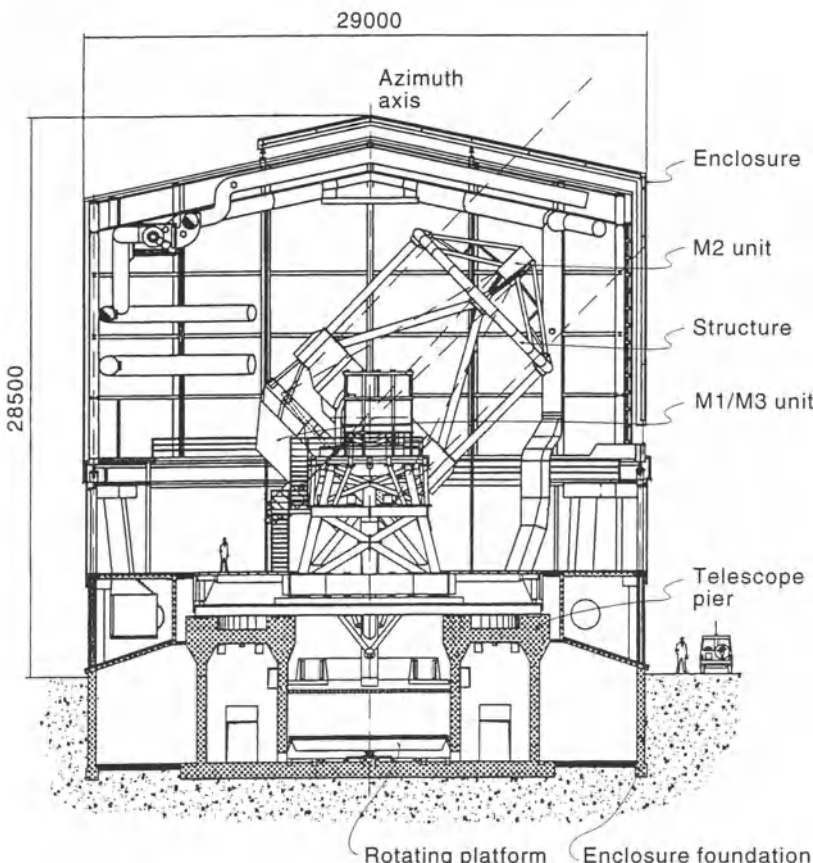


**Fig. 3.32.** The final version of the building of the 8 m VLT unit telescopes (after Schneermann et al. [3.86])

The first choice of blank material for the four 8 m primaries was glass ceramic (Zerodur from Schott, Mainz). A back-up solution – in view of the fact that no blank of this size in glass had ever been made – was aluminium with a Canigen (nickel) coat. Following the initial investigations for the NTT, such aluminium blanks have been very successfully produced up to a diameter of

1.8 m, and polished to high quality with (test) spherical forms – see § 3.3. The active optics concept is not only the key to supporting large, thin, monolithic blanks, but also the key to their *production*. Using a spin-casting procedure (see § 3.3), Schott has been able to make *thin* 8 m blanks ( $t = 175$  mm) in Zerodur because of the limitation of glass mass required. Classically *thick* blanks ( $A \sim 8$ ) in glass ceramic cannot be made in such sizes. This is the reason why a glass ceramic replacement of the borosilicate (Pyrex type) mirror of the Russian 6 m telescope could never be made.

Schott succeeded in casting the first 8.2 m VLT blank early in 1992 (Fig. 3.33), which was subsequently successfully ceramized (see § 3.3). This success, confirmed in November 1992 when ceramization was complete, represented a further milestone in the history of the reflecting telescope. In June 1993 it was transported to the new VLT optical shop of REOSC, near Paris. It is self-evident that the handling and transport of such large glass monoliths is a very delicate matter which has been the subject of careful technical studies at ESO, Schott and REOSC. The problems were considered soluble if appropriate care was taken. The relatively much lower sensitivity to handling and transport damage was one of the attractions of aluminium. However, the success of the manufacture and delivery programme of all 4 VLT primary blanks (the last being delivered in September 1996) gave final confirmation of a brilliant technical and organisational achievement by Schott, summed

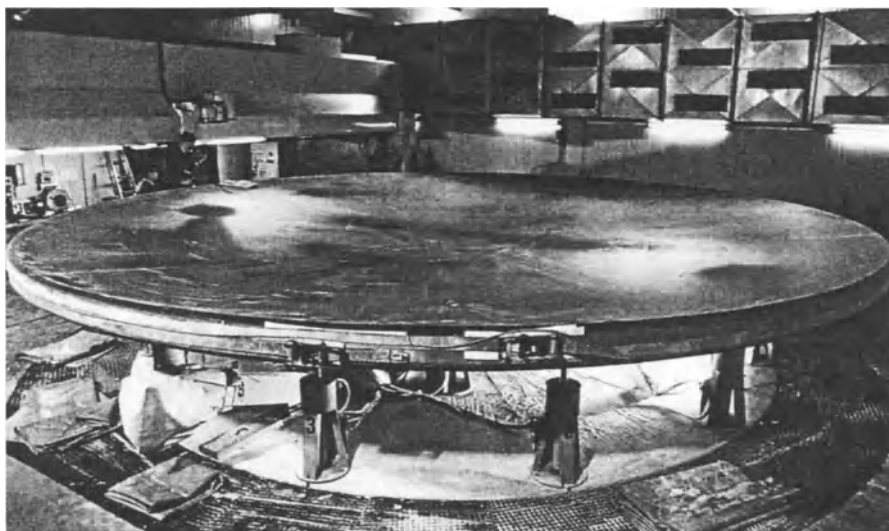


**Fig. 3.33.** The ESO 4 × 8 m VLT: the first 8 m telescope blank ever made, before ceramization at the Schott works, Mainz, early in 1992, intended for the first VLT telescope. The diameter here is about 8.5 m, the thickness about 250 mm. After ceramization, completed in November 1992, the diameter was reduced to 8.2 m and the thickness to slightly more than the final  $t = 175$  mm. The final weight is about 23 500 kg. (Courtesy Schott)

up by Morian et al. [3.87]. Another account is given in an excellent general paper on modern ground-based telescopes by Enard, Maréchal and Espiard [3.88]. This paper also gives an admirably clear summary of the figuring and test techniques at REOSC, dealt with in Chap. 1 above.

Figure 3.34, showing the first blank ground to its final dimensions before figuring at REOSC, gives a good impression of how thin the VLT primaries are relative to their diameter.

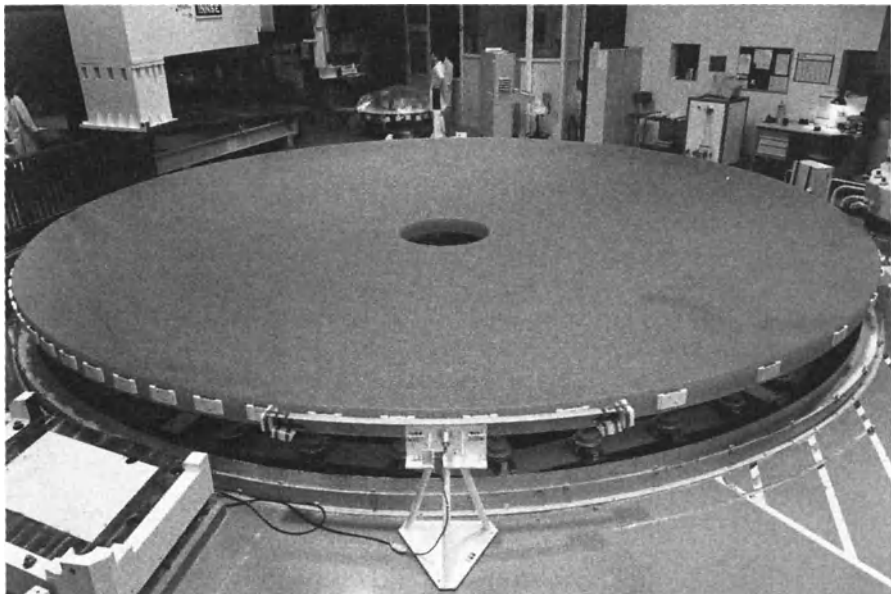


**Fig. 3.34.** The first VLT primary blank ground to its final dimensions before figuring at REOSC ( $D = 8.2\text{ m}$ ,  $t$  slightly more than the final 175 mm, i.e. 177.9 mm). (Courtesy REOSC)

A revealing way of understanding how flexible such modern meniscus blanks are, is to scale them according to the Couder Law of Eq. (3.2) to a diameter of 1 m, maintaining the same linear flexibility. The NTT primary, thus scaled, would have a thickness of only 18.9 mm. Such a test mirror was used for experiments in active optics [3.89] and seemed a very thin mirror by conventional standards. With the same scaling law, however, the VLT primaries would have a thickness of only about 2.6 mm – no thicker than large panes of window glass. This shows how far active optics technology has already advanced. Whereas the NTT could still work with moderate classical quality in the *passive* mode, the VLT cannot function at all without active optics. Nevertheless, ESO is confident that active control can be achieved in the VLT, using 16 controlled (natural flexure) modes (see § 3.5) in contrast to the 6 modes controlled in the NTT.

The optical quality specification for the VLT has been the subject of a rigorous analysis – see Chap. 4 – and is no longer based on the simple geometrical  $d_{80}$ -value used in the NTT and conventional telescopes. The error budget should give

$$d_{rms} \simeq 0.2 \text{ arcsec}$$

for a Fried parameter  $r_0 = 250 \text{ mm}$  (giving atmospheric seeing with FWHM  $\simeq 0.4 \text{ arcsec}$ ) and  $\lambda = 500 \text{ nm}$ . The above figure for  $d_{rms}$  includes *all* sources of error apart from the external atmosphere: it includes residual tracking error and local air effects. The latter represent the most problematic factor, as the NTT has demonstrated. The most powerful correction weapon against local air effects is a rapid correction cycle: in the VLT a correction cycle of 40 s is intended – see § 3.5.

Another large telescope project using thin meniscus technology which is largely completed is the Japanese *National Large Telescope (JNLT)*, now called *Subaru*. Originally, the JNLT envisaged an aperture of 7.5 m [3.90], but this was upgraded to 8 m under the name Subaru [3.91]. Reviews of its characteristics are given by Kodaira [3.90] [3.92]. In the latter, the aperture is given as 8.2 m. The following are the (original) essential optics characteristics [3.91] based on an aperture of 8 m:

Aperture	=	8.0 m [3.91] (8.2 m according to [3.92])
Primary focal length $f'_1$	=	15.0 m ( $f/1.875 - f/2.0$ according to [3.92])
Primary thickness ( $A$ )	=	200 mm (thin meniscus, $A = 40 - 41$ according to [3.92])
Blank material	=	ULE fused quartz (Corning)
Field of view at PF	=	30 arcmin (with corrector)
Cassegrain focus	=	$f/12.2$ (visual)
Field of view at Cassegrain	=	6 arcmin
Optical design	=	RC [3.92]
Cassegrain focus	=	$f/35$ (IR)
Nasmyth focus	=	$f/12.6$
Enclosure	=	flushing cylindrical type (rotates with alt-az telescope)

An artist's impression of the telescope, in its enclosure at the site on Mauna Kea, Hawaii, is given in Fig. 3.35, reproduced from the brochure [3.91]. The project is excellently documented in a series of JNLT Technical Reports, the first of which gives a general outline [3.93].

The technological approach using an actively controlled thin meniscus follows essentially the same concept as the ESO VLT. The primary is supported by 264 actuators, both axially and radially, located in bores in the mirror. This is an important technical difference from the VLT, which we shall discuss in § 3.4. Another technical difference from the VLT is that the



**Fig. 3.35.** The Japanese Subaru 8 m telescope project (reproduced from [3.91])

blank is made of Corning ULE fused quartz, not glass ceramic. Details of the optical specification of Subaru are given in [3.91]. In terms of the FWHM of the PSF, the values are given for the primary mirror (overall, including diffraction) as 0.10 arcsec; for the optical system overall as 0.11 arcsec; for the tracking overall as 0.12 arcsec; for local seeing overall as 0.12 arcsec; and for miscellaneous sources as 0.11 arcsec. The total effect of this specification is an *FWHM of 0.23 arcsec, overall, excluding external seeing*. This is very comparable with the specification of the ESO VLT – see above and Chap. 4.

A notable feature of the studies for the Subaru project are the systematic analyses, both theoretical and experimental, of the *local air conditions* and the *enclosure*. We shall return to these in § 3.6.

The Subaru project emphasizes its role as an optical-IR telescope using modern array detectors not only in the optical but also in the near IR. Combined with powerful instrumentation, the brochure gives a comparison [3.91] of *telescope sensitivities*, as the limiting photon flux detectable as a function of wavelength, for a number of projects [3.91]. This is reproduced in Fig. 3.36.

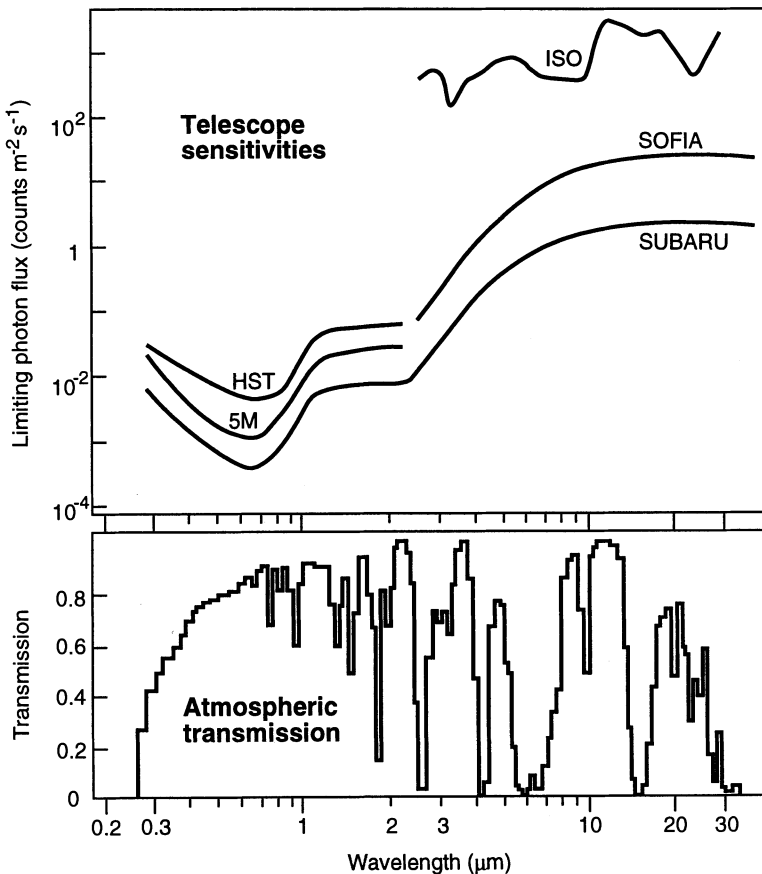


**Fig. 3.36.** The Subaru 8 m project compared with other telescopes from the point of view of *telescope sensitivity* over the optical-IR wavelength band, expressed as the minimum photon flux required as input (upper figure). The lower figure shows the atmospheric transparency windows for Mauna Kea, over which Subaru has high sensitivity. The upper figure refers to the high dispersion mode and IR data without the effect of the atmosphere. (After the Subaru brochure [3.91])

We shall return to the important matter of the sensitivity and efficiency of telescopes in relation to their optical specification in Chap. 4.

Subaru was planned to have “First Light” in 1998 [3.91]. According to Kodaira [3.93], the cost estimate followed the conventional telescope cost function given by Meinel and Meinel [3.94] in connection with the Chinese Optical Table Top concept. This was about \$ 100 million (1980). Kodaira pointed out that the aim of Subaru was not a *low cost* telescope but a *low risk, very high quality telescope*; also the infrastructure of the Subaru project and its relation to industry are different from those common in the US or Western Europe. Kodaira’s later cost estimate [3.92] was about \$ 250 million, tending to decrease.

The most recent general account of the further progress of the Subaru project has been given by Kaifu [3.95]. The ULE fused quartz blank for the primary, made by Corning, was delivered to Contravez, Pittsburgh, in 1995. The blank was produced by fusing 44 hexagonal ULE units together. Figuring was planned to be complete in the summer of 1997, enabling the “First Light” schedule to be met in the Cassegrain focus in the summer of 1998.

Another direction of thin meniscus technology, more revolutionary and more extreme in lightweighting, involves the abandonment of one-material mirrors in glass or metal and uses *lightweight fibre composites* in some form. This approach has above all come from the technology of radio telescopes, for which weight reduction with high stiffness was essential. Pioneer work was done by Dornier in Germany [3.96], who developed the first reflector of carbon fibre reinforced plastic (CFRP) in the late 1970s for a 2 m satellite antenna. This consisted of a sandwich structure with CFRP faceplates and an aluminium honeycomb core. The surface quality of 100  $\mu\text{m}$  was sufficient for direct use (CFRP is a conductor) for  $\lambda \geq 15$  mm. For shorter wavelengths a metal coating is required, which Dornier achieved by vacuum deposition of aluminium. Further developments were made in connection with the space projects FIRST (Far IR Sub-mm Space Telescope), for which an 8 m mirror with accuracy 10  $\mu\text{m}$  was required, and SOFIA (Stratospheric Observatory for IR Astronomy), for which a 3 m mirror to optical precision was required.

The firms MAN and Krupp in Germany have also been deeply involved in the application of CFRP to radio and submillimeter telescopes (SMT). An example of a 10 m SMT using CFRP is the SMT for Mt. Graham, Arizona, a joint project of the MPI for Radio Astronomy in Bonn and the Steward Observatory in Tucson, completed in 1990 [3.97]. For a shortest wavelength  $\lambda = 0.35$  mm, the required accuracy was 17  $\mu\text{m}$  rms. This work is particularly interesting from the point of view of *optical telescopes* because Krupp and collaborators at the Ruhr University in Bochum have undertaken the extension of similar technology into the optical domain. The origins of this go back to one concept [3.98] for the DGT 12 m project (see also § 3.2.1 above). At that time, the principal technical interest was the development of the hexapod (HP) mounting originally proposed by Felgett [3.99]. Since then, a smaller prototype telescope of aperture 1.5 m has been constructed: the *1.5 m HPT*. Although the hexapod mounting is still being applied and leads to the term HPT (Hexapod Telescope), the technical interest has shifted towards the novel concept for the optics [3.100] [3.101]. The principal idea of this concept is to consider the prime mirror *with its cell* as a single, fixed, actively-controlled unit. This is achieved by combining a thin Zerodur meniscus with a CFRP support/cell as a single hybrid structure. For the 1.5 m HPT, the Zerodur mirror is 55 mm thick ( $A = 27.3$ ). This is not particularly thin according to the standards of modern, actively-controlled menisci, but for this diameter such a level of weight reduction was considered adequate in view of the weight gain with the cell. According to Schnur [3.100], the same thickness could be maintained up to  $D = 4$  m ( $A = 72.7$ ): for larger

diameters, maintenance of the same thickness would lead to a problem of the CFRP structure optimization for expansion – see below. Also, with 4 m diameter and a thickness of 55 mm ( $A = 73$ ), the flexibility is similar to that of the VLT 8 m blanks: increase of diameter with this thickness could lead to insuperable handling problems.

Pausch and Stenvers [3.101] show a model of the 1.5 m hybrid mirror (Fig. 3.37). The main problem involved in this structure is the realisation of homogeneous temperature expansion, i.e. best adaptation of the CFRP structure to the low coefficient of expansion  $\alpha \simeq 0.065 \times 10^{-6} \text{ }^{\circ}\text{K}^{-1}$  of Zerodur, and the length of the CFRP tubes to get the most stable behaviour from the point of view of moisture absorption. This was solved by an optimization procedure. In any event, an active control of the hybrid structure is essential. Since the mass of the mirror is low, the *forced-based* concept of active optics as in the NTT is no longer appropriate and a *position-based* concept is used – we shall deal with this in § 3.5. There are 36 piezoelectric ceramic position actuators at the upper connecting points of the trusswork (Fig. 3.37). The specification calls for a figure control giving a wavefront aberration  $W \leq 36 \text{ nm rms}$  under all operating conditions [3.101]. Since the system has low inertia, there is the possibility, according to Schnur [3.100], to operate this correction not only in the normal *active* bandpass (§ 3.5) but also much faster in the *adaptive* bandpass. Current plans envisage an adaptive frequency limit of the order of 100 Hz, whereby “holes” in this adaptive bandpass (starting round 30 Hz)

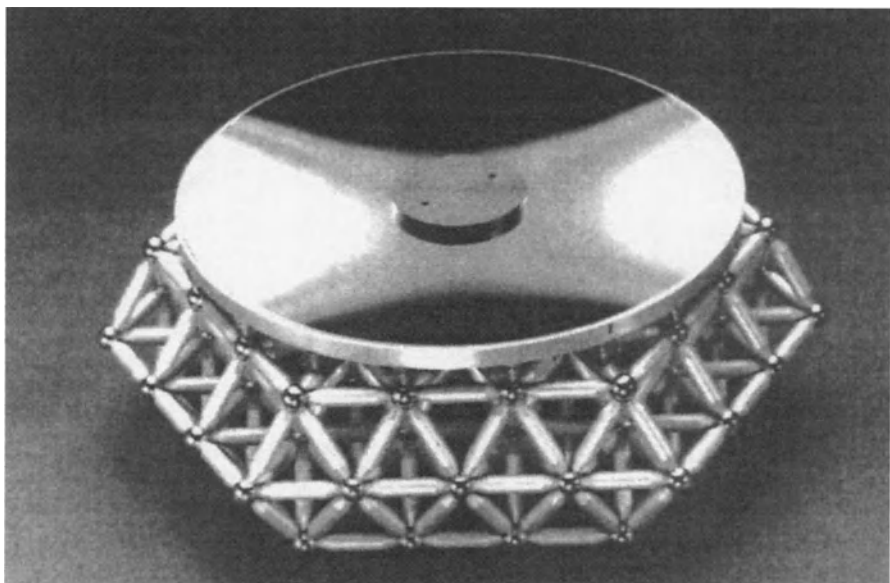


**Fig. 3.37.** Model of the hybrid primary mirror (Zerodur/CFRP) for the 1.5 m HPT (from Pausch and Stenvers [3.101])

would be left to avoid exciting the first or subsequent eigenfrequencies of the structure.

The active correction is in closed-loop using a Shack-Hartmann image analyser as in the NTT. In the adaptive bandpass, the problem of detection within the isoplanatic angle (§ 3.5 and Chap. 5) remains.

A picture of the HPT and more recent information has been given by von Appen-Schnur and Luks [3.102]. The project was finally realised by the German company VERTEX Antennentechnik. These authors mainly report a more ambitious development using the same basic concept: the ISLA project (International Stratospheric Laboratory for Astrophysics). The ISLA project will consist of two 4 m and four 2 m telescopes based on the HPT concept to achieve extreme lightweighting. They will be held on a platform in the stratosphere at a height of 15 km, maintained by helium-filled airships of a novel Russian design (Thermoplane). The great attraction of this concept is that a high proportion of the deleterious atmospheric effects, both of turbulence and absorption, are overcome at a fraction of the costs of a space enterprise. The seeing at optical wavelengths at this altitude is significantly less than 0.1 arcsec. The aim is that the 4 m telescopes will have diffraction-limited quality at these wavelengths (0.03 arcsec) by using simple adaptive optics with few elements. The interferometric mode should, of course, offer much higher resolution.

ISLA already has the support, in principle, of the German Space Agency DARA, but is too big a project for a single country. It is hoped to launch it as a European or international venture.

### 3.3 Blank production for new technology telescopes

#### 3.3.1 General considerations and physical properties

Development in blank technology for primary mirrors has been a central driver of progress since glass displaced speculum metal about 1860. We recall (see Chap. 5 of RTO I) that the 4-foot Melbourne reflector (1869) was the last major telescope to be equipped with a speculum mirror – with fatal consequences for its operation. The key to the replacement of speculum by plate glass was not a specific advance in glass casting technology, but the invention of chemical silvering on glass (see Chap. 5 of RTO I and [3.103]). Because of the higher reflectivity and freedom from need to repolish to maintain reflectivity, the classical glass blank (which was also lighter) represented an enormous gain which carried the reflecting telescope up to the 100-inch Mt. Wilson primary of Ritchey. Ritchey himself was acutely conscious of the problems associated with the thermal expansion ( $\alpha \simeq 8 \times 10^{-6} \text{ }^{\circ}\text{K}^{-1}$ ) and the high thermal capacity, both during manufacture and operation (Chap. 5 of RTO I). The classical crown glass was still supplied from Europe – St. Gobain in France. Only in 1927 did the production of large classical blanks start in

the U.S. for the Perkins 69-inch telescope. In the late 1920s, experiments started (Chap. 5 of RTO I) in connection with the Palomar 200-inch with both fused quartz and Pyrex (borosilicate glass). Corning supplied in 1932 a Pyrex blank for the Macdonald 82-inch (2.08 m) reflector with thickness 30 cm ( $A = 6.95$ ) and in 1933 a 74-inch (1.88 m) blank for the David Dunlap telescope [3.104]. The reduction of the expansion coefficient from about  $8.0 \times 10^{-6} \text{ }^{\circ}\text{K}^{-1}$  to about  $3.2 \times 10^{-6} \text{ }^{\circ}\text{K}^{-1}$  was so important that the classical crown glass blank disappeared for major telescopes after about 1930.

The Pyrex age for massive blanks of classical aspect ratio culminated in the Russian 6 m, still in use, but giving significant thermal problems (Chap. 5 of RTO I). The 5 m Pyrex blank for the Palomar development was a remarkable advance because the moderately lightweighted structure improved the thermal properties and gave the basis for the combined axial-radial support (Chap. 5 of RTO I).

The development of massive *fused quartz* blanks, which failed in the 1930s, was realised in the 1970s, giving a further reduction to  $\alpha \simeq 0.4 \times 10^{-6} \text{ }^{\circ}\text{K}^{-1}$ . Shortly afterwards, *glass ceramic* was developed with effectively negligible expansion for a defined temperature, to be followed by ULE (Ultra Low Expansion) fused quartz with similar negligible values. See Table 5.2 of RTO I for the use of Pyrex, fused quartz and glass ceramic in classical type blanks up to the William Herschel Telescope (WHT) completed in 1988.

Glass blanks still totally dominate the market for telescope mirrors: normal fused quartz largely removed the expansion problem; ULE and glass ceramic have removed it totally. Pyrex has made a come-back with the extreme lightweighted structures of Angel. These are the choices available for *glass* blanks today (in combination with modern support and ventilation technologies) which we deal with below. However, the fact that the expansion problem of glass has been solved does not mean that glass is the only, or necessarily the best choice for future telescope blanks, since other physical properties are also important, both mechanical and thermal.

Consideration of the thermal properties of blanks goes back to W. Herschel. Temperature effects on focus were well known. Ritchey's work, above all on the 100-inch Mt. Wilson telescope with its massive crown glass blank (Chap. 5 of RTO I), made very evident what he called the "edge effect", spherical aberration which he attributed to more rapid cooling at the edge than near the center of the prime mirror. A remarkable and far-sighted treatment of thermal aspects was given by Couder in 1931 [3.105]. He points out that the change of focus observed with crown glass mirrors is not just due to the basic expansion law of Gay-Lussac [3.106] for two temperatures  $t_0$  and  $t_1$  and expansion coefficient  $\alpha_t$

$$f_{t1} = f_{t0} [1 + \alpha_t(t_1 - t_0)] , \quad (3.3)$$

which assumes constant temperature in the blank, but due to a difference of temperature of the front and back surfaces with a linear gradient. In this case, there are no internal strains and the case can be treated as simple expansion of

parallel shells. The change of semi-aperture angle  $\theta$  at the center of curvature is

$$\delta\theta = \frac{y_b - y_f}{t} = \frac{y_f}{t} \alpha_t (t_b - t_f) , \quad (3.4)$$

where  $y_b$  and  $y_f$  are the semi-diameters of the mirror at the back and front faces respectively,  $t$  is the thickness,  $\alpha_t$  the expansion coefficient and  $t_b$  and  $t_f$  the temperatures. From simple geometry of the normals (this is the same procedure as the derivation of the wavefront aberration for change of focus [3.107]), we have

$$\delta r = -r \frac{\delta\theta}{\sin\theta} = -\frac{r^2}{y_f} \delta\theta \quad (3.5)$$

With  $r = 2f$ , this gives from (3.4)

$$\delta f = -2 \frac{f^2}{t} \alpha_t (t_b - t_f) \quad (3.6)$$

Couder gives an example with  $t = 0.1$  m,  $f = 6$  m,  $\alpha_t = 7.5 \times 10^{-6}$  for crown glass,  $t_b - t_f = 0.2$  °K and

$$\delta f = 1.08 \text{ mm}$$

This is over a hundred times higher than the change of focus corresponding to a uniform change of temperature of 0.2 °K according to Eq. (3.3). This latter case would occur for a mirror of infinite thermal conductivity and negligible thermal capacity in ambient air of changing temperature.

Spherical aberration effects due to radial gradients in crown glass mirrors were much more complex because stresses are introduced giving shearing moments. Such effects were well-known to amateurs and led to the recommendation to give the mirror an aspheric form of only about 80 % of the normal parabola as the usual cooling state of the mirror would distort its figure further from the sphere.

Such considerations led Couder to the conclusion that metal was thermally superior to glass because of the higher thermal conductivity. He proposed (actually as the reciprocal) the thermal quality criterion  $q_t$

$$q_t = \frac{\lambda_t}{\alpha_t c_t \rho_t} , \quad (3.7)$$

in which  $\alpha_t$  is the expansion coefficient,  $\lambda_t$  the thermal conductivity,  $c_t$  the specific heat and  $\rho_t$  the density. (The suffix  $t$  – thermal – is used in the normal German notation of these parameters to distinguish them from other symbols in optics). Without  $\alpha_t$ , the other parameters in (3.7) express the thermal diffusivity  $a_t$  of the material: the parameter  $1/\alpha_t$  measures the insensitivity to temperature change. The larger the value of  $q_t$ , the better the material. Couder showed that crown glass was 212 times worse than fused quartz, 42 times worse than steel and 28 times worse than cast iron. Earlier (1924–1927), he had made drum-shaped blanks of cast iron, had them enamelled

with a thickness about 1 mm and polished the enamel surface (enamel is essentially a fused layer of flint glass with high lead content). In experiments, he proved the excellent thermal insensitivity compared with crown glass.

Maksutov, apparently unaware of Couder's work, did similar work in the late 1930s [3.106] (see also Riekher [3.108]). Bearing in mind Ritchey's "edge effect" producing spherical aberration, he proposed the same thermal criterion as Couder in Eq. (3.7) but including Young's modulus  $E$  in the numerator giving

$$(q_t)_M = \frac{E\lambda_t}{\alpha_t c_t \rho_t} , \quad (3.8)$$

a high Young's modulus being favourable in giving higher stiffness against deformation. Maksutov performed numerous experiments with both solid metal mirrors and ribbed, lightweighted structures, confirming the enormous thermal advantage over crown glass or Pyrex. He proposed copper, bronze and aluminium with chromium coats, which take a good polish; or stainless steel, polished directly. In all cases they could be provided with reflecting coats of evaporated aluminium. Maksutov was convinced metal mirrors were preferable to glass and used a stainless steel mirror in a 0.7 m telescope for Pulkowa [3.109].

The situation today has evolved further, not only because of the invention of glass ceramic and ULE fused quartz but also because of active optics control of blanks, which can be made very thin, and extreme lightweighting of borosilicate glass (Pyrex). Table 3.4 shows the physical properties of most materials of interest for telescope mirror blanks [3.110]. The same thermal quality criterion  $q_t$  as Couder (in inverse form) is given, following Eq. (3.7). The best materials (highest  $q_t$ ) are the glass ceramic Zerodur, mainly as a result of its very low expansion coefficient ( $\leq 0.05 \times 10^{-6} \text{ }^{\circ}\text{K}^{-1}$  for best quality), with the value of  $q_t = 15.80$ ; and ULE fused quartz, which has an even higher nominal value (25.7). However, this depends on the interpretation of the expansion coefficient, where there is no real difference. The best metal is beryllium (7.33), followed by pure aluminium (3.74), alloys being somewhat inferior. Cast iron has 1.52, low alloy carbon steel 1.24. Stainless steels vary from 0.63 (best ferritic) to 0.33 (austenitic). Carbon fibre is very good parallel to the fibre, bad perpendicular to it. The worst materials are the classical optical glasses, above all heavy flints (0.038). Pyrex (borosilicate glass) has 0.19, a value little more than half that of the worst stainless steel.

These values of  $q_t$  entirely confirm the viewpoints of Couder and Maksutov concerning the great potential of metal mirrors. *Aluminium*, particularly, assumes greater interest than ever, in view of the proven possibilities of coating it with Canigen (ca. 91 % nickel) by chemical means, or with nickel coats by electrolytic processes, allowing excellent polish (see below). Aluminium has the great advantage over stainless steel that its density is only about 7 % higher than that of glass (Zerodur), whereas stainless steel has a value over 3 times higher. This makes lightweighting essential for large stainless steel

**Table 3.4.** Physical properties of potential mirror blank materials (from Wilson and Mischung [3.110]). (Continued overleaf)

Material	$\lambda_t$ Thermal conductivity $\frac{\text{W}}{\text{m}^\circ\text{K}}$	$c_t$ Specific heat $\frac{\text{J}}{\text{Kg}^\circ\text{K}}$	$\rho_t$ Density $10^3 \cdot \frac{\text{Kg}}{\text{m}^3}$	$a_t = \frac{\lambda_t}{c_t \rho_t}$ Thermal diffusivity $10^{-6} \cdot \frac{\text{m}^2}{\text{s}}$
Zerodur (1 quality)	1.63	820	2.52	0.79
Zerodur (2 quality)	1.63	820	2.52	0.79
Fused silica (transparent)	1.38	772	2.20	0.81
Fused silica (ULE)	1.3	766	2.21	0.77
BSC glass (Pyrex, Duran 50)	1.17	830	2.23	0.63
BK7 glass	1.11	858	2.51	0.52
SF3 glass	0.71	423	4.64	0.36
Al (pure)	221	920	2.70	89.0
Al (low alloy)	160	890	2.60	69.1
Fe (pure)	67	465	7.86	18.3
Carbon steel (low alloy)	49	460	7.85	13.6
Stainless steel (ferritic 13 % Cr, 4 % Ni)	25	480	7.86	6.6
Stainless steel (austen. 18 % Cr, 8 % Ni)	21	500	7.88	5.3
Invar (36 % Ni)	13	500	8.13	3.2
Beryllium (pure)	162	1000	1.84	88.0
Nickel (pure)	58	460	8.80	14.3
Canigen (90–92 % Ni)*	8	420	7.90	2.4
Titanium (90 % Ti, 6 % Al, 4 % V)	7	550	4.50	2.8
Silicon carbide (SiC)-CVD	193	712	3.21	84.4
Silicon carbide (SiC)-siliconized	156	670	2.92	79.7
Carbon fibre Type I – parallel to fibre	4.2	840	1.55	3.2
– orthog. to fibre	0.7	840	1.55	0.5
Carbon fibre Type II – parallel to fibre	5.5	840	1.55	4.2
– orthog. to fibre	1.3	840	1.55	1.0

\* (hardened at 100 °C)

**Table 3.4.** Physical properties of potential mirror blank materials (from Wilson and Mischung [3.110]). (Continued overleaf)

Material	$\alpha_t$ Thermal expansion $10^{-6} \cdot \frac{1}{^{\circ}\text{K}}$	$q_t = a_t/\alpha_t$ Thermal insensitivity $\frac{\text{m}^2}{\text{s}} \cdot ^{\circ}\text{K}$	Relative thermal insensitivity Zerodur = 1000	$E$ Young's Modulus $10^{10} \cdot \text{Pa}$
Zerodur (1 quality)	0.05	15.80	1000	9.1
Zerodur (2 quality)	0.10	7.90	490	9.1
Fused silica (transparent)	0.4	2.0	126	7.0
Fused silica (ULE)	0.03	25.7	1620	6.8
BSC glass (Pyrex, Duran 50)	3.3	0.19	12	6.3
BK7 glass	8.3	0.063	4.0	8.1
SF3 glass	9.5	0.038	2.4	5.6
Al (pure)	23.8	3.74	237	7
Al (low alloy)	22	3.14	198	7
Fe (pure)	12	1.52	96	21
Carbon steel (low alloy)	11	1.24	78	21
Stainless steel (ferritic 13 % Cr, 4 % Ni)	10.5	0.63	40	21
Stainless steel (austen. 18 % Cr, 8 % Ni)	16	0.33	21	20
Invar (36 % Ni)	1.2	2.67	170	14
Beryllium (pure)	12	7.33	465	30
Nickel (pure)	13	1.10	70	21
Canigen (90–92 % Ni)*	13	0.18	11	14.5
Titanium (90 % Ti, 6 % Al, 4 % V)	9	0.31	20	11
Silicon carbide (SiC)-CVD	2.10	40.2	2540	46.6
Silicon carbide (SiC)-siliconized	2.57	31.0	1960	31.1
Carbon fibre Type I – parallel to fibre	0.2	16.0	1010	13
– orthog. to fibre	35	0.014	0.9	8.5
Carbon fibre Type II – parallel to fibre	(–)0.9	4.6	292	22.6
– orthog. to fibre	32.5	0.031	6.3	7.3

\* (hardened at 100 °C)

**Table 3.4.** Physical properties of potential mirror blank materials (from Wilson and Mischung [3.110])

Material	$E/\rho_t$ Mechanical stiffness $10^7 \cdot \frac{J}{Kg}$	$H$ Hardness $10^8 \cdot Pa$	$H_{Kn}$ Hardness Knoop
Zerodur (1 quality)	3.6		630
Zerodur (2 quality)	3.6		630
Fused silica (transparent)	3.2		ca. 610
Fused silica (ULE)	3.1		
BSC glass (Pyrex, Duran 50)	2.8		ca. 440
BK7 glass	3.2		520
SF3 glass	1.2		330
Al (pure)	2.6	2	
Al (low alloy)	2.7	5	
Fe (pure)	2.7	6	
Carbon steel (low alloy)	2.7	12	
Stainless steel (ferritic 13 % Cr, 4 % Ni)	2.7	20	
Stainless steel (austen. 18 % Cr, 8 % Ni)	2.5	20	
Invar (36 % Ni)	1.7	14	
Beryllium (pure)	16.3	20	
Nickel (pure)	2.4	8	
Canigen (90–92 % Ni)*	1.8	50	
Titanium (90 % Ti, 6 % Al, 4 % V)	2.4	3	
Silicon carbide (SiC)-CVD	14.5		
Silicon carbide (SiC)-siliconized	10.7		
Carbon fibre Type I – parallel to fibre	8.3		
– orthog. to fibre	5.5		
Carbon fibre Type II – parallel to fibre	14.6		
– orthog. to fibre	4.7		

\* (hardened at 100 °C)

blanks, whereas aluminium can be used in thin meniscus form. Beryllium is very favourable, but cost and the poisonous nature of its dust make it less attractive for large blanks.

The criterion  $q_t$  is above all related, because  $\alpha_t$  is included in the denominator of Eq. (3.7), to the avoidance of *distortions* of the blank due to temperature differences. Of course, this situation is also influenced by *structure* in the blank and any *active thermal control process* – see below. However,

distortion of the blank is not the only important thermal aspect, particularly since (for unstructured meniscus blanks) such distortions will be above all in low spatial frequency modes and thereby correctable by active optics. The other aspect is associated with the influence of mirror blanks as heat sources (or sinks) in the ambient local air ("mirror seeing"). For this, the criterion  $a_t$  (thermal diffusivity) without  $\alpha_t$

$$a_t = \frac{\lambda_t}{c_t \rho_t} \quad (3.9)$$

is more appropriate. Table 3.4 shows that the metals beryllium and aluminium are by far the most favourable with this criterion. It measures, however, only the ability of a blank to get heat transfer from its interior to its surfaces: the transfer to the ambient air then depends on a complex situation of ventilation and convection. Heat radiation into space is a much more predictable phenomenon. If ventilation or thermal control means exist to drive the mirror into thermal equilibrium with the ambient air, then a high value of  $a_t$  can only be an advantage.

The criteria considered above assume that the expansion coefficient  $\alpha_t$  is a *constant* throughout the blank material. For large blanks this is by no means necessarily the case, and variations in  $\alpha_t$  can lead to distortions. This limitation must be borne in mind when applying the simple Gay-Lussac linear expansion law of Eq. (3.3).

### 3.3.2 Glass ceramic blank production

That a "glass ceramic" can exist with effectively zero expansion coefficient compared with normal glasses was discovered by accident at Corning. The manufacture of large blanks (up to 4 m diameter) was taken up by the firm Owens-Illinois in the U.S. in the 1960s and a number of telescopes (see Table 5.2 of RTO I) were equipped with blanks of the product "Cervit". Production was later ceased. At present there are three centers of production of glass ceramic: Schott in Germany ("Zerodur"), a factory in Russia ("Astro-Sitall") and a factory in Shanghai, China. The Schott product "Zerodur" is the best known and has achieved unsurpassed standards as well as the largest diameter blanks.

Glass ceramic achieves a quasi-zero expansion coefficient by a balance between the crystalline phase (approx. 70 % by volume) and the normal amorphous glass phase (approx. 30%) [3.111]. The glass phase exhibits the normal *positive* thermal expansion whereas the crystalline phase exhibits a *negative* thermal expansion. If this balance is optimized zero net expansion results, although there is a slight dependence on temperature, of the order of  $\pm 0.05 \times 10^{-6} \text{ }^{\circ}\text{K}^{-1}$  from  $0^{\circ}$  to  $50^{\circ}\text{C}$ . The mean value given for the NTT primary mirror was  $\alpha_t = -0.0026 \times 10^{-6} \text{ }^{\circ}\text{K}^{-1}$ . Good transparency can be realised for astronomical applications because the crystal size can be kept very small (ca. 50 nm). The chemical properties and hardness of the two phases

are very similar, so the uniformity of the material is excellent for polishing. Some details of the manufacturing process are given by Pfaender [3.112]. The blank is cast in a more or less normal way to produce a blank only in the glass phase. However, it contains additional materials (above all  $\text{TiO}_2$  and  $\text{ZrO}_2$ ) which can germinate the production of crystals. An essential feature is that the temperature region at which the maximum production of nuclei takes place is *lower* than that for maximum crystal growth. The glassy blank is reheated to about  $800^\circ\text{C}$  which initiates maximum production of nuclei; then to about  $1000^\circ\text{C}$  where maximum crystallisation occurs, the time determining the volume percentage of crystalline material. Crystal structures with negative expansion coefficient are, for example, lithium-alumo-silicates.

Müller and Höneß [3.111] give some major projects that have made use of Zerodur. Others are given in Table 5.2 of RTO I. Including more recent projects, Zerodur has been chosen, apart from a large number of smaller telescopes, for five 4 m class projects, including the ESO NTT and Italian TNG, for the 42 segments of the Keck 10 m primary and for the four 8 m blanks of the ESO VLT. It has also been used for the X-ray projects ROSAT B and AXAF. Figure 3.26 showed the 3.58 m primary of the NTT, with  $A = 15$ . This was produced by conventional casting, the glass mass being less than that used for previous conventional “thick” blanks of the same diameter, e.g. the 3.5 m MPIA telescope at Calar Alto or the 4.2 m WHT at La Palma (Table 5.2 of RTO I).

The 8 m blanks for the ESO VLT were a problem of a different order of magnitude. The essential parameter is the glass mass which means, for a given diameter of a monolithic blank, its *thickness*. The *active optics control* (§ 3.5) permits an aspect ratio ( $A = 46.9$ ) which would be unthinkable for classical passive blanks such as that for the Russian 6 m telescope. This is the key to the successful production of 8 m blanks in glass ceramic and the reason why manufacture of a “thick” 6 m blank for the Russian telescope failed: the 6 m is still equipped with a BSC glass (Pyrex type) mirror.

In an extensive development programme, Schott investigated [3.111] three different techniques of lightweighting Zerodur, also a technique of producing thin menisci by slumping flat plates. Promising results were obtained with diameters up to 1 m. However, the technique finally chosen for the VLT 8.2 m blanks was *spin-casting*, similar to the technique pioneered by Angel for his Pyrex blanks – see below. The convex meniscus back of the blank is produced by the mould form, while the spinning process produces the concave upper surface and transports the glass over the whole area. The volume ratio of mirror volume to blank volume increases from 0.16 to 0.53 and every aspect of the manufacture is made easier and cheaper. Tests with this technique on smaller diameters were started in 1987. Details concerning the successful production of *the first 8 m class blank ever produced* (see Fig. 3.33) were given by Morian and Müller [3.113]. Two 8.5 m blanks were cast in the glassy state, annealed and machined. The machining of the back face was a delicate stage, since it is at this face that uncontrolled ceramization takes place because of

the temperature gradient. If the “crust” is too thick, the blank may crack. Ceramization ( $8\frac{1}{2}$  months) was completed for the first blank in November 1992. After final machining, the blank was delivered to REOSC for figuring in June 1993 (see § 3.2.4 above).

The last of the 4 VLT primary blanks was delivered by Schott in September 1996. Handling of such blanks is a delicate matter, although the thickness at delivery was still appreciably more (250 mm) than the final thickness (175 mm). A three-point support would give tensile stresses of  $5 \text{ N/mm}^2$ , well above the tolerance of  $\leq 1 \text{ N/mm}^2$  [3.113], so a multi-point support, specially studied, was required.

One of the advantages of glass over metal for mirror blanks is their *transparency*, enabling strain measurements with polarised light. The principles of such strain measurement are given by Maksutov [3.114]. Conventional Zerodur blanks normally have a *compressive* bulk stress, which is favourable, of  $< 10 \text{ nm/cm}$ . Local defects may be accompanied by higher values which can be dangerous if they generate tension stresses.

The bubble and seed quality resulting from the spin-casting process is particularly high.

### 3.3.3 Fused quartz (silica) blank production

As was mentioned in Chap. 5 of RTO I, the first systematic development of fused quartz for telescope mirror blanks was by Thomson of GEC as a possibility for the Palomar 5 m telescope [3.115]. After great difficulties, he produced two 60 inch (1.52 m) blanks in 1931, but the experiments were then stopped because of the high costs and the decision taken in favour of Pyrex.

Manufacture of large fused quartz blanks for telescopes was taken up at Corning in 1958 with a 0.9 m blank for Stratoscope II [3.116]. In the period 1965 to 1967, four fused silica blanks were produced in the 2.6 to 4.0 m range. Two of these were for the KPNO 4 m and ESO 3.6 m telescopes – see Table 5.2 of RTO I. The breakthrough in technology, which Thomson had not managed for Palomar and which was essential for  $D \geq 2.5 \text{ m}$ , was the vertical sealing of separate pre-cast “boules” of fused silica, usually of diameter about 1.2–1.4 m. Once this technology was proven, there was in principle no limit to the size of fused quartz blanks that could be made, since only scaling up of furnace equipment was required: handling and transport would limit diameters, not manufacture.

After 1970, Corning concentrated more on lightweighted blanks for space use, the most notable example being for the 2.4 m HST primary (Fig. 3.21), made of ULE, Ultra Low Expansion fused silica. ULE is doped with titanium and quasi-zero expansion is claimed, compared with the small value  $0.4 \times 10^{-6} \text{ }^\circ\text{K}^{-1}$  for normal fused silica (see Table 3.4). Lightweighting fused silica structures is more demanding than solid blanks, since the structure shape must be maintained during the fusing process. The six 1.8 m primaries of the MMT were also Corning lightweighted fused silica blanks.

Corning has also made, since 1970, a number of large, thin blanks, up to 3 m diameter with aspect ratios  $A$  in the range 40 to 82.

Large blank manufacture, specifically for a 3 m blank but also suitable for 8 m blanks, involves the following steps [3.116]. Fused silica boules of 1.2 m diameter are sawn and ground to 50 mm thickness, then edge ground to hexagonal shape. The hexagons, together with triangular pieces for filling edge gaps, are assembled on a flat refractory bed and given a circumference wall of refractory material. The furnace is then heated to over 1500 °C (fused silica requires the highest working temperatures) to produce fusion of the vertical seams. After controlled cooling to room temperature, the blank is machined to a thickness of 35 mm and the required diameter. A refractory sag form is fabricated and ground on to the furnace turntable. The 3 m blank is then placed on the sag form and sagged at the appropriate temperature to the refractory shape. Controlled cooling gives fine annealing as the blank is cooled to room temperature.

For an 8 m blank, 1.4 m diameter boules of very high purity and refractive index homogeneity are selected [3.116]. Boules are sealed in stacks twice the required thickness so that top quality glass is available, after slicing in half, at the upper part of each slice for the “critical zone” containing the optical surface. Since, unlike Zerodur, the highest cost in a fused silica blank comes from the boule material itself, actively controlled thin meniscus blanks are also very favourable for this technology.

An important feature of fused silica blank technology is the possibility of repair. The only requirement is that the blank or parts can be put back in the furnace with no missing fragments and that the pieces being fused can have their surfaces properly cleaned.

The maximum stress appearing in 8 m blanks is 10 nm/cm, similar to glass ceramic.

Earlier, with blanks made in the 1960s, the vertical seals tended to produce bubbles. However, the ESO 3.6 m “thick” fused quartz blank was worked optically with complete success. Corning considers the current technology of vertical seals gives much improved bubble quality: there have not been any problems of bubbles opening up at the optical surface during grinding and polishing of modern fused quartz blanks.

Some European manufacturers have suspected that ULE gives problems of variable hardness. This is certainly not the case with classical fused silica. With active optics, the small residual expansion of  $0.4 \times 10^{-6} \text{ }^{\circ}\text{K}^{-1}$  is of little significance and the classical material is an excellent candidate if a glass is chosen. Once the vertical sealing of boules is mastered, the manufacturing process is simpler than that of glass ceramic; but in its nature, glass ceramic is probably better in bubble and seed quality.

A fairly thin meniscus primary of fused quartz (ULE) was the preferred solution in 1982 for the proposed Texas 7.6 m telescope [3.117], but this was never realised in practice. A thickness of 51 cm for 7 m diameter ( $A = 13.7$ ) was quoted by Nather [3.118]. This was considered as thin as reasonably

possible at the time, whereas the ESO VLT 8 m primaries now have only one third of that thickness.

At the present time (summer 1997), the 8.3 m *Subaru* ULE blank has been manufactured without problems by Corning and has now been polished at Contravez [3.95] (see also § 3.2.4 above). Similarly, following the decision to use thin meniscus technology (see § 3.2.3 above), the two 8.1 m *Gemini* ULE blanks have been successfully manufactured and shipped to REOSC for polishing [3.8]. The fusing technique with boules has advantages of flexibility in contracting for blanks. For example, boules were ordered in 1992 for the primary of a 3.5 m North Carolina project, based on the NTT, without further commitment at that time for delivery of a finished blank.

### **3.3.4 Modern blank production with BSC (borosilicate) glass (Pyrex)**

The era of classical “thick” blanks in BSC (“Pyrex”, “Duran”, etc.) with an expansion coefficient  $\alpha_t \simeq 3.3 \times 10^{-6} \text{ }^{\circ}\text{K}^{-1}$  effectively came to an end about 1970 when fused quartz and glass ceramic with negligible expansion became available. The last such classical BSC blank was the second blank used for the replacement primary of the Russian 6 m telescope, the finished mirror being inserted in the telescope in 1979 (see § 5.3 of RTO I). Such a blank was already an anachronism at that time: attempts to replace it with glass ceramic (Astro-Sitall) failed because of the high glass volume due to the thickness (see § 3.3.2 above).

Nowadays, the limit of supply of “Pyrex” or “Duran” solid blanks from normal production is  $D = 400$  mm. In *lightweighted* form, BSC glass blanks have been advocated and manufactured for many years by Angel, who gave a complete account of the rationale, technique developed and facilities for diameters up to 8 m in 1988 [3.119]. Essentially, this technology is a refinement and extension of that of the Palomar 5 m telescope.

The principle of the Angel lightweighted BSC blanks is a much finer structure (i.e. higher lightweighting) than was used in the Palomar 5 m, giving much lower thermal inertia, combined with a sophisticated ventilation system to maintain the mirror in thermal equilibrium, both internally and with the ambient air. The honeycomb hexagonal structure was chosen because of its inherent stiffness. BSC glass is cheap and has excellent chemical stability. Instead of pouring liquid glass as in classical casting, the mould is assembled and filled with many blocks of cold BSC glass which are simply melted together to fill the mould.

The thermal stabilization aspect is described by Cheng and Angel [3.120]. The important conclusion is that the maintenance of the reflecting surface within  $0.2 \text{ }^{\circ}\text{C}$  of the ambient air (giving, according to their calculations, a mirror seeing  $\leq 0.06$  arcsec) requires a faceplate which is thin (25 mm) and well-ventilated from the back, where the heat transfer rate must correspond

to a “good breeze at the front surface ( $10 \text{ W/m}^2/\text{°K}$ )”. Thermal equilibrium within the blank should be maintained to  $0.1^\circ\text{C}$ .

BSC glass of very high quality is required. Mostly, Angel has used E6 BSC glass from Ohara, Japan, supplied in blocks of about 4 kg. A high homogeneity in the thermal expansion coefficient of  $\delta\alpha_t \leq 10^{-8} \text{ °K}^{-1}$  is required and obtainable.

Technically, it is easiest to make blanks with a flat back. The honeycomb structure is optimized for loads due to gravity, polishing and wind during operation. Cell size is determined by the sag of the faceplate due to gravity and polishing pressure. The plate deflects roughly like a circular plate clamped at the edge under uniform pressure, giving a deflection (see § 3.4)

$$\delta z = \frac{3}{16} \frac{qa^4(1-\nu^2)}{Et^3}, \quad (3.10)$$

where  $q$  is the pressure applied,  $a$  the cell diameter,  $t$  the faceplate thickness,  $E$  Young's modulus and  $\nu$  Poisson's ratio. This is a fundamental formula governing all supports (see § 3.4). For  $t = 25 \text{ mm}$ , the cell spacing chosen for an 8 m blank study was 193 mm, or 223 mm across a diagonal. This gave a quilting of about 20 nm ptv for a modest polishing pressure of 1000 Pa.

The depth of the blank structure depends on the stiffness required in view of the support chosen. Ballio et al. [3.121] calculated that such a structure of average depth 630 mm and supported on 3 hard points, deflects by 410 nm rms, under a windload force of 61.3 Pa. Using whiffle-trees to spread the load, they estimate the effects are some 4 times smaller and  $< 0.06 \text{ arcsec}$ , the target value.

Such considerations led to the design for the 8 m Columbus (later LBT) and Magellan projects given in Table 3.5. We shall consider support aspects of such blanks in § 3.4. Angel compares the rigidity to wind loading with that of solid meniscus blanks of Zerodur of similar weight and gives deflections some 20 times higher than for his lightweighted blank (9.2  $\mu\text{m}$  rms instead of 410 nm rms under 61.3 Pa load). However, this does not take account of the possibilities of active correction – see § 3.5. Angel also points out the much

**Table 3.5.** Baseline design for the 8 m f/1.2 BSC honeycomb blanks for the Columbus (later LBT) and Magellan projects (from Angel [3.119])

Shape:	plano-concave
f/no:	f/1.2
Diameter:	8 m
Facesheet thickness:	25 mm
Rib thickness:	12 mm
Outer edge thickness:	0.84 m
Inner edge thickness:	0.43 m
Cell shape:	hexagonal
Cell spacing:	193 mm (across faces)
Mass of blank:	14 000 kg

lower thermal inertia of the lightweighted structure giving a time constant of < 1 hour compared with  $\sim 10$  hours for a meniscus. However, this argument assumes it is equally deleterious for mirror seeing if the mirror is too cold or too hot compared with the ambient air, which is not the case – see § 3.6. Furthermore, it neglects the possibility of automatic correction of mirror seeing in fairly rapid cycles – see § 3.5.

Angel introduced the concept of a rotating furnace to spin the upper surface to the right curvature. Figure 3.38 shows the casting process. The quality of the blanks depends on the quality of the mould. The hexagonal cores are made of ceramic fibre held down by silicon carbide bolts.

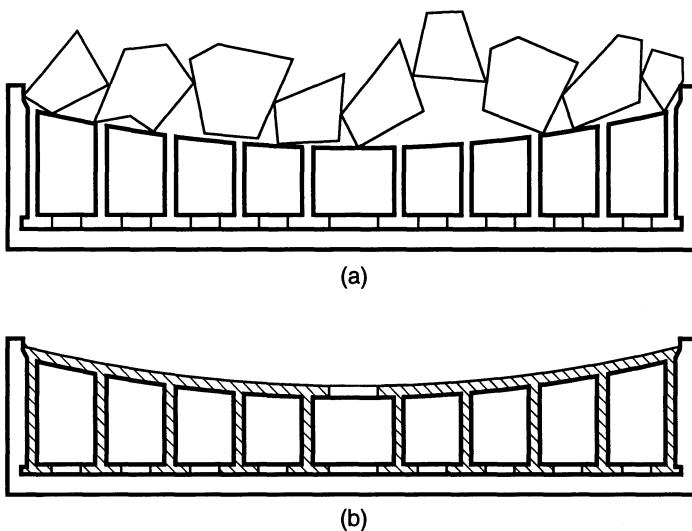


**Fig. 3.38.** Schematic diagram of the honeycomb sandwich casting process: (a) the glass blocks before firing, (b) after melting and spinning (from Angel [3.119])

In 1988, Angel reported [3.119] the successful casting of the first 3.5 m blank. This blank has been successfully polished and is used in the Apache Point telescope.

In 1992 Hill and Angel [3.50] reported the successful casting of the 6.5 m f/1.25 replacement blank for the MMT. The mould manufacture required 13 months. The level of lightweighting is 78 %. Figure 3.39 shows this blank soon after the successful casting.

The Steward Observatory Mirror Laboratory (Fig. 3.40) then prepared to tackle the primary blanks for the Magellan project (2  $\times$  6.5 m) [3.53] [3.122] and for the LBT (earlier Columbus) project (2  $\times$  8.4 m) [3.47] [3.123]. The available height of the test tower makes very fast primaries in this diameter essential: the LBT primaries have a relative aperture of f/1.142 and will be the most aspheric mirrors yet made.

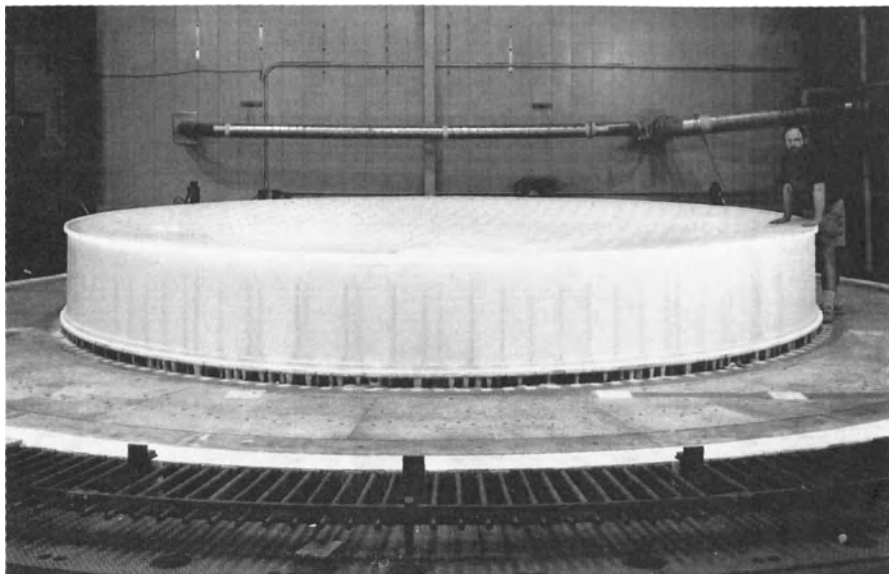


**Fig. 3.39.** The first 6.5 m blank cast at the U. of A. Steward Observatory Mirror Lab in April 1992 for the MMT replacement primary. The steep curvature ( $f/1.25$ ) is evident. The hexagonal blocks of ceramic fibre, here still in the casting, were subsequently removed, leaving a lightweighted blank appreciably less dense than water. (Original photo courtesy Roger Angel)



**Fig. 3.40.** The Steward Observatory facility for manufacturing and figuring lightweighted BSC glass blanks. It was built under the grandstands of the University of Arizona football stadium, which limits the height of the test tower. (Courtesy R. Angel)

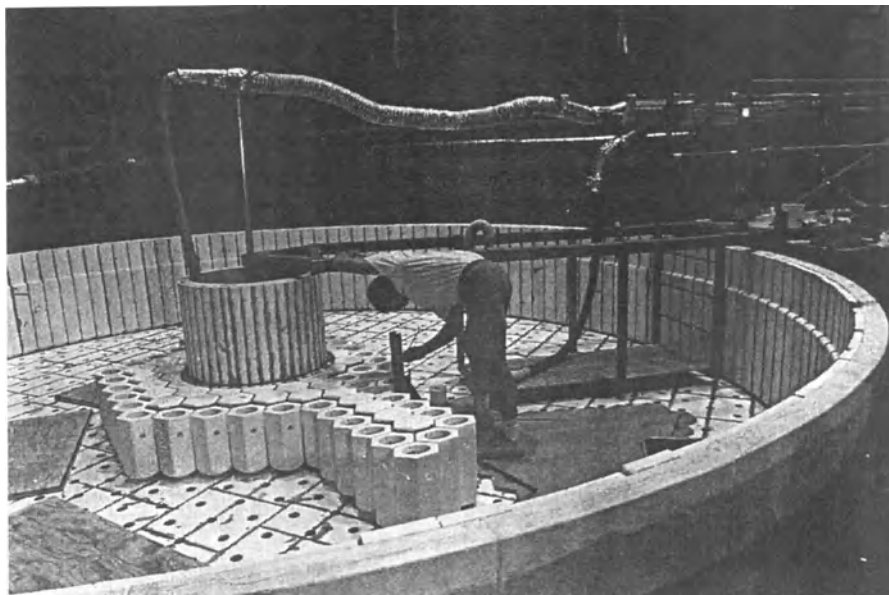


**Fig. 3.41.** Installation of core boxes in the mould of the 6.5 m blank for the MMT conversion (from Hill and Angel [3.50])

Figure 3.41 shows the installation of the core boxes in the mould of the 6.5 m blank for the MMT conversion [3.50]. It reveals the complexity of the mould structure and the remarkable technical ingenuity and care that has led to the successful production of such large honeycomb blanks.

### 3.3.5 Modern blank production in metal

We have referred in § 3.3.1 above to the earlier thermal analyses of Couder and Maksutov which revealed the advantages of metal mirrors from the point of view of conductivity compared with non-zero expansion glasses. This was demonstrated by the “thermal insensitivity”  $q_t$  column in Table 3.4, whereby aluminium is about 1/4 as good as top grade Zerodur. Active correction can easily compensate for this disadvantage. Of more significance today is “thermal diffusivity”  $a_t$ , enabling heat to be removed from the inner parts of a blank by surface cooling. Pure aluminium is the best of all the listed materials. Because of its favourable density and cost, aluminium (pure or alloy) seems the most favourable metal candidate for large primary blanks, though other alternatives may be equally or more interesting for smaller mirrors.

**3.3.5.1 Aluminium blanks.** Apart from the work of Couder and Maksutov referred to in § 3.3.1, no systematic attempt was made to re-introduce metal blanks after the demise of speculum metal about 1870, until Johnson [3.124]

used aluminium blanks for various sized telescopes, including primaries for two 60-inch photometric telescopes, in the 1960s. These telescopes, intended particularly for IR use, had *vase-shaped* primaries which were self-supporting. Johnson did not aim for high quality as his purpose was to produce *low-cost, single-purpose* photometric instruments. The first 60-inch telescope was claimed to give images of 3–4 arcsec at its Cassegrain focus (using a Pyrex secondary), the second one to give a stable quality of 1–2 arcsec [3.125] [3.126]. Forbes [3.127] also reported good results on a 40-cm lightweighted welded-segment aluminium alloy mirror. It seems that these bold and far-sighted experiments subsequently backfired because of considerable warping of the primaries, above all, as is to be expected, in the astigmatic mode. This was apparently in contradiction with Forbes' and Johnson's earlier published results [3.126], and was particularly unfortunate because it gave "metal" a bad reputation in the USA at a time when the field was wide open for further systematic development. In hindsight, it seems that the choice of a vase-shaped blank in aluminium alloy (i.e. changing not only the material but also the form of conventional glass blanks) was over-ambitious in the era of purely passive telescopes.

In 1969, a 1.37 m telescope with a solid primary of pure aluminium and 150 mm thickness went into operation in Merate, Italy. This design, due to Mottoni [3.128], was remarkable for its careful, logical concept and execution. The telescope was tested after 14 years of continuous use by an ESO team [3.129] and found to have an optical quality quite comparable to similar telescopes with glass mirrors. Only the lowest spatial frequency mode (astigmatism) showed a significant coefficient (about  $1\lambda \sim 500\text{ nm}$ ) which *might* have been partly due to a small amount of warping, but even this could not be proven compared with its original state. Even had the whole astigmatic effect been due to warping, its correction by an active support would today be trivial (see § 3.5).

The original definitions of the ESO 3.5 m NTT [3.69], as discussed in § 3.2.4 above, envisaged an aluminium primary as well as the Zerodur primary. The rationale was that the *active optics* concept of the NTT represented the logical partner for a *metal mirror*, since warping of a solid blank would be in a low spatial frequency mode (above all astigmatism as in the Johnson telescopes) and would be easy to correct actively. Nevertheless, since the extent of warping with aluminium and its alloys was a largely unknown quantity and the dynamic range of active correction must be defined by reasonable limits, it was decided to perform systematic thermal cycling tests on model blanks. The tests were performed on 18 blanks of 500 mm clear diameter made of either "pure" aluminium (99.5 %) or various standard types of alloys, and by various manufacturing techniques [3.130]. The blanks were given a standard concave spherical figure on a Canigen (chemically deposited nickel) coat for ease of testing and compared with a reference (uncycled) Zerodur mirror. Details of the thermal cycling regime and results of the figure deformations were given by Noethe et al. [3.131] [3.132]. Three types of cycle were applied:

“soft” with a temperature range from  $-5$  to  $+25$  °C; “hard” with  $-20$  to  $+50$  °C; “very hard” with  $-30$  to  $+90$  °C. One soft cycle was performed, a total of 50 hard cycles in seven groups of tests, and one very hard cycle. An interesting general result (in contrast with the vase-shaped mirrors of Johnson) was that warping was mainly in the axisymmetrical mode (defocus and spherical aberration). Some mirrors warped significantly with the soft cycle but stabilized with further warping during the hard cycles. Other mirrors warped mainly with the very hard cycle. Full details are given in [3.132]. The general conclusion was that a number of such blank compositions and production processes can give entirely satisfactory results provided correct heat treatment is applied to release stresses. Yoder [3.133] has emphasized the advantage of cycling to much *lower* temperatures than those used in the above experiments.

As a result of these experiments, offers were solicited for a 3.5 m blank in “pure” aluminium for the NTT. Perfectly valid offers were received, both for production by casting and forging; also for the deposition of nickel layers both by chemical means (Canigen) and electrolytic means. The costs were only about 35 % of those of Zerodur and the leadtime only about 50 % including nickel coating and extra transport. Furthermore, optical figuring costs would have been only marginally higher than for Zerodur, although the preparation of the aluminium blank surface prior to nickel coating is a delicate matter to prevent “breakthrough” of the relatively thin (at that time 400 µm thickness was envisaged) coating during figuring.

As mentioned in § 3.2.4, the aluminium primary was abandoned in the NTT solely for organisational, *not* technical reasons. This was above all because the investigative work for aluminium had absorbed considerable time which could not be pulled back by the shorter manufacturing time, since the Zerodur blank had been ordered much earlier. A proposal to order the aluminium blank on the VLT budget, as an intermediate step to an 8 m aluminium blank, was not accepted, partly because interest had switched more to stainless steel, which does not require a nickel coat (see § 3.3.5.2). Apart from this technical simplification, a possible bi-metallic effect between aluminium and nickel [3.127] is avoided.

Later, ESO reverted to aluminium as the best reserve alternative to glass ceramic for the 8 m VLT primaries. Experiments were performed with two 1.8 m diameter aluminium blanks, one manufactured by electron-beam (EB) welding of 4 quarter segments and the other by “build-up” (BU) welding, a process proposed by Mischung [3.110] [3.134] for the manufacture of stainless steel blanks but later applied with great success to aluminium. This work is described by Dierickx and Zigmann [3.135]. Build-up welding consists of building up a cylindrical blank by continuous deposition of a welding seam while rotating the blank. Figure 3.42 shows a 500 mm BU aluminium blank. It was concluded that either the BU or the EB process could be successfully extrapolated to 8 m. Either process should yield excellent homogeneity. The

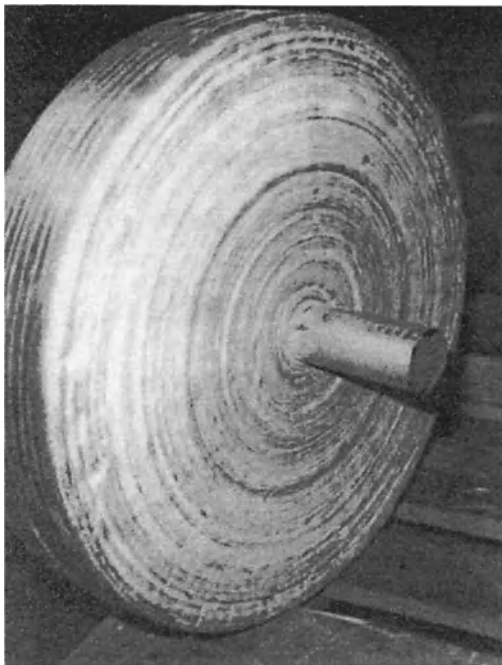


**Fig. 3.42.** A “built-up” (BU) welded blank in aluminium with a diameter 500 mm (from Dierickx and Zigmann [3.135])

EB process uses forged segments which show optimum homogeneity and very low porosity.

Independently of the ESO experiments for the VLT, this technology was pursued within the framework of multi-national EUREKA funding in the EC under the name of the LAMA project (Large Active Mirrors for Astronomy) managed by TELAS, a subsidiary company of Aérospatiale in France, in association with INNSE/TECNOL in Italy and REOSC/ONERA in France. The purpose of LAMA was to deliver a complete active mirror package.

The two 1.8 m blanks for the ESO VLT experiments had a thickness of 300 mm, flat backs and a spherically-machined front surface of  $f/1.67$  ( $r = 6$  m). After annealing and cryogenic stabilization, there followed rough grinding by REOSC and nickel coating by TECNOL (thickness ca.  $100 \mu\text{m}$ ). The surfaces were then fine ground and figured by REOSC to a modest spherical quality. This was sufficient, as the requirement was not top figuring quality but only precise measurement of the *differences* resulting from thermal cycling. The surface quality of the polished nickel was in all respects as good as glass.

Thermal cycling was done with cycles between  $-20$  and  $+40^\circ\text{C}$  over about 24 hours. Both mirrors underwent 32 cycles with interferometric measurements after 0, 4, 8, 16 and 32 cycles. Figure 3.43 shows the initial and final figures, and (what is the most important) the *difference* of the figure between 0 and 32 thermal cycles. The higher order results represent the figure after

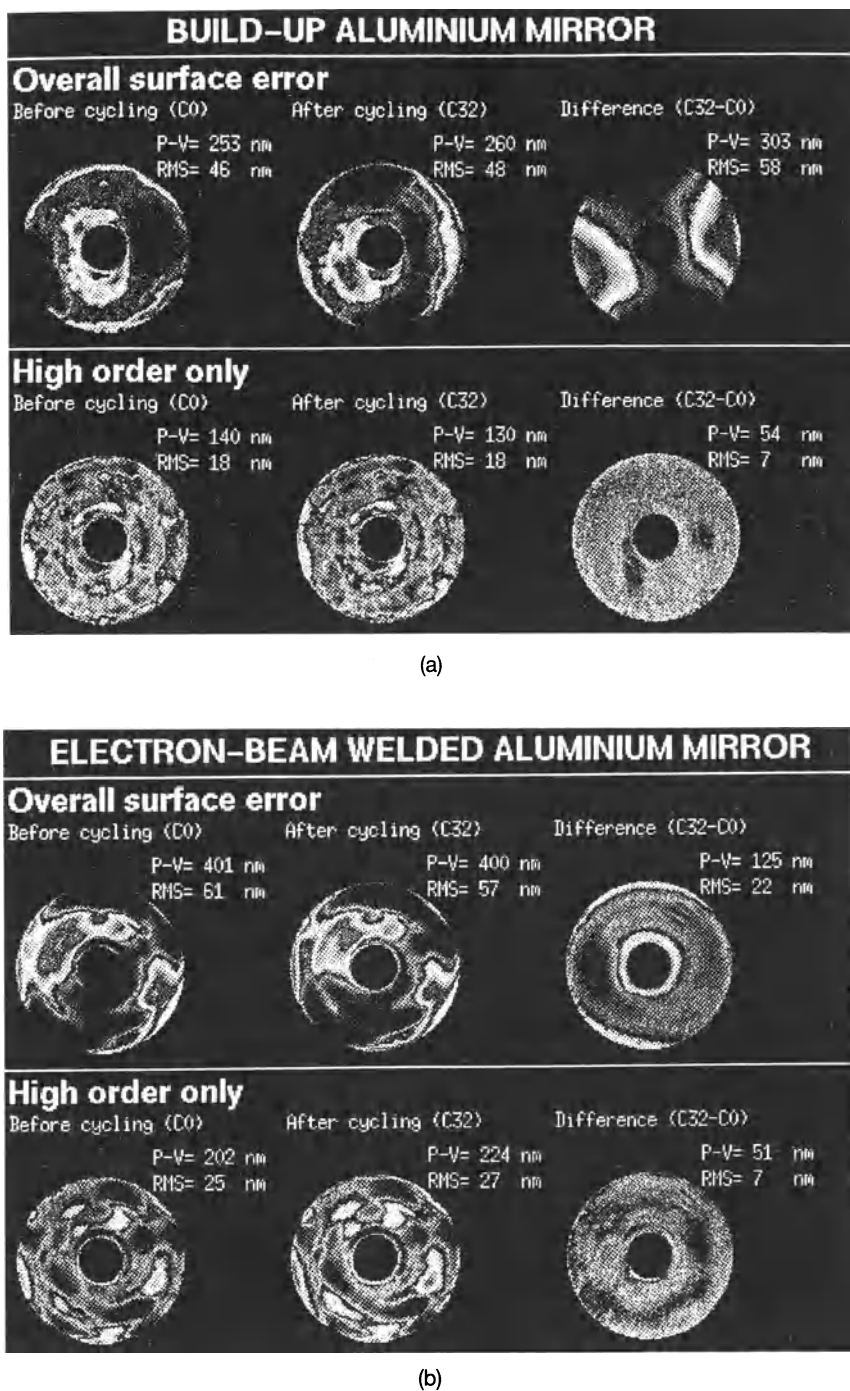


**Fig. 3.43.** Thermal cycling experiment at REOSC (Paris) on two 1.8 m aluminium blanks showing the interferometric figure before cycling, after 32 cycles and the difference. (a) BU welded blank. (b) EB welded blank. (From Dierickx and Zigmann [3.135])

mathematical removal of third order and fifth order errors. The conclusion is that both mirrors remain stable to  $\lambda/25$  rms for the overall surface errors and to  $\lambda/70$  rms for the higher order surface errors. Nearly all the variation occurred in the first cycles. The lower order errors can easily be corrected actively. Furthermore, it is estimated [3.135] that inhomogeneities in the expansion coefficient  $\alpha_t$  up to 5 % (a very large tolerance) would produce lower order effects which could be corrected actively.

There is clear evidence that aluminium technology for large blanks has reached an advanced stage of development. Up to 4 m, classical methods can be used and the modern variants of BU and EB welding can be used both for smaller blanks and large blanks without apparent limit. The astronomical community has always been cautious in adopting radical new technologies, but it seems that aluminium is poised for a major take-off. This will be initiated by the first 4 m class blank. The key to the successful application of aluminium to large primaries remains active optics control, as is fully accepted by the LAMA project. One of the most attractive features for very large blanks, as was recognised by the Gemini project for its 8 m blanks, is the higher security in handling compared with glass. The problem for a positive decision in favour of aluminium was the lack of proof in practical function of an intermediate blank size, say 4 m.

Further discussion of aluminium is given in a general summing-up on the use of metal for mirrors in § 3.3.5.4.

**3.3.5.2 Stainless steel blanks and other iron variants.** The use of stainless steel was pursued most systematically by Maksutov, as discussed in § 3.3.1, culminating in the 0.7 m stainless steel primary for Pulkowa [3.109]. Unfortunately, little systematic information on the stability of this mirror is available although it has been in operation for over 30 years.

A detailed analysis of the possibilities of stainless steel for large blanks was carried out by Mischung [3.110] [3.130], above all using BU welding for the manufacture, a well-known procedure for the manufacture of large pressure vessels in stainless steel. Metallurgical aspects of stainless steel are extremely complex, in their nature more so than for the aluminium alloys considered for telescope blanks. *Austenitic* stainless steels have a higher content of Cr and Ni than *ferritic* stainless steels. As Table 3.4 shows, the higher the alloy content of other elements compared with pure Fe, the higher the degradation of the thermal criteria  $a_t$  and  $q_t = a_t/\alpha_t$ , for austenitic stainless steels by a factor of about 5. For this reason, ferritic or martensitic stainless steels are preferable and are probably more stable. But even ferritic stainless steels have a thermal diffusivity  $a_t$  about 13.5 times worse than pure aluminium. Invar (36 % Ni) is 28 times worse, though its low expansion  $\alpha_t$  gives a comparable criterion  $q_t = a_t/\alpha_t$ . Invar seems of little interest compared with stainless steel. An even bigger disadvantage for very large blanks is the high density  $\rho_t$  which is nearly 3 times higher than that of pure aluminium. The inferior parameters  $\rho_t$  and  $a_t$  are the price one pays for the advantage of a directly polishable

surface, without a separate coat, and the *cost* advantage: for a given volume, stainless steel is the cheapest of all potential mirror blank materials.

If the weight of a thin, solid stainless steel blank is acceptable and active optics control is available, it may be a very attractive solution. Unfortunately, this is likely to be limited to blanks of diameter up to the order of 2 m. Beyond this, lightweighting becomes increasingly desirable. Young's modulus of stainless steel is about 3 times higher than that of pure aluminium, but this is almost exactly offset by the increase of density.

The experiments on thermal cycling of aluminium test blanks were repeated at ESO in modified form for stainless steel blanks, for the VLT programme, as reported by Enard et al. [3.134]. Some of these had only moderate lightweighting (cylindrical holes) while others had high lightweighting with finer structures. Those blanks with moderate lightweighting, which approximated to solid blanks, gave reasonably satisfactory results with modest warping largely in correctable low spatial frequency modes. But the highly lightweighted, finely structured blanks gave poor results with sharp high spatial frequency discontinuities. It was concluded that *fine-structured* stainless steel blanks, which would be essential for the VLT 8 m blanks because of the weight, were unsatisfactory without major further development and improvement in stability. For the VLT programme, interest therefore reverted to aluminium as the only viable fall-back solution compared with glass.

Nevertheless, stainless steel retains its interest in certain cases because of its low cost. For example, Lemaître and Wilson [3.136] proposed a stainless steel primary of diameter 1.8 m and thickness 40 mm (aspect ratio = 45) for the VLT auxiliary (interferometric) telescopes, to be made by stress polishing with tolerance relaxation for active optics control. The cost (July 1992) of the stainless steel meniscus blank from the firm Ferry-Capitain in France was about DM 22 200, almost an order of magnitude lower than that of a Zerodur blank.

Finally, the possibility investigated by Couder [3.105] and mentioned in § 3.3.1, of using cast iron covered with a layer of enamel (flint glass) should be borne in mind, since the thermal properties of pure iron are much superior to stainless steels and it is far cheaper. But the limitations of the enamelling process for reasonably sized mirrors would require further investigation.

**3.3.5.3 Beryllium blanks.** Reference to Table 3.4 reveals that beryllium has excellent thermal properties and easily the best mechanical stiffness  $E/\rho_t$  of all the materials listed. It suffers from two major disadvantages: very high cost and the poisonous nature of powder residues from machining or figuring. Its main application will probably be in space optics of modest dimensions. Even there, the advantage over lightweighted aluminium or zero expansion glasses may be too limited unless there are further technical breakthroughs. A further serious rival is silicon carbide (see § 3.3.6).

After an early preference for silicon carbide, beryllium was finally chosen for the *secondary* mirrors of the VLT 8 m telescopes. The excellent features

of low density and high mechanical stiffness (Table 3.4) were decisive in this case where servo oscillations up to about 15 Hz are envisaged for technical purposes (see § 3.3.6 below). The polishing and figuring of the Canigen coat has now (August 1997) been successfully completed for the first secondary by REOSC. According to Dierickx [3.137], the figure achieved in the *active mode* (i.e. the high spatial frequency quality) is 16 nm rms, an excellent result for such an aspheric mirror of 1.13 m diameter. This success could well bring beryllium into more general favour for the secondaries of modern ground-based telescopes.

**3.3.5.4 Summary of the situation regarding the use of metal for mirrors.** A conference was held in London in November 1992 specifically on the possibilities of the use of metal mirrors, particularly of appreciable size. The proceedings, edited by Bingham and Walker [3.138], still represent the best summary of the current situation. The main emphasis was on *aluminium*, with a number of excellent contributions, for example by Rozelot [3.139], Dierickx [3.140] and Bingham [3.141]. Stainless steel was discussed by Lemaître et al. [3.142] in the framework of the proposal of [3.136]. The general viewpoint of the contributors was that aluminium, above all in combination with active optics, was a perfectly viable candidate for mirrors up to about 4 m diameter and possesses significant thermal advantages over glass. A successful aluminium mirror of the 4 m class would provide the essential stepping stone to an 8 m aluminium mirror. The barriers to the use of aluminium are not technical but *psychological*, as discussed by Bingham et al. [3.143]. It is the same conservatism of the ground-based astronomical community which resisted the *inverse* switch from speculum metal to glass at the time of the Melbourne reflector (see RTO I, pages 410–414); or, more recently, the switch from the equatorial back to the alt-az mount, finally implemented by the Russian 6 m telescope (see RTO I, page 433). However, the increasingly negative funding situation, particularly in Europe, for new projects since 1992 may also have contributed to the fact that no 4 m project with an aluminium mirror has yet (1997) been launched.

### 3.3.6 Compacted powder, sintered or vapour-deposited materials for blanks

For smaller mirrors, above all for secondaries up to about 1.5 m diameter, a most interesting candidate for blanks has been recently developed in the form of *silicon carbide* (SiC). The possible application of this material to the active secondary mirrors of the ESO VLT 8 m telescopes has been considered in detail by Dierickx et al. [3.144]. The  $M_2$  units of the VLT are complex units with four active functions: focusing, active centering (coma) correction, IR chopping and field stabilization (fast tracking). The first two functions only require changes at a moderately slow rate; but chopping has square wavefront modulation at 0 to 5 Hz and field stabilization a sinusoidal modulation at 0 to

15 Hz. The two latter functions place severe demands on the mass, moment of inertia and stiffness of  $M_2$ . The size in the VLT case has been kept to a minimum by making it the pupil of the telescope: its full diameter is 1126 mm and the free diameter 1116 mm.

The manufacture of SiC blanks has been analysed in studies for ESO [3.145]. The two most interesting processes appear to be:

- a) *Chemical Vapour Deposition (CVD)*: This occurs in a vacuum chamber at about 1300 °C and produces potentially 100 % dense SiC. Lightweighted structures are produced in three steps:
  - An SiC layer is deposited on to a contoured graphite mandrel (up to 1 cm thick). This is interrupted, and
  - A graphite egg-crate structure is inserted on the back face of the layer.
  - The deposition is re-initiated to form a layer on the egg-crate structure which also bonds it to the first layer.
  - The graphite core is leached out by thermal methods after exposure by machining.

This process gives excellent structural properties, but only allows an open back. The CVD microstructure is polycrystalline and can be polished to  $\ll 10 \text{ \AA rms}$ . The hardness is much higher than glass ceramic and requires a pressure 4 times as high.

- b) *Siliconized SiC*: This process involves:
  - Fabrication of a pre-sintered green body (SiC grains or SiC grains plus free carbon) by processes called isostatic pressing, press moulding or slip casting, followed by sintering.
  - Infiltration with silicon at a temperature considerably higher than the melting point of Si.

Table 3.4 gives the physical properties of SiC as produced by CVD and siliconized SiC. Both thermally and mechanically, it is one of the best materials, fully comparable with beryllium. Environmentally, its stability is reported to be excellent, even after thermal cycles involving hundreds of degrees Celsius. Because of the limited number of existing samples, the question of temporal stability is not yet fully answered, but current data is favourable.

Mirror designs for the VLT secondary lead to a mass of 35 kg and an inertia of  $2.8 \text{ kg m}^2$  for a CVD solution (face sheet 4 mm thick and total thickness 125 mm), and corresponding figures of 20.5 kg and  $1.52 \text{ kg m}^2$  for the favoured “open tapered back” solution of the three siliconized SiC solutions investigated. These figures are to be compared with 100 kg and  $10 \text{ kg m}^2$  for a 75 % lightweighted glass ceramic mirror.

Optical figuring of such steep aspheric mirrors in SiC is by no means trivial, but the problems are considered soluble with known techniques and profiting from active optics tolerance relaxation (see § 3.5) [3.146].

Dierickx et al. [3.144] give the calculated mechanical and optical performances of the mirror and support system. The first eigenfrequencies of the

two possibilities are 602 and 691 Hz respectively. The estimated optical quality is 0.09 arcsec rms and 0.10 arcsec rms respectively, *after active correction*. Before active correction, the figures are 0.30 arcsec rms and 0.68 arcsec rms respectively.

The positive conclusion is that an SiC secondary for the VLT could yield comparable optical quality to that of a glass ceramic mirror; but is about 4 times more favourable in mass and inertia. Although the SiC mirror itself is more expensive than glass ceramic, it simplifies the design of the support unit because of its favourable mechanical properties: the total cost may therefore not be less favourable.

In spite of these favourable prospects of SiC for the VLT secondary mirrors, subsequent procurement problems and the uniformly excellent mechanical and thermal properties of beryllium led to a decision in favour of the latter.

### 3.3.7 Lightweight composite materials for blanks

The most interesting work in this area is in carbon fibre reinforced plastic (CFRP) and was described in some detail in § 3.2.4, above all in connection with the 1.5 m HPT development, using a hybrid of CFRP and Zerodur. The earlier form of Dornier had used the CFRP substrate directly with an evaporated aluminium coating. This work was applied later to space projects (FIRST and SOFIA).

### 3.3.8 Liquid mirror telescopes (Hg)

The technique of producing automatically a paraboloidal primary by rotating a bowl of mercury was first suggested and practised by Wood in 1908 [3.147] [3.148]. By varying the angular velocity, the focal length  $f'$  can be varied at will according to the formula [3.149]

$$f' = g/2\omega^2 , \quad (3.11)$$

where  $g$  is the acceleration due to gravity and  $\omega$  is the angular velocity in rad/s. It is easily shown that the balance of gravity and centrifugal force at right angles produces a perfect paraboloid. The levelling is very critical, an error producing a travelling wave on the surface. Wood also recognised that the stability of the angular velocity  $\omega$  was also very critical. Variations critically affect the focus, as is clear by differentiating Eq. (3.11), but also introduce travelling waves through the accelerations involved. Wood used a 20-inch flat-based pan with rubber drive through a magnetic clutch, the whole being placed in a well, 15 feet deep. At 12 rpm,  $f'$  was 15 feet according to Wood [3.148] but the correct value should have been 10.19 feet according to Eq. (3.11). Wood's principal problem was the variation of angular velocity  $\omega$ , causing ripples. These were damped fairly successfully with a glycerine layer on the mercury, giving resolution better than 5 arcsec. He observed the moon

and other objects using a 20 inch siderostat-type flat mirror, but recognised the serious limitation of the fixed vertical axis. Wood also suggested using a roughly paraboloidal pan with a thin mercury layer.

Liquid mirror telescopes (mercury) have recently been investigated more thoroughly by Borra et al. [3.149]. They are inevitably limited to a vertical axis and Borra et al. propose to use mercury primaries up to 1.2 m at f/4.58 in a drift-scan mode using a CCD. Their experiments were mainly carried out using a simple, fixed automatic film camera in the drift mode giving linear star trails with integrations of 2 minutes. The best images have been about 2 arcsec FWHM, about the limit of seeing at an indifferent site. On a 1 m mirror, knife edge tests were made in 1985 showing that the central part was of good quality. Ripples with amplitude  $< \lambda/10$  were detected. The angular velocity of the mirror should be stable to better than 1 part in  $10^6$ . Since they had no field corrector, the appreciable field coma at f/4.58 (3.3 arcsec at semi-field angle 6.17 arcmin) was a serious problem; also focusing performed visually with an eyepiece. Wind disturbance of the liquid mirror was prevented by covering it with a mylar sheet, but this increased the wings of the image because of high spatial frequency errors. Damping with oil films was also being investigated.

The authors viewed the work on natural stars to be a supplement to optical-shop tests. It seemed highly desirable to perform such tests in a modern form at the center of curvature using a null system and fixed artificial source to establish the real quality of the mirror surface in quantitative terms. Reference was made to a performance goal of 0.5 arcsec but there was no quantitative evidence to support that this is possible. It is claimed that limitations from the Earth's curvature and Coriolis forces would allow diameters up to 30 m.

The latest report (1996) [3.150] of this group's research into liquid mirror telescopes reveals most impressive progress, especially in state-of-the-art testing of the liquid surfaces with null systems at their centers of curvature. An interferogram of a 2.5 m mirror working at f/1.2 shows excellent quality with exposures of 1/60 s. This short exposure can detect rapid liquid movements, but makes the interferogram sensitive to seeing. Nevertheless, the rms wavefont quality is  $0.050\lambda$  with  $\lambda = 633$  nm. Artificial star images are clearly diffraction limited. Ideally, the rotation axis should coincide with gravity within 0.25 arcsec, though 1 arcsec may be tolerable. The authors have explored the possibilities of wide-field correctors of a type proposed by Richardson and Morbey [3.151] using 2 mirrors to correct the fixed parabolic primary. (These are wide-field solutions of the same basic type as some of those discussed in § 3.6.5 of RTO I, but used in inclined – off-axis – form.) They show a typical solution for a 4 m liquid f/5.25 mirror observing at a zenith distance (field angle) of  $7.5^\circ$  and having a field of view of 18 arcmin. They also use the technique of electronically stepping the pixels of a CCD, called time delay integration (TDI), for imagery, narrow band filter spectroscopy or slitless spectroscopy. An impressive CCD image, 5 arcmin wide,

is shown as observed with a 3 m liquid mirror telescope built by NASA. This reached about  $23''$  with an effective 100 s exposure and shows faint galaxies and stars. A 2.6 m LIDAR facility at the University of Western Ontario is also mentioned.

In view of the rapid advances that have been made in the manufacture of conventional solid mirrors in glass and other materials in the past decade, one should be cautious at this stage regarding the possibility of mercury mirrors becoming a major competitor in telescopes of the largest sizes. For a fixed primary, the “rotating shoe” form discussed in § 3.2.1 with a spherical primary scanned by a secondary arrangement, or the Hobby-Eberly telescope solution are likely to be more flexible and cost-effective for very large sizes than a fixed, vertical-axis paraboloid.

## 3.4 Mirror support systems in modern telescopes

### 3.4.1 The basic laws of axial supports for mirrors

The subject of mirror supports *during manufacture* was discussed in § 1.2.2.6. While there are common aspects in supporting the weight of the mirror against gravity with axis vertical, this case is both simpler and more complex than the general problem of support in a functioning telescope: it is simpler because the installation is fixed without tilt and no gravity edge support is required, but more difficult because lapping tool pressure and friction effects must be taken into account.

The basic law (Eq. (3.2)) concerning the flexure of mirror blanks under their own weight was given in 1931 by Couder [3.7] and its general significance was discussed in § 3.1. We must now consider the origin of this Couder Law.

The essential theory of the symmetrical bending of thin cylindrical circular plates, mounted with axis vertical and loaded symmetrically with regard to that axis, is given by Timoshenko and Woinowsky-Krieger [3.152], from which the following treatment is taken. Since the loading is axisymmetric, the deformation  $\omega$  is also axisymmetric. The solution was first given by Poisson in 1829 [3.153]. Following the notation of [3.152], it is shown for the situation of Fig. 3.44 (circular plate supported at its edge) that the differential equation

$$\frac{1}{r} \frac{d}{dr} \left\{ r \frac{d}{dr} \left[ \frac{1}{r} \frac{d}{dr} \left( r \frac{d\omega}{dr} \right) \right] \right\} = \frac{q}{D_E} \quad (3.12)$$

applies, where  $r$  is the radius of a zone whose deflection is  $\omega$ ,  $q$  is the intensity of the load distributed over the plate, an axisymmetrical function of  $r$  to be defined, and  $D_E$  is defined by

$$D_E = \frac{Et^3}{12(1 - \nu^2)} , \quad (3.13)$$

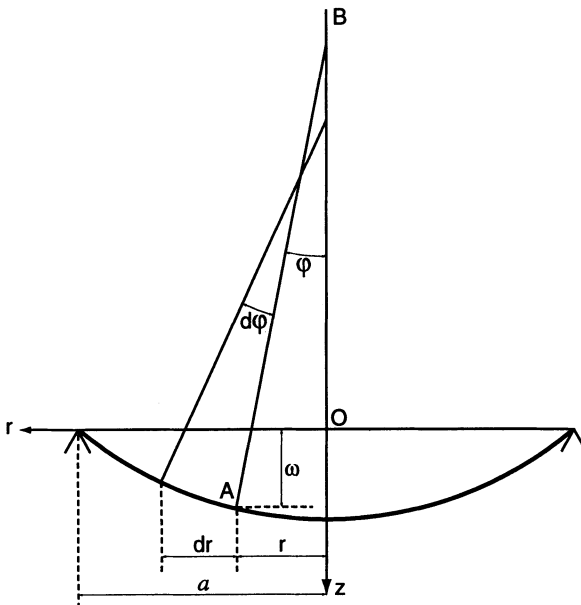


Fig. 3.44. Symmetrical bending of a thin cylindrical plate under an axisymmetric force (after Timoshenko, Woinowsky-Krieger [3.152])

where  $E$  is Young's modulus,  $\nu$  Poisson's ratio and  $t$  the thickness. At this stage, we assume the weight of the plate is negligible and that the axisymmetrical pressure distribution is produced by external means. The equation (3.12) can easily be integrated if the intensity  $q$  of the load is given as a function of  $r$ . Let  $Q$  be the basic vertical shearing force per unit length of a cylindrical section of radius  $r$ . Then the relation between  $Q$  and  $q$  is defined by

$$Q 2\pi r = \int_0^r q(r) 2\pi r \, dr , \quad (3.14)$$

where  $q(r)$  is a function of  $r$  in the general case. If we apply the restriction that the load intensity  $q$  is *constant* over the entire surface of the plate, i.e. a *constant pressure*, then (3.14) simplifies to

$$Q = q \frac{r}{2} \quad (3.15)$$

Triple integration then gives

$$\omega = \frac{qr^4}{64D_E} + \frac{C_1 r^2}{4} + C_2 \log_e \frac{r}{a} + C_3 , \quad (3.16)$$

for which the constants of integration  $C_1, C_2, C_3$  can be calculated for various defined cases. The case of a circular plate with horizontally clamped edges is important for many applications, but the case of interest for telescope mirrors is a *circular plate with freely supported edges*, which reduces to

$$\omega = \frac{q(a^2 - r^2)}{64D_E} \left[ a^2 \left( \frac{5+\nu}{1+\nu} \right) - r^2 \right] , \quad (3.17)$$

where  $a$  is the radius of the plate. Inserting  $r = 0$  gives the maximum deflection  $\omega_{max}$  at the center as

$$\omega_{max} = \frac{qa^4}{64D_E} \left( \frac{5+\nu}{1+\nu} \right) , \quad (3.18)$$

which, combined with (3.13), gives finally

$$\omega_{max} = \frac{3}{16} \frac{q}{E} (1-\nu^2) \left( \frac{5+\nu}{1+\nu} \right) \frac{a^4}{t^3} \quad (3.19)$$

for the case of the freely supported plate of negligible weight *under an external uniform pressure*  $q$ . The deflection therefore varies as the fourth power of the diameter and the inverse cube of the thickness. Equation (3.19) is the same as that given by Couder [3.154].

Following Couder, the case of Eq. (3.19) can be adapted at once to the case of a thin cylindrical plate supported freely at its edge and *deforming under its own weight*. The pressure  $q$  is then given by

$$q = g\rho t , \quad (3.20)$$

where  $g$  is the acceleration due to gravity and  $\rho$  the density. Combining (3.19) and (3.20) gives *Couder's Law* (Eq. (3.2)) for the flexibility due to gravity of a cylindrical mirror blank:

$$\omega_{max} = \frac{3}{16} \frac{g\rho}{E} (1-\nu^2) \left( \frac{5+\nu}{1+\nu} \right) \frac{a^4}{t^2} \quad (3.21)$$

The flexibility *under gravity* varies as the fourth power of the diameter and the inverse square of the thickness.

Timoshenko and Woinowsky-Krieger also treat the case of a thin circular plate of negligible weight exposed to a total load  $P$  applied uniformly over a narrow annulus of radius  $b$  (Fig. 3.45). The vertical shearing forces  $Q_1$  per unit length of the annulus are given by

$$Q_1 = P/2\pi b \quad (3.22)$$

To determine the deflection, the plate is divided into two zones, as shown by (b) and (c) in Fig. 3.45. The inner zone with  $b > r > 0$  is in a state of pure bending produced by the uniformly distributed moments  $M_1$ , while the outer zone with  $b < r < a$  is deformed by the moments  $M_1$  and the shearing forces  $Q_1$ . The authors derive the following expressions for the deflections of the outer and inner zones  $o$  and  $i$  of the plate respectively:

$$\omega_o = \frac{P}{8\pi D_E} \left\{ (a^2 - r^2) \left[ 1 + \frac{1}{2} \left( \frac{1-\nu}{1+\nu} \right) \left( \frac{a^2 - b^2}{a^2} \right) \right] + (b^2 + r^2) \log_e \frac{r}{a} \right\} \quad (3.23)$$

$$\omega_i = \frac{P}{8\pi D_E} \left\{ (a^2 - b^2) \left[ 1 + \frac{1}{2} \left( \frac{1-\nu}{1+\nu} \right) \left( \frac{a^2 - r^2}{a^2} \right) \right] + (b^2 + r^2) \log_e \frac{b}{a} \right\} \quad (3.24)$$

Following Couder [3.154] and substituting for  $D_E$  from (3.13), these equations can be written in the more revealing form for our purpose

$$\omega_{o,i} = \frac{3}{4\pi}(1-\nu^2)\frac{P}{E}U_{o,i}\frac{a^2}{t^3}, \quad (3.25)$$

with

$$\left. \begin{aligned} U_o &= 2(1 - \xi_E^2) + \left( \frac{1 - \nu}{1 + \nu} \right) (1 - \xi_E^2)(1 - \zeta_E^2) + 2(\xi_E^2 + \zeta_E^2) \log_e \xi_E \\ U_i &= 2(1 - \zeta_E^2) + \left( \frac{1 - \nu}{1 + \nu} \right) (1 - \xi_E^2)(1 - \zeta_E^2) + 2(\xi_E^2 + \zeta_E^2) \log_e \zeta_E \end{aligned} \right\}, \quad (3.26)$$

where  $\xi_E$  and  $\zeta_E$  are the normalized, dimensionless measures of the zonal radius and annular radius where the force  $P$  is applied:

$$\left. \begin{aligned} \xi_E &= r/a \\ \zeta_E &= b/a \end{aligned} \right\} \quad (3.27)$$

Equation (3.25) shows the third fundamental law of dependence of the deformation of a thin circular plate, whose weight is neglected and is freely supported at the edge. For a force  $P$  applied uniformly over a thin annulus (axisymmetrically), the deformation of any zone is proportional to the square of the diameter and the inverse cube of the thickness.

Suppose the annulus over which the force  $P$  is applied is reduced in radius so that  $b \rightarrow 0$ . Then  $Q_1$  in (3.22) becomes indeterminate, but  $P$  can remain finite and unchanged as a force at the axial point  $O$  in Fig. 3.45. Then the deformation is given by (3.25) with the simplification that  $\zeta_E$  in (3.26) becomes zero and only the outer zone corresponding to  $\omega_o$  and  $U_o$  remains. So the dependency of  $\omega_o$  on  $Pa^2/t^3$  is also true for a single symmetrical point force. The maximum deformation resulting at the center due to a point force  $P$  at that point is given from (3.25) by setting both  $\xi_E$  and  $\zeta_E$  equal to zero in (3.26) giving

$$(\omega_o)_{b=0}^{\max} = \frac{3}{4\pi}(1-\nu^2)\frac{P}{E} \left( 2 + \frac{1-\nu}{1+\nu} \right) \frac{a^2}{t^3} \quad (3.28)$$

If now, again following Couder [3.154], we consider the case of a thin cylindrical plate (mirror) supported freely at its edge and sagging with gravity under the uniform pressure of its own weight according to the Couder Law (3.21), we can now apply the result of (3.25) to the supplementary deformation produced by the free ring support round its edge with  $b = a$  (Fig. 3.45). Clearly, this must be zero because the reaction of the ring support balances the weight, giving a zero shearing force. The reaction force  $P$  applied upwards at the edge is simply the weight of the mirror, so that

$$P = -g\pi a^2 \rho t \quad (3.29)$$

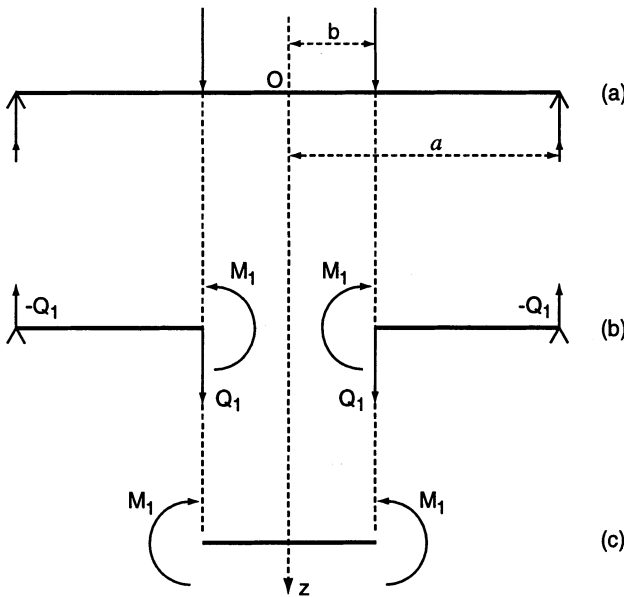


**Fig. 3.45a–c.** Deformation of a thin circular plate of negligible weight, freely supported at the edge and loaded axisymmetrically at a thin annulus by a total force  $P$  (after Timoshenko and Woinowsky-Krieger [3.152])

We now only have the internal zone and the supplementary deformation induced by the edge ring support is from (3.25) and (3.29)

$$(\omega_i)_{b=a} = -\frac{3}{4}(1-\nu^2)\frac{g\rho}{E}(U_i)_{b=a}\frac{a^4}{t^2} = 0 \quad , \quad (3.30)$$

since  $(U_i)_{b=a} = 0$  from (3.26). This supplementary term must be zero with  $b = a$ , since the sag of the plate for this case was completely described by the uniform gravity pressure effect for a free edge support by (3.21).

The general form of the deformation due to its own weight from the uniform pressure of gravity with a free edge support was given above by Eq. (3.17). Using the normalized parameters of (3.27), this can be immediately converted to the more convenient form of Couder

$$\omega_g = \frac{3}{16}\frac{g\rho}{E}(1-\nu^2)V\frac{a^4}{t^2} \quad , \quad (3.31)$$

where

$$V = \xi_E^4 - \left(\frac{6+2\nu}{1+\nu}\right)\xi_E^2 + \left(\frac{5+\nu}{1+\nu}\right) \quad (3.32)$$

The final form of the plate, sagging under gravity while supported by a sharp ring *not* placed at its edge ( $b < a$ ) is given by the combined effect of the deformation with a free edge support  $\omega_g$  according to Eq. (3.31) with the supplementary effect of the upward reaction of the ring to the weight.

The supplementary deformation  $\omega_s$  of the plate is given by substituting for  $P$  from (3.29) in (3.25) giving, as in (3.30)

$$\omega_s = -\frac{3}{4}(1-\nu^2)\frac{g\rho}{E}U_{o,i}\frac{a^4}{t^2} \quad (3.33)$$

The two deformations  $\omega_g$  and  $\omega_s$  can be combined by *linear superposition*, an important principle introduced by Saint-Venant as a consequence of the linear nature of Hooke's Law [3.155 (a)]. This gives the final general form of the Couder Law [3.154] for a thin cylindrical plate (mirror), held in equilibrium in the gravity field by one thin support ring of any radius  $b \leq a$ , expressing the deformation due to its own weight from (3.31) and (3.33) as

$$\omega = \omega_g + \omega_s = \frac{3}{4}\frac{g\rho}{E}(1-\nu^2)\left[\frac{1}{4}V - U_{o,i}\right]\frac{a^4}{t^2}, \quad (3.34)$$

with  $V$  defined by (3.32) and  $U_o$  and  $U_i$  by (3.26). Note that the dimensions of this equation are correct if  $E$  is expressed in pascal and linear dimensions in meters.

For the case of typical mirror glass with  $\nu = 0.25$ , Couder calculated the function  $(\frac{1}{4}V - U_{o,i})$  for seven values of  $\zeta_E$  and ten values of  $\xi_E$ , giving the result of Fig. 3.46. These curves show, on an arbitrary scale, the relative deformations of a mirror supported by a single thin ring at the different zones indicated. In the best case shown with  $\zeta_E = 0.667$ , the maximum deformation is only 3.6% of the maximum deformation of a mirror supported at its center. We note that the expression for  $V$  from Eq. (3.32) has three terms depending on the zero, second and fourth powers of the normalized aperture  $\xi_E$  which correspond to a constant, defocus and third order spherical aberration as wavefront aberrations.  $U_{o,i}$  contains similar terms but includes higher orders from the  $\log_e \xi_E$  and  $\log_e \zeta_E$  terms. However, these are small. Couder therefore approximated the functions of Fig. 3.46 by the simple polynomial

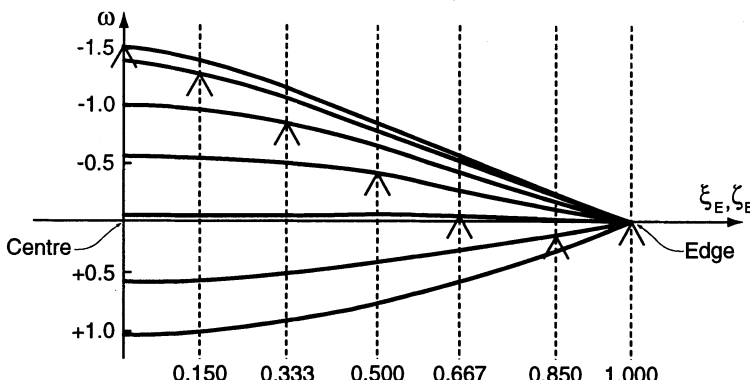


Fig. 3.46. Deformation functions  $\omega$  for the sag of a thin cylindrical plate (mirror) under gravity supported by a single thin support ring of seven different diameters (after Couder [3.154])

$$f(\xi_E) = \alpha + \beta\xi^2 + \gamma\xi^4 \quad (3.35)$$

and determined the coefficients  $\alpha$ ,  $\beta$ ,  $\gamma$  with zero points for the deviation at  $\xi = 0$ , 0.7 and 1.0 for the seven values of  $\zeta_E$  shown. Applying again the principle of linear superposition of Saint-Venant, the deformation resulting from any number of symmetrical support rings at radii  $b_1$ ,  $b_2$ ,  $b_3$  ... and supporting proportions  $m_1$ ,  $m_2$ ,  $m_3$  ... of the weight of the mirror can be deduced immediately from the extended form of (3.34). For 3 support rings, we have from (3.34) and (3.35):

$$\begin{aligned} \omega_3 = \frac{3}{4} \frac{g\rho}{E} (1 - \nu^2) \frac{a^4}{t^2} [ & m_1 (\alpha_1 + \beta_1 \xi_E^2 + \gamma_1 \xi_E^4) \\ & + m_2 (\alpha_2 + \beta_2 \xi_E^2 + \gamma_2 \xi_E^4) \\ & + m_3 (\alpha_3 + \beta_3 \xi_E^2 + \gamma_3 \xi_E^4) ] \end{aligned} \quad (3.36)$$

With three rings, it is clearly possible to achieve three zero points in the flexure function. Couder wished to have a support ring at the edge ( $\zeta_E = 1$ ) to give a stable base for the locating fixed points. Working in the pre-computer age, he chose the other two support radii arbitrarily, at even spacings. He then deduced the approximately optimum load distributions by trial, with the result of Table 3.6. The residual of spherical aberration was so small that a value of  $a^4/t^2$  ( $\text{cm}^2$ )  $> 2.3 \times 10^6$  would have been necessary to exceed the tolerance, whereas the largest telescope at that time (the 100-inch Mt. Wilson) had a value of  $0.284 \times 10^6$ .

**Table 3.6.** Three ring axial mirror support optimized by Couder in 1931 (from Couder [3.156])

Ring 1	Ring 2	Ring 3
$\zeta_{E_1} = 0.333$ $m_1 = 0.253$	$\zeta_{E_2} = 0.667$ $m_2 = 0.484$	$\zeta_{E_3} = 1.000$ $m_3 = 0.263$

Having solved by this remarkable piece of work the general problem of axisymmetric support, Couder turned his attention to the number of discrete support points  $n$  required per ring. Considering the section of each ring as a beam, he proposed the function

$$\omega_{az} = \frac{1}{n^4} V_{az}(n) \frac{a^4}{t^2} \quad (3.37)$$

as the determinant relation, where  $V_{az}(n)$  was some unknown function. He determined this roughly by experiment, plotting the function  $\omega_{az}$  against  $n$  to find where it tended to an asymptotic form. In this way, he established rules for the number  $n$  of supports for the edge ring, including fixed points, in terms of the flexibility  $a^4/t^2$ . Thus he established for a blank of diameter 1.92 m, with flexibility  $a^4/t^2$  ( $\text{cm}^2$ )  $= 0.374 \times 10^6$ , the value  $n = 15$  for ring 3

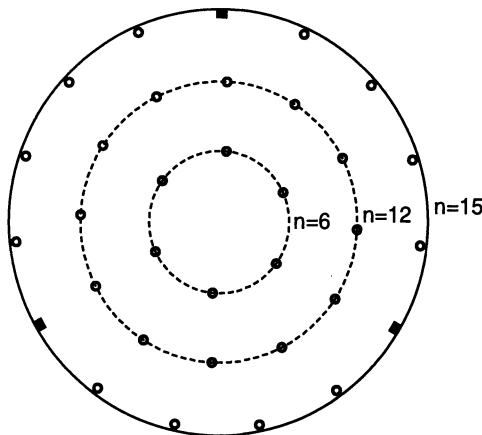


**Fig. 3.47.** 3-ring support proposed by Couder for a 1.92 m mirror (from Couder [3.156])

of Table 3.6. The complete 3-ring support, using astatic levers, had the form shown in Fig. 3.47.

With this classical work, Couder essentially laid down the basis of all modern passive mirror supports. The ESO VLT 8 m primary mirrors have six axial support rings. While the detailed analysis uses sophisticated modern methods, the basic principles remain those established by Couder.

Let us return to the general Couder Law of Eq. (3.34) for a mirror flexing in the gravity field while supported by a thin ring of any radius  $b \leq a$ . The flexibility criterion is  $a^4/t^2$ , so this is the *scaling law* for any such *passive support system*, extended also to any number of symmetrical support rings as shown in Eq. (3.36). Now the optimization procedure for the loads  $m_1, m_2, m_3$  in (3.36) to establish a passive support system in a classical fashion is essentially the same as the *active* correction (§ 3.5) of spherical aberration by varying these loads: the only difference is that the passive correction is done by calculation in advance and not subsequently changed, whereas the active correction changes it *on-line* according to the needs of the measured image. *It follows that the scaling law for active correction of a mirror supported in the gravity field is identical, i.e.  $a^4/t^2$ .* Timoshenko and Woinowsky-Krieger [3.152] give an elegant and simple proof that the same scaling law applies for *all types of active loading* for a mirror *supported in the gravity field*. We saw from Eq. (3.25) the effect of a force  $P$  distributed uniformly round a ring support. Owing to the complete symmetry of the plate and its boundary conditions, the deformation produced at its center by an *isolated* load  $P$  depends only on the magnitude of the load and on its radial distance from the center. This deformation is unchanged if the load  $P$  is moved to another point of the same zone. The deflection at the center also remains unchanged if the load  $P$  is replaced by several loads, the sum of which is equal to  $P$  and the radial distances of which are the same as that of load  $P$ . In other words, in calculating the deformation at the center, we can replace an isolated load  $P$  by a load  $P$  uniformly distributed along a circle whose radius is equal to

the radial distance of the isolated load. For a load uniformly distributed along a circle of normalized radius  $\zeta_E$ , the deflection at the center of a plate freely supported at its edge is given from (3.25) and (3.26) as

$$(\omega_i)_0 = \frac{3}{4\pi} (1 - \nu^2) \frac{P a^2}{E t^3} \left\{ \left[ 2 + \left( \frac{1 - \nu}{1 + \nu} \right) \right] (1 - \zeta_E^2) + 2\zeta_E^2 \log_e \zeta_E \right\} \quad (3.38)$$

So the deformation at the center follows the same scaling law  $Pa^2/t^3$  for an isolated load  $P$  as for the same load round the ring. Following the principle of linear superposition, the same is true for any number of isolated loads. Now, we shall see that active optics modulation of loads must always obey the law that the total support load must equal the weight of the mirror: some proportion of the mirror weight must always appear on the equivalent support circle. Therefore the substitution for  $P$  from (3.28), with some weight factor proportion  $m_P$ , will apply. This converts the scaling factor  $Pa^2/t^3$  into  $a^4/t^2$ , as in Eq. (3.30).

The important conclusion is that the *Couder scaling factor*  $a^4/t^2$  applies to all passive or active support deformations for a mirror deforming under its own weight in the gravity field in which it is held in equilibrium by any type of axial support.

If there is no gravity field, the transformations of Eqs. (3.29) and (3.20) do not take place and other scaling laws will apply (§ 3.5). In particular, if an external uniform pressure  $q$  is applied to a mirror in a weightless environment, the mirror being freely supported at its edge, then from Eq. (3.17) by introducing the Couder normalizing parameter  $\xi_E = \frac{r}{a}$ , the scaling law goes with  $qa^4/t^3$  from Eq. (3.13). If external forces  $P$  are applied, either locally or distributed uniformly over rings, then from Eq. (3.28) the scaling law is  $Pa^2/t^3$ .

It has been shown above that the Couder scaling law  $a^4/t^2$  applies to all influences due to the weight of a mirror in the normal gravity field, since the supports are only *reacting* to proportions of the weight of the mirror. If, however, an *external* force, independent of the gravity field is applied to the mirror, then the deformation follows the scaling law  $Pa^2/t^3$  of Eq. (3.28). Such a case can occur in ground-based telescopes, due to *wind-buffetting on thin primaries* (see § 3.5), resisted by the reaction only of the fixed points assuming the other supports are perfectly astatic. If the wind applies a uniform external pressure  $q$ , then we have again from (3.17) the scaling law  $qa^4/t^3$ . The case of wind-buffetting for ground-based telescopes is therefore similar to that for weightless mirrors in space.

The stresses induced in mirrors by passive or active supports are normally negligible compared with rupture limits. This is not the case for the *handling* of large, thin mirrors such as the ESO VLT 8 m primaries, which is a very delicate operation requiring carefully designed handling supports and tools. For the deformation cases treated above, equivalent formulae are given for the maximum bending moments by Timoshenko and Woinowsky-Krieger [3.152], to which the reader is referred.

These authors also deal with the deformation of a circular cylindrical plate with a circular central hole, a case of great importance for telescopes with a perforated primary. If the hole is negligibly small compared with  $2a = D$ , its effect is negligible.

The results derived above for the symmetrical bending of circular plates apply to the case of pure bending. The effect of shearing stresses and normal pressures on planes parallel to the surface of the plate on bending has been neglected. Hence only the solution for a plate bent to a spherical surface and the solution for an annular plate with moments uniformly distributed along the inner and outer boundaries are rigorous. All other results are approximations whose accuracy depends on the ratio  $a/t$ . More sophisticated theory, taking account of shearing stresses and lateral pressures, was initiated by Saint-Venant [3.155 (b)]. Timoshenko and Woinowsky-Krieger [3.152] treat some basic cases. For example, a circular plate freely supported at its edge and subjected to a uniform pressure  $q$  gave a maximum deformation at its center according to Eq. (3.18). Shearing stresses and lateral pressure lead to the additional term in

$$\omega_{max} = \frac{qa^4}{64D_E} \left[ \left( \frac{5+\nu}{1+\nu} \right) + \frac{4}{3} \left( \frac{3+\nu}{1-\nu^2} \right) \frac{t^2}{a^2} \right] , \quad (3.39)$$

which depends on  $(t/a)^2$ . For the primary of the ESO NTT, with  $t/2a = 1/15$ , the second term produces an additional deformation with  $\nu \simeq 0.25$  of about 2 %. Further developments of the modern theory of axial supports are discussed below. We will consider first some further important properties of basic theory.

Many modern telescopes are adopting *thin meniscus technology* (see § 3.2.4 above). Apart from its curvature, which is tending to increase as primary f/nos get smaller, the thin meniscus approximates to a uniform flat sheet whose size is very large compared with its thickness. Such a sheet must be axially supported by a large number of supports, the number being determined by the permissible sag between the supports. This may approximate to a rectangular network of supports on a raster of dimensions  $b_x$  and  $b_y$  as shown in Fig. 3.48. This case has been treated by Timoshenko and Woinowsky-Krieger [3.157] and the result is quoted by Cheng and Humphries [3.158] in an excellent review paper on supports. The maximum deformation at the symmetry point between supports is given by

$$\omega_{max} = \frac{qb_y^4}{384D_E} - \frac{qb_x^3b_y}{2\pi^3D_E} \sum_{m=2,4,\dots}^{\infty} (F_1 + F_2) , \quad (3.40)$$

where  $D_E$  was defined in (3.13) and  $F_1$  and  $F_2$  are functions of  $m$  and  $\alpha_m = m\pi b_y/2b_x$ . As in (3.20), the pressure  $q$  is equal to  $g\rho t$  in the gravity field. For the simplified case of a square support raster with  $b_x = b_y = b$ , Eq. (3.40) reduces to

$$(\omega_{max})_{b_y=b_x} = 0.00581g\rho \frac{12(1-\nu^2)}{E} \frac{b^4}{t^2} \quad (3.41)$$

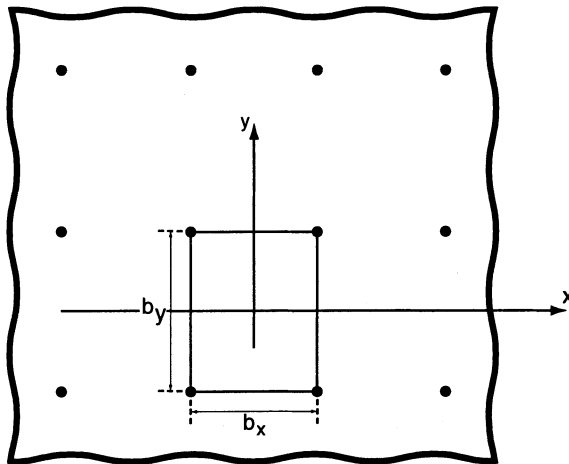


**Fig. 3.48.** Deformation of an infinite thin flat plate supported by a rectangular raster of support points (after Timoshenko and Woinowsky-Krieger [3.157])

Once again, because of the uniform pressure due to gravity, we have the Couder Law with  $\omega_{max}$  proportional to  $b^4/t^2$ . This has important consequences for basic support design. For we also have for the number of supports  $N$  per unit area, the *support density*,

$$N \propto 1/b^2 \quad (3.42)$$

and hence from (3.41)

$$\omega_{max} \propto 1/N^2 t^2 , \quad (3.43)$$

so that, for a given value of deformation  $\omega_{max}$ ,  $N \propto 1/t$ . Eq. (3.41) is the essential basis for deciding the number of supports and hence the number of support rings for all thin meniscus projects. The sag  $\omega_{max}$  leads to a high spatial frequency aberration and must be kept very small – see Chap. 4.

Another important aspect of mirrors, which is closely associated with support and deformation theory, is the property of the *eigenfrequencies* of mirror blanks. For a thin circular plate, these are given by [3.159] [3.160]

$$f_n = (k_f)_n \frac{1}{2\pi} \left( \frac{t}{a^2} \right) \left[ \frac{E}{12(1-\nu^2)\rho} \right]^{1/2} , \quad (3.44)$$

where  $(k_f)_n$  is a constant depending on the vibrational mode  $n$ . For the individual thin meniscus primaries of the ESO VLT, the full diameter is 8.2 m and the thickness 0.175 m, giving an aspect ratio  $A = 47$ . The lowest vibrational mode is always the first astigmatic mode which has in this case for a mirror in glass ceramic (Zerodur from Schott) a frequency  $(f_1)_{VLT} = 16.1$  Hz. These are followed by the first triangular mode ( $(f_2)_{VLT} = 37.9$  Hz) and the first axisymmetrical mode ( $(f_3)_{VLT} = 38.3$  Hz). For comparison, the NTT primary has a diameter of 3.6 m and  $t = 0.240$  m, giving  $A = 15$ . Scaling with the law  $t/a^2$  from (3.44) from the VLT value gives  $(f_1)_{NTT} = 114.6$  Hz, a value 7.12 times higher than for the VLT primary and which is totally damped

out by the axial support. This is also intended in the VLT support (upper hydraulic stage), but the frequency  $(f_1)_{VLT} = 16.1\text{ Hz}$  is more dangerous as it approaches the extended active optics bandpass (see § 3.5).

### 3.4.2 Modern work on the theory of mirror supports: axial support solutions

This is a very large and complex subject and only a brief review is appropriate in this book. Recently, finite element analysis (FE) has become a powerful tool for exact analysis. However, FE must be seen as a *complement*, not a substitute, for analytical investigations, since the latter remain essential for a physical insight into the flexure processes involved.

An excellent review of the modern theoretical basis of mirror supports was given by Schwesinger in 1968 [3.160]. He introduced the theory by two basic statements of approach to the general problem of support:

- The use of the polar coordinates  $r, \phi$  to describe the flexure modes because of the circular form of mirror blanks. Couder had already used a modal approach (see Eq. (3.35)) for axisymmetrical modes and the analysis of Timoshenko and Woinowsky-Krieger [3.152] also uses polar coordinates. But Schwesinger extended this to the definition of flexure modes by the general Fourier equation

$$\omega_n = k_n f_n(r) \cos n\phi , \quad (3.45)$$

in which  $n$  defines the flexure mode. This is particularly significant because essentially the same Fourier formulation is used in the formulation of the Hamilton Characteristic Function (§ 3.2.1 of RTO I) and Zernike polynomials (§ 3.9 of RTO I) for optical aberrations, although the boundary conditions are different.

- The *principle of Saint-Venant* governs the modal behaviour of flexure. Schwesinger states this as follows: "If we have within a limited region of an elastic body a system of forces in equilibrium with each other, the strain produced by these forces will decrease rapidly with increasing distance from the loaded region. The smaller that region, the shorter the radius of straining action." The consequence of this principle is illustrated by the case of a continuous sinusoidal load. Equilibrium then exists in each wave and, if the wavelength is short, the strain will not reach far into the body, i.e. it will cause little flexure. Now in the Fourier modal definition, each mode above  $n = 0$  forms waves in the azimuthal direction and for each mode there are an integral number of waves. From Saint-Venant's principle, the lowest modes form the longest waves and will produce the highest flexure: the higher the mode number  $n$ , the less will be the flexure. However, this consequence is only true for  $n \geq 2$ . The axisymmetrical mode with  $n = 0$  produces no azimuthal wave: its radial waves are shorter than the azimuthal waves for  $n = 2$ . The mode  $n = 1$  is also a special

case corresponding to tilt or coma of some order. Because of its one-axis symmetry, compared with two-axis symmetry for  $n = 2$ , it is a less natural deformation mode. The best illustration is the simple bending of a piece of paper about one axis to produce a cylindrical form ( $n = 2$ ). To produce coma ( $n = 1$ ), an antisymmetric bending along an axis is required. Thus astigmatism ( $n = 2$ ) is the flexure mode requiring lowest energy as is reflected in the eigenfrequencies quoted in § 3.4.1 above.

These two basic statements are fundamental to the active optics control of monolithic mirrors, as we shall see in the next section.

Schwesinger illustrates the Saint-Venant convergence with  $n \geq 2$  by the simple example of a mirror floating in a liquid in a force-free environment (the equivalent of a perfect axial support) subjected at its edge to an external point force  $P$ . As discussed above, the deformation law will be in the form of Eq. (3.28), the amount of deformation depending on the mode  $n$ . Then

$$\omega_{rms}^* = \frac{Pa^2}{Et^3} \left( \sum_n k_n^2 \right)^{1/2}, \quad (3.46)$$

where  $k_n$  expresses the deformation function of the mode and  $\omega^*$  implies that defocus and tilt are removed. Table 3.7 gives the function  $k_n$  for the first six modes. These values demonstrate the predominance of the astigmatic mode  $n = 2$  and the convergence, following Saint-Venant, of the amplitudes of the modes with  $n > 2$ . Of course, the very small value of  $k_0$  is because the point of application of  $P$  is at a maximum distance from the central symmetry point.

**Table 3.7.** The flexure function  $k_n$  in different modes for a cylindrical plate floating in a liquid and subjected to an external point force  $P$  at its edge (from Schwesinger [3.160])

Flexure mode $n$	Modal flexure function $k_n \cdot 10^2$
0	0.425
1	1.846
2	26.50
3	5.42
4	1.90
5	0.85
6	0.45

Schwesinger concludes that the principal aim of support design must be to avoid astigmatism. This was certainly true for passive telescopes, but is no longer so for actively controlled telescopes.

So far we have considered only *axial* supports. But an inclined telescope also requires a *lateral* support for the mirrors. Schwesinger [3.161] investigated

in an exhaustive paper the deformations of a vertical mirror (horizontal axis) in various support systems. The principal deformation induced is again astigmatism, which is worse the steeper the curvature of the mirror. We shall see that a lateral support principle is possible which largely eliminates astigmatism.

The axial support theory based on thin plates above is only an approximation to real telescope mirrors, though the approximation is closer for modern, thin menisci than for classical “thick” ( $A \sim 6\text{--}8$ ) blanks with a flat back. Reissner [3.162] [3.163] developed a theory for thick circular plates that includes shear deformations. This theory was used by Selke [3.164] [3.165] to deduce more accurate values of deformations for a thick cylindrical plate supported axially against gravity by one concentric ring and two concentric rings respectively. For an optimum one-ring support, the maximum difference between the deformation from classical and Reissner theory is about 6.5 % (increase). For two rings the differences are larger, as would be expected since the residuals are themselves much smaller. Schwesinger and Knohl [3.166] used a similar theory to that of Reissner, due to Green [3.167]. They applied this to the deformation of a mirror with a large central hole on a single ring support. They pointed out the high sensitivity of the support radius.

Malwick and Pearson [3.168] used a method called dynamic relaxation [3.169] to analyse the deformations of a 4 m blank with a 2-ring axial support and various lateral support systems. This was effectively the blank of the 4 m KPNO telescope (see Chap. 5 of RTO I). We shall return to the results for the lateral support systems below. A similar analysis for 2.3 m and 1.54 m mirrors was later given by Malwick [3.170], above all for lateral supports for shop testing using points, bands, mercury bag and sinusoidal systems (see below).

For the ESO 1.47 m primary of the Coudé Auxiliary Telescope (CAT), Schwesinger calculated in 1979 [3.171] a 1-ring axial support using his thick plate theory. He had already pointed out [3.160] the high sensitivity of the support radius for single ring supports. His work confirmed this high sensitivity and, as a corollary, the high quality obtainable with a single ring if a relatively high defocus effect with tilt of the telescope is acceptable. Figure 3.49 shows the normalized rms deformation  $\omega_0$  on a logarithmic scale as a function of  $\beta$  ( $\equiv b$ ), the normalized radius of the ring support. The optimum radius is  $\beta = 0.6907$ . The function is so sharp that even a change  $\delta\beta = \pm 0.02$  doubles the  $\omega_0$  residual. Twelve individual supports were required for this mirror with  $A = 9.3$ . It is instructive to compare this result with the curves of Couder in Fig. 3.46, who, using the simple classical thin plate theory, established an optimum support radius of 0.667. Couder’s curves also indicate the sensitivity of the radius.

In 1980, Mack [3.172] analysed the deformations and supports of the 4.2 m alt-az mounted WHT (see Chap. 5 of RTO I). This is above all interesting for the significance of the *alt-az* mounting on the *lateral* support, which will be discussed below.

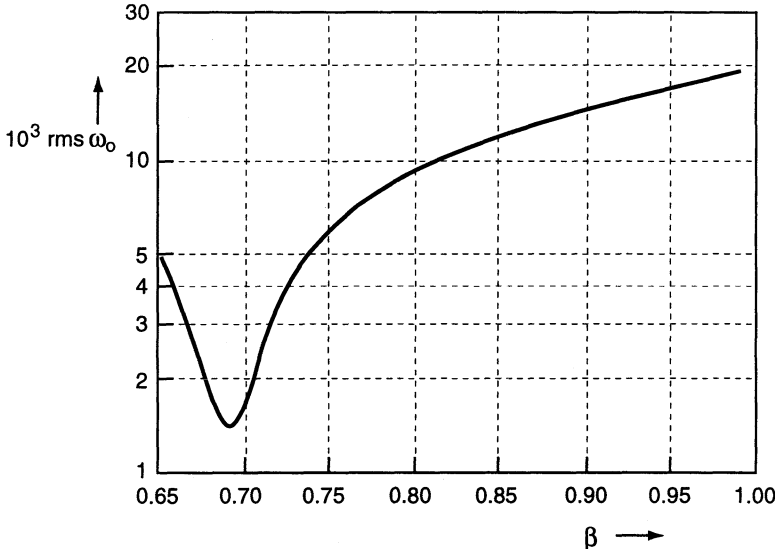


**Fig. 3.49.** Single ring axial support designed by Schwesinger for the ESO 1.47 m CAT. The normalized deformation  $\omega_0$  is the rms deformation referred to the best fit parabola (focus). (After Schwesinger [3.171])

In connection with the ESO active 3.5 m NTT, Schwesinger [3.173] used his analytical theory to establish the passive axial 4-ring support and calibrations for the active corrections both for the full-size primary and the 1 m test mirror. He also designed the push-pull radial support, discussed below. Schwesinger's paper, at my suggestion, gives a synopsis of his analytical theory both for the axial and radial supports. The support design is fundamental to the active optics concept: we shall return to this in § 3.5.

Fine tuning in support design can be done either with sophisticated analytical theory, as discussed above, or by FE calculations. For structured mirrors, it may prove very difficult with analytical methods to derive the “equivalent plate” from the flexure viewpoint. Analytical methods and FE calculations are completely complementary: they provide an excellent mutual cross-check. It is a dangerous illusion to suppose that FE methods make the theory superfluous, since errors which can easily occur remain undetected.

The modern axial support is essentially based on a number of concentric support rings, laid out in the way used by Couder (Fig. 3.47), with refinements of the modern theory. For modern, thin blanks the actual number of individual supports, the support density, is derived from the Couder Law for an infinite plate (Eqs. (3.41)–(3.43)), which largely determines the number of rings and supports on them. Conventionally “thick” mirrors have 1–4 rings, depending on size: the ESO CAT 1.4 m, 1 ring; KPNO 4 m, 2 rings; Palomar 5 m, 3 rings (hexagons); Russian 6 m, 4 rings. The latter two incorporate the lateral support with the axial support in bores – see § 3.4.3 below. The 3.5 m (semi-thin) NTT primary has 4 rings; the thin 8 m VLT primary 6 rings.

The nature of the individual supports disposed round the various rings can be mechanical, pneumatic or hydraulic. The classical mechanical solution was the *astatic lever* as invented by Lassell in 1842 [3.174]. This was discussed in Chap. 5 of RTO I (Fig. 5.4). The principle of a modern construction is shown in Fig. 3.50. The lever arm AOB rotates round the horizontal axis  $O$ . The gravity force  $F_A$  of the weight at  $A$  is multiplied by the ratio  $AO/BO$  to give the force  $F_B$  applied to the mirror back at  $C$  by a link which is, in principle, frictionless at  $B$  and  $C$ . If the telescope is tilted to zenith angle  $Z$  in the plane of the diagram, the force exerted decreases with  $\cos Z$ . The same  $\cos Z$  relation applies also if the telescope is tilted at right angles to the plane of the diagram. Since the weight of the mirror in the axial direction is also a function of  $\cos Z$ , this means the astatic lever *automatically* adjusts in the gravity field to the reduced axial support force required when the telescope is tilted away from the zenith. This is a marvellous property, not fully understood by the inventor Lassell [3.174], since the adjustment for tilt in conventional passive supports requires no change or energy consumption. This property is not necessarily true of pneumatic or hydraulic supports, though they have other advantages.

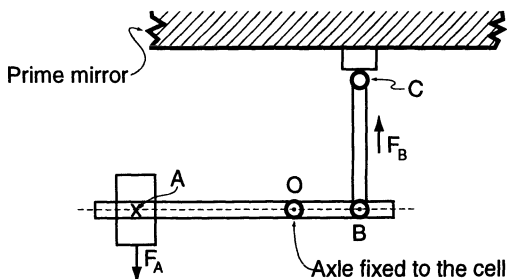


**Fig. 3.50.** The principle of the modern astatic lever

The term *astatic* refers to another remarkable property of such a lever. The mirror cell supporting it will, with conventional construction, inevitably suffer flexure several orders of magnitude greater than the flexure tolerances of the mirror. The lever absorbs this flexure, which may be of the order of 1 mm, by a slight tilt. For this tilt angle, the cosine effect is negligible and other effects on the force  $F_B$  are theoretically zero if the points  $A$ ,  $O$  and  $B$  lie on a straight line. The forces exerted by such a lever system are thus independent of small movements of the lever parallel to the mirror axis, i.e. it is *astatic*. This is normally only possible for a *force-based support*, whereby the mirror is essentially floating on a system which does not constrain it in position: in other words, the mirror is floating in a force field and the forces determine the shape it assumes. The classical solution for location of the mirror in space is to provide, in addition to the astatic supports, three *fixed points*, usually distributed on an equilateral triangle with corners on one of the outer rings. Classically, the fixed points, by subtraction of the sum of

the astatic loads from the mirror weight, should carry the same load as the astatic supports on the ring in question. Modern telescopes sometimes replace real fixed points by virtual fixed points distributed over three equal sectors, a system introduced by Carl Zeiss for the MPIA 2.2 m and 3.5 m telescopes (see Chap. 5 of RTO I).

Such an astatic support is also called a “soft” support because it does not attempt to constrain the mirror positionally. It has many advantages, above all in solving the problem of cell flexure in a most elegant manner, but has the disadvantage that it offers, in its nature, no resistance (except that provided by inertia) to external forces applied through the mirror, above all due to wind-buffetting. We shall return to this issue in § 3.5.

A “hard” support, by contrast, links the mirror firmly to a cell of high rigidity whose flexure must be very small. Such a solution was discussed above (§ 3.2.4) in connection with the German 1.5 m HPT project.

Modern mirror supports frequently make use of an invention made by T. Grubb about the same time as Lassell’s invention. This was the *whiffle-tree*, used in a multi-tier form for the Lord Rosse 6-foot reflector completed in 1845 – see § 5.1 of RTO I and Fig. 5.2. A succession of triangular plates on universal joints converted a 3-point support into a 81-point support for the whole mirror.

According to Bahner [3.175], whiffle-tree systems with 9 points were used for mirrors up to 1.9 m diameter. Meyer [3.176] proposed an 18 point support. Such systems were analysed in complete form by Hindle [3.177]. An excellent résumé is given by Yoder [3.178]. Hindle’s basic idea was that each support should carry the same share of the mirror weight. This can be achieved with a 3-point support but a 9-point support cannot achieve this in azimuth because the two rings have 3 and 6 points. To achieve equal weight sharing, 18 points are required with 6 on one ring and 12 on the other. Figure 3.51, reproduced from Yoder [3.178], shows the geometry. Yoder gives the equations defining the radii of the various circles which were also analysed by Hindle. The 18-point support (Fig. 3.51 (c)) uses three pairs of triangular supports, each pair being linked by a bar using universal joints. Yoder gives for the geometry with  $D = 2R_{max}$ :

$$\left. \begin{aligned} R_E &= 0.28868D \\ R_O &= 0.40825D \\ R_I &= 0.21133D \\ R_S &= 0.33333D \end{aligned} \right\} \quad (3.47)$$

These values of  $R_I$  and  $R_S$  do not correspond exactly to the geometry giving equilibrium between the inner and outer zones of the central disk inside  $R_E$ . The small departure is normally accepted in order to space the 12 outer supports equally and to make the support triangles equilateral.

Modern support systems often combine the essential features of the Lassell-Couder ring supports with additional Grubb whiffle-trees to distribute

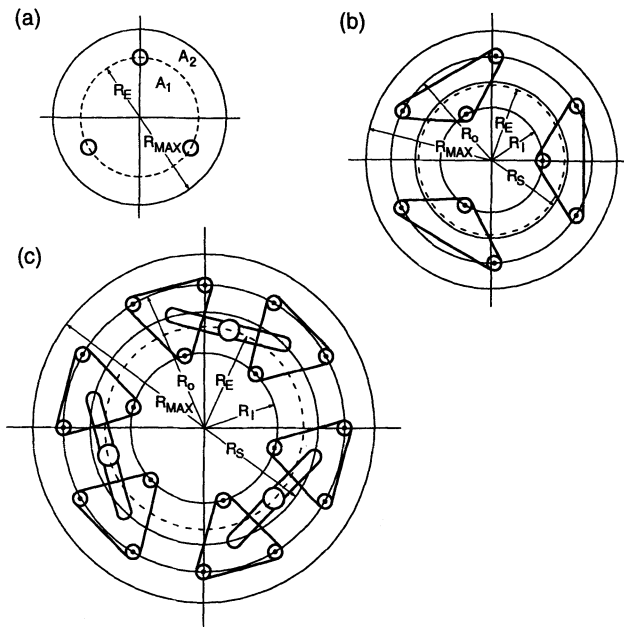


**Fig. 3.51.** Hindle-type whiffle-tree supports with (a) 3-point, (b) 9-point, (c) 18-point configurations (after Yoder [3.178])

the loads further. It should be noted that, in its basic concept, the Grubb whiffle-tree support was *not* astatic. In modern systems using pneumatic or hydraulic supports, with or without whiffle-trees, full astaticity may not be essential or technically feasible.

Although the basic ideas of Couder and Hindle give a sound basis for modern axial supports, analytical theory and FE analysis will define the final layout. For technical details of various approaches, including pneumatic and hydraulic designs, the reader is referred to the excellent account by Yoder [3.178].

Support systems are also strongly influenced by active optics concepts – see § 3.5.

### 3.4.3 Lateral (radial) supports for mirrors

**3.4.3.1 The classical case: radial supports.** In his classic work on axial supports for large primary mirrors, Couder [3.7] attempted to deduce the flexure limits for vertically mounted (horizontal axis) mirrors by a simplified theory and by experiment. He clearly felt unable to deal with the flexure produced under these asymmetrical conditions by theoretical means in the general sense and approached the problem by considering the sag of a narrow, vertical strip of a curved mirror, supported against gravity on the edge of this strip. He concluded that the increase in vertical curvature, due to the sag

induced by the asymmetry of the concave reflecting surface compared with the flat back surface, was undetectable for a diameter of 1.2 m, an aspect ratio of 9 and a focal length of 7.2 m ( $f/6$ ). His experiments seemed to confirm this, from which he concluded that astigmatic errors would only become significant for lateral supports, operating at the outer edge of the mirror, for diameters  $\geq 3$  m.

At that time (1931) no telescope of 3 m diameter existed, but design studies were underway for the Palomar 5 m telescope. For this telescope, the lightweighted structure of the Pyrex blank (see Chap. 5 of RTO I) not only provided 36 cylindrical bores for the axial supports within the mirror block, but also the possibility of combining these with an internal lateral support, thereby avoiding the whole issue of flexure produced by a lateral support operating at the edge. The lever mechanism is described by Bowen [3.179] and shown in its original form in Fig. 3.52. The support band  $B$ , which makes contact with the mirror, is placed in a plane normal to the optical axis through the center of gravity of the mirror. As the zenith angle increases, the lower end of the support system, including the weights  $W$ , attempts to swing about the gimbals  $G_1$ , thereby exerting a lateral force on the band  $B$  through the gimbals  $G_2$  in a direction normal to the optical axis. The weights and lever arms are so adjusted that the forces exerted just balance the component in the opposite direction of the pull of gravity on the section of the mirror assigned to the support. Likewise, the weights  $W$  pivot about bearings  $P$  in such a way as to exert a force along the rod  $R$  which is transmitted to the ring  $S$  by the gimbals  $G_2$ . These weights and lever arms are so adjusted that the force exerted balances the component parallel to the optical axis of the pull of gravity on this same section of mirror. The mirror is therefore floating on these support systems, and, if the function is perfect, no forces are transmitted across the mirror. In practice, friction presented a problem and amounted to over 1 % of the force applied, whereas calculation had shown that the forces had to be correct within 0.1–0.2 % if the optical specification was to be met. The friction problem was solved in 1948 by a redesign of the lower part of the support system, in which the simple lever of Fig. 3.52 was replaced by a compound lever with greatly lengthened lever arms. This led to the successful Hartmann tests reported in 1950 – see § 5.2 of RTO I.

For lightweighted mirrors with such internal support possibilities, the Palomar 5 m telescope approach still represents, in its principle, the state of the art, though other technical solutions than mechanical levers may be applied. Lever solutions, analogous to Palomar, are often used for combined axial – lateral supports in secondary mirrors.

In 1954, Schwesinger [3.161] published a paper as fundamental to lateral supports as that of Couder [3.7] to axial supports. Schwesinger's paper was based on his earlier thesis [3.180]. He considers the general theory of concave mirrors, with a flat back, mounted with horizontal axis and various edge support conditions. His approach, illustrated by Fig. 3.53, represented a major advance not only because of its generality but also because he introduced

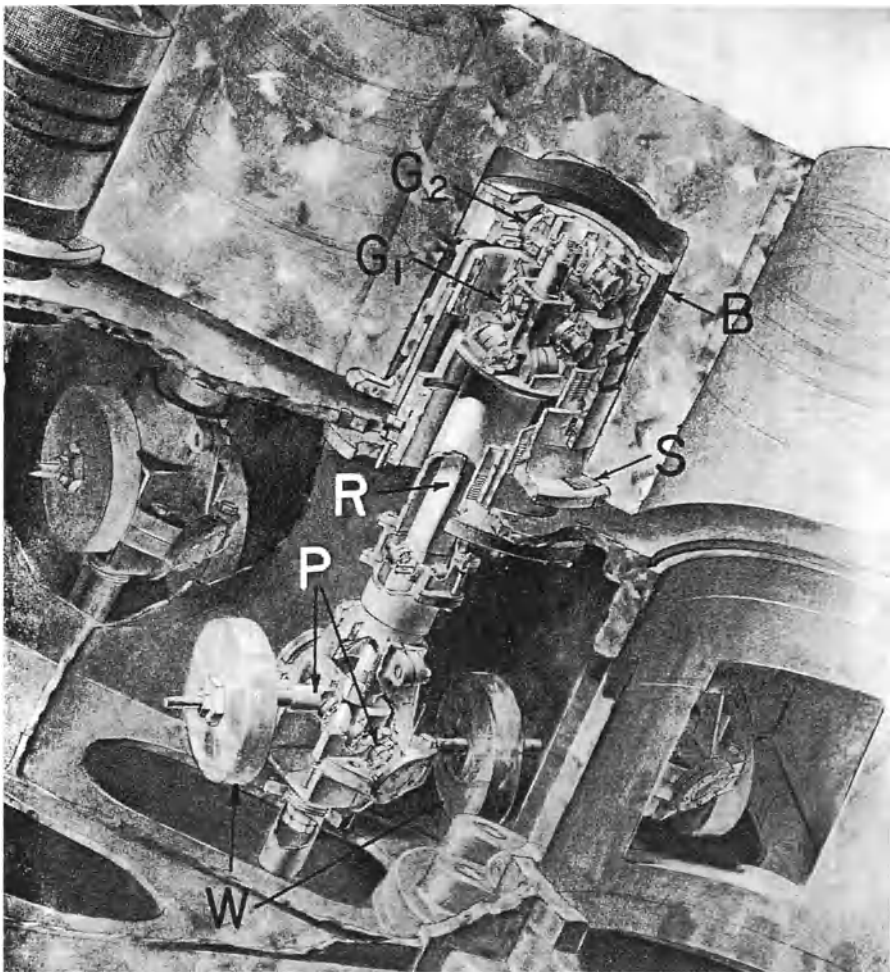


**Fig. 3.52.** Palomar 5 m telescope: function of the mirror support levers (from Bowen [3.179])

*modal* analysis in terms of a Fourier treatment of the flexure modes analogous to optical aberrations defined by Zernike polynomials (see § 3.9 of RTO I). We shall see in the next section that this has profound significance for the development of active optics. The mirror is supported at its edge by some system of forces, which does not have to be defined to derive the general nature of the flexure. Regardless of their specific distribution, these forces, usually compressive stresses, are equivalent to the action of two systems of forces. The first system comprises normal stresses, tensile or compressive, which vary along the circumference but are uniformly distributed across the edge, i.e. parallel to the optical axis. These normal boundary forces are transmitted through the mirror body so as to balance the weight of each volume

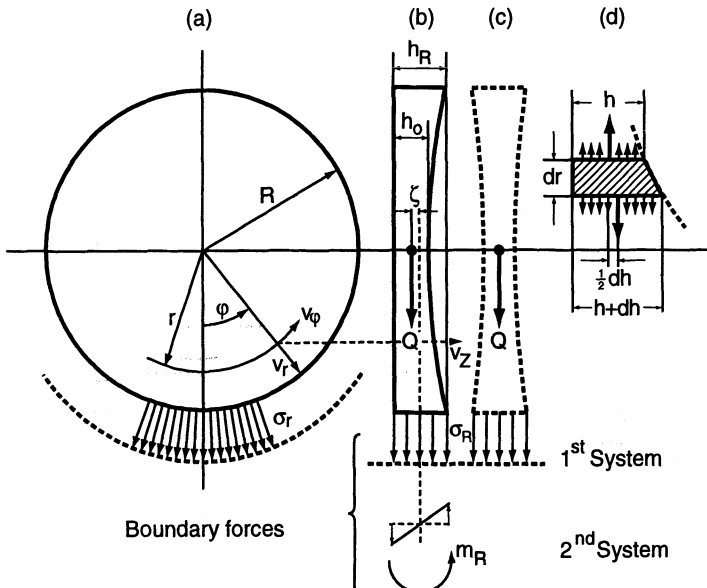


Fig. 3.53a–d. Flexure of horizontal-axis mounted mirrors: quantities entering the flexure problem (from Schwesinger [3.161])

element. A plane through the middle of the cylindrical edge, parallel to the back, is defined as the middle plane of the mirror. If the mirror were symmetrical about its middle plane, as in Fig. 3.53 (c) with equal curvature on both sides, there are no bending moments and the deformation in the  $z$ -direction (optical axis) is determined by the first system of forces acting symmetrically about the middle plane. In the notation of Schwesinger, the deformation  $v_z$  is caused only by the transverse contraction or dilatation of the mirror material, as determined by Poisson's ratio  $\nu$ .

In practice, Schwesinger considered a flat-backed mirror with concave front face, Fig. 3.53 (b). This asymmetry leads to bending moments, arising from the displacement  $dh/2$  of the stress resultants as shown in the section element of Fig. 3.53 (d). The sum of these bending couples over the entire mirror furnishes a resultant of the amount  $Q\zeta$ , where  $Q$  is the weight of the mirror and  $\zeta$  the distance of its center of mass from the middle plane. The resultant moment  $Q\zeta$  is balanced by a distribution of bending moments  $m_R$  round the edge. This is the second boundary force system mentioned above. The result is a bending of the disk in such a manner that its middle plane is deformed in a wavy fashion, but without radial or tangential stretching.

Schwesinger defines the following parameters:

$$\left. \begin{array}{ll} \delta = h_o/2R & (\text{thickness parameter or aspect ratio}) \\ m = f/2R & (\text{aperture number or f/no}) \\ \rho = r/R & (\text{normalized radius}) \\ \kappa = R^2/4h_o f & (\text{normalized shape factor}) \\ h = h_o(1 + \kappa\rho^2) & (\text{thickness function for any practical mirror surface}) \end{array} \right\} \quad (3.48)$$

It follows that

$$\kappa = 1/16\delta m \quad (3.49)$$

Schwesinger demonstrates that these two systems of boundary forces can be expressed as a Fourier series of the azimuth (polar) angle  $\varphi$ , measured from the downward pointing radius of the disk. Apart from the mode  $n = 1$ , the optical effect of the force systems is largely determined by the nature of the support. The resulting deformations can be expressed by Fourier expansions of the form

$$\left. \begin{array}{l} v_r \\ v_\varphi \\ v_z \end{array} \right\} = (\gamma R^2/E) \sum_{n=0}^{\infty} a_n \begin{pmatrix} F_n(\rho) \\ G_n(\rho) \\ H_n(\rho) \end{pmatrix} \cos n\varphi \quad (3.50)$$

$$w = (\gamma R^2/E) \sum_{n=0}^{\infty} b_n K_n(\rho) \cos n\varphi , \quad (3.51)$$

in which  $a_n$  and  $b_n$  are coefficients appearing in similar functions of the normal stress  $\sigma_R$  and the bending moment  $m_R$  respectively. In these equations,  $v_r$ ,  $v_\varphi$  and  $v_z$  are the deformations in the corresponding directions due to the *first system* of forces on the assumption of a *symmetrical* mirror as in Fig. 3.53(c); whereas  $w$  is the axial deformation of the actual *unsymmetrical* mirror (to the central plane) due to the bending moments (Fig. 3.53(b) and (d)) of the *second system* of forces. In most cases of practical importance, the two systems of boundary forces follow the same law, so that

$$a_n = b_n$$

$\gamma$  is the density of the material,  $E$  Young's modulus, while the functions  $F_n$ ,  $G_n$ ,  $H_n$  and  $K_n$  involve Poisson's ratio  $\nu$  and the parameters  $\kappa$  and  $\delta$  defined in (3.48) and (3.49).

Schwesinger then interprets the deformation effect in terms of the Strehl intensity ratio – see Eq. (3.465) of RTO I. With the normalized wavefront aberration as

$$W = 2z/\lambda \text{ wavelengths}$$

and  $\overline{W}$  as the rms value, then the Strehl ratio  $S$  is given by

$$S = 1 - 4\pi^2 \overline{W}^2 , \quad (3.52)$$

valid provided  $1 - S \ll 1$ , for small aberrations. He then combines his Fourier definition with (3.52) and derives

$$\overline{W} = (2\gamma R^2/E\lambda) \left[ \sum_{n=0}^{\infty} a_n^2 Y_n \right]^{1/2}, \quad (3.53)$$

in which the numbers  $Y_n$  are termed the optical influence numbers. We already encountered similar modal analysis in connection with the general theory of axial supports (Table 3.7). Table 3.8 shows these influence numbers for the first ten Fourier modes and four different values of  $\kappa$ , the normalized shape parameter of (3.48). Only the mode  $n = 1$  (coma, since Schwesinger removes tilt) is of fixed amount, independent of the support, and is extremely small, which can be explained from the principle of Saint-Venant. Mode 0 is small because the principal effect, defocus, has been removed and spherical aberration is small. The table shows the massive dominance of the astigmatic mode  $n = 2$ .

**Table 3.8.** Influence numbers  $Y_n$  for the different modes  $n$  with a mirror supported at its edge with horizontal axis (after Schwesinger [3.161])

Mode $n$	$\kappa = 0$	$\kappa = 0.1$	$\kappa = 0.2$	$\kappa = 0.3$
0	0	1.01	4.04	9.1
1	0	0.0331	0.132	0.30
2	4.59	140.5	465	978
3	3.45	20.7	52.5	99
4	2.76	8.89	18.5	32
5	2.30	5.49	10.1	16
:	:	:	:	:
10	1.25	1.92	2.74	3.7

Schwesinger then analyses various types of edge support using the above theory, considering the following cases:

- (a) *Ideal mirror radial edge support*: This is the cosine distribution with tensile forces in the upper half and compressive forces in the lower half, normally known as the push-pull support (Fig. 3.54(a)). All modes except  $n = 1$  are eliminated. Schwesinger considered it was impossible to realise in 1954; but it has since been commonly applied. For example, it was used in the 4 m KPNO and 2.2 m and 3.5 m MPIA telescopes.
- (b) *Optimum distribution of compressive edge forces*: Schwesinger shows that this is closely approximated by the force function  $(1 + \cos \varphi)$  – see Fig. 3.54(b). This force distribution gives an adequate suppression of the astigmatic mode only if the forces are accurate to a fraction of one percent. The simplest way of achieving such a distribution is an elastic lining giving uniform radial stress. If this radial stress just compensates

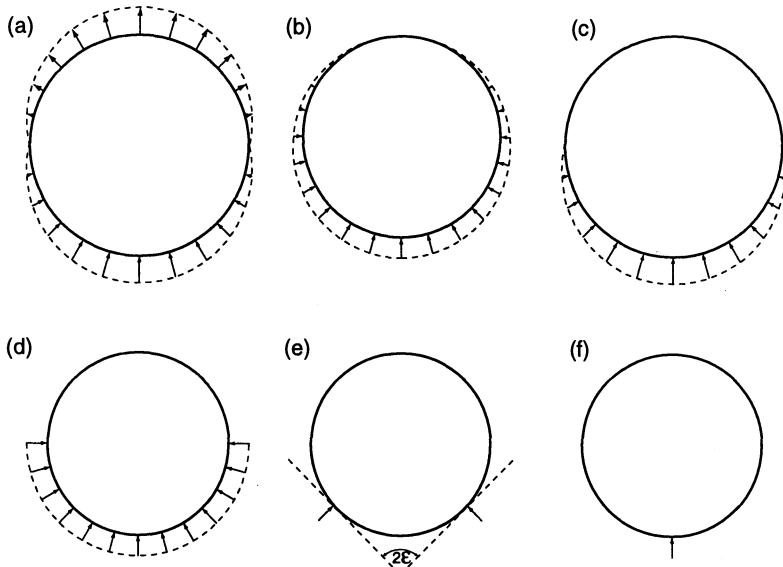


Fig. 3.54a–f. Various radial edge support force distributions

the weight of the mirror, the distribution (b) will be achieved. However, it is not easy to achieve uniform stress with an elastic lining. Various devices have been used, including mercury bags.

- (c) *Half compressive distribution:* If the radial stress of the elastic lining in (b) is progressively reduced, the case (c) is produced where compressive forces only operate over the lower half, giving the lower half of the cosine wave distribution. Although this is a fairly common type, it is not very good: Schwesinger shows that a significant astigmatic term remains.
- (d) *Optimum distribution of compressive forces along the lower half edge:* The optimum distribution given by Schwesinger is relatively complex but approximates to a flat function. In practice, this can be achieved by a flat belt or band, or by two flexible cables, covering the lower half of the circumference (Fig. 3.54 (d)). This is then a square wave function with sharp cut-off and the normal stress  $\sigma_R$  can be expressed as the Fourier expansion

$$\sigma_R = - \left( \frac{\pi}{4} + \cos \varphi - \frac{1}{3} \cos 3\varphi + \frac{1}{5} \cos 5\varphi \mp \dots \right) \quad (3.54)$$

Clearly, this support is free from astigmatism, the principal deformation being the triangular term in  $\cos 3\varphi$ . The popularity of a belt suspension is therefore justified. Schwesinger states it is only 9% less favourable than the optimum lower-half distribution.

- (e) *V-support:* The astigmatic mode disappears if the angle  $2\varepsilon = 90^\circ$  in Fig. 3.54 (e). Thus a right-angled V-support is almost the optimum and gives a big improvement over a pure edge support.

(f) *Single edge support (V-support with  $\varepsilon = 0$ ):* This is the most primitive case, also considered by Couder. The numerical values given by Schwesinger indicate a maximum astigmatic wavefront aberration difference of about  $\lambda/3$  for the 1.2 m mirror investigated by Couder, a value normally detectable by fairly simple detection devices.

Table 3.9 indicates the comparative values of  $\bar{W}$  for the above 6 cases, normalized by dividing by the factor  $(2\gamma R^2/E\lambda)$  in Eq. (3.53). Schwesinger also gives a diagram of mirror diameters, with ordinates in terms of the shape and aperture parameters  $\kappa$  and  $m$ , indicating the maximum size for values of  $\bar{W} = 1/15$  and  $1/30$ .

**Table 3.9.** Comparative deformation given by the six edge supports discussed by Schwesinger (after Schwesinger [3.161])

Case	Type of support	$\kappa = 0$	$\kappa = 0.1$	$\kappa = 0.2$	$\kappa = 0.3$
(a)	Ideal support (push-pull)	0	0.0018	0.0036	0.0055
(b)	Prestressed elastic lining	0	0.0132	0.0289	0.0464
(c)	Unstressed elastic lining	0.00920	0.0508	0.0926	0.1350
(d)	Belt-type suspension	0.00743	0.0182	0.0301	0.0421
(e)	V-support, $\varepsilon = 45^\circ$	0.0548	0.0832	0.1152	0.148
(f)	On-edge-support, $\varepsilon = 0$	0.0673	0.148	0.246	0.346

It should be noted that Schwesinger's original analysis does *not* take account of the effect of shear stresses or central holes in primary mirrors. Nevertheless, this analysis remains the standard concerning the nature of aberrations generated by lateral supports. We shall consider extensions to meniscus mirrors and the specific requirements of alt-az mounts below.

Modern computing techniques enable a general solution of the 3-dimensional elastic equations. Malwick and Pearson [3.168] used the technique called dynamic relaxation to analyse the deformations of a 4 m diameter mirror having a large central hole and a flat back. Results were given as height contours for 4 axial support distributions with vertical axis, 8 distributions with horizontal axis and 2 axial + radial distributions at  $45^\circ$  inclination. Qualitatively, the results for the horizontal axis, which include all the 6 cases of Schwesinger, illustrate admirably the essential truth of his modal analysis. Figure 3.55 gives four examples. Further, more refined calculations were given by Malwick [3.170] for mirrors of 2.30 m and 1.54 m diameter.

**3.4.3.2 The uni-directional case: alt-az mounted telescopes.** So far, we have considered lateral supports as strictly *radial* force distributions as shown in Fig. 3.54. As long as telescopes were *equatorially* mounted, the radial arrangement was natural because the orientation of the mirror cell could vary widely relative to the direction of gravity. For alt-az mounted telescopes, now the commonest solution for large telescopes, this is no longer the case:

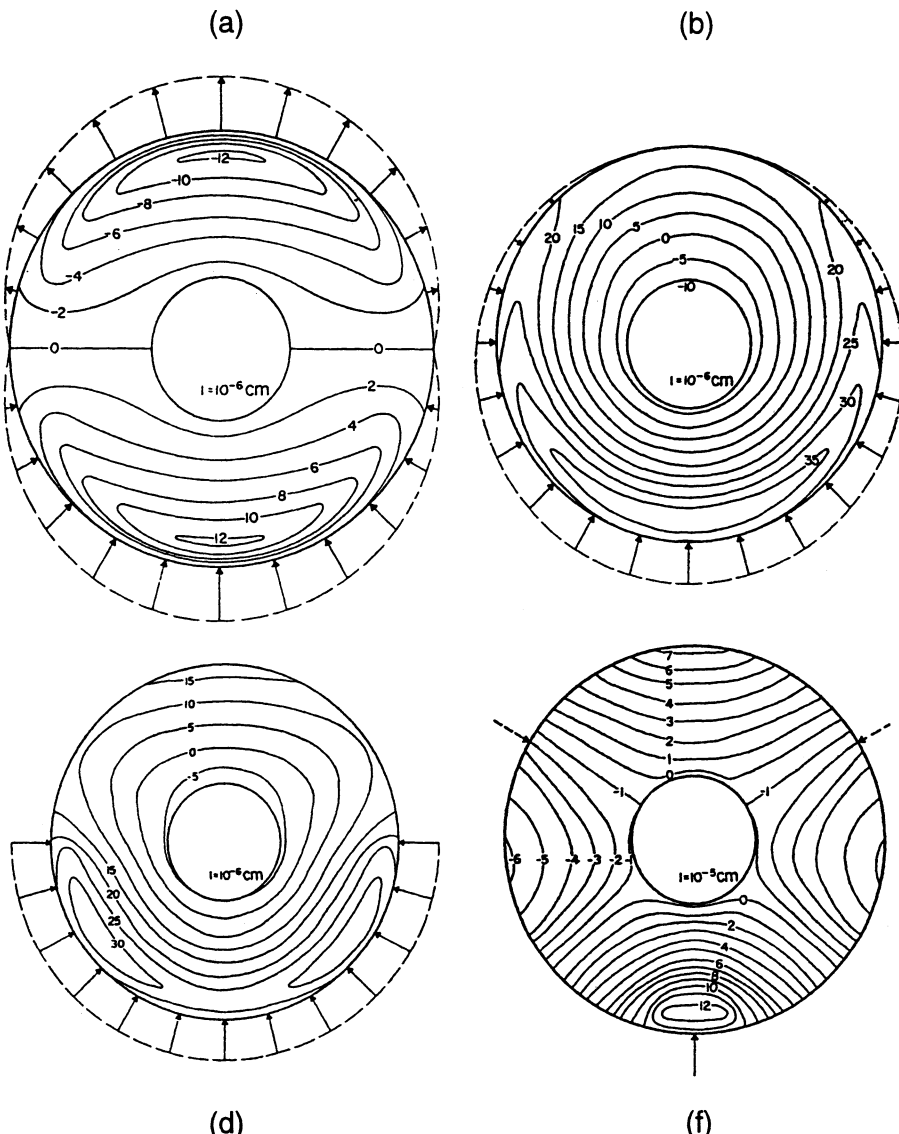


**Fig. 3.55.** A 4 m diameter mirror supported in three different ways with axis horizontal. Numerical determination of flexure by dynamic relaxation for the following cases from Table 3.9: (a) push-pull through c. of g., (b) mercury bag, (d) belt type, (f) single lower support (from Malwick and Pearson [3.168])

tilt of the cell only occurs across one diameter of the mirror. The significance of this uni-directional tilt has been investigated by Mack [3.172] for the 4.2 m primary (flat back, aspect ratio 8) of the alt-az- mounted WHT – see Chap. 5 of RTO I. Mack pointed out that, while the radial push-pull arrangement of Fig. 3.54 (a) will also work in the alt-az case, the horizontal forces are not

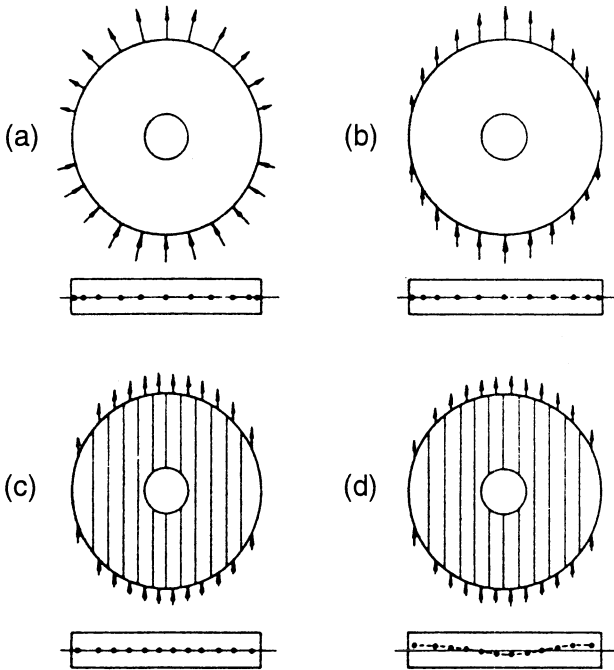


**Fig. 3.56.** Edge force distributions for alt-az mounted mirrors. (a) Conventional radial push-pull; (b) Using vertical components of (a); (c) Equal transverse force distribution in the plane of the c. of g. of the mirror; (d) Equal transverse forces acting through the c. of g. of individual slices. (From Mack [3.172])

strictly required to carry the weight which only requires vertical forces. Mack distinguishes between the four cases shown in Fig. 3.56 and analyses the flexures by finite element (FE) techniques. (a) is easily the worst, followed by (d). Cases (b) and (c) are almost equally good, but (c) is more convenient in practice because of the uniformity of the forces applied. In the normal push-pull case, as was shown by Schwesinger above, we are only concerned with deformations of the mode  $n = 1$ , i.e. the deformations of the first type associated with Poisson's ratio. According to Mack, this is also true of case (d), whereas (c) introduces bending moments. This is disputed by Schwesinger [3.173] (see below), who considers Mack's FE result for the ordinary push-pull radial support consistent neither with shell theory nor with the results of dynamic relaxation given by Malwick and Pearson [3.168].

The 3.5 m primary of the NTT, also alt-az mounted, has a meniscus primary with aspect ratio 15. A lateral support system with 24 supports was designed by Schwesinger [3.173] which appears similar to that of Mack, but has an important difference. The equal, vertical push-pull edge forces are evenly spaced along the *circumference*, as shown in Fig. 3.57, in the plane containing the c. of g. of the mirror. Schwesinger shows that this distribution leads only to deformation in the mode  $n = 1$ , as with the radial push-pull support. He shows that the equal slice approach leads not only to the mode  $n = 1$  but also  $n = 3$  and will, in the presence of a central hole, also be more sensitive to higher orders. Schwesinger concludes, therefore, that the equal vertical distribution along the circumference is, above all, more favourable for

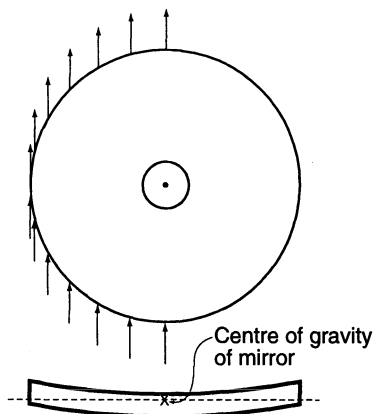


**Fig. 3.57.** Lateral edge support (push-pull) for the primary of the ESO NTT: equal vertical loads at equal spacing along the circumference (after Schwesinger [3.173])

active correction (see § 3.5) since third order coma is the easiest of all aberrations to correct at the secondary, and fifth order coma can also be corrected in modest amounts at the primary. He investigates also the effect of three different values of radial and tangential forces, distributed evenly round the circumference, as cosine and sine functions of  $\varphi$  (Fig. 3.53) respectively. The fraction  $\beta$  of the weight is supported by the tangential forces. Figure 3.58 shows the residual errors for different values of  $\beta$ . The case  $\beta = 0.5$  corresponds to the vertical forces of the NTT support. Clearly, the agreement with the third order coma component is much better than with a pure radial support with  $\beta = 0$ . This agreement is even better with  $\beta = 0.8$  but the rms aberration is 50 % higher.

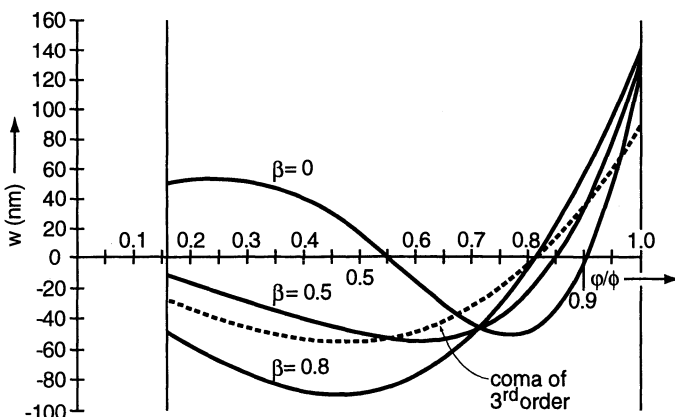


**Fig. 3.58.** Lateral edge support (push-pull) for the ESO NTT: the effect of the fraction  $\beta$  of the weight supported by a tangential force system (equal spacing round the circumference) compared with the radial force system (after Schwesinger [3.173])

The possibilities of further improvement by systematic optimization of the parameter  $\beta$  have been further investigated by Schwesinger with remarkable success in connection with the 8 m ESO VLT primaries [3.181]. Following his previous modal approach, he points out that a well-designed lateral, push-pull edge support will suppress all Fourier modes except the inevitable mode  $n = 1$  and high orders starting at  $n = m_s - 1$ , where  $m_s$  is the number of edge supports. Since  $m_s = 24$  for the NTT and 48 for the VLT, these high order modes will be very small because of convergence according to the Saint-Venant principle. The VLT primaries have an aspect ratio of 47 and a meniscus curvature corresponding to f/1.8. It is therefore not possible to apply lateral radial forces at the outer edge, perpendicular to the optical axis, such that they lie in the plane of the c. of g. of the mirror, as was done in the NTT. If such forces are not in this plane, they cause bending moments which will be absorbed by a reaction of the axial supports, normally the fixed points or equivalent. Such effects can be compensated actively by the axial system but this uses up some of the dynamic range available. A better method is to introduce either an axial force in the edge support, giving a resultant with the radial force no longer perpendicular to the optical axis, or bending moments. Both of these would also have cosine distributions. If equilibrium is maintained by axial forces at the outer edge, then we are only concerned with the mode  $n = 1$ . With  $\beta = 0.5$  as in the case of the NTT, corresponding to equal vertical forces with equal spacing along the circumference, the mode  $n = 1$  (coma) has an rms deflection value of 4000 nm, a very large value even in an active telescope. Above all, the coma orders above the third order would cause serious problems. However, if  $\beta$  is increased to about 0.75, the aberration of the mode  $n = 1$  reduces at once by about two orders of magnitude. Such a support is termed by Schwesinger a *push-pull-shear* support. The appearance of the force distribution is shown in Fig. 3.59. The rms error is a sensitive function of  $\beta$  and can reverse its sign near the optimum. Figure 3.60 shows the variation of the function in the range  $0.745 < \beta < 0.760$ . The optimum value in this case is  $\beta = 0.7529$  giving an rms deflection value for the mode  $n = 1$  of only 8.9 nm, i.e. a wavefront rms value of only 18 nm, an amazingly small value for a diameter of 8 m! It is only about 0.22 % of the equivalent value with  $\beta = 0.5$  and the function is just as smooth.

This result was so good that there is hardly scope for further improvement. With the original arrangement with  $\beta = 0.5$ , ESO had proposed an improvement by supporting some of the weight in the central hole. Schwesinger investigated an optimization including a 20 % weight support in the central hole with  $\beta_0 = 0.5$ , an outer edge  $\beta_1 = 0.71$  and shifts of the force application of  $\pm 20$  mm from the mid-edge points of the edges, as well as balancing of axial forces at the edge and at the central hole. But the result was much inferior to the straight optimization with  $\beta$  above. Above all, considerable higher order aberration is introduced.

These results are so remarkable that they seem to present a definitive solution to the problem of lateral supports for alt-az-mounted solid mirrors.

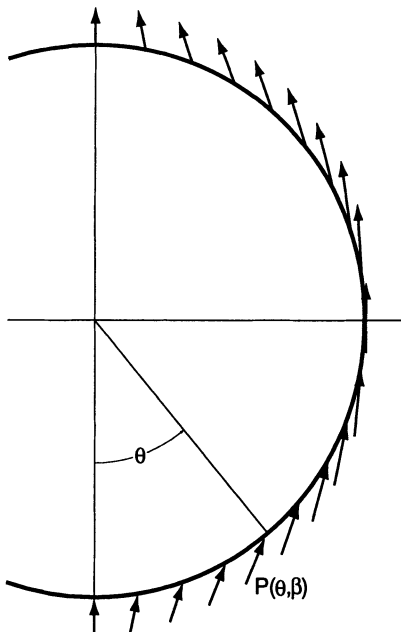


**Fig. 3.59.** Lateral outer edge support for the ESO 8 m VLT primaries showing the modification by introducing tangential shearing forces corresponding to  $\beta = 0.680$  in this diagram (from Schwesinger [3.181])

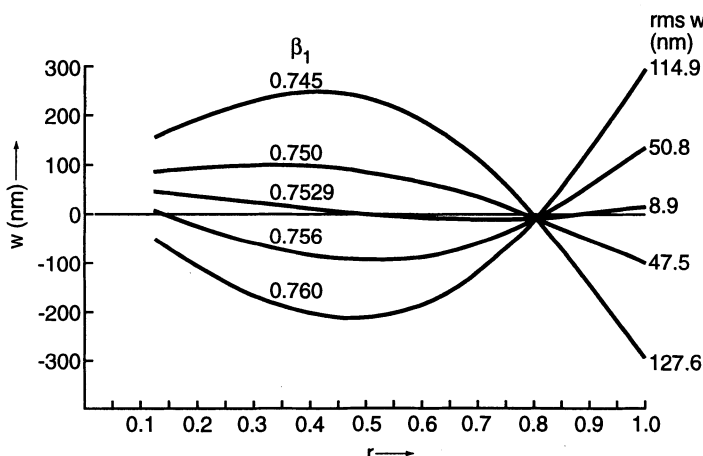


**Fig. 3.60.** Lateral outer edge support for the ESO 8 m VLT primaries showing the optimization of the residual error  $w$  in the mode  $n = 1$  by a shear fraction  $\beta = 0.7529$  (from Schwesinger [3.181])

Schwesinger throws up the question as to whether structured mirrors could also profit from this approach, instead of internal lateral supports. Certainly, for solid blanks, the addition of bores to permit internal lateral supports seems to lose its interest compared with the optimized push-pull-shear edge support.

This viewpoint is supported by a further paper by Schwesinger [3.182] on the same approach, but with further refinements in the optimization. The final residue left above from optimization with  $\beta$  alone is further improved by optimizing with axial shearing forces applied at the inner (hole) and outer edges, as well as with  $\beta$ . The final results for the VLT 8.2 m mirror (case no. 1) and for the SOAR primary (full diameter 4.035 m, aspect ratio 20, f/2.0) (case no. 2) are given in Table 3.10. The parameters  $\tau$  and  $\varepsilon_0$  are related to the position of the lateral support forces on the edge relative to the mid-edge point and the relative axial forces at hole and edge respectively. The final results for the rms deflection are 0.25 nm and  $< 0.1$  nm, effectively zero. Whether, in an active telescope, this improvement from the case with optimization of  $\beta$  alone is worth it, is doubtful: the small amount of 18 nm rms wavefront aberration in the VLT case is largely third order coma and its removal actively is trivial. Nevertheless, it is important to have the theoretical proof that an optimized edge support with additional axial shearing forces at edge and hole can yield absolutely negligible aberration.

**Table 3.10.** Lateral support optimization with three parameters for 8 m (mirror no. 1) and 4 m (mirror no. 2) meniscus mirrors (from Schwesinger [3.182])

Mirror no.	$\beta$	$10^5 \cdot \tau$	$10^5 \cdot \varepsilon_0$	rms $w$ (deflection) nm
1	0.7529	0	0	8.9
1	0.7566	-6.231	0	5.8
1	0.7518	0	-0.438	0.83
1	0.7521	-0.652	-0.449	0.25
2	0.7698	0	0	5.9
2	0.7497	0	-6.00	$< 0.1$

### 3.4.4 Mirror handling

The basic theory of stresses induced by mirror handling (lifting) devices for large mirrors is given by Cheng and Humphries [3.158]. The normal and most convenient way of handling primary mirrors is a lifting device round the central hole. For thick mirrors (aspect ratio  $\sim 6$ ), a relatively modest flange round the back of the central hole is safe enough; but as mirrors get larger and thinner the device becomes much more critical.

From thin plate theory [3.152], the maximum tangential stress is

$$\sigma_{max} = k\rho g \frac{D^2}{t} , \quad (3.55)$$

where  $k$  is a constant depending on the radius of the support ring and on  $R_0/R$ , the ratio of the central hole radius to the radius of the mirror. This equation supposes the forces are applied at the neutral surface so that compressive stress underneath and tensile stress at the top of the blank are

equal. Nevertheless, it gives a useful approximation for practical cases. For  $R_0/R = 0.25$ ,  $\rho = 2500 \text{ kg m}^{-3}$  and  $\nu = 0.3$ , Eq. (3.55) assumes the form for a mirror lifted on a narrow flange round the hole:

$$\sigma_{max} = 2.63 \times 10^4 \frac{D^2}{t} \text{ N m}^{-2} \quad (3.56)$$

Thus, for a given diameter  $D$ , the maximum induced stress is proportional to  $D/t$ , the aspect ratio. Figure 3.61 shows this relationship as a function of  $D$  and for various values of  $D/t$ .

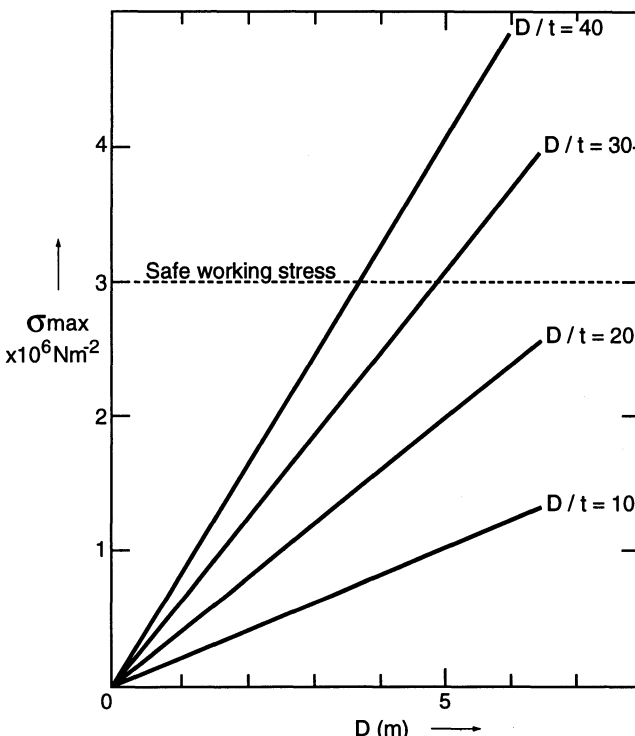


Fig. 3.61. Maximum induced stress as a function of  $D$  for various values of  $D/t$  for a mirror lifted round the periphery of its central hole with  $R_0/R = 0.25$ ,  $\rho = 2500 \text{ kg m}^{-3}$  and  $\nu = 0.3$  (after Cheng and Humphries [3.158])

The tensile strengths of optical materials lie typically in the range  $35 \times 10^6 \text{ N m}^{-2}$  for flint glass to  $110 \times 10^6 \text{ N m}^{-2}$  for Pyrex. Zerodur is given as ca.  $90 \times 10^6 \text{ N m}^{-2}$ . However, a safety factor of at least 10 is used for glass mirrors of telescopes. Furthermore, a further factor of 3–5 must be applied because of defects such as bubbles, inclusions or non-polished edges. The unpredictability of glass in this respect is its great weakness compared with metals such as aluminium. Cheng and Humphries give a safe working stress in Fig. 3.61 of  $3 \times 10^6 \text{ N m}^{-2}$  (MPa). For the ESO VLT primaries, a value

of 3–5 MPa is laid down. The validation of this figure is given in a Schott Technical Note for Zerodur [3.183]. Graphs are given of breakage probability for stepwise increase in bending stress, for samples produced by various grinding finishes. The acceptable bending stress is also a function of time: in this sense, breakage probabilities for repeated processes like handling must be accumulated.

Cheng and Humphries give figures showing the tangential and radial stress arising from mirrors being lifted by single ring supports of radius  $0.25R$ ,  $0.67R$  and  $1.0R$ . The consequences of breakage during handling of very large primaries such as 8 m blanks are so daunting that the handling tools must be the subject of intensive study. The handling tool for the 8.2 m VLT primaries at the glass manufacturers (Schott) consisted of 18 suction pads operating at the front face. Such a system operating at the front face would be impractical for the optical figuring contractor (REOSC). The handling tool there operates on the back face through the central hole and uses 3 support points round the central hole and 12 support points near the outer edge.

## 3.5 Active optics control systems

### 3.5.1 Introduction and definitions

The purpose of *active optics* control systems is, in the most general sense, the improvement of the quality of the telescope image (effectively, of a natural star image near the field center) by some systematic process involving the relative positioning of the mirrors and the modification of their form by their supports, whereby this systematic process may be carried out at any time frequency from dc (i.e. once only at set-up) up to a certain limit. This upper limit is a highly technical point to be discussed in detail below and which is closely linked with the lower time frequency limit of *adaptive optics*. With the definitions which we shall give below, *active optics* [3.69] is therefore a low time frequency bandpass control process, whereas *adaptive optics* is a high frequency bandpass control process, essentially concerned with correction of the “external seeing” (atmosphere).

The above definition is arbitrary and other definitions have been used: for example, irrespective of temporal frequency, that “adaptive” should refer to a closed-loop control, “active” to an open-loop [3.184]. But the preferred definition above is now widely accepted and has a good semantic base. The low time frequency errors are the classical “telescope” errors arising from fabrication, mal-adjustments and other sources associated with conventional “*passive*” telescopes. The semantic opposite of “*passive*”, for a telescope capable of correcting such errors, is “*active*”. “*Adaptive*” is then reserved for the higher time frequency effects of the atmosphere. This definition is also in agreement with that of Woolf [3.185], referring also more specifically to the application of such systems to telescopes. The aspect of “closed-loop” or

“open-loop” is, however, also very important and will be discussed in detail below.

Attempts to improve image quality by manipulating mirror supports, above all at the primary, go right back through telescope history. But the first suggestions of a systematic process seem to have been made by Couder in 1931 [3.186] and by Maksutov in 1948 [3.187].\* Couder noted the high sensitivity to *astigmatism* of a primary mirror under test when supported at only two points at the ends of a diameter. This led him to the idea that such a “regular” aberration as astigmatism (in modern terms, we would say a “low spatial frequency” aberration) could be corrected by “a system of forces suitably applied”. He experimented with a system of spring blades applying push-pull forces at right angles and concluded that astigmatism polished into a mirror could be corrected by such a device. Intuitively, as the excellent practical optical engineer that he was, Couder recognised that astigmatism was by far the most sensitive flexure mode long before Schwesinger introduced the formal Fourier analysis of flexure modes [3.180] [3.161]. Maksutov, apparently unaware of these experiments by Couder, proposed that mirror counterweights could be adjusted after set-up to correct errors observed in an ocular or with a Foucault knife-edge, including errors left by the manufacturer. He also observed that such a general correction was only valid for one zenith angle. He gives no algorithm for correlating the force changes with the image error and states the process is more an art using trial-and-error. Nevertheless, this was a highly perceptive observation at the time and pointed out the advantage of the generalised Lassell astatic lever support system for such processes. However, it did not lead to further systematic activity.

In 1969, the author, while working at Carl Zeiss, became aware of the approach of Schwesinger [3.188] [3.161] whereby support-induced errors were treated systematically by a Fourier expansion. Schwesinger treated the flexure errors in a way giving an interpretation which fitted in naturally with optical wavefront aberration theory and the concept of the Strehl Intensity Ratio (see § 3.10.5 of RTO I). For some time, it had been clear to me that the tolerances for decentering coma in Cassegrain telescopes could never be maintained in large telescopes and that only a *feedback* system could control this aberration, which was essentially identical to Schwesinger’s Fourier mode with  $n = 1$  (see § 3.4.3.1). The Fourier treatment of Schwesinger was effectively identical in form, though with different boundary conditions, to the optical aberration formulations of Hamilton’s Characteristic Function and Zernike’s circle polynomials (see §§ 3.2 and 3.9 of RTO I). This led, in the framework of the ESO 3.6 m (passive) telescope development and test [3.189], to the basic proposal in 1977 for an “optical feedback telescope” or an “active optics” telescope [3.190] using these concepts systematically. This was essen-

---

\* I am indebted to D. Enard and K. Bahner for drawing my attention to these proposals by Couder and Maksutov respectively.

tially identical with the concept used later in the ESO 3.5 m NTT, which is described in detail below.

In connection with the 2.4 m HST, work in active control of mirror figure had also been initiated in the late 1960s in the United States. Accounts of this work were mainly given in NASA reports, but a paper was published in 1970 in the journal "Automatica" by Creedon and Lindgren, [3.191], a journal not normally known in the astronomical and optical community. Neither this nor the NASA reports made wide impact at the time – the author only became aware of them in the mid-1980s when the NTT development was in the manufacturing phase. The astronomical community in the United States, with a few exceptions such as Meinel, showed little awareness or interest in the potential of active optics until the late 1980s.

The results of the NASA studies were summarised by Howell and Creedon in 1973 [3.192]. It should be borne in mind that all this work was intended for a *space telescope* application, not for normal ground-based telescopes. They were concerned with initial figuring errors, the change from 1 g to 0 g, and changing temperature gradients in orbit. The aim was to sense figure errors on the primary mirror and to correct them by appropriate deformation. The technique was successfully applied (on the ground) to a 30-inch diameter model mirror with 0.5-inch thickness (aspect ratio 60). Using 58 actuators, the initial error of  $\lambda/2$  rms ( $\lambda = 0.633 \mu\text{m}$ ) was reduced to  $< \lambda/50$  rms. The control system was a *modal* one, the modes used being the *natural vibration modes* of the mirror [3.191]. The mode shapes are referred to as eigenvectors of the mirror and the frequencies are eigenvalues. These were determined by numerical calculation. The use of modal control in general, and natural modes in particular, was an important contribution to the subject of active optics and natural modes were later used for part of the correction process in the ESO NTT and also in the VLT [3.193]. The control matrix had 58 eigenvalues. The output of the matrix operations was a set of modal coefficients which describe the desired force change patterns to be distributed on the mirror to correct these modes. Assuming these to be corrected in a quasi "steady state" in space, the residual error was then supposed to be the rms wavefront error of the higher, *uncontrolled* modes. However, the assumptions made on the ground might not be correct in space, leading to a control error. Since the authors had a complex scheme for determining the 58 actuator positions so as to compensate for uncontrolled higher orders, these positions might no longer be optimum.

The authors considered two possibilities for treating the errors: "deterministic" and "uncorrelated". For the deterministic case, it was found that the "best" actuator locations (i.e. those locations that minimized the steady-state error) were very sensitive to error distribution. Also the locations had to be found by laborious trial-and-error computing techniques, including the use of the steepest gradient algorithm. For this reason, and because the quasi steady-state errors would be expected to vary slowly from thermal causes, the uncorrelated approach was preferred. This simplified the determination

of actuator location and reduced the sensitivity of locations, although more actuators were required for a specific assumed error.

Further details of the active optics correction of the 30-inch test mirror are given in a subsequent NASA report [3.194] describing the study carried out at the Perkin-Elmer Co., now Hughes Danbury Optical Systems (HDOS). One of the objectives was to determine the optimum positioning of the actuators and distribution of actuator forces in order to minimize the number of control channels required and to decouple their action so as to optimize system response. The mirror influence coefficients were determined *experimentally* by measuring the displacement of the stressed mirror at various points, from interferograms. The authors state clearly the advantage of *modal control* compared with attempting to make the wavefront aberration zero over a matrix of actuator points. This was exactly the same conclusion as that reached independently by the ESO team [3.69], an important point to which we shall return. Thermal tests were carried out to investigate the performance of the active optics system in the presence of thermal disturbances and to determine the response of the thin mirror to various applied thermal gradients.

The original modal concept [3.191] proposed the determination of actuator locations at or near nodal contours of higher order modes, which followed a simple pattern for a flat plate model. However, Robertson [3.194] found that there was no such simple pattern of the nodal contours for the thin, spherical mirror when more than 8 modes were considered. Further, it was discovered that by including the fifteen dominant modes, which comprised 99 % of the specified figure error for  $1\lambda$  rms amplitude, it was not possible at that time to determine their placement to obtain anywhere near  $\lambda/50$  rms error with the control system because of the very large number of possible actuator position configurations. Robertson therefore applied a simplified modal approach using seven sensed points, 4 controlled and 3 uncontrolled. The function of a modal controller operating on these lines was tested for various error signals.

The above work programme was a remarkable pioneering effort, although its application was finally rejected for the Hubble Space Telescope. Had it been accepted and had the dynamic range been adequate to correct the large third order spherical aberration due to matching error (see § 3.2.3), the most serious setback in that whole project might have been averted. However, in spite of the many positive aspects of the active optics proposals, notably the modal approach using natural modes and the closed-loop concept of measuring and correcting the errors in the primary, the total concept was extremely complex, above all because of the ambitious concept of considering all modes: a large number of controlled modes and also the higher order uncontrolled modes for which the actuator positions were, in the original modal concept, to be determined. This is in contrast to the ESO system [3.69], described in detail below, in which *any* fixed actuator positions suitable for a normal passive support can be used modally and the number of modes to be controlled emerges naturally from the stiffness function of the mirror, the convergence following from the Saint-Venant principle, the Fourier definition of elastic

aberrations due to Schwesinger [3.160] [3.161] and the similar nature of optical errors such as defocus, decentering coma and spherical aberration from matching error.

Another weakness of the NASA studies was that they concentrated on errors of the *prime mirror alone*, using only corrections by elastically bending the mirror. This gives a problem of sensing the errors of the prime mirror alone, which was discussed by Meinel [3.195]. He also refers to the desirability of measurements of the Cassegrain image to determine decentering coma and to the open-loop, laser alignment system of the MMT (which was later abandoned). Here also, it seems a major advantage of the ESO system that it used for error sensing the obvious natural source for all optical errors in the total optical system, namely the image of a natural star in the field of the Cassegrain (or final) focus, normally the offset guide star. This is then a natural *closed-loop* control system, whereby all error sources are measured, including figure errors of the secondary and the errors of its position: decentering coma for lateral error and defocus for axial error. However, in 1970, the essential technological element of modern image analysers, the CCD detector, was not yet available.

So far, we have been concerned with *monolithic* primaries whose active control implies deforming them elastically. But active optics can also be applied to *segmented* primaries or to co-phasing separate telescopes as in the MMT. The most important examples of these two types, the Keck 10 m telescope and the 4.4 m equivalent MMT were discussed in § 3.2.1 and § 3.2.2 respectively. The requirement here is more complex than with monoliths as the separate segments or telescopes can have piston (phase) error, as well as tilt errors. The prime mirror control system of the Keck 10 m telescope is essentially a highly sophisticated (and apparently very successful) open-loop control system (in the sense that it does not use a natural star). However, a natural star was used in setting up the system and checking the effective image quality from individual segments and the stacked group as well as centering errors. A complete aberration analysis and description of the set-up and alignment procedure is given by Nelson et al. [3.196]. A continuous monitoring with an image analyser was apparently not envisaged at that stage (1992), although it seems a logical addition to exploit the system to the full, e.g. for decentering coma and defocus errors.

Active phasing of mosaic (segmented) mirrors was proposed in the 1970s by several authors, for example Muller and Buffington [3.197]. At a simpler, lower quality level for a very cheap IR spectroscopic telescope (light collector), it was also pursued in France for a 4 m telescope which was abandoned in 1975 for lack of support [3.198]. The aim here was a telescope of similar size to the 3.6 m CFHT with a budget of only about 1% of that telescope. The prime mirror was spherical with  $D = 4.2$  m working at  $f/1.43$  and consisting of 36 square segments. A servo-system controlled the segments. This project clearly proposed closed-loop active control of the tilt of the segments (phasing in piston was uncritical for the quality aimed for) by using an optical offset

guide star. The authors also recognised that telescope errors only required a low servo-bandpass ( $10^{-2}$  to  $10^{-3}$  Hz). The detector for the servos was a circular aperture passing flux to a photo-multiplier for each of the 36 segments. The quality aimed for was 10 arcsec and the servo-stacking seemed capable of achieving this, but the individual segments were of poorer quality, so that the effective image was more like 20–30 arcsec in size. If more money had been available to build an IR telescope on similar lines but diffraction limited at 10  $\mu\text{m}$ , more interest might have been generated. A short summing-up of this project was given by Connes in 1989 [3.199]. He states: “As to interest in a test-bench device on which budding active optics techniques had been demonstrated, and could be further refined, there was none whatsoever”. This does indeed correctly reflect the deep conservatism at the time of the bulk of the astronomical world towards new technology. However, no attempt was apparently made to discuss the matter with ESO at the time, where (at least on the technical side) thinking in the direction of a complete, high-performance active concept for telescopes was underway. Nevertheless, although the development was not known to the ESO engineers at the time, this project came in many ways closest to the ESO NTT concept.

### 3.5.2 The principles of the ESO active optics system, as developed for the 3.5 m NTT

The essential elements of this system were given by Wilson in 1977 [3.190] and more explicitly in 1982 [3.200]. A complete account of the principles is given by Wilson et al. in [3.69] under the title “Active Optics: I. A system for optimizing the optical quality and reducing the costs of large telescopes”. This definition is important, for the NTT has proven that it *is* possible to improve markedly the effective optical quality while *reducing* the costs compared with conventional telescopes.

There are 3 basic factors limiting image quality in ground-based telescopes: diffraction, atmospheric seeing and telescope quality. In space, the second factor is absent.

Apart from the fundamental limitation of *diffraction* (see § 3.10.3 of RTO I), which is small for large telescopes at visible wavelengths but not necessarily so at IR wavelengths, the practical limiting factor of *ground-based telescopes* should be *atmospheric turbulence (seeing)*. This implies that the third factor, *telescope quality*, should produce an image degradation small compared with that due to external seeing. Unfortunately, this is rarely the case over the bulk of the life of real telescopes. Earlier, fabrication errors set the limits. In more recent times (say since the Palomar 5 m), the limits have been increasingly set by *thermal* and *maintenance* aspects. The purpose of active optics is to make telescope errors, from all sources, negligible compared with the best external seeing. This aim can be more clearly defined now that scientifically-based and reliable *external-seeing monitors* are becoming commonly available – see Chap. 5.

If we aim with active optics to correct all optical telescope errors in order to make them small compared with external seeing, we must start by defining *all the sources* of optical error in telescopes. Table 3.11 gives the ten possible sources affecting imagery in ground-based telescopes, apart from diffraction which is inevitable and continuous, together with their bandpasses. Optical design and optical manufacture are once-for-all (dc) operations. We shall show below, in connection with the principle of Saint-Venant, that active optics is only concerned with the *axial* image quality: imagery *in the field* relative to the axis is an essentially fixed, higher order function which cannot normally be influenced by active optics. Optical design is therefore normally of little consequence since correction of the axial image is trivial. However, it may be disturbed by additional elements such as detector windows, above all by chromatic effects.

**Table 3.11.** The ten sources of error giving degradation of image quality in ground-based telescopes, and their corresponding bandpasses. Diffraction, which is inevitable and continuous, is excluded since (for a given signal wavelength) it cannot be influenced. In space, the three errors dependent on air vanish. (From Wilson et al. [3.69])

Source of error		Bandpass (Hz)	
(1)	Optical design	dc	(fixed)
(2)	Optical manufacture	dc	(fixed)
(3)	Theoretical errors of: – Mirror supports – Structure (focus, centering)	$dc \rightarrow 10^{-3}$ $10^{-3}$	(fixed $\rightarrow$ minutes) (minutes)
(4)	Maintenance errors of the structure and mirror supports	$10^{-6} \rightarrow 10^{-5}$	(weeks $\rightarrow$ days)
(5)	Thermal distortions: – Mirrors – Structure	$10^{-5} \rightarrow 10^{-4}$ $10^{-3}$	(days $\rightarrow$ hours) (minutes)
(6)	Mechanical distortion of mirrors (warping)	$10^{-7}$	(years)
(7)	Thermal effects of ambient air (telescope, dome and site “seeing”)	$10^{-4} \rightarrow 10^2$	(hours $\rightarrow$ 0.01 s)
(8)	Mirror deformation from wind gusts	$10^{-2} \rightarrow 10^1$	(minutes $\rightarrow$ 0.1 s)
(9)	Atmospheric turbulence (external “seeing”)	$2 \cdot 10^{-2} \rightarrow 10^3 +$	(50 s $\rightarrow$ $< 10^{-3}$ s)
(10)	Tracking errors	$5 \rightarrow 10^2$	

The most important feature of the bandpass column in Table 3.11 is that all the error sources are dc or of bandpass  $< 10^{-2}$  Hz except (8), (9) and (10) and partly (7). This is of central importance, because this is roughly the frequency limit of *normal* active optics correction *in closed-loop* and implies that two thirds of all the errors listed are amenable to it.

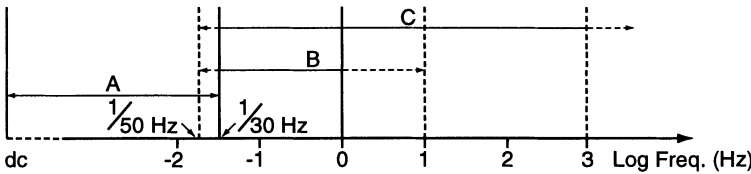


**Fig. 3.62.** The bandpasses for active and adaptive optics correction (from Wilson and Noethe [3.201])

The definition of the *correction bandpass* is an essential feature of any control system. Our definitions are shown in Fig. 3.62 [3.69] [3.201]. The *normal active optics bandpass* A, as in the NTT, goes from dc to  $1/30 \text{ Hz}$ . The limit  $1/30 \text{ Hz}$  simply corresponds to the well-known fact that, in the presence of excellent atmospheric (external) seeing, an integration time of 30 s is sufficient to integrate out the external seeing completely, giving a round image corresponding to the integrated external seeing quality, the classical definition of “seeing”. For a frequency  $\nu > 1/30 \text{ Hz}$  (for inferior seeing at somewhat lower frequencies), we enter into the *adaptive optics bandpass* C, going from  $1/30 \text{ Hz}$  to beyond  $10^3 \text{ Hz}$ . In this bandpass, we are confronted with the phenomenon of the *isoplanatic angle*  $\Theta_S$  (see Chap. 5), that angle over which the phase of the error introduced by atmospheric seeing remains essentially constant.  $\Theta_S$  is a function not only of the wavelength and the Fried parameter  $r_0$  defining the seeing, but also of the frequency  $\nu$ : the higher the frequency, the smaller the isoplanatic angle. However, even at the lowest frequencies of bandpass C, the angle  $\Theta_S$  at visible wavelengths is only one or two arcminutes at most. This has a very important consequence for bandpass B, which we call the *extended active optics bandpass*, going from  $1/30 \text{ Hz}$  to about  $10 \text{ Hz}$ . We shall see that an essential feature of the normal active optics system is its *closed-loop nature*, referring to the image of a natural star through the telescope in its final image plane. Normally, it is not practicable to use as a reference light from a star in the actual observation field, at the field center, because all photons are required for the observation and a suitable star may anyway not be present in the observation field. In practice, therefore, a star near the edge of the telescope field is used, normally the offset guide star. Such guide stars are almost always well outside the isoplanatic angle centered on the field center [3.201]. In bandpass B, it follows that the wavefront error component corresponding to the atmospheric effects in this bandpass are only valid for the field point measured and are wrong for the field center. *With a single measurement* in this bandpass, it is impossible to separate the errors due to sources (7) and (8) and possibly (10) (each of which has *no* isoplanatic limitation) from the normally dominant source (9). If a number  $p$  of detectors are distributed over the field, a statistical separation is possible [3.201], but the gain is proportional to  $p^{1/2}$  from normal statistics, a procedure which is normally too inefficient, since image analyser detectors are not trivial units and a large field area is rarely free. It follows that there is a fundamental

problem of closed-loop *detection* of the errors in this bandpass B and this makes the active correction of source (8) and the higher frequency part of (7) very much more difficult than that of the errors with bandpass  $< 10^{-2}$  Hz. It is emphasized that this fundamental problem is one of *detection of the signal*, not of its correction. Whether the servo-loop is capable of correcting a known signal in this frequency band is quite another matter, depending on the hardware involved.

We shall return to the matter of active optics correction in the bandpass B below, in connection with the ESO VLT, for which it is particularly important for error source (8) (wind-buffetting deformation of the primary mirror) and the part of error source (7) (thermal effects of the ambient air) with  $\nu > 1/30$  Hz. Error source (10) can also have problems of atmospheric confusion, but the frequencies, directions and amplitudes may be more predictable in this case. Correction in bandpass C is the domain of *adaptive optics*, dealt with in Chap. 5.

We return now to the *normal active optics bandpass A*. There are five basic reasons why correction in this bandpass should be treated as a separate technical system from adaptive optics correction:

- a) *Field.* In bandpass A there is no limitation of isoplanatic angle: the errors are the same over any reasonable field.
- b) *Correction at or near the telescope pupil.* Correction in bandpass A at or near the telescope pupil will automatically provide correction over the *whole field*. For *adaptive optics*, usually only one isoplanatic field can be corrected, which is very small. This enables a small field lens and a transferred pupil to a small, low-inertia correcting element (see Chap. 5) capable of operating at the high frequencies required.
- c) *Bandpass.* The low bandpass A enables one to work naturally and advantageously with heavy support units which would be impossible for high frequency adaptive correction. A separate active system for bandpass A has the huge advantage that *not a single observational photon needs to be lost due to the active system*. Any adaptive system, by contrast, is bound to have an optical throughput substantially  $< 1$  (see Chap. 5).
- d) *Wavefront amplitudes required for correction.* In its nature, the active system in bandpass A will be capable of correcting, and required to correct, amplitudes in certain modes that are neither possible nor required in the normal adaptive system.
- e) *Physical origin of errors.* In general, the physical origin of the errors involved in bandpass A is quite different from those of bandpass C: mainly induced by elasticity in bandpass A, a consequence of the physics of the atmosphere in bandpass C. Even error source (7), the thermal effects of the ambient air, has, in general, different characteristics from external seeing. It therefore does not follow that algorithms or correction procedures which are optimal for bandpass A will also be optimal for bandpass C.

The ESO active optics concept for bandpass A is essentially based on practical experience of optical defects in telescopes which may be induced (or corrected) either by movements of the secondary relative to the primary (in the normal Cassegrain form) or by deforming the primary (or secondary). In an optical train, the best surface to deform, theoretically, is that nearest the pupil, usually the primary. Deformation is usually easier to introduce into the support systems of primaries, but it may sometimes be more convenient at the secondary. If the surface is not at the pupil, there is a shearing effect of the correction over the pupil which increases linearly with angular field. This shearing effect should be kept negligible compared with the correction itself, the tolerances depending on the *modes* corrected – see below. Following Schwesinger [3.161], the concept is based on three laws of physics:

a) *The law of linearity (Hooke's Law of elasticity)*

Passive support systems have always been calculated on the basis of linearity. Glass materials obey Hooke's Law *exactly* right up to fracture, metals up to the elastic limit. The dynamic range for active optics will never be more than a tiny fraction of these limits. The linearity law allows linear superposition of the effects of any sets of forces. Furthermore, it implies that a given change of force distribution will always produce the same *change* of flexure independent of the initial state of the force field, i.e. independent of the initial shape of the mirror.

b) *The law of convergence (the Principle of Saint-Venant)*

We encountered this important principle in §§ 3.4.2 and 3.4.3 in connection with Schwesinger's support theory. The consequence is that the higher the spatial frequency of flexure modes defined by the Fourier equations (3.50) and (3.51), the higher the forces required to generate a given amplitude. This is intuitively obvious as a consequence of thermodynamics and it is of capital importance in active optics. Beyond a certain spatial frequency, a flexure mode cannot be generated by forces that can *either* occur naturally in the system *or* be generated actively in practice. This leads to a simple but important axiom: *if a mirror is flexible enough to develop a given elastic error mode in the gravity field, then the same error can also be corrected by applying active forces of the same order of magnitude as the passive support forces*. Conversely, if a higher spatial frequency mode can never appear as an elastic error because the forces required are higher than can occur, then it will not be correctable by active optics. This is the case with “ripple”, an error generated by resonance effects in polishing which have nothing to do with elasticity. Active optics can do nothing about ripple: its amplitude must be kept low by a hard specification to the optician for such high spatial frequency errors. The task can be made easier by relaxing the low spatial frequency specification.

c) *The law of orthogonality (Fourier or Zernike Law)*

The term  $\cos n\phi$  in Eqs. (3.50) and (3.51) implies that the different modes  $n$  are mathematically and physically orthogonal and independent and can be controlled independently without “cross-talk”.

On this basis, the test and correction polynomial of Table 3.12 was used, the terms being chosen from experience and the Schwesinger formulation originating in the Saint-Venant Principle. (This polynomial is very similar to that given in § 2.3.3.2 for the general off-line testing of telescopes). In the general Fourier equation

$$W = k_{nm} \rho^m \cos(n\phi + \theta_{nm}) , \quad (3.57)$$

$W$  is the wavefront error,  $k_{nm}$  is the optical aberration coefficient defined in Table 3.12,  $\rho$  the radius in the pupil,  $\phi$  the azimuth angle in the pupil to an arbitrary origin,  $\theta_{nm}$  the phase angle of the aberration and  $n, m$  are positive integers. Terms with the same  $n$  in this polynomial are not orthogonal. Strict orthogonality can be achieved by using Zernike polynomials (see § 3.9 of RTO I) and this is indeed a fully valid alternative. In practice, though, it makes little or no difference since the only non-orthogonalities in the corrected terms • in Table 3.12 are tilt with coma, and defocus with spherical aberration. In a least squares solution for the coefficients, the solution can be found with the first term alone of these pairs or with both terms. They anyway have to be separated and the accuracy is, in practice, excellent with the above definition. Furthermore, the image analyser used does not measure  $W$  but the local slope of the wavefront  $\partial W / \partial x, \partial W / \partial y$  and these derivatives of Zernike polynomials are no longer orthogonal [3.202].

The validation of the choice of such terms is finally the practical proof of what terms occur in the telescope. This was first tested at the set-up of

**Table 3.12.** Fourier expansion and terms used in the ESO active optics system for the NTT. The seven terms marked • are corrected, the first of which is simply the auto-guiding. (From Wilson et al. [3.69])

Fourier Equation: $W = k_{nm} \rho^m \cos(n\phi + \theta_{nm})$	
$k_{00}$	constant
• $k_{11} \rho \cos(\phi + \theta_{11})$	tilt (pointing or tracking error)
• $k_{02} \rho^2$	defocus
• $k_{13} \rho^3 \cos(\phi + \theta_{13})$	decentering coma (3rd order)
• $k_{04} \rho^4$	spherical aberration (3rd order)
• $k_{22} \rho^2 \cos(2\phi + \theta_{22})$	astigmatism (3rd order)
• $k_{33} \rho^3 \cos(3\phi + \theta_{33})$	“triangular” error
• $k_{44} \rho^4 \cos(4\phi + \theta_{44})$	“quadratic” error
$k_{06} \rho^6$	spherical aberration (5th order)
$k_{15} \rho^5 \cos(\phi + \theta_{15})$	coma (5th order)
$k_{24} \rho^4 \cos(2\phi + \theta_{24})$	astigmatism (5th order)

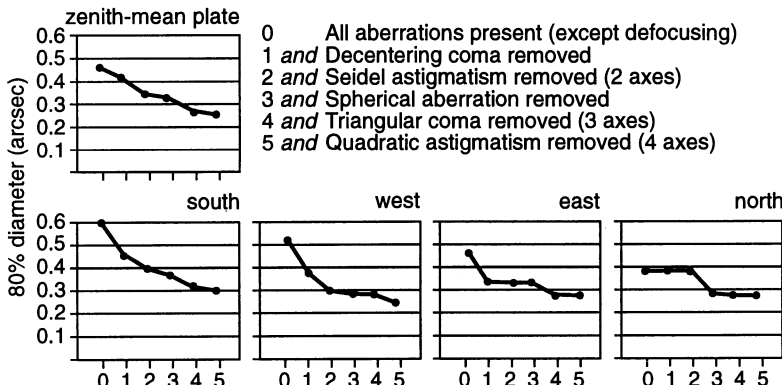


**Fig. 3.63.** Results of classical Hartmann tests of the conventional ESO 3.6 m telescope in 1976 [3.189], illustrating the theoretical improvement after successive removal of polynomial terms. The mean right-hand point of the functions gives the *Intrinsic Quality* (IQ) of this telescope. (From Wilson et al. [3.69])

the conventional (passive) ESO 3.6 m telescope in 1976 [3.189], from which Fig. 3.63 is taken and which illustrates the term “*Intrinsic Quality*” (IQ) of a telescope. The five graphs show the  $d_{80}$  quality criterion (star image diameter containing 80 % of the geometrical energy) for various telescope attitudes: near zenith and at ca.  $45^\circ$ – $60^\circ$  in the S, W, E and N directions. The left-hand point gives the actual, measured quality of the telescope after careful adjustment at set-up. The other points show the improvement that would be achieved if the residual terms shown were successively removed. In this passive telescope these were simply fictitious, mathematical values since there was no means available for such correction in that telescope. The left-hand part and the form of the 5 functions (which must, by definition, reduce monotonically from left to right or remain flat) is highly variable, which demonstrates that the terms involved are sensitive to the changes in telescope attitude. But the right-hand point, within the error of measurement at the time, is *invariant* and an intrinsic property of the telescope: we termed it the “*Intrinsic Quality*” (IQ) of the telescope. It is that quality a telescope would have, if all the terms that can vary during the function of the telescope and induced by the error sources of Table 3.11 up to the bandpass limit of 1/30 Hz were corrected. The aim of an *active* telescope is to achieve the *intrinsic quality* or a quality very close to it. The (unachievable) IQ of the passive 3.6 m telescope was, from Fig. 3.63,  $d_{80} = 0.27$  arcsec. For comparison, the *active* 3.5 m NTT has an (in principle, achievable) IQ of  $d_{80} = 0.125$  arcsec. The IQ is a measure of the total high spatial frequency residual errors left in the entire system, both from residual figuring errors and from all other sources (in practice, source (7), the thermal effects of the ambient air, as we shall see from further analysis of the NTT results).

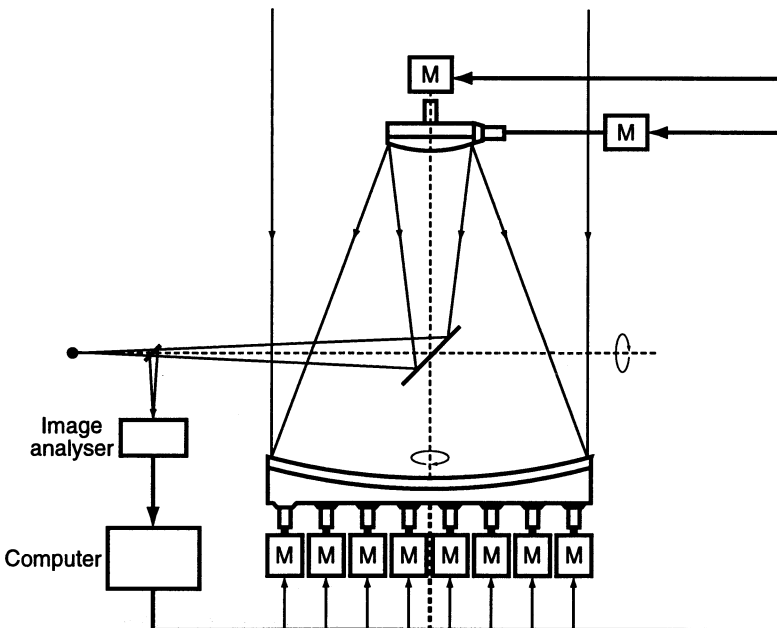


**Fig. 3.64.** Active optics correction for the low frequency bandpass A: principle of the ESO closed-loop control technique for optimizing image quality (from [3.69])

Figure 3.64 shows the principle of the feedback loop in the ESO closed-loop active optics system. The image analyser either “borrows” the light from the offset guide star for 30 s while the telescope relies on absolute tracking (the original system of the NTT) or a proportion of the light is permanently deflected by a beamsplitter to the analyser (final system of the NTT). The image analyser used in the NTT is of the Shack-Hartmann type (see § 2.3.3.2) and functions excellently. Other possibilities are discussed in Chap. 2. The raw data from the S-H image analyser, the lateral aberrations for the sub-apertures defined by the S-H raster, are processed in the microcomputer to derive the centroids of the S-H spots and then the coefficients  $k_{nm}$  of Table 3.12 are derived by least-squares reduction. From pre-stored *calibrations* for the different modes, signals are then sent either to the secondary  $M_2$  to correct 2 of the six terms (apart from tilt  $\equiv$  autoguiding), namely defocus and decentering coma, or to the primary support system to correct the other 4 terms. The essential features are the *modal* control and the fact that the correction at the primary is done by *force changes* applied to a “soft” (astatic) axial support system. *Automatically*, with this concept, the geometry of any adequate passive support system (see § 3.4.1, in particular Eqs. (3.41)–(3.43)) will provide sufficient sampling over the aperture to correct the low spatial frequency modes required. The modal correction, since the coefficients are measured for the final image, applies to all possible sources of error affecting the final image in this bandpass: whether the astigmatism measured is

induced by an axial or lateral support, at the primary or secondary, is of no consequence, since the total final vector will be corrected. The principle of correction would also work equally well with a “hard”, position-based support. But this requires an extremely stiff prime mirror cell which cannot normally be realised in a large telescope. Hence, the classical “soft” solution was chosen in the NTT. The soft support has no disadvantages in the normal bandpass A; but it does have in the extended bandpass B. We shall return to this concerning the ESO VLT.

Why is modal control so essential for a successful active optics system? This is discussed in ref. [3.69]. Mathematically, it seems simple and elegant to set up a square influence matrix (stiffness matrix) for the prime mirror support by applying a standard force change to each support and measuring the corresponding wavefront change for the same sampling points as the supports. Then, assuming linearity from Hooke’s Law, we have the unique solution to correct the wavefront at these sampling points

$$\Delta F_j = A_{ji}^{-1} \cdot \Delta W_i , \quad (3.58)$$

where  $\Delta F_j$  is the column vector component of force changes at the actuators,  $\Delta W_i$  the column vector component of desired wavefront changes at the sampled (actuator) points, and  $A_{ji}$  the component of the stiffness matrix. By modifying this basic algorithm, in a way used commonly in optimization programs for optical design [3.69] [3.203], the square stiffness matrix can be made rectangular in either sense. With this “wavefront approach”, one would then establish the stiffness matrix in advance. The on-line correction operation would consist of an image analysis followed by matrix inversion giving the force changes required to reduce the aberrations at the sampled points to zero.

In spite of its simplicity and elegance which have often led to its proposal, the method has serious disadvantages [3.69] and the modal approach is superior in all respects. The essential reason why this is so, is that the wavefront approach is blind to the physical realities behind the Schwesinger flexure theory (see § 3.4.3). The arbitrary sampling forces the full correction of higher order modes that can only be corrected by very high forces, if at all. The result is a highly ill-conditioned solution matrix with poor accuracy and very high forces, normally outside a reasonable dynamic range of the system. Another poor feature is that the wavefront sampling approach has no learning potential: a heavy matrix inversion operation is performed every time, but there is no indication what is the nature of the error: whether a support error causing astigmatism, or decentering or whatever other error source is involved. All such problems are automatically resolved by the modal approach, whereby the precise nature of the modes is not very critical provided they reasonably correspond to the physical reality. Three of the four most important modes occurring in telescopes are only indirectly, if at all, associated with elasticity: defocus, decentering coma and spherical aberration. Defocus occurs above all because of thermal effects in the tube structure.

Decentering coma is essentially due to lateral shear of the secondary (or a corrector) relative to the primary axis (see §2.1). It produces a very pure third order coma. Spherical aberration can occur from wrong image position (despace – see §2.1), but the commonest source by far is *matching error* in manufacture (see §1.3.4) due to errors in null systems used for testing. This will be mainly third order spherical aberration, but the order distribution will depend on the nature of the null system. It does not follow that this order distribution will be matched by natural flexure modes. On the other hand, all errors originating from supports, leading to astigmatic or higher orders of mirror flexure, will be best compensated by *natural vibration modes*. These are discussed in detail by Noethe [3.203] and were first suggested by Creedon and Lindgren [3.191]. In the NTT, a mixed system of modes is used: natural modes for the fixed dc correction and the polynomial of Table 3.12 for the on-line correction – see below.

A very important feature of the active optics system is the *calibration* of required force changes. For each mode, Schwesinger calculated the force change distribution required to produce a coefficient of 500 nm, with an adequate degree of purity, i.e. whereby the higher order residuals, whose correction would require very high forces, have a negligible effect on the image quality. Some details of these calibrations are given by Wilson et al. [3.69], more complete information by Schwesinger [3.173]. The lowest mode is, of course, third order astigmatism. A maximum load change of about 3 % of the mean passive load is sufficient to produce an astigmatism coefficient of 500 nm in the NTT primary. These calculations are complex but are all done in advance, once only, the results being stored in the microcomputer. Once the coefficients have been derived from the image analyser measurements, the calculations of the required force changes are trivial, since they consist solely of setting the precalibration forces in linear proportion to the measured coefficient and then summing the force changes for all the modes by linear superposition.

The modal procedure can formally be represented by the matrix operation analogous to (3.58)

$$(\Delta \tilde{F}_j)_{nm} = A_{ji}^{-1} \cdot (\Delta \tilde{W}_i)_{nm} , \quad (3.59)$$

in which  $(\Delta \tilde{F}_j)_{nm}$  is a force change distribution which produces a nominal change  $(\Delta \tilde{W}_i)_{nm}$  to the aberration mode  $n, m$  with the necessary radial purity, i.e. that purity which allows cross-talk in radial modes with negligible effect on the image. The force calibrations could be derived from the stiffness matrix  $A_{ji}$ , but were, in fact, derived from analytical theory. They are derived for  $\theta_{nm} = 0$  in Eq. (3.57) and for the standard change of aberration coefficient  $\Delta k_{nm}^U$ . We will give them the symbol  $(\Delta \tilde{F}_j^U)_{nm}$ . Then the total force change is given by

$$\sum F_j = \sum (\Delta \tilde{F}_j^U)_{nm} \cdot \frac{\Delta k_{nm}}{\Delta k_{nm}^U} , \quad (3.60)$$

where the summation refers to the modes chosen. For the NTT, the four modes  $n, m$  controlled at the primary are, from Table 3.12, 04, 22, 33 and 44. The linear procedure of (3.60) is a consequence of Hooke's Law. A similar linear law exists for the other two modes controlled at the secondary, 02 and 13, the calibrations being obtained directly from Eq. (2.16) for defocus and from Eqs. (2.1) and (2.4) for decentering coma, which are also pre-stored in the computer. The modal algorithm therefore permits any complex calculation to be done in advance: the on-line calculations are trivial compared with those required for centroiding the S-H images. A more complete discussion is given in ref. [3.69].

The use of an image analyser in the telescope field implies that field aberrations are also measured. This does not matter since, as mentioned above, the field aberrations of a telescope are higher order functions which are affected to a negligible extent by the error sources of Table 3.11. It is therefore entirely sufficient to deduct the theoretical (optical design) values of the field aberrations from the measurement for the indicated position of the image analyser (guide probe) in the field. Since we are only concerned with low spatial frequency terms, this means deducting third order field astigmatism (which, from Table 3.1 of RTO I, grows with the square of the field) for an RC telescope such as the NTT; or, additional, third order field coma (growing linearly with the field) for a classical Cassegrain telescope. As discussed in § 2.2.1, the effective position in the field of the "optical axis" of the telescope, resulting from the set-up and alignment procedure, must also be taken into account; further, the effect of telescope decenter on the field astigmatism if the decenter exceeds the limits analysed therein.

The theoretical limits of the normal active optics bandpass A of Fig. 3.62 are dc and 1/30 Hz. Since fabrication errors represent a dc (once-off) correction process, it was decided to achieve the dc correction in the NTT with springs, which are independent of the  $\cos Z$  effect of gravity with zenith angle. For a *passive* support, astatic levers are advantageous here, since they automatically compensate for  $\cos Z$  (see Fig. 3.50). But a dc *active* correction should, by definition, stay constant, independently of  $Z$ . Figure 3.65 shows schematically one of the 75 active supports, disposed with 3 fixed points over a 4-ring passive support geometry, with 8, 16, 24 and 30 supports respectively [3.69] [3.72] [3.204]. The levers are a two stage system, to save weight, with an average force magnification of 16. An important parameter of the system, closely linked to the  $\cos Z$  effect, is the *dynamic range* of correction, which was analysed in detail on the basis of manufacturing tolerances and the errors from Table 3.11 in the light of experience [3.205]. It was expected that the bulk of the correction would be dc. This was even more the case than had been assumed – see below. The following correction scheme in 3 levels was envisaged:

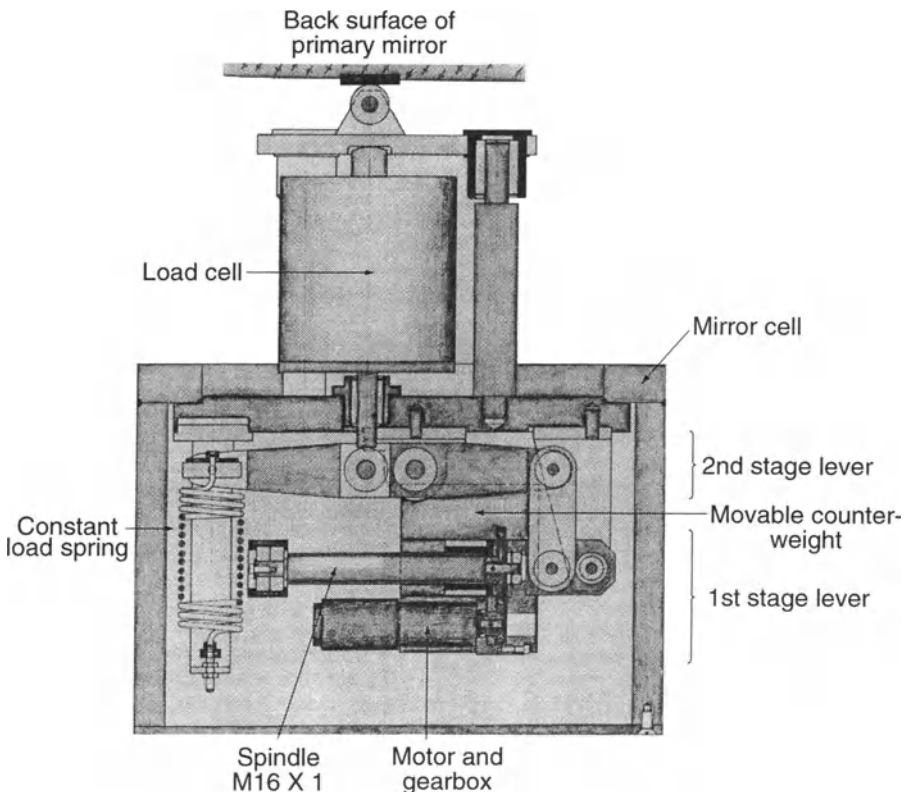


**Fig. 3.65.** One of the 75 active supports (schematic) of the ESO 3.5 m NTT primary axial support. The dc errors are corrected by tension springs (through the levers), the other (variable) errors by the movable counterweights. (From Wilson et al. [3.69])

- *First level:* dc correction with springs.
- *Second level:* Diurnal correction with the counterweights, performed at dusk near the zenith before telescope operation.
- *Third level:* Correction during operation with the counterweights whenever the altitude of the telescope has significantly changed.

The system was designed such that an image analysis and correction could be made *during the observation and without disturbing it*. It was necessary to learn how to operate the third level of correction. It was intended to automate this level fully with an automatic correction cycle about every 10 minutes. This matter is discussed below in the section (§ 3.5.3) on the operating results of the NTT.

It was considered essential to test the principles and practice of correction thoroughly on a 1 m diameter test model mirror. The results were described by Noethe et al. [3.204]. This model mirror was scaled according to the Couder

Law (see § 3.4.1) to give the same flexibility as the full-size NTT primary. This gave a thickness of 18.9 mm for a full diameter of 1050 mm, an aspect ratio of 56. The support geometry could then be taken over unchanged from the NTT, the loads being scaled according to the weights.

The results of the manufacture of the NTT optics by Carl Zeiss, Oberkochen, were given in § 3.2.4 above in the general description of the NTT. Details are given in [3.71]. It must simply be repeated here that the essential specification was the *active* one, namely the *Intrinsic Quality* for the high spatial frequency residuals assuming full correction of the actively controlled low spatial frequency terms. The specified IQ was  $d_{80} \leq 0.15$  arcsec; but Carl Zeiss surpassed this and achieved  $d_{80} = 0.125$  arcsec. This referred to the whole optical train comprising 3 mirrors for the Nasmyth focus. This quality has even been surpassed for the Italian TNG optics (§ 3.2.4). With the experience of the 1 m model mirror, the active correction of the low spatial frequency residuals of the NTT primary, under test at Carl Zeiss, was a simple operation. To achieve the IQ *passively*, if at all possible, would have cost an order of magnitude more than the contract price; but the active correction was done in a matter of minutes.

Of course, matching error between the primary and secondary was not revealed by the above tests on the primary alone. Such an error was present and was revealed (and afterwards corrected) by the functional tests of the telescope.

### 3.5.3 Operational results for the ESO 3.5 m NTT and conclusions from its performance

A complete account of the set-up procedure, active optics application and optimization, and the results of the first test period, was given in “Active Optics IV” by Wilson et al. [3.70]. Some of these results were briefly mentioned in § 3.2.4 above. Details of modifications and the state of technical completion of the NTT from the point of view of active optics in the summer of 1992 were given in refs. [3.72] and [3.73]. Here, only a few of the essential aspects will be reviewed.

The basic set-up and alignment [3.70] followed essentially the system used for passive telescopes (see § 2.2). This led to what was termed “Technical First Light”, giving the first images with an eyepiece and television, but before the final adjustment (by tilt) of the prime mirror cell was performed to achieve the basic (passive) correction of decentering coma. This was performed a month later when the image analyser was available to measure the amount and direction of the coma. The necessary tilt of the  $M_1$  cell was only  $\pm 1.25$  mm (or 1.98 arcmin), but this small error (mechanically) caused the huge coma coefficient of 12788 nm ( $\equiv 4.52$  arcsec for 100 % enclosed energy). This gives a good measure of the high sensitivity of modern, short telescopes to decentering coma and illustrates well how essential active centering is. These relations are given by Eqs. (2.1) and (2.4). The vector direction of the

coma must be interpreted in the physical coordinates of the prime mirror, which is not a trivial matter, but of prime importance since the machining of the flexion bars was a major operation. In fact, about 95 % of this coma was removed: the residual 5 % was well within the dynamic range of the active  $x$ - $y$  correction system at the secondary.

The full determination of the coefficients of the (fixed) aberrations in the zenith, for dc correction with the springs, led to no surprises except for the spherical aberration coefficient which, when local air variations were removed, had a value between  $-3500$  and  $-4000$  nm. For 100 % included energy, an image diameter at optimum focus corresponding to 1 arcsec has a coefficient with NTT geometry of 4241 nm, so the effect was well outside the *passive* specification. This error could be completely removed actively (using the natural mode which used somewhat lower forces), although it absorbed a considerable portion of the dynamic range. In many ways, the correction of this “matching error”, as it proved to be, was the most powerful validation of the active concept of the NTT. For, as a passive telescope with this quality, it would have been a failure. The alternative of a contractual replacement of the defective primary would have been immensely expensive and time-consuming. Subsequent analysis by Carl Zeiss revealed a systematic positional error of the null systems used to test the primary of 1.8 mm which gives a coefficient of about  $-3000$  nm. The remaining aberration (which happened to have the same negative sign) was due to extra weight of lateral support pads added after the support design had been done. The active correction of the spherical aberration at the primary did, therefore, remove the error at its source. Had the error been on the secondary, correction at the primary would have caused a small departure from the RC system, thereby introducing a field coma of 0.18 arcsec at a field radius of 10 arcmin. As it was, no field coma could be detected in the corrected system.

After the completion of the *first level* (dc) correction with the springs and a preliminary correction at the *second level* with counterweights of small residuals, the telescope was in a well-adjusted state *near the zenith* and ready for “Astronomical First Light”. It must be borne in mind that any telescope at this stage can only have rudimentary tracking quality. In addition, the field rotation facility, essential for an alt-az mounted telescope, was not yet operating. This meant that only very short exposure times were possible, of the order of 10 s. Since this is inadequate to fully integrate normal seeing, good results are only possible with exceptional seeing. Fortunately, the seeing *was* exceptional, better than 0.3 arcsec FWHM as it emerged. Also the local air conditions (ventilation) were remarkably favourable. The CCD was dismounted from the image analyser (the telescope was, therefore, actively “blind” during the night of the first observation) and mounted directly at the focus, giving a field  $12 \times 12$  arcsec. The globular cluster  $\omega$  Centauri was observed. These first pictures gave best star images of 0.33 arcsec FWHM. A comparison showing the gain in resolution and depth was set-up by West [3.206], reproduced in [3.70]. Figure 3.66 reproduces this comparison. The

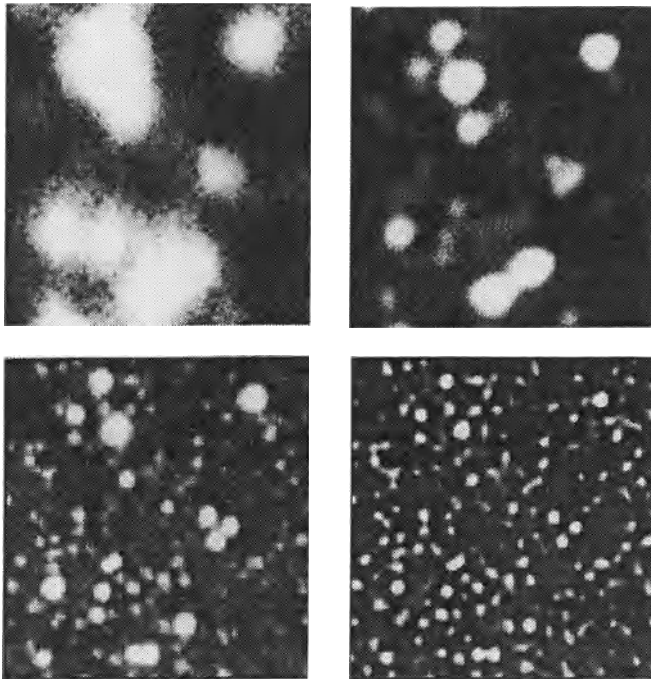


**Fig. 3.66.** CCD pictures obtained at “Astronomical First Light” with the ESO 3.5 m NTT, compared with previous photographic records of the same field (globular cluster  $\omega$  Centauri). (From West [3.206])

frame at the upper left shows a considerable enlargement of a small area of a plate taken with the ESO 1m Schmidt telescope in 1984 under modest seeing conditions (ca. 2 arcsec). The plate taken at the Cassegrain focus of the passive 3.6 m telescope (upper right) with seeing about 1 arcsec was considered extremely good by normal standards. The NTT raw frame (lower left) was probably the best image ever recorded at the time and showed the immense gains that active optics could bring, not only in resolution but also in depth (limiting magnitude for a given integration time). The frame at the lower right shows the further gain that can be achieved by post-detection deconvolution techniques [3.206].

The efficiency of the NTT proved to be so high that the correction process (image analysis, correction, check image analysis), taking 5 min or more, was relatively too slow for the aims of *third level* correction (see § 3.5.2 above). The most rapid correction can be achieved by precalibration of errors as a function of zenith angle. This is particularly simple and effective with decentering coma. There were difficulties with astigmatism due to friction, acting in the axial direction, but originating in the lateral support system. This problem was removed by a modification of the lateral support, and astigmatism is now reproducible and can be largely calibrated. Also the force setting oper-

ation is much simplified [3.72]. For technical reasons, defocus is the hardest aberration to control to the necessary quality, coma the easiest. Table 3.13 summarises the conclusions regarding the achievable optical quality with the NTT. It shows that, if the active control system is operated correctly, the low spatial frequency aberration residuals are effectively negligible with a value  $d_{80} \sim 0.075$  arcsec. Temperature and wind sensors have now been introduced, which should permit further optimization of the local air conditions, which even at best, were still the dominant factor in the measures of Table 3.13. Potentially, the NTT is capable of an image quality, excluding external seeing, with  $d_{80} < 0.20$  arcsec but this requires optimum operation of the total system, above all of the building conditions. Since external seeing  $< 0.20$  arcsec FWHM has been recorded at Paranal, it is clear the effort is worthwhile.

**Table 3.13.** Optical quality potential of the NTT (excluding external seeing). This table shows that the practical limitation is the local air (source (7) in Table 3.11), in spite of the excellent building design. (From Wilson et al. [3.70])

Error	$d_{80}$ (arcsec)
Low frequency aberration residuals	0.075
Total high frequency (smoothed), consisting of:	0.22
– High frequency from optical system	0.125
– High frequency from local air and measuring noise	0.18
Total with statistical addition	0.23

The aim was to fully automate the third level of correction with an automatic correction cycle of about 10 min. If conditions are excellent, most errors (including defocus) change very slowly and will be corrected by this cycle. This includes the bulk of the local air effects, *if local ventilation and temperature conditions are optimal*. If the local air is producing significant high frequency error, it is the best measure of deteriorating local conditions. The *automatic* nature of the correction cycle is the only way the optical maintenance problem of telescopes can, in practice, be solved. The nature of this maintenance problem, which above all requires active optics, will be further discussed in Chap. 8. Suffice it to say here that automation of the active correction essentially converts the (normal and unfavourable) *analogue* optical maintenance situation into a (favourable) *digital* one.

The best practical measure of what had been achieved by 1992, and what remained to be achieved, is shown by Fig. 3.67, which gives a rough practical comparison of the total optical quality of the best telescopes at the ESO La Silla observatory [3.73] as well as the external seeing as measured by the seeing monitor. For the three older telescopes (3.6 m, 1.54 m Danish, 2.2 m (II) MPIA), the values are an average over 5 years. The external seeing values from the seeing monitor at La Silla were only available for 4 months but

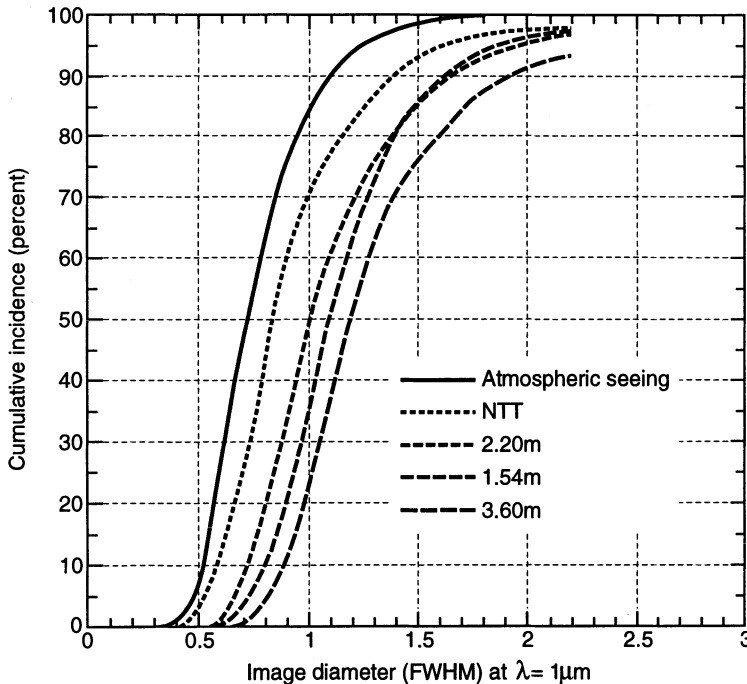


**Fig. 3.67.** Cumulative/integrated incidence of external seeing and image quality of the major telescopes at the ESO observatory La Silla. External seeing and NTT 1 year (1991), the other telescopes 5 years (1987–1991). Normalized for  $\lambda = 1\mu\text{m}$  and zenith position ( $Z = 0$ ). (From Wilson et al. [3.73])

they could be used to give an equivalent curve for the whole year of NTT measurements by comparing the median (most probable) image quality of the NTT, on the assumption that external seeing is the dominant factor limiting its performance, which is clearly the case. The data for the telescopes are only approximate, since they are normalized for a wavelength of  $\lambda = 1\mu\text{m}$  and for the zenith (air mass = 1,  $Z = 0$ ) on the assumption that the *only effect* is external seeing, giving for the image size [3.207] (see also Chap. 5)

$$d \propto \lambda/r_0 \propto \lambda^{-1/5}(\cos Z)^{-3/5}, \quad (3.61)$$

$r_0$  being the Fried parameter and  $Z$  the zenith angle. For observations at  $\lambda = 500\text{ nm}$  and  $Z = 45^\circ$ , the correction factors are then 0.87 and 0.81 respectively for the cumulative incidences of Fig. 3.67 or their reciprocals for the image diameters. However, the departures of the telescope images from the seeing disk are due to errors in the telescope optics and local air (dome and local seeing), for which the correction factors do not follow Eq. (3.61) and will normally be nearer to unity. Therefore this representation tends to compress slightly the real differences between the telescopes and thereby represent the 3.6 m over-optimistically. On the other hand, the image quality in this telescope has been significantly improved since 1987 by improvements in the

air-conditioning system and insulation of the telescope, so in measurements for 1991 it might be closer to the 2.2 m telescope. In any event, the global impression is certainly a reasonable approximation to the true situation, not only at La Silla, but at observatories in general.

Table 3.14 gives the median (i.e. most probable) seeing corresponding to the functions of Fig. 3.67. This table also gives a measure of the “optical efficiency”  $E$ , expressed as  $(d_0/d)^2$ , where  $d_0$  is the median FWHM of the external seeing and  $d$  that of the telescopes. This simple criterion, whose validity will be discussed in Chap. 4, is thereby normalized to 1 for a “perfect” telescope, i.e. the external seeing value  $d_0$ . As we would expect, the active NTT was easily the best telescope. However, we were convinced that the automation of the 10 min correction cycle together with the completion of the thermal sensor investigation and improvements would reduce the gap between the external seeing and NTT curves in Fig. 3.67 to half, or less, of that value. The efficiency  $E$  with a median seeing of 0.76 arcsec in Table 3.14, instead of the 0.82 arcsec measured, would rise from 0.73 to 0.85. Such an efficiency, 85–90 %, should be the aim of highest quality active telescopes, even at the best sites – or, indeed, *precisely at those best sites*, so that the best available seeing is exploited to the full. This exploitation will normally imply “flexible scheduling” of the observations, so that programmes requiring optimum seeing will be able to benefit from it.

**Table 3.14.** Median (most probable) image quality (FWHM) and “optical efficiency”  $E$  in five cases at La Silla corresponding to Fig. 3.67. Normalized for  $\lambda = 1 \mu\text{m}$  and  $Z = 0$ . (From Wilson et al. [3.73])

Telescope	Perfect Telescope (External Seeing)	NTT	2.2 m	1.54 m	3.6 m
Median seeing FWHM (arcsec)	0.70	0.82	0.99	1.08	1.17
$E = (d_0/d)^2$	1	0.73	0.50	0.42	0.36

The figures of Table 3.14 for the other telescopes deserve comment from the aspect of active optics. From the point of view of the optical quality of the mirrors, the 3.6 m and 2.2 m (II) telescopes are of comparable quality [3.68] [3.189], the 1.54 m somewhat inferior because its specification was less severe. But, in practice, the 3.6 m was significantly inferior to the 2.2 m because of variable decentering coma introduced by its top-end mechanics and its inferior dome seeing. An active optics upgrade, comprising only image analysis and active correction of decenter and focus could immediately produce a major improvement. Even without further correction possibilities at the primary, the on-line image analysis would at once give detailed information on the dome seeing problems and indicate what changes are required. A model of an automation approach to upgrading an older telescope was the improvement

programme of the Cerro Tololo 4 m telescope, applying the NTT principles insofar as they were applicable to a classical thick primary. Baldwin et al. [3.208] show that a considerable improvement is possible at relatively low cost.

The curves of Fig. 3.67 permit a further interesting comparison concerning the *matching error* of the NTT, which was completely corrected actively as indicated above. If this error had been left uncorrected, a passive error as in the other passive telescopes, the quality of the NTT could have been about the same as that of the 1.54 m.

Latest information (November 1997) concerning the status and perspectives of the active optics system of the NTT has been kindly provided by P. Gitton through L. Noethe of ESO, Garching. P. Gitton is the optics specialist of the team formed at the beginning of 1994 by D. Baade for the maintenance and upgrading of the NTT. This team was long overdue and a serious decline in performance had occurred between 1991 and 1994. It is largely due to the efforts of P. Gitton (of course, with excellent support from colleagues) that the optical quality has been restored and further advances in the system made within the framework of revised VLT-compatible software.

The *third level* of the active optics control, as defined above, is now functioning routinely, still in a *non-automatic* mode, for all correctable aberrations except *defocus*. This means that all the aberrations, apart from defocus, are controlled to give a low spatial frequency image quality of  $d_{80} \leq 0.15$  arcsec using image analysis (IA) before each new observation (preset) or after each significant change of zenith angle. Focus control is still performed with the old-fashioned “through-focus” sequence or with the focus wedge. A precalibration of focus change from a measured instrument offset has long been intended, but has so far not been reliable enough. It is hoped to solve the problem by logging data as a function of rotator angle and adapter temperature.

Active correction based on *precalibration* (open loop for the third level) is still not operating, though much of the necessary base work for it has already been completed. An important feature has been a re-optimization of the zenith  $M_1$ -support load distribution between the springs and counterweights, essential for effective third level astigmatism control. Further data of image analysis as a function of zenith angle  $Z$  is required and software implementation (and test) of defocus as a function of Serrurier truss temperature and  $Z$ .

The *automatic function* of the third level of active optics is still not operating. This was envisaged in the original design and should enable automatic active correction *in parallel with the observation* (i.e. without disturbing the observation and, indeed, without the astronomer being aware of it!). For several years, the main problem was the lack of an automatic guide star facility. This is now solved by the availability of the HST guide star data base. However, there are still technical problems of guide star acquisition and centering. The automation of focus control is limited by the pointing stability problems

of the  $M_2$  focus mechanics – the TNG (Galileo) telescope has a much improved system. It is stated by Gitton that coma correction also introduces pointing shift although this should not be the case with the principle of coma correction by rotation round the  $M_2$  center of curvature. It may generally be necessary to close the shutter (for the observation) when  $M_2$  is being moved to correct either defocus or coma, re-opening it when the slight pointing error has been corrected by the software.

A bonus compared with the original design intentions of the active optics system has been achieved with regard to additional aberrations induced by the *instruments* of the NTT. Specifically, a spherical aberration contribution ( $d_{80} \simeq 0.35$  arcsec) has been identified in the EMMI spectrograph. The active optics software has been modified to allow the addition of such contributions to those of the IA measurements. Further measurements on the instruments EMMI and SUSI are required to determine the contributions to all the aberrations.

The above résumé by Gitton confirms notable and excellent work in recovering and improving on the optical quality achieved in the early period of operation of the NTT. It is to be hoped that this good work will be further pursued and that full automation of the third level of the active optics will be achieved, including considerable use of precalibrated correction. Full automation of defocus correction, without closing the observation shutter, will probably require new  $M_2$  focus mechanics on the lines of the TNG design. Only then will the original design goals of the NTT opto-mechanical system have been fully realised.

### 3.5.4 Extension of the active optics system to the ESO 8 m VLT

The full blank diameters ( $D$ )/thickness ( $t$ ) of the NTT primary and the VLT primaries respectively are 3.6 m/0.240 m and 8.2 m/0.175 m, giving aspect ratios of 15 and 47. Originally, 200 mm thickness was envisaged for the VLT blanks, but 175 mm was finally the maximum thickness that could be guaranteed in Zerodur. The Couder flexure law  $\propto D^4/t^2$  gives a flexibility nearly 51 times greater for the VLT primary. Whereas it was a subsidiary requirement imposed on the NTT that it should also be capable of normal image quality in a purely *passive* mode (hence the aspect ratio of 15, not higher), no such requirement was placed on the VLT which is defined as a telescope that can only function in the *active* mode.

An analysis of the basic modal correction, using a 6-ring “passive” axial support geometry with 152 axial supports, was given by Schneermann and Cui [3.209], at that time (1988) for a thickness  $t = 200$  mm. The passive sag between supports gave a residual error, after subtraction of tilt and piston, of 33 nm rms. Natural mode correction – see Noethe [3.203] – for the active optics system was preferred to Zernike modes, because (as would be expected for the elastic corrections) it gives a more favourable dynamic range. Noethe proves two important properties of natural (or minimum energy) modes: firstly, the

*orthogonality* of the functions and, secondly, that the *pressure fields are proportional to the deformations* (Appendix A and B in [3.203]). Within the approximations of the theory, calibrations are then essentially a scalar process. The high flexibility of the VLT primaries means that many more modes must be controlled. For the thickness  $t = 200$  mm, the first 20 modes, with eigenfrequencies, are shown in Fig. 3.68. The amplitudes generated by a force field with a given maximum force will be roughly inversely proportional to the square of these frequencies. This is a statement of the modal convergence resulting from the Saint-Venant Principle. Schneermann and Cui [3.209] give the frequencies of the first 10 modes of Fig. 3.68 together with the percentage of the mean passive load for the maximum force required to generate 500 nm rms of wavefront aberration. These percentages go from 0.06 % for the first (astigmatic) mode with eigenfrequency 18.4 Hz ( $t = 200$  mm) to 6.34 % for the tenth mode with frequency 182 Hz, the corresponding force being 108.9 N. The *dynamic range* of the correction system must be laid out to cover the correction requirements from the various error sources of Table 3.11, for the normal active optics bandpass A of Fig. 3.62. Table 3.15 gives the distribution

\*  
**The two modes marked → with frequencies 407 Hz (n=1) and 471 Hz (n=0) are not induced by normal axial forces giving all the other modes, but by radial forces.**

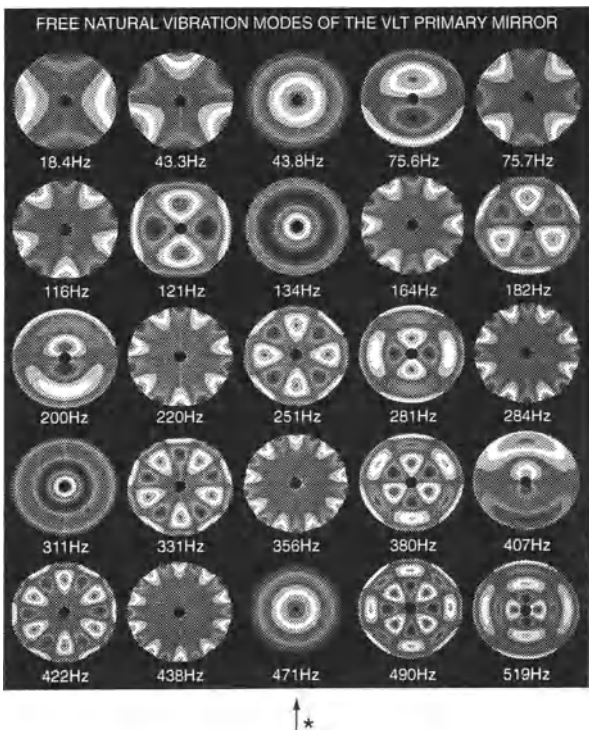


**Fig. 3.68.** The first 25 natural modes, with eigenfrequencies, for a VLT primary with  $t = 200$  mm (courtesy M. Schneermann, ESO)

**Table 3.15.** Dynamic range of the active optics system for the VLT 8 m primary mirrors (after Noethe [3.210])

Error source	Active forces (N)		Dependence on zenith angle $Z$
	Positive	Negative	
Change to Cassegrain	413	156	constant
Figuring	120	120	constant
Lateral supports	50	50	$\sin Z$
Axial supports	80	65	$\cos Z$
Wind	50	50	unknown
Local air	50	50	unknown
One chamber hydraulic system	188	188	$\sin Z$

[3.210] for the final thickness  $t = 175$  mm. The biggest item is the conversion from Nasmyth to Cassegrain, which, because of an appreciable axial image shift, introduces about  $20\lambda$  of spherical aberration.

The axial support hardware consists of a 2-stage system: a *passive* part (top stage) consisting of a hydraulic whiffle-tree system [3.211] [3.212]. An *active* spring-based (lower stage) applies the active corrections. Figure 3.69 shows this system schematically. The active stage, based on a spring of finite length, is not astatic, but the extent of non-astaticity is acceptable for the correction cycle proposed and the given flexibility of the cell. The basic active correction cycle proposed is 40 s. Since the integration time for image analysis must be 30 s, this is technically about the fastest cycle possible. It will be about 15 times faster than the 10 min cycle intended for the NTT. The fast correction cycle has great advantages. It allows higher non-astaticity of the active support, but above all should correct the bulk of the low spatial frequency errors originating in the ambient air (source (7) of Table 3.11). This should include most of the *mirror seeing*, though this should anyway be low because of the thermal regime (see § 3.6). Furthermore, in the VLT more modes are controlled than in the NTT, giving also for this reason more control of errors from the local air.

Active optics is a linear *differential* correction system, so *absolute* setting to a given force is not very important: what is important is accurate differential forces, which is much simpler. However, it is essential that the total *absolute* force remain sufficiently constant over the correction cycle. Again, the shorter the correction cycle, the easier this is to achieve. The requirements for the axial support system are discussed by Noethe et al. [3.213]. Assuming random force errors over 150 supports, the accuracy of a single force should be 0.1 N. The minimum force step is 0.05 N. These limits are set by the first, astigmatic mode.

Originally, a push-pull axial support was envisaged. It was decided, however, that a purely “push” system, as in the NTT, was adequate, in spite of

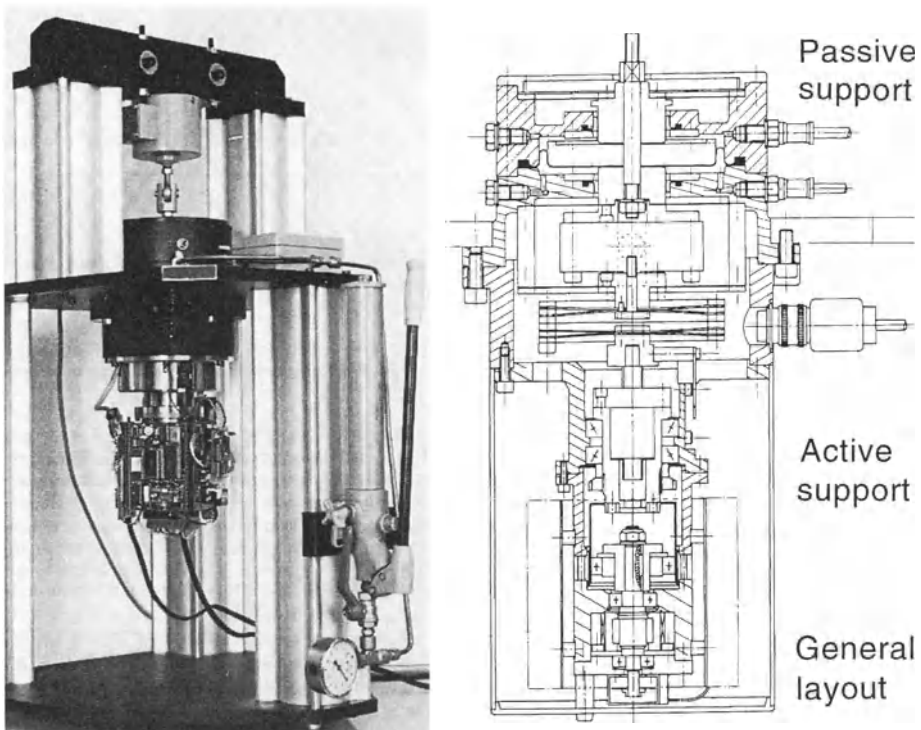


**Fig. 3.69.** Axial support unit (schematic) for the VLT 8 m primary mirrors (from Schneermann et al. [3.212])

the  $\cos Z$  limitation near the horizon. A “push” system can apply no active correction at  $Z = 90^\circ$  because there is no gravity load to push against.

So far we have considered the normal active optics bandpass A of Fig. 3.62. In the VLT, however, wind-buffetting of the primary can cause deformation of the mirror form in the *extended active optics bandpass B*. The problems of *detection* of these errors due to confusion with the atmosphere were explained in § 3.5.2 and given in detail in ref. [3.201]. From experiments measuring the power spectra of wind at the NTT with a dummy mirror, Noethe [3.213] has deduced that the maximum tolerable pressure at individual sensors at the VLT primary for wavefront aberrations of 50 nm rms are of the order of  $1 \text{ N/m}^2$  rms. Useful correction would require a bandpass up to 10 Hz or more, which cannot be achieved with the VLT axial support. 1 Hz would be about the limit of its practical operation. The safest approach is therefore an enclosure design which limits the pressures to  $1 \text{ N/m}^2$  rms. However, this has consequences for the natural ventilation, which, as the NTT has proved, is so important for good thermal conditions of the ambient air.

These conditions might be relaxed if a satisfactory method of measuring the wind-buffetting deformation were available. This problem has been ad-

dressed by Wilson et al. [3.214]. The possibility of detection by direct strain measurements on the mirror blank was considered, but sub-molecular strain values would be necessary to detect the astigmatism limits required. It was concluded that only an optical method could give the required accuracy. By the definition of the bandpass B, a closed-loop (natural star) method is not appropriate in this bandpass [3.201], so an artificial source must be used. The most promising method seems to be the so-called *front detection method* based on the well-known Hindle sphere geometry (see § 1.3.5.2). The application of this geometry to wind-buffetting deformation detection is shown in Fig. 3.70. It requires small auxiliary Hindle-type mirrors to be attached to the primary, near the central hole or outer edge or both, which operate in autocollimation via the secondary from a source in the image plane. The authors [3.214] consider several other front-detection systems, some of which may be easier to realise in practice; also back-detection systems of the sort proposed by Tull [3.215], but these seem to be less practicable from a space point of view. If the feasibility of one of these front-detection systems can be confirmed, this should be a major step in removing this last weakness of active, thin-meniscus technology. However, the support response will have to be adapted to the bandpass requirements for wind-buffetting. A somewhat thicker primary than  $t = 175$  mm for the VLT would ease the situation since

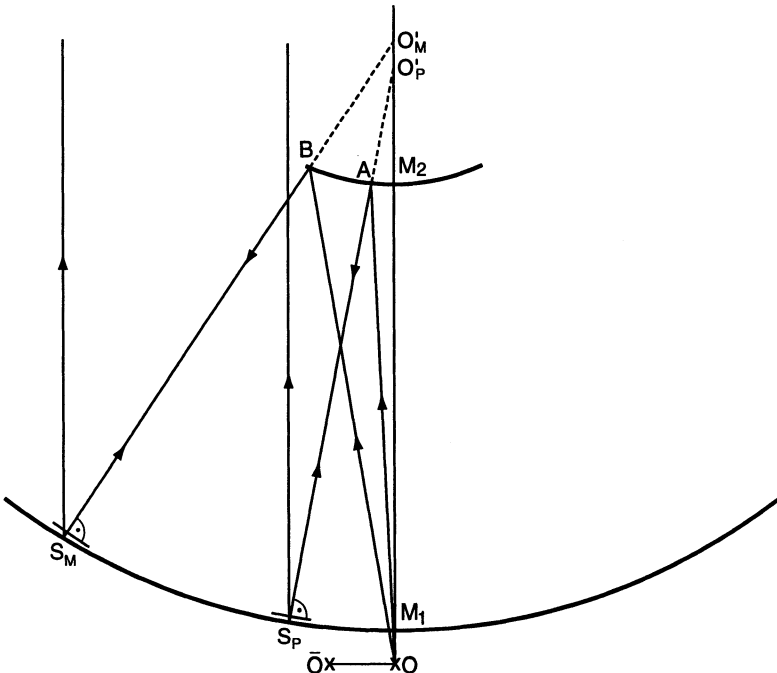


**Fig. 3.70.** Hindle sphere arrangement for detecting wind-buffetting deformation of primaries (from Wilson et al. [3.214])

the scaling law for deformation due to an external force or pressure goes with  $t^{-3}$  (see § 3.4.1). Another advantage of the scheme of Fig. 3.70 is that the effects of the local air in the path between the mirrors are also measured in double pass.

Further experiments seemed to confirm the feasibility of this detection system, but it has not finally been applied to the VLT. Even if it gave accurate values of wind-induced astigmatism in the bandpass B, the normal active support system, designed for bandpass A, would not be able to apply correction at these higher temporal frequencies.

The situation in October 1997 regarding wind-buffetting prevention of the VLT primaries, shortly before the first unit telescope was scheduled for "First Light", has been kindly communicated to me by L. Noethe of ESO. The system intended is a development of thinking initiated at NOAO and mentioned by L. Barr in connection with the Subaru project – see § 3.5.5.1 below. The possibilities of sensing wind forces at the three fixed points were considered and Barr mentioned the possibility of a hydraulic connection between the three fixed point sectors. The Gemini project extended the idea by the possibility of a hydraulic "switching system" between 3 sectors and 6 sectors. For the VLT, this concept has been developed further on the following basis.

A system with 3 fixed points (sectors) is the natural basis for a "soft", active support. A constant (uniform) pressure by the wind produces identical reaction forces at the fixed points and only the deformation modes  $n = 0$  and  $n = 3$ . A "tilt" (linear) pressure function over the mirror produces 3 non-identical reaction forces and generates all deformation modes in a "filtered" form. All other pressure distributions in elastic modes produce deformations with identical elastic modes, a consequence of the important property mentioned above in this section, as though the mirror were in free space. Above all, the most sensitive wind pressure mode with  $n = 2$ , but also the two other significant modes with  $n = 0$  and  $n = 3$  (see the eigenfrequencies of Fig. 3.68), are transmitted to the mirror. Suppose, however, that each sector is divided into two, linked by a pipe in the hydraulic system which can be opened or closed by a valve. If the valve is open, we have the normal 3-sector support; if it is closed, we have 6 sectors. Such a 6-sector support is largely a "position control" system. The modes that can be transmitted are  $n = ks$  and  $n = ks \pm 1$ , where  $s$  is the number of sectors and  $k = 0, 1, 2, \dots$ . This can then transmit the modes

$$n = (0, 1), (5, 6, 7), (11, 12, 13), \dots$$

Of the three most important wind-induced modes  $n = 2, 3, 0$ , it follows that the first two (above all, astigmatism) are excluded. In fact, the mode  $n = 3$  can also be transmitted if the nodes correspond with the fixed points; but this requires accurate azimuthal angular agreement which is statistically improbable. Suppose at a given moment the valve is closed (6 sectors) and an astigmatism measurement is performed over 40 s. If the valve is then opened,

this can be corrected, after which the valve is closed again. The problem with this technique is that an astigmatism induced at high temporal frequency is frozen in by the correction for the next 40 s cycle. The optimum technique is, therefore, to reduce the diameter of the pipe, acting as a valve, such that the oil viscosity allows flow at frequencies *lower* than about 1/40 Hz, thereby allowing normal active correction with 3 sectors; but such that it blocks the flow at *higher* frequencies than about 1/40 Hz, giving effectively 6 sectors. Thus, low temporal frequency wind effects are corrected by the normal active optics, while effects of higher temporal frequency in bandpass B are, to a considerable extent, blocked. The limitations to this higher frequency blocking are:

- Modes  $n = 0$  and  $n = 1$  are not blocked
- Intermediate frequencies in the range 0.1–0.5 Hz are inadequately blocked
- The cell has a finite stiffness which, although much higher than the mirror, allows some additional deformation under the wind pressure on the mirror with 6 sectors

Noethe has estimated that the net efficiency of wind deformation blockage should be ca. 50 %. While this cannot rival a complete detection and active correction system in bandpass B (perhaps realisable with actuators at the secondary of a telescope in which the primary corrects in bandpass A), it nevertheless represents an elegant and valuable partial solution of the wind-buffetting problem for large telescopes with thin meniscus primaries. Above all, it allows a higher *flushing speed* for control of thermal effects, as discussed in § 3.6.3.4 below, than would be acceptable with no control of wind deformation.

### 3.5.5 Other active optics developments in current projects

It should be remembered that, at the end of 1992, only two telescopes were actually functioning with an active optics system: the ESO 3.5 m NTT with its closed-loop, on-line system; and the Keck 10 m telescope with open-loop prime mirror control. However, since then, there has been much development work with active telescope systems, some of which will be briefly reviewed here. The nature of the active optics solution is essentially determined by the nature of the primary: thin meniscus monolith; lightweighted monolith; segmented mirror; very light, rigid, positional monolith. The advantages and disadvantages of these approaches for active optics control in ground-based telescopes are considered by Noethe [3.216]. Separate areas of active optics development are space telescopes and radio telescopes.

### 3.5.5.1 Thin meniscus projects

**Further NTT-type projects.** Plans existed for a number of projects intended to reproduce the ESO NTT, with or without modifications or size upgrades. The most advanced is the Italian “Galileo” (TNG) project, effectively now complete (October 1997). This has some important new features, above all concerning the mechanics of  $M_2$  and  $M_3$ . However, the essential features of the active optics system are those of the NTT. Another such project, already clearly defined in 1992, was the 4 m SOAR project (Southern Observatory for Astronomical Research) of the Universities of North Carolina and Columbia. The quartz primary was intended to have a thickness of 200 mm giving an aspect ratio of 20 and to work at f/2.0. These are very reasonable extrapolations of the NTT parameters and do not require a change of the active optics concept. A number of similar proposals have been held up or abandoned because of funding problems.

**The 2.5 m Nordic Optical Telescope (NOT).** The 2.5 m NOT, set up at the excellent site of La Palma, is considered to be one of the best telescopes in the world for its optical quality. The optics, made by Korhonen of OPTEON in Finland as a passive telescope, were specified to have a quality of  $d_{80} \leq 0.4$  arcsec. Tests [3.217] of the functional telescope confirmed that this had been easily met with an average of  $d_{80} \simeq 0.35$  arcsec. However, there were the inevitable variations of astigmatism and spherical aberration giving values up to 0.42 arcsec at zenith and higher at large zenith angles. Since the primary is quite thin (average AR = 16.8, thinner than the NTT), the telescope is clearly well adapted to an active optics approach, although this was not originally envisaged. The system planned as a modification was described by Ardeberg and Andersen [3.218]. The axial supports contain pneumatic bellows which can be regulated to give the required force changes. Figure 3.71 shows the improvements to be expected from existing image analyses. The effective gain in average image diameter is about a factor of 2 for the basic telescope quality. Coma is controlled at  $M_2$ , the other four aberrations at  $M_1$ . The system is therefore identical with that of the NTT, except that defocus is not mentioned; but that can easily be added. Precalibration of aberrations with  $Z$  was envisaged, as in the NTT, and is certainly a good feature. The calibrations of the force changes for the four elastically controlled aberrations were done by FE calculations [3.219], not from analytical theory as in the NTT.

With this system in operation, the NOT, with its excellent site and building design, has been able to equal the NTT in optical quality. This modification to an existing passive telescope confirms the great advantage of the ESO active optics system and algorithm in that it can be applied to any existing passive support geometry. Even classically stiff mirrors will allow correction of astigmatism, as the application to the 4 m Cerro Tololo mirror (§ 3.5.3) demonstrates.

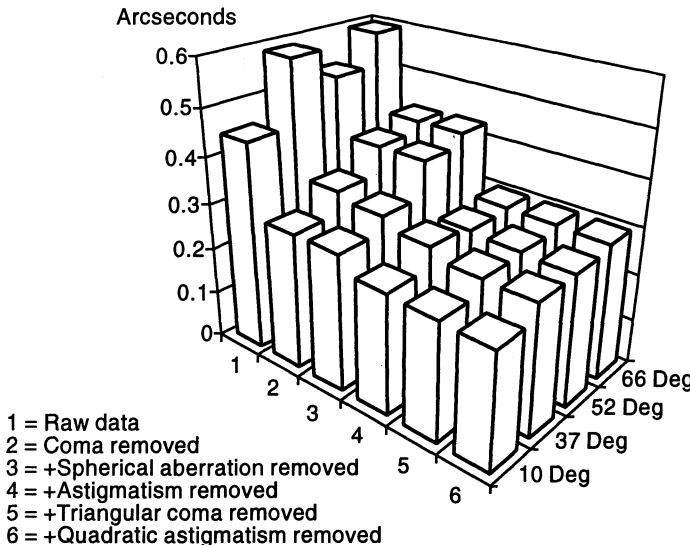


**Fig. 3.71.** 2.5 m Nordic Optical Telescope (NOT): the expected improvements by addition of the active optics control system for various zenith angles (from Ardeberg and Andersen [3.218])

**A complete active concept for manufacture and operation of a telescope.** In § 1.2.2.4, an account was given of the stress polishing technique used by Lemaître and its possible combination with operational active optics to give a unified active concept for producing and operating thin meniscus primaries. This led to a proposal by Lemaître and Wilson [3.136] [3.142] for the fabrication of a thin 1.8 m prototype primary ( $f/1.8$ ), potentially suitable for the ESO VLT auxiliary telescope primaries, using a stainless steel blank as discussed in § 3.3.5.2.

The active optics concept is based on low spatial frequency tolerance relaxation, because of subsequent correction in operation, and a very high polishing quality of non-correctable high spatial frequencies, corresponding to an excellent Intrinsic Quality (IQ). The combination with stress polishing is clearly ideal because the stress polished surface is spherical, ensuring an IQ of a quality which would be difficult to match by normal aspheric polishing. Furthermore, the relaxation of low spatial frequency tolerances, above all of astigmatism, is a major simplification of the stress polishing technique.

The proposal would be valid, with minor modifications, for a blank in Zerodur, aluminium or stainless steel. However, for reasons of cost and the fact that any subsequent warping in such a solid meniscus could easily be corrected actively, the stainless steel option was preferred. The aspect ratio is in the range of 30 to 45. Compared with Zerodur, the blank costs are enormously reduced (about 20 KDM compared with 180 KDM). The combination

of active optics, stress polishing and thin stainless steel menisci appears to be unbeatable for achieving high optical quality at a low price.

Recently, Lemaître has extended the elastic theory for vase-shaped mirrors (Lemaître et al. [3.220]) and analysed in depth in a classic paper [3.221] the cases of equal curvature and equal constraint cantilevers, giving further developments of formulae due to Euler and Clebsch [3.155]. He is thus equipped with the necessary theory for the active production of a very wide range of mirror forms and materials.

**The Japanese 8.2 m Subaru project.** The 8.2 m Subaru project is an active telescope based on a thin meniscus primary and on the lines of the ESO NTT and VLT concepts [3.91]. The 8.2 m quartz primary has a thickness of 200 mm and is somewhat stiffer than the ESO VLT mirrors with 175 mm. This is an advantage, above all in the extended active optics bandpass with regard to wind buffetting.

The active optics aspects have been analysed and tested on model mirrors with great care. Three papers [3.222] describe the development of the Shack-Hartmann image analyser, an active experiment with a 0.62 m glass mirror tested holographically and a further experiment with the same mirror, tested with the Shack-Hartmann analyser for various gravity-related inclinations. The latter was seen as an extension of the ESO model experiment with a 1 m test mirror with a vertical axis [3.204]. Satisfactory agreement between the two measuring systems and with FE calculations was attained. Above all, the third paper gave careful experimental evidence of successful active correction also for inclined positions, as was later demonstrated in the functional NTT [3.70] [3.72]. The active concept of the Subaru project was thereby confirmed. 264 computer controlled actuators are envisaged for the primary mirror. Further details of the active support, including its hardware, are given by Iye [3.223]. A notable technical feature is the high precision load cell (relative error  $\leq 10^{-4}$ ). The working principle is that it measures the frequency modulation of a small tuning fork which is subject to a strain force externally applied. High precision actuators with a relative error  $\leq 10^{-4}$  and a dynamic range 0–60 kp are to be used. These actuators combine an active axial force with a passive radial force and are embedded in bores in the mirror, as in the Palomar 5 m concept. The active force variation is achieved by driving a spring, as in the ESO VLT.

Wind-buffetting of the primary is intended to be controlled, as in the ESO VLT, by an enclosure design limiting the windspeed perpendicular to the mirror surface to  $\leq 1.5$  m/s. A further possibility is to apply reaction forces through the actuators up to a frequency of 1 Hz. Position control was considered but abandoned except for the fixed points. Barr [3.224] states that wind forces up to 10 m/s could be coped with to an accuracy of  $< 0.003$  arcsec of image degradation by an interconnected hydraulic piston support, arranged in three sectors. He does not give the bandpass. No comment is made on the detection problem addressed in § 3.5.4.

**The Gemini 2 × 8 m project.** As was indicated by Randall [3.54], the decision on the nature of the primary mirror blanks was scheduled to be taken in the autumn of 1992. The result was confirmed in September 1992, the choice being a meniscus blank supplied by Corning. This choice was made on the basis both of cost and technical security in the supply of the blank. The Gemini selection board [3.225] believed that the work being carried out on the ESO VLT and the Japanese Subaru projects, using a similar meniscus solution, would lead to satisfactory solutions also in the two aspects considered to be critical: wind-buffetting and mirror seeing.

### 3.5.5.2 Projects using lightweighted primaries

**LBT (Columbus) 2 × 8 m and Magellan 6.5 m projects.** It is now generally accepted that even stiff, lightweighted blanks of the type offered by Angel will, in diameters such as here envisaged, flex to an extent that will require active optics control. This was already recognised and proposed in 1983 [3.226]. The possibilities of active optics control of such mirrors were also confirmed in connection with the Gemini studies, although doubts were expressed concerning the dynamic range of deformation amplitude available before high spatial frequency structure printhrough appears. The finer the structure, the higher the danger. In general, the higher stiffness will give a lower dynamic range of correction. This will not matter for flexure errors in operation, since the requirements are automatically correspondingly reduced. But the other aspect of active optics, compensation of manufacturing errors from relaxed low spatial frequency tolerances, can be much less favourable. The classical example is the Hubble Space Telescope where the lightweighted primary was far too stiff to give the dynamic range for correction of the spherical aberration from the matching error of the mirrors. The same would have been true for the NTT primary if it had had a stiff lightweighted primary.

In the extended active optics bandpass B, the increased stiffness compared with thin menisci is a definite advantage. The wind-buffetting situation is certainly more favourable.

The thermal aspects of structured mirrors in borosilicate glass, already favourable, should be further improved by active optics. This has been amply confirmed by experiments in connection with the 3.5 m WIYN new technology telescope of NOAO, completed in 1994 (see Table 3.17 below, with literature references). This telescope was an important development in that it combined the 3.5 m BSC honeycomb blank with full thermal control *and* an active optics correction system. The conclusion of Goble et al. [3.258] was that *both* are necessary for a honeycomb blank of this size. The excellent results reported for this telescope [3.259] have fully confirmed this concept.

**3.5.5.3 Active optics in telescopes with segmented primaries.** The Keck 10 m telescope is the standard here and its system for control was mentioned in § 3.5.1, the aberration analysis being given in detail by Nelson

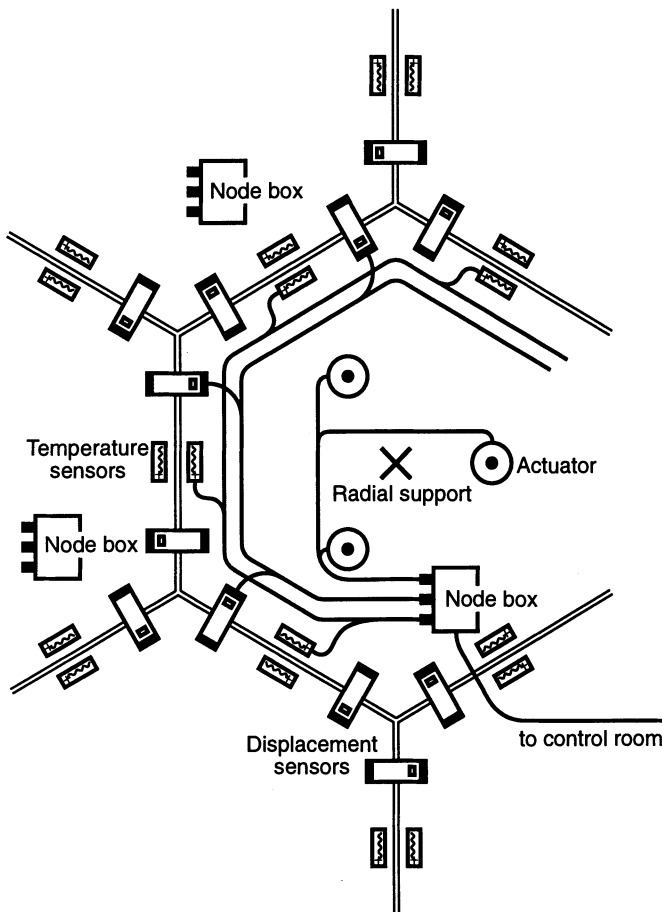


**Fig. 3.72.** Keck 10 m telescope: schematic of the control system arrangement around one segment (from Meng et al. [3.227])

et al. [3.196]. The function of the prime mirror active control system is given by Meng et al. [3.227]. The mirror figure is set from natural star observations made during calibration. Maintaining this figure requires the recall of the mirror relative positions set at calibration time, detecting changes and then appropriately re-adjusting the mirror segments. Figure 3.72 shows one of the 36 segments of the mirror with its gaps to the next segment and control elements. Although each segment has 12 displacement sensors (2 on each of its 6 sides), they are shared by adjacent segments, so readout is 6 per segment. Since innermost and outermost segments do not have 6 neighbours, there are, in fact, 168 displacement sensors for the entire mirror. Repositioning the mirror once a figure error is detected is achieved by changing the distance of one or more attachment parts to the subcell support. Each segment sits on a central fixed post about which it may be tilted by the action of any or all

three actuators arranged in a triangle round the fixed post. The segment can also be moved in piston owing to the flexibility of attachment at the fixed post. The temperature sensors continuously monitor the temperature at each joint. Readout is every 10 ms, actuator movement commands every 500 ms.

The evidence is that this complex system functions very well for the total specification requirements of the telescope ( $d_{80} \leq 0.42$  arcsec of which  $d_{80} \leq 0.34$  arcsec for the primary mirror alone [3.23]). The limitations (§ 3.5.1) are solely in the quality of segments (see § 3.2.1), particularly as the quality of the secondary (see § 1.3.3) is apparently extremely high ( $\sim \lambda/10$ ) [3.27] [3.28]. However, the *open-loop* active control system only controls the form of the primary. Otherwise, only dc active correction is applied in *closed-loop* with a natural star, at set up and calibration. If this remains the case, there is no on-line control of decentering coma, defocus or low frequency ambient air errors. It is to be hoped that this feature, with a real-time image analyser, will be added, since this is missing for a full active optics system.

**3.5.5.4 Mixed closed-loop and open-loop concepts.** The Keck 10 m telescope has a sophisticated open-loop control system for its segmented primary, calibrated in dc with a natural star (closed-loop) and correcting in open-loop up to a frequency of 2 Hz.

The meniscus projects discussed in § 3.5.5.1 all operate in closed-loop, on the principles of the NTT, for the *normal* active optics bandpass A of Fig. 3.62. For large, flexible meniscus primaries, the weakness is the effects of wind-buffetting in the *extended* active optics bandpass B. A fully satisfactory solution to this problem has not yet been proposed: in general (e.g. ESO VLT and Japanese Subaru) the aim is *prevention* of wind-buffetting by appropriate design of the enclosure. But this has dangers in restricting natural ventilation, which could lead to increased errors from the ambient (local) air. The optimum system would be a general active optics system covering fully both bandpasses A and B.

Since the central problem up to now has been the *detection problem* of wind-buffetting errors in closed-loop systems, the methods of *open-loop detection* discussed in § 3.5.4 (Fig. 3.70) might provide the basis for a general active optics system covering both bandpasses A and B. The active support of a large, thin primary would then have an *open-loop* controlled support, capable of functioning over the modest dynamic range required for reasonable wind-buffetting up to about 10 Hz. Below about  $10^{-1}$  to  $10^{-2}$  Hz this would be complemented by a normal, low frequency, *closed-loop* support system of the type intended for the VLT or Subaru, which would have a much higher dynamic range.

How such a general, combined support system would function from the point of view of hardware remains a matter for further development.

**3.5.5.5 Extremely stiff mirrors with positional active optics control.** If a mirror cell unit can be made so stiff that gravity-induced deformations become of the dimensions of optical tolerances, other possibilities

are opened up. Normally, the flexure of large mirror cells is at least 3 orders of magnitude higher than the optical tolerances. This fact has favoured the “soft” (flotation) type of support ever since its invention by Lassell in 1842. The possibilities of fibre composites, particularly CFRP, discussed in § 3.2.4 may provide sufficient stiffness to use “hard” supports with positional control based on the stiff cell as an absolute mechanical reference with optical stability quality. This is the optical concept of the 1.5 m Hexapod Telescope (HPT) [3.100] [3.101]. Since inertia is low, there is even the intention of operation in the lower part of the adaptive bandpass C, beyond bandpass B [3.100]. This is the most ambitious project in active optics currently under development. The results will be very interesting, whatever emerges from the practical tests.

**3.5.5.6 Space telescope applications.** Since space has no atmosphere, there is, by definition, no need of *adaptive* optics: it has no meaning in space. But *active* optics is even more important in space than for ground-based telescopes for four reasons [3.70] [3.72]:

- Because of the absence of atmospheric seeing, diffraction-limited performance (also in the UV) is highly desirable. This can only reasonably be achieved, from a manufacturing viewpoint, if low spatial frequency tolerance relaxation is available.
- The thermal regime in space is extreme. All those error sources in Table 3.11 whereby thermal effects on mechanics or optics apply, will require to be corrected by active optics.
- Although (orbital) space is a zero gravity regime, the manufacture and assembly are done under 1 g and launch involves 5 g or more. Active optics is, again, the answer to the errors induced by these changes.
- The moon also counts as space. Here gravity is only one sixth of that on earth, but not zero.

Much work has been going on for a considerable time concerning the application of active optics to space telescopes, above all in the United States [3.228].

The principles of the ESO active optics system, as outlined in § 3.5.2, can be taken over directly to space applications. Since there is no gravity weight, push-pull supports are essential. This is a simplification of the principles, not a complication, although it involves bonding the supports to the mirror. The laws governing the effect of forces are no longer the Couder Law, arising out of the gravitational effect, but the basic flexure laws of independent point force ( $\propto D^2/t^3$ ) or independent pressure ( $\propto D^4/t^3$ ), from Eqs. (3.25) and (3.19) respectively. The modal concept of flexure will apply in space exactly as for ground-based telescopes. The optical relations governing the sensitivity of the secondary to decentering coma and defocus are unaffected by the space environment: only the specification and correction tolerances will be much tighter.

Much of this approach was studied in detail by MATRA Espace [3.229]. The first part deals with the study, manufacture and test of a “Shack-Hartmann” image analyser using a CCD detector. In fact, the preferred form does not use a Shack lenslet raster, but a screen containing an array of pin-holes, whose diameter and spacing can be optimized. It is therefore essentially of the type described by Bahner and Loibl – see § 2.3.3.2. The authors conclude that this analyser can be successfully applied in space applications. With a  $20 \times 20$  sampling mask, this sensor was able to measure deformations of a thin meniscus ( $D = 820$  mm,  $t = 5$  mm, i.e. AR = 164) using 111 actuators to a measurement sensitivity of  $< 0.02 \lambda$  rms. Part 2 was concerned with a validation of the active control of the meniscus. Corrections from several wavelengths of error down to  $\lambda/10$  rms wavefront error were achieved. It is pointed out that, for space applications, attention should be paid to the linear behaviour of the actuators and solid friction effects inside them. The experimental results are in good agreement with NASTRAN predictions. Friction effects led to the need of two or three iterations to acquire the final accuracy.

This study seems to confirm completely that the active optics concept can be applied in space. As in ground-based astronomy, the evidence is that it will not only give the best results but will also be the cheapest way of achieving top quality.

The initial matching error of the HST remains the best proof that active optics is essential in space telescope optics. Furthermore, it demonstrates that mass reduction by the use of thin flexible menisci, giving not only the possibility of active modal control in orbit but also of large dynamic range with corresponding tolerance relaxation in fabrication (e.g. for matching error) is a more general solution than mass reduction by stiff, lightweighted primaries. With the modern technologies of figuring and testing described in Chap. 1, such thin menisci can also be manufactured to the necessary high spatial frequency quality (IQ).

**3.5.5.7 Active optics in radio telescopes.** Radio telescopes as such are outside the scope of this book. However, active optics techniques in the visible waveband may have great significance for the optimization of short wave radio telescopes in the mm or sub-mm wavebands.

A résumé of the situation for the main reflector is given by Gallieni [3.230]. He quotes the requirement of the measuring accuracy as  $\lambda/20$ , that of the control positioning system as  $\lambda/200$ , the total accuracy requirement being  $\lambda/20$  rms. The measurement system considered optimum is based on microwave holography [3.231]. The time needed for evaluation is given by Tarchi and Comoretto as about 1 week, but it can be carried out without disturbing normal operations. Gallieni considers the knowledge is available for a test system, routinely included in radio telescopes and independent of its geometry and structure, enabling the verification within 1 hour of the shape and alignment of the optical system.

If basic calibration is done with high accuracy by the above method of microwave holography, the remaining problem is one of detecting *differential* changes from this calibrated state at a higher frequency, i.e. up to the highest frequency flexure generated by wind. If optical mirrors are attached to the main reflector, as discussed in § 3.5.4 and ref. [3.214] and shown as an example in Fig. 3.70, with sufficient sampling to provide information on the significant bending modes, which will have the same elastic nature as for optical mirrors, then an optical detector of the Shack-Hartmann type could register the *differential* modal changes at any frequency required. Alternatively, the optical supplementary mirrors could follow the parabolic shape of the reflector and the S-H detector work in *closed-loop* on a natural star. But this system, in contrast to the *open-loop* front detection methods such as that shown in Fig. 3.70, would be limited to bandpass A by the atmosphere.

Gallieni points out that the panel nature and requirements are similar, in principle, to those of the Keck 10 m telescope primary: a similar “self-reference”, open-loop control and test system for the main reflector is possible. Apart from its own control signals, this system could react, possibly with an overlay control system, to the signals given by the optical detector measuring the complete system quality, including alignment. As a two-tier system, this is analogous to the proposal of § 3.5.5.4 for large optical telescopes, but in the radio case, *both* tiers could be open-loop systems without use of a natural star.

### 3.5.6 Conclusions on the current state of development and future potential of active optics in telescopes

By 1992, active optics was so firmly implanted in *ground-based* telescope technology that it could be considered as “state of the art”. However, there were still only two “active” telescopes already functioning, though many were in various stages of development. These two were, firstly, the ESO 3.5 m NTT, based on a consistent scheme (Table 3.11) for low bandpass (Fig. 3.62), closed-loop operation on a natural star, in operation since early 1989; and, secondly, the Keck 10 m telescope with its internal (open-loop in the sense that it does not rely on a natural star) prime mirror control extending well into the bandpass B of Fig. 3.62, but without the closed-loop control of secondary movements to correct decentering coma and focus in the normal bandpass A.

An excellent overview of active optics technology has been given by Ray [3.232], including 105 annotated references. This is limited to ground-based systems, including military applications. Support aspects for large mirrors are given much emphasis. The SOFIA 2.5 m IR telescope, to be carried by an aircraft, is mentioned as a special case since it imposes special problems by its airborne nature apart from normal low bandpass active correction. Ray emphasizes, with the support of many references, the enormous gain in efficiency and observing time resulting from active optics improvement of image quality in telescopes. We shall return to this aspect in Chap. 4. Ray

also points out clearly that after much earlier resistance of the astronomical community, which has always reacted conservatively to technical change, the validity and advantages of active optics in large telescope systems are no longer in doubt.

Since 1992, there has been a steady advance of active optics on a broad front, above all with the development work associated with the largest ground-based telescopes, notably the ESO VLT, the Japanese Subaru project and the international Gemini project, accounts of which are given above. On a smaller scale, the development of the 3.5 m Galileo (TNG) telescope and the “activation” of the 2.5 m NOT are notable. Although the latter was not planned as an active telescope, its relatively thin primary (see § 3.5.5.1 above) and general concept were ideally suited to this conversion. Apart from ref. [3.218], this is documented in a number of reports of the Nordic Optical Telescope Scientific Association. Today (1997), the NOT may be considered a fully functioning active telescope of excellent optical quality. The question is often asked, what the minimum size for a ground-based telescope would be, below which an active concept is not justified? My own view is that it is still justified at 1.5 m diameter, but marginal at 1 m.

In contrast to ground-based developments, there is still not a single active telescope *in space*. This is partly due to the modest apertures of space telescopes compared with large ground-based instruments, but also to the deep-rooted aversion to *mechanisms* which may fail in space and vitiate a whole, costly mission. However, as discussed in § 3.5.5.6, the advantages of active optics for space telescopes are enormous and irrefutable. Furthermore, if the mechanisms involved can be made sufficiently reliable, there is no serious technical problem in the realisation [3.229]. Above all, with the experience of the 2.4 m HST, it seems clear that any future project of comparable or larger size will be based on active optics control. This was the tenor of the workshop held at Pasadena in March 1991 concerning the design principles of a future space telescope of the order of 6 m in diameter.

## 3.6 Local environmental aspects of telescopes

### 3.6.1 Definition of “local air” and its importance

“Local air turbulence” is a term used in this book to cover all those aspects of image deterioration provoked by the air in and around the telescope installation. It covers the error sources commonly called “mirror seeing”, “telescope structure seeing”, “dome seeing”, and “site seeing”. By definition, there is no isoplanatic angle limitation as with external (atmospheric) seeing. “Site seeing” has no clear division from the general, larger-scale effects of heat stored in the ground and liberated at night to influence the lower layers of the general atmosphere: but it can often be identified as a specific local influence of nearby roads, ramps, paved areas or buildings.

Local air effects on the image have been known for 100 years or more, but were earlier masked by manufacturing, support or expansion-induced errors (see Table 3.11). The general introduction of low or quasi-zero expansion materials for mirrors was accompanied after about 1940 by the rapid and increasingly general introduction of electronics, accompanied by major heat sources. Ritchey's telescopes (see Chap. 5 of RTO I) had virtually no heat sources except human beings and early electric motors. The last big refractors at the end of the nineteenth century introduced huge buildings and domes, but astronomers were accustomed by visual observation to working in cold and uncomfortable conditions.

Between 1950 and about 1980 telescope optics went through a relatively conservative consolidation phase after the technical advances of the Palomar 5 m telescope. This included the construction of massive buildings and domes, usually including office space, workshops, etc. The inevitable heat sources, worsened by increasing use of electronics at the telescope and instruments, had the result that the advantage in image quality from zero expansion materials and improved manufacture was often thrown away by "dome seeing" effects. Since the statistics of the local air effects usually (but not always) produced round images and no scientific measure of external seeing was available on-line, it was concluded, globally, that the "seeing" was inferior. Of course, there were a minority of astronomers and engineers who were well aware of the "dome seeing" problem and did their utmost to improve thermal conditions. Of the classical "Bowen-type" telescopes (Chap. 5 and Table 5.2 of RTO I), the 3.6 m CFHT and the 3.9 m AAT were probably the most successful because of clear awareness and support of the management in these endeavours. The ESO 3.6 m telescope was equipped in 1980 with a sophisticated temperature sensing system, but this was unfortunately not used in a systematic programme for dome seeing improvement, although there were sporadic improvements. The global situation is reflected, together with other technical weaknesses of passive telescopes, in Fig. 3.67. Recently (1997), the optical quality of this same telescope has been markedly improved by a systematic programme analysing and correcting error sources.

The *aim* of these sophisticated buildings was laudable in that it was hoped to achieve a micro-climate corresponding to the night situation and protect the telescope from the sunshine and heat of the day. But the aim was often sabotaged by the air volume involved and the internal heat sources permitted in incorporating other functions in the building. The two *essential purposes* of the enclosure were then lost sight of: not only should the telescope be protected from heat sources during the day, but the enclosure should allow maximum adjustment of the telescope to the night conditions. At night, therefore, the optimum enclosure is one giving the necessary *wind-buffetting* protection with maximum ventilation: at low windspeeds, *no* enclosure is the best. Compared with the delicate compromise concerning wind, the provision of a shelter to protect the telescope from rain, snow, etc., is a relatively simple matter. In other words, thermal control is the central problem.

Until recently, two technical measuring devices were missing in the necessary equipment for fully scientific advance in local seeing effects: a sophisticated detector or image analyser and an external (atmospheric) seeing monitor. The former enables one to separate effects and analyse the errors from different local sources [3.70]; the latter is essential to separate the external seeing and to know the extent of the total local errors (Fig. 3.67). Both of these devices are available at the ESO NTT, but even today, few installations have a seeing monitor and even fewer have an image analyser capable of modal analysis. We shall see below, from notable work at the 3.6 m CFHT, that excellent measures of local air errors can also be obtained with classical telescopes without modal analysis if a suitable detector is applied in a systematic programme. Apart from the image sensor aspect, the thermal parametric situation in a telescope-enclosure structure is extremely complex and requires a sophisticated sensor installation (essentially for temperature differences and air speeds) in order to get systematic information. Only recently have such general systems, incorporating all requirements, become available. This is the reason that earlier work, although valuable, could usually give only *qualitative* results.

This is well illustrated by the classic paper of Lowne [3.233], who performed the first *quantitative* investigations of "mirror seeing". Lowne referred to previous work [3.234] [3.235] [3.236] and concluded that there were too many factors that could not be adequately controlled in a real telescope. At the suggestion of R. G. Bingham, he therefore investigated mirror seeing with a *laboratory experiment* in carefully controlled conditions. First of all, qualitative observations were made with a heated mirror about 5 °C warmer than the ambient air. With a horizontal mirror (vertical axis), once thermally stabilized with regularly rising air bubbles under otherwise extremely stable conditions, the deterioration of the Airy diffraction pattern was minimal over a period of 20–30 s. However, the slightest general air movement was sufficient to upset these stable conditions, giving major image degradation due to slow turbulent motions. A fan producing a lateral air velocity across the mirror surface of 0.1 m/s produced no improvement. With a lateral wind-flushing velocity raised to about 1 m/s, the warmed air was stripped from the surface and the Airy pattern was largely restored, although with movement in the diffraction rings. Inclining the mirror improved the situation as warmed air could convect off more readily. Lowne found that these effects could still be observed with a temperature differential of only 1–2 °C, values typically measured in the 2.5 m INT (see Table 5.2 of RTO I) and other telescopes.

Quantitative results were then obtained at the center of curvature of a spherical mirror of zero-expansion substrate with 254 mm aperture and 2 m radius of curvature. The image was magnified 250 times by a microscope objective giving an effective focal length of 500 m. A calibrated iris diaphragm was then used to measure the energy passing through different diameters. Figure 3.73 shows the results for a horizontal (vertical axis) mirror at a temperature 6 °C above ambient and with three different flushing air velocities

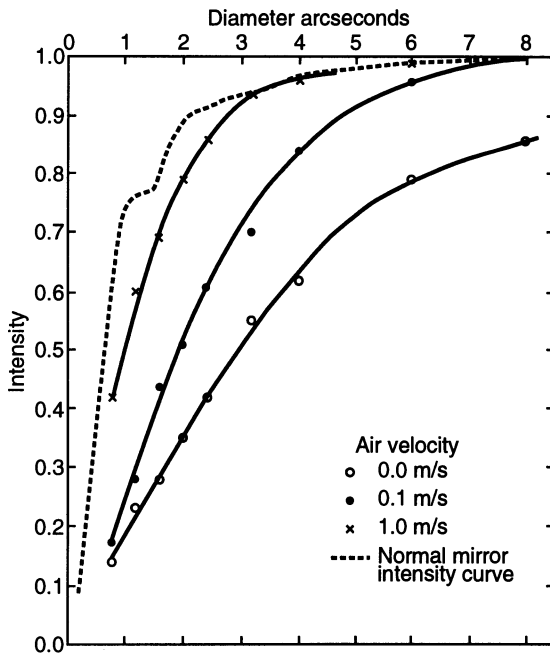
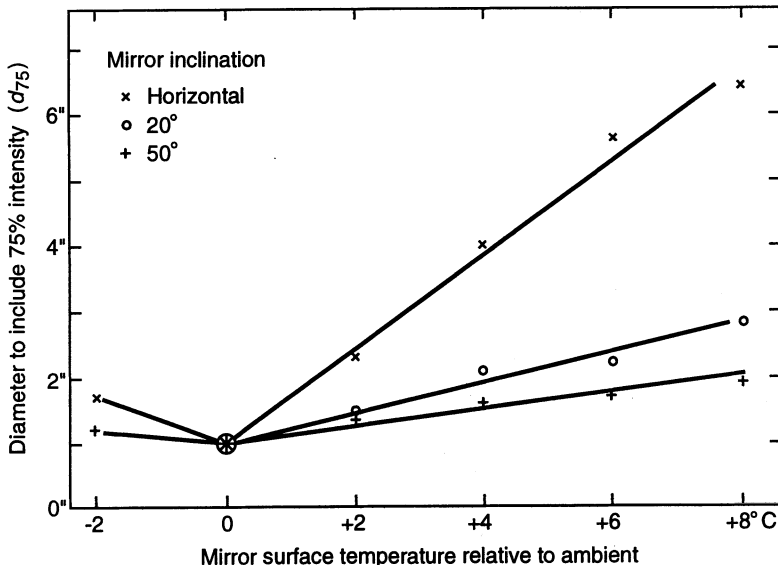


Fig. 3.73. Encircled energies in images given by a mirror of 254 mm diameter, horizontal (axis vertical), at 6 °C above ambient temperature and with three different horizontal flushing air velocities (from Lowne [3.233])

across the mirror. The dashed curve shows the undisturbed image (without heating) of the mirror and is essentially the diffraction image encircled energy function given in Fig. 3.104 of RTO I. Without any flushing, the image degradation for the horizontally disposed mirror surface, the worst case, was about a factor of 4 in encircled energy diameter for 6 °C above ambient temperature. The dramatic improvement with a 1 m/s flushing air velocity is apparent.

Lowne also demonstrated the dramatic improvement produced by inclining the mirror from the horizontal in the absence of flushing air (Fig. 3.74). If observations are weighted towards zenith distances  $Z \sim 10^\circ$ , the slope of the line for positive temperature differences is about  $\tan^{-1} 1/2$ , i.e. a positive temperature difference of  $\Delta T$  degrees C of the mirror produces a mirror seeing of the order of  $\Delta T/2$  arcsec. Since Lowne's work, this has been the accepted rule-of-thumb in astronomical observatories using big telescopes. Lowne also measured the effect of a negative  $\Delta T$ , i.e. of a mirror colder than the ambient air. Lowne's results suggest that a cooler mirror is much less deleterious, but the negative range of -2 °C was insufficient to quantify this accurately. Since then, a factor of 3 has often been quoted as a measure of the relative image degradation of a warm compared with a cold mirror with the same  $|\Delta T|$ ; but later measurements (see below) suggest that this important matter is by no means clearly settled.

Lowne showed that air flushing still functioned well with an inclined mirror and performed experiments simulating a radial flushing system operating



**Fig. 3.74.** Image degradation measured by  $d_{75}$  in arcsec induced by the heated 254 mm diameter mirror ( $6^{\circ}\text{C}$  above ambient temperature) with natural convection at different inclinations  $Z$  from horizontal (axis vertical) (from Lowne [3.233])

outwards from the central hole. His results were very positive in reducing the excess (positive) surface temperature, in removing warmed air in laminar flow and in randomizing the warm air cells to a more uniform fine structure.

Lowne's work was the first clear proof of the remarkably beneficial effects of modest laminar air flushing and the serious consequences of *lack* of flushing in the presence of a significant positive  $\Delta T$  of the mirror ( $\Delta T$  more than  $+1$  to  $+2^{\circ}\text{C}$ ). This was the essential basis for the NTT building concept: natural ventilation and a prime mirror always cooler than the ambient air.

### 3.6.2 Recent evolution in telescope enclosures and “local air” error measurements in functioning telescopes

As mentioned above, the concept of an expensive building with a dome enclosing reflecting telescopes is relatively modern. The Melbourne 4-foot reflector of 1869 (Fig. 5.7 of RTO I) had simply a roll-off shed to protect it, observations being done with the free-standing telescope. After their introduction for the last big refractors, the building-dome structures swelled to the opulent designs for the Palomar 5 m telescope and the succeeding telescopes of the “Bowen-type” of 3.5–4 m aperture. Figure 3.75, taken essentially from Nelson [3.237], shows a comparison of the cross-sections of the enclosures of a number of typical telescopes in comparison with that of the Keck 10 m telescope. The ESO NTT and VLT enclosures have been added, on the same scale, to Nelson's nine figures. Note that the included circle shows the aperture

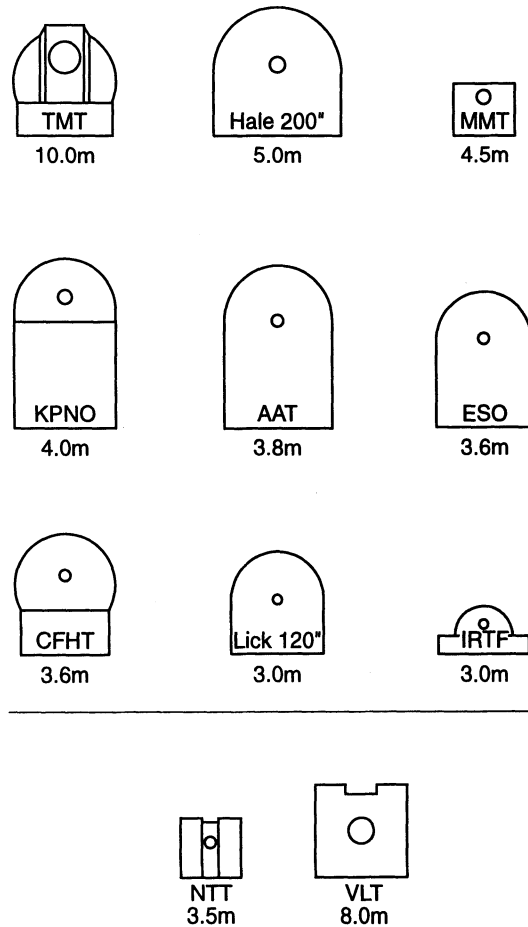


**Fig. 3.75.** The cross-sections of a number of typical telescope enclosures in comparison with the Keck 10 m telescope enclosure. Note that the included circle shows the relative apertures of the telescopes. (From Nelson [3.237] with the ESO NTT and VLT enclosures added)

of the telescope to the same scale. The reduction in size of the enclosures relative to the telescope aperture is striking in the more modern designs of the 4.4 m MMT, 3.5 m NTT, 10 m Keck and 8 m VLT. There is a corresponding reduction in the volume of local air enclosed. This huge air volume, together with the high thermal capacity of classical primaries, has been the principal problem of the preceding Bowen-class telescopes. The dome and mirror seeing problem of such telescopes was illustrated by the comparison of the ESO 3.6 m telescope with the NTT and other La Silla telescopes in Fig. 3.67. Improvements have been made recently, but dome and mirror seeing remain a major limiting factor of this telescope. The 3.8 m AAT has probably been more successful with its very powerful ventilation system, and the 3.6 m CFHT the most successful of these telescopes because of the systematic analysis and improvement programmes. Comprehensive results have been reported by Racine [3.238], certainly the most valuable and complete investigation of local air errors yet carried out in a functioning telescope.

Earlier work by Bely [3.239] had demonstrated the importance of analysis and control of local air seeing.

The detector for the work reported by Racine was the fast guiding imager high-resolution CCD camera (HR Cam) used regularly for several years at the PF of the CFHT. In 1986 thermal and wind sensors (thermistors) were installed in and around the telescope and dome, read out every 10 minutes to a data logger. The thermal data was, in fact, limited to two key temperature differences,

$$\Delta T_m = T_m - T_t$$

$$\Delta T_d = T_t - T_o ,$$

where  $T_o$  is the outside temperature (i.e. the local air outside but near the dome),  $T_m$  the surface temperature of the primary mirror and  $T_t$  the temperature at the top of the Serrurier trusses, 8.5 m above the primary. (For comparison, a similar but more comprehensive temperature logging system was installed on the ESO 3.6 m telescope in 1980, together with a TV system displaying the image profile; but, in contrast to the CFHT, the will and interest to exploit it systematically was absent at the time). Racine gives distributions showing the correlations between  $T_t$  against  $T_o$  and  $T_m$  against  $T_t$ .

The image quality was measured with the HR Cam and given as the FWHM in arcsec. Experience showed that the fast tracking facility of the HR Cam reduced the FWHM by a factor of about 1.3 by removing wavefront tilt effects present in the normal slow-guiding mode. Figure 3.76 shows the raw image quality data, a log-normal curve being fitted to the total population in the histogram and to the shape of the distribution at  $\text{FWHM} > 0.60 \text{ arcsec}$ . The absence of values below 0.40 arcsec is explained by the limit imposed by the quality of the optics, estimated as  $0.38 \pm 0.02 \text{ arcsec}$ . The hatched histogram is for image quality data when  $\Delta T_m < +0.5^\circ\text{C}$ . This improves the median value from 0.62 to 0.56 arcsec. Image quality distributions are also given as a function of sec  $Z$ , the zenith angle, and these plots show qualitatively that, for a given  $\Delta T$ , mirror seeing is more critical than dome seeing.

The separation of the effects of external seeing, optical system errors, mirror and dome seeing is achieved by a simple model based on Kolmogorov turbulence as given by Fried (see Chap. 5). The angular spread is then given, in Racine's notation, by

$$\omega \propto \left[ \int C_T^2 dl \right]^{3/5} \quad (3.62)$$

Thus image degradation from different turbulent layers add according to the 5/3 power law,  $C_T$  being proportional to the temperature gradient across a layer. The air layer between two points separated by a distance  $l$  and differing in temperature by  $\Delta T$  will therefore produce an angular image spread

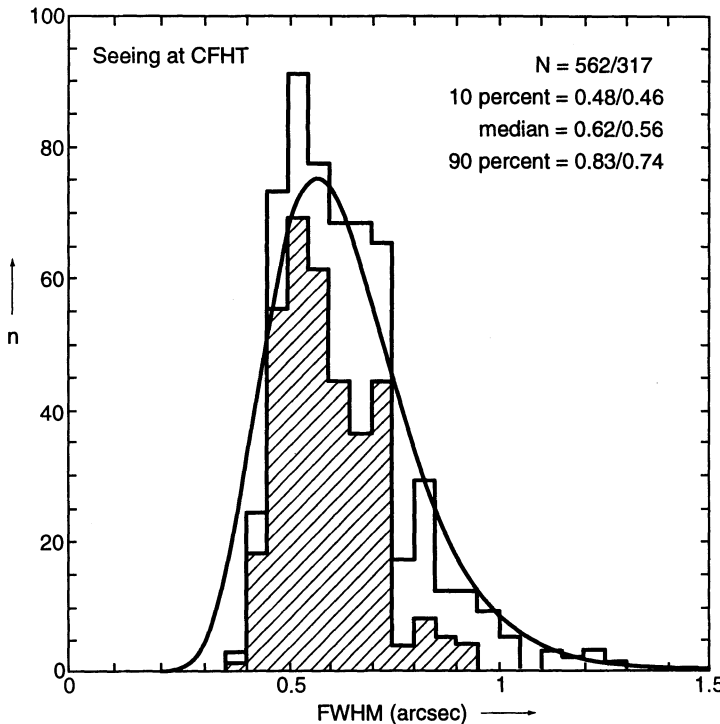


**Fig. 3.76.** Histogram, also with the log-normal fit, of image quality at the CFHT prime focus measured on HR Cam CCD frames. The hatched histogram is for measurements when  $\Delta T_m < +0.5^\circ\text{C}$ . (From Racine [3.238])

$$\omega \propto \frac{\Delta T^{6/5}}{l^{3/5}} \quad (3.63)$$

Furthermore, in a horizontally stratified layer, such as the external atmosphere producing  $\omega_n$ , we have for the air mass dependence  $dl = dl_0 \sec Z$ , so that

$$\omega_n(Z) = \omega_n(0)(\sec Z)^{3/5} \quad (3.64)$$

Racine assumes the isotherms for an inclined mirror remain parallel to its surface as they rise into a vertical air cylinder and their temperature decreases (by mixing with ambient air) with a scale height  $h_0$ . By integrating Eq. (3.62) along light rays within the cylinder of rising turbulence and averaging over the (cylindrical) beam, Racine deduces

$$\omega_m^{5/3} \propto \Delta T_m^2 (1 - e^{-D \cot Z / h_0}) \quad (3.65)$$

If  $D/h_0 \gg 1$ ,  $\omega_m$  is hardly affected by  $Z$  since the turbulent cells decay while still in the light path. If  $D/h_0 \ll 1$ ,  $\omega_m$  decreases rapidly with  $Z$ , as  $(D \cot Z / h_0)^{3/5}$ , because only the air near the mirror surface is subject to mirror turbulence. Taking, for  $D = 3.6\text{ m}$ , the value of  $h_0 \sim 0.5\text{ m}$  as typical,

following Iye et al. (to whose work we shall return below), Racine concludes that mirror seeing will be effectively independent of  $Z$  for  $Z < 70^\circ$ . He also assumes the change of decentering coma (roughly proportional to  $\sin Z$ ) and other errors of the telescope optics will vary little with  $Z$ . Then, in general, the median global image spread  $\omega$  for the CFHT can be written

$$\omega^{5/3} = \omega_n^{5/3} \sec Z + \omega_{opt}^{5/3} + \alpha_m^{5/3} \Delta T_m^2 + \alpha_d^{5/3} \Delta T_d^2 , \quad (3.66)$$

where

$\omega_n$  = median external seeing at  $Z = 0$

$\omega_{opt}$  = median angular aberration of the optics

$\alpha_m$  = coefficient of mirror seeing

$\alpha_d$  = coefficient of dome seeing

Using Eq. (3.66), the data were used to determine the coefficients  $\alpha_m$  and  $\alpha_d$ .

Figure 3.77 shows the angular image spread resulting from *mirror seeing*. The ridge line drawn through the data represents a plateau of  $\text{FWHM} = 0.56 \text{ arcsec}$  to which a mirror seeing of  $\omega_m = \alpha_m \Delta T_m^{6/5}$  is added as a  $5/3$

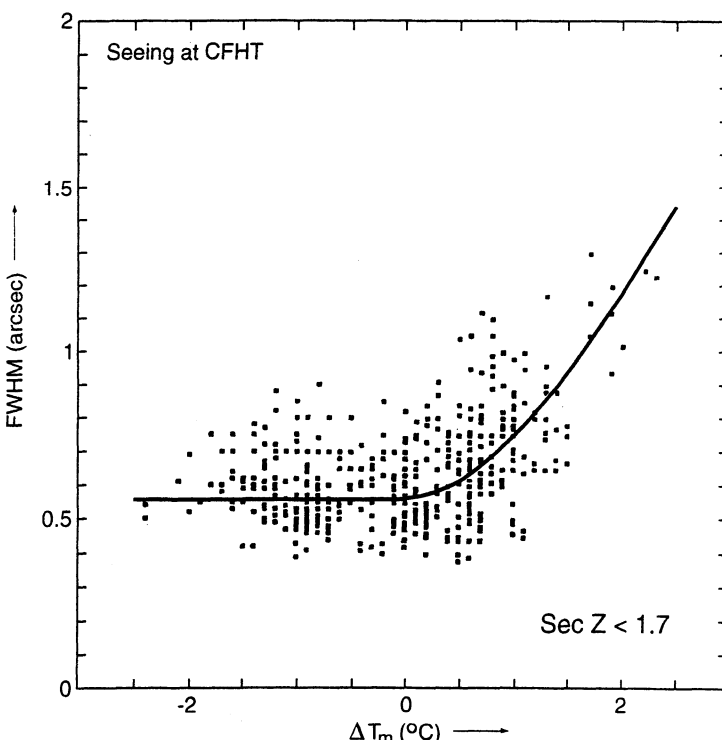


**Fig. 3.77.** Angular image spread due to *mirror seeing* in the CFHT. The mirror seeing contribution occurs only at  $\Delta T_m > 0$  and is superposed on the constant plateau  $0.56 \text{ arcsec}$  due to other sources. (From Racine [3.238])

power law for  $\Delta T_m > 0^\circ\text{C}$ . A least squares fit yields for the median coefficient of mirror seeing

$$\alpha_m = 0.40 \pm 0.05 \text{ arcsec } /{}^\circ\text{C}^{6/5} \quad (3.67)$$

The plateau represents the other terms of Eq. (3.66) apart from that in  $\alpha_m$ . This result is of great importance not only as a practical determination of  $\alpha_m$  in a functioning telescope but also as indicating that a *colder* mirror ( $\Delta T < 0$ ) is very much less deleterious to seeing than a warmer one. Figure 3.77 suggests the effect of the colder mirror for temperature differences down to  $\Delta T = -2.5^\circ\text{C}$  is not detectable. Cautiously, Racine deduces that the effect is at most 1/3 of that of a warmer mirror, referring to the rule-of-thumb in use. We shall see below that this is supported by Iye et al. and compare the results with other experiments.

Racine deduces a similar function for *dome seeing* (Fig. 3.78), deriving in a similar way

$$\alpha_d = 0.10 \pm 0.05 \text{ arcsec } /{}^\circ\text{C}^{6/5} \quad (3.68)$$

The value for  $\alpha_d$  is thus 4 times smaller than  $\alpha_m$ . Racine suggests that the mixing length  $l_0$  between air volumes across the dome slit, which one would expect to be of the order of the slit width (6 m), is larger than the scale height of convection above the mirror  $h_0$  by a factor of ca.  $4^{5/3} \sim 10$ .

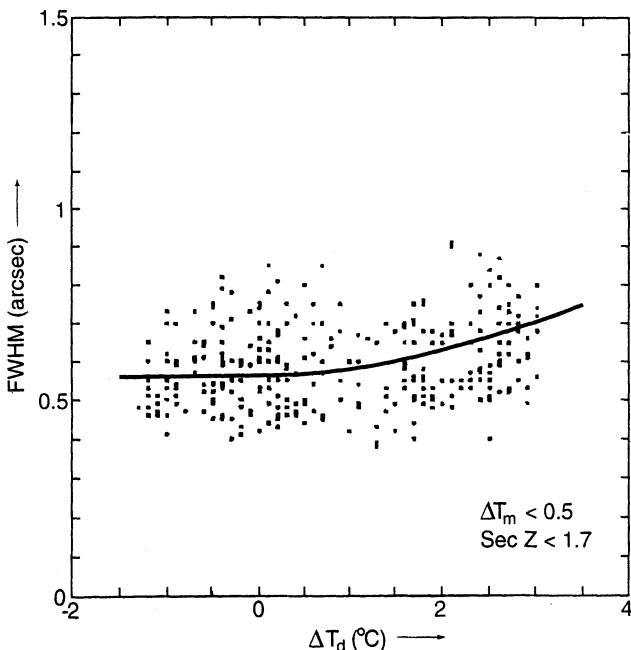


**Fig. 3.78.** Angular spread due to *dome seeing* in the CFHT, for  $\Delta T_m < 0.5^\circ\text{C}$ . Again, the dome seeing contribution occurs only at  $\Delta T > 0$  and is superimposed on the constant plateau 0.56 arcsec due to other sources. (From Racine [8.238])

This would be consistent with the value assumed above for  $h_0$  and a slit width of 6 m. It is important to note that, according to Fig. 3.78, a  $\Delta T_d = +3.5^\circ\text{C}$  can still generate dome seeing of about 0.4 arcsec, even though the coefficient  $\alpha_d$  is smaller than  $\alpha_m$ . Such  $\Delta T_d$  values can readily occur in the Bowen-type telescopes, if attention is not given to heat source prevention and reasonable ventilation. Rapidly falling external temperatures are particularly dangerous, since there is inevitably a thermal time lag with the high mirror and air masses. As an example, around 1980, when the dome conditions of the ESO 3.6 m telescope were much worse than today, the effective final seeing corresponding to Eq. (3.66) was largely determined by whether the outside temperature was tending to fall or rise, the latter giving markedly better seeing. At the CFHT, the biggest improvements in dome seeing have been achieved by the refrigerated observing floor and elimination of air leaks and heat sources above it. It is estimated that the residual solar radiation (heating power) entering the dome during a sunny day amounts to about 30 kW. This would raise the temperature about  $5^\circ\text{C}$  if the heat were not absorbed by the cooled floor and air chiller units in the telescope area.

Other specific sources of dome seeing have been identified at the CFHT, notably air venting from the top louvers, radiative heat loss from the outer skin and slit edge turbulence. Further work was under way, for example, cooling the primary by ducted air from the dome air chillers.

The above work on the CFHT was admirable in demonstrating the progress that can be made in removing local air errors with a classical thick mirror and large building, if the matter is approached systematically. Another admirable example, attacking local air errors in the framework of a general upgrade using active optics principles, is the work of Baldwin et al. [3.208] on the 4 m Cerro Tololo telescope.

One aspect of great importance that could not be addressed in Racine's work on the CFHT was the effect of *wind flushing*, since this is not normally available inside a classical dome unless fans are specifically built on to the telescope structure, as Lowne suggested.

Although the above work with the CFHT has shown that good dome and mirror seeing results can be achieved with classical telescopes and building concepts, the modern trend is undoubtedly away from such enclosures. The second row in Fig. 3.75 shows classical enclosures which are relatively high, the aim being to get above "ground seeing". But the advantage of this has never been confirmed. At the ESO La Silla observatory, both the 2.2 m MPIA telescope and the 3.5 m NTT are much lower than the 3.6 m telescope but have appreciable superior dome seeing, although neither telescope is sited at a marked local peak like the 3.6 m. They are, however, on the main ridge with the prevailing wind roughly orthogonal to the ridge.

The 4.4 m MMT enclosure (Fig. 3.15) marked a milestone in the development of telescope enclosures. For the first time since its introduction, the classical "dome" construction with a slit was abandoned. (Of course, the step towards a symmetrical building rotating with the telescope was a logical

consequence of the alt-az mount, but this step had not been taken for the Russian 6 m telescope or the 4.2 m WHT). Essentially, opening the building implied taking the lid off a rectangular box, giving an opening of the same area as the telescope area itself. This has obvious advantages for convectively removing hot air. Considerable attention was also given to temperature differences between the ambient air and the enclosure and telescope structures (i.e. “dome” and “telescope” seeing), including a thermogram and radiation cooling analysis by Beckers and Williams [3.240]. The thermograms revealed the strong radiation cooling from enclosure and telescope structure and calculations gave  $\Delta T = -8^\circ\text{C}$  for the enclosure roof relative to the ambient air, in reasonable agreement with the measured value of  $\Delta T = -6^\circ\text{C}$ . That this can produce a dangerously unstable colder air layer compared with the air in the telescope chamber, was first pointed out by Meinel [3.241] and is now quantitatively confirmed by the CFHT experiments of Racine [3.238] discussed above. At the MMT, the floor and yoke were covered with wood and styropor insulation, while other surfaces were tested with various surface covers:  $\text{TiO}_2$  paint, Al paint, Al foil and “Maxorb”. As a result, wherever possible, the surfaces were covered with *adhesive Al foil*. This is a relatively simple solution to apply and is a procedure from which other telescopes could certainly profit. It confirms, too, the trend away from “white” enclosures to ones constructed of aluminium panels (at La Silla, for example, the 2.2 m MPIA and 3.5 m NTT enclosures). The aim is to reduce the IR emissivity. According to Beckers [3.242], the 10 m Keck telescope was also treated to reduce radiation cooling (above all to prevent thermal warping affecting the pointing). In this case, a special aluminium paint was applied.

Gillingham [3.236] identified a correlation between image motion and temperature excess in the AAT dome, using pairs of 5 cm holes of a Hartmann type mask. The question of such dome-induced image motion was pursued by Forbes at the MMT [3.243]. Using microthermal sensors mounted 3 m above the floor and near the opening, Forbes also found a correlation between an increase of microthermal activity and image blur. He concluded that, in agreement with Gillingham and Young [3.244], such microturbulence causes image movement in a small aperture telescope and blur (speckle) in a large aperture telescope. This is to be expected from the small air cell size of the microturbulence.

Following Racine’s argument concerning the link between slit size in a classical dome and the mixing length  $l_0$  between air volumes across the dome slit, i.e.  $l_0$  being of the same order as the slit width, it is clear that an opening (slit) no smaller than the telescope chamber itself, as in the MMT, should bring a major advantage in dome seeing compared with classical domes.

The enclosure of the 3.5 m ESO NTT (Fig. 3.27) was essentially the same concept as the MMT building, but with the important modification that the back wall of the MMT telescope chamber was removed to allow *free natural ventilation* through the NTT “building slit”. Like the MMT building, the side walls are vertical, allowing free convection. If the louvers are opened behind

the telescope and the windshield is down, the NTT is effectively open at the top, front and back. We shall return below to the remarkable potentialities of the NTT as a test bench of the dome, mirror and site seeing. Here, two examples will be given which were recorded soon after “first light” and which illustrate “mirror seeing” and “telescope structure seeing” (from radiation cooling) respectively [3.70]. It must be borne in mind that, at this early stage of its operation, no thermal sensors were available and that the building thermal control was far from optimal because of technical work. In general, the primary mirror probably had a  $\Delta T_m > 0$ , but the effects could be mitigated by natural ventilation in a way that would be impossible in a classical dome.

The “mirror seeing” effect was observed near zenith as third order spherical aberration. Under stable air conditions (poor ventilation), axisymmetrical modes are to be expected near the zenith and this is the lowest such mode apart from defocus. Figure 3.79 shows the evolution over about 2 h as the wind slowly increased to about  $5 \text{ ms}^{-1}$  and “blew away” the hot air layer. The initial coefficient of Sph3 of about  $-1630 \text{ nm}$  corresponded to a  $d_{80} \sim 0.3 \text{ arcsec}$  or FWHM  $\sim 0.2 \text{ arcsec}$ . Unfortunately  $\Delta T_m$  was not known at that time.

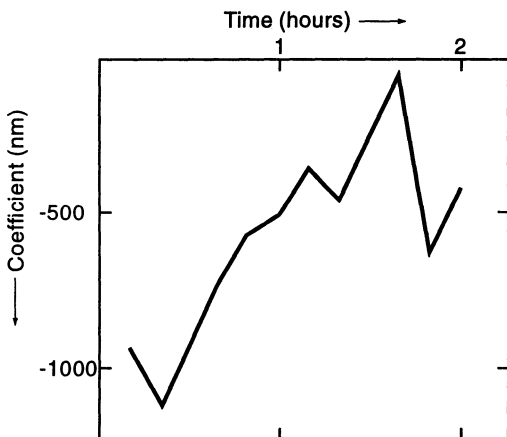


**Fig. 3.79.** Mirror seeing in the ESO 3.5 m NTT during a night in March 1989 shortly after “first light”. The histogram shows the evolution of the first axisymmetrical natural mode. The coefficient of  $-1000 \text{ nm}$  (equivalent to a coefficient of Sph3 of about  $-1630 \text{ nm}$ ) was reduced over about 2 hours to a mean level of about  $-350 \text{ nm}$  by a modest ventilating wind. (From Wilson et al. [3.70])

The second example, illustrating “telescope structure seeing” (possibly in combination with convection effects from the “warm” primary) was the observation over more than 1 hour of a very stable quadratic astigmatism ( $\propto \cos 4\phi$ ) aberration, the telescope being at  $Z \sim 50^\circ$  and pointing *away* from the wind, i.e. with the wind behind the primary so that ventilation was poor. The coefficient corresponded repeatedly to  $d_{80} \sim 0.2 \text{ arcsec}$  and was so stable that we sought an explanation in mechanical flexure. However, there is no evident source of such a flexure mode due to  $Z \sim 50^\circ$  in the NTT. The experiment was made of observing a star at  $Z \sim 50^\circ$  with an azimuth change of  $\sim 180^\circ$ , thus observing *into* the wind. The systematic aberration vanished completely. Since temperature sensors were not available, we could not prove

it, but the most plausible explanation was a radiation and conduction cooling effect of the spiders holding  $M_3$  leading to 4 cold nodes and a  $\cos 4\phi$  mode.

These examples show the power of image analysis for investigating local air errors. We return to this below.

### 3.6.3 Other recent investigations by laboratory experiment or theory: mirror seeing

**3.6.3.1 Cooled, lightweighted blanks.** One of the principal advantages claimed for lightweighted, honeycomb type blanks of the sort developed by Angel using borosilicate glass (see § 3.3.4) is the low mass and accessibility of the material to air cooling. Woolf [3.245] claimed that this provided the best solution to the mirror seeing problem, a viewpoint that has repeatedly been presented.

The design and demonstration of such a system of thermal control for a honeycomb blank was given by Cheng and Angel [3.246]. The general aim is to follow the ambient temperature while maintaining low internal temperature gradients. Essentially, air jets at ambient temperature are directed into the mirror structure. The aim is to limit the angular effect of *support forces and mirror seeing* to  $\leq 0.1$  arcsec, the temperature difference to the ambient air being then defined as  $\Delta T_m \leq +0.2^\circ\text{C}$ . These two figures are in excellent agreement with the subsequent experimental determinations of Racine (see Eq. (3.67)) for a conventional, massive blank. The temperature gradients should be limited to  $0.1^\circ\text{C}$ . These goals must be maintained for cooling at  $0.25^\circ\text{C}/\text{hour}$  in a typical observatory environment. The general scheme for such forced convective ventilation is shown in Fig. 3.80. Streams of air, all at the same ambient temperature, are directed against all the internal, edge and back surfaces of the mirror. The cooling rate should match the convective cooling of the front face. However, *active* temperature control is envisaged to give more flexibility. The system used an exchanger and servo system to control the temperature of the ventilating air. The test results, stated to be valid for blanks up to 8 m diameter, were able to meet the requirements defined above. A time constant of less than one hour for the overall response

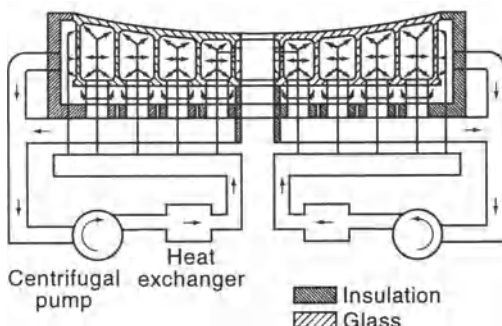


**Fig. 3.80.** Lightweighted honeycomb blanks of borosilicate glass: schematic of the mirror ventilation system (from Cheng and Angel [3.246]).

was readily achieved. It was concluded that such a system would remove all problems of expansion of the BSC glass as well as mirror seeing.

Further information and confirmation was given by Cheng and Angel in a later paper [3.120], addressed more specifically to 8 m honeycomb blanks. The target for mirror seeing is a blur with  $\text{FWHM} \leq 0.06 \text{ arcsec}$ . Regarding Lowne's suggestion of introducing fans to reduce convective turbulence, Cheng and Angel doubt whether a laminar flow could be maintained over an 8 m mirror: at least, this remains to be proved. The authors show that their cooling system can achieve the stringent aims for an ambient cooling rate of  $0.25^\circ\text{C}/\text{hour}$ , the front face temperature lag being  $\sim 0.2^\circ\text{C}$  for a wide range of convective wind conditions. At  $0.5^\circ\text{C}/\text{hour}$ , the lag increased to  $0.31\text{--}0.47^\circ\text{C}$ ; but this is a rapid ambient air cooling rate which may well produce poor conditions from other sources.

**3.6.3.2 Internal cooling in meniscus mirrors.** The possibilities of internal cooling of thin menisci in low expansion glass have been considered in detail by Barr et al. [3.247]. From the results of the investigations by Lowne and the work at the CFHT, Barr et al. concluded that the front surface of an 8 m mirror should be within the range  $+0.1$  to  $-0.2^\circ\text{C}$  of ambient temperature. This factor of only 2 between warmer and colder mirrors seems over-cautious in view of the results of Iye, to be considered below, and Racine [3.238]. The authors consider menisci of the geometry proposed for the 8 m VLT or Subaru telescopes with a thickness about 200 mm. The elegant solution proposed is to assemble hexagonal boules of ULE fused quartz in a sandwich construction consisting of a front and back faceplate fused to a central element in which linear grooves have been milled on each side. These then provide the channels for coolant. Although not experimentally demonstrated at the time, it was considered that such a sandwich was quite feasible with state-of-the-art quartz fusing technology. The coolant channel geometry is analysed in detail: the geometry giving a short time constant and small instantaneous surface temperature variation. The latter aspect is important, as it is effectively a thermal "printthrough" effect. This has been one ground for suspicion of this proposal in a glass material with essentially low heat conductivity. However, Barr et al. show curves with maximum "printthrough" temperature differences well under  $0.1^\circ\text{C}$ . The time constant for a  $2^\circ\text{C}$  temperature difference is shown to be about 30 minutes with internal cooling, whereas it would be several hours for a 200 mm thick blank exchanging heat only by normal air convection at its front and back surfaces. The estimated fluid flow (water) required for an 8 m blank with  $t = 200 \text{ mm}$  containing 200 channels would be a maximum of 143 l/min. This is for a worst case with air temperature falling  $0.6^\circ\text{C}/\text{hour}$ . The question of cooling the mirror during optical tests in manufacture is also considered.

**3.6.3.3 Meniscus mirrors in aluminium.** The potential of aluminium as a material for mirror blanks was treated in § 3.3.5.1. The most attractive

features are its high thermal conductivity, or better, thermal diffusivity (see Table 3.4) and its mechanical properties in handling. The high thermal diffusivity makes it a most attractive candidate for *active cooling*, either by fluid coolant channels at the back or by air cooling at the back. However, I am not aware of specific studies in these directions.

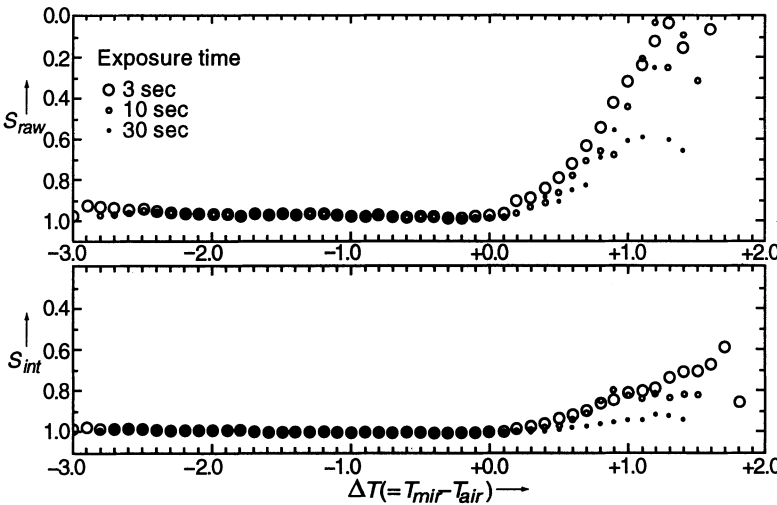
**3.6.3.4 Further laboratory experiments on mirror seeing.** Barr et al. [3.248] carried out experiments with a 1.8 m diameter BSC glass honeycomb mirror using the test tower above a 4 m polishing machine. The mirror temperature was controlled by a 1.8 m diameter liquid cooled “radiation plate” close to the mirror back surface. Testing was performed with CCD camera interferograms and detection of variations due to mirror seeing was far better than the fixed errors in the system. Notable was a systematic Zernike polynomial analysis of the test data. The authors concluded that FWHM was not a good measure of the mirror seeing effects and that the Strehl Intensity Ratio was more appropriate. They found insignificant image degradation for the range  $\Delta T_m = \pm 0.5^\circ\text{C}$  and only small effects in the range  $\pm 1^\circ\text{C}$ . This seems more generous than other authors in the positive range. Larger positive  $\Delta T_m$  values (up to  $2^\circ\text{C}$ ) produced significant degradation in the Strehl ratio. It is significant that no appreciable deterioration was produced by the *cold* mirror, even with larger  $\Delta T_m$ , until the fans were turned on, disturbing the natural convection. For  $\Delta T_m > 0$ , flushing produced some improvement.

A further notable experiment on mirror seeing with a 62 cm mirror was reported by Iye [3.249]. The image analysis was performed with a Shack-Hartmann analyser. The degradation in image quality was evaluated over 90 days and nights. Both the effect of  $\Delta T_m$  on mirror seeing and the effect of a flushing air flow were measured. The set-up was originally designed for an active optics experiment. The temperature variation was that produced by the natural diurnal cycle without active temperature control. The temperature was monitored at one point on the front surface of the mirror, 2 points at the back of the mirror, at the support actuators and at 6 heights between the mirror and the S-H detector at the center of curvature.

The image analysis, as in active optics, was carried out in *modal* form, using 27 Zernike modes. The global criterion used was the Strehl Intensity Ratio.

Flushing wind was achieved by a fan and flat nozzle, 70 cm wide and 2 cm high, at 13, 33, 60 or 88 cm above the mirror surface and near the edge of the beam.

The maximum  $\Delta T_m$  relative to the air measurements was about  $\pm 2^\circ\text{C}$ , produced by mirror inertia in the diurnal cycle. Between 9 and 18 hours, the mirror was colder than the air. Both the coefficient Ast3 and the Strehl criterion reflected precisely the period when the mirror was colder with negligible changes, whereas marked degradation occurred from 18 hours to 9 hours when the mirror was warmer. *With a flushing air flow of the order of  $1\text{ ms}^{-1}$ , the turbulent effect when the mirror was warmer was largely removed.*



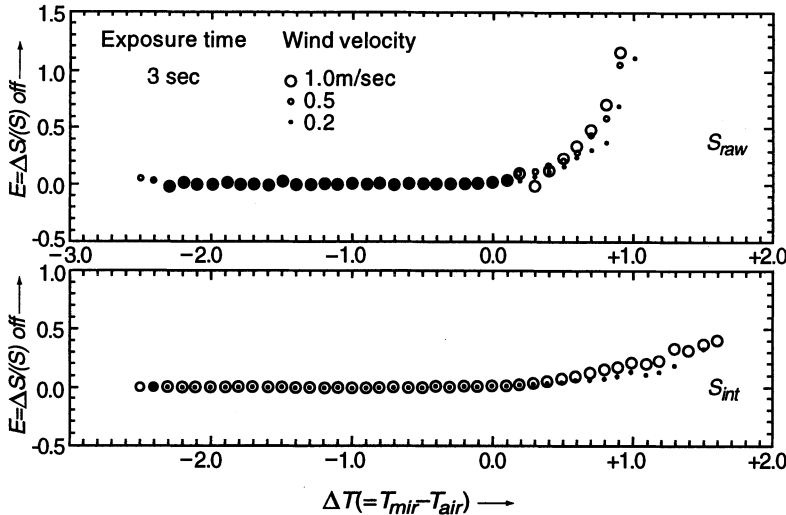
**Fig. 3.81.** Mirror seeing experiments showing the Strehl criterion  $S_{raw}$  and  $S_{int}$  as a function of  $\Delta T_m$  (from Iye et al. [3.249])

Figure 3.81 shows the effect of the diurnal cycle on the “raw” Strehl criterion  $S_{raw}$  (complete function) and the function with wavefront tilt and defocus removed  $S_{int}$ , plotted for three exposure times: 3 s, 10 s and 30 s. The degradation is lowest for the longest exposure, as we would expect from the integrating effect. The similarity to the result of Racine in Fig. 3.77 is so excellent that it gives one great confidence that they provide a solid basis for conclusions on the nature and extent of mirror seeing. This agreement is in spite of the fact that different image quality criteria were used. It is particularly noteworthy that the measurements of Iye et al. confirm that the degradation by a cold mirror is far less than the rule-of-thumb  $1/3$  value compared with a warm mirror, particularly for the range  $0 > \Delta T > -2^\circ\text{C}$ , where the degradation of the cold mirror is not detectable. For  $S_{int}$  this is true out to  $-3^\circ\text{C}$ .

The flushing efficiency is also demonstrated. As expected, it is much more efficient at 13 cm height than higher up.

Figure 3.82 shows the flushing efficiency  $E$  as a function of flushing air velocity, for exposure times of 3 s. This result is remarkable in showing that, although the stronger velocity of  $1\text{ ms}^{-1}$  gives the best results, the result with  $0.2\text{ ms}^{-1}$  is only slightly inferior. The effectiveness of a given windspeed, however, will depend on the mirror size and the exposure time. It was noted that, for a cold mirror with  $\Delta T < -2^\circ\text{C}$ , flushing slightly degrades the quality by disturbing a convectively stable situation. This effect was also noted by Barr et al. [3.248].

Iye et al. also analyse the convective situation, deducing the mixing length of about 7 cm as discussed above by Racine. In practice, they state that convective bubbles will overshoot by a factor of 2 or 3 the thickness of this



**Fig. 3.82.** Mirror seeing experiments: efficiency of a flushing wind (from Iye et al. [3.249])

unstable zone, giving a convection zone thickness  $\sim 20$  cm in this experiment. This explains why the flushing wind is still reasonably effective at 33 cm height, but hardly at all at 88 cm. They deduce a bubble velocity of about  $2 \text{ cm s}^{-1}$  and a turnover time for a bubble of about 15 s.

It should be remembered that the experiment was done in a closed laboratory without active ventilation and that the light beam is conical, not cylindrical. This latter aspect may make the flushing more efficient than in a normal telescope. Nevertheless, the experiment fully confirms Lowne's proposals and measurements. As we shall see below, it also confirms qualitatively what we have observed at the ESO 3.5 m NTT.

The possibilities for thermal control to maintain a budget limit of 0.05 arcsec FWHM for mirror seeing from an 8 m *thin meniscus* blank have been investigated by Rayboult [3.250] for the *UK large telescope project*, equally relevant to the  $2 \times 8$  m *Gemini project*. Rayboult concludes that the active fluid cooling technique of Barr et al. [3.247] (§ 3.6.3.2) would meet the above error budget at all times on the site of Mauna Kea. However, he considers there are technical problems in delivering the coolant and possible problems of induced deformation of the mirror face due to the hydrostatic head pressure differences as the telescope moves away from zenith. The alternative is forced air cooling of the mirror to keep it at, or below, ambient temperature, which may involve significant negative values of  $\Delta T_m$ . Rayboult mentions the condensation risk if this is too large. His assessment of the mirror seeing effect of  $\Delta T_m$  is based on Lowne's work [3.233] (§ 3.6.1): for a colder mirror he assumes image degradation of  $0.125 \text{ arcsec}/^\circ\text{C}$  (minus) and concludes that the specification for the mirror of 0.05 arcsec FWHM could

only be met at Mauna Kea for 50 % of the night. However, the subsequent work of Racine (Fig. 3.77) and Iye et al. (Fig. 3.81) suggests strongly that Rayboult's assumption from Lowne for *colder* mirrors is too pessimistic.

Further work on thermal control of thin menisci to eliminate mirror seeing has been performed for the *ESO 8 m VLT primaries* by Cullum [3.251].

He considers first of all the *passive* ability of an 8 m VLT primary ( $t = 175$  mm) to follow the outside ambient temperature at the proposed Paranal site. Temperature data for the outside ambient air over 17 nights were considered and appear representative. A figure of merit  $\psi$  as the average  $\Delta T_m$  (mirror minus air) was formed with weighting factors 1.0 for  $\Delta T > 0$  and 0.33 for  $\Delta T < 0$ . The temperature  $T_{opt}$  of the mirror at the start of the nights was calculated to minimize  $\psi$ . The value of  $\psi$  varied from  $0.09^\circ\text{C}$  on the most favourable night to  $0.55^\circ\text{C}$  on the least favourable. An error of  $\pm 0.5^\circ\text{C}$  in  $T_{opt}$  has little effect on  $\psi$ . Figure 3.83 shows the temperature functions of the ambient air and the mirror if cooled initially to the temperatures  $T_{opt} + 0.5^\circ\text{C}$  and  $T_{opt} - 0.5^\circ\text{C}$ . Figure 3.83 (b) confirms Rayboult's view that passive thermal adaptation of thin menisci is not adequate: in this case, assuming correct achievement of  $T_{opt}$  by the cooling system of the ambient air *in the enclosure* during the day, the maximum discrepancies with the Cullum criterion are  $\Delta T_m = -3.0^\circ\text{C}$  and  $+1.2^\circ\text{C}$ . A positive overhang is inevitable in the latter part of any night where a rapid fall of ambient temperature is occurring. The Cullum criterion is probably cautious in taking a weighting

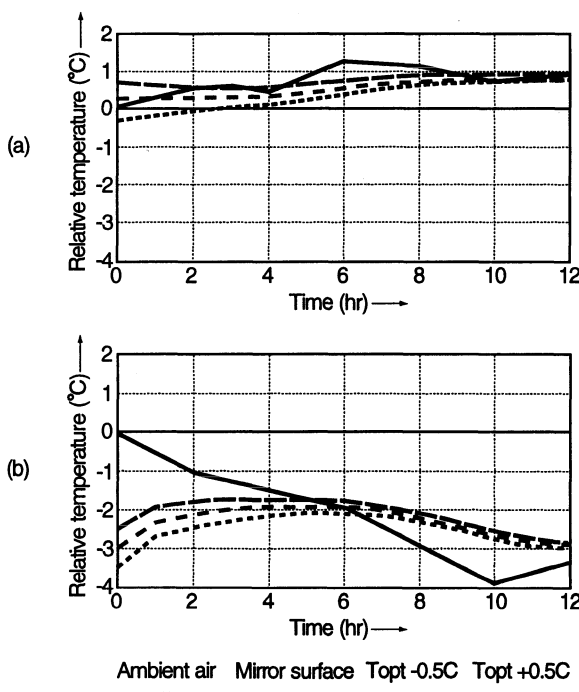


**Fig. 3.83.** ESO 8 m VLT primaries at Paranal: *passive* thermal adaptation if cooled initially to the optimum temperature  $T_{opt}$  (between the two curves): (a) most favourable night, (b) least favourable night (from Cullum [3.251]).

factor of 0.33 for  $\Delta T_m < 0$ , in view of Racine's and Iye's results discussed above. But a lower weighting factor would increase the negative initial  $\Delta T$  values to values of the order of  $-5^\circ\text{C}$ , which may lead to dewpoint problems or overburden the cooling system in the enclosure.

The establishment of  $T_{opt}$  is a matter for the general air-conditioning system inside the enclosure *during the day* and must cope with the thermal inertia of the mirror. Cullum shows a typical cooling scenario for the mirror and steel plates of various thicknesses (Fig. 3.84). The enclosure daytime ambient air is reduced over one hour to  $3^\circ\text{C}$  below the final target temperature of the mirror and  $5^\circ\text{C}$  below the initial mirror temperature, held 2 hours at this temperature and then allowed to converge linearly over 1 hour to the target temperature. The cycle to cool the mirror  $2^\circ\text{C}$  thus requires 3 hours. The calculations for steel plates of various thicknesses are intended to show the effect of the cycle on the steel telescope structure.

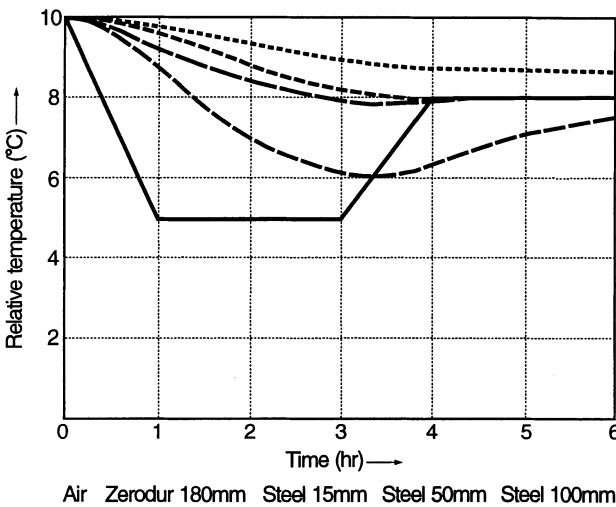
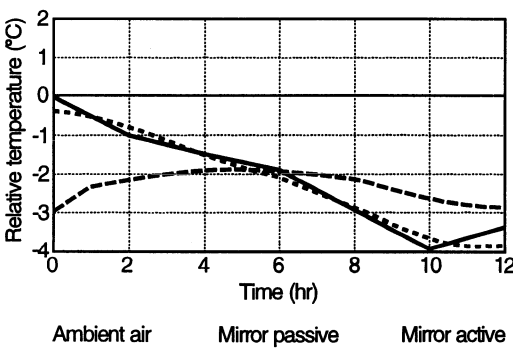


Fig. 3.84. Surface cooling of the ESO 8 m VLT primary and various steel plates with an enclosure daytime ambient air cycle  $3^\circ\text{C}$  below the target temperature, assuming an air velocity of  $1\text{ ms}^{-1}$  on both sides of the mirror and one side for the steel plates (from Cullum [3.251])

From Fig. 3.84 and more extreme examples, it appears feasible to achieve  $T_{opt}$  for the VLT primaries at Paranal within acceptable tolerances of reasonable predictions, though enclosure air cycles up to  $7^\circ\text{C}$  below the initial mirror temperature may be necessary. However, such temperature excursions are large and might lead to dewing problems on metal parts. For the VLT, a dewpoint "fuse" could be envisaged which would prevent a temperature excursion leading to dewing. More serious is the positive temperature over-

hang of the mirror in the second half of an unfavourable night as shown in Fig. 3.83 (b).

To get a better adaptation of the mirror to the outside ambient air, Cullum suggests an additional element in the thermal chain, namely a metal plate built into the prime mirror cell, a few cm below it, which is cooled by liquid through attached channels. A metal cooling plate was used by Barr et al. [3.248] in their laboratory experiment on mirror seeing, but Cullum's suggestion to use such a device *in the functioning telescope* seems to provide the definitive solution for suppressing mirror seeing from thin meniscus primaries. Such a cooling plate was under study for the VLT, but it seemed probable that some 90 % of the back surface of the primary (i.e. 10 % for supports) could be achieved as a cooling surface. Since, in the VLT telescopes, the top end of the tube tends to be somewhat too heavy, the additional weight of a suitable plate is no problem at all. The ideal material seems to be aluminium because of excellent thermal conductivity and low mass. The time constant of such a liquid-cooled plate is therefore very low, giving far greater flexibility of control than with the enclosure air-conditioning system. Cullum supposes (during observation at night) a cooling plate 5 °C below the outside ambient air and calculates the thermal control possible for the VLT primary *without prediction*, i.e. forced cooling takes place only when  $\Delta T_m > 0$ ; if  $\Delta T_m < 0$ , the plate is at the outside ambient temperature. Figure 3.85 shows the cooling result for the same unfavourable outside ambient air temperature scenario as Fig. 3.83 (b). The initial  $\Delta T_m \simeq -0.3$  °C with plate cooling, but this is un-critical. The *active* cooling curve shows a maximum positive  $\Delta T_m \simeq +0.2$  °C and a maximum negative  $\Delta T_m \simeq -0.5$  °C. The *passive* cooling curve  $T_{opt}$  of Fig. 3.83 (b) is also shown for comparison with  $(\Delta T_m)_{max} \simeq +1.2$  °C and -3.0 °C respectively. It is clear that, if the weighting factor of the criterion  $\psi$  for  $\Delta T_m < 0$  were reduced to zero with active cooling, that positive values of  $\Delta T_m$  would be completely eliminated without producing negative values exceeding -1 °C. This technology therefore seems able to eliminate mirror seeing completely in a flexible, technically simple and reliable way. Compared with internal fluid cooling of the meniscus blank itself, as proposed by Barr



**Fig. 3.85.** Active cooling online at night of the ESO 8 m VLT primaries with a cooling plate compared with passive cooling for the case of Fig. 3.83(b) (from Cullum [3.251])

et al. [3.247] but which is inevitably a complex process, the cooling of a plate is technically trivial since deformations are of no significance. The only limitation would be the dewpoint of the plate; but the temperature excursions required are probably less than those required for the enclosure daytime ambient air to establish  $T_{opt}$  for passive cooling. With the plate, furthermore, no accurate temperature predictions are required.

More recently (1997), Cullum has confirmed [3.252] that his proposed active cold plate is indeed being built into the prime mirror cells of the VLT unit telescopes. Furthermore, the same concept has been taken over for the Gemini project, although the mirror support structure is somewhat less favourable than in the VLT.

Cullum points out a further important and advantageous aspect of his active cooling system. Plots of statistical data of external seeing, as recorded by the ESO seeing monitor, reveal that the best seeing with *rising* night temperature is markedly worse than that with *falling* night temperature, the best recorded median FWHM values in this sample being about 0.50 arcsec and 0.37 arcsec respectively. This can be interpreted as the effect of a weather change producing rising temperature, whereas falling temperature corresponds to stable conditions for the “normal” case. In any event, it is precisely nights of falling temperature which require *active* cooling to prevent a positive temperature overhang of the primary (Fig. 3.85). With *passive* cooling, the external seeing gain is vitiated by the mirror seeing with  $\Delta T > 0^\circ\text{C}$ .

Further work on the matter of mirror and dome seeing for the ESO VLT was carried out by Zago [3.253]. Zago was concerned with the enclosure ventilation and mirror seeing aspects in view of the primary mirror wind-buffetting pressure limitation (assuming no correction possibilities of the primary in the extended active optics bandpass – see § 3.5.4) of  $1 \text{ N/m}^2$  established by Noethe et al. [3.213]. With this limitation, he deduced a limit windspeed on the mirror of about  $1.35 \text{ ms}^{-1}$  for  $Z > 35^\circ$  to about  $2.6 \text{ ms}^{-1}$  at  $Z = 10^\circ$ . Zago emphasized the need for correct *scaling laws* for mirror and dome seeing so that model experiments such as those of Lowne, Barr et al. or Iye et al. can be extrapolated to 8 m diameters. For the *free convection* case, he assumes Kolmogorov statistics as does Racine (Eq. (3.62)) and derives the scaling law

$$\text{FWHM} \propto \Delta T_m^{6/5} L^{1/5} \quad (3.69)$$

for the dependence on temperature difference  $\Delta T_m$  and dimensional scale  $L$ . Natural convection may be free or turbulent but all the evidence is that only *turbulent* natural convection produces mirror seeing. In the case of *mixed convection*, when natural convection is disturbed by forced convection with an independent airspeed  $U$ , Zago derives an approximate scaling law on certain assumptions:

$$\text{FWHM} \propto \Delta T_m^{3/2} L^{1/2} U^{-3/5} \quad (3.70)$$

He performed a laboratory experiment on a very small scale (a 4 cm mirror) and applied the scaling law (3.69) to the results of mirror seeing produced by

$\Delta T_m > 0$ , the FWHM being given from (3.62) as  $F_{rad}$  in this experiment by

$$F_{rad} = 0.987 \frac{\lambda}{r_0} , \quad (3.71)$$

where  $r_0$  is the Fried parameter. For free convection with  $\Delta T_m$  varied between +10 and +100 °C, he gives the coefficient  $a = F/\Delta T_m^{6/5}$ , both for the open mirror and when enclosed by a simple cardboard “dome”. For the larger  $\Delta T_m$  values, this coefficient converges on a mean value about  $a = 0.17 \text{ arcsec}/^\circ\text{C}$ , both with and without “dome”. Scaling according to (3.69) for  $L$  gives then  $a \simeq 0.43 \text{ arcsec}/^\circ\text{C}$  for a 3.5 m mirror and  $0.49 \text{ arcsec}/^\circ\text{C}$  for an 8 m mirror, a relatively small difference because of the weak dependence on  $L$ . This value of  $a$  agrees well with the value  $a = 0.40 \text{ arcsec}/^\circ\text{C}^{6/5}$  given by Racine [3.238] – see Eq. (3.67) – for the 3.6 m CFHT primary.

Using his scaling laws, Zago also compares the results of his experiment with those of Iye et al. [3.249], given above. Extrapolating the flushing-wind effect to an 8 m mirror with  $\Delta T_m = +1^\circ\text{C}$ , he derives the function for mirror seeing against flushing speed given in Fig. 3.86, converting Iye et al.’s data from the Strehl criterion to FWHM. The agreement is good except in the low flushing-speed domain < ca. 1.5 m/s. This is because the relative turbulence intensity tends to increase with low speeds so that the pure convection case with speed zero is not approached in practice and mirror seeing is worse. The important conclusion drawn by Zago from Fig. 3.86 is that a flushing speed of about  $2 \text{ ms}^{-1}$  is required to “blow away” mirror seeing with  $\Delta T_m = +1^\circ\text{C}$  at the scale of an 8 m primary.

Regarding cooler primaries ( $\Delta T_m < 0$ ), Zago concludes that the conditions of free convection remained laminar over his whole negative temperature range. At the 8 m scale, this may not be the case. If the flow becomes

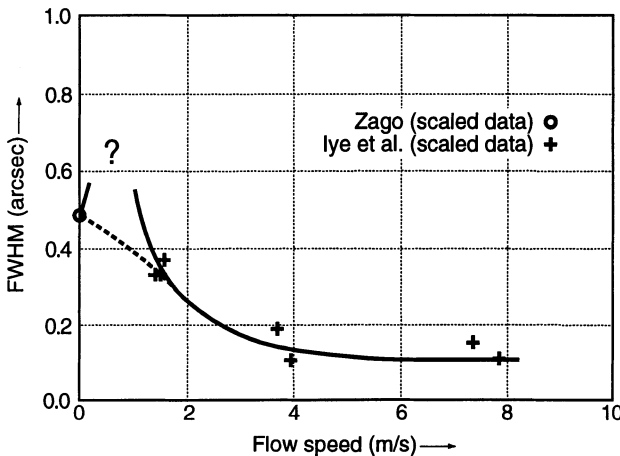


**Fig. 3.86.** Extrapolation predictions for the flushing windspeed effect on mirror seeing for the ESO 8 m VLT primaries and  $\Delta T_m = +1^\circ\text{C}$ , based on Iye et al. (from Zago [3.253])

turbulent, mirror seeing can also result at negative  $\Delta T_m$  values, as was noted by Iye et al. when flushing disturbed the laminar flow conditions. Previous experiments had not covered a sufficiently large negative range of  $\Delta T_m$  to do scaling predictions concerning incidence of turbulence.

Summarising for the ESO 8 m VLT, one may conclude from Zago's work:

- Without active correction for wind-buffetting in the extended active optics bandpass, the maximum windspeeds incident on the primary must be 1.5 to  $2.5 \text{ ms}^{-1}$ , depending on  $Z$ .
- Preliminary investigations for the enclosure envisaged will permit maximum flushing winds of  $1\text{--}2 \text{ ms}^{-1}$ .
- Scaling laws predict a mean *mirror seeing*

$$\text{FWHM} \simeq 0.5 \Delta T_m^{6/5}$$

for  $\Delta T_m > 0$ .

- Dome seeing effects were believed by Zago to be interaction effects aggravating mirror seeing rather than independent effects. Small air motions worsen local seeing, whereas stronger laminar flushing improves it. This conclusion agrees with both Lowne and Iye et al.
- At the 8 m scale, a flushing speed  $\geq \sim 2 \text{ ms}^{-1}$  is required to flush away mirror seeing. However, the evidence is very approximate and  $1 \text{ ms}^{-1}$  may prove to give useful improvement.
- The 8 m VLT primaries should have  $\Delta T_m \leq +0.2^\circ\text{C}$ , the negative limit being unclear but certainly more generous.  $\Delta T_m = +0.2^\circ\text{C}$  would give a FWHM  $\sim 0.1 \text{ arcsec}$  of mirror seeing.
- A large  $\Delta T_m$  range of experimental data is required to establish correct scaling to the 8 m class for  $\Delta T_m < 0$ .

Later, in 1995, Zago produced a major work as a doctoral thesis [3.254] on the effects of the local atmospheric environment on observational seeing. This is certainly one of the most (if not *the* most) comprehensive treatments of the subject currently (1997) available. The chapter headings are:

- Introduction
- The image quality of a telescope
- Telescope enclosures
- Telescope aerodynamics
- Local seeing
- Systems engineering
- Conclusions

There is also a valuable bibliography of 65 references, as well as two appendices.

### 3.6.4 Further work on “dome seeing” in general

**3.6.4.1 The ESO 3.5 m NTT as a test bench for local air seeing.** Reference was made in § 3.6.2 to image analyses which revealed by their modal nature effects due to mirror seeing (spherical aberration) and (probably) to seeing effects from the  $M_3$  spider support (quadratic astigmatism). At that time (March 1989), no temperature or wind sensors were available. About a dozen temperature and windspeed sensors were later installed and (in November 1992) largely linked to the computer-monitor system. A programme was intended which would seek systematic correlations between the various temperature differences of mirror, telescope and dome from the ambient air, together with windspeed in the building slit (Fig. 3.27), and the image quality error modes measured by the image analyser. There was also continuous monitoring of the external (atmospheric) seeing from the seeing monitor. The output data from the image analysis [3.70], together with the external seeing, permits a complete separation and modal identification of local air seeing errors up to the temporal bandpass limitation of the 30 s integration of the image analysis. Since, at normal tracking speeds, the telescope optics errors are, with the exception of defocus, largely stable over periods of the order of 30 min, variations in the low spatial frequency (controlled) aberrations are due to local air variations and are normally a sign of inferior thermal conditions. A sensitive indicator is the high spatial frequency rms wavefront residual  $W_{HF\,rms}$ , after removal of the controlled terms. This term contains the fixed high spatial frequency errors of the optics (the “Intrinsic Quality”) and the measuring noise of the system. The lowest value recorded up to 1992 was

$$W_{HF\,rms} = 0.09 \text{ arcsec rms ,}$$

a value corresponding to superb thermal conditions in the NTT and enclosure. Values up to 0.12 arcsec rms indicate good local conditions. However,  $W_{HF\,rms}$  is a very sensitive and non-linear indicator of the local thermal conditions in general: empirically, it has been established that a value  $> 0.15$  arcsec rms implies (for NTT standards) poor thermal conditions. Measurements on other telescopes with the ANTARES off-line image analyser confirm the value of this indicator. In the ESO 3.6 m telescope, for example, “dome seeing” could at that time easily produce values of 0.35 arcsec rms or more. Apart from the low spatial frequency modes, it remained extremely important to seek correlations in the NTT between  $W_{HF\,rms}$  and the temperature and wind differences.

**3.6.4.2 The 2.5 m Nordic Optical Telescope (NOT).** This is a telescope for which highest quality has been a consistent aim. This requires careful attention to the thermal environment [3.255]. The building has 4 “wall gates” which can be opened at will during observing to get adequate air flushing, an excellent feature. The normal “passive” thermal control comprises the usual cooling and air-conditioning system. However, it was intended

to “activate” the thermal control by reference to an extensive temperature measuring system, including 172 temperature probes, repeatable to  $0.1^\circ\text{C}$ . This was intended to lead to a model for optimizing the temperature of the dome ambient air whose variation was to be modelled as closely as feasible.

**3.6.4.3 The significance of a fast active optics control loop for local seeing in general.** The qualitative evidence from the NTT (§ 3.6.4.1) is that good thermal conditions are associated with *slowly* varying low spatial frequency terms of small amplitude. As the thermal conditions deteriorate, both the amplitude and temporal frequency of such terms induced by local air increase, together with a rise (much more rapid than linear) in high spatial frequency errors. This situation corresponds qualitatively to that described by Zago (§ 3.6.3.4) for the transition from a stable or laminar convective situation to a turbulent one. The NTT is a test bench which enables the accurate investigation of the errors near the optimum conditions. If thermal conditions are good, the evidence from image analysis is very clear that an *automatic correction cycle* every 10 min (as envisaged for the final automation of the NTT optics system) will correct the bulk of residual local seeing effects, as discussed by Wilson et al. [3.73]. Only if thermal conditions are bad will this cycle be too slow: but in this case, the thermal conditions must be improved by better predictions of outside ambient temperature. In other words, if the thermal control system is operated correctly with the temperature sensors, residual local air seeing should always be largely correctable by the 10 min automatic correction cycle.

This feature should be even more true of the ESO 8 m VLT, for which a 40 s active optics correction cycle is envisaged [3.73], 15 times faster than for the NTT. However, more investigation will be required to quantify what temperature differences can be allowed under what air-flushing conditions in order to limit the local air effects to a bandpass  $< 1/40 \text{ Hz}$  and to correctable spatial frequencies.

**3.6.4.4 “Dome” or “tube” seeing monitors.** The scheme proposed by Wilson et al. [3.214] (Fig. 3.70) for detecting wind-buffetting deformation of thin meniscus primaries in the extended active optics bandpass B (Fig. 3.62) is also a “dome” or “telescope” seeing monitor, measuring the air conditions in *double pass* in a conical beam extending from the primary via the secondary back to the Cassegrain or Nasmyth image. Such a conical beam corresponds to the conical beam measured by Iye et al. [3.249] (§ 3.6.3.4) between a concave mirror and its center of curvature. The detection system proposed in Fig. 3.70 can detect only the lowest modes since it is primarily intended for wind-buffetting detection, for which these are fully adequate. However, within this modal limitation and that of its conical beam path, it can detect local air effects in both bandpasses A and B.

A specific proposal for a dome seeing monitor, together with first experimental results, has been made by Iye et al. [3.256]. The technique proposed

is termed a “differential dome seeing monitor” (DDSM), although, as the authors emphasize, it really measures only that part of the “dome seeing” which is within the telescope tube and is therefore really a “tube seeing” monitor. However, the authors are probably right that this constitutes the major part of the dome seeing, particularly in modern, more open types of enclosure. But in classical hemispherical domes with a relatively narrow slit, the seeing induced at and around the slit may be equally or even more significant, depending on the effectiveness of the thermal regime.

The working principle of the DDSM is shown in Fig. 3.87, as realised at the Newton focus of the 1.88 m telescope of the Okayama Astrophysical Observatory. It should be noted that this arrangement, disposed at the Newton focus and blocking a significant part of the telescope aperture, was intended for an *experimental* set-up and would not be suitable without modifications for use in a *functioning* Cassegrain telescope, whereas the system proposed

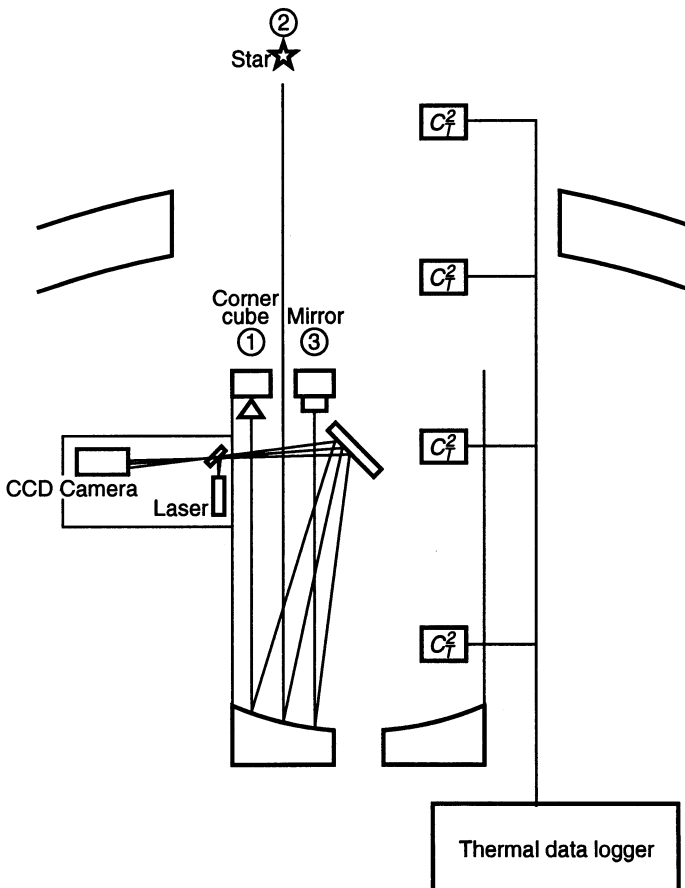


**Fig. 3.87.** Principle of the differential dome seeing monitor (DDSM) set up at the Newton focus of a 1.88 m telescope (from Iye et al. [3.256])

by Wilson et al. [3.214], above, is intended for measurements in a functioning telescope without disturbing observations. The DDSM of Iye et al. uses autocollimation in double pass against the plane reflecting elements of a mask (1) (3) placed in the incident beam. This mask also lets light pass from a natural star. Various types of masks are considered. The first type, realised for the experiment, consists of a plane-parallel glass plate of 400 mm diameter which can be masked at will. The masking used had two circular transparent windows of diameter 70 mm ( $A$  and  $B$ ) disposed near the edge at 90° spacing. Outside the rim, two corner-cubes return the collimated light along its incident path, thereby eliminating angular aberrations and giving reference spots on a CCD detector. With this arrangement, three pairs of spots appear on the CCD:

$C_1, C_2$	from the corner cubes
$S_A, S_B$	from the natural star by transmission through the windows $A$ and $B$
$M_A, M_B$	from the artificial pinhole source in double pass by reflection from the plate at $A$ and $B$ (4 % Fresnel reflection)

Of these,  $C_1$  and  $C_2$  give reference positions which should be stable within the mechanical stability of the source-optics-detector system. The others have movements interpreted as follows:

- The *common movement* of the star spot images, represented by  $S_A + S_B$ , carries information on the common wavefront tilts in the *entire optical path* (tilts from outer atmospheric turbulence, tilts due to tube and local turbulence, tilts due to vibration or tracking errors).
- The *differential movement* of the star spot images, represented by  $S_A - S_B$ , carries information on the wavefront aberrations higher than “tilt” in the *entire optical path*, i.e. from the atmosphere or the local environment.
- The *common movement* of the mirror spot images, represented by  $M_A + M_B$ , carries information of common wavefront tilts *in the telescope tube* or rotational vibrations of the mask plate.
- The *differential movement* of the mirror spot images, represented by  $M_A - M_B$ , carries information on the wavefront aberrations higher than “tilt” *in the telescope tube* or bending vibrations of the mask plate.

In the experiment reported, sag of the mask plate produced serious astigmatism in both star and mirror images, 4 times larger in the latter case because of reflection compared with refraction, as expected. This astigmatism was a limitation on the centroiding accuracy, but the astigmatic lines contained some information on aberrations higher than “tilt”.

The image monitoring was done with a video-rate monitoring camera, limiting the bandpass to 30 Hz. But this was ample to observe the essential features of atmospheric and dome seeing from the point of view of image motion over the sampling apertures. Figure 3.88 shows results both without any

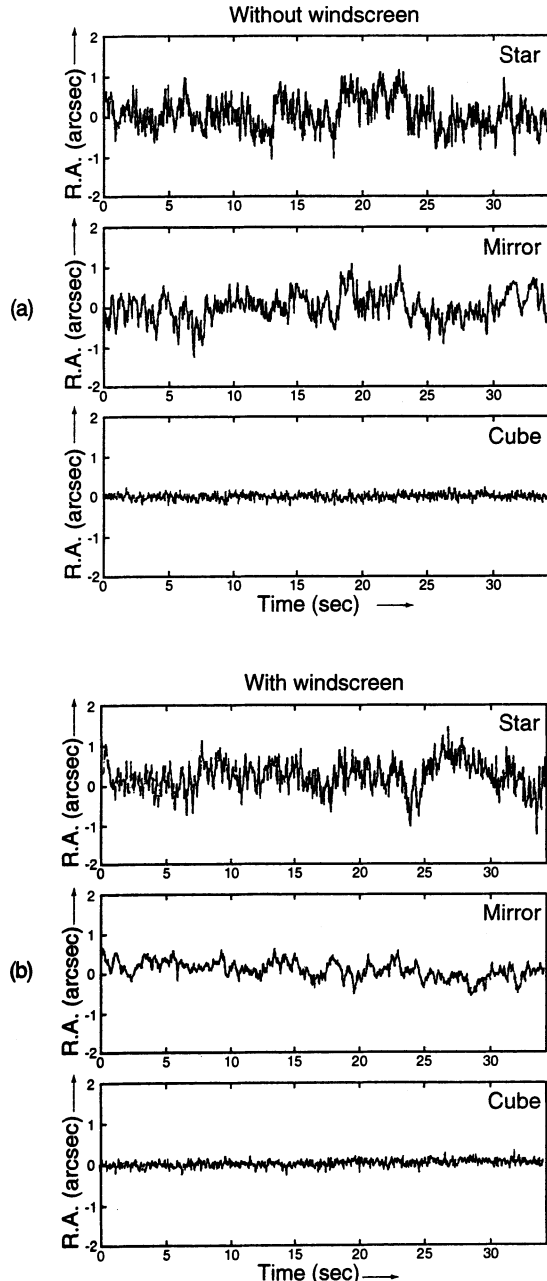


**Fig. 3.88.** Experiments on image motion (wavefront tilt) with the DDSM at a 1.88 m telescope showing the results for the images from a star, mirrors and corner cubes respectively: (a) without windscreening, (b) with maximum windscreening (from Iye et al. [3.256])

windshielding (telescope near zenith with slit pointing into the wind of wind-speed  $\sim 3\text{--}4 \text{ ms}^{-1}$ ) and with the windscreens to give maximum protection from wind.

Figure 3.88 shows that there is a major reduction in image motion from the mirrors ( $M_A + M_B$ ) when windscreening was applied. Not only was the amplitude reduced, but also the temporal frequency, thereby reducing the spectral power. Table 3.16 gives the standard deviations of the image motions.

**Table 3.16.** Standard deviation  $\sigma$  of image motions for the images from the star, mirrors and corner cubes in the DDSM experiment (from Iye et al. [3.256])

Windscreen applied or not	Direction	Star $\sigma (S_B)$ (arcsec)	Mirror $\sigma (M_B)$ (arcsec)	Corner cube $\sigma (C_1)$ (arcsec)
Yes	R.A.	0.36	0.22	0.05
Yes	Dec.	0.43	0.19	0.05
No	R.A.	0.39	0.34	0.08
No	Dec.	0.38	0.35	0.06

Iye et al. conclude that there is a significant improvement in dome seeing by preventing disturbance of the enclosure air by external wind. However, wind flushing may well be beneficial or essential to remove effects of *internal* heat sources (such as mirror seeing). They suggest windscreening should be applied if the latter are small compared with the former. They also suggest that cylindrical buildings of the modern type will be better than classical hemispherical domes because the hemispherical dome allows the wind blocked by the windscreens to “climb up” the enclosure and disturb the slit area used by the light beam, whereas a cylindrical building blocks this effect.

### 3.6.5 General conclusions on local air seeing and enclosures

Compared with elastic and manufacturing errors which dominate the solid elements of telescope optics and which can be largely suppressed by the systematic application of modern technology, local air seeing (error source No. 7 of Table 3.11) is increasingly, apart from external (atmospheric) seeing, the most serious source of image degradation. If care is not taken, as has often been the case in the last 40 years with heat sources within the enclosure, local air seeing may well be more serious than external seeing on a very good site. Only since the work of Lowne in 1979 [3.233] has systematic, quantitative research been done. However, the discussion above shows that rapid progress is now being made and the understanding of the complex parametric situation is growing. However, clear analytical prescriptions are still not available. This is not surprising if we reflect how complex the thermal behaviour of an air mass is which may involve many thousands of cubic meters of air in a complex interaction of a glass-metal structure, enclosure and site.

The modern, compact, alt-az mounted telescopes have produced a revolution in enclosures initiated by the MMT. The reduction of air volume is a huge gain in itself (Fig. 3.75).

“Mirror seeing” has been intensively investigated and the work, above all, of Racine [3.238] and Iye et al. [3.249] gives a good basis for design of the thermal environment of large primary mirrors. Positive temperature differentials ( $\Delta T_m > 0$ ) are certainly far more deleterious than negative ones. For small negative values  $0 > \Delta T > -1^\circ\text{C}$ , the evidence is that the errors produced are negligible. Active thermal control of the enclosure air can be very effective for modest sizes, but the largest sizes ( $\sim 8\text{ m}$ ) can scarcely be adequately controlled by this means. As Cullum [3.251] [3.252] has shown, a fluid-cooled metal cooling plate in the mirror cell appears to be by far the simplest and most effective thermal control technique. This technique works adequately for glass mirrors and would be even more effective for aluminium ones with their high heat conductivity.

The benefits of flushing air flow against mirror seeing have been well demonstrated by the NTT [3.70] and are clearly revealed by the experiments of Iye et al. [3.249]. However, as Zago [3.253] points out, unless a certain minimum flushing speed is achieved, dependent on the size of the telescope, flushing may make the mirror seeing worse, not better.

“Dome seeing” is still less well understood. As Zago indicates, there may be a complex interaction between thermal differences in the structure and mirror seeing convection. This viewpoint is supported by the experiments of Iye et al. with the differential dome seeing monitor, whereby flushing air apparently *worsens* the tube seeing image motion. Thermal differences in the metal structure of telescope and building will be inevitable from radiation cooling and should be countered, as advocated by Beckers [3.240] [3.242], by insulation. More experiments on functioning telescopes are required and the NTT, with its complete image analysis, external seeing monitor and thermal and windspeed sensors, is an ideal testbench. It can then perform modal analysis, as performed by Barr et al. [3.248], enabling a full understanding of the nature of the thermally-induced aberrations.

The most delicate and difficult purpose of a telescope enclosure is to protect the telescope from *wind*. The wind loading of telescopes was considered in a general way by Forbes and Gabor [3.257]. In the classical dome, with its concept of a stable micro-climate, this was solely a matter of designing a building with sufficient stability against wind forces; but, with modern enclosures, the design has become far more complex if natural wind flushing is desired. Above all the NTT has shown the merit of this approach, building on the experience of the MMT. The “wall gates” of the 2.5 m NOT are a similar feature in this direction. For stiff primaries, the only requirement is to avoid wind-shake of the telescope structure, causing tracking errors. Some modern projects (e.g. the ESO VLT) envisage a fast-tracking facility with the secondary mirror unit. This may relax the wind-shake tolerances of the telescope structure. For thin menisci, there remains the problem of

wind-buffetting deformation of the primary. This was discussed in § 3.5.4 and the detection systems proposed by Wilson et al. [3.214] may help to solve this general problem. As mentioned in § 3.6.4.4, this system can also measure “tube seeing”. If wind-buffetting deformations of the primary can be actively corrected in the extended active optics bandpass B (Fig. 3.62), then higher flushing windspeeds can be allowed and the enclosure designed accordingly. But if this is not the case, a windspeed limit will be set for avoiding wind-buffetting deformation of the primary, as determined for the ESO VLT by Noethe [3.213] and Zago [3.253] (see also § 3.5.4). The extent to which flushing is useful will depend on the thermal control, above all of the primary. These compromises are currently a key area of development in telescopes with meniscus technology.

The above considerations are particularly relevant to meniscus technology. The experimental work has also been largely performed with solid blank primaries or experimental mirrors. For lightweighted, stiffer primaries, the wind-buffetting problem is much more favourable, but the thermal control of the mirror is very critical because of the BSC glass used and its associated expansion coefficient (see § 3.6.3.1). When larger lightweighted blanks are in use for the modified MMT or for the LBT, more practical experience will be gained.

Segmented primaries such as the 10 m Keck have an internal control system [3.227] with relatively high bandpass (up to 2 Hz – see § 3.5.5.3) and are quite favourable against wind-buffetting. Since the effective aspect ratio of the primary as a total meniscus of 10 m and thickness 0.075 m is very high, 133, as a result of the segmentation (see Fig. 3.4), the glass mass involved is particularly favourable for mirror seeing. The aim of the thermal control system [3.26] is to establish an internal micro-climate adjusted as nearly as possible to the outside ambient air, banish all heat producing sources to an annex building and insulate [3.26] [3.245] the telescope structure and inside dome walls to reduce radiation transfer.

This book is concerned with telescope optics, not telescope engineering in general. But it is very clear that the telescope enclosure, with its local air system, is one of the fundamental aspects of the total optical train. Thus, the design of the enclosure must go hand in hand with the global optical concept for achieving high image quality.

### 3.7 Optical data of the major ground-based telescope projects using new technology

Table 3.17 gives the basic optical characteristics of the major large ground-based telescope projects *using new optical technology*, following essentially the same presentation as that used in Table 5.2 of RTO I for “conventional” telescopes. It is not claimed that this list is complete, for the definition of a “telescope project” is often fluid until full funding has been achieved. The

**Table 3.17.** Basic optical characteristics of the major large ground-based telescope projects using new optical technology

Telescope	Diameter	Completion date	Blank material	Blank nature and support	f/no primary	Optical form	Mount	References
MMT (Original) (U.S.)	$6 \times 1.8\text{ m} \equiv 4.4\text{ m}$ equivalent	1979	Fused silica	Egg-crater – passive	$6 \times f/2.72$	Classical Cassegrain with beam combination	MMT alt-az	[3.40] § 3.2.2.
NTT (ESO)	3.5 m	1989	Zerodur	Thin meniscus – active	f/2.2	RC	alt-az	[3.70] [3.72] § 3.2.4
TNG (Galileo) (Italy)	3.5 m	1997	Zerodur	Thin meniscus – active	f/2.2	RC	alt-az	[3.77] § 3.2.4
WIYN Telescope (U.S.)	3.5 m	1994	BSC	Lightweighted (honeycomb) – active	f/1.5		alt-az	[3.258] [3.259] § 3.5.5.2
LAMOST (China)	4.0 m	?		Segmented – with additional general active control	f/5.0	Schmidt with reflecting corrector	Fixed with corrector plate as coelostat	[3.49] § 3.2.2
Keck I (U.S.)	10.0 m	1992	Zerodur	Segmented (hexagonal) with open-loop active control	f/1.75	RC	alt-az	[3.22] [3.23] § 3.2.1
Keck II (U.S.)	10.0 m	1996	Zerodur	Segmented (hexagonal) with open-loop active control	f/1.75	RC	alt-az	[3.29] § 3.2.1
HET (Hobby-Eberly Telescope) (U.S., Germany)	9.5 m equivalent (11 m full)	1997	Zerodur	Segmented (hexagonal)	f/1.38	Spherical primary with PF corrector	Fixed zenith distance with az mount and image tracker	[3.18] § 3.2.1

**Table 3.17. (continued) Basic optical characteristics of the major large ground-based telescope projects using new optical technology**

Telescope	Diameter	Completion date	Blank material	Blank nature and support	f/no primary	Optical form	Mount	References
Subaru (Japan)	8.2 m	1998	ULE fused silica	Thin meniscus – active	f/2.0	RC	alt-az	[3.91] [3.92] § 3.2.4
VLT (ESO)	<i>Four telescopes:</i> Each 8.0 m equivalent (8.2 m full)	1998–2000	Zerodur	Thin meniscus – active	f/1.8	RC	alt-az	[3.82] [3.83] § 3.2.4
MMT (Upgrade) (U.S.)	6.5 m	1998	BSC	Lightweighted (honeycomb) – active	f/1.25	Classical Cassegrain	alt-az	[3.42] § 3.2.2
Magellan 1 (U.S.)	6.5 m	1998	BSC	Lightweighted (honeycomb) – active	f/1.25	Classical Cassegrain and Gregory	alt-az	[3.53] § 3.2.3
Magellan 2 (U.S.)	6.5 m	?	BSC	Lightweighted (honeycomb) – active	f/1.25	?	alt-az	[3.53]
Gemini North (U.S., U.K., Canada, Chile, Argentina, Brazil)	8.0 m equivalent (8.1 m full)	1998	ULE fused silica	Thin meniscus – active	f/1.8	RC	alt-az	[3.8] [3.54] § 3.2.3
Gemini South (U.S., U.K., Canada, Chile, Argentina, Brazil)	8.0 m equivalent (8.1 m full)	2000	ULE fused silica	Thin meniscus – active	f/1.8	RC	alt-az	[3.8] § 3.2.3
LBT (Large Binocular Telescope) (U.S., Italy)	<i>Two telescopes:</i> Each 8.4 m	2001–2003	BSC	Lightweighted (honeycomb) – active	f/1.142	Classical Cassegrain and Gregory	MMT-type alt-az	[3.47] § 3.2.2

term "large" here implies a diameter greater than the 5 m of the Palomar telescope. However, a few notable new technology telescopes of the  $3\frac{1}{2}$ –4 m class have been included, again without claim to completeness. I have limited the list to those projects which, to my knowledge, are finished, under construction or officially approved. Many other interesting projects are under study, some of which have been discussed in this chapter.

A recent book by Moore [3.260] gives an excellent list of major telescopes, both historical and functioning, as well as a list of large projects in preparation. This book's most valuable feature, however, is the inclusion of 64 colour plates of excellent quality showing the major telescopes and observatories.

## 4. Image quality specification and optical efficiency criteria

### 4.1 Classical specification criteria: geometrical angular or wavefront aberration

Atmospheric seeing and “total” telescope seeing have been estimated in terms of *angular aberration*, normally arcsec for historical reasons, virtually since the invention of the telescope. For visual observation, this was closely linked to the quest for angular resolution on objects in the solar system. That the angular resolution could be limited by atmospheric seeing as well as telescope errors was well-known long before the diffraction limit was formulated by Airy in 1835 [4.1] (see § 3.10.3 of RTO I), mainly as a result of smaller refractors of excellent quality due to Fraunhofer and the development of the wave theory of light by Young, Fresnel and Fraunhofer. This led in 1879 to the first formulation by Rayleigh [4.2] of optical tolerances as a *phase error* of the wavefront (see § 3.10.5 of RTO I), leading to the rough general rule that a system was still effectively diffraction limited provided the wavefront error did not exceed  $\lambda/4$  (*Rayleigh limit*). For small telescopes, for which the diameter of the Airy disk  $d_{Ad}$  is given according to Eq. (3.447) of RTO I by

$$d_{Ad} = 2.44(\lambda/D)(206\,265) \text{ arcsec} , \quad (4.1)$$

the diffraction limit defined by the Rayleigh limit was a reasonable specification for the required manufacturing quality. Such a specification remained reasonable as long as the aperture  $D$  of the telescope was not so large that  $d_{Ad}$  was no longer a significant fraction of the atmospheric seeing. Visual observation permitted the instantaneous use of excellent seeing so that diffraction limited quality up to  $D \sim 75$  cm could still occur on exceptional occasions ( $d_{Ad} = 0.335$  arcsec with  $\lambda = 500$  nm). However, the largest reflectors had exceeded this diameter since W. Herschel in 1789 and the largest refractors exceeded it by 1888. In such instruments, secondary spectrum anyway exceeded the Rayleigh limit for more than a small spectral range.

The general introduction of photography meant that the *integrated* atmospheric seeing over an extended period, not the instantaneous best seeing, became the essential criterion. This was only rarely as low as 1 arcsec. Until the Palomar 5 m telescope, an optical quality “specification” hardly existed: the effective quality was a result of the optician’s skill in figuring, his test procedures, the thermal conditions of the blank material (with its relatively high

expansion coefficient) and the supports and structural stability (centering). If the resulting point spread function (PSF) of a star image was comparable with the best integrated atmospheric seeing PSF,  $d_{at}$ , for a significant fraction of the observing time, the telescope was certainly a success.

In 1902 Strehl [4.3] introduced the general optical quality criterion known as the *Strehl Intensity Ratio* or *Strehl criterion* (see § 3.10.5 of RTO I), whereby the reduction due to aberrations in the intensity of the central diffraction peak should not exceed 20 %. The Strehl criterion was as arbitrary as a global limit as the Rayleigh  $\lambda/4$  limit and the theoretical rationalisation was given by Maréchal [4.4] in 1947. As shown in § 3.10.5 of RTO I, this leads to the very important relation of Eq. (3.465) in RTO I which we will repeat here in the form

$$S_{SIR} \equiv \frac{I(Q)}{I_0} = 1 - \left( \frac{2\pi}{\lambda} \right)^2 W_{rms}^2 , \quad (4.2)$$

where  $S_{SIR}$  is the Strehl Intensity Ratio. Maréchal gave the relationship between the individual, or grouped, aberration coefficients and their  $W_{rms}^2$  values, thereby deriving the values of the coefficients for the standard criterion of  $S_{SIR} = 0.80$  (see Table 3.26 of RTO I). This work established a systematic physical basis for the effect of *small* aberrations on the diffraction image, “small” implying that the essential structure of the central diffraction peak with the first dark diffraction ring is retained. For larger aberrations giving major reduction in  $S_{SIR} \sim < 0.5$ , this is no longer the case and the single information parameter  $S_{SIR}$  is no longer adequate to describe the effect of the aberration on the image. From Eq. (4.2), this is equivalent to saying that, for *small* aberrations,  $W_{rms}$  provides a necessary and sufficient criterion of the physical effect on the image, i.e. the precise nature of the wavefront aberration is unimportant. For larger aberrations, the effect depends on the nature of the aberrations composing the wavefront error  $W$ : its physical effect on the image requires a more sophisticated approach such as the Fourier treatment by Duffieux [4.5] in 1945 of the Optical Transfer Function (OTF) – see § 3.10.7 of RTO I. The effect of specific aberrations on the real part of this function, the Modulation Transfer Function (MTF), was largely worked out in the 1950s by Hopkins [4.6] and his collaborators.

For the “Bowen class” of telescopes (see Chap. 5 of RTO I) developed after 1950, there were therefore *two* basic approaches available for defining optical specifications: the classical approach of angular aberration of the PSF in comparison with atmospheric seeing; or the wavefront aberration approach, above all for smaller aberrations, as  $W_{rms}$  giving  $S_{SIR}$ . The more general MTF approach only became possible later, about 1970, when computer programs for the calculations became available.

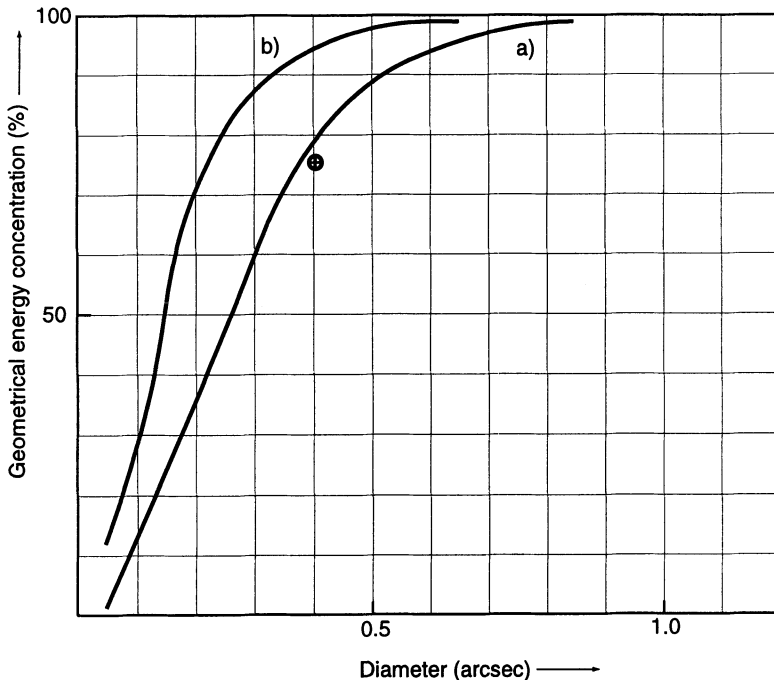
A strong argument for using the simple *angular aberration* concept for specifications was that, until recently, too little was known about atmospheric seeing for it to be handled in any other way than as an angular aberration, normally as the Full Width Half Maximum (FWHM) of its PSF.

Since the large telescopes after the Palomar 5 m were all > ca. 3 m, the diameter of the Airy disk  $d_{Ad}$  from (4.1) for  $\lambda = 500 \text{ nm}$  was  $< 0.10 \text{ arcsec}$ . It was therefore not unreasonable at that time to ignore diffraction as a negligible effect compared with the other errors specified to produce a PSF comparable with the best atmospheric seeing expected, then accepted to be  $(d_{at})_{FWHM} \geq 0.5 \text{ arcsec}$  for the best sites. Ignoring diffraction means that the calculation of the PSF is performed by the laws of *geometrical optics* alone and is greatly simplified: effectively, all that is required is the calculation of *spot diagrams* (see § 3.2.5.3 of RTO I) using a sufficient number of rays over the entrance pupil that the ray density (assuming equal light intensity per ray if a square mesh rectangular sampling grid is used) gives the intensity function of the geometrical PSF. Using the equations of Nijboer (see § 3.3.1 of RTO I), an inverse Fourier transform gives the wavefront aberration over the pupil. Conversely, if the wavefront error is measured by an interferometer, the Fourier transform gives the spot-diagram for any chosen focus and, by a count of ray intersections with this plane, the *encircled energy percentages* corresponding to Fig. 3.104 of RTO I for the case of pure diffraction. Such functions can be measured in the finished telescope by one of the techniques described in Chap. 2, giving a function which can be compared with the specification. A typical case was shown in Fig. 2.22. Another example, the ESO 3.6 m telescope [4.7], is shown in Fig. 4.1. In the case of this telescope, the geometrical encircled energy was specified for one point only, i.e. for 75 % encircled energy:

$$\begin{aligned} \text{Prime focus (assuming a perfect corrector): } & d_{75} \leq 0.40 \text{ arcsec} \\ \text{Cassegrain focus: } & d_{75} \leq 0.50 \text{ arcsec} \end{aligned} \quad \{ \quad (4.3)$$

Sometimes, the specification is given for two percentile values, as in Fig. 2.22 with 70 % and 90 %. The slope of the function falls off rapidly towards 100 %, since all the “wings” of the PSF induced by high spatial frequency polishing errors as well as diffraction effects are then included. The form of the function will reflect the spatial frequency spectrum of figuring errors left by the manufacturer. For the optical quality specifications of the Bowen-type telescopes, the evidence is that a single specification value, say  $d_{80}$ , identifies the function sufficiently. Other examples are given in the literature of Chap. 2.

The geometrical encircled energy specification of the type shown in (4.3) is still the commonest in use today (1997) and has the great merits of simplicity of form and ease of comprehension, calculation and measurement. For these reasons, it is unlikely to be displaced in the future for many “normal” telescopes, for which the image quality requirements are not pushed to the current technological limits. At the time when the specification of the ESO 3.6 m telescope was fixed (about 1969), the values of (4.3) were considered to be about at the practical limit and the successful manufacture of such telescopes was a great technical achievement. Tighter specifications



- a) Decentering coma only removed
- b) All polynomial terms removed
- ESO-REOSC contract

**Fig. 4.1.** Geometrical energy concentration at best focus measured at the PF of the ESO 3.6 m telescope with Gascoigne plate corrector (near zenith), compared with the specification (from Franz et al. [4.7])

than  $d_{80} \leq 0.30$  arcsec are rare, even today, and difficult to achieve in *passive* telescopes with  $D >$  ca. 2 m.

If the telescope diameter is sufficiently modest that the Airy disk  $d_{Ad}$  becomes more than about a quarter of the  $d_{80}$  geometrical specification, the neglect of diffraction may significantly falsify the real energy distribution. If the geometrical aberrations are near the diffraction limit, the angular aberrations calculated from them will be too pessimistic in that the diffraction core is not much increased but the convolution with the diffraction function of Fig. 3.102 of RTO I will spread energy out for percentiles above  $d_{80}$ . Programs are available today which allow calculation of the encircled energy including diffraction. For *space telescopes*, of course, diffraction limited quality for the minimum wavelength of observation is highly desirable. Hence diffraction must be included, either for the encircled energy or for a specification according to the Strehl criterion or the OTF. A simple geometrical angular aberration specification is *not* suitable in such cases.

Apart from the percentile encircled energy specification, geometrical angular aberrations can also be given as  $d_{FWHM}$  (normal for atmospheric seeing) or as  $d_{rms}$ . Schwesinger [4.8] analysed in 1969 the relative merits of optimizing lateral supports for large primaries following a specification in terms of  $d_{rms}$  compared with one in terms of  $W_{rms}$ . His analysis followed his Fourier modal approach (see § 3.4.3.1). He optimized the radial support for certain cases (including  $D = 5\text{ m}$  and  $7\text{ m}$ ) on the basis of  $d_{rms}$  and  $W_{rms}$  and calculated the corresponding MTF. The MTF function was similar for the lower spatial frequencies but markedly better for the higher spatial frequencies when optimized for  $W_{rms}$ . Schwesinger made a comparison with an estimated MTF of atmospheric seeing, in order to determine the weight to be given to higher spatial frequencies. At that time, the classical work of Kolmogorov and Fried on atmospheric turbulence (see Chap. 5) was not generally known and Schwesinger followed Scheffler [4.9] in assuming a Gaussian distribution. He also assumed a quality of best atmospheric seeing giving an energy concentration of 95 % in 0.2 arcsec diameter, a value which even today, when the expectations of excellent atmospheric seeing are indeed higher than in 1969, would be at or beyond the limits of the best sites. The Fourier transform gave an atmospheric MTF with diffraction limited performance for a 2 m telescope. In current terminology, this corresponded to a Fried parameter  $r_0$  of about 2000 mm, a value that exceeds anything ever recorded. On this basis, Schwesinger concluded that  $W_{rms}$  is a better optimization criterion for support errors than  $d_{rms}$ . This is what one would expect if the Strehl criterion of the errors is fairly near the diffraction limit, as it was for his extreme assumptions on atmospheric seeing.

In addressing this question as to whether  $W_{rms}$  or  $d_{rms}$  is the better criterion for establishing telescope optics specifications, Schwesinger dealt with a matter which is still of central importance. We shall see below that Dierickx comes to opposite conclusions concerning the ESO 8 m VLT, based on the modern theory of atmospheric seeing and a less extreme reference value of atmospheric seeing.

## 4.2 Specifications for modern ground-based telescope projects

The inauguration of the 4.4 m MMT in 1979 (see § 3.2.2) introduced the revolution in modern telescopes with fundamental departures from the classical design principles. The new concepts, together with the spectacular advances in manufacture and test technology (Chap. 1) and in the theory of atmospheric seeing (Chap. 5), enabled further significant advances in the realisable optical quality delivered by the manufacturer. Active optics (§ 3.5) relaxes manufacturing tolerances and automates the optical maintenance. All of this calls for more sophisticated optical specifications than the fixing of a  $d_E$  limit

for the PSF, where  $E$  is some energy percentage  $\sim 80\%$ . Above all, specifications should reflect more closely a global optimization of the parameters affecting the final image.

However, the attractions of the classical  $d_E$  specification are so strong that only the most recent projects depart from it. The *Keck 10 m telescope* (started in 1977) has a systematic error budget [4.10] based entirely on  $d_{80}$ , as given in Table 4.1. It should be noted that the  $d_{80}$  value assumed for the atmosphere (for Mauna Kea (Hawaii), accepted as one of the best, if not *the* best in the world) is 0.95 arcsec, compared with the value  $< 0.2$  arcsec taken by Schwesinger above. The telescope as a whole is allowed  $d_{80} = 0.42$  arcsec, with values 0.34, 0.16 and 0.19 for the primary, secondary and misalignment respectively, whereby the figure of 0.34 arcsec for the primary was not initially achieved because the segment figuring quality averaged 0.28 arcsec even after ion beam correction [4.11] – see § 3.2.1 – instead of the 0.24 specification. Nevertheless, even if the specification were not fully achieved, the Keck telescope would still represent a remarkable technical achievement. The active concept of the Keck was discussed in § 3.5.5.3. While the primary is active, with its internal sensor system with a bandpass up to 2 Hz, the telescope is passive for the position of the secondary (focus and decentering coma). The budget errors for these are severe for a passive telescope but generous compared with those of the ESO active telescopes, the NTT and VLT.

**Table 4.1.** Keck 10 m telescope optical error budget (from Nelson and Mast [4.10])

Item	Image Diameter (arcsec) $d_{80}$		
Atmosphere			0.95
Telescope			0.42
– Primary mirror		0.34	
– segment figuring	0.24		
– segment thermal distortion	0.15		
– segment support	0.10		
– segment alignment – passive	0.12		
– segment alignment – active	0.10		
– Secondary mirror		0.16	
– surface	0.15		
– support	0.05		
– alignment	0.05		
– Misalignment		0.19	
– tracking	0.05		
– defocus	0.15		
– other misalignment	0.10		
<i>Note:</i> For Gaussian errors – $d_{FWHM} = 0.66 d_{80}$			
For atmospheric seeing – $d_{FWHM} = 0.50 d_{80}$			

According to Salmon (quoted in [4.12]), the atmospheric seeing at the 3.6 m CFHT on Mauna Kea is  $< 0.2$  arcsec FWHM for ca. 10% of the time. The figure of  $d_{80} = 0.95$  arcsec for the atmosphere in the error budget of Table 4.1 corresponds to  $d_{FWHM} = 0.48$  arcsec and is relatively generous compared with the modern estimate of best seeing. However, the telescope budget is in good balance with the chosen figure and the segment manufacturing experience indicates that the specified error budget is about at the limit for existing technology with direct segmentation. The error budget of the ESO 8 m VLT telescopes, discussed below, is more severe, being based on a requirement that all telescope errors shall have a relatively small effect (10–15%) on an atmospheric seeing of 0.40 arcsec FWHM. However, it remains to be proved that this can be realised in practice.

The *ESO 3.5 m active NTT*, operating since 1989, was defined optically in 1980–1981, its specification also still being based on the classical  $d_E$  for encircled energy (see § 3.2.4 and § 3.5.2). The optical specification for the manufacturer was based on the active concept and had two elements. For the *whole optical train* ( $M_1$ ,  $M_2$ ,  $M_3$ ) for the Nasmyth focus:

$$\left. \begin{aligned} (d_{80})_{Pas} &\leq 0.40 \text{ arcsec} \\ (d_{80})_{Act} \equiv IQ &\leq 0.15 \text{ arcsec} \end{aligned} \right\} \quad (4.4)$$

The “passive” specification  $(d_{80})_{Pas}$  implied that only the first four terms (constant, tilt, defocus and decentering coma) in the polynomial of Table 3.12 were removed from the test wavefront, whereas the “active” specification  $(d_{80})_{Act}$  implied that four additional terms (third order spherical aberration and astigmatism, triangular and quadratic effects) were *also* removed to give the Intrinsic Quality (IQ). The passive specification was intended to ensure that the active correction remained well within the defined dynamic range of the system and was a relatively cautious value placing somewhat higher demands than those of (4.3) for the classical 3.6 m telescope. Nominally, the manufacturer was well within  $(d_{80})_{Pas}$ ; but the “matching error” revealed in function [4.13] implied that  $(d_{80})_{Pas}$  was nearly 0.6 arcsec from this source alone (§ 3.5.2). Full active correction was still possible for  $Z \leq$  ca.  $65^\circ$ , but the dynamic range of the NTT has thus been exploited close to its limit. This confirms that a double specification is necessary even for active telescopes. Nevertheless, it is  $(d_{80})_{Act} \equiv IQ$  which determines the limit quality of the telescope from the manufacturing point of view. Carl Zeiss achieved an even better result than the specification with  $(d_{80})_{Act} = 0.125$  arcsec.

The limits of the optical quality in the NTT have been analysed by Wilson et al. [4.13] and are given in Table 3.13. The conclusion was that, with optimum operation, the actively controlled terms can be made negligible ( $d_{80} \sim 0.075$  arcsec) and that the practical limits are set by the high frequency errors, above all residues from the local air even under optimum ventilation conditions. The ultimate for all errors apart from external seeing might be  $d_{80}$  somewhat less than 0.20 arcsec, including measuring noise,

or  $(d_{FWHM})_{Tel} < 0.14 \text{ arcsec}$ . This should be compared with best atmospheric seeing measures on Mauna Kea or Paranal with  $(d_{FWHM})_{Atm} < 0.20 \text{ arcsec}$ . For such superb seeing the equivalent best value for the telescope of 0.14 arcsec for  $(d_{FWHM})_{Tel}$  is not really good enough. This means that a specification for  $(d_{80})_{Act} \equiv IQ < 0.10 \text{ arcsec}$  would be justified if the local air conditions can be further improved. It is hoped that improved thermal control and a fully automatic correction cycle can achieve this improvement in local air conditions [4.12]. The performance without such a cycle and where the third level of active control (§ 3.5.2) was often not operating, is shown in Fig. 3.67 and Table 3.14.

The above conclusions for the NTT were based on the classical procedure of statistical addition of  $d_{80}$  values for different sources, which is only a crude approximation to a true convolution procedure for error sources which are by no means strictly statistical in their nature. We believe that a more modern approach with more sophisticated criteria, as attempted by Schwesinger [4.8] above or applied to the ESO VLT – see below – may well indicate that the simple treatment of the NTT above leads to conclusions which may be too pessimistic. But a change from the current evaluation system with  $d_{80}$  can only be meaningful in the NTT once the automatic correction cycle and thermal control are fully operational.

In § 4.1 above, it was mentioned that the PSF can today readily be calculated *including the effect of diffraction*. This raises the question whether the extension of the geometrical angular aberration concept  $d_E$  to include diffraction is the most useful way of profiting from the power of modern computers. This question was addressed by Brown [4.14] on the basis of great experience in testing large telescope optics to meet classical specifications based on the geometrical  $d_E$ . Brown dealt first with the well-known problems of a specification based on  $d_E$  arising from the finite sampling in the pupil of the test system and the spatial frequency of the error. The higher the spatial frequency, the higher will be the equivalent  $d_E$  for a given amplitude. But, beyond a certain high spatial frequency, an averaging effect over the test sub-aperture will take place, giving falsified results for the maximum angular aberrations. Brown suggested that a true prediction of performance could only be obtained by taking account of the necessary sampling and combining the effects of atmospheric seeing, manufacturing errors and diffraction. One way is to calculate the diffraction PSF of the telescope and convolute it with the PSF of the atmosphere. However, the combination is easier in Fourier space using the MTF, for which the final result is simply the product of the individual MTFs (see § 3.10.7 of RTO I). The inverse Fourier transform then gives the final combined PSF, but Brown considered it preferable to use the simpler approach that the *Central Intensity Ratio*, in the Strehl sense, of the final image is directly available from the normalized MTF from

$$\text{CIR} = \int_0^{s_m} \int_0^{t_m} (\text{MTF}) \, ds \, dt , \quad (4.5)$$

a relation referred to in § 3.10.7 of RTO I and given explicitly by Wetherell [4.15]. In fact, Brown gives the CIR as the integral under the *square* of the MTF; which is not correct if the usual definition of the MTF as an *intensity* function is taken. This error was corrected by Brown in a later paper [4.16].

Brown derived the degradation of the CIR, as a function of telescope size, due to “average” and “good” atmospheric seeing for a perfect telescope and for a telescope with a typical quality specification at the time (1979). This is shown in Fig. 4.2. Brown suggested that a specification in terms of the CIR would lead to a much more predictable performance. He also felt that the typical quality requirement of the time was, from Fig. 4.2, fully adequate for the smaller apertures but produced too big a loss of CIR compared with the perfect diffraction limited telescope for  $D \sim 4$  m. This was probably true in view of the many other sources of error (see Table 3.11) apart from the two he considered: atmospheric seeing and manufacturing errors. His conviction that the optical performance in operation could be more predictable was certainly too optimistic in view of the normal degradation in image quality of passive telescopes arising from decentering, support errors and local air seeing.

Brown’s suggestion of the use of the Central Intensity Ratio, based on the Strehl criterion but generalised to include atmospheric seeing, as an optical quality criterion for ground-based telescopes was a major advance. However, it made little impact at the time.

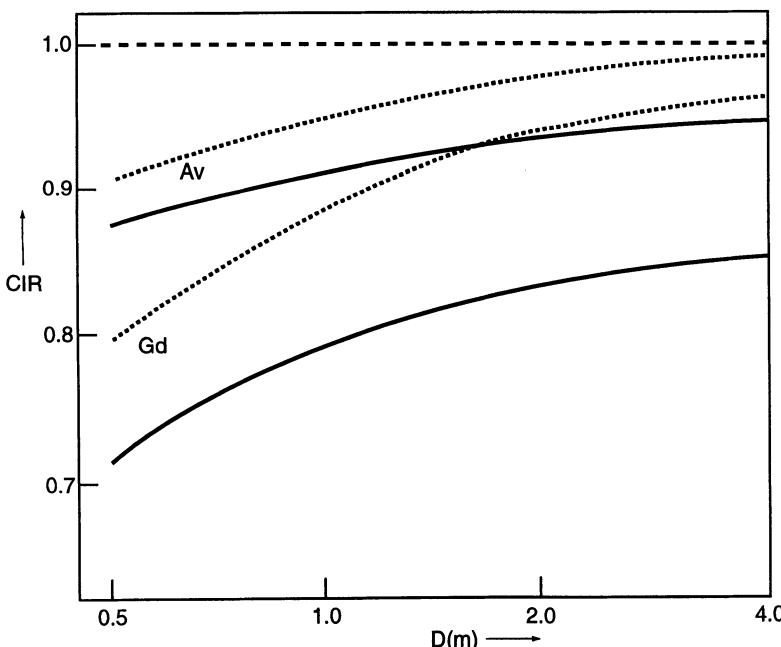


**Fig. 4.2.** The Central Intensity Ratio (CIR), calculated for “average” and “good” atmospheric seeing for a perfect telescope (*dashed curves*) and for a telescope with a typical specification for 1979 (*full curves*) (after Brown [4.14])

In the investigations for the *ESO 8 m VLT*, Dierickx [4.17] independently proposed the CIR as the general criterion of image quality, but now taking account, in a general error budget, of all possible sources of error.

Dierickx first derives the MTF for an annular aperture (i.e. the normal case of a telescope with a central obstruction) *in a vacuum*,  $M_v(\nu)$ , from the autocorrelation integral (see § 3.10.7 of RTO I), where  $\nu$  (in the notation of Dierickx) is the normalized spatial frequency. Using the normal procedure of approximating the MTF by a Taylor expansion [4.18], he derives the result, assuming *at this stage only axisymmetrical aberrations*,

$$M_v(\nu) \simeq 1 - \frac{4\nu}{\pi(1-\varepsilon)} - 2\sigma^2\nu^2 + \frac{2\nu^3}{3\pi} \left( 8\delta^2 + \frac{1}{\varepsilon(1-\varepsilon)} \right), \quad (4.6)$$

in which  $\varepsilon$  is the linear obstruction ratio and the quantities  $\sigma$  and  $\delta$  are defined by

$$\sigma^2 = \left( \frac{k^2}{1-\varepsilon^2} \right) \int_{\varepsilon}^1 \left( \frac{dW}{d\rho} \right)^2 \rho d\rho \quad (4.7)$$

and

$$\delta^2 = \left( \frac{k^2}{1-\varepsilon^2} \right) \left[ \left( \frac{dW}{d\rho} \right)_{\rho=1}^2 + \varepsilon \left( \frac{dW}{d\rho} \right)_{\rho=\varepsilon}^2 \right], \quad (4.8)$$

where  $k = 2\pi/\lambda$ ,  $W$  is the wavefront aberration and  $\rho$  the normalized (dimensionless) aperture radius. The quantity  $\sigma$  is thus the normalized rms slope error of the wavefront aberration and  $\delta$  is a function of the slope errors at the outer and inner edges of the pupil. The linear term in Eq. (4.6) gives 1% error (accuracy) up to  $\nu \sim 0.3$  (bandpass limit normalized to 1) if  $W = \sigma = \delta = 0$  and  $\varepsilon = 0$ . The accuracy including the third term is < 1% up to  $\nu \sim 0.6$ .

Dierickx now introduces the MTF of the atmosphere,  $M_a(\nu)$ , as (see Chap. 5)

$$M_a(\nu) = \exp \left[ -c(\zeta\nu)^{5/3} \right], \quad (4.9)$$

in which  $\zeta = D/r_0$  and  $c$  is a constant.  $D$  is the telescope diameter and  $r_0$  the Fried parameter or time-averaged atmospheric coherence length.

The multiplicative combination of  $M_v(\nu)$  and  $M_a(\nu)$  then gives the MTF for both atmospheric and axisymmetrical telescope errors

$$M(\nu) \simeq \left[ 1 - \frac{4\nu}{\pi(1-\varepsilon)} - 2\sigma^2\nu^2 + \frac{2\nu^3}{3\pi} \left( 8\delta^2 + \frac{1}{\varepsilon(1-\varepsilon)} \right) \right] \times \exp \left[ -c(\zeta\nu)^{5/3} \right] \quad (4.10)$$

Figure 4.3 shows a typical example of the “long-exposure” (i.e. time-averaged for atmospheric seeing) MTF according to Eq. (4.10) with  $W$  corresponding to a third order spherical aberration (Zernike polynomial) of 500 nm peak-to-valley and an atmospheric turbulence defined by  $\zeta = 10, 20$  and  $30$ . For

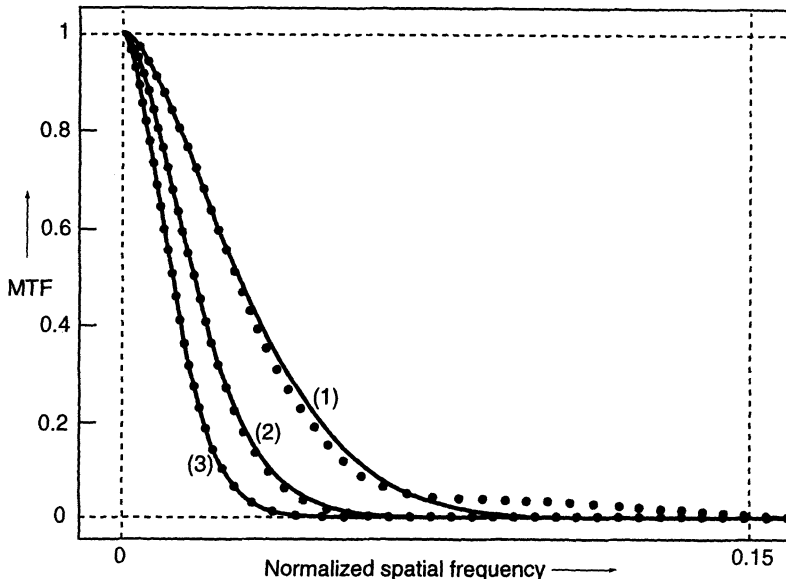


**Fig. 4.3.** Long-exposure MTF with a third order spherical aberration of 500 nm ptv (Zernike) combined with atmospheric seeing defined by (1)  $\zeta = 10$ , (2)  $\zeta = 20$ , (3)  $\zeta = 30$  (from Dierickx [4.17])

$D = 4$  m, these  $\zeta$  values correspond to atmospheric seeing 0.26, 0.51 and 0.76 arcsec FWHM respectively. These values assume there is no central obstruction, i.e.  $\varepsilon = 0$ . In this case, the diameter of the geometrical image would be about 0.32 arcsec rms. The solid lines in Fig. 4.3 give the MTF to high accuracy computed by means of two successive Fourier transforms of the pupil complex transmittance  $\tau$  with  $\lambda = 500$  nm. The maximum discrepancy with the approximation of Eq. (4.10) is about 0.026 in the absolute MTF for the case  $\zeta = 10$  and  $< 0.01$  for  $\zeta = 20$ .

Equation (4.10) shows that the effect on the MTF of any axisymmetrical aberration, of whatever source apart from the atmospheric turbulence, is determined by the rms slope of the wavefront (given in normalized form by  $\sigma$ ) and the wavefront slopes at the edges of the pupil (given in normalized form by  $\delta$ ). Equation (4.10) gives, in general, good accuracy when the rms diameter of the geometrical image is smaller than half the atmospheric seeing angle. If this is not the case, the telescope is anyway optically not in the top class, unless the atmospheric seeing is exceptionally good (see the results for the NTT above).

The normalized intensity distribution  $\psi(r)$  of the “long-exposure” PSF is proportional to the Fourier transform of the MTF. For an axisymmetric PSF, the Fourier transform can be replaced by the Hankel transform. Dierickx then derives the “long-exposure” PSF as

$$\psi(r) = \frac{1}{\zeta^2} \left[ \psi_0(r) - \frac{1}{\zeta} \psi_1(r) - \frac{1}{\zeta^2} \psi_2(r) \right], \quad (4.11)$$

in which

$$\psi_0(r) = \sum_{j=0}^{\infty} d'_j \left( \frac{r}{\zeta} \right)^{2j} \quad (4.12)$$

represents the pure normalized PSF of the atmosphere,

$$\psi_1(r) = \left( \frac{1}{1-\varepsilon} \right) \sum_{j=0}^{\infty} \left( \frac{4b'_j}{\pi} - \frac{1}{\varepsilon} \frac{2d_j}{3\zeta^2\pi} \right) \left( \frac{r}{\zeta} \right)^{2j} \quad (4.13)$$

represents the perturbation produced by the diffraction at the aperture of the perfect telescope, and

$$\psi_2(r) = \sum_{j=0}^{\infty} \left( 2c'_j \sigma^2 - \frac{16d'_j \delta^2}{3\zeta\pi} \right) \left( \frac{r}{\zeta} \right)^{2j} \quad (4.14)$$

represents the perturbation produced by the aberrations  $W$  of the telescope. Equation (4.13) becomes singular if  $\varepsilon = 0$ , since the calculation assumes  $\varepsilon \geq \nu$ , because otherwise the obstruction circles in the autocorrelation integral leading to (4.6) no longer overlap: if  $\varepsilon = 0$  the quantity  $1/\varepsilon$  in (4.13) must be set equal to 1. The quantity  $r/\zeta$  is the radius in the image plane and is expressed in units of  $\lambda/r_0$ : these are the natural units of “seeing”, equivalent to the natural units of  $\lambda/D$  for diffraction. The quantities  $a'_j$ ,  $b'_j$ ,  $c'_j$ ,  $d'_j$  are dimensionless coefficients. Dierickx gives as an example the PSF profile according to Eq. (4.11) for the case of  $\zeta = 30$  and  $\lambda = 500$  nm together with spherical aberration of 500 nm and 1000 nm peak-to-valley (Seidel), with  $\varepsilon = 0$ . For a 4 m telescope the atmospheric seeing is 0.76 arcsec FWHM. The Strehl intensities are, of course, totally dominated by the atmospheric seeing and are about 0.0011, 0.00105 and 0.0009 respectively for the three cases of a perfect telescope and the two given amounts of spherical aberration respectively.

From Eq. (4.11), the  $d_{FWHM}$  or  $d_{80}$  values can be deduced. In seeing units  $\lambda/r_0$ , Dierickx gives for the case of  $\psi_0(r)$  for the atmosphere alone

$$\begin{aligned} (d_{FWHM})_a &= 0.976 \lambda/r_0 \\ (d_{80})_a &= 1.848 \lambda/r_0 \end{aligned}, \quad (4.15)$$

giving a ratio  $(d_{80}/d_{FWHM})_a \simeq 1.9$ . A Gaussian distribution gives a ratio  $\simeq 1.5$ , showing that Gaussian fitting, as used to be done [4.8] [4.9] before the modern theory was developed (Chap. 5), is not appropriate.

Dierickx compares the effects of the given quantities of spherical aberration, in the presence of atmospheric turbulence defined by  $\zeta = 30$ , on the encircled energy  $d_{80}$  and  $d_{FWHM}$  with that on the *equivalent* Strehl ratio. He concludes, exactly as did Brown [4.14] above, that the equivalent Strehl ratio is much preferable as a quality criterion.

The Strehl ratio  $\Psi$  is the normalized measure for the intensity at the center of the image. Equations (4.11) and (4.12) yield

$$\Psi = \frac{1}{\zeta^2} \left( 1 - \frac{1}{\zeta} \Psi_1 - \frac{1}{\zeta^2} \Psi_2 \right) \quad (4.16)$$

for the *Strehl ratio  $\Psi$  of the total system of atmosphere, telescope and site*, assuming that  $D \gg r_0$  and the angular errors of the telescope and site are appreciably smaller (not more than about half) than the atmospheric seeing. The other quantities to be defined are:

$$\Psi_1 = \left( \frac{1}{1 - \varepsilon} \right) \left( \frac{4b'_0}{\pi} - \frac{2d'_0}{3\zeta^2 \pi \varepsilon} \right) \quad (4.17)$$

$$\Psi_2 = 2c'_0 \sigma^2 - \frac{16d'_0}{3\zeta \pi} \delta^2 \quad (4.18)$$

and

$$\Psi_0 = \frac{1}{\zeta^2} \left( 1 - \frac{1}{\zeta} \Psi_1 \right) \quad (4.19)$$

$\Psi_0$  is the Strehl ratio of the equivalent perfect telescope, limited only by diffraction, *in the same atmosphere*.  $\Psi_1$  and  $\Psi_2$  are the effects of diffraction and aberration respectively in the actual telescope *in the same atmosphere*. If diffraction is negligible for a large telescope compared with atmospheric seeing, then  $\frac{1}{\zeta} \Psi_1 \ll 1$  in (4.19) and the Strehl ratio of a ground-based, diffraction-limited telescope is approximately  $1/\zeta^2$ . This corresponds to the very low value of 0.0011 quoted above for  $\zeta = 30$ .

We can now define the *proposed optical quality parameter  $I_0 \equiv \text{CIR}$  (Central Intensity Ratio)* as

$$\text{CIR} \equiv I_0 = \frac{\Psi}{\Psi_0} = \frac{\Psi}{\frac{1}{\zeta^2} \left( 1 - \frac{1}{\zeta} \Psi_1 \right)} \quad (4.20)$$

The CIR is more practical than the Strehl ratio of Eq. (4.16) since the latter yields very small values in practice, whereas the CIR is normalized to unity for the performance of an aberration-free, diffraction-limited telescope. From (4.16), (4.17) and (4.18), we can write (4.20) as

$$I_0 = 1 - \frac{2}{\zeta^2} \left[ \frac{c'_0 \sigma^2 - \frac{8d'_0}{3\zeta \pi} \delta^2}{1 - \frac{1}{\zeta(1-\varepsilon)} \left( \frac{4b'_0}{\pi} - \frac{2d'_0}{3\zeta^2 \pi \varepsilon} \right)} \right] \quad (4.21)$$

In practice, for most cases of large telescopes, we have  $\zeta \geq 20$  and  $\varepsilon > 0.1$ , so (4.21) can be approximated by

$$I_0 \simeq 1 - \frac{2}{\zeta^2} \left[ c'_0 \sigma^2 - \frac{8d'_0}{3\zeta \pi} \delta^2 \right] \left[ 1 + \frac{4b'_0}{\zeta \pi (1 - \varepsilon)} \right] \quad (4.22)$$

For the definition of the dimensionless coefficients  $a'_0$ ,  $b'_0$ ,  $c'_0$ ,  $d'_0$ , the reader is referred to Dierickx' paper [4.17]. The values are given as  $a'_0 = 1$ ,  $b'_0 =$

$0.483\,197$ ,  $c'_0 = 0.306\,969$ ,  $d'_0 = 0.235\,430$ . Equation (4.22) shows that the loss of central intensity  $\Delta I_0$  is approximately proportional to  $1/\zeta^2$  and to  $\sigma^2$ , the square of the rms wavefront slope error. Since the radius of the seeing image is  $r/\zeta$  in  $\lambda/r_0$  units in Eqs. (4.12), (4.13) and (4.14), it follows that the loss  $\Delta I_0$  will also be proportional to  $d_a^2$ , where  $d_a$  is the angular atmospheric seeing. The CIR expresses the *weight* of the telescope aberrations relative to the atmospheric seeing: with poor seeing, the weight of the aberrations becomes less and the CIR improves. Precisely this effect was shown in Fig. 4.2 as presented by Brown [4.14].

It is interesting and important that Dierickx arrives at precisely the opposite conclusion, with regard to the essential parameter measuring the physical effect of the aberrations  $W$ , from that of Schwesinger [4.8] discussed in § 4.1 above. Dierickx concludes that  $\sigma \equiv d_{rms}$ , the rms geometrical angular aberration, is determinant, whereas Schwesinger concluded that  $W_{rms}$  was better. Schwesinger did not have the modern theory of atmospheric seeing and assumed a reference value of  $d_a$  which was extremely severe even by present standards. He therefore gave more weight to higher spatial frequencies. Dierickx' analysis is based on the modern theory of Fried and puts more weight on the lower spatial frequencies. This seems closer to reality for the current

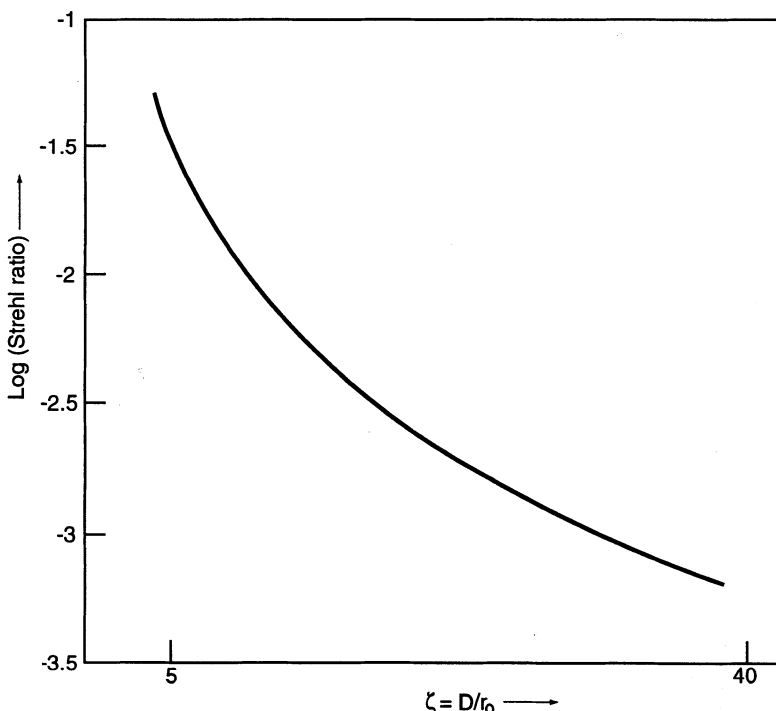
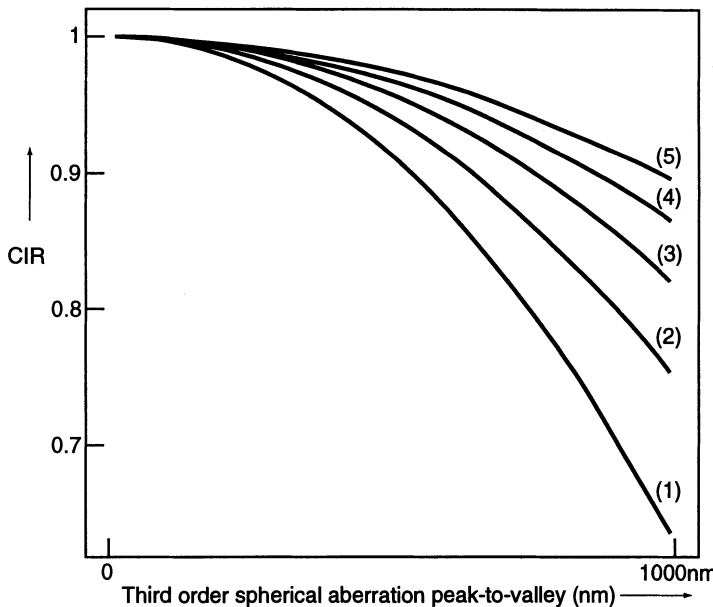


Fig. 4.4. Absolute Strehl ratio of a perfect telescope. The wavelength  $\lambda = 500$  nm and  $\varepsilon = 0$ . (From Dierickx [4.17])



**Fig. 4.5.** Central Intensity Ratio (CIR) against peak-to-valley third order spherical aberration (Seidel) for  $\lambda = 500 \text{ nm}$  and  $\zeta$  equal to (1) 20, (2) 25, (3) 30, (4) 35, (5) 40 (from Dierickx [4.17])

situation, since the absolute Strehl ratios are always very low in practice. This is shown for a perfect telescope in Fig. 4.4. Even for  $\zeta = 5$ , a value for a 4 m telescope giving  $r_0 = 0.8 \text{ m}$ , the Strehl ratio of a perfect telescope is only about 0.03. Dierickx gives an example of the effect on the CIR of varying amounts of third order spherical aberration, for various values of  $\zeta$  (Fig. 4.5).

Dierickx also derives a relation giving the effect of *image motion* on  $I_0$ . Let  $\eta$  be the rms image motion in diffraction (i.e.  $\lambda/D$ ) units. Then, using the MTF for random image motion given by Mahajan [4.19], he derives the approximate relation

$$I_0 \simeq 1 - \frac{2\pi^2 c'_0}{\zeta^2} \eta^2 \left[ 1 + \frac{4b'_0}{\zeta \pi (1 - \varepsilon)} \right] \quad (4.23)$$

Dierickx shows that, for relatively good seeing and a large telescope with  $\zeta = 20$ , an rms image motion of only about 0.12 arcsec is as damaging as spherical aberration of 1000 nm ptv as shown in curve (1) of Fig. 4.5. This is proof of the extremely tight tolerances on tracking quality to achieve modern telescope optical quality standards.

The theory above was derived by Dierickx for the case of axisymmetrical aberrations for which analytical expressions could be derived. However, the definition of the CIR can be made perfectly general as

$$\text{CIR} \equiv I_0 = \frac{\Psi}{\Psi_0}, \quad (4.24)$$

in which the Strehl ratio  $\Psi$  includes all sources of error: atmosphere, local air and telescope errors.  $\Psi_0$  is again the Strehl ratio of the perfect telescope *in the same atmosphere* but excluding all aberration effects occurring close to and within the telescope. Equation (4.24) is formally the same as (4.20) but, in the general case of (4.24), the function  $\Psi$  must be calculated *numerically*. However, numerical simulations confirm that the key geometrical parameter is still  $\sigma$ , the rms slope error of the wavefront. If the diffraction effect is negligible, Eq. (4.24) can still be represented approximately by

$$I_0 \simeq \zeta^2 \Psi , \quad (4.25)$$

provided that  $\zeta$  is sufficiently large ( $\zeta \geq 20$ ). In general, the numerical procedure preferred is the one suggested by Brown – see Eq. (4.5). The wavefront error is determined numerically over a square raster of sampling points, as for a spot-diagram calculation or for Shack-Hartmann measures, and the two-dimensional Fourier transform gives the MTF. This is combined with the atmospheric MTF as in (4.10), except that the first square bracket term has been derived numerically rather than analytically, and the integral under the resulting function gives  $\Psi$ .

Since the ESO 8 m VLT unit telescopes have the same *active optics* concept as the 3.5 m NTT, the optical quality specification must be defined, together with the error budget, to take account of *all* the sources of error in the image of the functioning telescope, be this from manufacture, supports, adjustment, operation and maintenance, including tracking. In other words, all the error sources of Table 3.11 must be taken into account.

The VLT optical error budget had still not been fully finalised in November 1992, but its essential form had already been given in detail by Dierickx [4.20]. The budget is based on the goal:

$$\Delta \text{CIR} \leq 0.2 \quad \text{with } r_0 = 250 \text{ mm} , \quad \lambda = 500 \text{ nm} \quad (4.26)$$

A value of  $r_0 = 250$  mm corresponds to an atmospheric seeing of about 0.40 arcsec FWHM at  $\lambda = 500$  nm. With the three parameters  $\text{CIR} = 0.8$ ,  $r_0 = 250$  mm,  $\lambda = 500$  nm, the resulting rms diameter  $d_{rms}$  of the geometrical image from all error sources apart from atmospheric seeing and diffraction will be about 0.2 arcsec. The FWHM of 0.40 arcsec of the pure atmospheric seeing would be degraded to about 0.44 to 0.46 arcsec, about 10–15%; the  $d_{80}$  from 0.74 arcsec to 0.78 to 0.81 arcsec, about 5–10%.

From Eq. (4.22), within a reasonable approximation if  $\zeta \geq 20$  and the angular aberrations are appreciably smaller than the atmospheric seeing, we have

$$\text{CIR} \equiv I_0 \sim 1 - 2c'_0 \left( \frac{\sigma}{\zeta} \right)^2 \quad (4.27)$$

It follows, since  $(d_{FWHM})_a \propto \zeta$ , that the approximation

$$\Delta \text{CIR} \propto \left( \frac{\sigma}{(d_{FWHM})_a} \right)^2 \quad (4.28)$$

is also valid – see also (4.15). For a fixed aberration, then,  $\Delta\text{CIR}$  diminishes roughly as  $1/(d_{FWHM})_a^2$  as the atmospheric seeing deteriorates. For the parameters fixed by the goal defined above, the CIR thus increases from the defined 0.80 for  $(d_{FWHM})_a = 0.40$  arcsec to 0.975 for 1.2 arcsec.

The “Error Tree” for the VLT [4.20] [4.12], giving the basic groups of image errors, is shown in Fig. 4.6. The quasi-dc factors embrace all the error sources which fall within the normal active optics bandpass A of Fig. 3.62. The remaining error sources, wind and local air, involve bandpass B as well as A. As we saw in Chap. 3, these error sources are those about which scientific information has only recently become available, so that error budgeting is most difficult for these. The “Error Tree” leads to the Optical Error Budget [4.20]. Fig. 4.7 gives a *provisional* form of this budget and shows clearly the many factors which must be considered in the total image quality chain implicit in Table 3.11 for an active telescope. It is clearly an immense advantage to have a quality criterion which allows simple combination of individual errors. From Eq. (4.27) the individual, independent contributions to  $\Delta\text{CIR}$  can be added linearly according to the rule

$$1 - \text{CIR} = \sum_{k=1}^N (1 - \text{CIR}_k) \quad (4.29)$$

The budget of Fig. 4.7 applies to the on-axis image and zenith angles  $\leq 70^\circ$ .

Dierickx has also considered the problem [4.21] of directly measuring the CIR in practice. Essentially, the problem reduces to a calibrated measurement

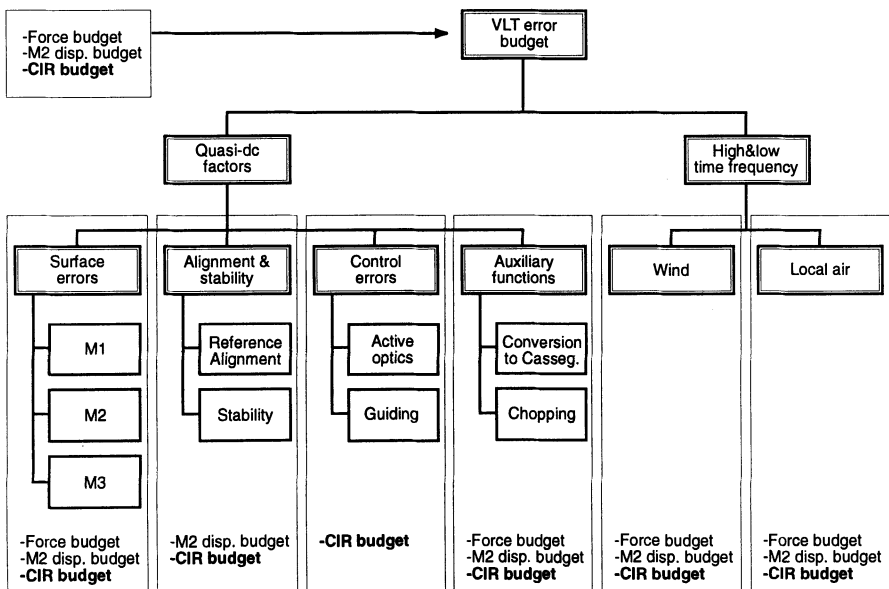


**Fig. 4.6.** “Error Tree” for the ESO 8 m VLT telescopes (from Dierickx [4.20] or Wilson et al. [4.12])

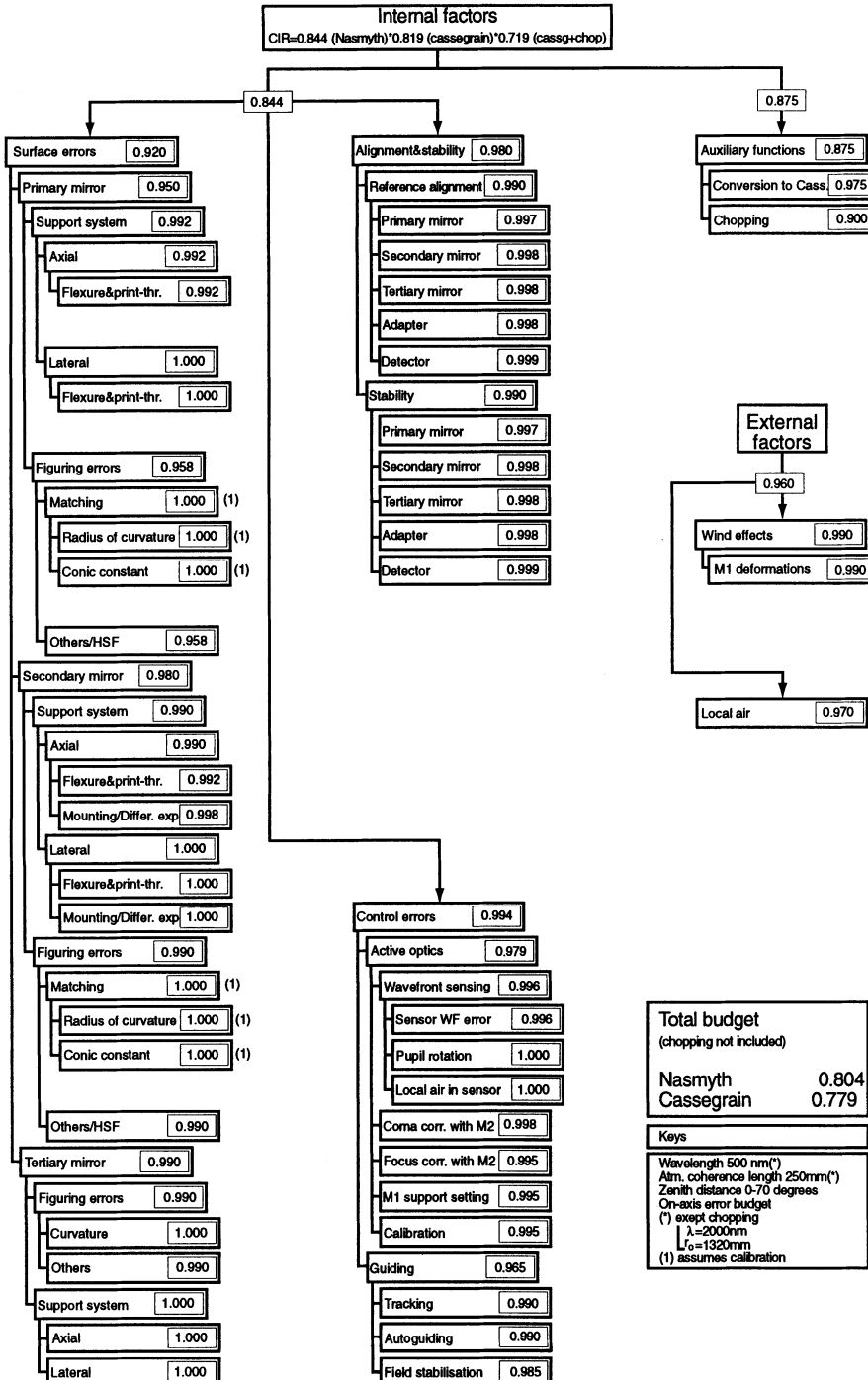


Fig. 4.7. Overall Optical Error Budget for the ESO 8 m VLT unit telescopes (from Dierickx [4.20])

for a known error. He suggests a fixed known amount of *defocus* error which gives a calculable reduction in the CIR. The method assumes that all other error factors are constant over the calibration measurement. This may be difficult with atmospheric seeing. The measurement can still be done with varying seeing if the *ratio* of the seeing values (not their absolute values) is accurately known.

Since the ESO VLT was the most advanced of the new 8 m class projects, its error budget analysis was probably the most detailed and advanced in 1992. However, the Japanese *Subaru* 8 m project was also advancing well and diffraction theory was applied to the performance evaluation [4.22]. The essential elements of the Optical Error Budget are given in the Subaru brochure [4.23], the criterion being the classical  $d_{FWHM}$ . Table 4.2 gives the budget items quoted. The overall optical budget error is

$$d_{FWHM} \leq 0.23 \text{ arcsec}$$

corresponding to (see (4.15) et seq.)

$$d_{80} \leq 0.345 \text{ arcsec},$$

on the assumption of statistically independent errors.

**Table 4.2.** Optical Error Budget for the Japanese 8 m Subaru project (after Subaru Project Office [4.23])

Item	Image Diameter $d_{FWHM}$ (arcsec)		
<b>Primary mirror</b>		0.10	
– diffraction ( $\lambda = 500 \text{ nm}$ )	0.013		
– figuring (higher order residuals)	0.07		
– active support system	0.07		
– Shack-Hartmann measurement	0.02		
<b>Optics overall</b>		0.11	
<b>Tracking</b>		0.12	
– mechanical settings	0.017		
– control loop error	0.060		
– auto-guider	0.033		
– wind load ( $7 \text{ ms}^{-1}$ )	0.050		
<b>Local seeing</b>		0.12	
<b>Miscellaneous</b>		0.11	
<b>Overall error</b>			0.23

### 4.3 Optical efficiency criteria

Virtually throughout its entire history, the aim in telescope development has been to make the aperture bigger, as big as technically possible at the time, on the implicit assumption that “bigger is better”. This simple concept is out-of-date.

Already before the introduction of photography, the efficiency of telescopes had been carefully analysed for visual use, above all because the larger the aperture, the larger the magnification required to get the full exit beam into the eye (see Chaps. 1 and 2 of RTO I). In a classic paper, W. Herschel [4.24] established a formula for the *penetrating power* into space by telescopes. In our notation, this was

$$\text{Penetrating power} = \frac{D_t}{D_e} [(1 - \varepsilon^2) \tau_t]^{1/2} , \quad (4.30)$$

$D_t$  and  $D_e$  being the diameters of the telescope and eye pupil respectively,  $\varepsilon$  the linear obstruction ratio and  $\tau_t$  the throughput (transmission) of the total telescope system. The linear dependence on aperture comes from the decrease of brightness of objects with the square of distance so that the penetrating power is proportional to the square root of the light entering the eye. Herschel assumed  $D_e = 0.2$  inch for faint objects and a value of  $\tau_t$  for a 12-inch Newton telescope of 0.429. To satisfy the formula  $m \geq D_t/D_e$ , he required a minimum magnification for his 48-inch reflector of  $m = 240$ . But seeing sometimes limited the usable magnification to no more than 60, so the telescope was stopped down to about 12 inches by his eye. This was one of the reasons that his largest telescope produced relatively few results compared with the 24-inch, which was also much less cumbersome to operate.

Similarly, the 72-inch reflector of Lord Rosse (Chap. 5 of RTO I) was inevitably frequently used at magnifications well below that required to get the exit beam through the eye pupil.

Stellar photography was effectively introduced by W. C. and G. P. Bond about 1850. This removed the limitation of an eye pupil since the telescope was simply a photographic camera with large aperture, long focal length and small angular field. The efficiency was very low because of the very low quantum efficiency of the emulsions, but the *effective light efficiency*  $E$  depended on the area of the effective PSF on the emulsion giving the simple formula

$$E \simeq k_c \left( \frac{D}{d} \right)^2 , \quad (4.31)$$

where  $D$  and  $d$  are the diameters of the telescope and star image (PSF) respectively and  $k_c$  is a constant. The formula (4.31) has certainly been known for at least a century, but its significance was not generally recognised. In modern terms, it means that, for a given detector and throughput determining  $k_c$ , the integration time required to reach a given limiting magnitude will roughly depend on  $(D/d)^2$ . This assumes a direct imaging mode, a photon-limited regime and adequate sampling of the PSF by the pixels of the detector. Other observation modes will have different efficiency laws and require a much more sophisticated analysis. But classical direct imagery remains one of the most demanding, usually *the* most demanding, observation mode. If the observation is background or detector noise limited, again more sophisticated formulae are required, but (4.31) remains a simple baseline formula for

considering the efficiency. If  $D$  is doubled and  $d$  is also doubled (because of increased technical difficulties) then there is no gain in efficiency, but a great deal more money will have been spent (see § 3.1 on diameter-cost laws). It is clear then, from this classical formula, that the building of larger telescopes as "light buckets" of low quality makes no sense at all unless they are to be used only in special modes of observation not related to direct imagery. An example might be photometry, if a minimum diaphragm of 10 arcsec is used. But, even here, if a "light bucket" has a significant high spatial frequency component in its generous error budget, it will spread the energy of the PSF into broad wings which may easily exceed 10 arcsec.

The practical validity of Eq. (4.31) was demonstrated virtually every night with the ESO 3.5 m NTT, during its initial operation, compared with the older "passive" 3.6 m telescope (itself an excellent telescope of the Bowen class – Chap. 5 of RTO I) in that the integration times for a given limiting magnitude were only a fraction if the atmospheric seeing was excellent [4.12] [4.13] – see Fig. 3.67 and Table 3.14 in which a similar efficiency criterion was applied to a number of telescopes.

The requirement of high image quality is now recognised for all modern telescopes and it is desirable to have more scientifically-based criteria of efficiency. Dierickx [4.17] considers this matter on the basis of the performance criteria for the VLT. For the direct imaging case, photon limited, and for an ideal detector with 100% efficiency, zero noise and infinite pixel sampling of the PSF, he derives the criterion for *Optical Efficiency*  $E_O$

$$E_O \simeq \frac{Ik^2}{16f^2} \tau_a r_0^2 \tau_t D^2 I_0 , \quad (4.32)$$

where  $k = 2\pi/\lambda$ ,  $f$  is the focal length,  $D$  the telescope diameter,  $r_0$  the Fried parameter,  $\tau_a$  and  $\tau_t$  the transmission factors of the atmosphere and telescope respectively,  $I$  is the photometric intensity of the point source, and  $I_0$  is the CIR as defined in § 4.2 above. The quantities  $I$ ,  $\tau_a$ ,  $r_0$ ,  $\tau_t$  and  $I_0$  are all wavelength dependent. The site determines the parameters  $\tau_a$  and  $r_0$ ; the telescope with its local environment determines  $\tau_t$ ,  $D$  and  $I_0$ , of which  $D$  is decided in advance.

The relation (4.32) leads at once to the definition of the *effective diameter*  $D_{eff}$  of a telescope as

$$D_{eff} = D(\tau_t I_0)^{1/2} \quad (4.33)$$

The product  $(\tau_t I_0)^{1/2}$  has the same weight as  $D$ : if either  $\tau_t$  or  $I_0$  is not maintained at its potential optimum, then the effective diameter is reduced. If we set

$$\tau_t I_0 = T^2 , \quad (4.34)$$

then

$$D_{eff} = DT , \quad (4.35)$$

where  $T^2$  can be seen as a measure of the *technological optical efficiency*  $E_t$  of the telescope, i.e. the parameter that can be influenced by efficient maintenance and operation. The weight of parameter  $\tau_t$  draws attention to the fundamental importance of the throughput, i.e. efficient coatings and cleanliness (see Chap. 6). Although it cannot enter into the efficiency defined by (4.32), cleanliness is even more important from the point of view of diffusion of light over the image plane, increasing the background noise. The linear response of modern electronic detectors makes this much more serious than with photographic plates as detectors. In applying Eq. (4.33) it is important to remember the wavelength dependence of both  $\tau_t$  and  $I_0$  and that  $I_0$  is also strongly dependent on seeing. In optimizing  $T$ , it may be a better compromise to accept a small degradation in  $I_0$  from multidielectric coats in order to increase  $\tau_t$  by a more significant amount than the loss in  $I_0$ .

In a recent discussion (February 1998), Dierickx kindly pointed out to me that the wavelength dependence of  $I_0$  (=CIR), referred to above, is, in practice, weak. Since, from Eq. (4.27),  $\Delta I_0$  is proportional to  $(\sigma/\zeta)^2$ , it follows that the CIR will approach unity at extremely long and short wavelengths, with a flat minimum somewhere near the visible waveband. For the VLT primary No. 1, this minimum CIR is of the order of 0.87 with  $r_0 = 500$  mm (exceptionally good seeing of about 0.2 arcsec FWHM at  $\lambda = 500$  nm). The minimum lies at about  $\lambda = 350$  nm or further into the UV, but has virtually the same value at  $\lambda = 500$  nm. It follows that, in practice, CIR values calculated for visible or UV wavelengths will represent more or less a “worst case”, the CIR improving in the IR or further into the UV.

If diffraction is neglected for  $\zeta \equiv D/r_0 \sim 30$ , which permits further approximations in Eq. (4.22) for  $I_0$ , then (4.32) can be expressed as [4.12]

$$E_O \sim t \frac{D^2}{\lambda^2} (1 - \sigma_*^2) , \quad (4.36)$$

where  $\sigma_* = \sigma/\zeta$  and  $t$  is a constant. Because of the normalizing factor  $k = 2\pi/\lambda$  in (4.7), defining  $\sigma$  as the rms slope error of the wavefront, and because  $\zeta$  is a normalized, dimensionless parameter, both  $\sigma$  and  $\sigma_*$  are dimensionless. It is interesting to compare this with the simple classical formula of (4.31). This can be reduced at once to the approximate form

$$E \simeq k_c \frac{D^2}{d_0^2} \left( \frac{d_0}{d} \right)^2 \sim k_c \frac{D^2}{d_0^2} \left( 1 - 2 \frac{\Delta d}{d_0} \right) , \quad (4.37)$$

where  $d_0$  is the diameter of the atmospheric seeing image, measured in the same way as  $d$  and  $\Delta d = d - d_0$ , the increase due to aberrations from all sources, assuming  $\Delta d \ll d_0$  for a “good” telescope. (Figure 3.67 shows that the neglect of higher terms in (4.37) will not be justified for many telescopes in practice). Setting the constant  $t = k_c \lambda^2 / d_0^2$ , Eqs. (4.36) and (4.37) have the same basic form to this rough approximation. The fact that the bracket term in (4.36) contains the square of  $\sigma_*$ , while the equivalent bracket term in (4.37) contains the first power of  $\Delta d$ , simply reflects the fact that (4.36) measures

the degradation of image quality as a reduction in the central intensity of the image while (4.37) measures it in terms of the classical angular diameter.

Since  $\sigma$  is the rms *slope* error of the wavefront,  $\sigma$  will remain constant with increase of telescope size if the amplitudes of the aberrations increase linearly with the diameter. This agrees with the conclusion that has been drawn in the past using the classical performance criterion  $d_E$ .

Dierickx also considers the efficiency of a telescope with the same approach in the presence of *sky background noise*. This gives an illuminance in the focal plane  $E_B$  independent of the optical quality of the telescope

$$E_B = \pi\tau B \frac{D^2}{4f^2} , \quad (4.38)$$

where  $\tau = \tau_a \tau_t$  and  $B$  is the photometric brightness of the sky background. The signal/noise ratio  $S/N$  is then

$$\frac{S}{N} = \frac{E_O}{E_B} = \frac{I}{B} \frac{r_0^2 k^2}{4\pi} I_0 , \quad (4.39)$$

i.e. the  $S/N$  is proportional to the CIR =  $I_0$ . Substituting from (4.15) to replace  $r_0$  by  $(d_{FWHM})_a \equiv d_0$  gives

$$\frac{S}{N} \simeq 2.99 \frac{I}{B} \frac{I_0}{d_0^2} \quad (4.40)$$

The  $S/N$  is therefore directly proportional to  $I_0$  and inversely to the square of the diameter of the atmospheric seeing angle. The dependence on  $\lambda$  is expressed by  $I(\lambda)/\lambda^{2/5} B(\lambda)$ .

Dierickx gives a similar relation for *IR emission* of the atmosphere showing that the IR emission  $B_s$  is effectively included in  $B$ :

$$\frac{S}{N} = \left( \frac{I\tau}{\tau B + B_s} \right) \frac{r_0^2 k^2}{4\pi} I_0 \quad (4.41)$$

In considering the optical efficiency of telescopes, it is important to remember that relatively few telescopes have had their *functional* performance measured at all. Only recently have image analysers become available as off-line devices for measuring the optical quality (Chap. 2). In November 1992 the ESO 3.5 m NTT was still the only large functioning telescope with an *on-line* image analyser, though a number of telescopes were planning to add this facility or were being designed to incorporate it. It is therefore still of immense value if image analysers of the Shack-Hartmann or other types can yield information in the classical geometrical  $d_E$  form. This gives comparative data in a consistent system [4.25]. Furthermore, software is available today whereby the measured information can afterwards be processed to include diffraction and give better efficiency criteria as discussed above.

## 5. Atmospheric optics, adaptive optics, telescope quality for interferometry

### 5.1 Atmospheric optics

Whereas the basic theory of elasticity of solid bodies was already worked out before the twentieth century, understanding of the thermodynamic behaviour of large air masses has only become significant for telescope optics in the last 35 years. It is therefore logical and inevitable that the subject of telescope optics has reached a stage where the mechanical, opto-mechanical and optical production problems (see Table 3.11) are largely solved, whereas the residual problems associated with the local air mass and, even more, of the atmosphere itself, are increasingly dominant and the subject of an increasing proportion of research and development effort.

There are three classical areas of influence of the atmosphere on the telescope image: extinction (atmospheric absorption), “seeing” quality (atmospheric turbulence) and refraction (including atmospheric dispersion). It is significant that an excellent general work on astronomy published as late as 1967 [5.1] devoted less space to the second topic (seeing) than to the other two and limited its factual data to the statement that the “seeing disk” varied between 0.5 and 10 arcsec. The first aspect of extinction is of great importance in photometry and in site selection, above all from the point of view of water vapour content for extinction in the IR. Sophisticated measuring techniques are now available and in general use in major observatories. Since extinction is not primarily related to image quality, I refer the reader to specialised astronomical literature and site selection documentation such as that of ESO [5.2]. Such documentation includes monitoring of wind velocity and direction and temperature, parameters of increasing importance for the control of local telescope conditions (see § 3.6). Technically, sensors are readily available today for the monitoring of such parameters.

We are principally concerned in this section with the atmospheric phenomena of refraction and “seeing”, whereby the latter represents the most important limitation on image quality of sophisticated ground-based telescopes.

### 5.1.1 Atmospheric refraction and atmospheric dispersion

The basic theory of atmospheric refraction and atmospheric dispersion was given in RTO I, § 4.4, in connection with atmospheric dispersion correctors. Atmospheric dispersion is simply the differential of atmospheric refraction with respect to the “effective” refractive index – wavelength function of the atmosphere and leads to the formation of an image spectrum in the direction of telescope altitude. As we saw, the effect is very serious for wide spectral bandwidths: about 10 arcsec for the bandwidth 300–800 nm for zenith distance  $Z = 70^\circ$ . The differential effect of atmospheric dispersion is the aspect affecting image quality and the basic theory of refraction currently available is quite adequate for  $Z \leq \text{ca. } 70^\circ$ . This covers most observational requirements.

Refraction itself is a much larger effect introducing a positional error and therefore important for astrometry. An excellent review paper of the historical development of atmospheric refraction theory and its state at the time was given in 1962 by Mahan [5.3]. The first scientific approach was that of Cassini in 1656, whose derivation is also given by Barlow and Bryan [5.4]. Cassini assumed a concentric, homogeneous atmosphere and derived for a small value of refraction  $\delta Z$  in radians

$$\delta Z = (n - 1) \tan Z (1 - q \sec^2 Z + q^2 \sec^4 Z - q^3 \sec^6 Z + \dots) , \quad (5.1)$$

where  $Z$  is the *apparent* zenith distance,  $n$  is the refractive index and  $q = h/r_E$  with  $h$  the height of the homogeneous atmosphere and  $r_E$  the earth’s radius. Using measurements on two stars, Cassini could deduce  $h = 6.82$  km and  $n = 1.000284$  for  $r_E = 6377.36$  km. The value of  $q$  is therefore 0.00107 and the terms in (5.1) higher than that in  $\sec^2 Z$  can normally be neglected. Equation (5.1) then reduces to

$$\delta Z = (n - 1)[(1 - q) \tan Z - q \tan^3 Z] \text{ rad} , \quad (5.2)$$

the same form as (4.92) in RTO I if  $q$  is considered negligible. Cassini’s formula (5.1) clearly fails with  $Z \rightarrow 90^\circ$  because of singularity. In fact, Cassini also had an exact formulation, within the limitations of his homogeneous atmospheric model, in terms of Snell’s law of refraction and the law of sines for the refraction triangle [5.3]. By observations on two stars, he could eliminate the refractive index  $n$  from the refraction equations. Substitution from the two law-of-sines equations enabled a fourth degree equation in  $h$  to be set up, in which  $Z_1, Z_2, \delta Z_1, \delta Z_2$  are known for the two stars, as well as the quantity  $r_E$ . The correct root of this equation gave him the effective value of  $h$  and thence, by substitution,  $n$ . These are the values quoted above and were derived for  $Z \leq 70^\circ$ . Beyond this, they yield values of  $\delta Z$  which are too small. However, unlike Eq. (5.1), the formulation in terms of  $\sin Z$  is not singular at  $Z = 90^\circ$ . Hence, if the two reference stars are chosen with  $Z$  approaching  $90^\circ$ , a higher effective value of  $h$  is derived. This dependence of  $h$  on  $Z$  is a consequence of the limitations of the homogeneous atmospheric model. Cassini’s calculations gave 59, 159 and 1940 arcsec for  $Z = 45^\circ, 70^\circ$

and  $90^\circ$  respectively, the latter being over half a degree and more than the diameter of the sun. Refraction is therefore a very large effect at high values of  $Z$ . Beyond  $Z \approx 70^\circ$ , Eq. (5.2) starts to give significant errors. The Cassini value for  $Z = 90^\circ$  (horizontal refraction) is inevitably too low and is over 4 arcmin lower than modern values [5.3].

Soon after Cassini, it was recognized that the homogeneous atmosphere did not correspond to reality and the much better model of concentric layers with decreasing refractive index upwards was proposed (Fig. 5.1). To illustrate the theoretical analysis, Mahan [5.3] shows in this figure a final thick layer of constant index  $n_{(l+1)}$ , but the concentric model assumes, of course, a monotonic height – index function. The theory leads to the “refraction integral”, first derived independently by Newton, Bouguer and Simpson according to Mahan, who gives the derivation. The refraction integral is

$$\delta Z = \int_1^{n_E} \frac{n_E r_E \sin Z}{[n^2(r_E + h)^2 - n_E^2 r_E^2 \sin^2 Z]^{1/2}} \frac{dn}{n} , \quad (5.3)$$

the equation which is the basis of virtually all subsequent theories. If  $n_E$  at the height of the observer is known and  $n$  as a function of the height  $h$  to the limit of the atmosphere, then  $\delta Z$  can be calculated. However, the integration was not a trivial problem, apart from the fact that reliable information on the  $n - h$  function was not available until modern times.

A simplification of the general form of the refraction integral results if the earth's curvature is neglected to give a plane parallel layer model. This leads to an equation similar to the Cassini formula, but giving 1 arcsec accuracy up to  $Z \leq 65^\circ$ :

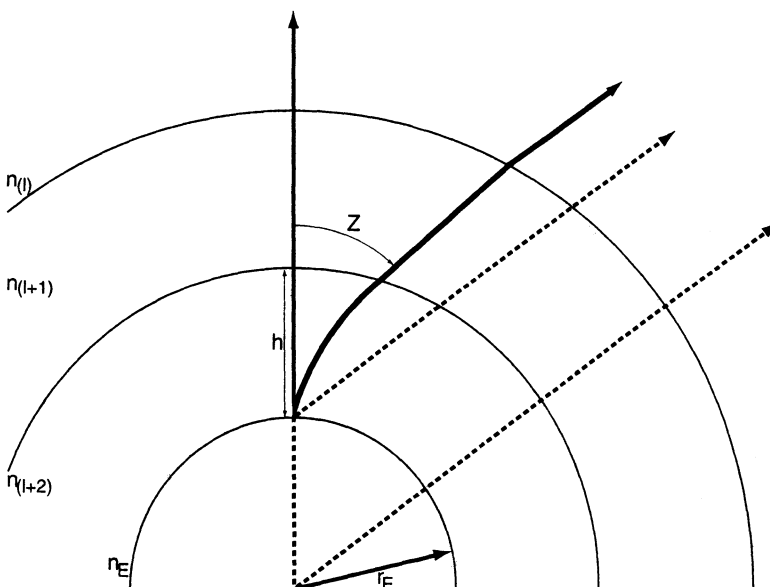


**Fig. 5.1.** The concentric shell model for astronomical refraction (after Mahan [5.3])

$$\delta Z = (n_E - 1) \tan Z + \frac{(n_E - 1)^2}{2} \tan^3 Z + \frac{(n_E - 1)^3}{2} \tan^5 Z \dots \quad (5.4)$$

At  $Z > 65^\circ$ , the values from (5.4) are too large.

Progressive attempts were made to interpret the  $n - h$  function by meteorological parameters. Bessel [5.3] abandoned attempts to improve the analytical solution and proposed the empirical form

$$\delta Z = \alpha (P T_P)^A T_a^\lambda \tan Z , \quad (5.5)$$

in which  $P$  represents corrections for pressure,  $T_P$  temperature corrections for the barometer,  $T_a$  temperature corrections for the ambient air, and the quantities  $\alpha$ ,  $A$  and  $\lambda$  are functions of  $Z$ . Further work and refinements are given by Mahan [5.3]. He quotes Newcomb (1906) as writing that, in spite of the enormous amount of work, the theory of refraction was still in a very unsatisfactory state. For  $Z = 90^\circ$ , it was still not possible to predict refraction to better than 5–10 arcsec in 1962. What is needed is a value for  $n$  at all heights with an accuracy of at least  $10^{-7}$ .

The case of refraction is extremely instructive as it reveals that *even the apparently very simple phenomenon* of average image shift is by no means simple if high accuracy in extreme cases is required. It is not surprising that the much more complex phenomenon of seeing defied all attempts at analytical treatment until quite recently. We shall see in the next section that the refractive index – height function can be defined by the function of the refractive index structure constant,  $C_n$ , with height. Although this function is now reasonably well-known for paths near the zenith, near-horizontal propagation still poses major problems because of limitations like the outer scale of turbulence.

### 5.1.2 Atmospheric turbulence (“seeing”)

Genuine scientific progress in the theory of the effect of atmospheric turbulence on the plane wavefront of a star was initiated in 1941 by Kolmogorov [5.5] and Obukhov [5.6], following work by Khinchin in 1938 [5.7]. A general treatment of the theory following this approach was given by Tatarski in an English translation in 1961 [5.8]. Shortly afterwards, the complete theoretical formulation was achieved, first by Hufnagel and Stanley [5.9] but above all by Fried and collaborators [5.10] [5.11] [5.12] [5.13] [5.14] [5.15]. In 1981, a classical review paper was published by Roddier [5.16]. It may be argued that the works of Tatarski [5.8], Fried [5.12], [5.13] and Roddier [5.16] represent the most important publications in the theory of telescope optics since Schwarzschild’s classical paper on the aberration theory of reflecting telescopes in 1905 (see RTO I, Chap. 3).

Only the major points of the theory will be given here, above all following the cited works of Tatarski, Fried and Roddier. For details, the reader is referred to the extensive literature given by Roddier [5.16].

**5.1.2.1 Statistical properties of atmospheric turbulence.** The laminar flow of a fluid is stable only as long as the Reynolds number  $\text{Re}$  is less than a critical value  $\text{Re}_{cr}$ , i.e. if

$$\text{Re} = V_o L_o / \nu_o < \text{Re}_{cr}, \quad (5.6)$$

where  $L_o$  characterizes the length,  $V_o$  the velocity of the flow, and  $\nu_o$  is the kinematic viscosity.  $L_o$  arises from the nature of the boundary conditions. Since  $\nu_o \sim 15 \times 10^{-6} \text{ m}^2 \text{s}^{-1}$ , then  $L_o \sim 15 \text{ m}$  and  $V_o \sim 1 \text{ ms}^{-1}$  give  $\text{Re} \sim 10^6$ , a value far beyond  $\text{Re}_{cr}$ . The normal state of the atmosphere corresponds therefore to fully developed turbulence.

Suppose that for some reason a velocity fluctuation  $v'_l$  occurs in a region of size  $l$  of a basic laminar flow. The time involved is  $\tau = l/v'_l$  and the energy per unit mass is  $v'^2_l$ . Then the amount of energy per unit time transferred from the laminar flow to the fluctuational motion is of the order of  $v'^2_l/\tau \sim v'^3_l/l$ . If  $\text{Re}_{cr}$  is only modestly exceeded, then the velocity fluctuations  $v'_l$  associated with a length  $l$  have a Reynolds number  $\text{Re}_l < \text{Re}_{cr}$  and are stable. With further increase in the basic flow with  $\text{Re} = vL/\nu$  considerably exceeding  $\text{Re}_{cr}$ , then a point is reached when the “first order” velocity fluctuations with  $v_l$  lose stability and transfer energy to “second order” fluctuations. In other words, *the kinetic energy of larger scale motions is transferred to smaller and smaller scale motions*, a principle first enunciated by Kolmogorov [5.5] [5.8] [5.16]. When the Reynolds number  $\text{Re}_l$  of some order of fluctuation becomes small enough that  $\text{Re}_l < \text{Re}_{cr}$ , the fluctuation generation ceases and the energy is dissipated as heat by viscous friction. The rate of such dissipation into heat depends on the local velocity gradients in these smallest perturbations, which are given by  $\nu_o/l_o$ . The energy  $\varepsilon_o$  dissipated per unit mass per unit time is then given by  $\varepsilon_o \propto \nu_o v_o^2/l_o^2$ . *For all velocity fluctuations of scale greater than this very smallest scale, the energy transfer law given above, namely  $\varepsilon \propto v'^3/l$  applies, giving*

$$v'_l \propto \varepsilon^{1/3} l^{1/3} \quad (5.7)$$

To calculate the dimension  $l_o$  of the smallest fluctuations, we use  $\varepsilon \propto \nu_o v_o^2/l_o^2$  and  $v_o \sim (\varepsilon l_o)^{1/3}$  from (5.7) giving

$$l_o \propto \left( \frac{\nu_o^3}{\varepsilon} \right)^{1/4}, \quad v_o \propto (\nu \varepsilon)^{1/4} \quad (5.8)$$

The quantity  $l_o$  can also be expressed in terms of the largest fluctuations  $L$ , which are comparable to the dimension of the flow as a whole. Then  $\varepsilon \propto v_L^3/L$ , which gives by substitution in (5.8)

$$l_o \propto \frac{L}{(\text{Re})_L^{3/4}}, \quad v_o \propto \frac{v_L}{(\text{Re})_L^{1/4}} \quad (5.9)$$

The larger the Reynolds number of the flow as a whole, the smaller the size of the velocity inhomogeneities that can arise.

These principles give the basis for a more rigorous theory.

If we term  $L_o$  that scale which gives rise to the turbulence in general, then  $L_o$  is termed the *outer scale* of the turbulence, while  $l_o$  is the *inner scale* at which viscous heat dissipation commences.

Kolmogorov [5.5] [5.8] found the solution to the problem of handling the random nature of the variations of the physical parameters involved in the atmosphere. For non-stationary random functions of time  $t$ , such as the atmospheric case, the problem is to decide which changes should enter into a mean value of a parameter and which should be viewed as smooth variations. He introduced the so-called *structure functions* which could be applied to a random system  $f(t)$  with *stationary first increments*. The difference  $F_\tau(t) = f(t + \tau) - f(t)$  is then a stationary random function if  $\tau$  is not too large, and this function is not affected by slow changes in the function  $f(t)$ . The basic structure function is then of the form

$$\underline{D}_f(\tau) = \langle |f(t + \tau) - f(t)|^2 \rangle , \quad (5.10)$$

i.e. the mean value of the square of the difference. The assumption that the differential of a physical function is more stable than the function itself occurs throughout physics. We have encountered essentially similar phenomena in RTO I, Chap. 3, with regard to the increasing stability of optical aberrations with increasing order; or in Chap. 3 concerning the convergence and increasing stability of higher order effects resulting from the Principle of Saint-Venant in elasticity.

In Kolmogorov theory applied to the velocity field, it is accepted that the largest scale fluctuations cannot be isotropic, since they are influenced by the geometrical properties of the total flow with scale  $L_o$ . However, these properties no longer influence the fluctuations of a high order, i.e. sufficiently small scale  $l$ , so these may be considered as *isotropic*. We are then dealing with a *locally isotropic random field with stationary increments of the velocity vector  $\vec{v}(\vec{r})$* . Tatarski [5.8] shows that it has the general vector structure function  $\underline{D}_{ik}(\vec{r})$  which can be expressed in terms of a longitudinal structure function  $\underline{D}_{rr}$  of the same form as (5.10) and a transverse one  $D_{tt}$ . But these are not independent and are related by

$$\underline{D}_{tt} = \frac{1}{2r} \frac{d}{dr} (r^2 \underline{D}_{rr}) \quad (5.11)$$

Thus  $\underline{D}_{rr}$  is sufficient to determine the tensor  $\underline{D}_{ik}(\vec{r})$ .

We now make the important limitation

$$l_o \ll r \ll L_o , \quad (5.12)$$

implying that the results established will lose their validity as we approach either the inner or outer scale of turbulence. Then the velocity difference at points  $\vec{r}_1$  and  $\vec{r}'_1 = \vec{r}_1 + \vec{r}$  is mainly due to fluctuations with dimensions comparable to  $r$ . We saw above in Eqs. (5.7)–(5.9) that such fluctuations are totally characterized by the energy dissipation rate  $\epsilon$ . Then  $\underline{D}_{rr}(r) = F(r, \epsilon)$ . Since the energy requires the dimensions of velocity squared, i.e.  $\underline{D}_{rr}(r) \propto$

$v_r^2$ , the only combination of the quantities  $r$  and  $\varepsilon$  which can satisfy the requirements is, from (5.7)

$$\underline{D}_{rr}(r) = C(\varepsilon r)^{2/3} , \quad (l_o \ll r \ll L_o) , \quad (5.13)$$

where  $C$  is a dimensionless constant. This is the famous Kolmogorov-Obukhov "two-thirds law" [5.5] [5.6] [5.8], which forms the basis of the entire theory. Its physical significance is that the spatial correlation of turbulence decreases in proportion to the two-thirds power of spatial separation.

If  $r \ll l_o$ , we are outside the range of validity of (5.13), but the relative motions are laminar: the structure function has a parabolic form in this range.

If  $r \gg L_o$ , (5.13) is again invalid since large fluctuations, which are not isotropic and homogeneous, start to influence the structure function velocity differences. It can only be stated, in Tatarski's theory, that the growth of  $\underline{D}_{rr}(r)$  slows down in this region. Figure 5.2 shows the general form of the structure function.  $L_o$  is that value of  $r$  where saturation becomes significant;  $l_o$  is defined as that value for which the parabolic function cuts the function of (5.13). Its value is then given by

$$l_o = \left[ \frac{(15C\nu_o)^3}{\varepsilon} \right]^{1/4} \quad (5.14)$$

It is important not only to derive results for the velocity structure functions themselves but also for their spectral distributions  $E(\kappa)$ , the Fourier transforms. Since, for the velocity field,  $\underline{D}_{rr}(r)$  has the form  $\langle (v_r - v')^2 \rangle$ , the

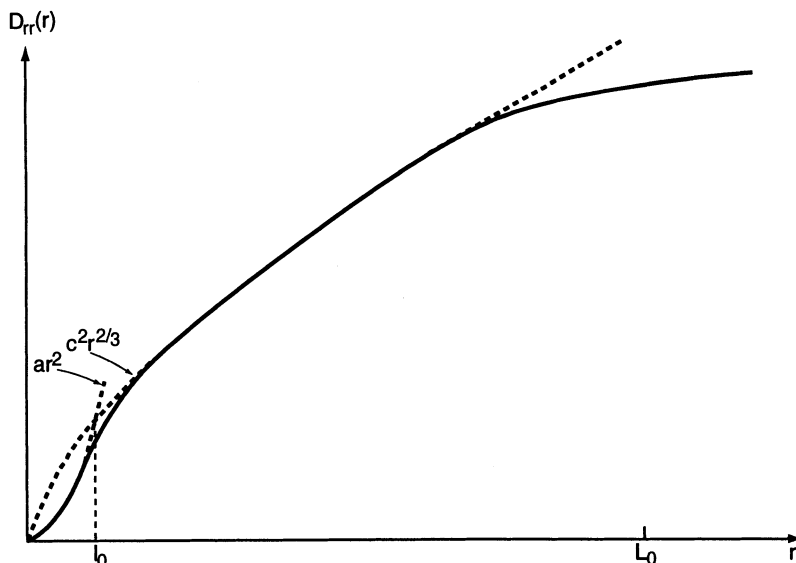


Fig. 5.2. General shape of the structure function  $\underline{D}_{rr}(r)$  showing  $L_o$  (outer scale) and  $l_o$  (inner scale) (from Tatarski [5.8])

function  $E(\kappa)$  is an energy distribution. Tatarski derives the 1-dimensional spectral distribution  $E_1(\kappa)$  corresponding to the “two-thirds law” as

$$E_1(\kappa) = A_1 \varepsilon^{2/3} \kappa^{-5/3}, \quad (5.15)$$

where

$$A_1 = \frac{\Gamma(\frac{5}{3}) \sin \frac{\pi}{3}}{2\pi} C, \quad (5.16)$$

in which  $\Gamma$  represents the gamma function. Roddier [5.16] derives the  $\kappa^{-5/3}$  dependence directly from (5.7), since the energy  $E_1(\kappa) d\kappa$  between  $\kappa$  and  $\kappa + d\kappa$  is proportional to  $v^2(\kappa)$ , giving with  $l \propto 1/\kappa$

$$E_1(\kappa) d\kappa \propto \kappa^{-2/3} \quad \text{or} \quad E_1(\kappa) \propto \kappa^{-5/3},$$

as in (5.15).

In the more general, 3-dimensional case for which we assume isotropy in accordance with the above theory, we must integrate over a sphere so that the proportionality to  $\kappa^{-5/3}$  in (5.15) is raised by  $\kappa^{-2}$  to  $\kappa^{-11/3}$ . Tatarski gives

$$E(\kappa) = A \varepsilon^{2/3} \kappa^{-11/3} \quad (5.17)$$

with

$$A = \frac{11\Gamma(\frac{8}{3}) \sin \frac{\pi}{3}}{24\pi^2} C \quad (5.18)$$

Equation (5.15), expressing the Kolmogorov-Obukhov law for the spectral distribution corresponding to (5.13), has the equivalent reciprocal limitation on its range of validity, namely  $l_o^{-1} \gg \kappa \gg L_o^{-1}$ .

According to Roddier, the inner scale  $l_o$  ranges from a few mm near the ground to about 1 cm near the boundary troposphere-stratosphere.  $L_o$  is of the order of the thickness of turbulent layers, i.e. about 100 m. Near the ground, it is of the order of the height above the ground. The theory will prove that the size of the fluctuations disturbing the wavefront and producing “seeing” ranges from a few cm to the size of the telescope aperture. The validity range of the Kolmogorov-Obukhov law is therefore entirely sufficient, even for the largest apertures of modern telescopes of the order of 10 m. However, for an interferometric mode with path lengths of the order of 100 m, its validity becomes doubtful (Fig. 5.2).

In 1949, Obukhov [5.17] and Yaglom [5.18] introduced an important extension into the Kolmogorov-Obukhov theory, namely, the concept of “conservative passive” additives to the atmosphere. “Conservative” implies that no chemical reaction with the air takes place, i.e. the concentration  $\psi$  of the additive does not change; “passive” implies that the additive does not affect the dynamical regime of the turbulence. To a good approximation, the Kolmogorov-Obukhov law also applies to additives such as water vapour or the parameter temperature, resulting in a mixture of cooler or warmer air. The temperature field case was the one dealt with by Obukhov and Yaglom.

A quantity  $\bar{N}$  is defined which is the rate at which the fluctuation (in this case temperature) is dissipated by molecular diffusion and is analogous to the energy dissipation rate  $\varepsilon$ . The structure function is defined by analogy with (5.10) as

$$\underline{D}_\psi(\vec{r}_1 - \vec{r}_2) = \langle [\psi(\vec{r}_1) - \psi(\vec{r}_2)]^2 \rangle \quad (5.19)$$

Obukhov [5.17] showed that  $\underline{D}_\psi(r)$  is a function only of  $\bar{N}, \varepsilon, r$  and deduced, from dimensional considerations, the physical basis of which is given by Tatarski [5.8],

$$\underline{D}_\psi(r) = a^2 \bar{N} \varepsilon^{-1/3} r^{2/3} , \quad (l_o \ll r \ll L_o) , \quad (5.20)$$

where  $a$  is a numerical constant. This is the Obukhov “two-thirds law” for the concentration  $\psi$  of a conservative passive additive. If  $r \ll l_o$ , in the laminar regime, the function  $\underline{D}_\psi(r)$  is again a parabola, as in Fig. 5.2, but leading to a definition of  $l_o$  given by

$$l_o = \left( \frac{27a^6 D_d^3}{\varepsilon} \right)^{1/4} , \quad (5.21)$$

where  $D_d$  is the molecular diffusion coefficient of the additive. The structure function  $\underline{D}_\psi(r)$  can then be written as the general form of the Obukhov law

$$\underline{D}_\psi(r) = \begin{cases} C_\psi^2 r^{2/3} & \text{for } l_o \ll r \ll L_o \\ C_\psi^2 l_o^{2/3} \left( \frac{r}{l_o} \right)^2 & \text{for } r \ll l_o \end{cases} , \quad (5.22)$$

where  $C_\psi \equiv C_T$  is called the additive (temperature) structure constant and is defined by

$$C_T^2 = a^2 \bar{N} \varepsilon^{-1/3} \quad (5.23)$$

The inner and outer scales  $l_o$  and  $L_o$  in such cases are similar to the basic values given above for the velocity field. Similar expressions to (5.22) apply to humidity variations.

*Refractive index fluctuations*  $\delta n$  of the atmosphere can be considered as a case of conservative passive additives where the additives are temperature and humidity, of which  $\delta n$  is a function. Roddier [5.16] states that the terms due to humidity may be neglected in the astronomical seeing case, so that  $\delta n$  is effectively only a function of temperature. It follows that the structure function for  $\delta n$  has the same form as that of the Obukhov law for temperature and is given by

$$\underline{D}_n(r) = \begin{cases} C_n^2 r^{2/3} & \text{for } l_o \ll r \ll L_o \\ C_n^2 l_o^{2/3} \left( \frac{r}{l_o} \right)^2 & \text{for } r \ll l_o \end{cases} , \quad (5.24)$$

where  $C_n$  is the *refractive index structure constant*. Roddier gives for  $C_n$  the relations

$$\left. \begin{aligned} C_n &= \overline{A} C_T \\ \overline{A} &= (80 \times 10^{-6}) P / T^2 \end{aligned} \right\}, \quad (5.25)$$

where  $C_T$  is defined by (5.23),  $P$  is the air pressure in millibars and  $T$  the absolute temperature.

The spectral distribution corresponding to the Obukhov law of (5.20) is given by

$$\Phi_n(\kappa) = 0.033 C_n^2 \kappa^{-11/3}, \quad (l_o^{-1} \gg r \gg L_o^{-1}) \quad (5.26)$$

Numerical values of  $C_n^2$  are given by Roddier [5.16]. For points near the ground ( $h = 12$  m), he gives about  $10^{-13} \text{ m}^{-2/3}$  during daytime and about  $10^{-14} \text{ m}^{-2/3}$  during night-time. A height dependence

$$\begin{aligned} C_n^2 &\propto h^{-4/3} && (\text{unstable daytime conditions}) \\ C_n^2 &\propto h^{-2/3} && (\text{stable night-time conditions}) \end{aligned} \quad (5.27)$$

is quoted. A minimum value of about  $10^{-17} \text{ m}^{-2/3}$  is given for  $h$  around 6–9 km, followed by a maximum near the tropopause and steady decrease in the stratosphere.

**5.1.2.2 Complex amplitude calculations for a plane, horizontal, monochromatic wavefront from a zenith star passing through the atmosphere.** Tatarski derived solutions using the simplification of geometrical optics, ignoring diffraction. This is valid if the condition  $\lambda \ll l_o$  is satisfied. However, diffraction effects must be taken into account in the region of the outer scale  $L_o$ . The geometrical optics approximation is only valid for  $L \ll L_{cr}$  with  $L_{cr} = l_o^2/\lambda$ .

Tatarski's treatment [5.8] uses approximations derived from assumptions of "small" and "smooth" perturbations. Roddier [5.16] uses an approach proposed by Lee and Harp [5.19] called the "thin screen approximation". This assumes the atmosphere is still and homogeneous except for a thin horizontal layer between  $h$  and  $h + \delta h$ . The layer thickness must be chosen to be large compared with the correlation scale of the perturbations but small enough for diffraction effects to be negligible over  $\delta h$ . Each point of the atmosphere is designated by a horizontal coordinate vector  $\vec{x}$  and a height  $h$ . The scalar vibration at  $(\vec{x}, h)$  is described by its complex amplitude

$$\Psi_h(\vec{x}) = |\Psi_h(\vec{x})| \exp[i\phi_h(\vec{x})] \quad (5.28)$$

With the thin screen approximation, at the layer input  $\Psi_{(h+\delta h)}(\vec{x}) = 1$ , giving at the output

$$\Psi_h(\vec{x}) = \exp[i\phi(\vec{x})], \quad (5.29)$$

in which  $\phi(\vec{x})$  is the phase shift introduced by index fluctuations  $n(\vec{x}, h)$  within the layer

$$\phi(\vec{x}) = k \int_h^{h+\delta h} n(\vec{x}, z) dz, \quad (5.30)$$

where  $k = 2\pi/\lambda$ , the wave number, and  $z$  is the layer coordinate in the height direction. Both Tatarski and Roddier introduce the correlation function as the second order moment of the complex random field  $\Psi_h(\vec{x})$ . At the layer output, Roddier terms this the *coherence function* defined by

$$B_h(\vec{\xi}) = \langle \Psi_h(\vec{x}) \Psi_h^*(\vec{x} + \vec{\xi}) \rangle \quad (5.31)$$

With (5.29), this gives

$$B_h(\vec{\xi}) = \langle \exp i[\phi(\vec{x}) - \phi(\vec{x} + \vec{\xi})] \rangle , \quad (5.32)$$

which can be written because it has Gaussian statistics

$$B_h(\vec{\xi}) = \exp -\frac{1}{2} \langle |\phi(\vec{x}) - \phi(\vec{x} + \vec{\xi})|^2 \rangle , \quad (5.33)$$

or

$$B_h(\vec{\xi}) = \exp -\frac{1}{2} \underline{D}_\phi(\vec{\xi}) , \quad (5.34)$$

where  $\underline{D}_\phi(\vec{\xi})$  is the two-dimensional (i.e. horizontal for the thin screen approximation) structure function. Roddier then introduces the refractive index fluctuations from (5.30) into  $\underline{D}_\phi(\vec{\xi})$  and finally deduces with  $\zeta = z' - z$  and after introducing Obukhov's law from (5.22) into the index structure function the results

$$\underline{D}_\phi(\vec{\xi}) = 2.91 k^2 C_n^2 \delta h \xi^{5/3} \quad (5.35)$$

and, from (5.34),

$$B_h(\vec{\xi}) = \exp -\frac{1}{2} (2.91 k^2 C_n^2 \delta h \xi^{5/3}) \quad (5.36)$$

Tatarski derives the equivalent result to (5.35) with his "small" and "smooth" perturbation approximation except that the thin screen approximation height difference  $\delta h$  is replaced by  $L$  with the condition  $\xi > (\lambda L)^{1/2}$ . The two approaches therefore give the same result.

The complex field at ground level is the field diffracted by the layer. Roddier shows that

$$B_o(\vec{\xi}) = B_h(\vec{\xi}) , \quad (5.37)$$

giving from (5.34)

$$B_o(\vec{\xi}) = \exp -\frac{1}{2} \underline{D}_\phi(\vec{\xi}) \quad (5.38)$$

Strictly, since the complex field  $\Psi_o(\vec{x})$  at ground level fluctuates in both amplitude and phase, it is not correct to interpret  $\underline{D}_\phi(\vec{\xi})$  in (5.38) as the phase structure function at ground level. However, the error can be shown to be small in the astronomical "seeing" case. Taking  $\underline{D}_\phi(\vec{\xi})$  to be the phase structure function at ground level is called the *near-field approximation*.

Roddier generalises the above treatment to take account of multiple layers and thick layers. For a continuous distribution of turbulence, he deduces from (5.36)

$$B_o(\xi) = \exp -\frac{1}{2} \left[ 2.91k^2 \xi^{5/3} \int C_n^2(h) dh \right] , \quad (5.39)$$

the integral being extended over the earth's atmosphere.

So far, we have assumed a plane wave originating at a star in the zenith. At an angular distance  $Z$  from the zenith, the thickness  $\delta h$  of each layer varies as  $(\cos Z)^{-1}$ , so that (5.39) can be generalised as

$$B_o(\xi) = \exp -\frac{1}{2} \left[ 2.91k^2 (\cos Z)^{-1} \xi^{5/3} \int C_n^2(h) dh \right] \quad (5.40)$$

This expression is of fundamental importance for determining the effect of "seeing" in long-exposure images. Doubts have been cast concerning the validity of (5.40) from the point of view of the outer scale limit  $L_o$  and also the inner scale  $l_o$  [5.20] [5.21]. These seem founded for horizontal propagation near the ground, but not under conditions of astronomical observation.

**5.1.2.3 Long-exposure images.** When a stellar image is observed through a telescope under high magnification, the appearance of a star image is determined by the atmospheric turbulence if the other sources of error listed in Table 3.11 are negligible, which is rarely the case with larger telescopes. If atmospheric turbulence is dominant, the appearance depends strongly on the aperture of the telescope and the quality of the "seeing". The pattern changes rapidly with time. With smaller apertures a random motion of the image is often the dominant effect, while with larger apertures a "speckle structure" is observed, i.e. a patch of rapidly varying lighter areas over a fainter background. Exposure times of the order of milliseconds are necessary to freeze the speckle image. If the exposure time exceeds a certain minimum, depending on the seeing quality, the random motions average out and leave a round image whose diameter is a measure of the "integrated seeing", as discussed in § 3.5 in connection with image analysis for active optics where the effect of the atmosphere is effectively eliminated by this integration process.

Here we are concerned with the size and intensity distribution in this integrated seeing function, i.e. the nature of long-exposure images formed only by atmospheric turbulence.

Using the equivalent of Eq. (5.35), Tatarski gave as early as 1961 [5.8] a relation for the mean square fluctuation of the angle  $\alpha$  of arrival of light forming a star image, i.e. the "image motion" part of the "seeing". He considered the case of two interferometer slits separated by a distance  $b_i$ . Then the mean square phase shift  $\langle \phi^2 \rangle$  corresponding to image movement (wavefront tilt) is related to  $\langle \alpha^2 \rangle$  by

$$\langle \phi^2 \rangle = k^2 b_i^2 \langle \alpha^2 \rangle \quad (5.41)$$

with  $k = 2\pi/\lambda$ . But

$$\langle \phi^2 \rangle = \underline{D}_\phi(b_i), \quad (5.42)$$

giving  $\langle \alpha^2 \rangle = \frac{\underline{D}_\phi(b_i)}{k^2 b_i^2}$ , in which  $\underline{D}_\phi(b_i)$  has the form of (5.35) and (5.40). This gives

$$\langle \alpha^2 \rangle \equiv \sigma_m^2 = 2.91 b_i^{-1/3} (\cos Z)^{-1} \int C_n^2(h) dh \quad (5.43)$$

This result is only an approximation, since  $b_i$  must be replaced in practice by  $D$ , the diameter of a telescope. It indicates that the rms image motion angle would vary as  $(\cos Z)^{-1/2}$  and decrease very slowly with  $b_i^{-1/6}$ . We shall return to this matter of image motion in connection with the short-exposure image case (§ 5.1.2.4).

Fried [5.12] represents the wavefront in terms of a least squares fit to a truncated series of six orthonormal polynomials which represent over the pupil a uniform phase change, a wavefront tilt change, a “spherical” change (i.e. defocus) and a “hyperbolic” change (i.e. third order aberration). The statistics of the atmosphere are expressed by a phase structure function following the Obukhov law (5.35) as

$$\underline{D}(r) = \underline{A} r^{5/3} \quad (5.44)$$

Fried then introduced the “Fried parameter”  $r_o$ , now accepted as the fundamental parameter for astronomical seeing, as

$$r_o \simeq (6.88/\underline{A})^{3/5} \quad (5.45)$$

giving

$$\underline{D}(r) = 6.88(r/r_o)^{5/3} \quad (5.46)$$

The significance of the factor 6.88 will be made clear below. The value is derived from  $2[(24/5)\Gamma(6/5)]^{5/6}$ .

Fried's polynomial analysis revealed that the coefficients of the terms corresponding to wavefront tilt (image motion) were much larger than those corresponding to defocus and aberrations. Since these terms are mean square errors which are simply proportional to  $(D/r_o)^{5/3}$ , the convergence of the coefficients is a general property which parallels that of the optical aberration function or that arising out of the Saint-Venant principle in elasticity (see § 3.4 and § 3.5). Fried pointed out that the phase structure function corresponding to tilt depends on  $r^2 = r^{6/3}$ , instead of the  $r^{5/3}$  dependence of (5.44), leading to Gaussian behaviour. This is further discussed in § 5.1.2.4 in connection with Tatarski's equation (5.43).

In 1966, Fried [5.13] gave a similar treatment of the subject in terms of the Fourier transform of the star image, the Optical Transfer Function (OTF) discussed in RTO I, § 3.10.7, an approach first used by Hufnagel and Stanley [5.9]. Roddier [5.16] derives the fundamental result, for long-exposure images, that

$$L(\vec{s}) = B(\vec{s}) \cdot T(\vec{s}) , \quad (5.47)$$

where  $\vec{s}$  is the frequency,  $L(\vec{s})$  the normalized OTF of the total system,  $T(\vec{s})$  the OTF of the telescope (in RTO I, § 3.10.7) and  $B(\vec{s})$  is the atmospheric OTF which is equal to the coherence function, equivalent to (5.40). Equation

(5.47) is simply the normal multiplicative property of the OTF arising out of Eq. (3.505) in RTO I.

Fried introduced the concept of characterising the effect of atmospheric turbulence in terms of the Strehl ratio (see RTO I, § 3.10.5). In Chap. 4 we saw the significance of the Central Intensity Ratio, equivalent to the Strehl ratio but including atmospheric turbulence, for deriving optical tolerances for telescopes. The Strehl ratio can be derived from the time-averaged MTF as the integral over that function for the whole spatial frequency range, relative to the diffraction limited case (RTO I, § 3.10.7) [5.22]. Fried terms this MTF integral the “resolution”  $\underline{R}$ . We shall see below that it is in close agreement with the classical definition of resolution, or resolving power, based on the radius of the Airy disk. This quality definition is also analogous to the bandwidth in electronics. Following Roddier [5.16], the results of this treatment can be summarised as follows. The angular resolution is

$$\underline{R} = \int B(\vec{s}) T(\vec{s}) d\vec{s} \quad (5.48)$$

For a small, diffraction-limited telescope of diameter  $D$ , the turbulence effects of  $B(\vec{s})$  are negligible.  $T(\vec{s})$  is the same function as Eq. (3.501) in RTO I and the integral gives for  $\underline{R}_d$ , limited by diffraction only

$$\underline{R}_d = \int T(\vec{s}) d\vec{s} = \frac{\pi}{4} \left( \frac{D}{\lambda} \right)^2 \quad (5.49)$$

For an infinitely large telescope, the effect of diffraction is negligible and we have

$$\underline{R}_\infty = \int B(\vec{s}) d\vec{s} \quad (5.50)$$

From (5.36) or (5.40) we have

$$B(\vec{s}) = B_o(\lambda \vec{s}) = \exp -K s^{5/3} \quad (5.51)$$

where  $K$  defines the seeing conditions contained in (5.36) and  $s = |\vec{s}|$ . Integration gives

$$\underline{R}_\infty = (6\pi/5) \Gamma(6/5) K^{-6/5} , \quad (5.52)$$

where  $\Gamma$  is the gamma function. Fried’s parameter  $r_o$  is now introduced according to the definition

$$\int B_{r_o}(\vec{s}) d\vec{s} = \int T_{r_o}(\vec{s}) d\vec{s} , \quad (5.53)$$

which means that the asymptotes to the long-exposure curve A of Fig. 5.3 meet at  $D/r_o = 1$ . Setting  $D = r_o$  in (5.49) and equating it with (5.52) leads to

$$K = [(24/5)\Gamma(6/5)]^{5/6} (r_o/\lambda)^{-5/3} = 3.44(r_o/\lambda)^{-5/3} \quad (5.54)$$

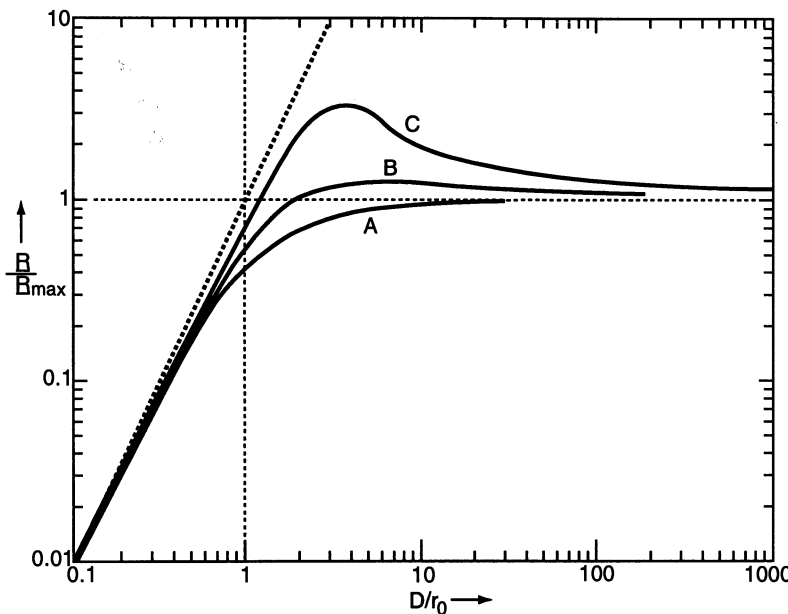


**Fig. 5.3.** Dependence of normalized resolution  $\underline{R}/\underline{R}_{max}$  on normalized telescope diameter  $D/r_o$ . *Curve A* for the long-exposure image. *Curve B* for averaged short exposures (ASE) “far-field” results. *Curve C* for averaged short exposures (ASE) “near-field” results. (After Fried [5.13])

Substitution of (5.54) in (5.51) gives

$$B(\vec{s}) = \exp -3.44(\lambda s/r_o)^{5/3} \quad (5.55)$$

or

$$B_o(\vec{\xi}) = \exp -3.44(\xi/r_o)^{5/3} \quad (5.56)$$

For uniformity of nomenclature with  $r_o$ , this can also be written in the one-dimensional Fried form

$$B_o(r) = \exp -3.44(r/r_o)^{5/3} \quad (5.57)$$

From (5.52) and (5.54), the limiting resolution for an infinitely large telescope is  $\underline{R}_{max} \equiv \underline{R}_\infty$  and is given by

$$\underline{R}_{max} = \underline{R}_\infty = \frac{\pi}{4} \left( \frac{r_o}{\lambda} \right)^2 , \quad (5.58)$$

in agreement with (5.49) and as given by Fried except that he uses the form of cycles squared per unit area in the focal plane by converting angular measure with the focal length of the telescope.

Figure 5.3 summarises the results derived by Fried [5.13], both for the long-exposure and the averaged short-exposure cases. Curve A is for the long-exposure case and shows the asymptotic convergence of  $\underline{R}$  to  $\underline{R}_{max}$  with

$D/r_o \rightarrow \infty$  and the intersection of the asymptotes at coordinates  $\underline{R}/\underline{R}_{max} = D/r_o = 1$  following the definitions of (5.53) and (5.54). The averaged short-exposure cases of curves B and C will be discussed in the next section. The complete integral function of the MTF to give curve A for the long-exposure (LE) case, corresponding to (5.48), is given by Fried as

$$\begin{aligned} \underline{R}_{LE} = & \frac{4D^2}{\lambda f} \int_0^1 u \, du \left[ \cos^{-1} u - u(1-u^2)^{1/2} \right] \\ & \times \exp \left[ -3.44 \left( \frac{D}{r_o} \right)^{5/3} u^{5/3} \right], \end{aligned} \quad (5.59)$$

in which  $f$  is the telescope focal length and  $u = r/D$ . The first part gives the diffraction effect (see Eq. (3.501) in RTO I) and the exponential term the atmospheric effect. This is the equivalent of  $\int L(\vec{s}) \, d\vec{s}$  from (5.47).

If we now equate (5.40) and (5.56), we can derive the relation between the Fried parameter  $r_o$  and the square of the refractive index structure constant  $C_n^2(h)$  as

$$r_o = \left[ 0.423k^2(\cos Z)^{-1} \int C_n^2(h) \, dh \right]^{-3/5}, \quad (5.60)$$

with  $k = 2\pi/\lambda$ . The dependence of  $r_o$  on the wavelength  $\lambda$  is therefore

$$r_o \propto (\lambda^{-2})^{-3/5} \propto \lambda^{6/5}, \quad (5.61)$$

a result of great importance which has been confirmed experimentally [5.16] [5.23] [5.24]. Since the limiting resolution  $\underline{R}_{max}$ , as defined by (5.58), depends on  $(r_o/\lambda)^2$ , it increases only as

$$\underline{R}_{max} \propto \lambda^{2/5} \quad (5.62)$$

Roddier [5.16] gives the normal limits of  $r_o$  (for zenith observations and  $\lambda \simeq 500$  nm) as about 2 cm and 20 cm. Fried and Mevers [5.14] analysed data from two major observatories supplied by Hoag and Meinel and gave a median value at  $\lambda = 550$  nm as  $r_o \simeq 11.4$  cm with a log-normal distribution and a one standard deviation factor of 1.36.

It should be noted from (5.60) that  $r_o$  reduces with the zenith angle  $Z$  according to

$$r_o \propto (\cos Z)^{3/5} \quad (5.63)$$

The relation between  $r_o$  and the angular seeing  $\omega$  in radians is defined by Roddier [5.16] as follows. We saw above that the Fried resolution  $\underline{R}$  was deduced from the integral of the MTF function (5.47) as

$$\underline{R} = \int L(\vec{s}) \, d\vec{s} \quad (5.64)$$

$L(\vec{s})$  is derived from the Fourier transform of the long-exposure illumination  $\langle I(\vec{\alpha}) \rangle$  in the PSF of the star image, where  $\alpha$  is the angular deviation from

the image center. The long-exposure (or “integrated”) seeing angle  $\omega$  is defined as *that angle which would contain the same total intensity as that of the actual image but assuming uniform illumination identical with the image center  $\langle I(\vec{\alpha}) \rangle$* . With this definition

$$\frac{\pi}{4}\omega^2 = \int \left[ \langle I(\vec{\alpha}) \rangle / \langle I(\vec{0}) \rangle \right] d\vec{\alpha} = 1/\underline{R} , \quad (5.65)$$

giving the angular *radius* of the equivalent uniform long-exposure seeing disk as

$$\omega = \left( \frac{4}{\pi \underline{R}} \right)^{1/2} \text{ rad} \quad (5.66)$$

For a small diffraction-limited telescope corresponding to the lower part of curve A in Fig. 5.3, we can insert  $\underline{R}_d$  from (5.49) giving

$$\omega_d = \frac{4}{\pi} \frac{\lambda}{D} = 1.273(\lambda/D) \quad (5.67)$$

This is very close to the classical definition of resolution based on the radius of the Airy disk and given in Eq. (3.446) in RTO I as  $1.22\lambda/D$ . Similarly, for an infinitely large telescope giving the maximum resolution  $\underline{R}_{max}$  limited only by atmospheric seeing, we have from (5.58) for the minimum seeing angle for the long-exposure image

$$\omega_{min} = \omega_\infty = \frac{4}{\pi} \frac{\lambda}{r_o} = 1.273(\lambda/r_o) \quad (5.68)$$

Referring to (5.60) and (5.61), we see from (5.68) that

$$\omega_{min} = \omega_\infty \propto \lambda^{-1/5} (\cos Z)^{-3/5} \quad (5.69)$$

This relation shows that although the gain with wavelength of  $r_o$  from (5.61) is slightly more than linear, the gain of *angular seeing* with wavelength is very weak: between visible light ( $\lambda = 0.5 \mu\text{m}$ ) and the thermal IR ( $\lambda = 16 \mu\text{m}$ ), the gain in  $\omega_{min}$  is only a factor of 2 whereas the gain in  $r_o$  is a factor of 64! This is the reason why Young [5.25] spoke of the supposed gain in seeing in the IR as “the Infrared Myth”. However, other gains, such as in isoplanatic angle, may be important. The  $(\cos Z)^{-3/5}$  dependence may be compared with Tatarski’s result for image motion alone given by (5.43), whereby a dependence  $(\cos Z)^{-1/2}$  was derived in accordance with Krasilnikov [5.26]. The difference to the power  $-3/5$  is small. Separation of image motion is of importance for short-exposure imaging which we consider below.

The angular long-exposure seeing disk (in arcsec) is the normal way of considering the practical significance of the quantity  $\omega$  from (5.66) (and for  $\omega_d$  and  $\omega_{min}$ ) in relation to the measures currently used. The theoretical profile, being a symmetrical function, can be calculated by taking the Hankel transform of (5.40). Table 5.1 gives results for  $r_o = 10 \text{ cm}$  calculated by Kadiri [5.27] and given by Roddier [5.16]. Since the profile is a result of the Fourier transform of (5.40) which contains the Obukhov 5/3 power in the exponential,

**Table 5.1.** Theoretical profile of the long-exposure atmospheric PSF obtained from the Hankel transform of Eq. (5.40) for  $r_o = 10$  cm and  $\Delta\alpha = 0.16$  arcsec (after Kadiri [5.27] and Roddier [5.16])

$\alpha/\Delta\alpha$	$I(\alpha)/I(0)$	$\alpha/\Delta\alpha$	$I(\alpha)/I(0)$
0	1.00000	18	0.00083
1	0.92893	19	0.00067
2	0.74724	20	0.00055
3	0.52615	21	0.00045
4	0.33039	22	0.00038
5	0.19005	23	0.00032
6	0.10364	24	0.00027
7	0.05567	25	0.00023
8	0.03052	26	0.00020
9	0.01751	27	0.00018
10	0.01062	28	0.00016
11	0.00681	29	0.00014
12	0.00459	30	0.00012
13	0.00322	31	0.00011
14	0.00234	32	0.00010
15	0.00175	33	0.00009
16	0.00134	34	0.00008
17	0.00104	35	0.00007

the intensity distribution is *not* Gaussian since this would require a power  $2 = 6/3$ . However, the difference in power is modest, giving an image “core” which approximates closely to a Gaussian function, down to intensity values of the order of a few percent [5.16] [5.28]. The subsequent fall-off in the wings is less steep than that of a Gaussian function. Experimental results are found to be entirely consistent with the  $5/3$  power law [5.16].

The PSF of a long-exposure star image in a perfect telescope includes the effect of diffraction. It is therefore formally impossible to form an rms value of the angular distribution, since this is equal to the standard deviation which is infinite, as it is for the diffraction effect forming the Airy pattern (Fig. 3.102 of RTO I).

The natural angular measure of seeing which is normal practice with astronomical telescopes is the diameter corresponding to the Full Width Half Maximum (FWHM), denoted in Chap. 4 by  $d_{FWHM}$ . This can be deduced from Table 5.1 and gives a result very close to the value given to high accuracy by Dierickx [5.29] from the relation

$$(d_a)_{FWHM} = (0.975\,863)(\lambda/r_o) , \quad (5.70)$$

where  $d_a$  refers to the atmospheric turbulence alone. Dierickx also gives relations enabling the encircled energy to be calculated to high accuracy (up to values of encircled energy over 90 %). A commonly used value is  $d_{80}$  (Chap. 4), for which Dierickx gives

$$(d_a)_{80} = (1.847\,934)(\lambda/r_o) \quad (5.71)$$

We see that the ratio  $(d_a)_{80}/(d_a)_{FWHM}$  is 1.894 whereas it is about 1.5 for a Gaussian distribution. Applying the factor ca. 1.9 from the FWHM width from Table 5.1, we see that there are already marked discrepancies in the encircled energy from the Gaussian case even for diameter cut-offs with  $I(\alpha)$  between 5 and 10 %. An approximate Gaussian fit for the core must therefore be treated with considerable caution. If such a Gaussian is taken, then  $(d_a)_{68.3}$  corresponds to the standard deviation  $\sigma$  and is thus a crude approximation to a  $(d_a)_{rms}$  value, a term used by some authors [5.25].

Since from (5.68) we have  $\omega_{min} = \frac{4}{\pi}(\lambda/r_o)$ , the various measures of angular seeing can be compared directly, as shown in Table 5.2. From Table 5.1, it is seen that  $2\omega_{min}$  corresponds to an intensity value at the cut-off of < 3 %. The corresponding enclosed energy is 90.8 %.

**Table 5.2.** Relation between the angular measure of the diameter of the long-exposure atmospheric PSF given by Roddier (2  $w_{min}$ ) and commonly used measures (after Dierickx [5.29] and private communication)

Units	$2\omega_{min}$ Eq. (5.68)	$(d_a)_{FWHM}$ Eq. (5.70)	$(d_a)_{80}$ Eq. (5.71)	$(d_a)_{68.3}$ (ca. $(d_a)_{rms}$ for a Gaussian approximation)
$2\omega_{min}$	1	0.384	0.727	0.583
$\lambda/r_o$	$8/\pi$ $= 2.546$	0.976	1.848	1.485
Encircled energy (%)	90.8	42.2	80	68.3
Arcsec for $r_o = 250$ mm, $\lambda = 500$ nm	1.050	0.403	0.763	0.613

**5.1.2.4 Short-exposure images.** We saw in the previous section that both Tatarski [5.8] (Eq. (5.43)) and Fried [5.12] made important deductions concerning the characteristics of the “image motion” (wavefront tilt) term of atmospheric seeing. In his MTF treatment, Fried [5.13] deduced expressions for the “resolution”  $R_{LE}$ , the case for the long-exposure image (LE) being given by (5.59). He also deduced equivalent expressions for the *averaged short-exposure* (ASE) case, assuming a negligible exposure time which is then averaged to give the average resolution designated by  $\underline{R}_o$ . The meaning of the ASE case is that the *image motion part* of the long-exposure (LE) atmospheric turbulence is removed, leaving only the focus and aberration terms of Fried’s polynomial [5.12], since it no longer affects the sharpness of the PSF, only its position. The ASE case is divided into two sub-cases, the *near-field* case and the *far-field* case, characterized by  $D \gg (L\lambda)^{1/2}$  and  $D \ll (L\lambda)^{1/2}$  respectively. In each case, a further term is multiplied into the exponential term of (5.59): in the near-field case  $(1-u^{1/3})$ , in the far-field case  $(1-\frac{1}{2}u^{1/3})$ , where  $u = r/D$ . The resulting ASE functions  $(\underline{R}_o)_{FF}$  and  $(\underline{R}_o)_{NF}$  are shown

in Fig. 5.3 as curves B and C for the far-field and near-field cases respectively. For the long-exposure MTF, there is no distinction between the near-field and far-field cases, giving the single equation (5.59).

The practical significance of the *ASE case* is that the removal of the image motion term gives a gain in resolution as shown by curves B and C compared with A. This effect has been known for a very long time in astronomy, principally from the better maximum resolution obtainable visually compared with photographic integration. The effect of image motion on the *long-exposure* (LE) case can be removed by fast automatic guiding, if the technical means to do this are available. The residual image degradation is termed “blurring”. The term “blurring” without image motion can be applied to both the short-exposure case and the long-exposure case.

A complete treatment of “angle-of-arrival fluctuations” (as “image motion” is more rigorously termed in the developments following Kolmogorov’s law) and averaged short-exposure images (ASE) is given by Roddier [5.16]. He derives the Tatarski law of image motion of (5.43) in the later form given by Tatarski [5.30] for a circular telescope aperture and by Fried [5.13] as

$$\sigma_m^2 \simeq \left( \frac{3.44}{\pi^2} \right) \lambda^2 D^{-1/3} r_o^{-5/3} \simeq 0.36 \left( \frac{\lambda}{D} \right)^{1/3} \left( \frac{\lambda}{r_o} \right)^{5/3}, \quad (5.72)$$

whereby Tatarski points out that the correction compared with his simple derivation of (5.43) from two interferometer slits of separation  $b_i$  is only a factor 0.97 if we set  $b_i = D$ .

Equation (5.72) confirms that average  $\sigma_m$ , the rms averaged image motion, should decrease slowly with increasing telescope size, i.e. with  $D^{-1/6}$ , a result which seems at first sight in conflict with the limiting resolution of curve A in Fig. 5.3. But this is not the case, as is demonstrated by Roddier [5.16]. The deviation  $\vec{\alpha}'$  of the image from its average position has a Gaussian probability density

$$\underline{P}(\vec{\alpha}') = \frac{1}{\pi \sigma_m^2} \exp \left( -\frac{|\vec{\alpha}'|^2}{\sigma_m^2} \right) \quad (5.73)$$

Applying the same arguments to the improved long-exposure blurring (ASE), due to removal of image motion, as for the total long-exposure image represented by Eqs. (5.64) and (5.65), he shows the MTF as the Fourier transform of  $\underline{P}(\vec{\alpha}')$  is

$$\tilde{\underline{P}}(\vec{s}) = \exp -3.44(\lambda s/D)^{1/3} (\lambda s/\vec{r}_o)^{5/3}, \quad (5.74)$$

giving for the MTF of  $I_o(\vec{\alpha})$

$$\langle \tilde{I}_o(\vec{s}) \rangle = T(\vec{s}) \exp -3.44(\lambda s/\vec{r}_o)^{5/3} [1 - (\lambda s/D)^{1/3}], \quad (5.75)$$

the square bracket term at the end being the Fried “near-field” correction term mentioned above for the ASE case compared with the LE result for resolution of Eq. (5.59). The corresponding integral gives for the case of long-exposure blurring a resolution

$$\underline{R}_o = \int \tilde{I}_o(\vec{s}) \cdot d\vec{s} , \quad (5.76)$$

after removal of image motion. With the same argumentation as for Eqs. (5.65) and (5.66), we have for the ASE blurred image with image motion removed

$$\omega_o = \left( \frac{4}{\pi \underline{R}_o} \right)^{1/2} \text{ rad} \quad (5.77)$$

The normalized function  $\underline{R}_o$  is given from Fried [5.13] in Fig. 5.3 as curve C for the near field case. Fried also gives tabulated values of the function in logarithmic steps of  $D/r_o$ .

The averaged spread angle  $\omega_m$  for image motion is similarly defined from

$$\underline{R}_m = \int \tilde{P}(\vec{s}) \cdot d\vec{s} \quad (5.78)$$

as

$$\omega_m = \left( \frac{4}{\pi \underline{R}_m} \right)^{1/2} \text{ rad} = 2\sigma_m \quad (5.79)$$

Roddier [5.16] shows the relationship between  $\omega$ ,  $\omega_o$  and  $\omega_m$  in a very instructive form which is reproduced in Fig. 5.4, based on Fried's curves A and C in Fig. 5.3 which correspond to  $\omega$  and  $\omega_o$ . The line for  $\omega_m$  represents the  $D^{-1/6}$  dependence of averaged image motion expressed by (5.43) and (5.72) and shows how this is compensated by the function  $\omega_o$  to give the total effect  $\omega$ . This effect is also discussed by Young [5.25], but in terms of the assumption

$$\omega^2 = \omega_o^2 + \omega_m^2 + \omega_d^2 \quad (5.80)$$

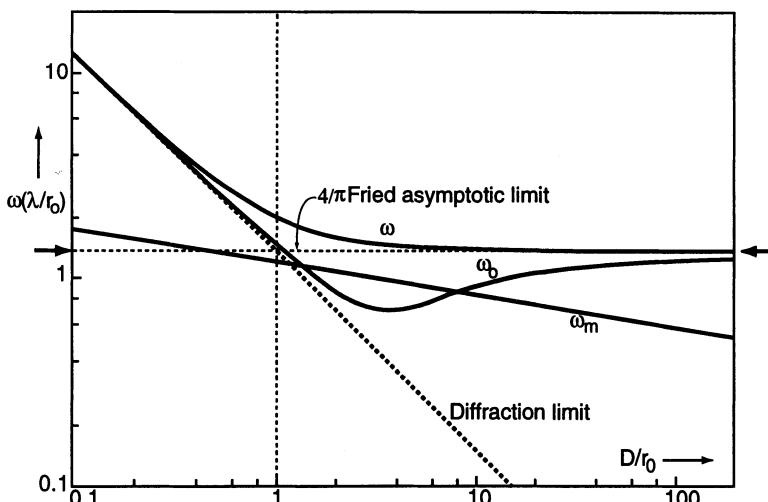


**Fig. 5.4.** Image motion  $\omega_m$ , “blurring”  $\omega_o$  and total “seeing”  $\omega$  in angular measure ( $\lambda/r_o$  units) for normal long exposures (after Roddier [5.16])

This assumption is often made as an approximation, but is not strictly correct, as Roddier points out, since the functions have infinite standard deviations.

The blurring function  $\omega_o$  has a minimum at  $D/r_o \simeq 3.7$ . For smaller values of  $D$ , diffraction is dominant, for larger values the turbulence is defined by  $r_o$ . For large values of  $D/r_o$ , the image motion is over-estimated according to Roddier because the outer scale of turbulence must be taken into account. Fig. 5.4 shows that the maximum gain in resolution due to image motion removal occurs at  $D/r_o \simeq 3$  and is of the order of a factor 2.

Young [5.25] comments that the normal subjective impression is that image motion is negligible for large telescopes, i.e. the PSF is governed entirely by a “speckle” regime. But according to the  $D^{-1/6}$  power law the  $\sigma_m$  of the 5 m Palomar telescope is still about half that of a 10 cm telescope. He points out that this impression may be due to the fact that the time frequencies of the motion are only about 0.2 Hz for the 5 m, but about 10 Hz for the 10 cm, the latter being much more noticeable to the eye.

Young also points out that the image motion  $\sigma_m$  is only correctable in practice in a long-exposure if the offset guider is able to work within the *isoplanatic angle*, the coherence angle, of  $\sigma_m$  at the time frequency of the correction. For a field of  $\pm 25$  arcsec, he gives a limit frequency of 1 Hz; for  $\pm 30$  arcmin a limit frequency of 1/60 Hz.

The isoplanatic angle of the functions  $\omega$  or  $\omega_o$  will, of course, be a fundamental aspect of adaptive optics (§ 5.2). The general theory is treated by Roddier [5.16].

The function  $\omega_o$  in Fig. 5.4 is based on the concept of short exposures but gives averaged results (ASE) with the purpose of establishing the gain from removal of image motion in long exposures. Genuine short exposures can also be used in a variety of post-detection techniques, including speckle interferometry, as discussed by Roddier [5.16]. A direct method of using short exposures is called *frame selection* and relies on chance to provide a high quality frame from many exposures. The probability of getting a high quality image has been investigated by Hufnagel [5.31] and Fried [5.15]. Fried derives a formal expression for the probability of obtaining a “good” SE image, the term “good” being defined by the limit for the rms phase wavefront distortion over the aperture as 1 rad:

$$\text{Prob} \simeq 5.6 \exp[-0.1557(D/r_o)^2] , \quad (5.81)$$

with the condition  $D/r_o \geq 3.5$ . It is thus applicable to all “large” telescopes, even at excellent sites. The probability according to (5.81) decreases very rapidly with increasing  $D/r_o$ : for 4 we have about 1 in 3 chance; for 5 about 1 in 10; for 6 about 1 in 50; for 7 about 1 in 300; for 10 about 1 in a million. The technique is above all interesting for solar astronomy using reduced apertures because of the bright source; or in the IR domain for large telescopes because of the increase of  $r_o$  with wavelength from Eq. (5.61).

**5.1.2.5 Seeing monitors and site selection.** Roddier's review paper [5.16] again gives an excellent summary of the situation up to 1981. Before the development of the Kolmogorov-Fried theory of the effect of atmospheric turbulence on the image, the experimental work on measurements of "seeing" lacked the necessary theoretical background. It is now universally accepted that the Fried parameter  $r_o$  is the best practical measure of seeing quality. Furthermore, "seeing" is not only the most difficult of the basic parameters characterizing a site to measure; it is also the most important. Reference was made above to early determinations by Fried and Mevers [5.14] of the value of  $r_o$  at good astronomical sites as about 11 cm. But more convenient methods of measurement were required.

Assuming image motion is negligible, Eq. (5.68) shows that  $r_o$  is of the order of  $\lambda/\omega$  if  $\lambda$  is set to about 0.5  $\mu\text{m}$ . But slow image motion (see the comments of Young above) can falsify the results as it is often not perceived. The most reliable method seems to be based on a measurement of image motion giving  $\sigma_m^2$  from which  $r_o$  is deduced from (5.72). But direct measurements of image motion are falsified by telescope vibrations. The fundamental solution to this problem was the *differential method* proposed by Stock and Keller in 1960 [5.32]. It is essentially a Hartmann screen test with only two apertures. This method has been developed further by Roddier [5.16]. Such a seeing monitor, termed DIMM (Differential Image Motion Monitor) has been built for the ESO VLT site-testing programme. The construction of the DIMM and results obtained with it are given by Sarazin et al. [5.33] [5.34] [5.35] [5.36]. It consists of a classical Cassegrain telescope with  $D = 350$  mm of compact construction ( $f/2.15$ ). The entrance pupil (at the primary) is transmitted by an achromat to a conjugate plane in which a pupil mask, containing the two Hartmann holes, is accurately placed. A prismatic beam splitter separates the beams via a camera objective to a CCD detector. A detailed description, together with the theoretical basis and data processing is given by Sarazin and Roddier [5.37]. In order to test the accuracy of the seeing measurements with the DIMM, it was mounted in 1988 [5.36] directly on the side of the prime mirror cell of the 2.2 m MPIA telescope at the ESO observatory at La Silla. The FWHM of the images of the 2.2 m telescope were measured directly. The two telescopes thus had the same dome seeing conditions. A correlation coefficient for the best linear fit of 0.97 was achieved [5.36] [5.37]. The instrument has been extremely successful and several copies have been built. In the normal mode of operation, a bright star is observed 2 hours before and 2 hours after the passage of the meridian. The variance of the differential movement is calculated from a series of 200 images with exposure time 10 ms, then converted into the FWHM equivalent every 2 minutes.

Another method of determining  $r_o$  is by *atmospheric soundings*, giving measurements of  $C_n^2$  as a function of  $h$  and hence  $r_o$  from (5.60). Such a technique is SODAR (SOund Detection and Ranging), described by Sarazin [5.33]. Roddier [5.16] gives a brief résumé. It is possible to combine soundings with image motion measurements. Roddier concludes that scintillation mea-

surements give the best results above 1 km; thermal sensors the best results near the ground; a sensitive image motion monitor the best results between ca. 25 m and 1 km. C. Roddier [5.38] has constructed a rotation interferometer which could be used for this purpose.

In conclusion, we can say that the activity starting with Kolmogorov, Tatarski and Fried was only slowly understood and adopted by the astronomical community, but that a veritable revolution has taken place since 1980. One of the consequences of the developments in atmospheric optics in general has been the burst of activity in adaptive optics.

## 5.2 Adaptive optics

### 5.2.1 Definitions and aims: active and adaptive optics

In § 3.5 we discussed the correction of “telescope errors” in the low temporal bandpass which, in agreement with Woolf [5.39], we termed the *active optics bandpass* [5.40]. This is the bandpass A of Fig. 3.62, extending from a time frequency  $(\nu_t)_{act}$  defined by  $0 \leq (\nu_t)_{act} \leq$  ca.  $(1/30)$  Hz for good atmospheric seeing conditions. The upper limit is, by definition, roughly the frequency at which the atmospheric or *adaptive optics bandpass* C starts, so that the latter is defined by ca.  $(1/50)$  Hz  $\leq (\nu_t)_{ad} < \nu_m$ , where  $\nu_m$  may be ca.  $10^3$  Hz or more. Table 3.11 listed the sources of error which can affect the quality of the telescope image: some of these (local air effects, wind-buffetting deformation of large thin mirrors, and tracking errors) can extend into the lower end of the adaptive bandpass. This overlap bandpass region was termed the *extended active optics bandpass B* and its significance discussed in § 3.5.4. The aim of the active optics systems discussed was to eliminate or, in practice, reduce to negligible amounts, the wavefront deformations (phase errors) for the active bandpass. If this aim is extended to the entire bandpass in the general form

$$\int_o^{\vec{r}_m} \int_o^{\nu_m} \int_{\lambda_1}^{\lambda_2} W(\vec{r}, t, \lambda) d\vec{r} dt d\lambda \leq (W_{rms})_{diff} , \quad (5.82)$$

where the function  $W(\vec{r}, t, \lambda)$  is a general phase error function over the aperture for the entire bandpass up to  $10^3$  Hz or more, and  $\lambda_1, \lambda_2$  define respectively the UV cut-off wavelength of the atmosphere (ca. 300 nm) and the wavelength at which the telescope becomes diffraction limited without correction.  $(W_{rms})_{diff}$  is some criterion based on the Strehl ratio, such as the Maréchal criterion of Eq. (3.470) in RTO I, defining the image quality as effectively diffraction limited. If the aim of (5.82) could be achieved, all the errors of Table 3.11 would be effectively corrected: apart from photon losses in the correction system, the errors plaguing the image quality of the ground-based telescope since its invention in 1610 would all be removed. Apart from the inevitable atmospheric absorption and the technically-induced photon losses,

the ground-based telescope would be the equivalent of a space telescope with perfect active optics correction.

In spite of remarkable progress in the last twenty years and pioneer thinking going back to Babcock in 1953 [5.41], the current situation (1997) is still a very long way from a complete solution according to (5.82). As we saw in § 3.5, active optics is capable of fulfilling the requirements in the bandpass A from the point of view of elasticity effects, and progress has been made in bandpass B. In the adaptive bandpass C, impressive results have been obtained in the IR for a limited temporal bandpass. But a general solution for the higher temporal frequencies and above all at visible wavelengths near  $\lambda_1$  in (5.82) is still not available.

In fact, even Eq. (5.82) does not cover the full theoretical formal requirements as far as the atmosphere is concerned. Fried [5.13] pointed out in 1966 that the stellar image is not only affected by the wavefront errors  $W$  but also by intensity variations across the wavefront due to *scintillation*, which we can consider as a form of random apodisation [5.42] over the aperture. This is considered further by Fried in a later paper [5.43]. Atmospheric turbulence produces a complex phase shift of the two-dimensional vector  $\vec{r}$

$$\phi(\vec{r}, t) - i l(\vec{r}, t) , \quad (5.83)$$

where the real part  $\phi(\vec{r}, t)$  represents the phase shift of the wavefront which we call “atmospheric seeing”, while the imaginary part  $l(\vec{r}, t)$  is a logarithmic measure of the intensity variation across the aperture plane, called the *scintillation*. The theory of scintillation is also treated by Tatarski [5.8] and Roddier [5.16]. Fried [5.43] considers the theoretical requirements regarding anisoplanatism (coherence errors with field) for both a limited (real part only) and general adaptive optics system. In practice, a random apodisation correction would be a further major complication to a technical problem which is already immensely complex: current attempts are only concerned with the real part correction of the wavefront, as indicated in (5.82).

There are five fundamental differences between active and adaptive optics as defined above, as discussed by Wilson et al. [5.40] and by Merkle [5.44]:

- The temporal bandpass for adaptive optics is far higher, as shown in Fig. 3.62.
- The field of phase coherence is unlimited for active optics but severely limited to the so-called *isoplanatic angle* for adaptive optics.
- The dynamic range of correction, i.e. the range of values of  $W$  to be corrected, is far higher for active optics than for adaptive optics. This is due to the normal convergence of amplitude with frequency, both spatial and temporal.
- The physics of active optics is essentially based on elasticity theory, i.e. physics of solid bodies, whereas the physics of the atmosphere is that of a gas and is far more complex. Optimum algorithms for correction may not be the same.

- e) Because of the limited isoplanatic angle, it is convenient and logical to perform the correction in adaptive optics at the transferred pupil. Active optics, on the other hand, can best be performed at or near the telescope entrance or exit pupil. This not only gives correction of variable effects over the whole telescope field but also causes no loss of photons, whereas some loss is inevitable in a transferred pupil device. The significance of the small isoplanatic field for the use of the transferred pupil is shown in Fig. 5.5. Since the isoplanatic field is very small, the additional size due to this transmitted field for the diameter of the optical elements Col and Cam is very small compared with that determined by the aperture. The correcting element Cor can therefore be made small and light, suitable for high frequency operation with relatively small dynamic range. The transferred pupil position can also be chosen to be conjugate with a plane other than the telescope entrance pupil.

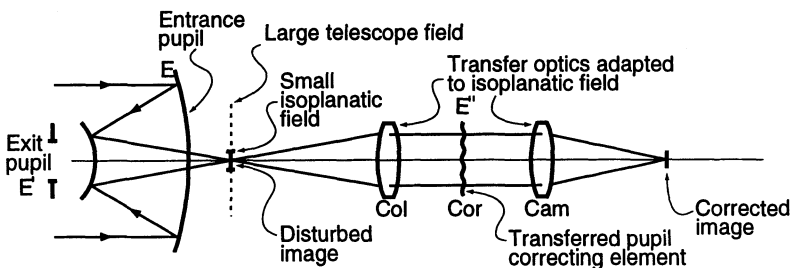


**Fig. 5.5.** Principle of transferred pupil technique for adaptive optics based on the small isoplanatic field (from Wilson et al. [5.40])

### 5.2.2 The principles of adaptive optics

Many accounts exist in the literature. We shall refer here above all to the works of Merkle [5.44] and Roddier [5.16] [5.45].

The element Cor in Fig. 5.5 is shown for simplicity as a transmission element. In practice, however, all schemes proposed use a deformable mirror in a closed-loop control system of the sort shown in Fig. 5.6. The surface of the adaptive mirror is adjusted in real time to correct  $\phi(\vec{r}, t)$  of (5.83). The beamsplitter, or beam selector within the isoplanatic angle, deflects the beam from a suitable star (or artificial reference star) to the wavefront sensor (image analyser). As in active optics, the wavefront error is determined and compensation information sent to the adaptive mirror to achieve the spatial and temporal correction function

$$\phi(\vec{r}, t) = \sum_{n=1}^N a_n(t) f_n(\vec{r}) \quad (5.84)$$

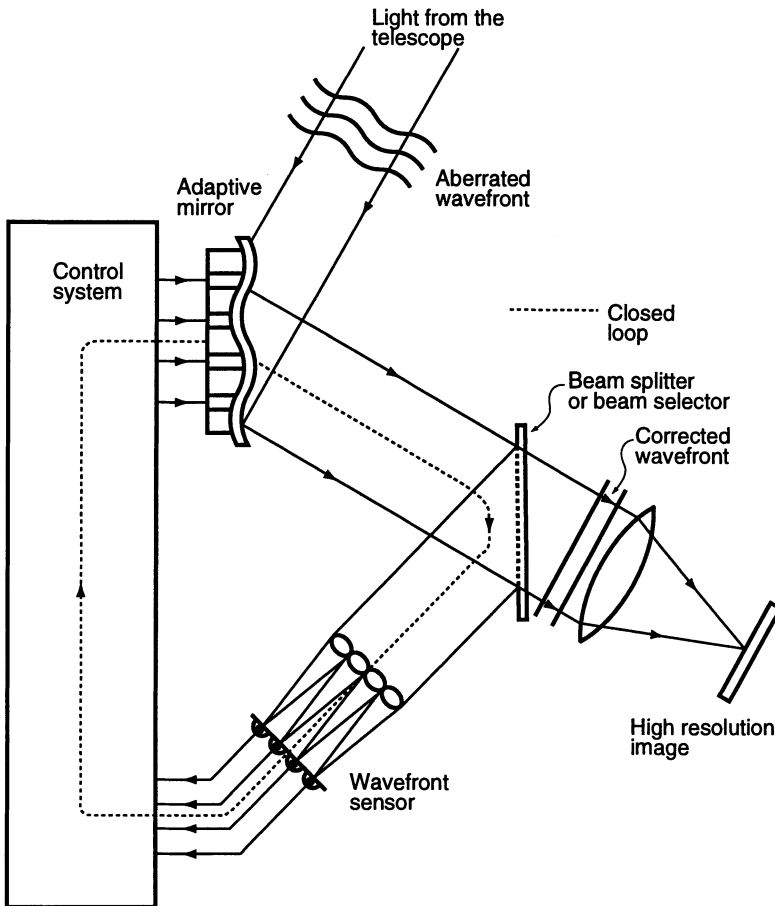


**Fig. 5.6.** Principle of adaptive optics in astronomy using an adaptive mirror (after Merkle [5.44])

The spatial function  $f_n(\vec{r})$  can, in principle, be a zonal or modal function of the aperture, but a modal function (again as with active optics) is advantageous in all respects.

The atmospheric parameters which are determinant for the design of the adaptive system are the refractive index structure constant  $C_n$  (Eq. (5.40)) and the associated Fried parameter  $r_o$  (Eq. (5.60)), together with the isoplanatic angle  $\theta_o$ . According to (5.60), we have for the zenith with  $Z = 0$

$$r_o = \left[ 0.423k^2 \int C_n^2(h) dh \right]^{-3/5}, \quad (5.85)$$

where  $k = 2\pi/\lambda$  gives the dependence on  $\lambda^{6/5}$ . From (5.70) and Table 5.2, we saw that the image size  $(d_a)_{FWHM} \simeq \lambda/r_o$  for pure seeing. The broad nature of the function  $C_n^2(h)$ , with dimensions  $m^{-2/3}$ , was given by Fried [5.43] and

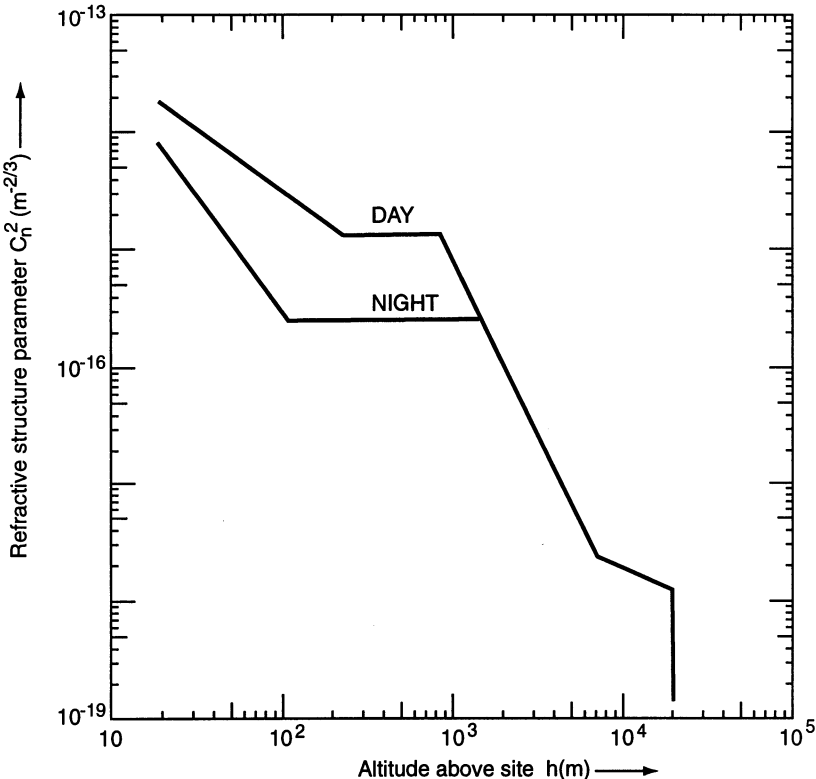


Fig. 5.7. Vertical distribution of the square of the refractive index structure constant  $C_n^2$  (from Fried [5.43])

is shown in Fig. 5.7. The night-time function is the one required for stellar astronomy, the daytime function for solar astronomy. For  $h >$  ca. 1 km the two functions are identical.

The spatial sampling over the pupil for the wavefront sensing will depend essentially on the number of speckles  $N_{sp}$  in the image which depends on the coherence area  $\sigma$  [5.16] and is given by Roddier [5.45] as

$$N_{sp} = \frac{\pi D^2/4}{\sigma} = 2.3(D/r_o)^2 \quad (5.86)$$

The necessary number of sub-apertures  $N$  to achieve a certain Strehl ratio  $S$  has been given by Brown [5.46] [5.44] as

$$N = \frac{(0.051 k^2 C_n^2 R D^{5/3})^{6/5}}{\ln(1/S)}, \quad (5.87)$$

where  $R$  is the height of the atmosphere for the path concerned. According to Merkle [5.44] this can be simplified to

$$N \simeq (D/r_o)^2 \quad (5.88)$$

and is therefore directly proportional to  $N_{sp}$ . Merkle gives graphical representations of the rapid fall-off in Strehl ratio obtained if the sub-apertures are inadequately sampled by the actuators of the adaptive mirror or if the temporal cut-off frequency is too low. Since  $N \propto r_o^{-2}$  it follows from (5.61) and (5.63) that  $N \propto \lambda^{-12/5}$  and  $(\cos Z)^{-6/5}$ .

The temporal function of the wavefront is determined by the so-called correlation time or speckle lifetime given by Roddier [5.45] for full aperture applications such as adaptive optics or speckle interferometry as

$$\tau \simeq r_o / \Delta v , \quad (5.89)$$

where  $\Delta v$  is the standard deviation of the wind velocities weighted by  $C_n^2$ . Typical lifetimes in the visible are given by Roddier as ranging from about 3 to 30 ms, in agreement with the exposure time for speckle interferometers using TV cameras. From (5.89), taking  $r_o = 10$  cm gives  $\Delta v \simeq 5$  m/s. Since  $\tau$  is directly proportional to  $r_o$  it has the same dependence as  $\lambda^{6/5}$  and  $(\cos Z)^{3/5}$ . If we take 3 ms as a limit for the shortest lifetime, the maximum correction frequency  $\nu = 1/\tau$  required is about 330 Hz.

Merkle [5.44] gives the dynamic (correction) range required for the actuators as

$$\Delta z \propto \lambda (d_{sa}/r_o)^{5/6} , \quad (5.90)$$

where  $d_{sa}$  is the diameter of the sub-apertures selected for correction, a relation deriving from an equation given by Roddier [5.16] for the standard deviation  $\sigma_z$  of the optical path difference. From (5.61) it follows that  $\Delta z$  is independent of  $\lambda$ . For the 8 m telescopes of the ESO VLT, the dynamic range  $\Delta z \simeq \pm 12.5 \mu\text{m}$ .

The final parameter of fundamental importance is the *isoplanatic angle*  $\theta_o$ . Fried [5.46] first derived an expression for this in 1979 and dealt later [5.43] with the general effect of anisoplanatism in adaptive optics systems. This definition is also given by Roddier [5.16] and by Loos and Hogge [5.47], who carried out practical measurements of  $\theta_o$ . The parameter  $H_o$ , a measure of the height dispersion of turbulence layers and termed the “atmospheric scaling height” by Loos and Hogge is defined, following Fried [5.46], by

$$H_o = \left[ \frac{\int C_n^2(h) h^{5/3} dh}{\int C_n^2(h) dh} \right]^{3/5} \quad (5.91)$$

From (5.60) we have

$$r_o = \left[ 0.423 k^2 (\cos Z)^{-1} \int C_n^2(h) dh \right]^{-3/5} , \quad (5.92)$$

which leads for the normal case where  $D \gg r_o$  to the definition of the isoplanatic angle as

$$\theta_o = 0.314 r_o \cos Z / H_o \quad (5.93)$$

This definition by Fried is based on the average antenna gain of an adaptive optics laser transmitter and gives the *radius* of the isoplanatic patch from the central point to an angle at which the antenna gain falls to  $1/e$ . Substituting (5.92) in (5.91) gives the form

$$\left. \begin{aligned} \theta_o &= \left[ 2.905k^2(\cos Z)^{-1} \int C_n^2(h)h^{5/3} dh \right]^{-3/5} \text{ rad} \\ \text{or } \theta_o &= (0.528) \left[ k^2(\cos Z)^{-1} \int C_n^2(h)h^{5/3} dh \right]^{-3/5} \text{ rad} \end{aligned} \right\} \quad (5.94)$$

for the *radius* of the isoplanatic angle. With this definition, the *angular diameter*  $\Theta$  of the *isoplanatic patch* is given by

$$\Theta = 2\theta_o = (1.056) \left[ k^2(\cos Z)^{-1} \int C_n^2(h)h^{5/3} dh \right]^{-3/5} \text{ rad} \quad (5.95)$$

With a somewhat stricter definition of coherence, Merkle [5.44] gives a relation equivalent to

$$\Theta = (0.800) \left[ k^2(\cos Z)^{-1} \int C_n^2(h)h^{5/3} dh \right]^{-3/5} \text{ rad} \quad (5.96)$$

From (5.93) and (5.61)

$$\Theta \propto \lambda^{6/5} \quad \text{and} \quad \Theta \propto (\cos Z)^{8/5} \quad (5.97)$$

Measurements by Loos and Hogge [5.47] give values of  $\Theta$  with their definition of (5.95) varying from about 6 arcsec to about  $1\frac{1}{2}$  arcsec for  $\lambda = 0.5 \mu\text{m}$ . They found a close inverse correlation with the variance of the log amplitude of the scintillation and suggest that  $\theta_o$  could be measured directly by measuring the scintillation over a 10 cm aperture.

Apart from the dynamic range  $\Delta z$ , we see that all the basic parameters for adaptive optics relax rapidly with increasing wavelength  $\lambda$ . The significance is summed up, following Merkle, in Table 5.3. This table shows clearly the huge technical advantage in initiating adaptive optics in the IR. Following Roddier [5.45], Table 5.4 lists the dependence of the most important adaptive optics parameters on  $\lambda$  and  $\cos Z$ .

**Table 5.3.** Simplification of the basic parameters of adaptive optics at longer wavelengths (after Merkle [5.44])

$\lambda$ ( $\mu\text{m}$ )	0.5	2.2	5.0	10.0
$r_o$ (cm)	10	59	158	364
$N$	6400	183	25	5
$\tau$ (ms)	6	36	95	218
$\Theta$ (arcsec)	1.8	11	29	66
$\Delta z$ ( $\mu\text{m}$ )	$\pm 12.5$	$\pm 12.5$	$\pm 12.5$	$\pm 12.5$

**Table 5.4.** Basic parameters for adaptive optics and their dependence on  $\lambda$  and  $\cos Z$  (after Roddier [5.45])

Parameter	Dependence on wavelength $\lambda$	Dependence on zenith angle $\cos Z$
Fried parameter $r_o$	$\lambda^{6/5}$	$(\cos Z)^{3/5}$
Angular seeing $\omega$	$\lambda^{-1/5}$	$(\cos Z)^{-3/5}$
Coherence area $\sigma$	$\lambda^{12/5}$	$(\cos Z)^{6/5}$
Number speckles $N_{sp}$	$\lambda^{-12/5}$	$(\cos Z)^{-6/5}$
Number of degrees of freedom $N$	$\lambda^{-12/5}$	$(\cos Z)^{-6/5}$
Speckle lifetime $\tau$	$\lambda^{6/5}$	$(\cos Z)^{3/5}$
Isoplanatic angle $\Theta$	$\lambda^{6/5}$	$(\cos Z)^{8/5}$
Dynamic (correction) range $\Delta z$	$\lambda^0$	$(\cos Z)^{-1/2}$

With regard to the size of the isoplanatic patch  $\Theta$ , Roddier [5.45] points out that the effective value can be increased by a reduction of  $H_o$  in (5.93) achieved by placing the adaptive mirror at a plane conjugate with some height  $h$  above the telescope representing the center of gravity of the turbulence layers. This could be deduced from Fig. 5.7. If the entrance pupil were then defined as being at, say  $h \simeq 240$  m, the resulting vignetting at the telescope may be acceptable for the modest isoplanatic fields achievable, but there will be insuperable optical problems arising from the final pupil image position in large Cassegrain telescopes. Consider the case of an 8 m ESO VLT telescope with  $f = 120$  m. The second principal plane (see Chap. 2 in RTO I) will then be 120 m from the Nasmyth image plane, in front of the telescope. For any optical system, the minimum distance between a real object and image is  $4f + PP'$ , where  $PP'$  is the separation of the principal planes, giving magnification  $m = -1$ . From Newton's law of conjugate shifts (Eq. 2.3 in RTO I)), the position of the pupil image would, in this case, be at a distance  $f = 120$  m beyond the normal focus and its diameter 8 m! But a height  $h \simeq 240$  m would mean the entrance pupil would only be about  $f$  from the principal plane, so its image would be roughly at infinity. A value  $h \simeq 360$  m would be necessary to give  $m = -1$ . From Newton's law, a value  $h \simeq 2f + nf$  would give a pupil image shifted from the normal image by  $f/n$ . Clearly  $n$  would have to be quite large to give an acceptable pupil position and size. With  $n = 8$  the height  $h \simeq 10f = 1200$  m for the VLT. Of course, the supplementary collimator of the adaptive system (see Fig. 5.5) gives freedom in positioning the final pupil image, but the collimator has to be large enough to accept the rays forming the pupil image.

### 5.2.3 Practical systems for adaptive optics in astronomical telescopes

The pioneer work of Babcock [5.41] in 1953 proposed the detection of the seeing errors by a rotating knife-edge (Schlieren) system operating on the

transferred image using an image orthicon detector. The adaptive mirror element (Fig. 5.6) consisted of an “Eidophor”, a device invented for projection television and permitting wavefront correction by the effect of a modulated electric charge on the thickness of a thin layer of oil covering a mirror. No information was given on results of a practical system operating on this basis.

The first practical results in astronomy were reported by Buffington et al. in 1977 [5.48] using a specially developed “image-sharpening telescope” of modest aperture. The 30 cm aperture telescope was masked to 30 cm  $\times$  5 cm aperture to reduce the number of correcting elements, which were six mirrors adjustable in wavefront phase (piston) by piezoelectric supports. The bandwidth was about 20 Hz. First tests were made with both laser and white light objects through 250 m of turbulent atmosphere and achieved essentially diffraction-limited performance with objects as faint as 5<sup>m</sup>.

Mounted equatorially at Lick Observatory, this telescope converted a FWHM of inferior seeing (ca. 4½ arcsec) to about 1 arcsec. With additional “gating”, whereby only the best 5–10 % of the imaging light beam was accepted for correction, a FWHM of about 0.6 arcsec was achieved compared with a value of 0.4 arcsec from diffraction.

Pioneering work was also carried out by Hardy [5.49], who developed adaptive systems for both military and astronomical applications. He pointed out clearly the logic of applying active optics in the general sense, namely for low frequency telescope errors using a segmented actively-controlled primary, and also for the partial correction of the higher frequency atmospheric turbulence errors using a transferred pupil with a small flexible adaptive mirror.

Since then, many groups have been active, both for stellar and solar astronomy [5.44]. As a typical project with notable success, we shall refer here mainly to the adaptive system developed for the ESO VLT by a collaboration of ESO with groups in France at CGE, Observatoire de Meudon and ONERA [5.50].

An important aspect of the strategy of any adaptive optics system is the algorithm for the correction. This was discussed in § 3.5 in connection with low temporal frequency active optics: it was shown that a classical matrix inversion using zonal information over a circular or rectangular raster leads to serious problems of convergence from ill-conditioned matrices. The same applies to adaptive optics. In fact, image analysers and adaptive mirrors will almost always function zonally; but this does not imply that the correction algorithm must also be zonal. It is far more effective to use *modal* correction, which allows the correction, essentially, of a relatively small number of orthogonal functions. Even a very limited number of modes can bring a substantial gain. The classical analysis by Fried [5.12] in 1965 was already a modal treatment using a very small number of modes. The level of effectiveness was demonstrated by Wang [5.51], as shown in Fig. 5.8. In an important paper, Noll [5.52] analysed the applicability of Zernike polynomials to the atmospheric function and found that they permit an analytical evaluation of the residual wavefront error for any number of independent corrections.

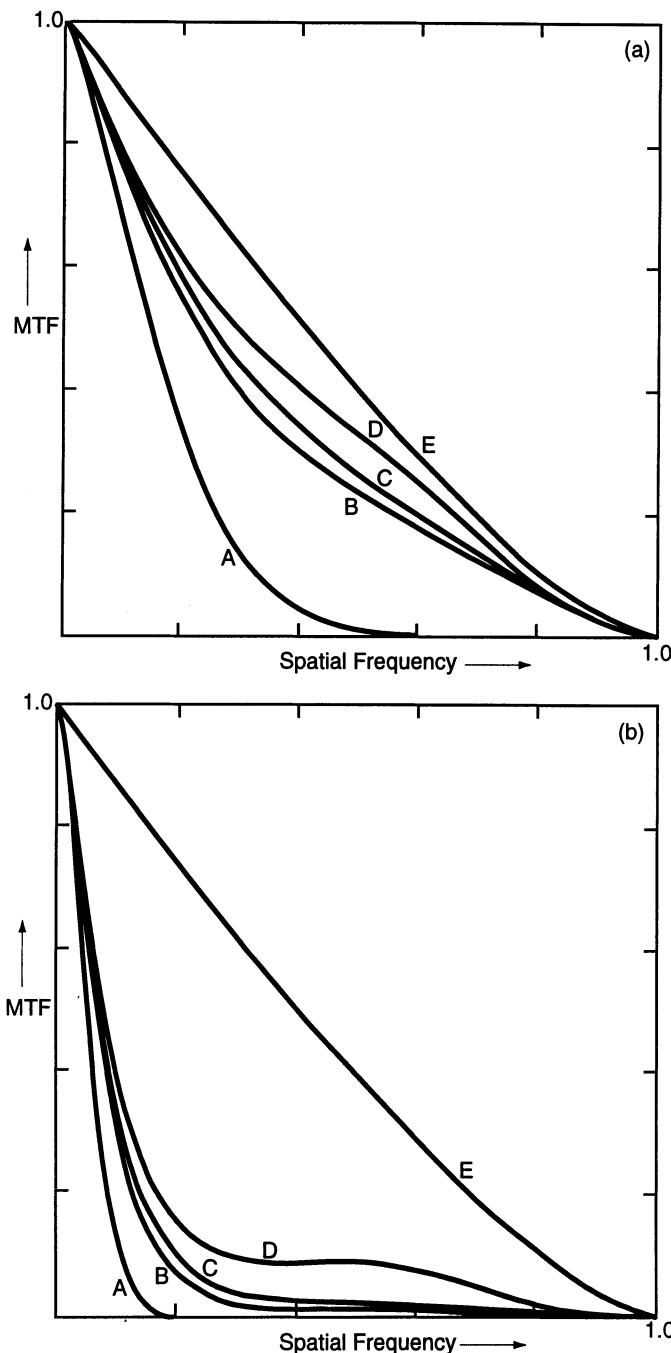


**Fig. 5.8.** Efficiency of adaptive correction using a small number of modes for (a)  $D/r_o = 2$ , (b)  $D/r_o = 7$ . Curve A, no correction; curve B, tilt correction; curve C, tilt plus focus corrections; curve D, tilt plus focus plus astigmatism corrections; curve E, ideal correction giving diffraction limited performance. (After Wang [5.51])

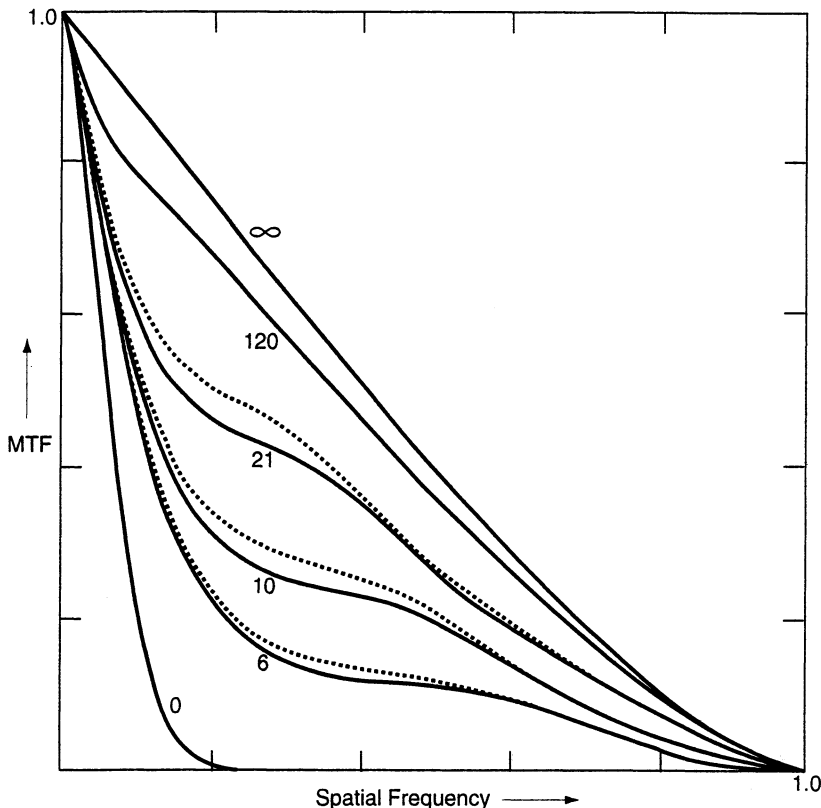


**Fig. 5.9.** Efficiency of adaptive correction using various numbers of Zernike polynomials (*continuous curves*) or Karhunen-Loeve functions (*dashed curves*) for the case  $D/r_o = 6$  (after Wang and Markey [5.53])

A later analysis by Wang and Markey [5.53] analysed the effectiveness of modal control with Zernike polynomials, compared with Karhunen-Loeve (K-L) functions. Figure 5.9 shows an example of the efficiency of correction using 0, 6, 10, 21, 120 and  $\infty$  polynomials or functions for  $D/r_o = 6$ . We see that the K-L functions are advantageous, if a relatively large number of functions are used, in raising the contrast in the normalized spatial frequency range about 0.1 to 0.5. The K-L functions are orthonormal and represent an optimum set of such functions in the sense that the square of the residual phase error averaged over the aperture is the minimum compared with any other orthogonal set for the same number of modes. The Zernike polynomials are near the optimum if the correction is confined to the low-order modes.

The three fundamental elements of an adaptive system for an astronomical telescope consist of:

- The adaptive mirror
- The image analyser (wavefront sensor)
- The detector

Merkle [5.44] considers two possible wavefront sensors: the shearing interferometer and the Shack-Hartmann sensor. As in active optics, the Shack-Hartmann sensor is the most commonly used. These sensors were discussed in Chaps. 1 and 2. The normal detector is, again as for active optics, a CCD which has optimum characteristics of sensitivity and stability.

The adaptive mirror is the most critical element. Merkle [5.44] shows the forms of deformable mirror which have been considered (Fig. 5.10). The forms are:

- Segmented mirrors
  - Piston only
  - Tilt only
  - Piston plus tilt
- Continuous thin-plate mirrors
  - Discrete position actuators
  - Discrete force actuators
  - Bending moment actuators
- Monolithic mirror
- Membrane or pellicle mirrors

Although other forms have been successfully tried, the continuous thin-plate mirrors seem the most favourable for the correction of atmospheric turbulence. Figure 5.11 shows such a device developed by the GEC Laboratories at Marcoussis in France [5.54] [5.55] for the so-called COME-ON project. The essential characteristics are as follows:

- 19 piezoelectric actuators
- Useful diameter 70 mm
- Actuator separation 17.5 mm
- Actuator stroke  $\pm 7.5 \mu\text{m}$
- Control voltage 1500 V
- Front plate: silicon, 1 mm thick, coated with silver
- Optical flatness:  $W \leq \lambda/4$  at 0.6  $\mu\text{m}$

The COME-ON system uses a separate tip-tilt mirror. (Systems have been developed for controlling tilt alone such as the ESO DISCO system [5.56]). The bandwidth of the complete system is about 30 Hz; this (see Table 5.3) will allow full correction for the speckle lifetimes corresponding to wavelengths  $\geq 2.2 \mu\text{m}$ .

The accuracy of correction is limited by three main sources of error: the wavefront fitting error ( $\sigma_F$ ), depending on how closely the adaptive mirror can match the actual wavefront error; the detection error ( $\sigma_D$ ), which is essentially inversely proportional to the  $S/N$  ratio of the wavefront sensor output, and the prediction error ( $\sigma_P$ ), which is caused by the time delay between the wavefront measurement and its correction. The overall phase error in waves is then given by

$$\sigma_R^2 = \sigma_F^2 + \sigma_D^2 + \sigma_P^2 \quad (5.98)$$

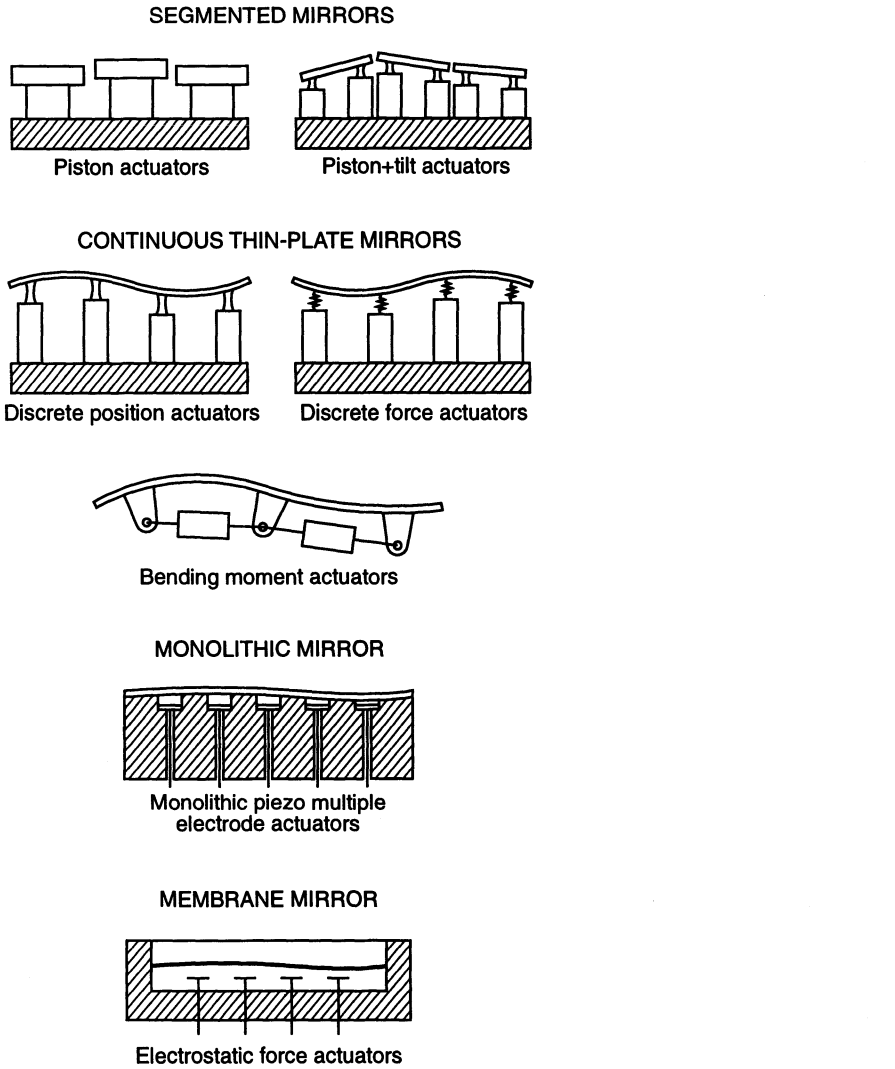
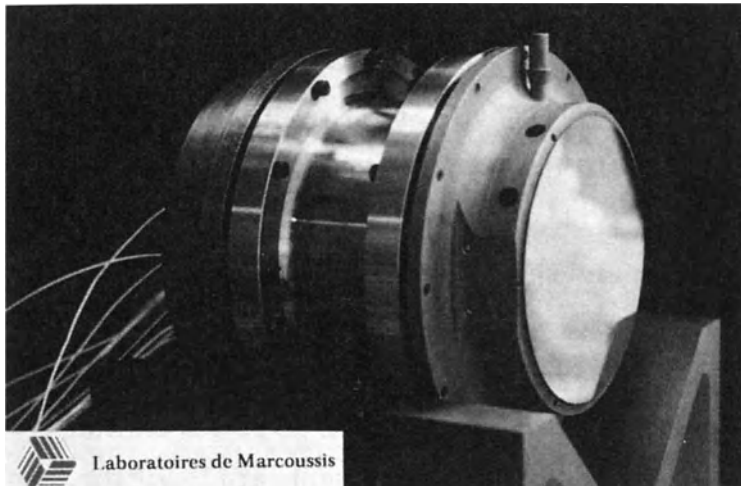


Fig. 5.10. Different types of deformable mirrors (from Merkle [5.44])

The wavefront fitting error  $\sigma_F$  can be described by

$$\sigma_F^2 = c \left( \frac{d_s}{r_o} \right)^{3/5} \text{ waves}^2 , \quad (5.99)$$

where  $d_s$  is the center-to-center spacing of the actuators and  $c$  is a parameter describing the slope for the correction mode. This important relation was established by Greenwood and Fried [5.57] and is further discussed by Greenwood [5.58] and Parenti and Sasiela [5.59].  $c$  has the value 1.07 for piston only, 0.14 for piston and tilt and various other values for continuous mirrors with differing influence functions. The function  $\sigma_F^2$  is related in its form and physi-



**Fig. 5.11.** Deformable adaptive mirror of the continuous thin-plate type driven by piezoelectric actuators developed by the GEC Laboratories at Marcoussis, France (from Merkle [5.50])

cal origins to the Fried structure function of Eq. (5.46), in which  $r$  is replaced by the outer scale  $L_o$  and  $d_s$  is analogous to  $L_o$ , as discussed by Greenwood [5.58].

Merkle [5.50] gives examples (Fig. 5.12) of the level of correction of the atmospheric MTF with the COME-ON adaptive mirror of Fig. 5.11 at  $\lambda = 1.0 \mu\text{m}$  and  $3.6 \mu\text{m}$  respectively. This illustrates again the huge gain in the IR implicit in Tables 5.3 and 5.4 for the number  $N$ : the level of correction with 19 actuators is nearly perfect at  $\lambda = 3.6 \mu\text{m}$  but minimal at  $1 \mu\text{m}$ . The effect of the other errors is discussed by Merkle [5.44].

#### 5.2.4 Limitations of the isoplanatic patch: artificial reference sources

The problems of wavefront fitting error and prediction error can also be solved, in principle, in the visible by investing in more actuators and larger bandpass. The problem of the isoplanatic patch (Eq. (5.96) and Table 5.3) is of a more fundamental nature and is indeed the most fundamental limitation to the practical application of adaptive optics in astronomy. It is in the nature of astronomical research that the majority of objects to be studied are near the limit of faintness observable with the telescope in question: otherwise a smaller telescope could do the observation equally well. Furthermore, the object may not be of a stellar nature, the ideal reference source. It is therefore unacceptable in the normal case to use a beam splitter to borrow light from the observed object for the purpose of adaptive correction. In *active optics* there is no problem, as we saw in § 3.5, because there is no isoplanatic angle

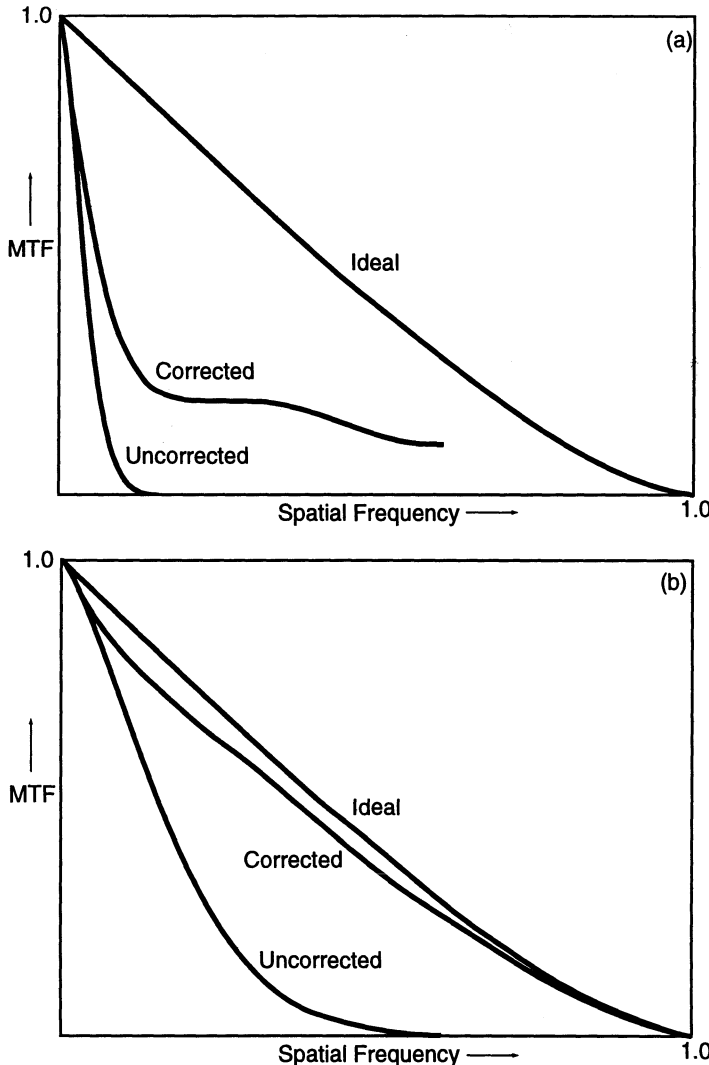


**Fig. 5.12.** Calculated MTF showing the extent of correction with the adaptive mirror of Fig. 5.11 (19 actuators) applied to a 2.2 m telescope with  $r_o = 10$  cm in the visible ( $\lambda = 500$  nm) for wavelengths (a)  $1\text{ }\mu\text{m}$  and (b)  $3.6\text{ }\mu\text{m}$  (after Merkle [5.50])

restriction and any convenient star in the entire telescope field is suitable. For *adaptive optics* the reference star must be within the isoplanatic patch. Tables 5.3 and 5.4 show again the rapid gain with wavelength ( $\propto \lambda^{6/5}$ ) of the isoplanatic patch. Merkle [5.50] gives (Table 5.5) the sky coverage with available stars of given magnitude for the same wavelengths as Table 5.3.  $m_{lim}$  is the limiting magnitude required on the assumption that 100 photons per sub-aperture are sufficient for a wavefront measurement with an integration

**Table 5.5.** Limitations of magnitude and sky coverage for adaptive optics at different wavelengths (after Merkle [5.44] [5.50])

$\lambda$ ( $\mu\text{m}$ )	0.5	2.2	3.6	10
$r_o$ (cm)	10	59	158	364
$m_{lim}$	7	13	15.5	17
$C_P$ (%)	$\simeq 0$	0.1	30	100
$C_E$ (%)	$\simeq 0$	0.3	100	100

time 10 ms or less. The available sky area  $C_P$  at the galactic poles and  $C_E$  at the equator goes from ca. 0 % at  $\lambda = 0.5 \mu\text{m}$  to 100 % at  $10 \mu\text{m}$ . This table shows that *with natural stars, adaptive optics in the visible is effectively impossible* except for special cases such as double stars or rare statistical cases. In the IR, however, with  $\lambda \geq$  ca.  $5 \mu\text{m}$ , the isoplanatic angle largely ceases to be a limitation – assuming that the wavefront information can be gathered and processed for these wavelengths. Fortunately, it is not necessary for the application of adaptive optics in the IR to use a wavefront sensor operating at these wavelengths, which would be technically very difficult. It has been demonstrated [5.44] that there is a strong correlation between the low spatial frequency MTF of atmospheric turbulence at visible and IR wavelengths so that a measurement in the visible is also valid in the IR for these low spatial frequencies.

The only way adaptive optics could become a soluble technical problem for general use *in the visible* is to obviate the necessity of a natural reference star in the isoplanatic patch. The first proposal of an artificial source was made by Foy and Labeyrie [5.60] in 1985. A so-called LIDAR system is envisaged whereby a high-power laser generates back scattering in the mesospheric layer of sodium atoms at 80–100 km height, giving a quasi point source in any required direction. Merkle [5.44] [5.50] discusses this possibility and shows the principles (Fig. 5.13). The laser propagation is in the form of a cone with its apex at the reflecting layer. If the latter is at a fairly low height, the difference between the conical beam and the cylindrical beam from a star is serious. The reflection should take place at as high a layer as possible; then the conical error (called “focus anisoplanatism”) is small for the most significant lower layers. With the LIDAR system, using an 80 cm telescope and a YAG laser of 0.5 J pumping a dye laser, about 5 photoelectrons were detected from a 300 m thick layer. With good seeing giving  $r_o \simeq 20 \text{ cm}$  at wavelength 590 nm, this could mean 5 photoelectrons per seeing cell or Hartmann spot. Foy and Labeyrie considered that a gain factor of 5 would be relatively easy with more powerful lasers and a gain of one or two orders of magnitude would be sufficient for operation.

Assuming a seeing-limited illuminated spot size (ca. 0.5 m at 100 km height), the artificial source produced would appear as an extended incoherent source featuring many speckles. Such a source may be of seeing di-

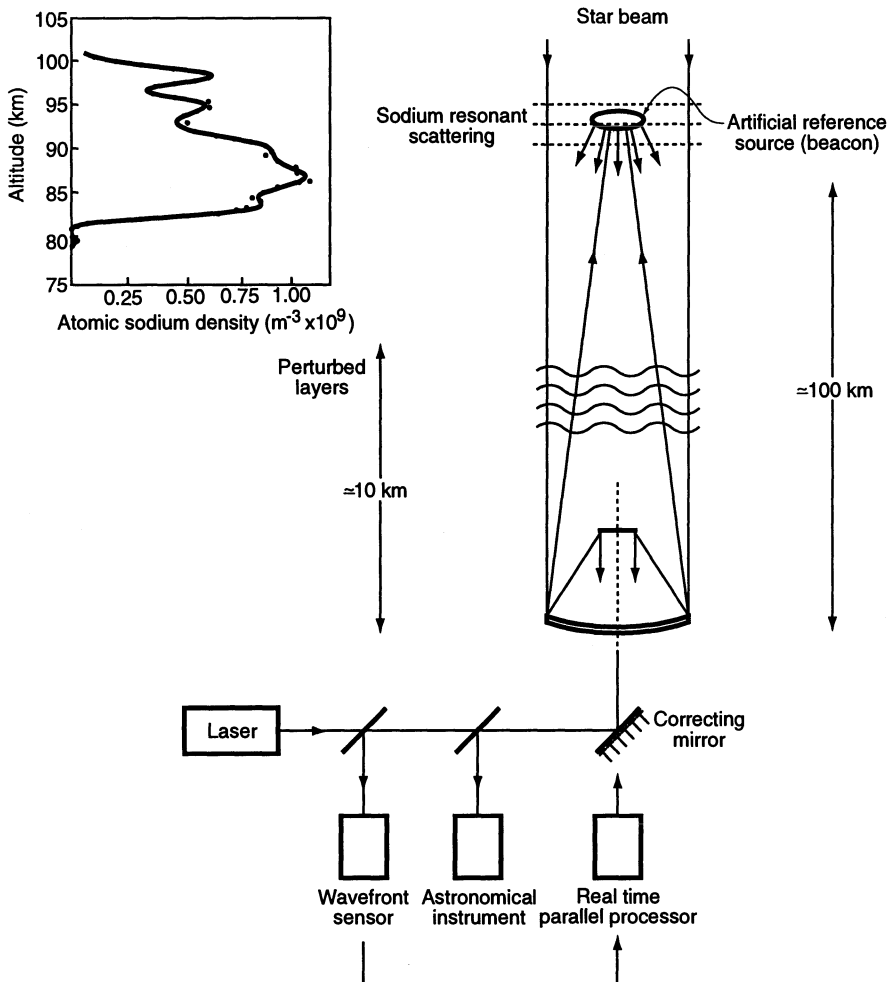


Fig. 5.13. Schematics of artificial reference star generation by a laser beam (from Merkle [5.44] [5.50])

mensions and still be quite suitable for Shack-Hartmann analysis. We saw in Chap. 2 that the Shack-Hartmann technique is very robust with regard to seeing quality and permits a resolution about an order of magnitude better than the integrated seeing.

Since the artificial source must be generated within the isoplanatic angle by the telescope itself, at a repetition rate synchronous with the adaptive correction rate, it would be necessary to gate the telescope during the sensing time. This would result in a modest loss, but the adaptive optics gain would be far greater. From Tables 5.3 and 5.5, it is clear that the potential of adaptive optics *in the visible*, as distinct from IR, depends entirely on progress in this field of generating artificial reference sources.

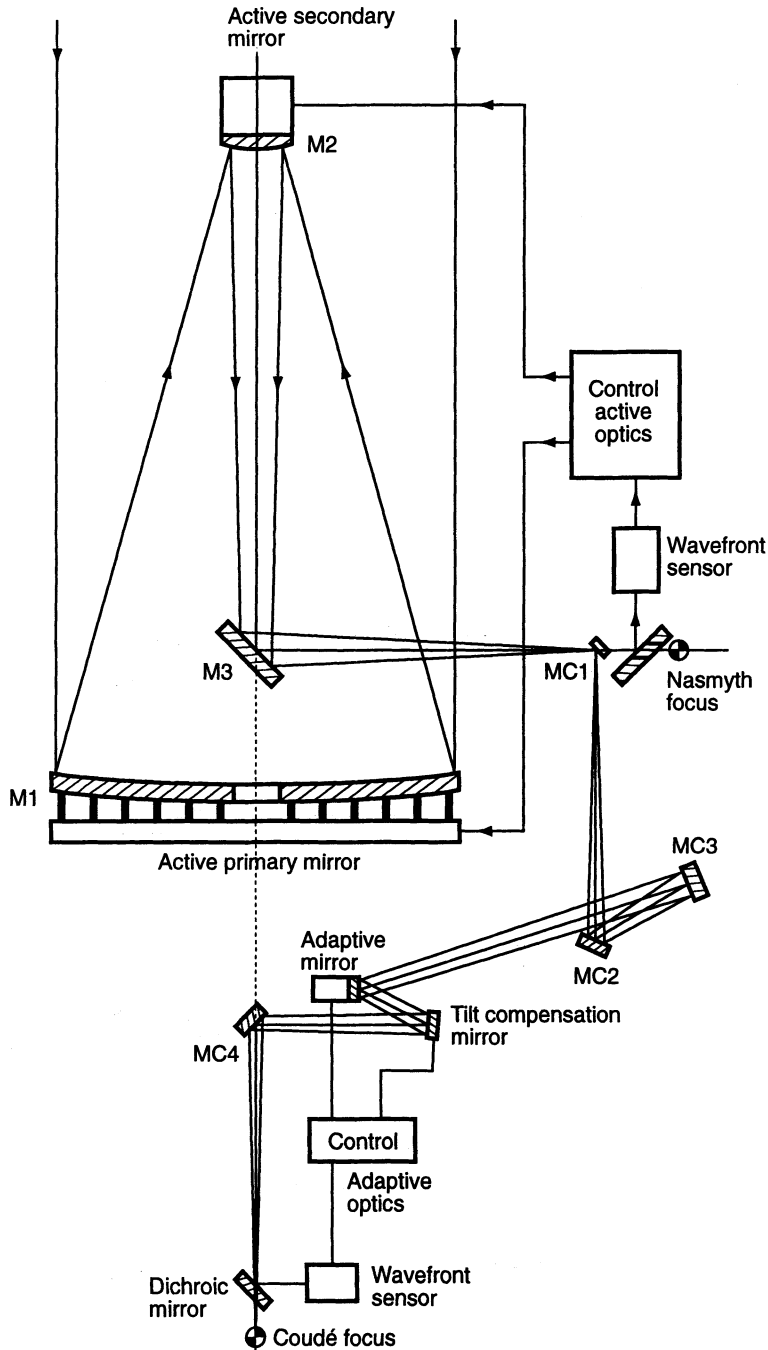
### 5.2.5 Adaptive optics for the ESO VLT and experimental correction results (COME-ON and COME-ON PLUS systems)

Figure 3.62 showed the total bandpass comprising the normal active optics bandpass A, the extended active optics bandpass B and the adaptive bandpass C. The active correction in bandpasses A and B was dealt with in § 3.5, whereby the correction in B is still (January 1998) a matter for experimental development. The adaptive optics correction, above all for the IR, is integrated into the coudé optical train. The complete scheme for bandpasses A and C is shown in Fig. 5.14, as given by Merkle [5.50]. A separate tilt compensation mirror and adaptive mirror are provided, the latter using the COME-ON piezoelectrically controlled mirror of the type shown in Fig. 5.11. The active and adaptive systems use two different wavefront sensors corresponding to the very different situations of isoplanatism and temporal frequency bandpasses A and C. The aim for the adaptive system [5.61] is about 400 measured sub-apertures controlling about 250 actuators with a stroke of ca.  $\pm 4\text{ }\mu\text{m}$  and a temporal bandpass of 100 to 200 Hz. The adaptive system, following Tables 5.3 and 5.5, should correct fully to the diffraction limit for  $\lambda \geq 2.2\text{ }\mu\text{m}$  and give partial correction at shorter wavelengths with rapidly diminishing returns towards the visible. Apart from the isoplanatic angle problem, a complete system for the visible would have to provide more than 6000 parallel control channels working up to 1000 Hz. No such hardware system is yet in view for astronomical use and only dedicated processors could handle the information flow. Such a system could only correct one isoplanatic patch.

In alt-az mounted telescopes, a field derotator is normally required. It is possible to integrate an adaptive system into the derotator optics [5.61].

The results achieved with the deformable mirror shown in Fig. 5.11, operating with 19 actuators in a closed-loop bandwidth extending to 25 Hz, have been described by Rigaut et al. [5.62] and by Merkle [5.63]. Tests were made using the ESO 3.6 m telescope and gave the striking result shown in Fig. 5.15 of diffraction limited correction in the IR at  $\lambda = 3.6\text{ }\mu\text{m}$ . The double star separation of the corrected, resolved image on the right is 0.38 arcsec. Rigaut et al. have defined a *critical wavelength*  $\lambda_{cr}$  as that wavelength at which the best resolution is obtained with a given active system. Further details at a later date are given by Rigaut et al. [5.64]. The performance is claimed to be the equivalent of the full correction of the first ten Zernike polynomials, giving diffraction limited performance in the IR down to  $1.7\text{ }\mu\text{m}$ . It must be emphasized, however, that all the experimental results with this system take no account of the problem of the isoplanatic angle: the objects chosen for adaptive improvement could either themselves provide the reference from part of their own light flux or contained very close reference stars.

Rousset et al. [5.65] report on a further development for a 4 m class telescope, the COME-ON PLUS project. The deformable mirror has 52 actuators



**Fig. 5.14.** Schematic diagram of the active/adaptive correction system of the ESO 8 m VLT unit telescopes (from Merkle [5.50])

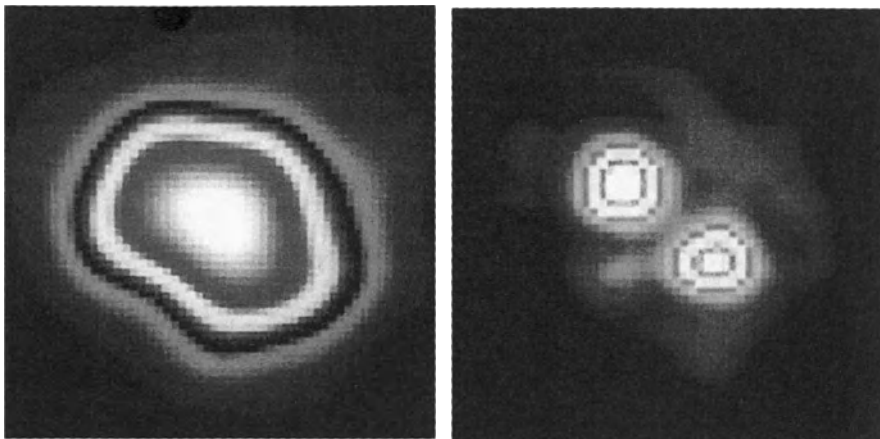


**Fig. 5.15.** Adaptive optics correction using the COME-ON system in the IR ( $\lambda = 3.6 \mu\text{m}$ ) of the image of the double star HR 6658 (separation 0.38 arcsec) with the ESO 3.6 m telescope. Left, without correction; right, with correction. (After Merkle [5.63])

working with a  $7 \times 7$  Shack-Hartmann wavefront sensor and a 30 Hz bandwidth. A special algorithm allows the number and bandwidth of the corrected modes to be optimized according to observing conditions. The throughput of COME-ON PLUS has been brought up to 30 %, compared with 3 % for COME-ON which was in no way optimized for throughput. Light loss of the order of 70 % is then the price that must be paid for an adaptive system using a transferred pupil compared with a throughput of 100 % for an active optics system. The limiting magnitudes for various levels of correction with the ESO 3.6 m telescope [5.65] are given in Table 5.6. The limiting magnitudes assume that all the light flux is available for the adaptive optics device.

**Table 5.6.** Adaptive optics with COME-ON and (predicted) COME-ON PLUS at the ESO 3.6 m telescope with  $r_o = 13 \text{ cm}$  at  $\lambda = 500 \text{ nm}$  (from Rousset et al. [5.65])

System	COME-ON		COME-ON PLUS	
Correction mode	Limits	Limiting magnitude $m_R$	Correction error at $\lambda = 2.2 \mu\text{m}$	Limiting magnitude $m_R$
Tilt only	13	13	$\lambda/3$	15.5
15 modes	11.5	11.5	$\lambda/5$	14
40 modes				11
				$< \lambda/3$
				$< \lambda/5$

### 5.2.6 Adaptive optics using laser reference sources for military purposes applicable to astronomy

Information on previously classified work for military purposes in the USA has now become available to the astronomical community and has produced very impressive results. Specifically the results of the SOR 1.5 m telescope, Generation II system, of the Phillips Laboratory Starfire Optical Range in New Mexico as reported by Fugate [5.66], Ellerbroek [5.67] and Ellerbroek et al. [5.68] refer to the astronomical applications. In fact, unknown to the astronomical community, the feasibility of using focused laser beams as artificial guide stars was already established in 1983 [5.66].

Compared with the proposal of Foy and Labeyrie to use back scattering from mesospheric sodium atoms at about 80 km height, these experiments used range-gated Rayleigh backscatter at a height of 6–10 km. Up to the end of 1991, all practical results of adaptive compensation with “laser guide stars” (LGS) have used such heights [5.68] [5.69]. (We will follow this terminology of the literature, although in the astronomical context the term “laser reference star” would be more appropriate). The Shack-Hartmann sensor sensed 146 sub-apertures to control 241 actuators of a continuous face sheet adaptive mirror made by ITEK. A separate track (tilt) sensor was used. The optical arrangement could switch between LGS and natural guide stars (NGS), permitting a comparison of the results. The closed-loop control bandwidth was 130 Hz. Fugate [5.66] quotes the following results:

- For “*short exposures*” (ca. 0.01 s), Strehl ratios of 0.64 and 0.48 were achieved for NGS and LGS operation respectively. The images had a FWHM of 0.13 arcsec, compared with  $\lambda/D = 0.12 \text{ arcsec}$  for  $\lambda = 0.88 \mu\text{m}$  representing the diffraction limit.
- For “*long exposures*” ( $\geq 1 \text{ s}$ ), Strehl ratios of ca. 0.25 and FWHM of ca. 0.18 arcsec were achieved with LGS. Intensity gains of ca. 15 times over uncompensated images were achieved at  $\lambda = 0.88 \mu\text{m}$ .

The improvement in the MTF is shown in Fig. 5.16 for these short and long exposure cases. CCD frames of astronomical fields show the high gain depth penetration (limiting magnitude) resulting from the energy concentration in faint star images.

Ellerbroek [5.67] reported results of *analytical predictions* of adaptive optics performance with an 8 m telescope in configurations employing either a single NGS, a single LGS in the mesospheric sodium layer (ca. 80 km), or a single LGS combined with a single dim NGS. He assumes  $r_o = 0.285 \text{ m}$  and an isoplanatic radius  $\theta_o = 18.6 \mu\text{rad}$  (see Eq. 5.94)). The characteristics of the adaptive system are:

- A continuous facesheet adaptive mirror with 529 actuators ( $25 \times 25$  square array)
- A Shack-Hartmann sensor with  $24 \times 24$  sub-apertures for the LGS

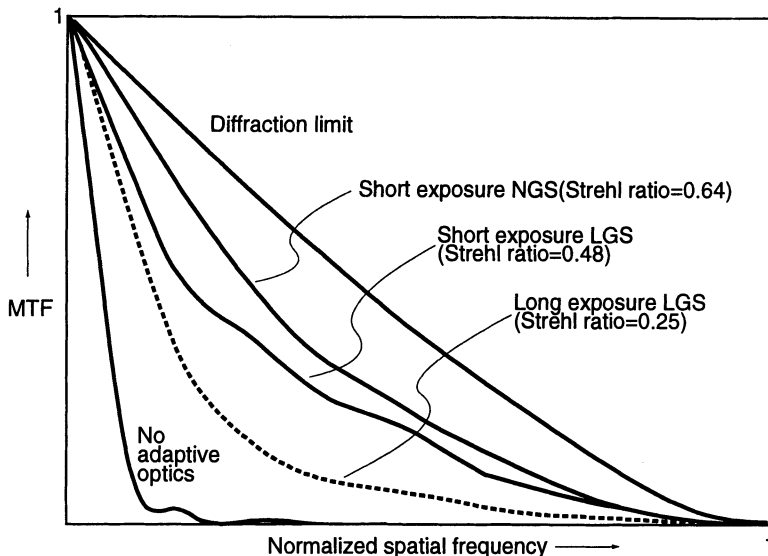


**Fig. 5.16.** Adaptive optics improvement of the MTF for the cases cited (after Fugate [5.66])

- A Shack-Hartmann sensor with  $4 \times 4$  sub-apertures for the dim NGS
- A closed-loop bandwidth of 20 Hz
- Wavefront sensor sampling rates of 200 Hz
- Guide star intensities sufficient to yield from 0.05 to 0.2 waves rms phase difference measurement accuracy at this sampling rate

The long-exposure Strehl ratio for a phase difference measurement accuracy of 0.1 waves rms is 0.21. The MTF is about 0.2 times that of the diffraction limited case for all spatial frequencies. These figures are for the optimum configuration with both a single LGS and a single dim NGS. The latter is required only to sense the low spatial frequency residues which would be dominant if an LGS were used alone. With a single LGS alone, the Strehl ratio is reduced from 0.21 to 0.12.

Ellerbroek et al. [5.68] have considered the current state of such systems and concepts for the future. Laser guide stars (LGS) open up immense possibilities, but there are a number of problems arising out of their nature.

The first is that the LGS technique is *insensitive to tilt error*. Tilt correction thus still requires a natural guide star (NGS), but this can be much fainter than is required for higher correction orders. Furthermore, the isoplanatic radius angle for tilt alone is somewhat larger than  $\theta_o$ . A sky coverage increase of a factor of 25 for a 6 m telescope imaging at  $\lambda = 0.6 \mu\text{m}$  has been estimated [5.70] using LGS adaptive optics in this way.

The second problem is *focus anisoplanatism* due to the conical form of the laser beam path. It may be shown [5.68] that the mean square phase error due to focus anisoplanatism increases with  $D^{5/3}$  for a given zenith angle and turbulence profile. They are already quite severe for a 4 m telescope with

an LGS generated at 20 km. Increasing the height will produce significant improvement, but even a height of 90 km using the mesospheric sodium layer gives non-negligible errors with  $D = 8$  m. This situation can be improved by increasing the number of guide stars at 20 km; or by using one such Rayleigh guide star together with a weak sodium guide star sensed only at low spatial frequency. However, it is clear that multiple artificial guide star solutions are bound to be technically complex.

The third problem is *tilt anisoplanatism* arising from an excessive angular separation of the NGS sensing atmospheric tilt from the observed object. Although this effect is less sensitive than common anisoplanatism, it is nevertheless appreciable at a radius  $\theta$  of 8 arcsec and serious at 20 arcsec [5.68].

A fourth problem occurs if the laser source is separated from the telescope, which may be technically much more convenient. This error has been discussed by Beckers [5.71] in connection with the ESO 8 m VLT telescopes and is termed by him the “perspective elongation effect”. It depends on the thickness of the reflecting (sodium) layer  $\Delta h_{Na}$  and the laser separation  $s_L$  from the telescope axis. The limit for  $s_L$  with the 8 m VLT is less than 4 m, so the effect is not normally acceptable and requires that the laser system operate through the telescope. However, Beckers proposes a method by which the elongation effect may be removed in the case of powerful lasers with short pulse times. The finite time involved in the elongation process is compensated by reading out the movement of the charges along the columns of the CCD of the Shack-Hartmann sensor at the appropriate clock rate, the CCD columns being aligned in the perspective elongation effect direction.

With such a compensation, the limit of separation  $s_L$  is set simply by considerations of the isoplanatic patch relative to the elongation. This will depend on the number of actuators  $N$ . For the planned value  $N = 200$ , Beckers gives  $(s_L)_{max}$  for the VLT as 71 m. This relaxes the whole technical layout and Beckers gives a possible layout relative to the four 8 m VLT telescopes at the Paranal site.

Ellerbroek et al. [5.68] mention the general possibilities of LSG for multiple field points and multi-conjugates for compensation at different heights (MCAO). Promising work on MCAO by the US Air Force is also reported by Roddier [5.72], the principal and most important aim being the extension of the isoplanatic angle. The 1992 ESO conference proceedings (see [5.61]) contains many papers revealing the intense activity now taking place. It represents a veritable frontal assault on the last, and now by far the most important limitation of the optical quality of ground-based telescopes.

### 5.3 Site selection in height

In spite of the impressive progress in adaptive optics, it is clear that the necessary technology for the visible spectral region is still in its infancy. As discussed above in § 5.1, the technical means for rational site selection are

now readily available. An excellent site remains the most effective form of “adaptive optics”, since, once the work of site selection itself is done, the benefits are automatic without any technical complication or loss of photons. High sites have obvious advantages and it is not surprising that Mauna Kea, Hawaii, at a height of about 4000 m is accepted as one of the best, if not the best, astronomical site currently available. The advantage of height is clear from Eq. (5.60) for  $r_o$  and the function  $C_n^2$  with height  $h$  shown in Fig. 5.7. Clearly, the contribution to the integral term  $\int C_n^2(h) dh$  in (5.60) becomes very small above 20 km. This is the basis of the “ISLA Proposal” (International Stratospheric Laboratory for Astrophysics) whose essential feature (see also § 3.2.4) is an *airship-held base* for a telescope array *at a height of 15 km* [5.73]. A conservative estimate of  $r_o$  is made at this height as about 1 m at  $\lambda = 0.5 \mu\text{m}$ , (i.e. in the visible), giving from Table 5.2 a  $(d_a)_{FWHM}$  of about *0.1 arcsec* for the residual atmospheric seeing disk. Similarly, from (5.95) the isoplanatic angle is deduced to increase by a factor of 30, going from about 4 arcsec to *120 arcsec*. It is proposed to have an array of several 4 m telescopes. With  $r_o = 1 \text{ m}$ , the number of sub-apertures  $N$  to be controlled for an adaptive optics system for the residual atmosphere *in the visible* would be only about 16 from Eq. (5.88), compared with about 1600 from the ground with an  $r_o = 0.1 \text{ m}$ . Referring to Table 5.3, we see that such a stratospheric platform at  $h = 15 \text{ km}$  brings the same advantages in the visible at  $\lambda = 0.5 \mu\text{m}$  that we get from a wavelength shift to about  $\lambda = 4 \mu\text{m}$  from the ground: indeed, even more for the isoplanatic angle. Furthermore, wavefront sensing in the visible can be applied directly at the same wavelength for correction.

There seems little doubt that such a platform at 15 km enables the complete solution of the adaptive optics problem even in the visible. Even with no correction the seeing angle has an FWHM of 0.1 arcsec, a value impossible to achieve from any ground-based observatory. Combined with active optics for telescope errors, which would be essential for a full field quality of 0.1 arcsec, the technical problem of achieving diffraction limited resolution over the adaptive field right down to the normal UV absorption limit of  $0.3 \mu\text{m}$  seems quite feasible. With adaptive optics for one isoplanatic patch, this already covers a field of about 2 arcmin diameter.

The analysis shows that airships using helium lifting gas could handle the payload of 4 lightweight telescopes of the hexapod type (see § 3.5.5.). The estimates of the project costs suggest that the procurement and operation costs are much nearer to those of ground-based installations than those of space projects.

It seems that the ISLA concept is extremely promising: technically, operationally and from the point of view of costs. With an array of several 4 m telescopes with the proposed baseline of 200 m, whereby the prospect of diffraction-limited performance can apply also in the visible, the potential in interferometry seems remarkable.

## 5.4 High resolution imaging apart from adaptive optics

We are concerned here essentially with three important techniques: Michelson interferometry, speckle interferometry and image reconstruction or improvement. Each of these is essentially outside the arbitrarily defined scope of this book, namely telescope optics in the sense of the factors affecting the image formed at some focus station of the telescope. Michelson interferometry is a complex subject in its own right and can better be seen as an instrument performing coherent processing of separate telescope images. Similarly, speckle interferometry requires an additional instrument recording short exposures used in a post-detection image reconstruction procedure. Image reconstruction techniques are, by definition, post-detection off-line procedures which have become of fundamental importance in astronomical observation and also form a separate subject in its own right.

We shall confine ourselves here, therefore, to brief considerations of the demands made on the optical quality of telescopes in order to permit Michelson and speckle interferometry.

### 5.4.1 Michelson interferometry

A brief, but excellent account of the optical requirements and the literature involved is given in his review paper by Roddier [5.16].

General adaptive correction will be essential unless the diameter of the two apertures giving the interfering beams is significantly less than  $r_o$ , in which case tilt correction alone is sufficient. The Australian SUSI operates on this basis [5.74]. At low light level the  $S/N$  ratio is proportional to the number of photons per “exposure”. The optical bandwidth has the fundamental condition that the beams must interfere. If the baseline is  $L_{int}$ , Roddier shows that the optical bandwidth  $\Delta\lambda$  is given by

$$\Delta\lambda \propto (r_o/L_{int})^{5/6} , \quad (5.100)$$

and the  $S/N$  by

$$S/N \propto r_o^2(r_o/v)(r_o/L_{int})^{5/6}$$

or

$$S/N \propto r_o^{23/6}v^{-1}L_{int}^{-5/6} , \quad (5.101)$$

where  $v$  is the velocity of the perturbations. These equations assume that the baseline  $L_{int}$  is smaller than the outer scale of turbulence  $L_o$ . Whether this is valid for some of the longer baselines proposed is questionable.

These are important results for the practice of interferometry. The optical bandwidth  $\Delta\lambda$  decreases almost linearly with the baseline. The  $S/N$  ratio varies almost as the fourth power of  $r_o$ . *For a given wavelength  $\lambda$ , this means from (5.68) or (5.70) that the  $S/N$  also varies almost with the inverse fourth power of the image diameter.* Since the possible observation time of fringes is

proportional to the square of the  $S/N$ , the *observation time* varies almost with the *eighth power of  $r_o$* . The same is true for speckle interferometry, underlining the fact that high image quality is a *sine qua non* of interferometric techniques with telescopes.

Michelson interferometry in a large, ambitious project like the ESO VLTI (Very Large Telescope Interferometer) places the highest demands on the telescope from an opto-mechanical viewpoint. The factors which influence fringe contrast have been analysed by Beckers et al. [5.75]. Simply as one example, one may quote the tolerance of  $4.7 \mu\text{m/s}$  for pathlength drift in the visible at  $\lambda = 0.6 \mu\text{m}$  at the final combined focus. Again, if in a normal telescope working incoherently the spider supporting the secondary causes an axial vibration of that mirror, then this will have no consequence at all unless it exceeds the focus shift tolerance corresponding to the integrated seeing disk. But, for interferometry, an axial oscillation equal to  $\pm\lambda/4$  will destroy the fringe contrast. Also, phenomena such as polarisation, which can normally be ignored for most observational modes, may become important.

In general, for small optical path differences  $\sigma_z$ , the effect on the fringe contrast is

$$\frac{\delta V}{V} = 2\pi^2 \left( \frac{\sigma_z}{\lambda} \right)^2 = \frac{\delta^2}{2} , \quad (5.102)$$

where  $\delta$  expresses small variations of fringe position in rad rms (1 fringe =  $2\pi$  rad). Thus a 1% loss of fringe contrast arises from  $\delta \simeq 0.1414$  or 1/44 fringe rms.

The adaptive optics system for the VLTI is described by Mariotti et al. [5.76].

The manufacturing tolerances for telescope systems, including the complete coudé train to the combining focus, are correspondingly stringent. For the auxiliary telescopes of the VLTI, moveable 1.8 m telescopes, the global requirement is

$$W_{rms} \leq 110 \text{ nm} ,$$

including figuring errors of all the eleven (coated) mirrors, supporting errors and alignment errors. In the wavefront analysis for the test, only the tilt term may be removed. If defocus is removed, the requirement is

$$(W_{rms})_f \leq 90 \text{ nm}$$

These represent hard manufacturing and assembly requirements.

### 5.4.2 Speckle interferometry

Again we shall follow the brief, but excellent résumé of the aspects concerned with telescope optics given by Roddier [5.16], [5.45], who also gives a listing of the essential literature to that date (1981). More recent accounts are given by Weigelt [5.77] [5.78].

Speckle interferometry was introduced by Labeyrie in 1970 [5.79], who recognized the significance of laser speckles for short-exposure stellar images. The method consists of a second order statistical analysis of the short-exposure image speckle pattern [5.16].

The aspect of greatest importance for telescope optics is the  $S/N$  ratio. Assuming photon noise only, the  $S/N$  ratio in the energy spectrum at very low light level is proportional to the number of photons per speckle. For a given optical bandwidth  $\Delta\lambda$  and exposure time  $t_{exp}$ , it is therefore proportional to  $r_o^2$  [5.45], as indicated by Eq. (5.88). The optical bandwidth limitation  $\Delta\lambda$  follows the same law as in Eq. (5.100) for Michelson interferometry. The exposure time  $t_{exp} \simeq r_o/\Delta v$ , where  $\Delta v$  is the dispersion of wind velocities in the turbulent layers [5.16] [5.45]. Similarly to the Michelson interferometry case of Eq. (5.101), we have then

$$S/N \propto r_o^{23/6} \Delta v^{-1}, \quad (5.103)$$

i.e. the  $S/N$  situation is the same as for Michelson interferometry except that  $v^{-1}$  is replaced by  $\Delta v^{-1}$ . Again the  $S/N$  increases with almost the fourth power of  $r_o$  and the possible exposure time  $t_{exp}$  of speckles almost with the eighth power of  $r_o$ . The limiting magnitude therefore depends strongly on the image quality. According to Dainty [5.80] [5.81], there is a gain of  $2.5^m$  in limiting magnitude if the seeing diameter decreases by a factor of 2, corresponding to a reduction by a factor of ten in brightness, a power law of 3.3 of the inverse image diameter. Telescope aberrations prejudice the results if they become comparable with the atmospheric seeing disk, as was shown by Dainty [5.81]. Striking results of diffraction-limited reconstruction of double stars and other objects are given by Weigelt [5.78]. Using a new triple correlation method reconstructing both modulus and phase of the Fourier transform (speckle masking), Weigelt shows absolutely clean diffraction limited reconstructions of double stars with separations of 0.184, 0.137, 0.159 and 0.463 arcsec, although the telescope used (the ESO conventional 3.6 m) was rarely capable of imagery better than 1 arcsec. With a 1 arcsec (FWHM) image quality, the 8 m VLT telescopes could achieve a limiting magnitude of  $20^m$ . Weigelt emphasizes the importance of excellent image quality, in agreement with (5.103), with particular emphasis on reducing local air effects (“dome and telescope seeing”) to an absolute minimum.

# 6. Mirror Reflecting Coats: Production and Cleaning

## 6.1 Introduction: evolution to the current situation

In Chap. 4 we considered criteria for the *optical efficiency* of telescopes. Following Dierickx, the effective diameter  $D_{eff}$  of a telescope was defined by Eq. (4.33) as

$$D_{eff} = D(\tau_t I_0)^{\frac{1}{2}} , \quad (6.1)$$

where  $D$  is the physical clear diameter,  $I_0$  the measure (CIR) of the optical quality and  $\tau_t$  the *throughput* of the total telescope system. The measure of optical efficiency  $E_t$  is then

$$E_t = (D_{eff}/D)^2 = \tau_t I_0 = T^2 \quad (6.2)$$

The quantities  $I_0$  and  $\tau_t$  enter into this expression with equal weight: neglect of either implies throwing away optical efficiency. Since the medium surrounding the optical elements of a telescope is almost always air, having a path length which is small compared with that through the atmosphere, the quantity  $\tau_t$  is effectively determined by the reflectivity of the mirrors and the transmissivity of any refractive elements. For the latter, the loss per surface reflection is, at the worst, that given by the Fresnel law  $[(n - 1)/(n + 1)]^2$  or 4% for  $n = 1.5$ . This can often be reduced by anti-reflection coating. Absorption is often a serious problem in the UV unless fused silica can be used but is otherwise usually a minor loss. The most serious source of reduction of  $\tau_t$  is therefore the reflectivity of mirrors, above all if there are a significant number in the optical train.

Up to the present (1997), there have been only three eras concerning reflectivity of “large” mirrors for telescopes: the speculum era from about 1660 to 1860, whereby the polished mirror surface was also the final reflecting surface; the chemically deposited silver on glass era from about 1860 to 1935, and the evaporated aluminium era which is still the standard solution for large mirrors (about 1935 to date). However, there is clear evidence that this third era is approaching its end, at least for the most advanced telescopes.

According to Riekher [6.1], the most favourable reflectivity of fresh speculum for the spectral bandpass of the eye (with sharp peak at about  $\lambda = 555$  nm) was about 66 %. In most cases, due to rapid tarnishing, a value of 60 % was favourable. Silver also tarnishes rapidly but Jamin showed already

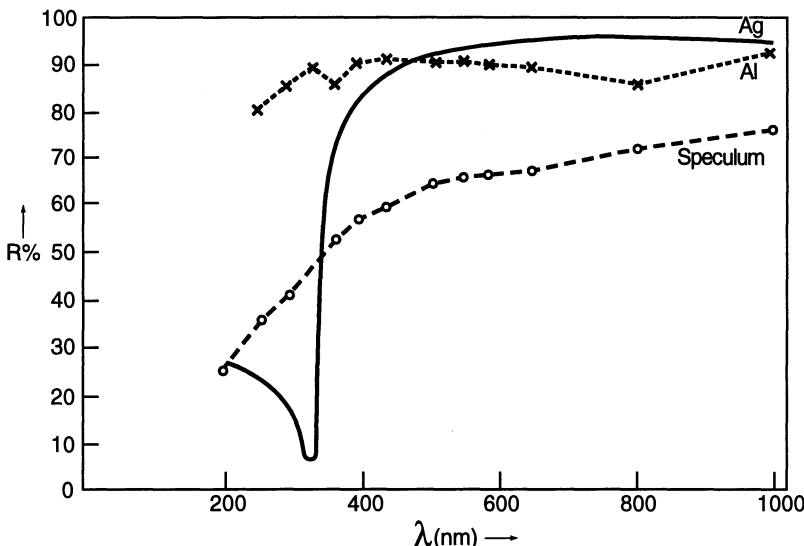


Fig. 6.1. Reflectivity  $R$  of fresh speculum, chemically deposited silver and evaporated aluminium (after Riekher [6.1])

in 1848 [6.2] that a mirror surface on freshly polished silver reflected about 50 % more light than speculum. Riekher [6.1] gives the reflectivity of fresh speculum, chemically deposited silver and evaporated aluminium (Fig. 6.1). The curve for speculum makes it clear why Herschel preferred oblique reflection at the primary to avoid a second reflection.

Chemical silvering on glass (high-expansion plate glass until borosilicate low-expansion glass was introduced in the 1920s to 1930s) was one of the most important developments in the history of the telescope. Not only was the reflectivity over 90 % in the visible range for a fresh film; even more important in practice was the ease of removal and renewal without the need for repolishing the mirror surface. A considerable art developed which is well described in older books [6.3] [6.4]. Essentially the processes described were based on the Brashears process, published in 1880 [6.5]. Although chemically deposited silver was a huge advance, the tarnishing problem due to moisture and, above all, sulphur, remained. Various protection measures were tried, above all lacquer diluted with amyl acetate. However, the protection was modest and lacquer was rarely used on large mirrors.

An excellent summary of the evaporation technique, which introduced the third era of aluminium coats, is given by Hass [6.6]. The first evaporated mirror coatings were prepared by Pohl and Pringsheim in 1912 [6.7]. However, vacuum technology was not adequate at that time and the real technological breakthrough was made, above all by Strong [6.8] [6.9] in the United States, between 1930 and 1937. Strong introduced the first really practicable method of producing pure evaporated aluminium films. With many refinements, the same process is still the standard method today. Details of the technology

are given by Holland [6.10] and by Hass and Turner [6.11]. Chemical cleaning is followed by ionic or electron bombardment cleaning. Unless an ultra-high vacuum (UHV) with  $p < 10^{-8}$  Torr is available aluminium evaporation must be done rapidly to prevent oxygen absorption, and the pressure must be below  $10^{-5}$  Torr. Al wets tungsten wire and can therefore be heated very conveniently to the required temperature. This is not true of other metals, such as silver, which must be held in "boats" or receptacles. Other metals of importance for mirrors, either directly or as intermediate coats, which can be evaporated by similar techniques to that for aluminium include silver, gold, copper, rhodium and platinum.

The percentage reflection  $R$  at normal incidence for these six metals as evaporated coats on glass substrates are shown in Table 6.1, as given by Hass [6.6] from his own measurements and those made by Bennett et al. [6.12] and Bennett and Ashley [6.13]. It is emphasized by Hass that the reflectivity of a good evaporated mirror coating is *always* higher than that of a polished or electroplated surface of the same material.

A graphical representation on a log wavelength scale of the reflectivities of UHV coatings with these metals is given by Jacobson et al. [6.14] in the extensive study commissioned for the Gemini project, adapted from Musikant [6.15] and Driscoll and Vaughan [6.16], reproduced in Fig. 6.2. I am indebted to M. Grössl of ESO for drawing my attention to this remarkable work of Jacobson et al.

The great advantage of evaporated aluminium over the unprotected silver of the chemically deposited silver era arose principally because it is much more resistant to tarnish on account of the rapidly developing oxide layer which grows to an ultimate thickness of 3–4 nm and protects the film from tarnish. The calculated reduction in reflectivity is only 0.1 % for  $\lambda \geq 1 \mu\text{m}$  and 1.6 % at  $0.22 \mu\text{m}$ .

The theoretical treatment of the normal reflectivity  $R$  of metals is given in standard works on physical optics [6.17] [6.18] and is re-capitulated by Jacobson et al. [6.14]. For *longer wavelengths*, for which the free electrons are largely responsible for the high reflectivity, the normal specular reflectivity  $R$  in air can be deduced from the refractive index  $n$  and the extinction coefficient  $\kappa$  of the reflecting medium. The complex index  $\hat{n}$  relates these two real quantities by

$$\hat{n} = n - i\kappa , \quad (6.3)$$

and the reflectivity is given by

$$R = \frac{(n-1)^2 + \kappa^2}{(n+1)^2 + \kappa^2} \quad (6.4)$$

Tables of the optical constants for thin metallic films are given by Hass [6.6] and by Jacobson et al. [6.14] for silver, the latter considering the values of Decker and Stanford [6.19] to be the most reliable. As an example, they take for  $\lambda = 10 \mu\text{m}$  the values  $n = 6.57$  and  $\kappa = 74.4$  giving from (6.4)  $R = 0.9953$ .

**Table 6.1.** Percentage reflectivities  $R$  at normal incidence of freshly evaporated coatings of six metals (from Hass [6.6])

$\lambda$ ( $\mu\text{m}$ )	Al	Ag	Au	Cu	Rh	Pt
0.220	91.5	28.0	27.5	40.4	57.8	40.5
0.240	91.9	29.5	31.6	39.0	63.2	46.9
0.260	92.2	29.2	35.6	35.5	67.7	51.5
0.280	92.3	25.2	37.8	33.0	70.7	54.9
0.300	92.3	17.6	37.7	33.6	73.4	57.6
0.315	92.4	5.5	37.3	35.5	75.0	59.4
0.320	92.4	8.9	37.1	36.3	75.5	60.0
0.340	92.5	72.9	36.1	38.5	76.9	62.0
0.360	92.5	88.2	36.3	41.5	78.0	63.4
0.380	92.5	92.8	37.8	44.5	78.1	64.9
0.400	92.4	95.6	38.7	47.5	77.4	66.3
0.450	92.2	97.1	38.7	55.2	76.0	69.1
0.500	91.8	97.9	47.7	60.0	76.6	71.4
0.550	91.5	98.3	81.7	66.9	78.2	73.4
0.600	91.1	98.6	91.9	93.3	79.7	75.2
0.650	90.5	98.8	95.5	96.6	81.1	76.4
0.700	89.7	98.9	97.0	97.5	82.0	77.2
0.750	88.6	99.1	97.4	97.9	82.6	77.9
0.800	86.7	99.2	98.0	98.1	83.1	78.5
0.850	86.7	99.2	98.2	98.3	83.4	79.5
0.900	89.1	99.3	98.4	98.4	83.6	80.5
0.950	92.4	99.3	98.5	98.4	83.9	80.6
1.0	94.0	99.4	98.6	98.5	84.2	80.7
1.5	97.4	99.4	99.0	98.5	87.7	81.8
2.0	97.8	99.4	99.1	98.6	91.4	81.8
3.0	98.0	99.4	99.3	98.6	95.0	90.6
4.0	98.2	99.4	99.4	98.7	95.8	93.7
5.0	98.4	99.5	99.4	98.7	96.4	94.9
6.0	98.5	99.5	99.4	98.7	96.8	95.6
7.0	98.6	99.5	99.4	98.7	97.0	95.9
8.0	98.7	99.5	99.4	98.8	97.2	96.0
9.0	98.7	99.5	99.4	98.8	97.4	96.1
10.0	98.7	99.5	99.4	98.9	97.6	96.2
15.0	98.9	99.6	99.4	99.0	98.1	96.5
20.0	99.0	99.6	99.4			
30.0	99.2	99.6	99.4			

There is considerable discrepancy between the values quoted from different sources. Equation (6.4) reveals clearly that high reflectivity is associated with high extinction coefficients  $\kappa$ . For a dielectric with high transmissivity such as glass,  $\kappa$  is effectively zero in (6.4) and the reflectivity  $R_G$  reduces to the Fresnel formula

$$R_G = \left( \frac{n-1}{n+1} \right)^2 \quad (6.5)$$

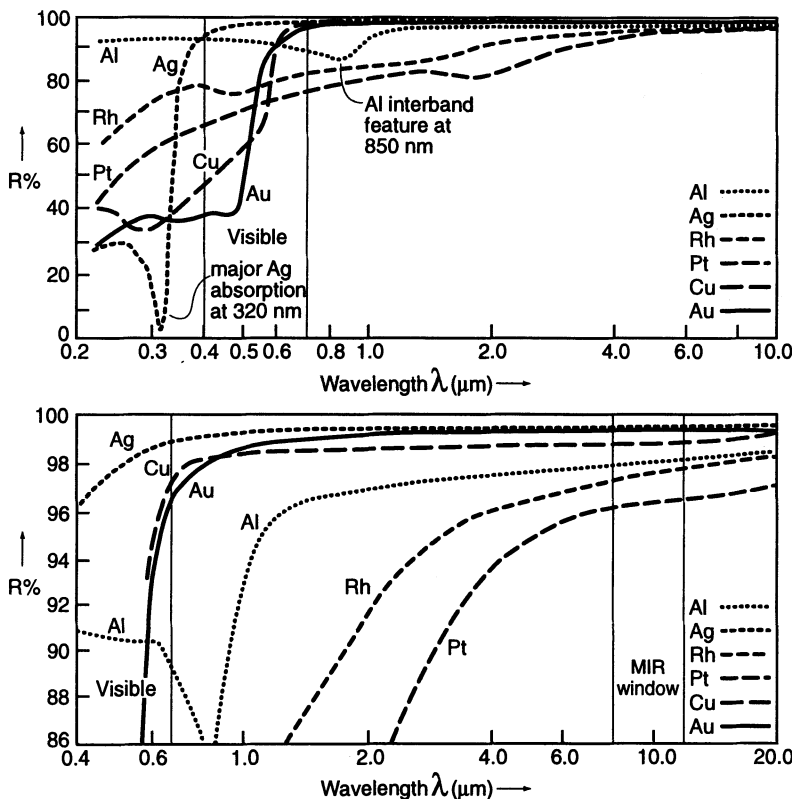


**Fig. 6.2.** Reflectivities  $R$  of coats produced by evaporation under UHV conditions of the six metals of Table 6.1 (from Jacobson et al. [6.14])

For longer wavelengths, since free electrons cause high electrical conductivity in metals, the approximate expression for  $R$  given by Hagen and Rubens [6.20] [6.17] [6.14] may be used. This is

$$R \simeq 1 - 2 \left( \frac{\nu}{\sigma} \right)^{1/2} = 1 - 2 \left( \frac{c}{\lambda \sigma} \right)^{1/2}, \quad (6.6)$$

where  $\nu$  and  $c$  are the frequency and velocity of light and  $\sigma$  is the dc conductivity of the metal. Jacobson et al. [6.14] deduce for silver at  $\lambda = 10 \mu\text{m}$  the value  $R = 0.9954$  from (6.6), in excellent agreement with that from (6.4) above.

For shorter and visible wavelengths, if reflectivities are lower, Eqs. (6.4) and (6.6) are no longer valid, since bound electrons affect the reflection and absorption. This case is treated further, following Drude-Lorentz theory, by Born-Wolf [6.17] and Jacobson et al. [6.14].

An important case is the normal reflectivity of a metal coat of optical constants  $n$  and  $\kappa$  covered with a non-absorbing dielectric film of refractive index  $n_1$  and thickness  $t_1$ . This is given by [6.6] [6.17]

$$R = \frac{r_1^2 + r_2^2 - 2r_1r_2 \cos(2\varphi - \delta)}{1 + r_1^2r_2^2 - 2r_1r_2 \cos(2\varphi - \delta)}, \quad (6.7)$$

where  $r_1 = (n_1 - 1)/(n_1 + 1)$  from (6.5) and, for longer wavelengths,

$$r_2 = \left[ \frac{(n - n_1)^2 + \kappa^2}{(n + n_1)^2 + \kappa^2} \right]^{1/2}, \quad (6.8)$$

by analogy with (6.4). The quantities  $\varphi$  and  $\delta$  are defined by

$$\varphi = \frac{2\pi n_1 t_1}{\lambda_o} \quad \text{and} \quad \tan \delta = \frac{2n_1 \kappa}{n_1^2 - n^2 - \kappa^2}, \quad (6.9)$$

where  $\lambda_o$  is the wavelength in vacuum and  $\delta$  is the absolute phase change at the dielectric-metal boundary. In the absence of the covering coat, Eq. (6.7) reduces to (6.4) by virtue of the fact that  $n_1 = 1$  in air and  $r_1 = 0$ .

The effect of angles of incidence other than zero is discussed by Hass [6.6] and depends on the polarisation of the light.

Classically, aluminium reflecting coatings on glass mirrors have been protected either by magnesium fluoride ( $MgF_2$ ) or silicon monoxide ( $SiO$ ) coats [6.6].  $MgF_2$  has disadvantages and is normally only desirable for the vacuum UV because of its low absorption. It can therefore be interesting in a space environment but not normally for ground-based telescopes. In principle,  $SiO$  has been more applicable to this case. It can be evaporated at a fairly low temperature (ca.  $1200^\circ C$ ) and forms a layer with excellent protection properties. The best coats are deposited slowly at rather high pressures (ca.  $8 \times 10^{-5}$  Torr of  $O_2$ ) and are highly oxidised,  $Si_2O_3$  rather than strictly  $SiO$ . They maintain the high reflectivity of aluminium coats down to  $\lambda \simeq 300$  nm, using protective coats about 275 nm thick. There is a strong absorption band at about  $\lambda = 10 \mu m$ . Other materials that were introduced quite early as protecting coats are  $SiO_2$  and  $Al_2O_3$ . These must be evaporated by electron bombardment [6.6].

Since these materials are hard and offer excellent protection, why have they not been routinely used in telescope optics, where unprotected (apart from its natural oxide coat) aluminium is still virtually universal practice for large telescopes? The answer is that the removal by chemical means is considered too difficult and dangerous for the mirror surface. Silicon oxide coats can be polished off with reasonable security, but this process is far too complex and expensive to be of interest for large optics. If the protecting coat could be produced in a highly perfect state, entirely free from blemishes such as pinholes or blisters, and if it never deteriorated, then such coats could be acceptable. But previous technology has not been able to provide this on large surfaces. A defective protection coat which cannot be removed and produces a patchy and non-renewable aluminium coat is much worse than simple aluminium which is easily removable with acids or caustic soda.<sup>1</sup>

<sup>1</sup> The prescription used at ESO, following practice at KPNO in the United States, is as follows [6.21]: a) Tap water rinse. b) Al removal by NaOH 5% with light

The theoretical curve for fresh aluminium given in Fig. 6.2 or Table 6.1 shows an average  $R$  in the waveband  $0.30\text{ }\mu\text{m}$  to  $1\text{ }\mu\text{m}$  of about 0.9. The reality of the primary mirrors of most of the world's large telescopes is very different: deterioration due to damp and dirt gives a normal average figure nearer 0.8, often less if there is reluctance to re-aluminize relatively often. In practice, the periodicity is of the order of 1–3 years. Secondary mirrors of Cassegrain telescopes are more favourable because they face downwards: re-aluminization is usually much less frequent.

The consequences of loss of reflectivity  $R$  are serious, above all if a number of mirrors are used to form the image. Four reflections with  $R = 0.8$  give a throughput, if every other loss were zero, of only 0.41. This has prevented the application of excellent 3 or 4 reflection telescope designs [6.22] (see also § 3.6.5.3 of RTO I) and has effectively limited the large telescope to the prime focus, Cassegrain or Nasmyth forms for high-throughput imagery. If durable coatings with  $R = 0.95$  were available, the throughput from 3 reflections would be 0.86; from 4 reflections 0.81. Several of the solutions discussed in Chap. 3 of RTO I, using 3 or 4 reflections at powered aspheric mirrors, can provide excellent wide-field solutions if  $R$  were adequate. The fact that no fundamental (and generally acceptable) advance has been made for *large optics* since Strong's work in 1933 is remarkable and implies clearly that too little investment has been made in this technological area: every other area of telescope optics has advanced dramatically since that time.

A further pressing reason for improvement is the small angle light diffusion due to reflecting surface deterioration, dust and other contamination. With modern linear detectors (CCDs), the increase of sky background due to diffusion of light from brighter objects in the field can become a serious limitation. This matter has been analysed by Greco et al. [6.23], who propose measurement techniques both for the manufacturing and operational phase of telescopes.

One of the most important reasons for improvement is the inevitable deterioration of the mirror surface due to cleaning prior to re-aluminization. However carefully this is done, some deterioration is inevitable. This is a major reason why re-aluminizing is often postponed even though the  $R$  values are unacceptable.

In the next sections we shall consider the developments now taking place which may well replace the classical unprotected aluminium coat, and modern methods for its cleaning and maintenance.

---

cotton wool swabbing (ca. 90 % Al removed). c) Tap water rinse. d) Residual Al removal by HCl 5 % plus CuSO<sub>4</sub> with light cotton wool swabbing. e) Tap water rinse. f) Distilled water rinse. g) Alcohol rinse with Propanol 99.7 %. Water residual removal and alcohol distribution using optical cleaning paper. h) Drying with optical cleaning paper.

## 6.2 Modern perspectives for reflecting coatings

### 6.2.1 Multi-coat enhancement of reflecting coats

If protective coats can also enhance the reflectivity of a metal reflecting layer, they become particularly interesting for astronomical telescopes. Such an enhancement is achieved over a fairly broad spectral region by coating the metal layer with alternate coats of dielectrics with low and high index [6.6] [6.24] [6.25]. To obtain the maximum enhancement, the metal layer is first coated with a low-index material until its reflectivity *decreases* to a minimum at the wavelength where enhancement is desired. Then the high-index material is applied until the reflectivity reaches a maximum. The addition of more such pairs gives further reflectivity increase. Under these conditions, the first low-index coat on the metal is effectively  $\lambda/4$  thick and all other coats are truly  $\lambda/4$  thick. The true thickness of the first coat on the metal is given by [6.6]

$$n_1 t_1 = \frac{\lambda}{4} \frac{\delta}{\pi} , \quad (6.10)$$

where  $t_1$  is the thickness and  $\delta$  the absolute phase change at the dielectric-metal boundary as defined by (6.9). For normal incidence, the maximum reflectivity of a metal surface with optical constants  $n$  and  $\kappa$  when coated with such a stack of dielectric pairs with indices  $n_L$  and  $n_H$  is given, in the notation of Hass [6.6], as

$$R = \left( \frac{1 - Y^{2x} Z}{1 + Y^{2x} Z} \right)^2 , \quad (6.11)$$

where  $x$  is the number of film pairs and

$$\left. \begin{aligned} Y &= \frac{n_H}{n_L} \\ Z &= n_L \left( \frac{1 + r_3}{1 - r_3} \right) \\ r_3 &= \left[ \frac{(n_L - n)^2 + \kappa^2}{(n_L + n)^2 + \kappa^2} \right]^{1/2} \end{aligned} \right\} \quad (6.12)$$

Hass gives the example of an Al coat enhanced by a single pair consisting of  $\text{MgF}_2$  and  $\text{CeO}_2$ , having  $n_L = 1.38$  and  $n_H = 2.35$  respectively. Taking the Hass values for the optical constants of Al in the visible ( $\lambda = 546 \text{ nm}$ ) as  $n = 0.82$  and  $\kappa = 5.99$ , Eq. (6.4) gives the reflectivity of the untreated Al coat as  $R_{Al} = 0.9163$ . Setting  $x = 1$  in (6.11) gives  $R_{Al(E)} = 0.971$  for the optimized wavelength, the bandwidth of enhancement extending from about 400 nm to 750 nm. With two pairs ( $x = 2$ ), a maximum reflectivity of 0.990 is obtained.

The potential of this approach for astronomical telescope mirrors has been investigated in detail by Browning et al. [6.26]. Their concern was twofold: to improve reflectivity and thereby reduce the IR emissivity of normal Al coats.

The best candidate was *silver* (Ag), but this must always be provided with a protecting coat. A dielectric coat over a metal always reduces reflectivity if it is thin. An increase in reflectivity is only possible if the dielectric coat is thicker, usually  $> \lambda/4$ . But the large values of the extinction coefficient  $\kappa$ , applying to most metals in the IR, reduce the sensitivity to this effect – see Eq. (6.8). Ag is excellent in the IR: its problems are poor reflectivity in the UV and the need for protection.

Dielectric multilayer coatings alone can give high reflectivity over limited spectral ranges typically of several hundred nm. They are based on the same quarterwave stack principle. If such stacks are placed over metallic high reflection coats, the stack boosts the reflection as shown above for the wavelength region  $\lambda_E$  giving  $\lambda/4$  thickness but reduces it outside this region at about  $2\lambda_E$ . For longer wavelengths, the reflectivity recovers to the basic value of the metal coat.

The enhanced Ag solution proposed by Browning et al. was

Air H L H M Ag

with H =  $Sb_2O_3$  or  $TaO_5$ , L =  $SiO_2$ , M =  $Al_2O_3$ , all quarterwaves referring to the reference (enhancing) wavelength of  $\lambda_E = 300nm$ . The theoretical reflectivity was excellent, with a minimum of 0.58 at  $\lambda = 315 nm$  and an average of about 0.95 in a smooth function from  $\lambda = 350 nm$  to  $700 nm$  and beyond. Such a result would be marvellous if it could be realised in practice, but typical coats produced with slightly different materials showed a serious dip (Fig. 6.3) from an enhanced maximum of about 0.97 at  $350 nm$  to a minimum of about 0.80 at  $390 nm$ . The authors point out that problems can arise

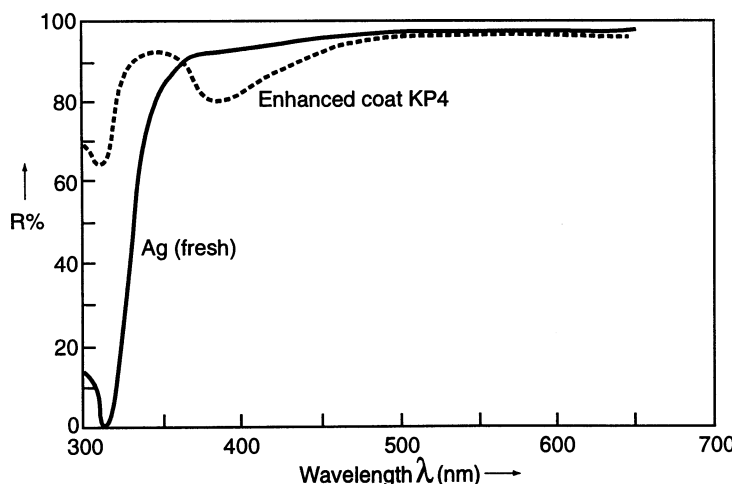


**Fig. 6.3.** Experimental reflectivity enhancement of an Ag coating using Air –  $SbO_3$  –  $Na_3AlF_6$  –  $Sb_2O_3$  –  $Si_2O_3$  – Ag with  $\lambda/4$  for  $\lambda_E = 300 nm$  (after Browning et al. [6.26])

because the  $\lambda/4$  stack is much more critical to thickness errors than normal metal coats.

Browning et al. found a second approach even more promising: the overcoating of an Al coat with a thin coat of Ag. The idea is that the Ag coat should be thick enough to dominate in the visible and IR but thin enough to permit sufficiently low absorption losses in the UV that the Al reflectivity predominates. Such an Ag thickness was estimated to be about 25 nm. The Ag and Al layers were separated by a barrier layer of  $\text{Al}_2\text{O}_3$  to prevent diffusion of the metals. The Ag coat was protected by an enhancing dielectric layer pair. The design was

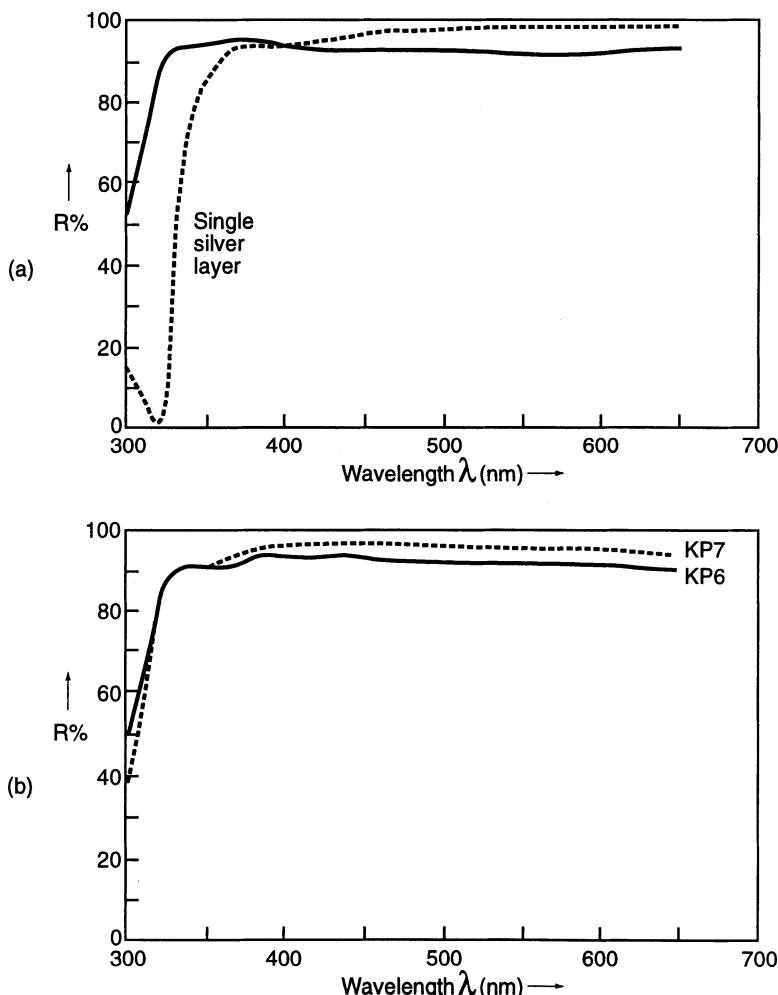


**Fig. 6.4.** Silver overcoating of an aluminium coat with dielectric enhancement in the UV, (a) theoretical, (b) experimental (after Browning et al. [6.26])

Air – H – M – Ag – M' – Al ,

with  $H = \lambda/4$  of  $Ta_2O_5$  or  $Sb_2O_3$ ,  $M = \lambda/5$  of  $Al_2O_3$ ,  $Ag = 25\text{ nm}$ ,  $M' = \lambda/40$  of  $Al_2O_3$ , the reference wavelength being  $\lambda_E = 200\text{ nm}$ . In the experiments, M was replaced by cryolite  $Na_3AlF_6$ . Figure 6.4 shows the theoretical and experimental results. The enhancement of the 2-layer dielectric stack in the UV is very successful. The reflectivity of the KP7 coat is 0.9 to 0.95 over the entire spectral range from 330 nm to 700 nm. KP7 has slightly more silver than KP6 giving a better  $R$  in the visible and a lower  $R$  in the UV.

Browning et al. concluded that this approach was extremely promising. Further enhancement of the UV would be possible with more layers in the dielectric stack: but this is a further technical complication and the increased thickness would increase the emissivity in the IR.

Subsequent improved results by Song and Macleod [6.27] for enhancing with a  $\lambda/4$  stack are quoted and discussed by Jacobson et al. [6.14] because of the use of  $TaO_5$  (tantalum), considered of great interest for its potential use in the Gemini project. The boosting coat was

Air –  $\lambda/4 TaO_5$  –  $\lambda/4 SiO_2$  –  $\lambda/4 TaO_5$  –  $\lambda/5 Al_2O_3$  – Ag

for  $\lambda = 300\text{ nm}$ . Figure 6.5 shows the result, in comparison with the enhanced Al coat overcoated with Ag, discussed above. The UV boosting of the  $\lambda/4$  stack is now most successful and the inevitable loss at  $\lambda \sim 500\text{--}550\text{ nm}$  is modest. This confirmed the practicability of both Ag protection and  $R$  enhancement in the UV.

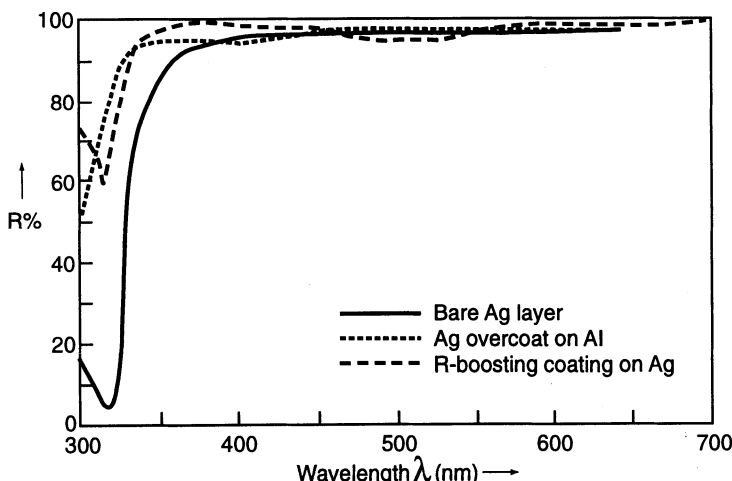


Fig. 6.5. Enhancement of  $R$  in the UV from an Ag coat using a  $\lambda/4$  stack compared with an Al coat with Ag overcoat and bare Ag (after Song and Macleod [6.27] from Jacobson et al. [6.14])

In spite of these highly interesting results, the technique has not been significantly applied to large optics to date because of the technical problems involved.

### 6.2.2 Silver reflecting coat with single protecting coat and other recent developments

The investigation by Jacobson et al. [6.14] for the Gemini project identifies protected *silver* as the most promising coating for the 8 m unit telescopes. Specifically, the investigation is concerned with low emissivity ( $E$ ) coatings, as a consequence of high reflectivity ( $R$ ). Transmissivity ( $Tr$ ) and absorption ( $A$ ) are defined by

$$R + Tr + A = 1 ; \quad A = E \quad (6.13)$$

The motivation for preferring Ag as basic reflecting material is the superior  $R$  compared with Al for all wavelengths  $\geq 380$  nm, as shown in Fig. 6.2. The emitted power  $P$  is given by

$$P = \sigma ET^4 , \quad (6.14)$$

where  $\sigma$  is the Stefan-Boltzmann constant and  $T$  the absolute temperature. The most effective parameter for reducing  $P$  would be  $T$ , but the dewpoint makes a significant reduction in  $T$  inapplicable in practice. Thus reduction in  $P$  can only be achieved by reduction in  $E$ , which is attained from (6.13) by an increase in  $R$ . At  $\lambda = 10\text{ }\mu\text{m}$  the best Ag coats have  $E$  about 0.005 whereas the best fresh Al coats give about 0.013 [6.13] [6.14].

The fundamental weakness of unprotected Ag coats, *tarnish*, can be attacked by two approaches: passivation and protection. *Passivation* implies doping Ag with small amounts of related metals such as Cu or Cr<sup>2</sup>. It is not yet clear to what extent this can be effective, so most effort has gone into *protection*. The authors consider the industrial coating of protected silver in low- $E$  architectural glass as a very favourable confirmation of the possibilities of protected silver. However, the *size* of very large telescopes (ca. 8 m) presents a special challenge.

The basic approach for the Gemini project (GP) is shown in Fig. 6.6. The layers involved are:

- Glass substrate.
- The lower adhesor/barrier layer will promote adhesion to the substrate and control interdiffusion between the substrate and the reflecting coat. This layer *may* include dopants. Thickness  $d < 100$  nm.
- The Ag reflective layer, which must have  $d > 100$  nm for UV/visible opacity.

---

<sup>2</sup> Attempts have been made to combine the positive properties of Ag and Al by using alloys. Apparently [6.14], these have not been successful: they promote the bad properties of each, not the good!

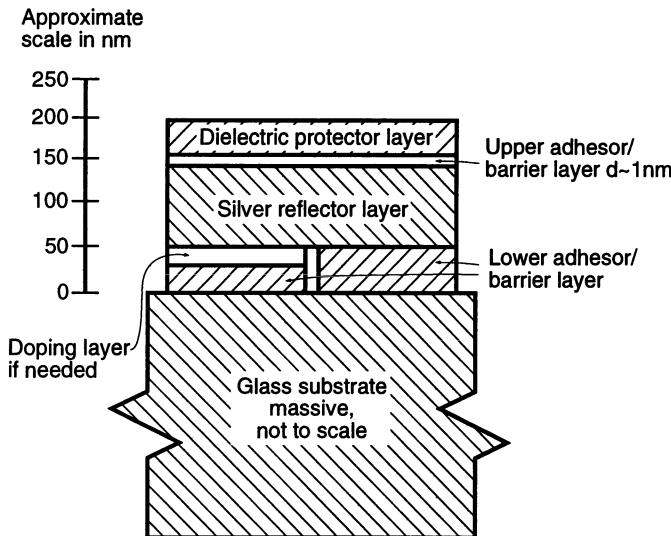


**Fig. 6.6.** Basic coating design for the Gemini project (GP) study (from Jacobson et al. [6.14])

- The upper adhesor/barrier layer will promote adhesion between the Ag and the topmost protective layer and will control interdiffusion. This layer must be very thin,  $d \simeq 1$  nm, to avoid reduction of  $R_{Ag}$ .
- The protective layer will protect the Ag layer from mechanical and chemical destructive agents. It should be thin enough (intended is  $d < 60$  nm) to minimize the increase of  $E$  from that of an ideal Ag layer.

When *evaporating* Ag coatings, high  $R$  depends above all on the purity of the Ag (0.99999+) and UHV conditions ( $\sim 10^{-9}$  Torr). The study considers, however, that *sputtering* is the best deposition method for large optics and is well suited to the properties of silver. Sputtering, like evaporation, is a physical vapour deposition (PVD) process, but differs in its nature markedly from evaporation. In the sputtering process, the source material is mobilized not by heating, but by the impact of ions on a large solid plate of source material known as the target. The ions are accelerated by strong electric fields. This gives much higher energies to the particles ejected from the target than occur in evaporation, leading to a film with higher adhesion and cohesion. Figure 6.7 shows the schematics of a large sputtering plant proposed for the Gemini 8 m primaries. The diameter is about 10 m but the height only about 2 m, the small value of the latter being a big advantage compared with an evaporation installation. The lower part of the vessel would essentially be a vehicle and rotator for the mirror with its cell. The essential guidelines for successful sputtering are:

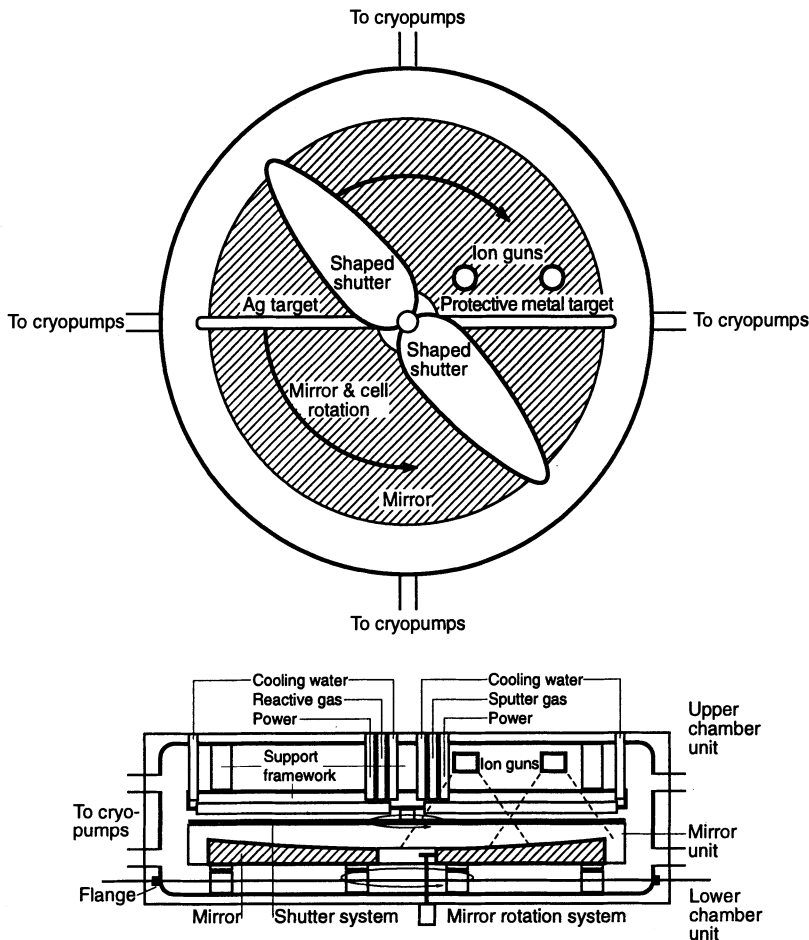


**Fig. 6.7.** Schematics of a proposed very large magnetron sputtering plant for the 8 m mirrors of the Gemini project (from Jacobson et al. [6.14])

- Pressure  $< 10^{-7}$  Torr
- A small  $h$  between target and mirror
- High purity of Ag and argon (Ar) sputtering gas

Low- $E$  architectural glass is produced by sputtering, but the Ag coat is only 10–20 nm thick.

The Gemini study identifies four materials as the most promising for the protective dielectric coating:

- Silicon nitride  $\text{Si}_3\text{N}_4$
- Hafnium oxide (hafnia)  $\text{HfO}_2$
- Tantalum oxide (tantalum)  $\text{Ta}_2\text{O}_5$
- Yttrium oxide (yttria)  $\text{Y}_2\text{O}_3$

The positive criteria for their selection included high optical  $Tr$ , amorphicity, low compression stress, hermeticity,  $H_2O$  insolubility, etchability (i.e. possibility of chemical removal), hardness, experience and cost. The ratings of all four were good (though high cost is a major problem for yttria), but the preferred materials were silicon nitride and hafnia. The reflectivity  $R$  of an Ag coat protected by various thicknesses of hafnia, as given by Decker and Stanford [6.19] and reproduced by Jacobson et al. [6.14] are shown in Fig. 6.8. The gains in the UV and blue result in corresponding losses between 0.7 and 4  $\mu m$ . Analogous results are given for the other materials [6.19] [6.14].

$Si_3N_4$  cannot be deposited by evaporation but can be by reactive or magnetron sputtering. It has the minor disadvantage of an absorption feature at  $\lambda = 11.5 \mu m$ , but this is negligible for  $d < 60 nm$ . The etchability is also relatively poor compared with hafnia, but it can be etched with dilute nitric and hydrochloric acids. The hardness and protection are optimum.

$HfO_2$  is less hard but still gives excellent protection. Its etchability by acids is more favourable than that of  $Si_3N_4$ .

Regarding the upper adhesor layer,  $Si_3N_4$  requires such a layer since it does not adhere well to Ag. The Gemini study considers the evidence is that a thin layer of NiCr will achieve what is required. For the other protective materials using oxides of a metal M, they suggest a thin layer ( $d \simeq 1 nm$ ) of M between the Ag and  $MO_x$  coats.

For the lower adhesor layer, the strongest candidates are given as Cu, Cr or NiCr alloys.

The tone of this most comprehensive and detailed study by Jacobson et al. [6.14] is cautiously optimistic. The sputtering results for Ag seem extremely good, giving superior  $R$  in the near IR for magnetron sputtered coats to that for evaporated coats. In general, the sputtered coats are fully the equal of the best evaporated ones. The Cu underlayers seem to reduce the corrosion rate of unprotected Ag coats, but the key to success appears nevertheless to be the removable protecting coat.

The above information on the Gemini project coating studies was already available in 1992 from the comprehensive report of Jacobson et al. [6.14]. An important update of this work has recently been given (1996) by Mountain, Gillett and Kurz [6.28]. These results have already been mentioned in § 3.1 above as some of the most important in current telescope development. Table 6.2 and Fig. 6.9 give a résumé of the status reported.

It is clear from Fig. 6.9 that silver gives a substantial boost in throughput over a conventional aluminium coated telescope for all wavelengths beyond about 400 nm. From Table 6.2 it is also clear that the protected Ag coat is close to meeting the UV specification, apart from the gain over Al in the region  $\lambda > 400 nm$ .

Latest information (November 1997) kindly supplied by F. Gillett [6.29] has confirmed that the report given by Mountain et al. [6.28] effectively represents the current situation. A more complete account will be presented by Jacobson et al. at the SPIE telescope conference in 1998 [6.30]. Further

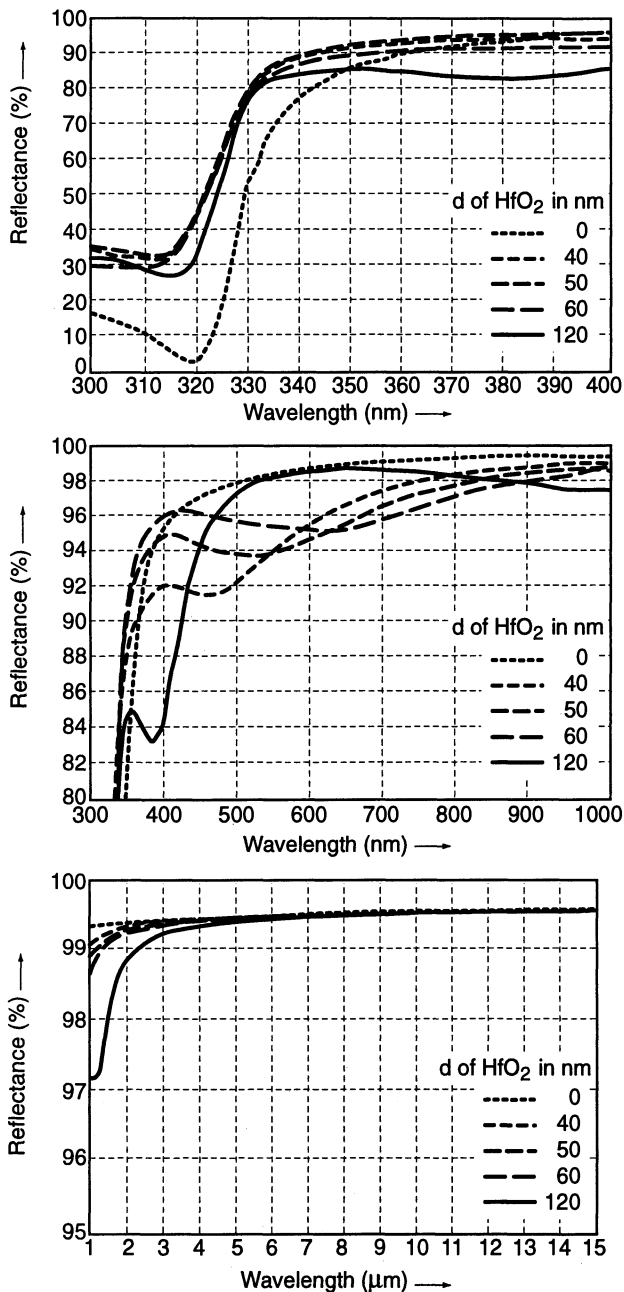


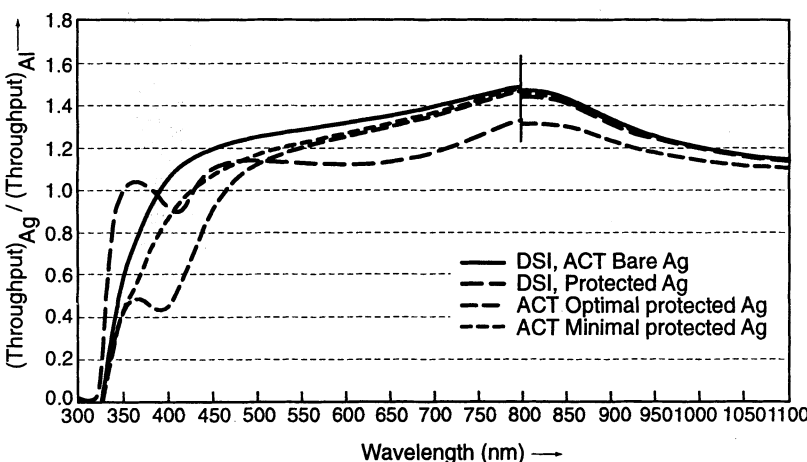
**Fig. 6.8.** A model of a coating Air –  $\text{HfO}_2$  (of variable  $d$ ) – Ag ( $d = 100 \text{ nm}$ ) – Cu ( $30 \text{ nm}$ ) – Glass showing the variation of  $R$  with  $d$  of  $\text{HfO}_2$  (after Decker and Stanford [6.19] reproduced by Jacobson et al. [6.14])

**Table 6.2.** Al and Ag Sample Reflectivity as reported for the Gemini coating program in 1996 (from Mountain, Gillett and Kurz [6.28])

Wavelength range ( $\mu\text{m}$ )	0.33–0.40	0.40–0.70	0.70–1.1
Bare Al	<u>0.87</u>	<u>0.89</u>	<u>0.90</u>
Bare Ag	0.80	<u>0.97</u>	<u>0.98</u>
Minimal protected Ag	0.76	<u>0.95</u>	<u>0.98</u>
Protected Ag	0.86	<u>0.92</u>	<u>0.96</u>

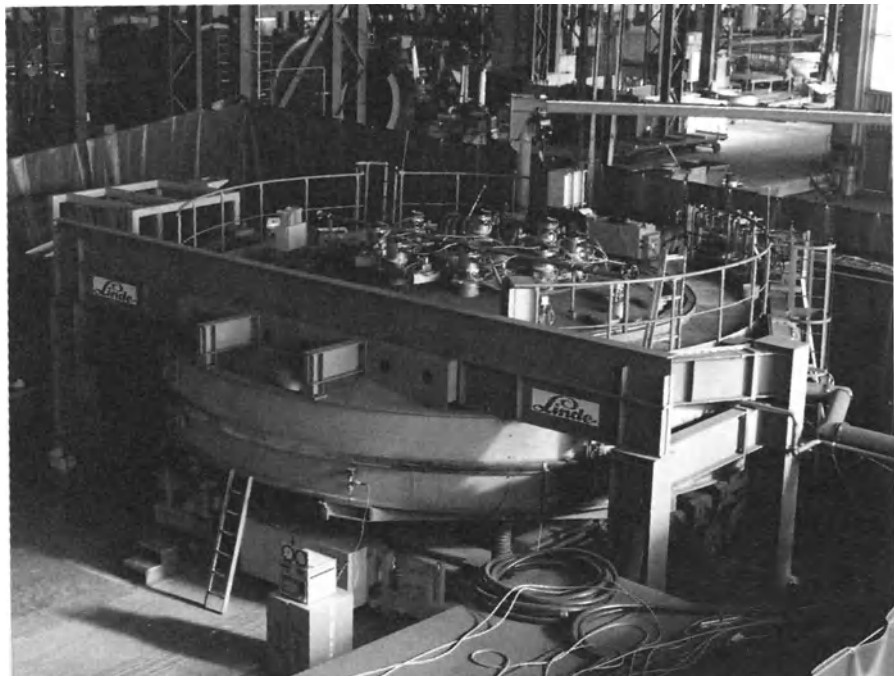
— ≡ Meets requirements

□ ≡ Meets goals

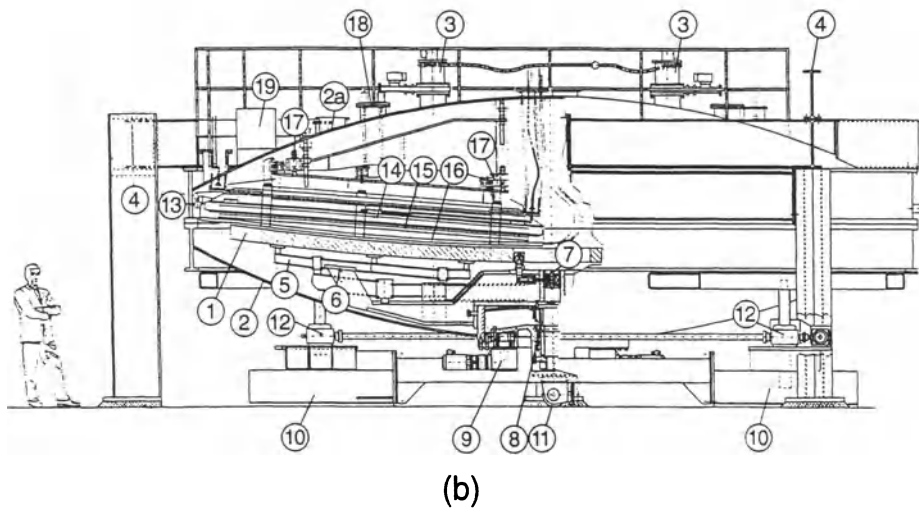
**Fig. 6.9.** The relative throughput of an “all aluminium” telescope (3 reflections) compared with that of an “all silver” telescope (3 reflections) for a variety of silver coatings (after Mountain, Gillett and Kurz [6.28])

experimentation with the coating plant is scheduled to start in December 1997 prior to the delivery of the first primary in March 1998. For “First Light”, a conventional Al coating is envisaged, but a new protected Ag coating is intended for the start of astronomical observation. F. Gillett thinks that water or moisture is still the main enemy of the Ag coat, even with its protecting coat. He believes it will be necessary to clean the new coat regularly with “snow” (see below) to prevent moisture degradation effects settling on the coat. Several years of use of a coat before renewal are hoped for: one year would be an absolute minimum that is acceptable. Thus the new Ag coats are not really seen as a revolution in *robustness* as compared with Al: their justification is the improved reflectivity.

It seems probable that protected Ag coats will replace Al coats for large telescopes in the near future. If so, this will be a great advance, above all if  $\lambda/4$  stack enhancement can be done.



(a)



(b)

**Fig. 6.10.** The ESO sputtering facility for the VLT 8m primaries (concept M. Grössl): (a) Photograph of the complete installation before shipment to Chile, (b) Section showing the basic design (courtesy M. Grössl, ESO, and Linde AG, München). For key see opposite page

**Fig. 6.10.** Key

1. VLT Primary Mirror with 8.2 m outer diameter and 28 800 mm radius of curvature.
2. Vacuum vessel lower part (supported from the air cushion cart).
- 2a. Vacuum vessel upper part (suspended from the steel frame (4)).
3. Closed cycle cryogenic pumps and gate valve.
4. Construction steel frame.
5. Substrate support system (force balancing whiffle tree principle) where the mirror substrate is resting on 27 axial pads.
6. Support flange for the VLT M<sub>2</sub> and M<sub>3</sub> mirror substrates.
7. Lateral support system: the M<sub>1</sub> substrate is fixed by 6 pads distributed over the central hole as safety protection against lateral displacement in seismic events.
8. High vacuum rotary feedthrough (Ferro fluidics system) for the central shaft.
9. Rotary drive and gearbox: all mirror substrates will be rotated during pre-treatment and thin film deposition. The thin films are deposited either in single or multiple pass mode.
10. Air cushion housings: in order to load the mirror into the coating chamber, the lower vacuum chamber section is moved on the floor by the air cushion system.
11. Friction wheel drive of air cushion transporter.
12. Spindle lifting system: the lower vacuum chamber section with its large flange must be lowered below the sputtering source structure in order to allow its manoeuvering off from the fixed upper chamber section.
13. The Meissner Trap is cooled down to liquid nitrogen temperature accomplishing a big pumping capacity for water vapour.
14. Planar magnetron sputter source body and the high purity Al target directed face down.
15. Sputter source anode.
16. Shutter correcting the Al flow for the speed variation over the radius.
17. Shutter bearings to allow opening and closing the panels.
18. Shutter drive and flange with rotary feedthrough.
19. Arc diverter module for powering the magnetron sputter source with up to 150 Kw.

This is confirmed by work on other projects such as the ESO VLT, also with 8 m class primaries. Grössl [6.31] gives the reflection curve for an enhanced, protected Ag coat with  $R > 0.90$  for all wavelengths greater than 330 nm and with a small dip to 0.92 at  $\lambda \simeq 420$  nm. This coat was produced by, or to the specification of the firm MATRA in France. The reflectivity requirement for the VLT primary mirrors is  $R \geq 0.86$  for  $300 \text{ nm} < \lambda < 20 \text{ mm}$ .

Protected Ag is not the only approach to fulfilling the above requirement for the VLT primaries. A more conventional approach, using Al as the base reflecting material, has been studied for ESO by the firm Leybold in Germany. An enhancement of  $R$  for Al by  $\geq 5\%$  in the visible wavelength band was an aim of the study, using two layers of  $\lambda/4$  low/high index materials to form an enhancing dielectric protective coat. The deposition was by Planar Magnetron sputtering. Experiments were made using an Al sputter target with dimensions 694 mm  $\times$  232 mm  $\times$  12 mm, and the 25 coats produced all easily met the above specification. The minimum  $R$  at  $\lambda \simeq 800$  nm was  $\geq 0.87$ .

Latest information from M. Grössl (November 1997) concerning ESO plans for the VLT confirm that the intention for the 8m primaries is still the cautious one of coating with pure Al. However, the sputtering facility, following the concept of Grössl, is designed to be completely flexible concerning the nature of the reflecting coats. Thus a change from Al to protected Ag will be possible, with suitable preparation, at any time. Figure 6.10 shows the sputtering facility for the ESO VLT.

Another center which intended the development of protected Ag coatings for large telescopes was the Optikzentrum in Bochum, Germany. According to Schmidt-Kaler [6.32], an ambitious programme for developing 3 layer coats, consisting of a carrier layer on the substrate, the Ag reflecting layer and a single dielectric protective layer, was to be initiated in 1994.

### 6.2.3 Cleaning and maintenance of reflecting coats

In § 6.1 we emphasized the importance of high throughput  $\tau_t$  in telescopes as one of the two parameters determining the optical efficiency  $E_t$  of the telescope in a basic photon-limited observing mode. We also commented on the marked discrepancy between the  $R$  values of freshly deposited Al coats and the average operating state of telescopes. The primary is normally the most critical reflecting surface since it is facing upwards. The average  $R$  is taken as about 0.8 in practice, but the state of the coats on the primaries of some telescopes is a depressing sight. On the other hand, many observatories make a major effort to achieve cleanliness, an effort which is rewarded by higher  $R$  and longer periods between aluminizing with corresponding preservation of the initial high quality optical surface.

The principal enemy is *dust* in the most general sense of that term. However, oil may be a danger in falling from dome hatches or, in open building concepts like the NTT, bird droppings.

So far as dust is concerned, observatory sites which are otherwise excellent may be unfavourable for dust because of dry, sandy conditions and appreciable wind. However, the cleaner the “dome” or “enclosure” is kept, the better the situation will be. Giordano [6.33] proposes a “clean dome” concept whereby the internal air is kept, during daytime with the enclosure closed, at “clean environment” condition, which he defines as a dust content not exceeding 50 000 dust particles per cubic foot. Dusty atmospheres have values easily an order of magnitude higher than this. Filtration and particle removal are discussed briefly by Jacobson et al. [6.14] who quote Kozicki et al. [6.34] for a review of possibilities.

For smaller primaries, *washing* with mild detergent or demineralised water has been very successfully applied. The more frequently it is performed, the more effective it is because dust particles are less firmly anchored to the mirror surface. In its original concept, an internal semi-automatic washing system was intended for the ESO NTT, but it was never implemented in practice. It is a difficult procedure to operate with very large mirrors since

the liquids involved can easily contaminate other parts of the telescope and drying must be achieved without staining.

The classical procedure of a jet of gas (particle filtered, oil-free, dry) is often used for local dirt concentrations and is considered for Gemini [6.14]. But it can be dangerous for gritty dust.

Two techniques have been developed in the last decade which seem very promising: "CO<sub>2</sub> snow" cleaning and "plastic film peeling". The former was proposed by Hoenig [6.35] and has been analysed in detail for large optics by Zito [6.36]. The advantage of CO<sub>2</sub> snowflakes as a cleaning jet is that the mass of the flake is comparable to that of a dirt particle whereas a gas jet consists of much lighter molecules. A jet of CO<sub>2</sub> snowflakes can therefore impart a much higher velocity to the dirt particle and is correspondingly more efficient in removing it. Of course, it is essential that the snowflakes cause no scratching of the mirror (Al unprotected) coat. Zito found no evidence of scratching with dimensions greater than 0.05 μm, his resolution limit. This conclusion has been confirmed by other investigators.

The CO<sub>2</sub> snow technique is simple to apply [6.36]. Liquid CO<sub>2</sub> is forced through a nozzle under 750 psi and expands into a volume at 1 atm pressure, creating snowflakes. The flake size is determined simply by the nozzle.

Zito quotes a rise in reflectivity of a 24-inch primary compared with a standard reference of 86.0 % to 91.8 % in blue light and 91.5 % to 99.0 % in red light.

The second technique of plastic film peeling has been practised for a number of years at several American observatories, e.g. Cerro Tololo. A suitable resin is sprayed on to the reflecting surface. Such protection resins for optical elements are in common use. The resin film is then peeled off, the dirt adhering to it. Tests have been reported by Bennett et al. [6.37].

Tests of cleaning both by CO<sub>2</sub> snowflakes and plastic film peeling have been performed by Giordano [6.38] [6.39]. Measurements of reflectivity  $R$  were made with an excellent device  $\mu$ SCAN [TM] supplied by TMA Technology, USA. This also measures diffusion as the BRDF (Bidirectional Reflectance Distribution Function). Two Al coated test mirrors were exposed to dust and other contaminants for over 6 months and then cleaned by CO<sub>2</sub> snowflakes and peeling with a plastic film material called OPTI-CLEAN. The results are shown in Fig. 6.11. The CO<sub>2</sub> snowflake cleaning recovered about half of the reflectivity loss compared with a fresh Al coat, somewhat less in the UV, somewhat more in the red and near IR. The cleaning efficiency of peeling was quite remarkable, virtually the entire original reflectivity being recovered over the whole spectral range.

The greater efficiency of peeling is not surprising since the intimate contact of the resin with the oxide coat on the Al can apparently remove dirt from this coat in a way which is impossible with CO<sub>2</sub> snowflakes.

Giordano also did tests of a spray material used at Cerro Tololo called "Econ-o-cloth". This was also successful as a peeling device but increased the BRDF (diffusion) which was not the case with OPTI-CLEAN [6.40].

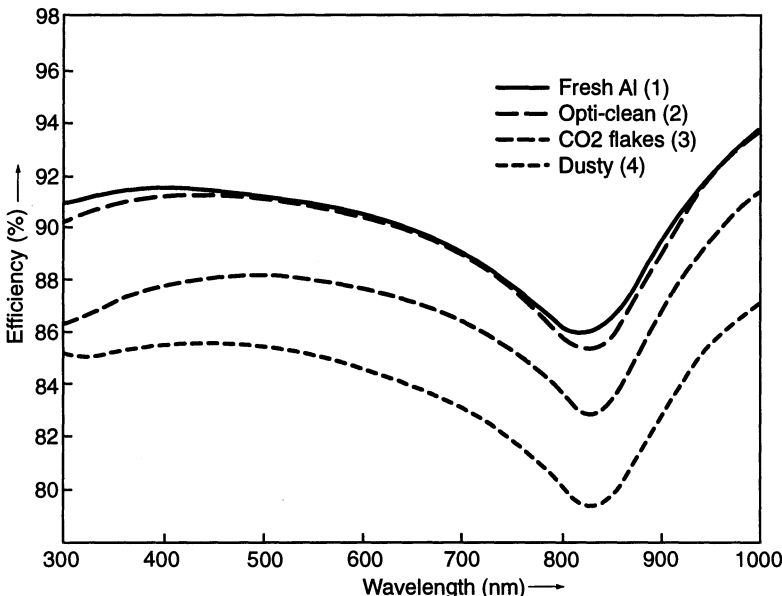


**Fig. 6.11.** Recovery of reflectivity losses due to cleaning of dusty samples (4) with CO<sub>2</sub> snowflakes (3) and peeling with OPTI-CLEAN (2), compared with fresh Al (1) (after Giordano [6.38] [6.39])

Further cleaning tests have been carried out by Giordano at the NTT [6.41], in order to develop a cleaning strategy for the optics of that telescope. Various cleaning techniques were applied to the “dusty” primary, prior to re-aluminizing.  $R$ -values were measured with  $\mu$ SCAN as percentages compared with a standard reference. The best results of all were achieved by peeling with *Collodion* films, Collodion being a cheap and readily available product used for surgical purposes and in photography. This produced an improvement of 8.15 %, even higher than that obtained from the subsequent new aluminium coat which gave 7.4 %. However, the peeling technique with Collodion was more difficult to apply and there are problems of toxicity. CO<sub>2</sub> snowflakes gave only 0.83 % improvement. Table 6.3 summarises the results. In practice, OPTI-CLEAN was considered the optimum solution, although more difficult to carry out than CO<sub>2</sub> snowflakes cleaning.

An analysis of the possibilities for cleaning in the case of the ESO VLT has been made by Dierickx and Giordano [6.42]. Experience has shown that the loss of reflectivity of primaries at the La Silla observatory is about 10 % per year, for a 3-mirror Nasmyth focus about 20 %, i.e. 1.8 % per month. The effective diameter  $D_{eff}$ , as defined by (6.1), would reduce for a VLT unit telescope from the initial value of 8.00 m to 7.17 m after 12 months and 6.43 m after 24 months. This illustrates how serious the normal loss of reflectivity would be. Such a loss in 12 months is the equivalent of the total loss from all sources affecting the optical quality parameter  $I_0$ . Clearly, this situation

**Table 6.3.** Percentage improvements in  $R$ , measured on the NTT primary relative to a standard reference, produced by various cleaning techniques (from Giordano [6.41])

Cleaning technique	Percentage improvement in $R$
$\text{CO}_2$ snowflakes	0.83
OPTI-CLEAN (peeling)	5.85
PL-25 (peeling)	3.25
Collodion (peeling)	8.15
New Al coat	7.4

would be transformed by a *cleaning procedure which reduces the loss of  $R$  to one tenth of the above values, i.e. 2% per year for a 3-mirror focus*. Re-coating could then be done every 4 years with only 8% loss. This is the declared aim for the VLT.

A report on the practical prospects of achieving the above aim is given by Giordano [6.43]. He concludes that *frequent* cleaning is the most important aspect of a cleaning programme. The frequency in practice will depend on the local contamination conditions and must be determined by an accurate and efficient monitoring device. Further experiments have confirmed the superiority in results of the OPTI-CLEAN peeling technique for unprotected Al surfaces. However, its application was still limited to an area of about  $0.25 \text{ m}^2$ . Clearly, the application to 8 m mirrors was felt to be problematic.

Recently, reports have been made [6.44] of effective cleaning for large primaries by a *laser bombardment* over several hours. This loosens the dirt, which can then be removed by suction devices. Figure 6.12 shows the striking results. Such cleaning could readily be done during daytime and – if its efficiency is proven by measurements of  $R$  – could well provide by far the simplest technique for large primaries.

Further details of laser cleaning in connection with the Gemini project have been given by Rayboult [6.45]. He quotes the firm STI Optronics, USA, in this connection, who are anxious to work with astronomical observatories. The need for laser wavelengths in the UV is emphasized. Molecular contaminants are removed by photochemical dissociation. Particles are removed by the generation of an opto-acoustic stress wave, requiring a pulsed laser source, such as an excimer laser. The power used in the UV was  $0.3 \text{ J/cm}^2$ . There is effectively no heating of the reflecting coating and no damage to it. Evidence is presented that the cleaning efficiency is far higher than with  $\text{CO}_2$  snowflakes.

Giordano [6.46] initiated an investigation into laser cleaning for the VLT. Preliminary results with an EXCIMER laser operating at  $\lambda = 308 \text{ nm}$  using test samples were very encouraging, the bulk of the dirt being removed by a single passage of laser irradiation of appropriate power and duration. The

### UV Laser Cleaning of $MgF_2$ coated Aluminium Mirror

- Contaminated with dust particles, solvent/oil residues
- Leftover surface features are pits and remnant scratches

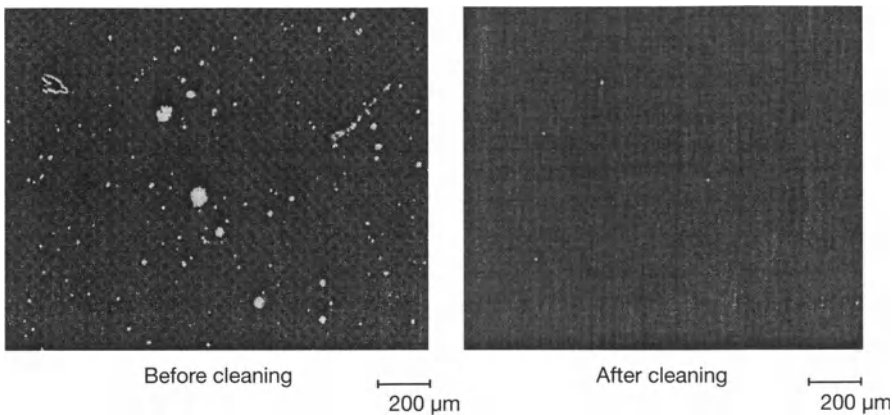


**Fig. 6.12.** Experiments for cleaning of telescope primaries by laser bombardment and suction removal of the loosened dirt (after Balick [6.44])

transfer of laser power to kinetic energy in the dust and dirt particles requires a wavelength in the UV. However, the wavelength must not attack an Ag or Al reflecting film.

A final report of this study, carried out for ESO by the Laser-Laboratorium Göttingen e.V., was submitted in 1994 [6.47]. This gives an excellent review of the potentialities and limitations of the method. The main conclusions were as follows:

- a) Laser cleaning with  $\lambda = 248\text{ nm}$  (30 ns pulse duration) was possible on all *aluminium* coated mirror samples provided by ESO.
- b) The gain in reflectivity increases with laser energy density (fluence), the upper limit to this fluence being determined by the damage threshold for the Al coating.
- c) At  $\lambda = 248\text{ nm}$ , the damage threshold for the (*aluminium*) coating and the glass substrate is markedly higher than the fluence required for effective cleaning. These fluence values converge as  $\lambda$  is reduced: for aluminium, the fluence required at  $\lambda = 193\text{ nm}$  for maximum reflectivity enhancement is very close to the damage threshold. This wavelength is therefore too short for practical cleaning of Al coats.
- d) The damage threshold for *silver* coats is less favourable than for aluminium. This is because of higher absorption by Ag than by Al. Cleaning of Ag with  $\lambda = 248\text{ nm}$  is therefore not possible. At  $\lambda = 351\text{ nm}$ , however,

cleaning of Ag coats should be possible as for Al coats at  $\lambda = 248\text{ nm}$ , since the absorptivity of Ag at  $\lambda = 351\text{ nm}$  is similar to that of Al at  $\lambda = 248\text{ nm}$ . Inevitably, the longer the wavelength, the higher are the fluence values required for effective cleaning. In this sense, the most efficient wavelength is therefore the shortest which allows sufficient safety margin to the damage threshold.

- e) The reflectivity increases with the number of pulses applied to a given site. The biggest increase results from the first few pulses and saturation occurs after 10–15 pulses.
- f) Relative reflectivity enhancement of up to 10 % (at roughly normal incidence) was achieved on strongly polluted mirror samples.
- g) Application of an auxiliary gas flow is necessary to avoid redeposition of detached particles.
- h) The cleaning efficiency is comparable to that of polymer film stripping (e.g. OPTI-CLEAN peeling).
- i) A solvent film on the sample surface strongly improves the laser cleaning efficiency.
- j) Laser spot sizes on the sample between  $0.6\text{ mm}^2$  and  $30\text{ mm}^2$  were used. In the case of one highly polluted sample, a small spot size (ca.  $0.56\text{ mm}^2$ ) gave a reflectivity gain of 10.0 % at 350 nm, whereas a large spot size (ca.  $12\text{ mm}^2$ , square) gave a gain of 7.5 %.
- k) Comparisons showed that OPTI-CLEAN peeling was more efficient in removing small particles, while laser cleaning is more successful in removing large particles.

In the general industrial sense, laser cleaning (and machining) is an area of intensive development. It is pointed out [6.47] that experience in other areas of application cannot be extrapolated to the case of test mirrors with different substrates. For example, Al coated silicon wafers have a damage threshold some ten times higher than that of the Al coated BK7-glass or Zerodur sample mirrors of ESO, because of the better thermal conductivity of silicon.

It is conceivable that the laser technique could also be used for removal of the reflecting coat, also its protecting coat, but it remains to be proved that this could be done without damaging the surface of the substrate.

An excellent review of the current situation regarding in-situ cleaning of ground-based telescope mirrors has been given by Giordano [6.48] [6.49].

In spite of the promise of UV laser cleaning, the risks were considered too high for its application at this stage to the ESO VLT. The fact that the VLT has 4 separate 8 m telescopes was considered a negative feature, as heavy equipment would have to be moved from telescope to telescope. The operation and maintenance of a suitable excimer laser is complex and expensive. A cleaning duration (ca. 10 hours) was considered too long, since safety precautions (laser beam reflections) limit dome access for other activities. Furthermore, the optical beam relays to scan such large mirrors would be by

no means trivial. Nevertheless, UV laser cleaning may well have an important future in ground-based telescopes. It will be necessary to gain experience on smaller sizes (say, a 1 m telescope) and step up from that to large sizes.

Peeling gives excellent results and is envisaged for the  $M_3$  mirrors of the VLT telescopes. Using the peel-off product XL Clean 5, Giordano reports [6.48] successful peeling operations on the ESO 3.6 m telescope at La Silla as well as tests on an 8.2 m VLT primary at the REOSC optical shop in France. Successful peeling was achieved on this  $M_1$  and a second coat applied as protection for packing and transportation to Paranal in Chile. Peeling may be used locally on the primaries on site and a peeling clean of the entire surface will be tried before the first scheduled re-coating of a primary.

The basic cleaning technique will be the CO<sub>2</sub> snowflake procedure. Although this cannot rival peeling or UV laser cleaning for seriously polluted mirrors, it is believed that, because of its ease of operation, it will prevent dirt sticking to the coating and thereby maintain good reflectivity over an extended period. The CO<sub>2</sub> snowflake and peeling techniques are therefore seen as complementary.

The development of hard protective coats will certainly facilitate and simplify all cleaning operations.

#### 6.2.4 Summary

In summary, techniques for producing reflecting coats for large optics and associated techniques for their maintenance and cleaning have clearly entered a period of active development and application after half a century of effective stagnation. This is certainly one of the most important trends in modern telescope optics. If hard protective layers become generally available, which are in any event required for Ag reflecting coats, the cleaning and maintenance problem will be greatly simplified.

## 7. Adapters and beam combination aspects, baffles

### 7.1 Adapters

#### 7.1.1 Background of adapter development

The term “adapter” is widely used to describe the more or less complex unit which is required at the focus stations of modern telescopes in order to control and operate the telescope. The modern adapter started to evolve when “offset guiding” replaced the old technique of a separate guiding telescope, normally a smaller refracting telescope rigidly attached to the main telescope. With increasing size and precision, this original solution was no longer adequate because of differential flexure problems, above all in the larger instrument. Offset guiding, i.e. guiding on a star image in the field of the main telescope, was a huge advance since only differential field effects caused errors. Of course, in many observing modes where the object is bright enough, guiding is done on the observed object itself or in the small instrument field.

Adapters for the “Bowen class” telescopes (see Chap. 5 of RTO I), most of which are still working and producing excellent results after conversion to modern electronic detectors, were originally designed for the photographic plate era. Furthermore, the transition to modern, TV-based monitors had not been completed. Hence the adapter for the Cassegrain focus of the ESO 3.6 m telescope, commissioned in 1977, still had to meet the requirement of supplying oculars for the astronomers, as a technical reserve. Since the aperture was 3.6 m, only low-power oculars made any sense. Magnifications of 288 and 480 were given by oculars of focal length 100 mm and 60 mm, large optical elements which had to be accessible to a human eye and fed with an image. They were never used in operation and barely used for technical purposes, but produced a major complication to the adapter. At the prime focus of this and similar telescopes, an observer’s chair was available for photographic work, above all using the Gascoigne plate corrector (see Chap. 4 of RTO I). The relatively large pointing error at that time (often approaching 1 arcmin) meant that a significant field with a lower power ocular was required to identify the object and center it in the field. At both foci, it was usually required to have a wide field/low resolution and a small field/high resolution system for observing the center of the field.

As television and other detector systems displaced the observer definitively from the telescope into the observing cabin, similar systems provided the fields on TV monitors, again with the limitations of the pointing at the time. Using the best pointing models, such as those developed by Wallace at the AAT, pointing accuracy with errors < ca. 5 arcsec rms were achieved under best conditions with such equatorially-mounted telescopes [7.1].

The adapters for such telescopes were essentially devices for mounting photographic plates (or the rapidly developing electronic detectors) and instruments, and also the center-field identification and monitoring equipment and offset-guider. Until television or other detectors released the astronomer from his historic chore, the offset guiding was done with an ocular. Television detectors were thus a huge advance in comfort and precision. *Field rotation* was not a problem at that time since all telescopes (except the Russian 6 m) were still equatorially mounted and had no significant field rotation.

Some telescopes of this epoch, e.g. the CFHT, provided a Cassegrain adapter with a large focus movement (ca. 700 mm) to allow for different focus positions. The mechanical precision required for focusing such a large, heavy unit is formidable.

### 7.1.2 The adapter for the ESO 3.5 m NTT (Nasmyth focus)

The case of the NTT is presented here simply as typical of modern telescopes featuring alt-az mountings, modern pointing specifications and a sophisticated active optics concept. The requirements will reflect the technological basis of the telescope: the adapter of the 10 m Keck telescope, for example, must have features reflecting its very sophisticated opto-electronic technology.

The NTT adapter has the following basic functions:

- To provide offset guiding facilities (using autoguiders)
- To provide image analysis facilities for the active optics control system
- To provide field rotation facilities both for orienting an instrument slit in the required direction and for compensating field rotation induced by the alt-az mounting
- To provide calibration facilities (about ten different calibration lamps and an integrating sphere)

**7.1.2.1 Guide-probes and image analysis.** Figure 7.1 shows a schematic plan-view of the adapter/rotator, designed by F. Franzia of ESO, looking along the optical axis from the Nasmyth image [7.2]. From the scale of the NTT ( $187\text{ }\mu\text{m} \equiv 1 \text{ arcsec}$ ), the effective linear diameter of the telescope field (nominal angular field 30 arcmin) is about 365 mm. The adapter/rotator diameter is about 1.6 m and the flange back focal distance is 500 mm. This relatively large value gives more freedom for mounting instruments but has the price that the *guide-probe* (GP) pick-up mirrors are correspondingly larger to receive the f/11 beam plus GP field.

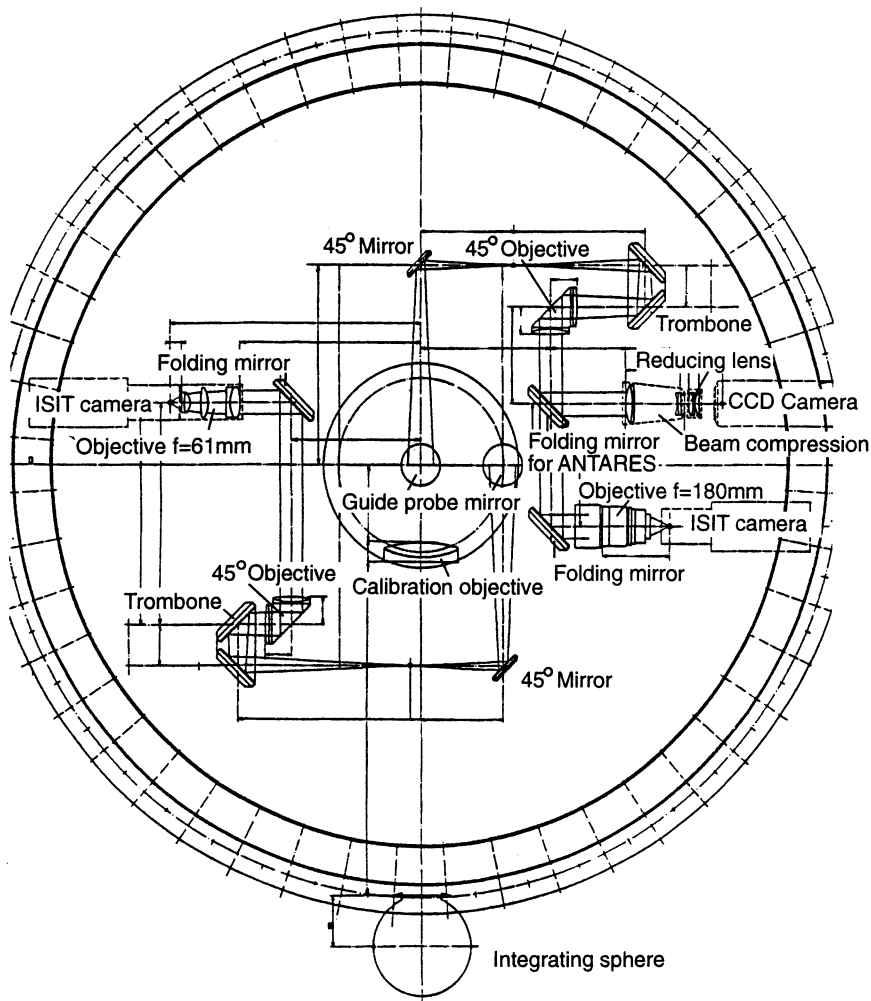


**Fig. 7.1.** The optical layout (schematic) of the ESO NTT adapter/rotator (from Franza [7.2] and ESO drawing NTT 30/11)

The GP pick-up mirror is shown in the center field ( $x = y = 0$ ), deflecting the beam (upwards in Fig. 7.1) perpendicular to the optical axis in the plane of the adapter/rotator (A/R). A  $90^\circ$  deviation precedes the image formation, at which point a reference point source can be switched in by a mirror (not shown) instead of the star image. The GP system can be moved over part of the field by an  $x$ - $y$  movement, so that this image position is also variable. However, it must be fed to a *fixed* optical train, feeding on one side of the A/R (the right-hand side in Fig. 7.1) a collimator objective combined with a  $45^\circ$  prism which, in turn, feeds either the image analyser or a TV camera for guiding via deflection mirrors. Later, the first of these deflection mirrors was

replaced by a dichroic mirror sending about 90% of the light to the image analyser (CCD camera) and about 10% to the guiding camera (ISIT camera). This permits continuous image analysis without disturbing the guiding in any way. With the original system, the absolute tracking quality was fully adequate over the time required for image analysis, but the switchover required human intervention.

On the left-hand side of Fig. 7.1, the fixed system consists only of the collimator and one guiding camera.

To accommodate for the variable distance of the star image (or reference) from the fixed collimators, each train has a two-mirror trombone system for absorbing these path length variations, so that a collimated beam is always produced. The collimator objectives focus the telescope exit pupil on the imaging optics of the three cameras.

It is an important feature of GPs with  $x$ - $y$  movements that only *half* the total field can theoretically be covered by one GP, two being required to cover the whole field because of the problem of going through the center. Anti-collision measures are necessary near the center.

The image analysis camera (so-called ANTARES system) consists of a beam compressor reducing the beam width from 46.4 mm to 25.4 mm, after which it passes through the Shack-Hartmann lenslet raster (see § 2.3.3.2 and § 3.5.2) to the reducing objective, which images the raster spots with a patch diameter of 9.5 mm on to the CCD (see Fig. 2.21 for the appearance, as shown on a photographic plate).

The guiding systems, originally using ISIT cameras<sup>1</sup>, are fed on the right-hand side (GP1) by an objective of focal length 180 mm giving 4.28 line pairs per arcsec, the camera normally used for guiding. The left-hand side (GP2) has an objective with focal length 61 mm giving 1.45 line pairs per arcsec. This system is faster with lower resolution and was intended above all for center-field identification for IR observation.

The scale of the NTT (187  $\mu\text{m}$  per arcsec) determines the *positioning accuracy* of the GP. This was fixed at  $6 \mu\text{m} \equiv 0.032$  arcsec. With movements in  $x$  and  $y$  of 168 mm and 336 mm respectively, this represents a stringent mechanical requirement for all altitudes of the telescope. GP position error will enter directly into the image error function as a form of *tracking error* (wavefront tilt). The search field for guide stars depends on the observing mode. Figure 7.2 shows the available search field using the EMMI spectrograph in its long-slit mode (upper half) or direct imaging (focal reducer) mode in the lower half. Based on the unvignetted field diameter of 30 arcmin delivered by the NTT, these areas provide sufficient guide stars, even at the galactic poles, if stars down to  $14^m$  can be used for image analysis [7.3]. The HST star catalogue is now available for the NTT and provides pre-determined guide stars of given magnitude. The GP field is 2 arcmin.

<sup>1</sup> During the major update of the NTT in 1996/1997, intended to unify its technology and software as far as possible with that of the VLT, the ISIT cameras were replaced by CCDs.

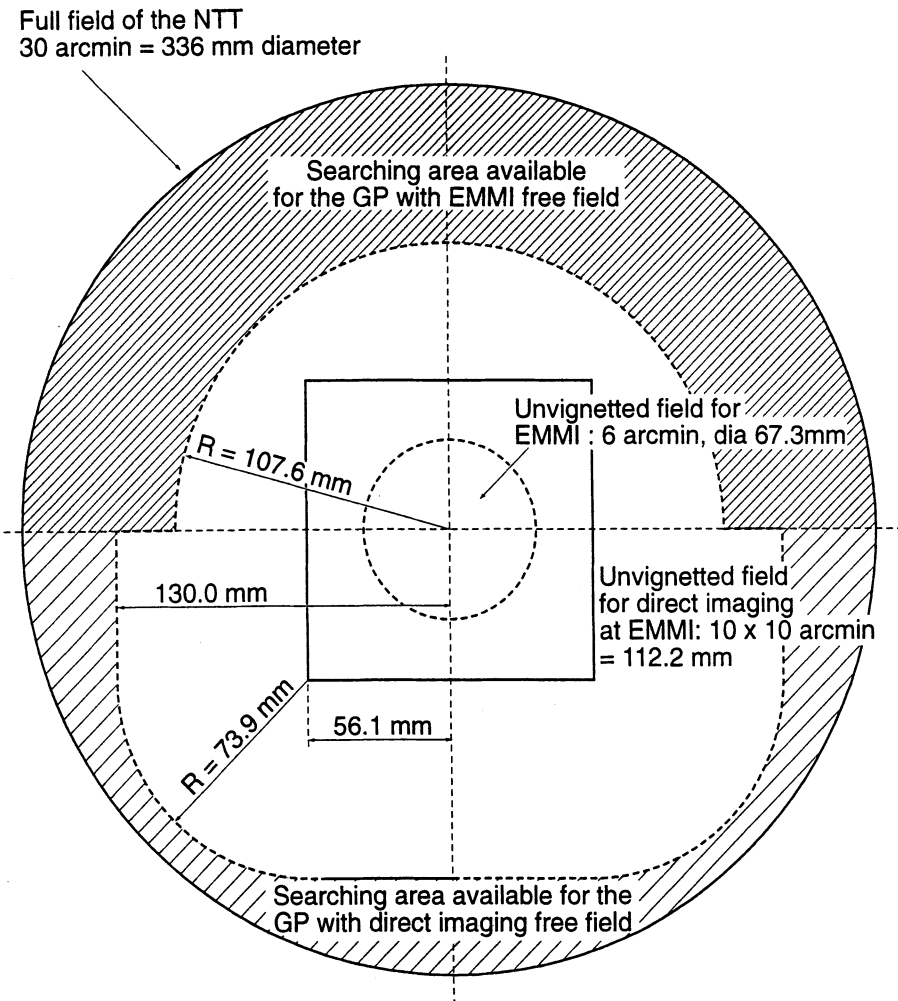


Fig. 7.2. Available search field for guide stars in the ESO NTT for two modes of observation with the EMMI spectrograph (from Franza [7.2])

An important technical point is that the trombones enable focus corrections to be made both for the field curvature of the telescope (radius of curvature 1881 mm – see Fig. 3.4(b) of RTO I) and for positioning errors (bias) of instruments up to  $\pm 10$  mm.

A considerable complication in the NTT adapter was the requirement that the CCD and ISIT cameras be accessible for service and/or exchange *without* dismounting the instrument. After 1993, this requirement could certainly have been dropped.

**7.1.2.2 Calibration System.** The *calibration* system is only shown schematically in Fig. 7.1 by the integrating sphere and the imaging objective. The integrating sphere simulates the pupil of the telescope and is imaged by the

objective on to the focal plane of the instrument via a folding mirror (not shown in Fig. 7.1).

The large number of calibration sources also represent a considerable complication in such an adapter.

**7.1.2.3 Rotation Facility.** In the NTT, the adapter/rotator is a single unit, the whole adapter being rotatable.

If a spectroscopic mode is used, the A/R must first be rotated to align the instrument slit to the required direction for an instrument like the spectrograph EMMI which turns with the rotator. The guide star is then selected (preferably from the HST catalogue with automatic selection of a star bright enough for image analysis). After lock-on of the autoguider, the automatic field rotation compensation is achieved by the rotator with the autoguider. Guiding errors can, in principle, originate from two sources: telescope tracking errors and field rotation tracking errors. To separate these requires *two* guide probes, which was one reason for having two such systems in the NTT. However, this requires two identical resolution ISIT cameras. In practice, the field rotation compensation is a trivial operation from the point of view of the encoder and the mechanical precision required<sup>2</sup>; whereas the general telescope tracking requirement (accuracy for the NTT quality 0.05 arcsec) is one of the hardest specifications in the entire telescope. Therefore it can be assumed that the tracking errors corrected by the autoguider are all telescope tracking errors, implying that only one guide probe is required for the autoguiding. This is the normal mode of operation of the NTT.

The integration time of the autoguider is an important and complex technical point. If it is set to be very short (< 1 second), there is confusion with the image movement due to the atmosphere (see Chap. 5). Use of such short integration times implies a fast tracking concept which the NTT was not designed to possess. Ideally, one would use the integration time of about 30 s which integrates out the atmospheric seeing, including image motion. But this slow control may allow too much tracking drift before correction is applied. In practice, integration times between 2 and 10 seconds may be applied.

Some instruments may be too heavy or bulky to mount on the rotator and are in a fixed mount in the extension of the altitude axis. Such a case with the NTT is the IR instrument IRSPEC. This requires its own optical de-rotator placed in front of the instrument. Such de-rotators are essentially part of the instrument optical system.

**7.1.2.4 Conclusions on the NTT Adapter/Rotator.** The A/R of the NTT is a highly complex element which is an essential feature of the telescope design. In many ways, it represents the maximum of sophistication in design, more than is required in the VLT because of relaxation of some of

---

<sup>2</sup> This will be clear if we consider the maximum angular rotation error corresponding to the position accuracy of the GP of  $6\text{ }\mu\text{m}$  at the edge of the field radius of about 175 mm: about 7 arcsec. The encoder has, in fact, a resolution of 0.5 arcsec.

the requirements on accessibility of detectors. The laboratory tests of the A/R [7.4] were an exhaustive process, but very successful. Figure 7.3 shows a photograph of the open adapter/rotator which gives an impression of its complexity. Mechanically,  $x$ - $y$  movements with the required precision are bound to be difficult precision units. The very different solution for the VLT adapters, discussed below, is a major simplification and advance.

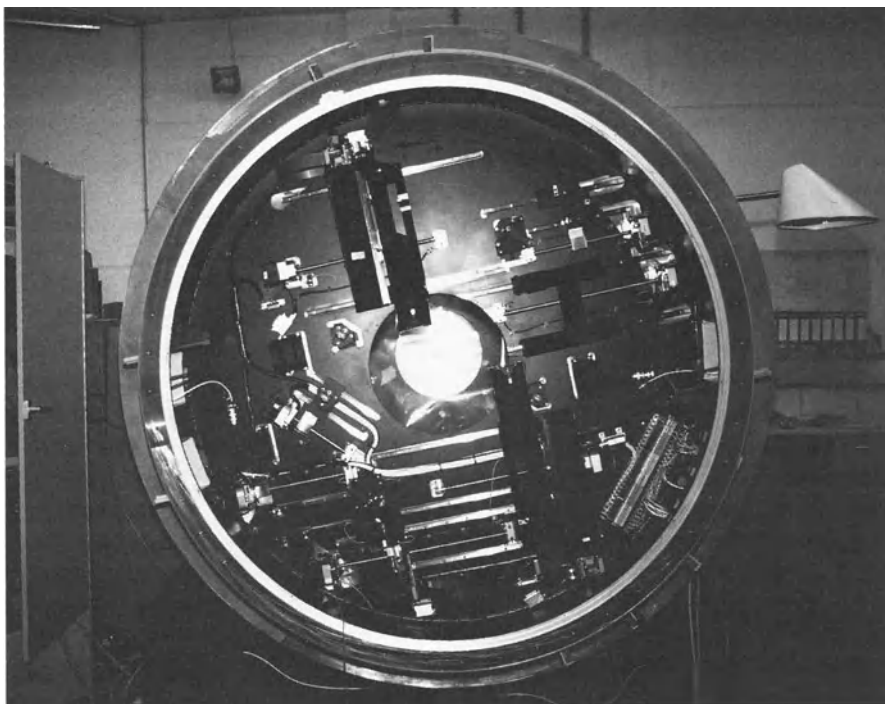


**Fig. 7.3.** Front view of the open NTT adapter/rotator seen from the image plane side (ESO photograph, courtesy F. Franza)

The rotator axis effectively defines the “axis” of the telescope. In Chap. 2, the issue of the definition of the “optical axis” was discussed and it was shown that this is very weakly defined in modern telescopes with aplanatic, or near-aplanatic, field correction. The effective optical axis is simply the altitude axis itself, to which the adapter/rotator axis will have some small error. If an instrument is mounted on the rotator, it will, in general, have a further centering error between its own “axis”, defined for example by the physical center of the slit, and the rotator axis. Such errors can be calibrated and their “tracking errors” removed by software corrections.

### 7.1.3 The adapters for the VLT 8 m unit telescopes

It is instructive to compare the essential characteristics of the adapter for the Cassegrain focus of the 8 m VLT unit telescopes with that of the NTT above.

In the VLT, the Nasmyth foci have the same angular fields (30 arcmin diameter) as the NTT but the Cassegrain has only 15 arcmin giving an effective linear field diameter of about 465 mm, about 100 mm more than the linear field of the NTT. Nevertheless, the diameter of the adapter/rotator is about the same, 1.6 m. This compactness relative to the NTT arises from certain simplifications such as relaxations regarding detector access and a reduced flange back focus of 250 mm instead of 500 mm, but, above all, because the  $x$ - $y$  movements of the guide probes have been replaced by an elegant double rotation concept introduced by D. Enard and designed by F. Franzia of ESO. This is shown in Fig. 7.4. In this solution, two independent rotations about the optical axis are required, an adapter rotation and a separate rotator ro-

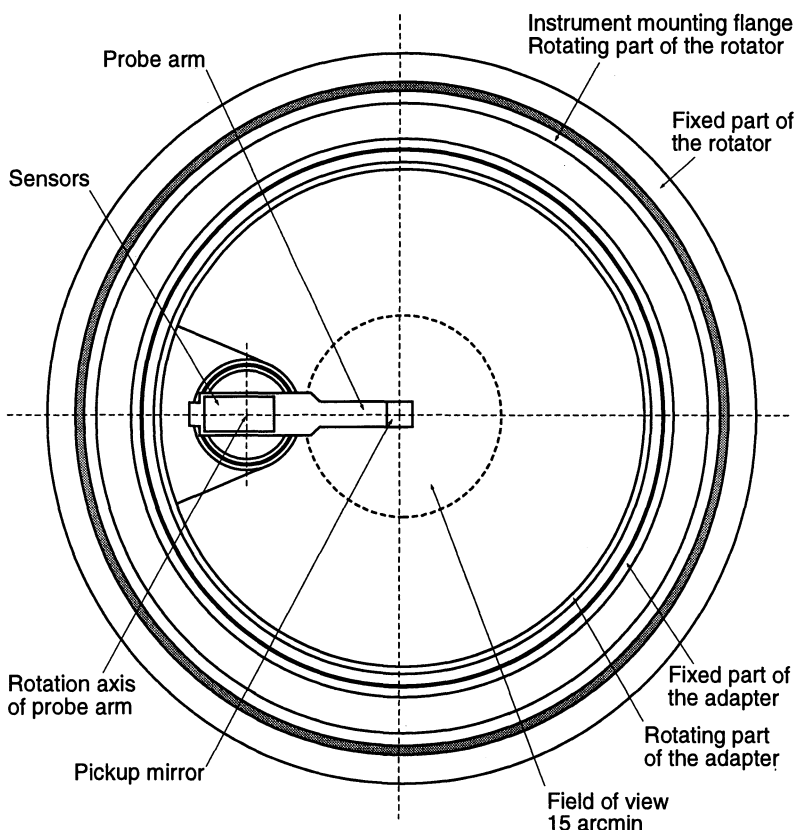


**Fig. 7.4.** Principle of the guide probe movements in the adapter/rotator of the 8 m VLT unit telescopes at the Cassegrain focus (ESO VLT drawing, courtesy F. Franzia)

tation. The single guide probe (GP) is mounted on an arm which can rotate over an arc which covers the 15 arcmin field, passing through the field center. In order to cover the entire field, the GP can be rotated through  $> 180^\circ$  by the adapter rotation bearing shown. Since rotations are mechanically far simpler and more precise than linear movements, the meeting of the GP stability requirement (positional accuracy) is far simpler than in the NTT, also because the telescope scale is over three times larger.

F. Franz has also informed me of a further elegant property of this GP rotation concept, again due to D. Enard. If the rotation axis of the GP arm shown in Fig. 7.4 is inclined to the direction of the optical axis of the telescope such that its projection passes through the center of the secondary mirror  $M_2$  (i.e. the center of the exit pupil in the VLT), then the GP pickup head describes with the rotation a conical motion through the field center, the apex of the cone being at  $M_2$ . If the  $45^\circ$  angle of the deflection mirror (see Fig. 7.5) is reduced by half this angular inclination of the axis, the beam is still sent centrally through the GP optics of the arm. Because of the symmetrical conical movement of the head, this will remain true for all rotation positions of the axis. Furthermore, the inclination also compensates a fraction of the field curvature of the RC system: only a fraction because the radius of the field curvature is much less than the distance  $L$  of the image plane from  $M_2$  (compare with Fig. 3.4(b) of RTO I for the NTT).

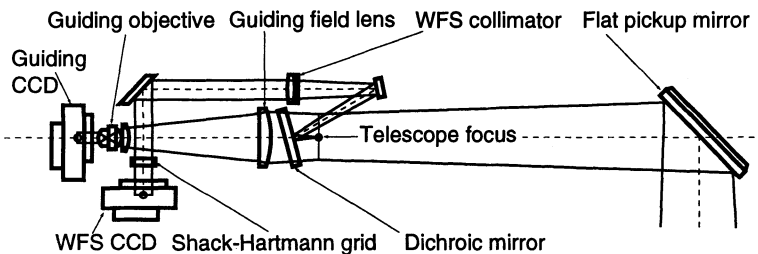


**Fig. 7.5.** Principle of the adapter GP sensor arm in the VLT adapter, Cassegrain focus (ESO VLT drawing, courtesy F. Franz)

The price to be paid for this rotation principle of the GP is that a separate rotator rotation is required so that the instrument slit can be set as required. But the concept remains far simpler than that of the NTT.

The design of the GP arm with the guiding camera and image analyser is also far simpler and more elegant than that of the NTT. This is made possible by dropping the requirement of accessibility to the detectors. It is assumed that they will have a life of ten years and they can only be serviced if the instrument is removed. Figure 7.5 shows the arrangement. Both cameras use CCDs. The telescope focus (guide star image) is at a fixed distance from the GP pick-up mirror and no trombone arrangement is needed. A dichroic mirror separates off the image analysis beam from the guiding beam, the collimated

beam and Shack-Hartmann lenslet raster having the same diameter as the CCD detector. The reduction optics required in the NTT are therefore no longer necessary, since a finer S-H raster with adequate sampling (ca. 20) over the CCD diameter is now available.

#### 7.1.4 Beam combination aspects

While these characteristics of the VLT adapters make them far simpler than those of the NTT, it would give a totally wrong impression if this were to imply that the *global problem* of operation regarding the object and pupil imagery were simpler in the VLT than in the NTT. Quite the opposite is the case, since the NTT imagery finishes at the Nasmyth focus whereas the VLT has a further complex coudé focus and beam combination system, including phase retention for the interferometric mode (see Figs. 3.29 and 3.30). At the coudé intermediate focus, the rotations of both the altitude and azimuth axes must be taken into account, not just that of the altitude axis alone.

Apart from aspects of equal phase and pupil imagery, the combination of the basic image field of several telescopes imposes difficult requirements which are usually non-existent for a single telescope, for which correct focus and lateral position (guiding) are the only Gaussian conditions *normally* required. Apart from these two conditions, unless the field is negligible, there will be three further geometrical conditions to be fulfilled in successful beam combination: equal *scales* of the individual telescopes (i.e. equal focal lengths), equal *azimuths* of the fields and absence of mirror-imaging or inversions of the fields relative to each other. Even for a single telescope there may be stringent requirements of constancy of both focus and scale over the period of an exposure, for example for multi-object spectroscopy with a prepared field mask. In an active telescope like the VLT, as envisaged by L. Noethe of ESO, the maintenance of constancy of both focus and scale will require control of the two geometrical parameters  $d_1$  and  $f'_1$  in the telescope. The necessary differential formulae for the sensitivities are given in § 3.8.1.1 of RTO I, apart from  $df'/df'_1$  which can be readily derived from the formulae given.

The general requirements of beam combination, above all for interferometry, are a complex subject in their own right. The field-of-view considerations for arrays have been analysed by Beckers [7.5]. He considers three basic types of array geometries. A detailed analysis of the design considerations for multiple telescope imaging arrays, in particular of the tolerances involved in lateral and longitudinal pupil geometry matching, has been given by Weaver et al. [7.6], who also list an extensive literature on this subject. The need for pupil matching in multiple telescope arrays was first recognized in a classic paper by Meinel [7.7]. The tolerances and requirements in the ESO VLT interferometer for the exit pupil configuration have been analysed by Beckers [7.8].

A deeper treatment of such beam combination aspects would lead us into the requirements of interferometry and instrument optics. The reader is referred to the literature cited.

### 7.1.5 Mountings and field rotation

With regard to field rotation problems arising from the currently favoured alt-az mount for telescopes, it must be admitted that this is the one major price which has to be paid for all its advantages of compactness and gravitational symmetry (see Fig. 3.3) compared with the equatorial mount. Richardson [7.9] [7.10] considers the field rotation complication to be so serious that the equatorial mount is to be preferred. He also disputes the significance of the alt-az mount for the compactness of the building or enclosure. While this seems to be a minority view, it does draw attention to the possibilities of spherical mounts, functioning either in a hydraulic or pneumatic mode, which are capable in compact form of operating in the equatorial mode. Richardson [7.9] calls his mount the "boule" telescope, the hollow boule containing the telescope floating in a water tank which supports the bulk of the weight and thereby relaxing the requirements on the polar axis. "Boule" telescopes with mechanical supports were introduced by Labeyrie [7.11] for an interferometer array. A similar concept to that of Richardson, but using a pneumatic support, has been proposed by Babcock [7.12] [7.13] as applied to an 8 m telescope.

It is not the purpose of this book to go further into the details of mountings. But these possibilities also have great relevance to *telescope optics* because of their removal of the field rotation consequence of the alt-az by virtue of their operation in the equatorial mode. Of less consequence, but also an advantage, is the removal of the limitation of the "dead angle" near the zenith for an alt-az, where the acceleration in azimuth becomes too rapid for practical operation.

## 7.2 Baffles

The purpose of baffles in any telescope is to prevent unwanted stray light reaching the defined image plane from parts of the object field which are outside the field angle of this image plane. The problem was well known in refracting telescopes which almost always had a continuous tube, usually cylindrical, connecting objective and ocular. Reflections could take place at the tube walls which, because of near grazing incidence, could be appreciable even with blackened tube walls. Danjon and Couder [7.14] show the classical solution using a number of baffles disposed along the tube as shown in Fig. 7.6. The extreme field rays forming the image defined by the field stop  $pq$  are  $Pp$  and  $Qq$ . The first baffle (1) in the system is formed by the end of the telescope tube leading to a smaller tube holding the ocular or detector. A ray

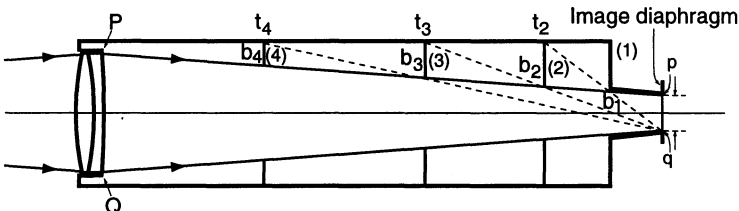


Fig. 7.6. Classical system of baffles in a refracting telescope with a continuous cylindrical tube (after Danjon and Couder [7.14])

is drawn from  $q$  through  $b_1$  to  $t_2$  which determines baffle (2). Similarly,  $qb_2t_3$  determines baffle (3), etc. Schmidt [7.15] has analysed the requirements in more detail and derived formulae which optimize more formally the number of baffles required. He gives a case where 2 baffles are sufficient whereas the simple geometrical process of Danjon and Couder requires 4. Such refractors have no direct relevance to modern large telescopes, but the case is a useful introduction to the situation in reflecting telescopes because it is apparently extremely simple in its geometry. However, even here the optimum solution is not obvious.

It should be noted from Fig. 7.6 that a similar baffling effect can be achieved simply by extending the telescope tube out forwards beyond the objective, either in conical form or with a larger cylindrical diameter to accept the field angle without vignetting. But the lengths required for efficient baffling are rarely acceptable. By contrast, one can also baffle at the exit pupil of the ocular, but this requires accurate mechanical centering if the baffle (stop) is to be exactly the size of the Ramsden disk of the exit pupil [7.14] – see also Fig. 1.8 and § 2.2.4 of RTO I.

A Cassegrain telescope is, in the nature of its ray path, more complex, but also because nearly all such telescopes in modern form have open structure tubes. Danjon and Couder refer briefly to the Cassegrain case and mention the use of a conical tube projecting up a certain distance above the primary. But they give no details of the design. They do not mention any baffle mounted at the secondary, although their preliminary remarks imply the logic and utility of such a baffle. However, the angular fields of the Cassegrain telescopes they were considering at that time were usually small and we shall see that a single baffle at the primary is then a reasonable solution.

One of the first treatments of systematic design of baffles for reflecting telescopes was given by Bouwers [7.16]. He discussed the use of two tubular baffles both at the primary and the secondary, essentially initiating the modern solution.

A graphical technique for designing baffles for Cassegrain telescopes was given by Sauer [7.17], who was concerned with the possibilities of daylight photography with amateur instruments. A simple, unbaffled Cassegrain telescope is virtually useless for daylight use because of the enormous contrast loss from stray light. This approach was analysed in detail in an important

paper by Young [7.18], who came to the surprising conclusion that *there is no formal analytical solution to the baffle problem in a Cassegrain telescope*. However, the subsequent work of Schmidt [7.15], as applied to Cassegrain telescopes, shows that optimal data for baffles can be deduced either from diagrams or from an associated analytical procedure which is by no means trivial. This is considered below in comparison with graphical procedures.

The general design principles of a 2-baffle system for a Cassegrain telescope are illustrated by Young as shown in Fig. 7.7. The marginal ray 1 of the axial beam passes through the telescope in the usual way to the Cassegrain focus  $F$ . The field ray 2 at semi-field angle  $u_{pr}$  strikes  $M_2$  at the maximum height and returns to the *highest* point of the image at  $F$ . The conical form of the front ( $M_2$ ) baffle is set by this field ray. The baffle follows the ray 2 to a point  $B$  to be decided. Ray 3 is then the inner ray of the axial beam, the height  $y_a$  determining the axial obstruction. The inner field ray 4 touches  $B$  and proceeds to  $M_2$  and thence to the *lowest* point of the image at  $F$ . The intersection of the rays 4, before reflection at  $M_2$ , and 2, after reflection at  $M_2$ , determines the end point  $B'$  and radius of the rear baffle.

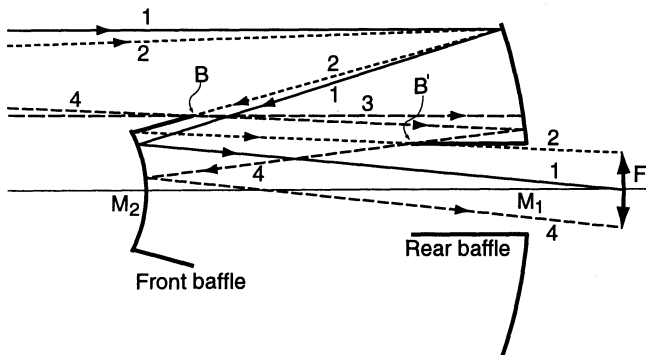


Fig. 7.7. General design principles of a 2-baffle system for a Cassegrain telescope (after Young [7.18])

The above procedure is simple and determinate except for one point: the point  $B$  determining the length of the front baffle is still arbitrary. If the size of the field were zero, the point  $B$  can be placed on  $M_2$  and the front baffle becomes redundant: the length of the rear baffle is set by the intersection with ray 1 for the baffle diameter chosen. Clearly, the larger the field, the further  $B$  must be moved from  $M_2$ , thereby increasing the central obstruction which must be larger than the field diameter to give a reasonable intersection point of rays 2 and 4. The effectiveness of the baffling against stray light entering the field will be completely determined by the choice of  $B$ . A procedure to optimize this choice is essential: if  $B$  is too near  $M_2$ , the central obstruction will be improved but the baffling inadequate; if  $B$  is too far from  $M_2$ , the baffling will be complete but the central obstruction larger than necessary.

Following the graphical approach of Sauer [7.17], Young derives equations for a semi-analytical formulation. The point  $B$  is fixed arbitrarily on a reasonable basis. Two procedures are established for checking whether the baffling is complete or excessive, (i.e. that light from the sky outside the nominal field just fails to reach the detector) and performing an iterative procedure to correct the position of  $B$ . One of these procedures is applicable for large fields (ca.  $D/5$ , where  $D$  is the telescope aperture), the other for small fields.

Young shows graphically a number of functions of central obstruction against different parameters. Obviously (see Chap. 2 of RTO I), the most important parameter in reducing the axial central obstruction  $R_A$  is a high magnification  $m_2$  of the secondary – see Eqs. (2.72) and (2.86) of RTO I. The obstruction including the field effect also follows this trend, but shows a flat minimum at about  $f/12$  in the Cassegrain focus for a primary focal ratio between  $f/4$  and  $f/2$ , with a field diameter of  $1^\circ$ . This minimum arises because, for smaller values of  $m_2$  the secondary is larger and the linear field smaller; whereas for larger values of  $m_2$ , the secondary is smaller but the linear field becomes larger. Young also shows that the central obstruction is a more or less linear function of field diameter. In a typical telescope, with  $D = 2.72$  m and an  $f/4$  primary with an RC configuration giving a  $1^\circ$  diameter field, the central obstruction is 25.6 % by area compared with 11.1 % for a zero field.

Although Young's paper gives a complete system for designing baffles for a Cassegrain telescope, I personally prefer the graphical procedure given by Prescott [7.19]. This was used with complete success for the design of the baffles of the ESO 3.5 m NTT. Prescott's approach has the advantages of complete generality (above all with the important freedom of the entrance pupil position, whereas the Sauer/Young method assumes the pupil to be at the primary), simplicity and clarity of the procedure, and sufficient accuracy for all practical cases if two iterations are performed.

The basis of the Prescott graphical method is the *paraxial* Gaussian ray-trace data of the telescope system. We saw in § 2.2.3 and § 3.1 of RTO I that the paraxial ray-trace laws are strictly linear. Refracting or reflecting surfaces are replaced by planes and, because of linearity, paraxial rays may be traced at any height  $y$ . This has the important advantage for a graphical procedure that vertical heights can be plotted to a larger scale than horizontal, giving much higher precision of ray intersections. Normally, Prescott uses a vertical scale some four times greater than the horizontal scale. Figure 7.8 shows the paraxial representation of the Cassegrain telescope in the same way as Fig. 2.12 of RTO I, but with the mirrors replaced by planes at  $M_1$  and  $M_2$ .  $P'_0$  defines the second principal plane and thereby the Cassegrain focal length  $f'$ .  $I'_0$  and  $I''_0$  are the prime and Cassegrain focal points respectively.  $E$  defines the position of the entrance pupil and  $u_{pr}$  is the semi-field angle in object space. Following Prescott, the ray numbers are the same for parallel rays, identified by 3, 3', 3'' etc.

Ray 1' is the marginal ray reflected in 2 to  $I'_0$  and 8 to  $I''_0$ . Rays 3 and 4 are extreme field rays defining the diameter of the image  $I''_0$ , similarly rays

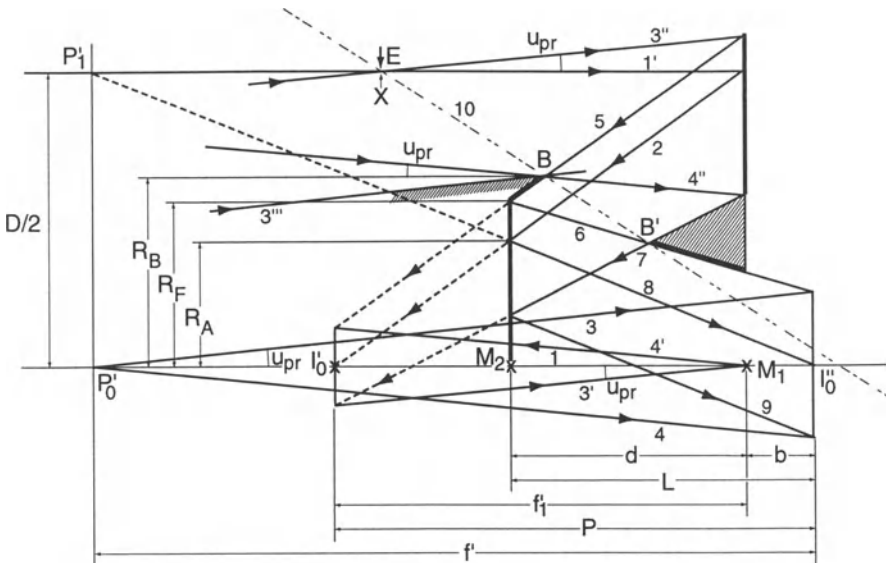


Fig. 7.8. Prescott's general graphical procedure for designing baffles in a Cassegrain telescope (after Prescott [7.19])

$3'$  and  $4'$  define the diameter of  $I'_0$ . Ray  $3''$  is then drawn to the limiting entrance pupil point  $E$  and reflected as ray 5 and 6 to the upper image point of  $I''_0$ . Point  $B$  is then arbitrarily chosen, as with Young's procedure, and ray  $4''$  drawn through  $B$  at the maximum downwards semi-field angle  $u_{pr}$ . This is reflected as 7 to the lowest point of  $I'_0$  and as 9 to the lowest point of  $I''_0$ . The intersection point  $B'$  of rays 6 and 7 defines the endpoint of the rear baffle corresponding to  $B$ , the endpoint of the front baffle. The ray 10 is then constructed through  $B$  and  $B'$  and represents the ray with the smallest angle to the axis 1 which can get past the baffle from the sky. We see in the case drawn that the baffling is inadequate, since the ray strikes the final image plane within the imaging field. The point  $B$  is therefore too low to give effective baffling – unless an extension tube of increased diameter blocks sky light entering to the right of point  $X$ . This shows that a modest extension tube can ameliorate the baffle situation markedly, but such an extension is rarely practicable for large telescopes.

Three obstruction ratios are shown, assuming the height of ray  $1'$  to be normalized to unity:  $R_A$  is the axial obstruction ratio,  $R_F$  the field obstruction ratio set by a secondary free from vignetting, and  $R_B$  the obstruction ratio imposed by the baffle system. Since the maximum half cone angle of the front baffle is set by the slope of ray 5, which is approximately the half aperture angle of the primary, and the point  $B$  must be set on this ray, it is clear that improving the baffling by shifting  $B$  upwards leads to a rapid increase in the central obstruction ratio  $R_B$ . This is the inevitable price of correct baffling with significant angular fields.

Prescott points out that the paraxial approximation may not be adequate for modern systems with fast primaries. This is true, but is no limitation to the method. After the approximate paraxial determination, it is a simple matter (above all with a CAD system) to feed in the true optical design data of the system, using real ray heights for the rays 3" and 4" combined with the real curvatures of the mirrors. With an iterative process, the possibilities of the accuracy of the graphical procedure can be rapidly reached, and this accuracy will be sufficient for any normal case.

Schmidt [7.15] gives a system for general optimization of baffles in a Cassegrain telescope analogous to his generalisation for refractors (see above). His aim is to establish an optimum in the sense that the central obstruction be a minimum with complete baffling and with no vignetting by the baffles. He gives an example of an RC telescope with  $D = 600$  mm and  $f/3.8$  with the large field diameter of  $1.5^\circ$  ( $u_{pr} = \pm 0.75^\circ$ ). The optimization gives a 4-baffle system:

- $B_1$  as an entrance stop at the end of a tube just inside the prime focus (the entrance pupil is at the primary)
- $B_2$ , the normal cylindrical rear baffle in front of the primary
- $B_3$ , the normal conical baffle at the edge of the secondary
- $B_4$ , a further conical baffle, with shallower cone angle, placed about half way between  $B_2$  and  $B_3$

Schmidt states that this system has been very successful in the RC telescope at the Hoher List observatory in Germany, allowing accurate stellar photometry even near the moon. Unfortunately, a comparison of the gain in central obstruction compared with a baffle system without  $B_4$  is not given. His formulation has the same limitation as Sauer/Young in that the entrance pupil is assumed to be at the primary.

It should be noted that the Prescott procedure can also fully take account of an entrance window  $B_1$ . The addition of  $B_4$  is probably only interesting in special cases where great weight is given to photometry, but can then be an important feature.

At the beginning of this section, the comment of Danjon and Couder [7.14] was quoted, namely that baffling for a refracting telescope can, in principle, be done by a baffle at the exit pupil of the ocular; but that this requires great precision of mechanical alignment since the baffle should then be the same size as the exit pupil. The same principle can be applied to any instrument. The ESO 8 m VLT unit telescopes, which have the exit pupils on the secondaries for IR reasons, follow this design concept: there are no baffles in the telescope, so all baffling must be done in the instruments. This will require high mechanical precision.

The ESO 3.5 m NTT, by contrast, with its entrance pupil at the primary, had a normal 2-baffle system laid out by the Prescott procedure – see above. For IR work it was envisaged that the  $M_2$  baffle could be removed and replaced by a “reflecting” stop of low emissivity, sending radiation from

the primary off to the side and stopping down  $M_2$  so that it becomes the exit pupil, thereby slightly reducing the aperture of the telescope. In practice, however, this possibility has not been pursued and baffling is performed within the IR spectrograph (IRSPEC).

The opposite extreme from the VLT no-baffle solution and thereby pushing the problem into the instruments is represented by careful baffling of the IR space telescope SIRTF, described by Bergener et al. [7.20]. This has a deployable aperture shade at the front of a tube more than twice the length of the telescope. This tube is provided with vanes normal to the surface beyond the telescope, oblique to the normal within the telescope. The usual  $M_2$  and  $M_1$  baffles are provided in addition. The stray light rejection performance is analysed with great care.

An even more extreme case is the work of Pompea et al. [7.21] for the Apache Point 2.5 m wide-field telescope. The difficulty of baffling in wide-field telescopes was also analysed for a telescope of similar size by Bowen and Vaughan [7.22]. Pompea et al. are concerned with a wide field telescope dedicated to CCD photometry and multifibre spectroscopy. They point out the important fact that modern telescopes usually have much more open enclosures than was earlier the case, in order to improve ventilation. This, however, aggravates the stray light problem. In the Apache Point telescope, there is a roll-off enclosure leaving the telescope completely open. Figure 7.9 shows the original baffle design, which is clearly extremely sophisticated and goes much further with intermediate baffles between  $M_1$  and  $M_2$  than the single additional baffle of Schmidt, mentioned above. As with the design principle of Fig. 7.8, the baffle vanes must essentially be parallel to ray paths, but are bound to block some light because of finite thickness and the field effect of their depth. Assuming 100% reflectivity of the mirrors, the area obstruction without and with baffles gives the throughputs of Table 7.1.

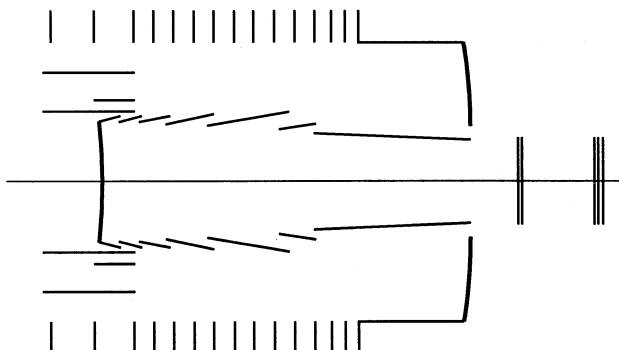


**Fig. 7.9.** Original baffle system for the Apache Point 2.5 m wide-field telescope (from Pompea et al. [7.21])

**Table 7.1.** Throughput of the Apache Point 2.5 m telescope without and with baffles (Fig. 7.9), assuming 100 % mirror reflectivity (from Pompea et al. [7.21])

Semi-field angle $u_{pr}$ (arcmin)	Throughput without baffles (%)	Throughput with baffles (%)
0	80.0	70.3
30	80.5	67.7
90	79.8	56.2

The baffle system of Fig. 7.9 was modified to give the layout of Fig. 7.10. The cylindrical baffles at the upper end were removed and the  $M_1$  baffle changed to have the same design form as the intermediate baffles.

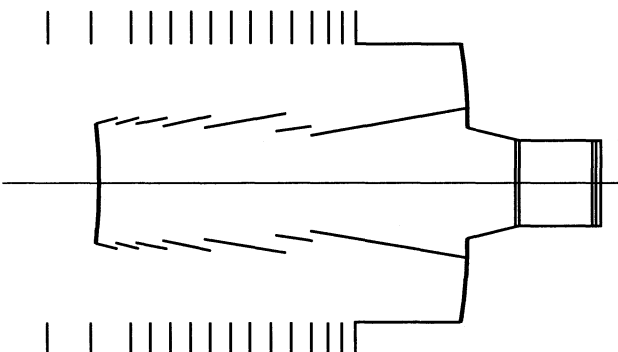


**Fig. 7.10.** Modified baffle system for the Apache Point 2.5 m wide-field telescope (from Pompea et al. [7.21])

The authors analyse the surface scatter models of this layout in detail. A promising diffuse black painted surface was identified, but the grazing incidence on the vanes is a major problem. Two models were used: specular reflection and the BRDF (Bidirectional Reflectance Distribution Function). The stray light was calculated for sources at various field angles. This work can serve as a model for computer analysis of stray light effects.

Further work by Pompea and McCall [7.23] and McCall et al. [7.24] investigates in detail the critical selection of paints or materials for producing black surfaces, both for ground-based telescopes and for space telescopes. Earlier, reflectance measurements were made by Pompea et al. [7.25] with an improved optical black for stray light rejection for wavelengths from 0.3 to 500  $\mu\text{m}$ .

More recently (1997), Pompea [7.26] has given a review of the current possibilities of stray light analysis in telescopes. He correctly emphasizes the importance and advantage of careful stray light analysis *early* in the design concept. This can bring substantial gains.

There is no doubt that the developments of the last two decades, with dramatic improvements in image quality, universality of *linear* detectors (CCDs) and their availability as *arrays*, giving increased angular fields, have upgraded the relative importance of optimized design for reducing stray light.

## 8. Maintenance and operation of telescope optics

### 8.1 Ground-based telescopes

The subject of “telescope optics”, as treated in the literature, is largely the remarkable story of the *development* of optical theory and design, manufacture and test procedures, going hand in hand with mechanics and then with electronics, to enable larger sizes with improved quality and observing convenience. However, the final criterion of the effectiveness of a telescope is determined in *operation*. The rich history of astronomical observation is full of examples of good results being achieved by brilliant use of modest equipment and telescopes of inferior quality. But, in general, the most spectacular work will be at or near the limits of the equipment available at the time. A telescope which has full state-of-the-art potential from its design and manufacture must then be *maintained* and *operated* to realise this potential, otherwise the investment is partially thrown away. This comment may seem banal, but it points to a major weakness of the modern ground-based optical telescope community. The pressures of funding and prestige, together with the interest of modern telescopes in generating industrial contracts (even though these are modest compared with most industrial activities), result in a massive over-emphasis on the *development* of new equipment, compared with the necessary infrastructure to *operate* it in the most cost-effective and productive way. Not only are the funds available for observatory operation usually reduced to an absolute minimum: maintenance is often viewed as lower-grade work than development and as fundamentally less attractive for competent staff. This is not the case in many areas of technical activity. For example, top-quality maintenance engineers are essential, and known to be essential, for modern airports or oil refineries.

An excellent illustration of the weight given to operation and maintenance of astronomical equipment compared with development is the number of conferences and workshops held. Conferences on telescope and instrument *development* are a major feature of the modern astronomical community and are an excellent driver of progress. But in about 40 years of active involvement with the optical telescope and instrument community, I have *never* known a conference on maintenance and operation.

It is instructive to consider how and when this mismatch between development and operation originated. In Chaps. 1 and 5 of RTO I, I gave a résumé of

the historical development of telescope optics. The work of William Herschel represented a perfect symbiosis between telescope development and productive operation leading to forefront astronomical research. Herschel combined, perhaps for the last time, the attributes of being the greatest telescope builder (in all its technical aspects) of his time *and* the greatest astronomer. Such a dual role is today impossible: telescopes are too complex. Herschel's small team of highly motivated assistants (mainly his own family) enabled him to oversee the requirements and possibilities in a global sense [8.1].

This tradition of a close link between telescope design, manufacture and observational use was maintained by many notable telescope builders such as Rosse, Lassell, Foucault and Nasmyth; but a dangerous break came with the Melbourne reflector in 1869. This was largely the design of a committee formed by the Royal Society under the chairmanship of T.R. Robinson. The tragic consequences of this project were discussed in § 5.1 of RTO I. The committee's design was good and advanced, except for the fatal error of the choice of a speculum mirror and the failure to understand the rapidly growing significance of photography compared with visual observation. The manufacturer, Thomas Grubb, was excellent. The director, R.L.J. Ellery, was dedicated but lacked experience. The fatal flaw was in organisation: neither the designers nor the manufacturer had any practical contact with the finished, functioning telescope, except Le Sueur, who had little weight. The close symbiosis which characterized William Herschel's or Lassell's work and which was essential for the operation of a speculum mirror telescope, was completely absent. The committee had totally failed to appreciate its importance and the significance of the distance and communication difficulty between Great Britain and Australia [8.2], even though William's son John Herschel was a key member of the committee!

With the completion of the Lick 36-inch and Yerkes 40-inch refractors, the dominance of Europe in observational astronomy passed to America towards the end of the last century. With the work of Keeler [8.3] at the Lick Observatory, this applied also to the use of reflecting telescopes, his work with the Crossley 36-inch reflector from 1898 till his early death in 1900 representing a milestone in astrophysics. Keeler converted a telescope in poor shape into one of the most powerful instruments of its time – see Fig. 5.9 of RTO I.

Keeler was a friend of G.E. Hale, director of the Yerkes Observatory with the largest refractor in the world. He also fully recognised the significance of the reflector and initiated the epoch-making work of G.W. Ritchey leading to the  $23\frac{1}{2}$ -inch, 60-inch and 100-inch telescopes (see § 5.2 of RTO I). The work of Keeler – Hale – Ritchey, together with the financing of Carnegie, was another period of remarkable symbiosis which completely revolutionised astrophysics and introduced the modern era of astronomical observation [8.4]. Ritchey was himself an astronomer who became one of the greatest telescope makers, but he maintained close contact with the function of his own telescopes.

Such a “rapport” between designers, builders and operators of telescopes is, unfortunately, much rarer today. To some extent, this is inevitable be-

cause no observatory can itself accomplish the relative volume of work that was possible in Ritchey's time. But the organisational problem of maintaining contact between designers, manufacturers and operators has been too little addressed. Perhaps one of the most positive examples of the continuous involvement of a great telescope designer through manufacture *and the early operation* of an ultra-modern, very large telescope is the role of J. Nelson in the Keck 10 m telescope, who spent 4 years (1990–1994) at the observatory on Hawaii [8.5].

This is a central issue in the concept of *active optics* control, as discussed in §§ 3.5.2 and 3.5.3. The original purpose was the *automation of optical maintenance* and this process of automation can be seen as the conversion of an *analogue* maintenance situation into a *digital* one [8.6]. Analogue degradation of optical quality is inherently dangerous because there is no clear point at which one can say a telescope "is not working properly". If the maintenance is automated, it will either be functioning to its prescribed standard, or not functioning at all – a digital situation. Figure 3.67 and Table 3.14 showed the strong effect that the maintenance situation, linked to the design parameters of the telescope, can have on optical quality. Optical quality can be quantified in terms of an efficiency criterion  $E_O$ , as discussed in Chap. 4 and defined by Eqs. (4.32), (4.33) and (4.36). However, although automation in this sense should be of fundamental importance in maintaining the very high standards of optical quality set by the specifications of modern telescopes (and without which, in a *passive* mode, their maintenance would be quite impossible), it is nevertheless no substitute for a correct organisational framework linking development with maintenance and operation. Both automation and this organisation are necessary.

What does this mean, in practice, for the development, set-up and integration, and operation of telescope optics?

This is best shown by a simple diagram giving the activities required at any given time in the life of a large, active, ground-based telescope to ensure top performance (Fig. 8.1). Whatever the nature and size of a ground-based telescope, a similar type of function will apply if high quality is to be achieved *and maintained*.

Time  $t_0$  represents the start of the design and development which is, by definition, 100 % technical time ( $T = 100$ ) of the team involved. This will remain the case until the point  $t_2$  is achieved, which was termed "astronomical first light" (AFL) for the NTT (see § 3.5.3). However, the technical team involved in the development must already be at the observatory before the point  $t_1$  ("technical first light" – TFL), working with observatory staff to achieve the *integration* of the total opto-mechanical system in the basic telescope mechanics leading up to AFL at time  $t_2$ . In the case of the NTT, the period  $t_1 - t_2$  was about 5 months of intensive work. For the first unit telescope of the VLT, it may well be appreciably longer and involve a bigger team.

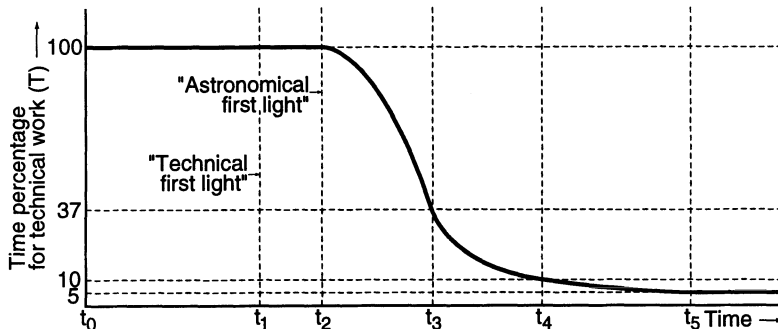


**Fig. 8.1.** Development-maintenance relationship for ensuring top quality optical performance of large, active, ground-based telescopes

After AFL, astronomical observation will start, to begin with in a preliminary way since technical aspects such as tracking and pointing will still have to be optimized. At some time  $t_3$ , the bulk of the technical problems will have been solved and the percentage  $T$  falls to about  $1/e$ , after which the slope of the function declines to a roughly constant value at  $t_4$  with a value of  $T$  which may be of the order of 10 %. The time  $t_2 - t_3$  for the NTT was about a year, but the organisation was then changed in a way that disturbed the above function. In the ideal case, full automation of the active optics (a learning process in the NTT, the first fully active telescope) should have been achieved by  $t_4$  or between  $t_4$  and  $t_5$ , whereas it is still not complete 8 years (1997) after AFT ( $t_2$ ), although it is hoped that this will soon be the case.

Point  $t_4$  normally implies that the opto-mechanical system, including tracking and pointing, is automated and essentially fulfilling the specification under the most rigorous (i.e. best) seeing conditions.

The time between  $t_4$  and  $t_5$ , when  $T$  may have fallen to a final steady value of the order of 5 % for normal maintenance, will above all be concerned with optimizing the *thermal conditions* and performing the necessary analyses with image analysis and thermal sensors to establish the specification regarding *local air* conditions. In most modern telescopes, this will be a relatively long and complex process which may lead to modifications or improvements of the telescope, enclosure and site. In the NTT, for the organisational reasons mentioned, this process is still not complete (December 1997).

Figure 8.1 gives an answer to the vexed and frequently posed question: "When will the telescope be finished?" The true answer to this from the optical viewpoint is: NEVER! In an ideal observatory, there will always be feedback and synergy between the development team and the on-site maintenance team to improve the telescope (above all, its control software). This intense cooperation starts at  $t_1$  and should continue indefinitely, although the numbers of staff involved will normally reduce markedly after point  $t_3$ . An essential organisational feature is a clear technically responsible person, both at the *development end* and at the *observatory* (on-site). This implies,

of course, that there be good mutual understanding and respect at both ends of the team.

The person responsible for the optical performance of a telescope at the observatory does not have to be formally an optics specialist by profession. Normally, the responsible person should be responsible for *all* technical aspects of the telescope. The best background for this is an electronic systems engineer with specialisation in software. After the point  $t_3$ , most problems will be associated with the control software in some way.

The efficiency criterion of Eq. (4.33) emphasized the importance of flux throughput of the telescope. In Chap. 6 we treated the matter of reflecting coatings and cleanliness. This is just as important as the maintenance of the optical quality and also requires the firm control of the technically responsible person for the whole telescope.

One of the most dangerous illusions, which unfortunately is not uncommon, is to assume that the development work is “finished” at some arbitrary point of time and to impose a step function between development and maintenance. This is unrealistic and harmful for a passive telescope, but particularly dangerous for an active telescope in which optical maintenance is built into the development concept. It can only hope to work if the ground-based telescope is built to space telescope standards (see § 8.2 below), implying enormous increase in costs.

For classical, *passive* telescopes, optical maintenance must be performed in the conventional *off-line* mode by the methods outlined in Chap. 2. The essential tools are an off-line image analyser (such as the ESO “ANTARES”) and a reflectivity measuring device such as that discussed in Chap. 6. Of course, adequate dedicated staff, again in good contact with the design team, are just as important (in fact, even more important if top-quality is aimed for) as for active telescopes.

In summary, the requirements for the maintenance of high quality performance of telescope optics are:

- a) A clearly nominated person at the observatory, *responsible* for the entire *technical* function of the telescope and who has sufficient time to concentrate on it. This person should feel the telescope is his/her personal “baby” and have all necessary power and support.
- b) A responsible *contact person* in the *development* team of the telescope who has complete understanding of its specification and potential, and good contact to the responsible person (a).
- c) Competent and motivated technical personnel at the observatory to assist the technically responsible person.
- d) For top-quality, modern, large telescopes, an *active optics* concept which is *fully automatic*, in order to *digitalize* and thereby simplify the maintenance situation of the optical quality (§ 3.5).
- e) For high-quality, *passive* telescopes of conventional design, an *off-line image analyser* and clear maintenance schedules as indicated in Chap. 2.

- f) A coating plant of high quality, a reflectivity measuring device and modern cleaning routines as outlined in Chap. 6.

## 8.2 Space telescopes

The maintenance situation for space telescopes is fundamentally different. Since intervention after launch beyond the normal operating control is rarely possible, there are two approaches:

- a) Very hard absolute tolerances and a high level of redundancy against failure.
- b) An active concept in which intervention is possible as optimization by the operating system.

The normal approach is (a), above all because there are not yet very large systems in space. Unlike ground-based telescopes, this does imply a step function at the equivalent of  $t_2$  in Fig. 8.1. The price of this approach, inevitable for space, is the well-known factor of cost for space projects compared with ground-based telescopes – over 2 orders of magnitude between the 3.5 m NTT and the 2.4 m HST, to quote an extreme case.

The second approach (b) is, in my view, far better for large systems in space, as the HST spherical aberration error (see §§ 3.2.3; 3.5.1; 3.5.5.6) clearly proved. However, the redundancy requirement for mechanisms in space may well absorb the cost savings on tolerances. Security against error will be the biggest advantage from the relaxed tolerances arising from active optics, rather than reduced costs.

## Appendix: Mathematical symbols

Appendix A of RTO I gave a complete listing of the mathematical symbols used in Vol. I of this work. This was possible, and in my view essential, because the optical design basis of telescope optics, the main subject of RTO I, requires strict adherence to a consistent nomenclature and sign convention. The aim in RTO I was therefore to have a unique significance for a given symbol, with as few exceptions as could reasonably be achieved.

The situation for the second volume (RTO II) is very different. Much material has been taken over unchanged from Vol. I, particularly in Chap. 2 but in general throughout the book. This material relates in its nature to the optical design basis and uses identical nomenclature to that of RTO I. In such cases, which are evident from the references to RTO I, the reader is referred to App. A of Vol. I. The symbols are therefore *not* redefined. Otherwise, the content of RTO II covers a far broader area of physics and engineering (and, indeed, other physical sciences as well) than the narrower material of RTO I. It was therefore not possible to maintain the principle of unique use of symbols. An equivalent of App. A of RTO I would consequently have been too cumbersome. In such cases, I have tried to define completely the symbols *in the sections where they are first used*. I hope I have been successful. In doubtful cases, I have preferred to repeat definitions, on the principle that a superfluous definition is much preferable to an absent one. In view of the vast range of choice of symbolism used in the international literature, I have usually modified the nomenclature to be more consistent with my own choice and to give more uniformity throughout the book, but, on occasions, it has seemed desirable to retain the nomenclature of the original author, since this simplifies reference to the original work for the reader.

# References

## Chapter 1

- 1.1 Dévé, Ch., 1936, "Le Travail des Verres d'Optique de Précision", Revue d'Optique, Paris; 1945, English translation "Optical Workshop Principles", Adam Hilger, London
- 1.2 Twyman, F., 1952, "Prism and Lens Making", Hilger and Watts, London
- 1.3 Maksutov, D.D., 1954, "Technologie der astronomischen Optik", VEB Verlag Technik, Berlin (translation of the Russian edition, Moscow, 1948)
- 1.4 Preston, F.W., 1922, Trans. Opt. Soc. London, **23**, 141 and 150
- 1.5 Preston, F.W., 1926, Trans. Opt. Soc. London, **27**, 181
- 1.6 Götz, J., 1968, Sprechsaal f. Keramik, Glas, Email, Silikate, **101**(13), 539
- 1.7 Beckstette, K., et al., 1992, private communication from Carl Zeiss, Oberkochen
- 1.8 Izumitani, T.S., 1985, "Optical Glass", Lawrence Livermore National Laboratory, Livermore, Cal., UCRL-Trans-12065. (Translation of the original Japanese version, 1984, Kyoritsu Shuppan Co., Tokyo)
- 1.9 Preston, F.W., 1927, J. Soc. Glass Techn., **9**, 42
- 1.10 Beckstette, K., Heynacher, E., 1988, Proc. ESO Conf. "Very Large Telescopes and their Instrumentation", Vol. I, ESO, Garching, 341
- 1.11 Kaufmann, H., 1965, "Praktische Optik" (private communication); also 1992, private communication
- 1.12 Kumanin, K.G., 1962, "Generation of Optical Surfaces", Focal Library, New York
- 1.13 Rupp, W., 1965, Appl. Opt., **4**, 743
- 1.14 Brown, D.S., 1971, Proc. ESO/CERN Conference "Large Telescope Design", ESO, Geneva, 273
- 1.15 Jones, R.A., Kadakia, P.L., 1968, Appl. Opt., **7**, 1477
- 1.16 Lysyannyi, Y.K., 1974, Sov. J. Opt. Technol., **41**, 262
- 1.17 Jones, R.A., 1977, Appl. Opt., **16**, 218
- 1.18 Jones, R.A., 1978, Appl. Opt., **17**, 1891
- 1.19 Jones, R.A., 1980, Appl. Opt., **19**, 2072
- 1.20 Facey, T.A., Nonnenmacher, A.L., Chadwick, D.P., 1990, SPIE Vol. 1236 "Advanced Technology Optical Telescopes", 597
- 1.21 Jones, R.A., 1982, Appl. Opt., **21**, 561
- 1.22 Nelson, J., 1980, Proc. Conf. "Optical and IR Telescopes for the 1990s", KPNO, Tucson, 11
- 1.23 Nelson, J., 1980, ibid, 631
- 1.24 Espiard, J., Gehl, R., 1988, Proc. ESO Conf. "Very Large Telescopes and their Instrumentation", ESO, Garching, 329
- 1.25 REOSC, 1989, Proposal for Figuring and Polishing the four 8.2 m VLT primary mirrors
- 1.26 Espiard, J., et al., 1992, private communication

- 1.27 Knohl, E.D., et al., 1985, Carl Zeiss "Study for the VLT 8 m Figuring"
- 1.28 Ewald, R., Himmes, A., 1990, SPIE Proceedings No. 1236 "Advanced Technology Optical Telescopes", 273
- 1.29 Jones, R.A., Plante, R.L., 1987, Precision Engineering, **9**(2), 65
- 1.30 Golini, D., Rupp, W.J., Zimmerman, J., 1989, SPIE Vol. 1113 "Reflective Optics II", 204
- 1.31 Jones, R.A., Rupp, W.J., 1991, Opt. Engineering, **30**(12), 1962
- 1.32 Jones, R.A. (ed), 1991, SPIE Vol. MS40 "Selected Papers on Computer-Controlled Optical Surfacing"
- 1.33 Heynacher, E., 1986, German Patent DE 3430499A1
- 1.34 Knohl, E.D., Schleth, A., Beckstette, K., Küchel, M., 1988, SPIE Conf. "Optical Design Methods, Applications, and Large Optics", SPIE Vol. 1013, 216
- 1.35 Korhonen, T., Lappalainen, T., 1990, SPIE Conf. "Advanced Technology Optical Telescopes IV", SPIE Vol. 1236, 691
- 1.36 Korhonen, T., Lappalainen, T., 1992, Test Protocols of the 1.2 m telescope optics for Geneva and Leuven, Opteon Oy, May 1992
- 1.37 Angel, J.R.P., Parks, R.E., 1984, OSA Workshop "Optical Fabrication and Testing", Monterey Cal.
- 1.38 Angel, J.R.P., 1984, Proc. IAU No. 79 "Very Large Telescopes, their Instrumentation and Programs", ESO, Garching, 11
- 1.39 Lubliner, J., Nelson, J.E., 1980, Appl. Opt., **19**, 2332
- 1.40 Martin, H.M., Angel, J.R.P., Cheng, A.Y.S., 1988, Proc. ESO Conf. "Very Large Telescopes and their Instrumentation", 353
- 1.41 Wizonowich, P., Angel, J.R.P., 1988, ibid, 363
- 1.42 Brown, D.S., 1986, OSA Workshop "Optical Fabrication and Testing", Digest 86: 16,48
- 1.43 Steward Observatory Mirror Lab., 1991, "Update on Progress at the Steward Observatory Mirror Lab.", Dec. 1991
- 1.44 Beckers, J.M., 1992, Internal Memo ESO, 15.01.92
- 1.45 Schmidt, B., 1932, Mitt. Hamburger Sternw., **7**, 15
- 1.46 Wenske, K., 1988, "Spiegeloptik", 4. Aufl., Verlag Sterne u. Weltraum, München, Taschenbuch 7, 92 and 131
- 1.47 Lemaître, G., 1972, Appl. Opt., **11**, 1630
- 1.48 Lemaître, G., 1981, Proc. ICO 12 Conf. "Current Trends in Optics", eds. F.T. Arecchi and F.R. Aussenegg, Taylor and Francis, London, 135
- 1.49 Lemaître, G., 1989, Proc. SPIE Conf. "Active Telescope Systems", Orlando Fa, SPIE Vol. 1114, 328
- 1.50 Nelson, J.E., Gabor, G., Hunt, L.K., Lubliner, J., Mast, T., 1980, Appl. Opt., **19**, 2341
- 1.51 Golden, L., Gillett, P., Radau, R., Richardson, J., Poczulp, G., 1982, Proc. Conf. "Advanced Technology Telescopes", SPIE Vol. 332, 357
- 1.52 Barr, L.D., Richardson, J.H., Shu, K.L., 1986, Proc. Conf. "Advanced Technology Telescopes III", SPIE Vol. 628, 550
- 1.53 Nelson, J.E., 1984, Proc. IAU Colloq. No. 79 "Very Large Telescopes, their Instrumentation and Programs", ESO, Garching, 755
- 1.54 Budiansky, M.P., 1984, Ten Meter Telescope Technical Note No. 95, Univ. of California, Berkeley
- 1.55 Mast, T.S., Nelson, J.E., 1988, Proc. ESO Conf. "Very Large Telescopes and their Instrumentation", ESO, Garching, 411
- 1.56 Pepi, J.W., 1990, Opt. Eng., **29**, 1366
- 1.57 Mast, T.S., Nelson, J.E., 1990, Proc. Conf. "Advanced Technology Telescopes IV", SPIE Vol. 1236, 670

- 1.58 Nelson, J.E., 1991, Conf. "Next Generation Space Telescope", Pasadena, March 1991
- 1.59 Wilson, S.R., Reicher, D.W., McNeill, J.R., 1988, Proc. SPIE Conf. "Advances in Fabrication and Metrology for Optics and Large Optics", SPIE Vol. 966, 74
- 1.60 Pileri, D., 1989, Proc. SPIE Conf. "Current Development in Optical Engineering and Commercial Optics", SPIE Vol. 1168, 25
- 1.61 Allen, L.N., Romig, H.W., 1990, Proc. SPIE Conf. "Advanced Optical Manufacturing and Testing", SPIE Vol. 1333, 22
- 1.62 Allen, L.N., Keim, R.E., Lewis, T.S., Ullom, J., 1991, Proc. SPIE Conf. "Advanced Optical Manufacturing and Testing II", SPIE Vol. 1531, 195
- 1.63 Allen, L.N., Hannon, J.J., Wambach, R.W., 1991, Proc. SPIE Conf. "Active and Adaptive Optical Components", SPIE Vol. 1543, 190
- 1.64 Wilson, T.J., 1990, Laser Focus World, 111
- 1.65 Kodak Brochure, revised April 16, 1992, "Optical Processing and Test Capabilities of Eastman Kodak Company's Federal Systems Division", 3
- 1.66 Wilson, R.N., Noethe, L., 1988, Proc. ESO Conf. "Very Large Telescopes and their Instrumentation", ESO, Garching, 373
- 1.67 Dierickx, P., et al., 1996, Proc. ESO/Lund/SPIE Conf. "Optical Telescopes of Today and Tomorrow", Landskrona, Sweden, SPIE Vol. 2871, 385
- 1.68 Espiard, J., 1997, private communication
- 1.69 Cheng, J., Humphries, C.M., 1982, *Vistas in Astronomy*, **26**, 15
- 1.70 Schwesinger, G., 1988, *J. Mod. Optics*, **35**(7), 1117
- 1.71 Beckstette, K., Küchel, M., Heynacher, E., 1989, *Astrophys. and Space Science*, **160**, 207 (Symposium on the JNLT, Tokyo, Nov.-Dec. 1988)
- 1.72 Wilson, R.N., Franzia, F., Giordano, P., Noethe, L., Tarenghi, M., 1989, *J. Mod. Optics*, **36**(11), 1415
- 1.73 Knohl, E.D., et al., 1992, Proc. ESO Conf. "Progress in Telescope and Instrumentation Technologies", ESO, Garching, 129
- 1.74 Malacara, D., 1978, "Optical Shop Testing", John Wiley, New York
- 1.75 Jenkins, F.A., White, H.E., 1937, "Fundamentals of Physical Optics", McGraw-Hill, New York
- 1.76 Twyman, F., Green, A., 1916, British Patent No. 103832
- 1.77 Twyman, F., 1919, British Patent No. 130224
- 1.78 Twyman, F., 1918, *Astrophys. J.*, **48**, 256
- 1.79 Michelson, A.A., 1918, *Astrophys. J.*, **47**, 283
- 1.80 Burch, C.R., 1940, *MNRAS*, **100**, 488
- 1.81 Hansen, G., 1955, *Optik*, **12**, 5
- 1.82 Ostrovskaya, M.A., Filimonova, N.F., 1969, *Sov. J. Opt. Tech.*, **36**, 563
- 1.83 Kingslake, R., 1925-1926, *Trans. Opt. Soc. London*, **27**, 94
- 1.84 Kingslake, R., 1926-1927, *Trans. Opt. Soc. London*, **28**, 1
- 1.85 Collier, R.T., Burkhardt, C.B., Lin, L.H., 1971, "Optical Holography", Academic Press, New York, 146
- 1.86 Houston, J.B., Buccini, C.J., O'Neill, P.K., 1967, *Appl. Opt.*, **6**, 1237
- 1.87 Swantner, W.H., Lowrey, W.H., 1980, *Appl. Opt.*, **19**(1), 161
- 1.88 Koliopoulos, C.L., 1986, "FAST" Operating Manual, Phase Shift Technology Inc., Tucson
- 1.89 Ingalls, A.G., ed., 1945, "Amateur Telescope Making", Book 1, Munn, New York, 96
- 1.90 Liu, Y.M., Lawrence, G.N., Koliopoulos, C.L., 1988, *Appl. Opt.*, **27** (21), 4504
- 1.91 Bruning, J.H., 1978, in Malacara [1.74], 409
- 1.92 Bruning, J.H., et al, 1974, *Appl. Opt.*, **13**(11), 2693
- 1.93 Jones, R.A., Kadakia, P.L., 1968, *Appl. Opt.*, **7**, 1477

- 1.94 Wyant, J.C., 1987, "Optical Testing and Testing Instrumentation", Opt. Sciences Center and WYKO Corp., Tucson, 43
- 1.95 Ichioka, Y., Inuiya, M., 1972, Appl. Opt., **11**(7), 1507
- 1.96 Takeda, M., et al., 1982, JOSA, **72**(1), 156
- 1.97 Itoh, K., 1982, Appl. Opt., **21**(14), 2470
- 1.98 Mertz, L., 1983, Appl. Opt., **22**(10), 1535
- 1.99 Macy, W.W., 1983, Appl. Opt., **22**(23), 3899
- 1.100 Womack, K.H., 1984, Opt. Eng., **23**(4), 391
- 1.101 Nugent, K.A., 1985, Appl. Opt., **24**(18), 3101
- 1.102 Wyant, J.C., 1975, Appl. Opt., **14**(11), 2622
- 1.103 Grievenkamp, J.E., 1984, Opt. Eng., **23**(4), 351
- 1.104 Kinnstaetter, K., et al., 1988, Appl. Opt., **27**(24), 5083
- 1.105 Massie, N.A., et al., 1979, Appl. Opt., **18**(11), 1797
- 1.106 Frantz, L.M., et al., 1979, Appl. Opt., **18**(19), 3301
- 1.107 Massie, N.A., 1980, Appl. Opt., **19**(1), 155
- 1.108 Schwider, J., et al., 1983, Appl. Opt., **22**(21), 3421
- 1.109 Hariharan, P., et al., 1987, Appl. Opt., **26**(13), 2505
- 1.110 Cheng, Y.Y., Wyant, J.C., 1985, Appl. Opt., **24**(18), 3049
- 1.111 Freischlad, K., Koliopoulos, C.L., 1990, JOSA A, **7**(4), 542
- 1.112 Koliopoulos, C.L., 1991, Proc. SPIE Conf. "Advanced Optical Manufacturing and Testing II", SPIE Vol. 1531, 119
- 1.113 Smythe, R., Moore, R., 1984, Opt. Eng., **23**, 361
- 1.114 Küchel, M., 1990, Proc. SPIE Conf. "Optical Testing and Metrology III", SPIE Vol. 1332, 655
- 1.115 Küchel, M., Heynacher, E., 1988, Proc. ESO Conf. "Very Large Telescopes and their Instrumentation", ESO, Garching, 495
- 1.116 Küchel, M., 1990, Proc. SPIE Conf. "Advanced Optical Manufacturing and Testing", SPIE Vol. 1333, 280
- 1.117 Küchel, M., 1991, German Patent DE 4014019A1
- 1.118 Torlötting, B., Béraud, P., 1991, "FLIP: Une nouvelle méthode de dépouillement d'interférogrammes pour le contrôle de grands miroirs", Proc. Int. Conf. on Space Optics "Horizon de l'optique", Toulouse (Sept. 1991), 295–302
- 1.119 REOSC, 1992, REOSC VLT Report to ESO No. 245
- 1.120 Espiard, J., et al., 1992, Proc. ESO Conference "Very Large Telescopes and their Instrumentation", ESO, Garching, 179
- 1.121 Miller, J., 1992, ESO Conference "Very Large Telescopes and their Instrumentation, *verbal* presentation only. A revised and updated (1997) *written* version, including work for Keck II, is in preparation at the Lick Observatory
- 1.122 Offner, A., 1978, in Malacara [1.74], 439
- 1.123 Couder, A., 1927, Rev. d'Opt., **6**, 49
- 1.124 Burch, C.R., 1936, MNRAS, **96**, 438
- 1.125 Burch, C.R., 1938, J. Brit. Astron. Ass., **48**, 99
- 1.126 Ross, F.E., 1943, Astrophys. J., **98**, 341
- 1.127 Dall, H.E., 1947, J. Brit. Astron. Ass., **57**, 201
- 1.128 Dall, H.E., 1953, in "Amateur Telescope Making", Book 3, ed. A.G. Ingalls, Scientific American, New York, 149
- 1.129 Hopkins, H.H., 1950, "Wave Theory of Aberrations", Oxford, 123
- 1.130 Wilson, R.N., 1968, Appl. Opt., **7**(2), 253
- 1.131 Offner, A., 1963, Appl. Opt., **2**, 153
- 1.132 Wilson, R.N., et al., 1991, J. Mod. Optics, **38**(2), 219
- 1.133 Wilson, R.N., 1990, The Messenger, ESO, **61**, 22

- 1.134 Brown, R.A., Ford, H.C. (eds.), 1991, "Report of the HST Strategy Panel: A Strategy for Recovery", Space Telescope Science Institute, Baltimore
- 1.135 Offner, A., 1969, *Appl. Opt.*, **8**, 1735
- 1.136 Hecht, J., 1990, *New Scientist*, **127**(1730), 18 August, 16
- 1.137 Parks, R.E., 1978, Proc. SPIE Conf. "Advances in Optical Metrology", SPIE Vol. 153, 56
- 1.138 Faulde, M., Fercher, A.F., Torge, R., Wilson, R.N., 1973, *Optics Communications*, **7**(4), 363
- 1.139 Martin, H.M., Burge, J.H., Ketelsen, D.A., West, S.C., 1997, Proc. Lund/ESO/SPIE Conf. "Optical Telescopes of Today and Tomorrow", ed. A. Ardeberg, SPIE Vol. 2871, 399
- 1.140 Burge, J.H., Andersen, D.S., Ketelsen, D.A., West, S.C., 1994, Proc. SPIE Conf. "Advanced Technology Optical Telescopes V", ed. L.M. Stepp, SPIE Vol. 2199, 658
- 1.141 Wilson, R.N., 1974, ESO Technical Report No. 3, ESO, Geneva, July 1974
- 1.142 Parks, R.E., Shao, L.Z., 1988, *Opt. Eng.*, **27**(12), 1057
- 1.143 Wetthauer, A., Brodhun, E., 1920, *Zeitschr. f. Instrumentenkunde*, **40**, 96
- 1.144 Hendrix, D.O., Christie, W.H., 1939, *Scient. American*, **161**(2)(August 1939), 118, in the monthly feature "Telescoptics" by A.G. Ingalls
- 1.145 Hochgraf, N.A., 1969, Opt. Sciences Center Newsletter, Jan.–March, 41
- 1.146 Espiard, J., Favre, B., 1970, *Nouvelle Rev. d'Opt.*, **1**(6), 395
- 1.147 Hu, Ningsheng, 1980, Proc. KPNO Conf. "Optical and IR Telescopes for the 1990s", Vol. I, App. A to paper by Meinel, A., et al., 88
- 1.148 Lytle, J.D., 1970, *Appl. Opt.*, **9**(11), 2497
- 1.149 Wilson, R.N., 1974, ESO Technical Report No. 4, ESO, Geneva, August 1974
- 1.150 Martin, L.C., 1950, "Technical Optics", Vol. II, Pitman, London, 303
- 1.151 Norman, B.A., 1957, *Sky and Telescope*, **XVII**(1), Nov. 1957, 38
- 1.152 Schmadel, L.D., 1974, *Sterne und Weltraum*, **13**(8/9), 282
- 1.153 Meinel, A.B., Meinel, M.P., 1983, *Appl. Opt.*, **22**(4), 520
- 1.154 Hindle, J.H., 1931, *MNRAS*, **91**(5), 592
- 1.155 Hindle, J.H., 1945, "Amateur Telescope Making", Vol. 1, ed. A.G. Ingalls, Munn, New York, 225
- 1.156 Silvertooth, W., 1940, *JOSA*, **30**(3), 140
- 1.157 Assus, P., 1992, Proc. ESO Conference "Progress in Telescope and Instrumentation Technologies", ed. M.-H. Ulrich, ESO, Garching, 219
- 1.158 Andersen, J., 1990, private communication: Report by the Rayleigh Optical Corporation
- 1.159 Dierickx, P., 1997, private communication (ESO)
- 1.160 Simpson, F.A., Oland, B.H., Meckel, J., 1974, *Opt. Eng.*, **13**, G101
- 1.161 Richardson, H.E., 1974, private communication
- 1.162 Espiard, J., 1991, REOSC VLT Report No. 5312
- 1.163 Common, A.A., 1888, *MNRAS* **48**, 105
- 1.164 Ritchey, G.W., 1904, *Smiths. Contr. to Knowledge* No. 1459, **34**, 25
- 1.165 Pierce, J.M., 1945, in "Amateur Telescope Making", Vol. 1, ed. A.G. Ingalls, Munn, New York, 241
- 1.166 Danjon, A., Couder, A., 1935, "Lunettes et Télescopes", re-issued 1983 by Blanchard, Paris, 501

## Chapter 2

- 2.1 Wilson, R.N., 1953, Ph.D. Thesis "The Production of Aspheric Surfaces", Imperial College, University of London, 1–10

- 2.2 Smart, W.M., 1947, "Text-Book on Spherical Astronomy", 4th Ed., Cambridge, 1
- 2.3 Wilson, R.N., Delabre, B., 1977, PASP, **109** (Jan.), 53
- 2.4 Bhatia, R., 1995, TNG Technical Report No. 43, Astron. Observatory Padova-Asiago; also SPIE Aerosense Conference, Orlando, Proc. No. 2479
- 2.5 Shack, R.V., Thompson, K., 1980, Proc. SPIE Conf. "Optical Alignment", San Diego, Vol. 251, 146
- 2.6 McLeod, B.A., 1996, PASP, **108** (Feb.), 217
- 2.7 Schroeder, D.J., 1987, "Astronomical Optics", Academic Press, San Diego
- 2.8 Taylor, H.D., 1894, "The Adjustment and Testing of Telescope Objectives", Cooke, Troughton and Simms (reissued 1946 by Grubb-Parsons, Newcastle)
- 2.9 Ingalls, A.G., 1945, "Amateur Telescope Making", Book 1, Munn and Co., New York, 428
- 2.10 Foucault, J.B.L., 1859, Ann. de l'Obs. de Paris, **5**, 197
- 2.11 Philbert, M., 1967, Optica Acta, **14**, 169
- 2.12 Berny, F., Slansky, S., 1970, Proc. ICO Conf. "Optical Instruments and Techniques", Reading, 1969, ed. J.H. Dickson, Oriel Press, Newcastle
- 2.13 Goad, L., Roddier, F., Beckers, J., Eisenhardt, P., 1986, SPIE Conf. "Advanced Technology Optical Telescopes", Vol. 628, 305
- 2.14 Wilson, R.N., 1980, ESO (La Silla) Internal Memo "Procedures and formulae for the adjustment of telescopes and analysis of their performance", 18 June 1980
- 2.15 Hartmann, J., 1904, Z. Instrumentenkde., **24**(1), 33 and 97
- 2.16 Bahner, K., 1967, "Teleskope" in "Handbuch der Physik", Vol. XXIX, 301
- 2.17 Hopkins, H.H., 1950, "Wave Theory of Aberrations", Oxford, 24
- 2.18 Lehmann, H., 1903, Z. Instrumentenkde., **23**, 289
- 2.19 Danjon, A., Couder, A., 1935, "Lunettes et Telescopes", Blanchard, Paris, reissued 1983, 504
- 2.20 Kingslake, R., 1928, Trans. Opt. Soc. London, **29**, 133
- 2.21 Beck, H.G., Fehlkamm, G., 1962, Jenaer Jb., **75**, 87; Jenaer Rundschau **7**, 116
- 2.22 Herzberger, M., 1958, "Modern Geometrical Optics", Interscience Publ., New York, 272
- 2.23 Mayall, N.U., Vasilevskis, S., 1960, Astron. J. **65**(5), 304; also Lick Observatory Bulletin No. 567
- 2.24 Franz, F., Le Luyer, M., Wilson, R.N., 1977, ESO Technical Report No. 8, ESO, CERN, Geneva
- 2.25 Platt, B., Shack, R.V., 1971, Optical Sciences Center Newsletter, Univ. of Arizona, Tucson, **5**(1), 15
- 2.26 Shack, R.V., Platt, B.C., 1971, JOSA, **61**, 656
- 2.27 Wilson, R.N., Franz, F., Noethe, L., Tarenghi, M., 1984, Proc. IAU Colloq. No. 79: "Very Large Telescopes, their Instrumentation and Programs", ESO, Garching, 119
- 2.28 Gale, M.T., Knop, K., 1983, SPIE Vol. 398, 347
- 2.29 Loibl, B., 1980, Astron. and Astrophys., **91**, 265
- 2.30 Franz, F., 1997, private communication from ESO
- 2.31 Franz, F., Delabre, B., 1997, private communication from ESO
- 2.32 Korhonen, T., 1984, SPIE Conf. "Advanced Technology Optical Telescopes II", Vol. 444, 249
- 2.33 Korhonen, T., Haarala, S., Piironen, J., Sillanpää, A., 1986, SPIE Conf. "Advanced Technology Optical Telescopes III", Vol. 628, 486
- 2.34 Korhonen, T., Haarala, S., 1988, ESO Conference "Very Large Telescopes and their Instrumentation", ESO, Garching, Vol. 1, 583
- 2.35 Korhonen, T., Lappalainen, T., 1991, NOT News, **4**, July 1991, 3

- 2.36 Wilson, R.N., 1979, Internal ESO Report on the 50 cm ESO telescope
- 2.37 Beckers, J.M., Williams, J.T., 1979, MMT Technical Memorandum 79-1
- 2.38 Roddier, F., 1987, NOAO R and D Note 87-3
- 2.39 Roddier, F., 1988, Appl. Opt., **27**(7), 1223
- 2.40 Roddier, F., Roddier, C., Roddier, N., 1988, SPIE Vol. 976, 203
- 2.41 Roddier, C., Roddier, F., Stockton, A., Pickles, A., Roddier, N., 1990, SPIE Vol. 1236, 756
- 2.42 Roddier, C., Roddier, F., 1991, SPIE Vol. 1531, 37
- 2.43 Roddier, F., 1990, Appl. Opt., **29**(10), 1402
- 2.44 Wilson, R.N., Franzia, F., Noethe, L., Andreoni, G., 1991, J. Mod. Optics, **38**, 219
- 2.45 Baldwin, J., Pérez, G., Gregory, B., Weller, W., 1992, Proc. ESO Conf., "Progress in Telescope and Instrumentation Technologies", ESO, Garching, Vol. 42, 247
- 2.46 Roddier, C., Roddier, F., 1993, JOSA A, **10**(11), 2277
- 2.47 Roddier, C., Graves, J.E., Northcott, M.J., Roddier, F., 1994, Proc. SPIE Conf. "Advanced Technology Telescopes V", SPIE Vol. 2199, 1172
- 2.48 Behr, A., 1973, Astron. and Astrophys., **28**, 355
- 2.49 Franzia, F., Wilson, R.N., 1980, Internal ESO Report on a Coma Experiment at the 1.54 m Danish Telescope
- 2.50 Wyant, J.C., 1975, JOSA, **65**, 2622
- 2.51 Hardy, J.W., Lefebvre, J.E., Koliopoulos, C.L., 1977, JOSA, **67**, 360
- 2.52 Koliopoulos, C.L., 1980, Appl. Opt., **19**, 1523
- 2.53 Bates, W.J., 1947, Proc. Phys. Soc. (London), **59**, 940
- 2.54 Smartt, R.N., 1979, SPIE Vol. 192, 35
- 2.55 Drew, R.L., 1951, Proc. Phys. Soc. B, **64**, 1005
- 2.56 Brown, D., 1954, Proc. Phys. Soc., **67**, 232
- 2.57 King, J.H., 1944, "Amateur Telescope Making II", ed. A.G. Ingalls, Munn and Co., New York, 104
- 2.58 Ronchi, V., 1958, Atti. Fond. G. Ronchi (Firenze), XIII **5**, 368
- 2.59 Cornejo-Rodriguez, A., 1978, "Optical Shop Testing", ed. D. Malacara, Wiley, New York, 283

## Chapter 3

- 3.1 Wilson, R.N., 1992, "Homage to Galileo", Ed. P. Mazzoldi, Invited Paper for Int. Conf. Univ. of Padua June 1992, Cleup Editrice, 359
- 3.2 Rule, B., 1971, Proc. ESO/CERN Conf. "Large Telescope Design", ESO, Geneva, 283
- 3.3 Meinel, A.B., 1978, Proc. ESO Conf. "Optical Telescopes of the Future", ESO, Geneva, 13
- 3.4 Meinel, A.B., 1979, Opt. Engin., **18**(6), 645
- 3.5 Meinel, A.B., 1982, JOSA, **72**(1), 14
- 3.6 Humphries, C.M., Reddish, V.C., Walshaw, D.J., 1984, IAU Colloq. No. 79, Proc. ESO Conf. "Very Large Telescopes, their Instrumentation and Programs", ESO, Garching, 379
- 3.7 Couder, A., 1931, Bulletin Astron., 2me Série, Tome VII, Fasc. VI, 201
- 3.8 Mountain, M., Gillett, F., Kurz, R., 1997, Proc. Lund/ESO/SPIE Conf. "Optical Telescopes of Today and Tomorrow", SPIE Vol. 2871, 15
- 3.9 Ingalls, A.G., 1951, Sci. Am., Jan. 1951, 60
- 3.10 King, H.C., 1955, "The History of the Telescope", Griffin, London, 206
- 3.11 Rosse, Lord, 1828, Edinb. J. Sci., **7**, 25

- 3.12 Mertz, L., 1970, "Optical Instruments and Techniques", Proc. Conf. at Reading 1969, Oriel Press, Newcastle, 507
- 3.13 Mertz, L., 1980, Proc. Conf. "Optical and IR Telescopes for the 1990s", KPNO, Tucson, Vol. II, 957
- 3.14 Barr, L., 1980, *ibid*, Vol. I, 23
- 3.15 Ramsey, L.W., 1988, Proc. ESO Conf. "Very Large Telescopes and their Instrumentation", ESO, Garching, 119
- 3.16 Ramsey, L.W., 1984, Proc. IAU Colloq. No. 79, ESO Conf. "Very Large Telescopes, their Instrumentation and Programs", ESO, Garching, 851
- 3.17 Ray, F.B., 1992, Proc. ESO Conf. "Progress in Telescope and Instrumentation Technologies", ESO, Garching, 91
- 3.18 Sebring, T.A., Ramsey, L.W., 1996, Proc. Lund/ESO/SPIE Conf. "Optical Telescopes of Today and Tomorrow", SPIE Vol. 2871, 32
- 3.19 Bash, F.N., Sebring, T.A., Ray, F.B., Ramsey, L.W., 1996, *ibid*, 576
- 3.20 Ardeberg, A., Andersen, T., Owner-Petersen, M., Jessen, N.C., 1996, *ibid*, 585
- 3.21 Owner-Petersen, M., 1996, *ibid*, 607
- 3.22 Gillingham, P., 1996, *ibid*, 2
- 3.23 Nelson, J.E., Mast, T.S., 1988, Proc. ESO Conf. "Very Large Telescopes and their Instrumentation", ESO, Garching, Vol. I, 7
- 3.24 Nelson, J.E., Mast, T.S., 1992, Proc. ESO Conf. "Progress in Telescope and Instrumentation Technologies", ESO, Garching, 3
- 3.25 Nelson, J.E., 1978, Proc. ESO Conf. "Optical Telescopes of the Future ", ESO, Geneva, 133
- 3.26 Nelson, J.E., Mast, T.S., Faber, S.M., eds., 1985, Keck Observatory Report No. 90 "The Design of the Keck Observatory and Telescope (10 m Telescope)"
- 3.27 Miller, J., 1992, ESO Conf. "Progress in Telescope and Instrumentation Technologies", *verbal* presentation only. A revised and updated (1997) *written* version, including work for Keck II, is in preparation at the Lick Observatory
- 3.28 Mast, T.S., Nelson, J.E., 1992, Proc. ESO Conf. "Progress in Telescope and Instrumentation Technology", ESO, Garching, 159
- 3.29 Smith, G.M., 1996, Proc. Lund/ESO/SPIE Conf. "Optical Telescopes of Today and Tomorrow", SPIE Vol. 2871, 10
- 3.30 Hügenell, H., 1992, Proc. ESO Conf. "Progress in Telescope and Instrumentation Technologies", ESO, Garching, 269
- 3.31 Appenzeller, I., 1988, Proc. ESO Conf. "Very Large Telescopes and their Instrumentation", ESO, Garching, 177
- 3.32 Aikens, R.S., et al., 1977, NGT Report No. 4, KPNO, Tucson
- 3.33 Appenzeller, I., et al., 1992, Proc. ESO Conf. "Progress in Telescope and Instrumentation Technologies", ESO, Garching, 109
- 3.34 Ardeberg, A., et al., 1992, Proc. ESO Conf. "Progress in Telescope and Instrumentation Technologies", ESO, Garching, 75
- 3.35 Sytchev, V.V., et al., 1996, Proc. Lund/ESO/SPIE Conf. "Optical Telescopes of Today and Tomorrow", SPIE Vol. 2871, 624
- 3.36 Rodriguez Espinosa, J.M., Alvarez Martin, P., 1996, *ibid*, 69
- 3.37 Beckers, J.M., Williams, J.T., 1980, Proc. Conf. "Optical and IR Telescopes for the 1990s", KPNO, Tucson, Vol. I, 108
- 3.38 Reed, M.A., 1978, Proc. ESO Conf. "Optical Telescopes of the Future", ESO, Geneva, 209
- 3.39 Carleton, N.P., 1980, Proc. Conf. "Optical and IR Telescopes for the 1990s", KPNO, Tucson, Vol. I, 491

- 3.40 Beckers, J.M., et al., 1981, "Telescopes for the 1980s", Annual Reviews Inc., Palo Alto, Cal., 63
- 3.41 Chaffee, F.H., 1991, Quarterly Summary Vol. 3, No. 4, of the MMT Conversion
- 3.42 West, S.C., et al., 1996, Proc. Lund/ESO/SPIE Conf. "Optical Telescopes of Today and Tomorrow", SPIE Vol. 2871, 38
- 3.43 Baranne, A., Lemaître, G., 1986, Proc. "Workshop on Large Telescopes", Hamburg, Mitt. der Astron. Gesellschaft No. 67, 1986, 226
- 3.44 Baranne, A., Lemaître, G., 1987, C. R. Acad. Sci. Paris, **305**, Série II, 445
- 3.45 Strittmatter, P.A., 1988, Proc. ESO Conf. "Very Large Telescopes and their Instrumentation", ESO, Garching, 29
- 3.46 Salinari, P., 1992, ESO Conf. "Progress in Telescope and Instrumentation Technologies", ESO, Garching, verbal communication only
- 3.47 Hill, J.M., 1996, Proc. Lund/ESO/SPIE Conf. "Optical Telescopes of Today and Tomorrow", SPIE Vol. 2871, 57
- 3.48 Wang, S., Su, D.-q., 1992, Proc. ESO Conf. "Progress in Telescope and Instrumentation Technologies", ESO, Garching, 105
- 3.49 Wang, S.-g., et al., 1996, Appl. Opt., **35**(25), 5155
- 3.50 Hill, J.M., Angel, J.R.P., 1992, Proc. ESO Conf. "Progress in Telescope and Instrumentation Technologies", ESO, Garching, 57
- 3.51 Martin, H.M., et al., 1996, Proc. Lund/ESO/SPIE Conf. "Optical Telescopes of Today and Tomorrow", SPIE Vol. 2871, 399
- 3.52 Shectman, S., 1992, Proc. ESO Conf. "Progress in Telescope and Instrumentation Technologies", ESO, Garching, verbal communication only
- 3.53 Johns, M., 1996, Proc. Lund/ESO/SPIE Conf. "Optical Telescopes of Today and Tomorrow", SPIE Vol. 2871, 49
- 3.54 Randall, L., 1992, Proc. ESO Conf. "Progress in Telescope and Instrumentation Technologies", ESO, Garching, 39
- 3.55 Osmer, P.S., 1992, Proc. ESO Conf. "Progress in Telescope and Instrumentation Technologies", ESO, Garching, 35
- 3.56 Huang, E.W., 1996, Proc. Lund/ESO/SPIE Conf. "Optical Telescopes of Today and Tomorrow", SPIE Vol. 2871, 291
- 3.57 O'Dell, C.R., 1981, "Telescopes for the 1980s", Annual Reviews Inc., Palo Alto, Cal., 129
- 3.58 Waldrop, M.M., 1990, Science, **249**, 13 July, 112
- 3.59 Chaisson, E.J., Villard, R., 1990, "Vistas in Astronomy", **33**, Pergamon Press, Oxford, 105
- 3.60 Schroeder, D.J., 1987, "Astronomical Optics", Academic Press, Inc., California, 213–220
- 3.61 Fienberg, R.T., et al., 1990, Sky and Telescope, **80**(4), October 1990, 340 and 352
- 3.62 Hecht, J., 1991, New Scientist, **129**(1760), 16 March 1991, 30
- 3.63 Allen, L., et al., 1990, "The Hubble Space Telescope Optical Systems Failure Report", NASA, November 1990
- 3.64 Hecht, J., 1990, New Scientist, **127**(1730), 18 August 1990, 16
- 3.65 Brown, R.A., Ford, H.C., eds., 1991, "Report of the HST Strategy Panel: A Strategy for Recovery", Space Telescope Science Institute, Baltimore
- 3.66 Benvenuti, P., Wilson, R.N., 1991, ST-ECF Newsletter, March 1991, 22 and 23
- 3.67 Fischer, D., Duerbeck, H., 1995, "Hubble: ein neues Fenster zum All", Birkhäuser, Basel. (English translation "Hubble: a New Window to the Universe", 1996, Copernicus, New York)
- 3.68 Tarenghi, M., Wilson, R.N., 1989, SPIE Conf. "Active Telescope Systems", ed. Roddier, Orlando, SPIE Vol. 1114, 302

- 3.69 Wilson, R.N., Franzia, F., Noethe, L., 1987, *J. Mod. Optics*, **34**(4), 485  
3.70 Wilson, R.N., et al., 1991, *J. Mod. Optics*, **38**(2), 219  
3.71 Wilson, R.N., et al., 1989, *J. Mod. Optics*, **36**(11), 1415  
3.72 Wilson, R.N., 1991, *Contemporary Physics*, **32**(3), 157  
3.73 Wilson, R.N., et al., 1992, Proc. ESO Conf. "Progress in Telescope and Instrumentation Technologies", ESO, Garching, 199  
3.74 Barbieri, C., 1997, TNG News No. 15 (Feb. 1997), 1  
3.75 Barbieri, C., et al., 1993, Proc. Int. Conf. "From Galileo's 'Occhialino' to Optoelectronics", Padua, June 1992, World Scientific, Singapore, 808  
3.76 Knohl, E.D., Schmidt, M., 1993, *ibid*, 769  
3.77 Knohl, E.D., et al., 1992, Proc. ESO Conf. "Progress in Telescope and Instrumentation Technologies", ESO, Garching, 129  
3.78 Barbieri, C., et al., 1994, SPIE Vol. 2199, 10  
3.79 Barbieri, C., 1996, Proc. Lund/ESO/SPIE Conf. "Optical Telescopes of Today and Tomorrow", SPIE Vol. 2871, 244  
3.80 Enard, D., 1988, Proc. ESO Conf. "Very Large Telescopes and their Instrumentation", ESO, Garching, 17  
3.81 Beckers, J.M., Tarenghi, M., 1992, Proc. ESO Conf. "Progress in Telescope and Instrumentation Technologies", ESO, Garching, 13  
3.82 Enard, D., 1992, *ibid*, 25  
3.83 Dierickx, P., et al., 1996, Proc. Lund/ESO/SPIE Conf. "Optical Telescopes of Today and Tomorrow", SPIE Vol. 2871, 385  
3.84 von der Lühe, O., et al., 1996, *ibid*, 498  
3.85 Zago, L., 1992, Proc. ESO Conf. "Progress in Telescope and Instrumentation Technologies", ESO, Garching, 235  
3.86 Schneermann, M., et al., 1996, Proc. Lund/ESO/SPIE Conf. "Optical Telescopes of Today and Tomorrow", SPIE Vol. 2871, 650  
3.87 Morian, H.F., et al., 1996, *ibid*, 405  
3.88 Enard, D., Maréchal, A., Espiard, J., 1996, *Reports on Progress in Physics*, **59**(5), 601  
3.89 Noethe, L., et al., 1988, *J. Mod. Optics*, **35**(9), 1427  
3.90 Kodaira, K., 1988, Proc. ESO Conf. "Very Large Telescopes and their Instrumentation", ESO, Garching, 47  
3.91 Subaru Project Office, 1991, Brochure "Subaru: An 8 m optical-infrared telescope project", National Astronomical Observatory, Tokyo  
3.92 Kodaira, K., 1992, Proc. ESO Conf. "Progress in Telescope and Instrumentation Technologies", ESO, Garching, 43  
3.93 Kodaira, K., 1991, JNLT Technical Report No. 1  
3.94 Meinel, A.B., Meinel, M.P., 1980, Proc. Conf. "Optical and IR Telescopes for the 1990s", KPNO, Tucson, Vol. I, 95  
3.95 Kaifu, N., 1996, Proc. Lund/ESO/SPIE Conf. "Optical Telescopes of Today and Tomorrow", SPIE Vol. 2871, 24  
3.96 Abt, B., et al., 1988, Proc. ESO Conf. "Very Large Telescopes and their Instrumentation", ESO, Garching, 615  
3.97 Mäder, H.F., et al., 1990, Technische Mitteilungen Krupp 1/1990, 27  
3.98 Schnur, G.F.O., Stenvers, K.-H., 1988, Proc. ESO Conf. "Very Large Telescopes and their Instrumentation", ESO, Garching, 151  
3.99 Fellgett, P.B., 1970, "Optical Instruments and Techniques", Proc. of Conf. at Reading 1969, Oriel Press, Newcastle, 475  
3.100 Schnur, G.F.O., 1992, private communication  
3.101 Pausch, K., Stenvers, K.-H., 1992, VDI Berichte No. 917 (English translation)  
3.102 von Appen-Schnur, G., Luks, T., 1996, Proc. Lund/ESO/SPIE Conf. "Optical Telescopes of Today and Tomorrow", SPIE Vol. 2871, 520

- 3.103 King, H.C., 1955, "The History of the Telescope", Griffin, London, 261–264
- 3.104 Riekher, R., 1990, "Fernrohre und ihre Meister", Verlag Technik GmbH, Berlin, 285, 291
- 3.105 Couder, A., 1931, Bulletin Astron., 2me Série, Tome VII, Fasc. VI, 201
- 3.106 Maksutov, D.D., 1954, "Technologie der astronomischen Optik", VEB Verlag Technik, Berlin, 22
- 3.107 Hopkins, H.H., 1950, "Wave Theory of Aberrations", Oxford, 13
- 3.108 Riekher, R., 1990, "Fernrohre und ihre Meister", Verlag Technik GmbH, Berlin, 295
- 3.109 Riekher, R., 1990, ibid, 376
- 3.110 Wilson, R.N., Mischung, K.N., 1986, "Future ground-based optical telescopes: mirror blank materials and fabrication, active optics", Table 2, 30 (unpublished ESO report)
- 3.111 Müller, R., Höneß, H., 1988, Proc. ESO Conf. "Very Large Telescopes and their Instrumentation", ESO, Garching, 313
- 3.112 Pfaender, H.G., 1986, Schott Glass Lexicon, mvg, Landsberg, 148
- 3.113 Morian, H., Müller, R., 1992, Proc. ESO Conf. "Progress in Telescope and Instrumentation Technologies", ESO, Garching, 47
- 3.114 Maksutov, D.D., 1954, "Technologie der astronomischen Optik", VEB Verlag Technik, Berlin, 47
- 3.115 Riekher, R., 1990, "Fernrohre und ihre Meister", Verlag Technik GmbH, Berlin, 304
- 3.116 Van Dyke, N., 1988, Proc. ESO Conf. "Very Large Telescopes and their Instrumentation", ESO, Garching, 319
- 3.117 Smith, H.J., Barnes, T.G., eds., 1982, "Report of the Optical Conference on the 7.6 m Telescope", University of Texas, Publ. in Astronomy No. 22, 307 et seq.
- 3.118 Nather, R.E., 1980, Proc. Conf. "Optical and IR Telescopes for the 1990s", KPNO, Tucson, Vol. I, 54
- 3.119 Angel, J.R.P., 1988, Proc. ESO Conf. "Very Large Telescopes and their Instrumentation", ESO, Garching, 281
- 3.120 Cheng, A.Y.S., Angel, J.R.P., 1988, ibid, 467
- 3.121 Ballio, G., et al., 1988, ibid, 451
- 3.122 de Jonge, M.J., 1994, Proc. SPIE Conf. "Advanced Technology Optical Telescopes V", SPIE Vol. 2199, 22
- 3.123 Hill, J.M., Salinari, P., 1994, ibid, 64
- 3.124 Johnson, H.L., 1968, "Vistas in Astronomy", **10**, 149
- 3.125 Forbes, F.F., 1968, Appl. Opt., **7**(7), 1407
- 3.126 Forbes, F.F., Johnson, H.L., 1971, Appl. Opt., **10**(6), 1412
- 3.127 Forbes, F.F., 1969, Appl. Opt., **8**(7), 1361
- 3.128 Mottoni, G. de, 1972, Sky and Telescope, **43**(5), 296
- 3.129 Delabre, B., et al., 1982, ESO Report (unpubl.), May 1982
- 3.130 Mischung, K.N., 1984, IAU Colloq. No. 79, Proc. ESO Conf. "Very Large Telescopes, their Instrumentation and Programs", ESO, Garching, 57
- 3.131 Noethe, L., et al., 1984, ibid, 67
- 3.132 Noethe, L., et al., 1986, Astron. and Astrophys., **156**, 323
- 3.133 Yoder, P.R., 1986, "Opto-Mechanical Systems Design", Marcel Dekker Inc., New York, 352
- 3.134 Enard, D., et al., 1986, Proc. SPIE Conf. "Advanced Technology Optical Telescopes III", SPIE Vol. 628, Tucson, 518
- 3.135 Dierickx, P., Zigmann, F., 1991, The Messenger, ESO, No. 65, Sept. 1991, 66
- 3.136 Lemaître, G., Wilson, R.N., 1992, "A meniscus mirror aspherized by active optics", proposal by the Observatoire de Marseille to ESO, October 1992
- 3.137 Dierickx, P., 1997, private communication from ESO

- 3.138 Bingham, R.G., Walker, D.D., eds., 1993, Proc. SPIE Conf. "Metal Mirrors", SPIE Vol. 1931
- 3.139 Rozelot, J.-P., 1993, *ibid*, 8 and 33
- 3.140 Dierickx, P., 1993, *ibid*, 78
- 3.141 Bingham, R.G., 1993, *ibid*, 100
- 3.142 Lemaitre, G.R., Wilson, R.N., Mazzanti, S., 1993, *ibid*, 66
- 3.143 Bingham, R.G., et al., 1993, *ibid*, 150
- 3.144 Dierickx, P., Merkle, F., Stanghellini, S., 1992, Proc. ESO Conf. "Progress in Telescope and Instrumentation Technologies", ESO, Garching, 223
- 3.145 United Technologies Optical Systems (UTOS), 1991, Feasibility Report on SiC for the VLT Secondaries, Oct. 1991
- 3.146 Carl Zeiss, Oberkochen, 1991, Feasibility Report on figuring of SiC secondaries for the VLT
- 3.147 Wood, R.W., 1909, *Astrophys. J.*, **29**, 164
- 3.148 Ingalls, A.G., 1945, "Amateur Telescope Making", Book 1, Munn & Co., Inc., New York, 319
- 3.149 Borra, E.F., et al., 1988, *PASP*, **100**, 1015
- 3.150 Borra, E.F., et al., 1996, Proc. Lund/ESO/SPIE Conf. "Optical Telescopes of Today and Tomorrow", SPIE Vol. 2871, 326
- 3.151 Richardson, E.H., Morbey, C.L., 1987, Conf. "Instrumentation for Ground-Based Optical Astronomy: Present and Future", Springer, New York, 720
- 3.152 Timoshenko, S., Woinowsky-Krieger, S., 1959, "Theory of Plates and Shells", McGraw-Hill (reissued 1987), Ch. 3
- 3.153 Poisson, S.D., 1829, *Mém. de l'Acad. Française*, Vol. VIII, 357–627
- 3.154 Couder, A., 1931, *Bulletin Astron.*, 2me Série, Tome VII, Fasc. VI, 219 et seq.
- 3.155 Saint-Venant, A.B. de, 1881, "Théorie de l'élasticité des corps solides", Dunod, Paris, (a) 363, (b) 337; translation with additions of the work by A.R.F. Clebsch, 1862, "Theorie der Elastizität fester Körper", Teubner, Leipzig
- 3.156 Couder, A., 1931, *Bulletin Astron.*, 2me Série, Tome VII, Fasc. VI, 266 and 275
- 3.157 Timoshenko, S., Woinowsky-Krieger, S., 1959, "Theory of Plates and Shells", McGraw-Hill (reissued 1987), 245–253
- 3.158 Cheng, J., Humphries, C.M., 1982, *Vistas in Astronomy*, **1.26**, Pergamon Press, 15
- 3.159 Prescott, J., 1946, "Applied Elasticity", Dover Publications, New York
- 3.160 Schwesinger, G., 1968, Proc. Symposium "Support and Testing of Large Astronomical Mirrors", KPNO and UA, Tucson, 11
- 3.161 Schwesinger, G., 1954, *JOSA*, **44**(5), 417
- 3.162 Reissner, E., 1945, *J. Appl. Mech.*, **12**, A-69
- 3.163 Reissner, E., 1947, *Quart. Appl. Math.*, **5**, 55
- 3.164 Selke, L.A., 1970, *Appl. Opt.*, **9**(1), 149
- 3.165 Selke, L.A., 1970, *Appl. Opt.*, **9**(6), 1453
- 3.166 Schwesinger, G., Knohl, E.D., 1972, *Appl. Opt.*, **11**(1), 201
- 3.167 Green, A.E., 1949, *Quart. Appl. Math.*, **7**, 223
- 3.168 Malwick, A.J., Pearson, E.T., 1968, *Appl. Opt.*, **7**(6), 1207
- 3.169 Day, A.S., 1965, *The Engineer*, **219**, 218
- 3.170 Malwick, A.J., 1972, *Appl. Opt.*, **11**(3), 575
- 3.171 Schwesinger, G., 1979, ESO Technical Report No. 9 (March 1979)
- 3.172 Mack, B., 1980, *Appl. Opt.*, **19**(6), 1001
- 3.173 Schwesinger, G., 1988, *J. Mod. Optics*, **35**(7), 1117
- 3.174 Lassell, W., 1842, *Mem. Roy. Astron. Soc.*, **XII**, 265

- 3.175 Bahner, K., 1967, "Teleskope" in "Handbuch der Physik", Vol. XXIX, Springer-Verlag, Heidelberg, 317
- 3.176 Meyer, F., 1930, Z. f. Instrumentenkde., **50**, 58
- 3.177 Hindle, J.H., 1945, in "Amateur Telescope Making", Book 1, A.G. Ingalls ed., Munn & Co., New York, 229
- 3.178 Yoder, P.R., 1986, "Opto-Mechanical Systems Design", Marcel Dekker Inc., Ch. 10, 302
- 3.179 Bowen, I.S., 1960, in "Telescopes", Kuiper and Middlehurst, eds., Univ. of Chicago, 3
- 3.180 Schwesinger, G., 1947, Dissertation "Über günstige Hohlspiegellagerungen hinsichtlich der Schwerewirkung senkrecht zur optischen Achse", Techn. Hochsch. Stuttgart
- 3.181 Schwesinger, G., 1991, J. Mod. Optics, **38**(8), 1507
- 3.182 Schwesinger, G., 1994, Appl. Opt., **33**(7), 1198
- 3.183 Schott Glaswerke Mainz, 1992, Technical Note "ZERODUR – Precision from glass ceramics", Ch. 3, 12
- 3.184 Pearson, J.E., Freeman, R.H., Reynolds, H.C., 1979, Applied Optics and Optical Engineering, Academic Press, New York, Vol. 7, 262
- 3.185 Woolf, N.J., 1984, IAU Colloq. No. 79, Proc. ESO Conf. "Very Large Telescopes, their Instrumentation and Programs", ESO, Garching, 221
- 3.186 Couder, A., 1931, Bulletin Astron., 2me Série, Tome VII, Fasc. VI, 243–245
- 3.187 Maksutov, D.D., 1954, "Technologie der astronomischen Optik", VEB Verlag Technik, Berlin, 74
- 3.188 Schwesinger, G., 1969, Astronomical J., **74**(10), 1243
- 3.189 Franzia, F., Le Luyer, M., Wilson, R.N., 1977, ESO Technical Report No. 8: "The 3.6 m Telescope: The Adjustment and Test on the Sky of the PF Optics with the Gascoigne Plate Correctors"
- 3.190 Wilson, R.N., 1977, Proc. ESO Conf. "Optical Telescopes of the Future", ESO, Geneva, 99
- 3.191 Creedon, J.F., Lindgren, A.G., 1970, Automatica, **6**(5), 643
- 3.192 Howell, W.E., Creedon, J.F., 1973, NASA Technical Note NASA TN D-7090, Jan. 1973
- 3.193 Noethe, L., 1991, J. Mod. Optics, **38**(6), 1043
- 3.194 Robertson, H.J., 1972, NASA Contractor Report NASA CR-2073, June 1972
- 3.195 Meinel, A.B., 1978, Proc. ESO Conf. "Optical Telescopes of the Future", ESO, Geneva, 23
- 3.196 Nelson, J., Mast, T., Chanan, G., 1989, SPIE Conf. "Active Telescope Systems", ed. Roddier, Orlando, SPIE Vol. 1114, 241
- 3.197 Muller, R.A., Buffington, A., 1974, JOSA, **54**, 1200
- 3.198 Chevillard, J.-P., et al., 1977, Appl. Opt., **16**(7), 1817
- 3.199 Connes, P., 1989, SPIE Conf. "Active Telescope Systems", ed. Roddier, Orlando, SPIE Vol. 1114, 238
- 3.200 Wilson, R.N., 1982, Optica Acta, **29**, 985
- 3.201 Wilson, R.N., Noethe, L., 1989, SPIE Conf. "Active Telescope Systems", ed. Roddier, Orlando, SPIE Vol. 1114, 290
- 3.202 Braat, J., 1987, JOSA A, **4**(4), 643
- 3.203 Noethe, L., 1991, J. Mod. Optics, **38**(6), 1043
- 3.204 Noethe, L., et al., 1988, J. Mod. Optics, **35**(9), 1427
- 3.205 Wilson, R.N., Franzia, F., Noethe, L., 1984, Proc. IAU Colloq. No. 79, ESO Conf. "Very Large Telescopes, their Instrumentation and Programs", ESO, Garching, 23
- 3.206 West, R., 1989, "The Messenger", ESO, Garching, No. 56, June 1989, 3

- 3.207 Merkle, F., 1986, VLT Report No. 47
- 3.208 Baldwin, J., et al., 1992, Proc. ESO Conf. "Progress in Telescope and Instrumentation Technologies", ESO, Garching, 247
- 3.209 Schneermann, M., Cui, X., 1988, Proc. ESO Conf. "Very Large Telescopes and their Instrumentation", ESO, Garching, 389
- 3.210 Noethe, L., 1991, ESO Internal VLT Report VLT-TRE-ESO-11120-0-4 (03.06.91)
- 3.211 Schneermann, M., 1987, in "Proposal for the construction of a 16 m VLT", ESO, Garching
- 3.212 Schneermann, M., et al., 1990, Proc. SPIE Conference, Tucson, Vol. 1236, 920
- 3.213 Noethe, L., et al., 1992, Proc. ESO Conf. "Progress in Telescope and Instrumentation Technologies", ESO, Garching, 195
- 3.214 Wilson, R.N., et al., 1993, PASP, **105**, 1175
- 3.215 Tull, R.G., 1984, "Report of the Optical Conference on the 7.6 m Telescope", Smith and Barnes, eds., Univ. of Texas, Publ. in Astronomy No. 22, 307
- 3.216 Noethe, L., 1992, Proc. EOS/SPIE Conf. in Berlin, "Lens and Optical Systems Design", SPIE Vol. 1780, 844
- 3.217 Korhonen, T., Lappalainen, T., 1991, NOT News No. 4, July 1991, 3
- 3.218 Ardeberg, A., Andersen, T., 1991, NOT News No. 4, July 1991, 21
- 3.219 Andersen, T., 1992, private communication
- 3.220 Lemaître, G.R., et al., 1997, Workshop "Science with Liquid Mirror Telescopes", Marseille Observatory, Univ. Aix-Marseille I, April 1997
- 3.221 Lemaître, G.R., 1997, Meccanica, **32**, 1
- 3.222 Iye, M., et al., 1989, Publ. Nat. Astron. Obs. Japan, Vol. 1, 49, 57, 63
- 3.223 Iye, M., 1991, JNLT Technical Report No. 2
- 3.224 Barr, L., 1991, JNLT Technical Report No. 2, in the discussion, 157
- 3.225 Wampler, J., 1992, private communication
- 3.226 Angel, J.R.P., 1983, Technical Bulletin of the McDonald Observatory, Jan./ Feb. 1983, 6
- 3.227 Meng, J.D., Minor, R., Merrick, T., 1989, SPIE Conf. "Active Telescope Systems", ed. Roddier, Orlando, SPIE Vol. 1114, 258
- 3.228 Cuneo, W.J., ed., 1980, "Active Optical Devices and Applications", SPIE Vol. 228
- 3.229 MATRA Espace, 1991, "Lightweight Deformable Mirror", Extension Phase, Phase 1 Report for ESA/ESTEC, Sept. 1991
- 3.230 Gallieni, W., 1992, ADS Report "Active Control of Radio Telescopes: Main Reflectors", ADS Italia, Lecco
- 3.231 Tarchi, D., Comoretto, G., 1990, "Holographic measurement of the Medicina VLBI radio telescope", Arcetri Technical Report No. 16, Firenze, 13.11.90
- 3.232 Ray, F.B., 1991, Proc. SPIE Conf. "Analysis of Optical Structures", SPIE Vol. 1532, 188
- 3.233 Lowne, C.M., 1979, MNRAS, **188**, 249
- 3.234 Stevenson, W.H., 1955, Vistas in Astron., **1**, 473
- 3.235 Murdin, P., Bingham, R.G., 1975, The Observatory, **95**, 180
- 3.236 Gillingham, P., 1978, AAT Progress Report "AAT Dome Seeing", AAT, Epping NSW Australia
- 3.237 Nelson, J.E., 1982, Proc. SPIE Conf. "Advanced Technology Optical Telescopes", SPIE Vol. 332, 109
- 3.238 Racine, R., 1991, PASP, **103**, 1020
- 3.239 Bely, P.-Y., 1987, PASP, **99**, 560

- 3.240 Beckers, J.M., Williams, J.T., 1982, Proc. SPIE Conf. "Advanced Technology Optical Telescopes", SPIE Vol. 332, 16
- 3.241 Meinel, A.B., 1960, "Telescopes", Kuiper and Middlehurst, eds., Univ. Chicago Press, 161
- 3.242 Beckers, J.M., 1992, ESO Memorandum, August 1992
- 3.243 Forbes, F., 1982, Proc. SPIE Conf. "Advanced Technology Optical Telescopes", SPIE Vol. 332, 185
- 3.244 Young, A.T., 1974, Ap. J., **189**, 587
- 3.245 Woolf, N.J., 1982, Proc. SPIE Conf. "Advanced Technology Optical Telescopes", SPIE Vol. 332, 193
- 3.246 Cheng, A.Y.S., Angel, J.R.P., 1986, Proc. SPIE Conf. "Advanced Technology Optical Telescopes III", SPIE Vol. 628, 536
- 3.247 Barr., L.D., et al., 1988, Proc. ESO Conf. "Very Large Telescopes and their Instrumentation", ESO, Garching, 595
- 3.248 Barr., L.D., et al., 1990, Proc. SPIE Conf. "Advanced Technology Optical Telescopes IV", SPIE Vol. 1236, 492
- 3.249 Iye, M., et al., 1991, PASP, **103**, 712
- 3.250 Rayboult, K., 1989, UK Large Telescope Project, Technical Report No. 4, UK Oxford Project Team
- 3.251 Cullum, M.C., 1992, ESO VLT Internal Memoranda, Feb. 1992 and Nov. 1992
- 3.252 Cullum, M.C., 1997, private communication, Oct. 1997
- 3.253 Zago, L., 1992, ESO VLT Technical Report VLT-TRE-ESO-12300-297, August 1992
- 3.254 Zago, L., 1995, Doctoral Thesis "The Effects of the Local Atmospheric Environment on Astronomical Observations", LASEN, Ecole Polytechnique de Lausanne, CH-Lausanne
- 3.255 Ardeberg, A., Erm, T., 1992, NOT News No. 6, Aug. 1992, 23
- 3.256 Iye, M., et al., 1992, PASP, **104**, 760
- 3.257 Forbes, F., Gabor, G., 1982, Proc. SPIE Conf. "Advanced Technology Optical Telescopes", Tucson, SPIE Vol. 332, 198
- 3.258 Goble, L.W., et al., 1992, Proc. ESO Conf. "Progress in Telescope and Instrumentation Technologies", ESO, Garching, 173
- 3.259 NOAO, 1994, brochure "WIYN Observatory", NOAO, Tucson, AZ
- 3.260 Moore, P., 1997, "Eyes on the Universe", Springer, London

## Chapter 4

- 4.1 Airy, G.B., 1835, Trans. Camb. Phil. Soc., **5**, 283
- 4.2 Rayleigh, Lord, 1879, Phil. Mag. (5), **8**, 261
- 4.3 Strehl, K., 1902, Z. f. Instrumentenkunde, **22**, 213
- 4.4 Maréchal, A., 1947, Rev. d'Optique, **26**, 257
- 4.5 Duffieux, P.M., Lansraux, G., 1945, Rev. d'Optique, **24**, 65, 151, 215
- 4.6 Hopkins, H.H., 1955, Proc. Roy. Soc. A, **231**, 91
- 4.7 Franzia, F., LeLuyer, M., Wilson, R.N., 1977, ESO Technical Report No. 8, Oct. 1977
- 4.8 Schwesinger, G., 1969, Astron. J., **74** (10), 1243
- 4.9 Scheffler, H., 1962, Z. Astrophys., **55**, 1
- 4.10 Nelson, J.E., Mast, T.S., 1988, Proc. ESO Conf. "Very Large Telescopes and their Instrumentation", ESO, Garching, Proc. No. 30, 7
- 4.11 Nelson, J.E., Mast, T.S., 1992, Proc. ESO Conf. "Progress in Telescope and Instrumentation Technologies", ESO, Garching, Proc. No. 42, 3
- 4.12 Wilson, R.N., et al., 1992, as [4.11], 199

- 4.13 Wilson, R.N., et al., 1991, *J. Mod. Opt.*, **38**(2), 219  
 4.14 Brown, D.S., 1979, "The Messenger", ESO, **19**, 16  
 4.15 Wetherell, W., 1980, "Applied Optics and Optical Engineering", Vol. 8, Academic Press, New York, 225  
 4.16 Brown, D.S., 1981, Proc. ESO Conf. "Scientific Importance of High Angular Resolution at IR and Optical Wavelengths", ESO, Garching, 181  
 4.17 Dierickx, P., 1992, *J. Mod. Opt.*, **39**(3), 569  
 4.18 Maréchal, A., Françon, M., 1960, "Diffraction: Structures des Images", Editions Rev. d'Opt., Paris, 137  
 4.19 Mahajan, V.N., 1978, *Appl. Opt.*, **17**, 3329  
 4.20 Dierickx, P., 1991, "Optical Quality Budget of the VLT", ESO Doc. VLT-tre-eso-02210-XXX, 24.09.91  
 4.21 Dierickx, P., 1992, ESO Tech. Note VLT-TEL-92/0200, 30.07.92  
 4.22 Myashita, A., Ando, H., 1991, JNLT Subaru Technical Report No. 13, Dec. 1991  
 4.23 Subaru Project Office, 1991, Brochure of the 8 m Subaru telescope, Tokyo, Oct. 1991  
 4.24 Herschel, W., 1800, *Phil. Trans. Roy. Soc.*, **90**, 49  
 4.25 Wilson, R.N., et al., 1984, Proc. IAU Colloq. No. 79 "Very Large Telescopes, their Instrumentation and Programs", ESO, Garching, 119

## Chapter 5

- 5.1 Schaifers, K., 1967, "Meyers Handbuch über das Weltall", Bibliogr. Institut, Mannheim, 159  
 5.2 Sarazin, M., 1992, "Update of environmental conditions at ESO Observatories", ESO VLT report VLT.TRE.ESO.17400  
 5.3 Mahan, A.I., 1962, *Appl. Opt.*, **1** (4), 497  
 5.4 Barlow, C.W.C., Bryan, G.H., 1944, "Elementary Mathematical Astronomy", Univ. Tutorial Press, London, 112  
 5.5 Kolmogorov, A.N., 1941, *Doklady Akad. Nauk SSSR*, **30**, 301 and **32**, 16 (German translation in "Sammelband zur statistischen Theorie der Turbulenz", Akademie-Verlag, Berlin, 1958, 71 and 77)  
 5.6 Obukhov, A.M., 1941, *Doklady Akad. Nauk SSSR*, **32**, 19  
 5.7 Khinchin, A.Y., 1938, *Uspekhi Mat. Nauk*, No. 5  
 5.8 Tatarski, V.I., 1961, "Wave Propagation in a Turbulent Medium", Dover, New York  
 5.9 Hufnagel, R.E., Stanley, N.R., 1964, *JOSA*, **54**, 52  
 5.10 Fried, D.L., Cloud, J.D., 1964, *JOSA*, **54**, 574A  
 5.11 Fried, D.L., 1965, Conf. "Atmos. Limitations to Optical Propagation", US Nat. Bur. Standards CRPL, March 1965  
 5.12 Fried, D.L., 1965, *JOSA*, **55** (11), 1427  
 5.13 Fried, D.L., 1966, *JOSA*, **56** (10), 1372  
 5.14 Fried, D.L., Mevers, G.E., 1974, *Appl. Opt.*, **13** (11), 2620 (Erratum: *Appl. Opt.*, **14** (11), 2567)  
 5.15 Fried, D.L., 1978, *JOSA*, **68** (12), 1651  
 5.16 Roddier, F., 1981, "Progress in Optics", Vol. XIX, 281  
 5.17 Obukhov, A.M., 1949, *Izv. Akad. Nauk SSSR, Ser. Geograf. Geofiz.*, **13**, 58 (German translation as in [5.5], 127)  
 5.18 Yaglom, A.M., 1949, *Doklady Akad. Nauk SSSR*, **69**, 743 (German translation as in [5.5], 141)  
 5.19 Lee, R.W., Harp, J.C., 1969, *Proc. I.E.E.E.*, **57**, 375  
 5.20 Lutomirski, R.F., Yura, H.T., 1971, *JOSA*, **61**, 482

- 5.21 Valley, G.C., 1979, *Appl. Opt.*, **18**, 984
- 5.22 O'Neill, E.L., 1963, "Introduction to Statistical Optics", Wesley Publ. Co., Reading, Mass., 88 and 106
- 5.23 Boyd, R.W., 1978, *JOSA*, **68**, 877
- 5.24 Selby, M.J., et al., 1979, *MNRAS*, **187**, 553
- 5.25 Young, A.T., 1974, *Astrophys. J.*, **189**, 587
- 5.26 Krasilnikov, V.A., 1949, *Doklady Akad. Nauk SSSR*, **65**, 291
- 5.27 Kadiri, S., 1979, Thèse de 3e. cycle, University of Nice
- 5.28 King, J.R., 1971, *PASP*, **83**, 199
- 5.29 Dierickx, P., 1992, *J. Mod. Optics*, **39** (3), 569
- 5.30 Tatarski, V.I., 1971, "The Effects of the Turbulent Atmosphere on Wave Propagation", English Translation, Jerusalem, 289
- 5.31 Hufnagel, R.E., 1966, "Restoration of atmospherically degraded images", *Nat. Acad. Sci.*, Washington, 11
- 5.32 Stock, J., Keller, G., 1960, "Stars and Stellar Systems", Vol. 1, "Telescopes", eds. Kuiper and Middlehurst, Chicago Univ. Press, 138
- 5.33 Sarazin, M., 1992, Thèse de Doctorat "Caractérisation des Propriétés Optiques de la Turbulence Atmosphérique", Univ. d'Aix-Marseille III
- 5.34 Sarazin, M., 1986, Proc. SPIE Conf. "Advanced Technology Optical Telescopes III", SPIE Vol. 628, 138
- 5.35 Sarazin, M., 1987, "The Messenger", ESO, **49**, 37
- 5.36 Pedersen, H., Rigaut, F., Sarazin, M., 1988, "The Messenger", ESO, **53**, 8
- 5.37 Sarazin, M., Roddier, F., 1990, *Astron. Astrophys.*, **227**, 294
- 5.38 Roddier, C., 1976, *JOSA*, **66**, 478
- 5.39 Woolf, N.J., 1984, IAU Colloq. No. 79, Proc. ESO Conf. "Very Large Telescopes, their Instrumentation and Programs", ESO, Garching, 221
- 5.40 Wilson, R.N., Franzia, F., Noethe, L., 1987, *J. Mod. Optics*, **34** (4), 485
- 5.41 Babcock, H.W., 1953, *PASP*, **65**, 229
- 5.42 Maréchal, A., Françon, M., 1960, "Diffraction: Structure des Images", Ed. Rev. d'Opt., Paris, 152
- 5.43 Fried, D.L., 1982, *JOSA*, **72**(1), 52
- 5.44 Merkle, F., 1986, "Adaptive Optics for ESO's VLT Project", VLT Report No. 47
- 5.45 Roddier, F., 1981, Proc. ESO Conf. "Scientific Importance of High Angular Resolution at IR and Optical Wavelengths", ESO, Garching, 5
- 5.46 Fried, D.L., 1979, *Optica Acta*, **26** (5), 597
- 5.47 Loos, G.C., Hogge, C.B., 1979, *Appl. Opt.*, **18** (15), 2655
- 5.48 Buffington, A., et al., 1977, *JOSA*, **67** (3), 298 and 304
- 5.49 Hardy, J.H., 1982, Proc. SPIE Conf. "Advanced Technology Optical Telescopes", Tucson, SPIE Vol. 332, 252
- 5.50 Merkle, F., 1988, Proc. ESO Conf. "Very Large Telescopes and their Instrumentation", ESO, Garching, 639
- 5.51 Wang, J.Y., 1977, *JOSA*, **67** (3), 387
- 5.52 Noll, R.J., 1976, *JOSA*, **66**(3), 207
- 5.53 Wang, J.Y., Markey, J.K., 1978, *JOSA*, **68**(1), 78
- 5.54 Kern, P., et al., 1988, as [5.50], 657
- 5.55 Gaffard, J.P., 1988, as [5.50], 729
- 5.56 Maaswinkel, F., et al., 1988, as [5.50], 751
- 5.57 Greenwood, D.P., Fried, D.L., 1976, *JOSA*, **66**(3), 193
- 5.58 Greenwood, D.P., 1979, *JOSA*, **69**(4), 549
- 5.59 Parenti, R.R., Sasiela, R.J., 1992, Proc. ESO Conf. "Progress in Telescope and Instrumentation Technologies", ESO, Garching, 419
- 5.60 Foy, R., Labeyrie, A., 1985, *Astron. Astrophys.*, **152**, L 29

- 5.61 Merkle, F., 1992, Proc. ESO Conf. "Progress in Telescope and Instrumentation Technologies", ESO, Garching, 461
- 5.62 Rigaut, F., et al., 1991, Astron. Astrophys., **250**, 280
- 5.63 Merkle, F., 1991, Physik in unserer Zeit, **22** (6), 260
- 5.64 Rigaut, F., et al., 1992, as [5.61], 399
- 5.65 Rousset, G., et al., 1992, as [5.61], 403
- 5.66 Fugate, R.Q., 1992, as [5.61], 407
- 5.67 Ellerbroek, B.L., 1992, as [5.61], 411
- 5.68 Ellerbroek, B.L., et al., 1992, SPIE and EOS Int. Symposium "Optical Systems Design", Berlin, Sept. 1992
- 5.69 Roddier, F., et al., 1991, PASP, **103**, 131
- 5.70 Rigaut, F., Gendron, E., 1992, LGSAO Workshop, Albuquerque, 582
- 5.71 Beckers, J.M., 1992, as [5.61], 505
- 5.72 Roddier, F., 1992, SPIE Working Group Letter on Adaptive Optics, Inaugural Issue June 1992, 1
- 5.73 Schnur, G., et al., 1992, Proc. ESA Colloquium "Targets for Space-based Interferometry", Beaulieu, France (ESA SP-354 Dec. 1992)
- 5.74 Dayton, L., 1991, New Scientist 20 April 1991, 24
- 5.75 Beckers, J.M., et al., 1989, "The VLT Interferometer Implementation Plan", VLT Report No. 59b, Ch. 3
- 5.76 Mariotti, J.M., 1992, "Coherent Combined Instrumentation for the VLTI", VLT Report No. 65, Ch. 3
- 5.77 Weigelt, G., 1982, as [5.49], 284
- 5.78 Weigelt, G., 1984, as [5.39], 337
- 5.79 Labeyrie, A., 1970, Astron. Astrophys., **6**, 85
- 5.80 Dainty, J.C., 1975, in "Laser Speckle and Related Phenomena", Topics in Appl. Physics, ed. J.C. Dainty, Springer-Verlag, Berlin, 255
- 5.81 Dainty, J.C., 1974, MNRAS, **169**, 631

## Chapter 6

- 6.1 Riekher, R., 1990, "Fernrohre und ihre Meister", Verlag Technik, Berlin, 223–224
- 6.2 Jamin, J., 1848, Ann. Chim. Phys., **22**, 311
- 6.3 King, H.C., 1955, "The History of the Telescope", Griffin, London, 270 et seq.
- 6.4 Ingalls, A.G., 1945, "Amateur Telescope Making", 4th ed., Munn and Co., New York, 157 and 397
- 6.5 Brashear, J., 1880, English Mechanic, **31**, 327
- 6.6 Hass, G., 1965, "Applied Optics and Optical Engineering", ed. Kingslake, Academic Press, New York, Vol. III, 309
- 6.7 Pohl, R., Pringsheim, P., 1912, Verh. deutsche physik. Ges., **14**, 506
- 6.8 Strong, J., 1933, Phys. Rev., **43**, 498
- 6.9 Strong, J., 1936, Astrophys. J., **83**, 401
- 6.10 Holland, L., 1970, "Vacuum Deposition of Thin Films", Chapman and Hall, London, Chap. 11
- 6.11 Hass, G., Turner, A.F., 1959, "Methods of Experimental Physics", Lark-Horowitz and Johnsons, eds., Vol. 6, Part A, Acad. Press, New York, Chaps. 2 and 5
- 6.12 Bennett, H.E., Silver, M., Ashley, E.J., 1963, JOSA, **53**, 1089
- 6.13 Bennett, J.M., Ashley, E.J., 1965, Appl. Opt., **4**, 221
- 6.14 Jacobson, M.R., et al., 1992, Gemini Project Investigation of Low Emissivity Durable Coatings, Optical Data Associates, Tucson

- 6.15 Musikant, S., 1985, "Optical Materials: An Introduction to Selection and Application", Dekker, New York
- 6.16 Driscoll, W.G., Vaughan, W., eds., 1978, "Handbook of Optics", McGraw-Hill, New York
- 6.17 Born, M., Wolf, E., 1964, "Principles of Optics", 2nd Ed., Pergamon Press, Oxford, 615
- 6.18 Jenkins, F.A., White, H.E., 1937, "Fundamentals of Physical Optics", McGraw-Hill, New York, 401
- 6.19 Decker, D.L., Stanford, J.L., 1971, JOSA, **61**, 679A
- 6.20 Hagen, E., Rubens, H., 1903, Ann. d. Physik, **11**(4), 873
- 6.21 Gilliotte, A., 1991, La Silla contribution in Proc. ESO Workshop on "Coating and Cleaning Large Mirrors" (Manuscript ed. M. Grössl), ESO, Garching
- 6.22 Wilson, R.N., 1994, "Karl Schwarzschild Lecture of the German Astronomical Society", Bochum, 1993, Reviews in Modern Astronomy, **7**, 1
- 6.23 Greco, V., et al., 1993, Astron. Astrophys., **277**, 345
- 6.24 Turner, A.F., 1946, JOSA, **36**, 711
- 6.25 Messner, R., 1947, Optik, **2**, 228
- 6.26 Browning, S.D., et al., 1982, Proc. SPIE Conference "Advanced Technology Optical Telescopes", Tucson, SPIE Vol. 332, 310
- 6.27 Song, D.Y., Macleod, H.A., 1985, SPIE Proc. Vol. 540, 156
- 6.28 Mountain, M., Gillett, F., Kurz, R., 1997, Proc. Lund/ESO/SPIE Conf. "Optical Telescopes of Today and Tomorrow", Landskrona, SPIE Vol. 2871, 15
- 6.29 Gillett, F., 1997, private communication by telephone, November 1997
- 6.30 Jacobson, M.R., et al., 1998, contribution "Development of the silver coatings options for the Gemini 8 m telescope project" to the SPIE Conf. "Astronomical Telescopes and Instrumentation", Kona, Hawaii, 20–28 March 1998
- 6.31 Grössl, M., 1991, as [6.21], contribution "ESO VLT"
- 6.32 Schmidt-Kaler, T., 1994, Astron. Nachr., **315**(4), 323
- 6.33 Giordano, P., 1992, ESO VLT Internal Memorandum 92/0100, 30.03.92
- 6.34 Kozicki, M., et al., 1991, "Cleanrooms: Facilities and Practices", Van Nostrand Reinhold, New York
- 6.35 Hoenig, S.A., 1986, Compressed Air Magazine, Aug. 1986, 22
- 6.36 Zito, R.R., 1990, Proc. SPIE Conf. "Advanced Technology Optical Telescopes IV", SPIE Vol. 1236, Part 2, 952
- 6.37 Bennett, J.M., et al., 1989, Appl. Opt., **28**(5), 1018
- 6.38 Giordano, P., 1991, as [6.21], contribution "Cleaning mirrors *in situ* in telescopes"
- 6.39 Giordano, P., 1992, VLT Doc. VLT-TRE-ESO-11942-0286, 03.08.92
- 6.40 Giordano, P., 1992, VLT Doc. VLT-TRE-ESO-11942-0301, 03.09.92
- 6.41 Giordano, P., 1992, VLT Doc. GEN-TEL-92/0274, 04.11.92
- 6.42 Dierickx, P., Giordano, P., 1991, VLT Doc. VLT-TRE-ESO-11942-05, 18.06.91
- 6.43 Giordano, P., 1993, VLT Doc. VLT-TRE-ESO-11942-0386, 03.02.93
- 6.44 Balick, B., 1992, "UV Laser Cleaning of Astronomical Telescopes", Univ. of Washington and STI Optronics
- 6.45 Rayboult, K., 1991, as [6.21], contribution of the Gemini project
- 6.46 Giordano, P., 1993, private communication
- 6.47 Laser-Laboratorium Göttingen e.V., 1994, Final Report "Feasibility Study for the UV Laser Cleaning of VLT Mirrors", commissioned by ESO, Garching

- 6.48 Giordano, P., 1997, Proc. Lund/ESO/SPIE Conf. "Optical Telescopes of Today and Tomorrow", Landskrona, SPIE Vol. 2871, 416
- 6.49 Giordano, P., 1997, "Operational Strategy in the Research of Cleaning Techniques for the VLT Mirrors", VLT Doc. VLT-TRE-ESO-11941-1533, 19.11.97, contribution presented at the Conf. "Mirror Coatings and Cleaning", Waikaloa, Hawaii, Nov. 1997

## Chapter 7

- 7.1 Wallace, P.T., 1978, Proc. ESO Conf. "Optical Telescopes of the Future", ESO, Geneva, 123
- 7.2 Franz, F., 1988, ESO internal document 1779 T (08.06.88) "The NTT Adapter/Rotator"
- 7.3 Allen, C.W., 1973, "Astrophysical Quantities", Athlone Press, London, 243
- 7.4 West, R.M., 1989, The Messenger, ESO, No. 56 (June 1989), 6
- 7.5 Beckers, J.M., 1986, Proc. Conf. "Advanced Technology Optical Telescopes III", SPIE Vol. 628, 255
- 7.6 Weaver, L.D., et al., 1988, Opt. Engineering, **27** (9), 730
- 7.7 Meinel, A.B., 1970, Appl. Opt., **9**, 2501
- 7.8 Beckers, J.M., 1989, VLT-IFP R & D Note 89-3
- 7.9 Richardson, H.E., 1987, Sci.Am., **257**(5), Nov. 1987, 40
- 7.10 Richardson, H.E., 1992 and 1996, private communications
- 7.11 Labeyrie, A., 1980, Proc. Conf. "Optical and IR Telescopes for the 1990s", Vol. II, KPNO, Tucson, 786
- 7.12 Babcock, H.W., 1985, Appl. Opt., **24**(9), 1248
- 7.13 Babcock, H.W., 1988, Proc. Conf. "Very Large Telescopes and their Instrumentation", ESO, Garching, Vol. I, 99 (also updated manuscript dated 21 August 1989)
- 7.14 Danjon, A., Couder, A., 1935, "Lunettes et Télescopes", reprinted 1983, Blanchard, Paris, 310
- 7.15 Schmidt, H., 1988, Feinwerk. u. Messtechnik, **96**(1/2), 19
- 7.16 Bouwers, A., 1946, "Achievements in Optics", Elsevier, Amsterdam, 54
- 7.17 Sauer, F., 1966, Sterne u. Weltraum, **4**, 141
- 7.18 Young, A.T., 1967, Appl. Opt., **6**(6), 1063
- 7.19 Prescott, R., 1968, Appl. Opt., **7**(3), 479
- 7.20 Bergener, D.W., et al., 1984, Proc. Conf. "Stray Radiation IV", SPIE Vol. 511, 65
- 7.21 Pompea, S.M., et al., 1992, Proc. Conf. "Stray Radiation in Optical Systems II", ed. R.P. Breault, SPIE Vol. 1753, 172
- 7.22 Bowen, I.S., Vaughan, A.H., 1973, Appl. Opt., **12**, 1430
- 7.23 Pompea, S.M., McCall, S.H.C.P., 1992, as [7.21], 92
- 7.24 McCall, S.H.C.P., et al., 1992, as [7.21], 158
- 7.25 Pompea, S.M., et al., 1984, Opt. Engineering, **23**(2), 149
- 7.26 Pompea, S.M., 1997, Proc. Lund/ESO/SPIE Conf. "Optical Telescopes of Today and Tomorrow", Landskrona, SPIE Vol. 2871, 193

## Chapter 8

- 8.1 Lubbock, C.A., 1933, "The Herschel Chronicle", Cambridge
- 8.2 Hyde, W.L., 1987, Optics News, Jan. 1987, 6
- 8.3 Osterbrock, D.E., 1984, "James E. Keeler: Pioneer American Astrophysicist", Cambridge

- 8.4 Osterbrock, D.E., 1993, "Pauper & Prince: Ritchey, Hale, & Big American Telescopes", Univ. of Arizona Press, Tucson
- 8.5 California Association for Research in Astronomy, 1997, Brochure "W.M. Keck Observatory"
- 8.6 Wilson, R.N., et al., 1992, Proc. Conf. "Progress in Telescope and Instrumentation Technologies", ed. M.-H. Ulrich, ESO, Garching, 199

# List of figures

## Chapter 1

1.1	Perkin-Elmer CCP head unit (Jones [1.17]) .....	5
1.2	Epicyclic tool configurations for Perkin-Elmer CCP (Jones [1.17]) .....	6
1.3	Figuring with the Perkin-Elmer CCP on a 1.8 m diameter lightweighted spherical f/1.5 mirror (Jones [1.19]) .....	7
1.4	Interferograms of a 1.8 m lightweighted spherical f/1.5 mirror, (a) initially, (b) after 72 hours of polishing with the Perkin-Elmer CCP (Jones [1.19]) .....	8
1.5	Segment improved using the Perkin-Elmer CCP (Jones [1.21]). The figure shows virtually no deviation at the edge .....	8
1.6	Computer Controlled Surfacing Technique (CCST) at REOSC [1.25] for mirrors up to 2 m diameter .....	9
1.7	CCST at REOSC [1.25] with a 60 cm test mirror. (a) The initial state, (b) after 7 polishing runs, (c) after a further 7 polishing runs .....	10
1.8	Petal tool for aspherizing by grinding or polishing considered by Carl Zeiss [1.27] for the ESO VLT 8.2 m primaries .....	11
1.9	Operations for a CCOS cycle (Litton ITEK [1.31]) .....	12
1.10	A block diagram showing key components of the “proportional option” CCOS algorithm (Litton ITEK [1.31]) .....	13
1.11	Arboga NC unit usable for CCOS and machining operations (Litton ITEK [1.31]) .....	13
1.12	Interferograms for a lightweight test piece after conventional and vacuum induced force surfacing (Litton ITEK [1.31]) .....	14
1.13	Gain in total machine time using microgrinding with CCOS (Litton ITEK [1.30]) .....	14
1.14	The principle of membrane polishing (Carl Zeiss [1.10] [1.33]) .....	15
1.15	Rectangular (strip) membrane tool for working axisymmetrical surfaces, e.g. primary mirrors (Carl Zeiss [1.10]) .....	16
1.16	Lapping of the ESO NTT 3.5 m primary (f/2.2) with two rectangular tools at Carl Zeiss in 1986 [1.10] [1.34] .....	17
1.17	Computer controlled figuring of a 60 cm test mirror (Korhonen and Lappalainen [1.35]) .....	18

1.18 Stressed-Lap Polishing Machine at Steward Obs. Mirror Lab (Martin et al. [1.40]) . . . . .	21
1.19 Schematic demonstration of avoiding lap mismatch through overhang by stressing a full-size lap with a coma term as well as spherical aberration. (a) Lap centered over workpiece, (b) decentered with supplementary comatic distortion, (c) the generated aspheric surface (Wizinowich and Angel [1.41]) . . . . .	22
1.20 Final interferogram of the Vatican (Lennon) 1.8 m, $f/1.0$ primary produced by stressed-lap technology (Steward Obs. Mirror Lab [1.43]) . . . . .	22
1.21 Principle of the dioptric elasticity method of stress polishing for the production of Schmidt plates proposed by Lemaître [1.47] . . . . .	25
1.22 Fringes of equal thickness of a plate made by the dioptric elastic (stress polishing) method (Lemaître [1.47]) . . . . .	26
1.23 Mirror forms for stressed polishing with constant thickness distribution (CTD) and variable thickness distributions (VTD) (Lemaître [1.49]) . . . . .	27
1.24 Coefficients describing deflections needed to transform a sphere into an off-axis parabola (segments with $a = 0.7\text{ m}$ , $r_0 = 40\text{ m}$ ). Best fitting sphere assumed. (Lubliner and Nelson [1.39]) . . . . .	29
1.25 Reconstructed interferograms of stress polishing on a 36 cm circular, off-axis segment of a paraboloid. (a) Original spherical mirror under stress before polishing ( $9.9\text{ }\mu\text{m rms}$ ); (b) Final result relative to the paraboloid with best fit position ( $0.03\text{ }\mu\text{m rms}$ ). The lower contour plots were generated from a fourth-order fit. (Nelson et al. [1.50]) . . . . .	30
1.26 Schematic of Kodak's ion figuring system [1.60] . . . . .	34
1.27 An interior view of Kodak's Ion Figuring Chamber showing preparation for the IBF of a 1.3 m workpiece (courtesy T.J. Wilson and the Eastman Kodak Company) . . . . .	35
1.28 Ion Beam Figuring at Kodak of one of the Keck primary mirror segments (courtesy T.J. Wilson and the Eastman Kodak Company) . . . . .	36
1.29 Ion Beam Figuring at Kodak of an off-axis, aspheric petal to a surface figure better than $0.01\text{ }\mu\text{m rms}$ in four iterations (courtesy T.J. Wilson and the Eastman Kodak Company) . . . . .	36
1.30 Pneumatic support for the figuring of the VLT 8.2 m primaries (courtesy REOSC, Works photo) . . . . .	38
1.31 Newly built (April 1992) optical production facility of REOSC for the ESO VLT 8.2 m primary mirrors (courtesy REOSC, Works photo) . . . . .	38

1.32 (a) The Computer Controlled Milling Machine (CCMM) installed at REOSC with one of the 8.2 m VLT primary mirror blanks mounted on the turntable. The relative thinness of the blank (175 mm, AR = 47) is noteworthy. (Courtesy REOSC, Works photo). (b) Another view during the grinding operation . . . . .	40
1.33 "Equal wear" petal-lap polishing form with possible modification (full lines) for zonal work on the ESO 8.2 m primaries at REOSC [1.25] . . . . .	41
1.34 A test operation being performed on one of the VLT primaries (courtesy REOSC, Works photo) . . . . .	42
1.35 Synthetic interferogram of the finished VLT primary #2 in the active mode (Intrinsic Quality) (Dierickx et al. [1.67]) . . . . .	43
1.36 Wavefront aberration (rms) generated by polishing pressure for 8 m mirrors with aspect ratios 20, 40 and 80 (Carl Zeiss [1.27]) . . . . .	44
1.37 Interferogram of the final figure of the 3.5 m, f/2.2 primary of the Galileo telescope: (a) before active correction, (b) after active correction (Carl Zeiss [1.73]) . . . . .	45
1.38 Schematic arrangement of a Fizeau interferometer using a lens collimator (after Malacara [1.74]) . . . . .	47
1.39 Fizeau interferometer without collimator for curved surfaces (after Malacara [1.74]) . . . . .	48
1.40 Simple arrangement for seeing Haidinger fringes with a quasi-parallel glass plate (after Malacara [1.74]) . . . . .	48
1.41 The basic form (equal path) of a Twyman-Green interferometer: (a) testing a plane mirror, (b) camera objective test arrangement .	49
1.42 Twyman-Green interferometer without a collimator (Williams type) (after Malacara [1.74]) . . . . .	49
1.43 Interference patterns for standard aberrations (after Malacara [1.74] and Kingslake [1.83] [1.84]) . . . . .	52
1.44 Basic version of LUPI designed by Houston et al. [1.74] [1.86] . . . . .	54
1.45 Set-up for testing parabolic telescope primaries with double-pass in autocollimation against a plane mirror (courtesy H. Kaufmann [1.11]) . . . . .	56
1.46 Phase and amplitude extraction in the direct phase detecting system of Ichioka and Inuiya [1.95]. The spectrum of the signal $S(t)$ or $C(t)$ is shown . . . . .	58
1.47 Separated Fourier spectra of a non-contour (i.e. tilted) type of fringe pattern. The $y$ -axis is perpendicular to the paper. (After Takeda et al. [1.96]) . . . . .	60
1.48 Layout of the Simultaneous Phase Shift Interferometer (SPSI). From Koliopoulos [1.112] . . . . .	67
1.49 Schematic of the test set-up at Carl Zeiss, Oberkochen, for large optics, including active vibration stabilization (from Küchel and Heynacher [1.115]) . . . . .	69

1.50 Interferogram evaluation with the Carl Zeiss DMI method. (a) Typical interferogram showing ring ghost reflection from the Offner-type null system. (b) Phase map modulo $2\pi$ . (c) Unwrapped phase map, showing astigmatism. (d) Phase gradients in the $x$ -direction. (From Küchel [1.116]) . . . . .	71
1.51 The Carl Zeiss DMI system: fringe scanning with tilt fringes at 45° to the pixel raster (after Küchel [1.117]) . . . . .	72
1.52 The Carl Zeiss DMI system in function. Reproduced from a Carl Zeiss brochure “Laser Interferometer DIRECT 100” (1991) (courtesy Carl Zeiss) . . . . .	73
1.53 Effect of testing a strongly aspheric concave mirror at its center of curvature without a null system . . . . .	76
1.54 Two ways of building a null system into a LUPI interferometer: (a) using an aberration-free diverger and a separate null system, (b) a combined diverger-null system . . . . .	77
1.55 Roughly afocal, 2-lens compensator used by Couder [1.123] in single pass for testing a paraboloid with the Foucault test (after Offner [1.122]) . . . . .	78
1.56 Double-pass lens compensator design by Ross [1.126] for testing the 5 m, f/3.3 Palomar primary (after Offner [1.122]) . . . . .	78
1.57 Single-pass plano-convex lens compensator due to Dall [1.122] [1.127] [1.128] . . . . .	79
1.58 Original principle of the Offner compensator using a field lens [1.131] [1.122] . . . . .	81
1.59 Effective function of a refracting Offner compensator, in which the “field lens” controls the higher order spherical aberration . . . . .	82
1.60 Single mirror Offner-type compensator [1.122] . . . . .	83
1.61 2-mirror Offner compensator [1.122] . . . . .	83
1.62 Technique for independently testing a null system. A computer-generated hologram (CGH), placed at the paraxial center of curvature, mimics the function of the primary (or test) mirror. (After Martin et al. [1.139]) . . . . .	85
1.63 The pentaprism test for spherical aberration (schematic) [1.146] [1.141] . . . . .	88
1.64 Test method using double reflection at primary [1.141] [1.130] . . . . .	90
1.65 Autocollimation test against the primary using a weak convex lens in front of the secondary . . . . .	91
1.66 The Lytle test [1.148] [1.141] [1.149] . . . . .	91
1.67 Test by a refraction through the secondary as a plano-convex Cartesian lens [1.141] [1.142] . . . . .	92
1.68 Test by reflection through the back surface due to Schmadel [1.152] . . . . .	93
1.69 The Hindle sphere test for secondaries [1.154] [1.155] . . . . .	95
1.70 The inverse Hindle test for concave hyperboloids: the Silvertooth test [1.156] . . . . .	96

1.71 The transmission meniscus Hindle sphere [1.141] [1.122] [1.160] ...	97
1.72 Matrix interference test for secondaries as used at Carl Zeiss [1.141] .....	98
1.73 Auxiliary convex lens in front of the secondary [1.141] .....	98
1.74 Richardson test [1.141] [1.161] .....	99
1.75 The Common-Ritchey test for plane mirrors [1.163] [1.164] [1.165] ...	101
1.76 Astigmatism due to a concave mirror imaging a parallel beam ...	102
1.77 General arrangement for testing afocal or quasi-afocal correctors in autocollimation against a spherical concave reference mirror ...	103

## Chapter 2

2.1 Combination of (a) field coma, growing linearly with the field radius, and (b) decentering coma, constant over the field .....	112
2.2 (a) "Pure" lateral decenter, (b) Coma-free Schießspiegler (CFS) (after Wilson and Delabre [2.3]) .....	113
2.3 Nature of the <i>binodal</i> decentering astigmatism function (after Shack and Thompson [2.5]) .....	115
2.4 Pointing correction necessitated by the coma-free Schießspiegler (CFS) (after Wilson and Delabre [2.3]) .....	121
2.5 Alignment of a Cassegrain telescope .....	123
2.6 The function of the pentaprism, an essential tool in telescope alignment .....	125
2.7 Foucaultgram of the MPIA 2.2 m telescope II after set-up at La Silla in 1983. This picture was obtained on a 6×6 cm photographic plate with 1 m exposure .....	133
2.8 Appearance of "pupil plates" showing geometrical adjustment error and the three basic third order aberrations [2.14] .....	135
2.9 Evaluation of the coma vector from a pupil plate [2.14] .....	137
2.10 Geometry of the coma patch with central obstruction [2.14] .....	137
2.11 Measurement of astigmatism from pupil plates [2.14] .....	139
2.12 Deduction of the third order spherical aberration coefficient from the relative obstruction ratio of intra- and extrafocal pupil plates [2.14] .....	141
2.13 Typical pupil plates, taken on one side of the focus with the 1.54 m Danish telescope at La Silla for the final centering. The negligible coma change on inclining the telescope showed the excellent mechanical centering stability of this telescope. Original image plate diameter ca. 2.5 mm .....	142
2.14 Extrafocal pupil plates taken in 1980 for the ESO 1 m telescope at La Silla showing ( <i>left</i> ) a "dent" at the top due to screw pressure on the edge of the secondary and ( <i>right</i> ) its correction by relaxing the pressure. The two figures at the right show schematically such an effect both extra- and intrafocally. The original pupil plate diameter was 3.5 mm .....	143

2.15 Geometry of the classical axisymmetrical Hartmann test (after Bahner [2.16]) . . . . .	144
2.16 The generalised Hartmann test for individual rays measured in 2 dimensions (after Bahner [2.16]) . . . . .	146
2.17 Contour map at intervals of $0.2\lambda$ , showing the surface of the 3 m Lick primary after correction of astigmatism on 3 January 1959 ( $\lambda = 500$ nm) (after Bahner [2.16]) . . . . .	147
2.18 Hartmann tests of the ESO 3.6 m telescope after set-up in 1976 at the prime focus with the Gascoigne plate correctors showing the effect of theoretical removal of the polynomial terms indicated (after Franza et al. [2.24]) . . . . .	149
2.19 Geometrical energy concentration of the image at best focus near zenith of the ESO 3.6 m telescope with the “red” Gascoigne plate and 10 mm filter glass. The specification required 75 % geometrical energy concentration within 0.4 arcsec for the primary alone. (After Franza et al. [2.24]) . . . . .	150
2.20 Construction (schematic) of basic Shack-Hartmann telescope test device for use with photographic plates or CCD detector (after Wilson et al. [2.27]) . . . . .	151
2.21 Typical S-H test plate exposed at the MPIA 2.2 m telescope II in 1983. The raster corresponding to the telescope image shows the form of the pupil of the telescope. The general raster comes from the reference source. (After Wilson et al. [2.27]) . . . . .	152
2.22 Image profile of the MPIA 2.2 m telescope II after set-up in October 1983 as given by the test S-H plate taken near the zenith, in comparison with the specification (from Wilson et al. [2.27]) . . . . .	156
2.23 Simplified S-H test arrangement as intended for the 8 m unit telescopes of the ESO VLT [2.30] . . . . .	157
2.24 The ESO off-line S-H test device ANTARES I, constructed in 1978 for use with photographic plates [2.31] . . . . .	158
2.25 Optical layout of the ESO general purpose off-line test device ANTARES II (1987), for use with a CCD detector. The figure shows the (switchable) optics for an f/11 telescope output beam [2.31] . . . . .	159
2.26 (a) Group of spots produced by a Hartmann plate in the classical way. (b) Interference effect produced by the same group of spots if the plate is exposed much nearer the image giving partial overlap and interference between spots. (After Korhonen [2.32]) . . . . .	160
2.27 Pupil plates showing strong “ripple” taken in 1979 at the ESO 50 cm telescope. The plates were taken with various exposures to reveal the zones, at the left intrafocally, at the right extrafocally. Original plate diameters 3.5 mm ( <i>left</i> ) and 2.8 mm ( <i>right</i> ). At this stage, the telescope still had 1.3 arcsec of decentering coma . . . . .	161

2.28 Curvature measurement following Roddier et al. [2.41] for testing telescopes .....	163
2.29 Contour plot of the reconstructed wavefront from curvature sensing of the primary of the 88-inch University of Hawaii telescope in April 1989 after removal of low spatial frequency terms. Increment 0.025 μm, dotted line positive, dashed line negative. (From Roddier et al. [2.41]) .....	164

## Chapter 3

3.1 The evolution of primary f/no in reflecting telescopes and its effect on their appearance. From top to bottom and left to right as in Table 3.1 [3.1] .....	170
3.2 The evolution of primary f/no in reflecting telescopes as a function of time [3.1] .....	171
3.3 “Sweep circles”, determining the enclosure size, for the ESO 3.6 m equatorial and the NTT 3.5 m alt-az telescopes [3.1] .....	171
3.4 The flexure-mass problem of classical mirror blanks and the solution through <i>segmentation</i> [3.1] .....	173
3.5 The “Rotating Shoe” concept for a large telescope due to Mertz [3.12]. Figure reproduced from Barr [3.14] as a proposal for the NGT .....	177
3.6 The 8 m Penn State Spectroscopic Survey Telescope (PSSST) project with an “Optical Arecibo” concept using a stationary, inclined, tessellated primary with azimuth rotation (from Ramsey et al. [3.15]) .....	178
3.7 A corrector design for the ELT similar to that for the HET. Mirrors $M_2$ , $M_3$ and $M_4$ are conic sections, while $M_5$ has higher order departures from the conic (after Bash et al. [3.19]) .....	179
3.8 Hexagonal segments (36) forming the primary mirror of the 10 m Keck telescope. (a) The complete mirror, (b) an individual segment during manufacture (figures kindly supplied by the Keck project) .....	180
3.9 The Keck 10 m telescope: the prime mirror cell and associated mechanics (figure courtesy of the Keck project) .....	181
3.10 The space frame structure of the Keck 10 m telescope [3.23] .....	182
3.11 Star image sizes (FWHM arcsec) for segments and for a full aperture ( $\lambda = 650$ nm). “Best” refers to the smallest of the averages for individual segments, “mean” is the average for all segments, “stack” is the combined image for all 36 segments. (After Gillingham [3.22]) .....	183
3.12 Drawing of the 10 m Keck I telescope in its dome. See also the photograph on the cover of this book. (Courtesy W.M. Keck Observatory, through J. Nelson and A. Perala) .....	184

3.13 Proposed segmentation schemes for the DGT primary mirror (after Appenzeller [3.31]) . . . . .	185
3.14 Optical layout ( <b>a</b> ) and primary mirror segmentation ( <b>b</b> ) for the Nordic 25 m telescope concept [3.20] . . . . .	186
3.15 The 4.4 m equivalent MMT with its synchronously rotating building . . . . .	187
3.16 MMT: Alignment system optical paths (from Reed [3.38]) . . . . .	188
3.17 MMT: Laser alignment beam optical paths (from Reed [3.38]) . . . . .	189
3.18 The Columbus project: $2 \times 8$ m MMT-type (recently renamed the Large Binocular Telescope (LBT)) . . . . .	190
3.19 The latest Large Binocular Telescope (LBT) design. Drawing by ADS Italia [3.47] . . . . .	191
3.20 Overview of the Chinese LAMOST telescope [3.49] . . . . .	192
3.21 The Hubble Space Telescope (HST): the primary mirror during polishing. The fine “egg-crate” structure of the fused quartz blank is clearly visible. Reproduced from Hecht [3.62] . . . . .	195
3.22 The Hubble Space Telescope (HST): predicted Strehl Intensity Ratio and FWHM corresponding to the specification $W \leq \lambda/21$ rms at $\lambda = 633$ nm and rms pointing error $\leq 0.007$ arcsec (reproduced from Schroeder [3.60]) . . . . .	195
3.23 The Hubble Space Telescope (HST): predicted encircled energy concentrations in two wavelength bands for the same quality specification as in Fig. 3.22. Note that $\alpha$ is the <i>radius</i> of the PSF in the Schroeder notation. (Reproduced from Schroeder [3.60]) . . . . .	196
3.24 The Hubble Space Telescope (HST): COSTAR solution for the correction of the spherical aberration error (from Benvenuti and Wilson [3.66]) . . . . .	197
3.25 Images before and after the repair mission of the HST: ( <b>a</b> ) The galaxy M 100 with WFPC II compared with WFPC I; ( <b>b</b> ) A highly magnified star image with the FOC before and after the addition of COSTAR. (Courtesy Fischer and Duerbeck [3.67]) . . . . .	198
3.26 The ESO NTT: the primary mirror (full diameter 3.58 m) mounted on its final support in its cell which is placed on the manufacturing table at Carl Zeiss for test in the test tower [3.68] [3.71] . . . . .	202
3.27 The ESO 3.5 m NTT in its rotating building at La Silla, Chile [3.70] . . . . .	203
3.28 The ESO 3.5 m NTT showing a view of the underside of the primary mirror cell with the 4-ring axial support geometry of the 78 supports, which are in the recesses under the covers shown [3.70] . . . . .	204
3.29 The ESO $4 \times 8$ m VLT: Nasmyth and coudé foci of the individual telescopes (after Enard [3.80]) . . . . .	206

3.30	The ESO $4 \times 8$ m VLT: principle of the beam combination showing the incoherent combined focus as well as the interferometric combination (after Enard [3.80]) . . . . .	207
3.31	The ESO $4 \times 8$ m VLT: layout proposed (summer 1992) for the 4 telescopes on Cerro Paranal, Chile. The <i>small circles</i> mark the possible stations for the auxiliary telescopes. (After Beckers and Tarenghi [3.81]) . . . . .	207
3.32	The final version of the building of the 8 m VLT unit telescopes (after Schneermann et al. [3.86]) . . . . .	208
3.33	The ESO $4 \times 8$ m VLT: the first 8 m telescope blank ever made, before ceramization at the Schott works, Mainz, early in 1992, intended for the first VLT telescope. The diameter here is about 8.5 m, the thickness about 250 mm. After ceramization, completed in November 1992, the diameter was reduced to 8.2 m and the thickness to slightly more than the final $t = 175$ mm. The final weight is about 23 500 kg. (Courtesy Schott) . . . . .	209
3.34	The first VLT primary blank ground to its final dimensions before figuring at REOSC ( $D = 8.2$ m, $t$ slightly more than the final 175 mm, i.e. 177.9 mm). (Courtesy REOSC) . .	210
3.35	The Japanese Subaru 8 m telescope project (reproduced from [3.91]) . . . . .	212
3.36	The Subaru 8 m project compared with other telescopes from the point of view of <i>telescope sensitivity</i> over the optical-IR wavelength band, expressed as the minimum photon flux required as input (upper figure). The lower figure shows the atmospheric transparency windows for Mauna Kea, over which Subaru has high sensitivity. The upper figure refers to the high dispersion mode and IR data without the effect of the atmosphere. (After the Subaru brochure [3.91]) . . . . .	213
3.37	Model of the hybrid primary mirror (Zerodur/CFRP) for the 1.5 m HPT (from Pausch and Stenvers [3.101]) . . . . .	215
3.38	Schematic diagram of the honeycomb sandwich casting process: (a) the glass blocks before firing, (b) after melting and spinning (from Angel [3.119]) . . . . .	229
3.39	The first 6.5 m blank cast at the U. of A. Steward Observatory Mirror Lab in April 1992 for the MMT replacement primary. The steep curvature ( $f/1.25$ ) is evident. The hexagonal blocks of ceramic fibre, here still in the casting, were subsequently removed, leaving a lightweighted blank appreciably less dense than water. (Original photo courtesy Roger Angel) . . . . .	230
3.40	The Steward Observatory facility for manufacturing and figuring lightweighted BSC glass blanks. It was built under the grandstands of the University of Arizona football stadium, which limits the height of the test tower. (Courtesy R. Angel) . . . . .	230

3.41 Installation of core boxes in the mould of the 6.5 m blank for the MMT conversion (from Hill and Angel [3.50]) . . . . .	231
3.42 A “built-up” (BU) welded blank in aluminium with a diameter 500 mm (from Dierickx and Zigmann [3.135]) . . . . .	234
3.43 Thermal cycling experiment at REOSC (Paris) on two 1.8 m aluminium blanks showing the interferometric figure before cycling, after 32 cycles and the difference. (a) BU welded blank. (b) EB welded blank. (From Dierickx and Zigmann [3.135]) . . . . .	235
3.44 Symmetrical bending of a thin cylindrical plate under an axisymmetric force (after Timoshenko, Woinowsky-Krieger [3.152]) . . . . .	243
3.45 Deformation of a thin circular plate of negligible weight, freely supported at the edge and loaded axisymmetrically at a thin annulus by a total force $P$ (after Timoshenko and Woinowsky-Krieger [3.152]) . . . . .	246
3.46 Deformation functions $\omega$ for the sag of a thin cylindrical plate (mirror) under gravity supported by a single thin support ring of seven different diameters (after Couder [3.154]) . . . . .	247
3.47 3-ring support proposed by Couder for a 1.92 m mirror (from Couder [3.156]) . . . . .	249
3.48 Deformation of an infinite thin flat plate supported by a rectangular raster of support points (after Timoshenko and Woinowsky-Krieger [3.157]) . . . . .	252
3.49 Single ring axial support designed by Schwesinger for the ESO 1.47 m CAT. The normalized deformation $\omega_0$ is the rms deformation referred to the best fit parabola (focus). (After Schwesinger [3.171]) . . . . .	256
3.50 The principle of the modern astatic lever . . . . .	257
3.51 Hindle-type whiffle-tree supports with (a) 3-point, (b) 9-point, (c) 18-point configurations (after Yoder [3.178]) . . . . .	259
3.52 Palomar 5 m telescope: function of the mirror support levers (from Bowen [3.179]) . . . . .	261
3.53 Flexure of horizontal-axis mounted mirrors: quantities entering the flexure problem (from Schwesinger [3.161]) . . . . .	262
3.54 Various radial edge support force distributions . . . . .	265
3.55 A 4 m diameter mirror supported in three different ways with axis horizontal. Numerical determination of flexure by dynamic relaxation for the following cases from Table 3.9: (a) push-pull through c. of g., (b) mercury bag, (d) belt type, (f) single lower support (from Malwick and Pearson [3.168]) . . . . .	267
3.56 Edge force distributions for alt-az mounted mirrors. (a) Conventional radial push-pull; (b) Using vertical components of (a); (c) Equal transverse force distribution in the plane of the c. of g. of the mirror; (d) Equal transverse forces acting through the c. of g. of individual slices. (From Mack [3.172]) . . . . .	268

3.57 Lateral edge support (push-pull) for the primary of the ESO NTT: equal vertical loads at equal spacing along the circumference (after Schwesinger [3.173]) . . . . .	269
3.58 Lateral edge support (push-pull) for the ESO NTT: the effect of the fraction $\beta$ of the weight supported by a tangential force system (equal spacing round the circumference) compared with the radial force system (after Schwesinger [3.173]) . . . . .	269
3.59 Lateral outer edge support for the ESO 8 m VLT primaries showing the modification by introducing tangential shearing forces corresponding to $\beta = 0.680$ in this diagram (from Schwesinger [3.181]) . . . . .	271
3.60 Lateral outer edge support for the ESO 8 m VLT primaries showing the optimization of the residual error $w$ in the mode $n = 1$ by a shear fraction $\beta = 0.7529$ (from Schwesinger [3.181]) . .	271
3.61 Maximum induced stress as a function of $D$ for various values of $D/t$ for a mirror lifted round the periphery of its central hole with $R_0/R = 0.25$ , $\rho = 2500 \text{ kg m}^{-3}$ and $\nu = 0.3$ (after Cheng and Humphries [3.158]) . . . . .	273
3.62 The bandpasses for active and adaptive optics correction (from Wilson and Noethe [3.201]) . . . . .	281
3.63 Results of classical Hartmann tests of the conventional ESO 3.6 m telescope in 1976 [3.189], illustrating the theoretical improvement after successive removal of polynomial terms. The mean right-hand point of the functions gives the <i>Intrinsic Quality</i> (IQ) of this telescope. (From Wilson et al. [3.69]) . . . . .	285
3.64 Active optics correction for the low frequency bandpass A: principle of the ESO closed-loop control technique for optimizing image quality (from [3.69]) . . . . .	286
3.65 One of the 75 active supports (schematic) of the ESO 3.5 m NTT primary axial support. The dc errors are corrected by tension springs (through the levers), the other (variable) errors by the movable counterweights. (From Wilson et al. [3.69]) . . . . .	290
3.66 CCD pictures obtained at "Astronomical First Light" with the ESO 3.5 m NTT, compared with previous photographic records of the same field (globular cluster $\omega$ Centauri). (From West [3.206]) . . . . .	293
3.67 Cumulative/integrated incidence of external seeing and image quality of the major telescopes at the ESO observatory La Silla. External seeing and NTT 1 year (1991), the other telescopes 5 years (1987–1991). Normalized for $\lambda = 1 \mu\text{m}$ and zenith position ( $Z = 0$ ). (From Wilson et al. [3.73]) . . . . .	295
3.68 The first 25 natural modes, with eigenfrequencies, for a VLT primary with $t = 200 \text{ mm}$ (courtesy M. Schneermann, ESO) . . . . .	299
3.69 Axial support unit (schematic) for the VLT 8 m primary mirrors (from Schneermann et al. [3.212]) . . . . .	301

3.70 Hindle sphere arrangement for detecting wind-buffetting deformation of primaries (from Wilson et al. [3.214]) . . . . .	302
3.71 2.5 m Nordic Optical Telescope (NOT): the expected improvements by addition of the active optics control system for various zenith angles (from Ardeberg and Andersen [3.218]) . . . . .	306
3.72 Keck 10 m telescope: schematic of the control system arrangement around one segment (from Meng et al. [3.227]) . . . . .	309
3.73 Encircled energies in images given by a mirror of 254 mm diameter, horizontal (axis vertical), at 6 °C above ambient temperature and with three different horizontal flushing air velocities (from Lowne [3.233]) . . . . .	317
3.74 Image degradation measured by $d_{75}$ in arcsec induced by the heated 254 mm diameter mirror (6 °C above ambient temperature) with natural convection at different inclinations $Z$ from horizontal (axis vertical) (from Lowne [3.233]) . . . . .	318
3.75 The cross-sections of a number of typical telescope enclosures in comparison with the Keck 10 m telescope enclosure. Note that the included circle shows the relative apertures of the telescopes. (From Nelson [3.237] with the ESO NTT and VLT enclosures added) . . . . .	319
3.76 Histogram, also with the log-normal fit, of image quality at the CFHT prime focus measured on HR Cam CCD frames. The hatched histogram is for measurements when $\Delta T_m < +0.5$ °C. (From Racine [3.238]) . . . . .	321
3.77 Angular image spread due to <i>mirror seeing</i> in the CFHT. The mirror seeing contribution occurs only at $\Delta T_m > 0$ and is superposed on the constant plateau 0.56 arcsec due to other sources. (From Racine [3.238]) . . . . .	322
3.78 Angular spread due to <i>dome seeing</i> in the CFHT, for $\Delta T_m < 0.5$ °C. Again, the dome seeing contribution occurs only at $\Delta T > 0$ and is superimposed on the constant plateau 0.56 arcsec due to other sources. (From Racine [3.238]) . . . . .	323
3.79 Mirror seeing in the ESO 3.5 m NTT during a night in March 1989 shortly after “first light”. The histogram shows the evolution of the first axisymmetrical natural mode. The coefficient of $-1000$ nm (equivalent to a coefficient of Sph3 of about $-1630$ nm) was reduced over about 2 hours to a mean level of about $-350$ nm by a modest ventilating wind. (From Wilson et al. [3.70]) . . . . .	326
3.80 Lightweighted honeycomb blanks of borosilicate glass: schematic of the mirror ventilation system (from Cheng and Angel [3.246]) . .	327
3.81 Mirror seeing experiments showing the Strehl criteria $S_{raw}$ and $S_{int}$ as a function of $\Delta T_m$ (from Iye et al. [3.249]) . . . . .	330
3.82 Mirror seeing experiments: efficiency of a flushing wind (from Iye et al. [3.249]) . . . . .	331

3.83 ESO 8 m VLT primaries at Paranal: <i>passive</i> thermal adaptation if cooled initially to the optimum temperature $T_{opt}$ (between the two curves): (a) most favourable night, (b) least favourable night (from Cullum [3.251]) . . . . .	332
3.84 Surface cooling of the ESO 8 m VLT primary and various steel plates with an enclosure daytime ambient air cycle $3^{\circ}\text{C}$ below the target temperature, assuming an air velocity of $1\text{ ms}^{-1}$ on both sides of the mirror and one side for the steel plates (from Cullum [3.251]) . . . . .	333
3.85 <i>Active</i> cooling on-line at night of the ESO 8 m VLT primaries with a cooling plate compared with passive cooling for the case of Fig. 3.83(b) (from Cullum [3.251]) . . . . .	334
3.86 Extrapolation predictions for the flushing windspeed effect on mirror seeing for the ESO 8 m VLT primaries and $\Delta T_m = +1^{\circ}\text{C}$ , based on Iye et al. (from Zago [3.253]) . . . . .	336
3.87 Principle of the differential dome seeing monitor (DDSM) set up at the Newton focus of a 1.88 m telescope (from Iye et al. [3.256]).	340
3.88 Experiments on image motion (wavefront tilt) with the DDSM at a 1.88 m telescope showing the results for the images from a star, mirrors and corner cubes respectively: (a) without windscreening, (b) with maximum windscreening (from Iye et al. [3.256]) . . . . .	342

## Chapter 4

4.1 Geometrical energy concentration at best focus measured at the PF of the ESO 3.6 m telescope with Gascoigne plate corrector (near zenith), compared with the specification (from Franz et al. [4.7]) . . . . .	352
4.2 The Central Intensity Ratio (CIR), calculated for “average” and “good” atmospheric seeing for a perfect telescope ( <i>dashed curves</i> ) and for a telescope with a typical specification for 1979 ( <i>full curves</i> ) (after Brown [4.14]) . . . . .	357
4.3 Long-exposure MTF with a third order spherical aberration of 500 nm pvt (Zernike) combined with atmospheric seeing defined by (1) $\zeta = 10$ , (2) $\zeta = 20$ , (3) $\zeta = 30$ (from Dierickx [4.17]) . . . . .	359
4.4 Absolute Strehl ratio of a perfect telescope. The wavelength $\lambda = 500\text{ nm}$ and $\varepsilon = 0$ . (From Dierickx [4.17]) . . . . .	362
4.5 Central Intensity Ratio (CIR) against peak-to-valley third order spherical aberration (Seidel) for $\lambda = 500\text{ nm}$ and $\zeta$ equal to (1) 20, (2) 25, (3) 30, (4) 35, (5) 40 (from Dierickx [4.17]) . . . . .	363
4.6 “Error Tree” for the ESO 8 m VLT telescopes (from Dierickx [4.20] or Wilson et al. [4.12]) . . . . .	365
4.7 Overall Optical Error Budget for the ESO 8 m VLT unit telescopes (from Dierickx [4.20]) . . . . .	366

## Chapter 5

- 5.1 The concentric shell model for astronomical refraction (after Mahan [5.3]) ..... 375
- 5.2 General shape of the structure function  $D_{rr}(r)$  showing  $L_o$  (*outer scale*) and  $l_o$  (*inner scale*) (from Tatarski [5.8]) ..... 379
- 5.3 Dependence of normalized resolution  $R/R_{max}$  on normalized telescope diameter  $D/r_o$ . *Curve A* for the long-exposure image. *Curve B* for averaged short exposures (ASE) “far-field” results. *Curve C* for averaged short exposures (ASE) “near-field” results. (After Fried [5.13]) ..... 387
- 5.4 Image motion  $\omega_m$ , “blurring”  $\omega_o$  and total “seeing”  $\omega$  in angular measure ( $\lambda/r_o$  units) for normal long exposures (after Roddier [5.16]) ..... 393
- 5.5 Principle of transferred pupil technique for adaptive optics based on the small isoplanatic field (from Wilson et al. [5.40]) ..... 398
- 5.6 Principle of adaptive optics in astronomy using an adaptive mirror (after Merkle [5.44]) ..... 399
- 5.7 Vertical distribution of the square of the refractive index structure constant  $C_n^2$  (from Fried [5.43]) ..... 400
- 5.8 Efficiency of adaptive correction using a small number of modes for (a)  $D/r_o = 2$ , (b)  $D/r_o = 7$ . *Curve A*, no correction; *curve B*, tilt correction; *curve C*, tilt plus focus corrections; *curve D*, tilt plus focus plus astigmatism corrections; *curve E*, ideal correction giving diffraction limited performance. (After Wang [5.51]) ..... 405
- 5.9 Efficiency of adaptive correction using various numbers of Zernike polynomials (*continuous curves*) or Karhunen-Loeve functions (*dashed curves*) for the case  $D/r_o = 6$  (after Wang and Markey [5.53]) ..... 406
- 5.10 Different types of deformable mirrors (from Merkle [5.44]) ..... 408
- 5.11 Deformable adaptive mirror of the continuous thin-plate type driven by piezoelectric actuators developed by the GEC Laboratories at Marcoussis, France (from Merkle [5.50]) ..... 409
- 5.12 Calculated MTF showing the extent of correction with the adaptive mirror of Fig. 5.11 (19 actuators) applied to a 2.2 m telescope with  $r_o = 10$  cm in the visible ( $\lambda = 500$  nm) for wavelengths (a)  $1\text{ }\mu\text{m}$  and (b)  $3.6\text{ }\mu\text{m}$  (after Merkle [5.50]) ..... 410
- 5.13 Schematics of artificial reference star generation by a laser beam (from Merkle [5.44] [5.50]) ..... 412
- 5.14 Schematic diagram of the active/adaptive correction system of the ESO 8 m VLT unit telescopes (from Merkle [5.50]) ..... 414

5.15 Adaptive optics correction using the COME-ON system in the IR ( $\lambda = 3.6 \mu\text{m}$ ) of the image of the double star HR 6658 (separation 0.38 arcsec) with the ESO 3.6 m telescope. Left, without correction; right, with correction. (After Merkle [5.63]) . . . . .	415
5.16 Adaptive optics improvement of the MTF for the cases cited (after Fugate [5.66]) . . . . .	417

## Chapter 6

6.1 Reflectivity $R$ of fresh speculum, chemically deposited silver and evaporated aluminium (after Riekher [6.1]) . . . . .	424
6.2 Reflectivities $R$ of coats produced by evaporation under UHV conditions of the six metals of Table 6.1 (from Jacobson et al. [6.14]) . . . . .	427
6.3 Experimental reflectivity enhancement of an Ag coating using Air – SbO <sub>3</sub> – Na <sub>3</sub> AlF <sub>6</sub> – Sb <sub>2</sub> O <sub>3</sub> – Si <sub>2</sub> O <sub>3</sub> – Ag with $\lambda/4$ for $\lambda_E = 300 \text{ nm}$ (after Browning et al. [6.26]) . . . . .	431
6.4 Silver overcoating of an aluminium coat with dielectric enhancement in the UV, (a) theoretical, (b) experimental (after Browning et al. [6.26]) . . . . .	432
6.5 Enhancement of $R$ in the UV from an Ag coat using a $\lambda/4$ stack compared with an Al coat with Ag overcoat and bare Ag (after Song and Macleod [6.27] from Jacobson et al. [6.14]) . . . . .	433
6.6 Basic coating design for the Gemini project (GP) study (from Jacobson et al. [6.14]) . . . . .	435
6.7 Schematics of a proposed very large magnetron sputtering plant for the 8 m mirrors of the Gemini project (from Jacobson et al. [6.14]) . . . . .	436
6.8 A model of a coating Air – HfO <sub>2</sub> (of variable $d$ ) – Ag ( $d = 100 \text{ nm}$ ) – Cu (30 nm) – Glass showing the variation of $R$ with $d$ of HfO <sub>2</sub> (after Decker and Stanford [6.19] reproduced by Jacobson et al. [6.14]) . . . . .	438
6.9 The relative throughput of an “all aluminium” telescope (3 reflections) compared with that of an “all silver” telescope (3 reflections) for a variety of silver coatings (after Mountain, Gillett and Kurz [6.28]) . . . . .	439
6.10 The ESO sputtering facility for the VLT 8 m primaries (concept M. Grössl): (a) Photograph of the complete installation before shipment to Chile, (b) Section showing the basic design (courtesy M. Grössl, ESO, and Linde AG, München) . . . . .	440
6.11 Recovery of reflectivity losses due to cleaning of dusty samples (4) with CO <sub>2</sub> snowflakes (3) and peeling with OPTI-CLEAN (2), compared with fresh Al (1) (after Giordano [6.38] [6.39]) . . . . .	444

6.12 Experiments for cleaning of telescope primaries by laser bombardment and suction removal of the loosened dirt (after Balick [6.44]) . . . . .	446
---	-----

## Chapter 7

7.1 The optical layout (schematic) of the ESO NTT adapter/rotator (from Franzia [7.2] and ESO drawing NTT 30/11) . . . . .	451
7.2 Available search field for guide stars in the ESO NTT for two modes of observation with the EMMI spectrograph (from Franzia [7.2]) . . . . .	453
7.3 Front view of the open NTT adapter/rotator seen from the image plane side (ESO photograph, courtesy F. Franzia) . . . . .	455
7.4 Principle of the guide probe movements in the adapter/rotator of the 8 m VLT unit telescopes at the Cassegrain focus (ESO VLT drawing, courtesy F. Franzia) . . . . .	456
7.5 Principle of the adapter GP sensor arm in the VLT adapter, Cassegrain focus (ESO VLT drawing, courtesy F. Franzia) . . . . .	457
7.6 Classical system of baffles in a refracting telescope with a continuous cylindrical tube (after Danjon and Couder [7.14]) . . . . .	460
7.7 General design principles of a 2-baffle system for a Cassegrain telescope (after Young [7.18]) . . . . .	461
7.8 Prescott's general graphical procedure for designing baffles in a Cassegrain telescope (after Prescott [7.19]) . . . . .	463
7.9 Original baffle system for the Apache Point 2.5 m wide-field telescope (from Pompea et al. [7.21]) . . . . .	465
7.10 Modified baffle system for the Apache Point 2.5 m wide-field telescope (from Pompea et al. [7.21]) . . . . .	466

## Chapter 8

8.1 Development-maintenance relationship for ensuring top quality optical performance of large, active, ground-based telescopes . . . . .	472
--	-----

# List of tables

## Chapter 1

1.1	Figuring control possibilities resulting from Preston's Law .....	4
1.2	Progress in figuring a 1.8 m lightweighted spherical f/1.5 mirror with the Perkin-Elmer CCP (Jones [1.19]) .....	6
1.3	Desired Zernike coefficients (microns) for extreme inner and outer segments (Mast and Nelson [1.57]).....	32
1.4	Segment quality before and after final correction with the warping harness for six segments (Mast and Nelson [1.57]) .....	32
1.5	Summary of the IBF correction results at Kodak on the Keck primary segment SN 009 [1.62] .....	35
1.6	Summary of the results for the first two ESO VLT 8.2 m primaries (Dierickx et al. [1.67]) .....	42

## Chapter 2

2.1	Parameters for the evaluation of Eqs. (2.34) and (2.35) in the case of the ESO 3.5 m NTT .....	117
2.2	Astigmatism values for the decentered NTT ( $\delta = 2.5$ mm) for various field points and in comparison with the centered system ..	119
2.3	Defocused image sizes for "pupil plates" for telescopes of sizes about 1.5 to 3 m [2.14] .....	134
2.4	Shack-Hartmann test results of the MPIA 2.2 m telescope II (RC focus) at La Silla in October 1983 (after erection and centering). All results are in arcsec and are the mean diameters corresponding to 80 % geometrical energy obtained from 4 S-H plates. (From Wilson et al. [2.27]) .....	155

## Chapter 3

3.1	Evolution of primary f/no in reflecting telescopes .....	169
3.2	Cost estimates by Meinel [3.5] showing the advantage of modern over conventional technology .....	172

3.3	The three key technologies which form the basis of the revolution in modern telescope optics (weight reduction, control of flexure and thermal problems) .....	175
3.4	Physical properties of potential mirror blank materials (from Wilson and Mischung [3.110]). (Continued overleaf) .....	220
3.5	Baseline design for the 8 m f/1.2 BSC honeycomb blanks for the Columbus (later LBT) and Magellan projects (from Angel [3.119]) .....	228
3.6	Three ring axial mirror support optimized by Couder in 1931 (from Couder [3.156]) .....	248
3.7	The flexure function $k_n$ in different modes for a cylindrical plate floating in a liquid and subjected to an external point force $P$ at its edge (from Schwesinger [3.160]) .....	254
3.8	Influence numbers $Y_n$ for the different modes $n$ with a mirror supported at its edge with horizontal axis (after Schwesinger [3.161]) .....	264
3.9	Comparative deformation given by the six edge supports discussed by Schwesinger (after Schwesinger [3.161]) .....	266
3.10	Lateral support optimization with three parameters for 8 m (mirror no. 1) and 4 m (mirror no. 2) meniscus mirrors (from Schwesinger [3.182]) .....	272
3.11	The ten sources of error giving degradation of image quality in ground-based telescopes, and their corresponding bandpasses. Diffraction, which is inevitable and continuous, is excluded since (for a given signal wavelength) it cannot be influenced. In space, the three errors dependent on air vanish. (From Wilson et al. [3.69]) .....	280
3.12	Fourier expansion and terms used in the ESO active optics system for the NTT. The seven terms marked • are corrected, the first of which is simply the auto-guiding. (From Wilson et al. [3.69]) .....	284
3.13	Optical quality potential of the NTT (excluding external seeing). This table shows that the practical limitation is the local air (source (7) in Table 3.11), in spite of the excellent building design. (From Wilson et al. [3.70]) .....	294
3.14	Median (most probable) image quality (FWHM) and “optical efficiency” $E$ in five cases at La Silla corresponding to Fig. 3.67. Normalized for $\lambda = 1 \mu\text{m}$ and $Z = 0$ . (From Wilson et al. [3.73]) ..	296
3.15	Dynamic range of the active optics system for the VLT 8 m primary mirrors (after Noethe [3.210]) .....	300
3.16	Standard deviation $\sigma$ of image motions for the images from the star, mirrors and corner cubes in the DDSM experiment (from Iye et al. [3.256]) .....	343
3.17	Basic optical characteristics of the major large ground-based telescope projects <i>using new optical technology</i> .....	346

**Chapter 4**

4.1 Keck 10 m telescope optical error budget (from Nelson and Mast [4.10]) .....	354
4.2 Optical Error Budget for the Japanese 8 m Subaru project (after Subaru Project Office [4.23]) .....	367

**Chapter 5**

5.1 Theoretical profile of the long-exposure atmospheric PSF obtained from the Hankel transform of Eq. (5.40) for $r_o = 10$ cm and $\Delta\alpha = 0.16$ arcsec (after Kadiri [5.27] and Roddier [5.16]) .....	390
5.2 Relation between the angular measure of the diameter of the long-exposure atmospheric PSF given by Roddier ( $2 w_{min}$ ) and commonly used measures (after Dierickx [5.29] and private communication) .....	391
5.3 Simplification of the basic parameters of adaptive optics at longer wavelengths (after Merkle [5.44]) .....	402
5.4 Basic parameters for adaptive optics and their dependence on $\lambda$ and $\cos Z$ (after Roddier [5.45]) .....	403
5.5 Limitations of magnitude and sky coverage for adaptive optics at different wavelengths (after Merkle [5.44] [5.50]) .....	411
5.6 Adaptive optics with COME-ON and (predicted) COME-ON PLUS at the ESO 3.6 m telescope with $r_o = 13$ cm at $\lambda = 500$ nm (from Rousset et al. [5.65]) .....	415

**Chapter 6**

6.1 Percentage reflectivities $R$ at normal incidence of freshly evaporated coatings of six metals (from Hass [6.6]) .....	426
6.2 Al and Ag Sample Reflectivity as reported for the Gemini coating program in 1996 (from Mountain, Gillett and Kurz [6.28]) .....	439
6.3 Percentage improvements in $R$ , measured on the NTT primary relative to a standard reference, produced by various cleaning techniques (from Giordano [6.41]) .....	445

**Chapter 7**

7.1 Throughput of the Apache Point 2.5 m telescope without and with baffles (Fig. 7.9), assuming 100 % mirror reflectivity (from Pompea et al. [7.21]) .....	466
--	-----

## Name index

- Aikens, R.S. 184, 185  
Airy, G.B. 349  
Allen, L. 196  
Allen, L.N. 34  
Andersen, J. 124  
Andersen, T. 305, 306  
Angel, J.R.P. 1, 19, 20, 22, 192, 193,  
    224, 227–231, 308, 327, 328  
Appen-Schnur, G.F.O., von, *see*  
    Schnur, G.F.O.  
Appenzeller, I. 185  
Ardeberg, A. 179, 185, 189, 305, 306  
Ashley, E.J. 425  
  
Baade, D. 297  
Babcock, H.W. 397, 403, 459  
Bahner, K. 144, 146, 147, 153, 155,  
    258, 275, 312  
Baldwin, J. 297, 324  
Balick, B. 446  
Ballio, G. 228  
Baranne, A. 188  
Barbieri, C. 205  
Barlow, C.W.C. 374  
Barr, L.D. 176, 177, 303, 307, 328–331,  
    334, 335, 344  
Bash, F.N. 178, 179  
Bates, W.J. 166  
Beck, H.G. 146, 148  
Beckers, J.M. 22, 161, 186, 187, 205,  
    207, 325, 344, 418, 421, 458  
Beckstette, K. 11, 15  
Behr, A. 165, 166  
Bely, P.-Y. 320  
Bennett, H.E. 425  
Bennett, J.M. 425, 443  
Benvenuti, P. 197  
Bergener, D.W. 465  
Bessel, F.W. 376  
Bhatia, R. 114  
Bingham, R.G. 238, 316  
  
Bond, G.P. 368  
Bond, W.C. 368  
Born, M. 427  
Borra, E.F. 241  
Bottema, M. 197  
Bouguer, P. 375  
Bouwers, A. 460  
Bowen, I.S. 148, 260, 261, 350, 465  
Brashear, J. 424  
Brodhun, E. 87  
Brown, D.S. 3, 20, 166, 356, 357, 360,  
    362, 364  
Brown, W.P. 400  
Browning, S.D. 430–433  
Bruning, J.H. 56, 62, 63  
Bryan, G.H. 374  
Buffington, A. 278, 404  
Burch, C.R. 49, 77, 82  
Burge, J.H. 85  
  
Carnegie, A. 470  
Cassini, J.D. 115, 118, 374, 375  
Chaffee, F.H. 187  
Chaisson, E.J. 194  
Cheng, A.Y.S. 19, 227, 327, 328  
Cheng, J. 43, 251, 272–274  
Cheng, Y.Y. 65  
Clebsch, A.R.F. 307  
Common, A.A. 101  
Comoretto, G. 312  
Connes, P. 279  
Couder, A. 77, 78, 145, 172, 217–219,  
    231, 237, 242, 244, 245, 247–249, 253,  
    255, 256, 259, 260, 266, 275, 290, 459,  
    460, 464  
Creedon, J.F. 276, 288  
Cui, X. 298, 299  
Cullum, M.C. 332–335, 344  
  
Dainty, J.C. 422  
Dall, H.E. 78, 79

- Danjon, A. 145, 459, 460, 464  
 Decker, D.L. 425, 437, 438  
 Delabre, B. 109, 113, 118, 120, 121,  
   157  
 Descartes, R. 92  
 Dévé, Ch. 2  
 Dierickx, P. 1, 41–43, 205, 233–235,  
   238, 239, 353, 358–366, 369–371, 390,  
   391, 423, 444  
 Driscoll, W.G. 425  
 Drude, P. 427  
 Duerbeck, H. 199  
 Duffieux, P.M. 350  
 Ellerbroek, B.L. 416–418  
 Ellery, R.L.J. 470  
 Enard, D. 205–207, 210, 237, 275, 456,  
   457  
 Epps, H.W. 188  
 Espiard, J. 210  
 Euler, L. 307  
 Facey, T.A. 7  
 Fehlkamm, G. 146, 148  
 Felgett, P.B. 214  
 Fischer, D. 199  
 Forbes, F.F. 232, 325, 344  
 Foucault, L. 470  
 Fourier, J. 284  
 Foy, R. 411, 416  
 Frantz, L.M. 64  
 Franzia, F. 124, 149, 150, 157, 165, 352,  
   450, 451, 453, 455–457  
 Fraunhofer, J. 349  
 Freischlad, K. 65  
 Fresnel, A. 349, 423, 426  
 Fried, D.L. 320, 336, 353, 362, 376,  
   385–388, 391–397, 399–402, 404, 408,  
   409  
 Fugate, R.Q. 416, 417  
 Gabor, G. 344  
 Gale, M.T. 152  
 Galileo, G. 170  
 Gallieni, W. 312, 313  
 Gay-Lussac, L.J. 217, 223  
 Gillett, F. 175, 437, 439  
 Gillingham, P. 182, 183, 325  
 Giordano, P. 442–445, 447, 448  
 Gitton, P. 297, 298  
 Goad, L. 132, 166  
 Goble, L.W. 308  
 Götz, J. 2  
 Greco, V. 429  
 Green, A.E. 255  
 Greenwood, D.P. 408, 409  
 Grievenkamp, J.E. 62, 65  
 Grössl, M. 425, 440–442  
 Grubb, T. 3, 169, 258, 470  
 Haarala, S. 160, 161  
 Hagen, E. 427  
 Hale, G.E. 470  
 Hansen, G. 49  
 Hardy, J.H. 404  
 Hariharan, P. 65  
 Harp, J.C. 382  
 Hartmann, J. 144, 145  
 Hass, G. 424–426, 428, 430  
 Hecht, J. 195  
 Herschel, J. 470  
 Herschel, W. 89, 169, 217, 349, 368,  
   424, 470  
 Herzberger, M. 146  
 Heynacher, E. 15, 69  
 Hill, J.M. 190, 229, 231  
 Hindle, J.H. 94, 258, 259  
 Hoag, A.A. 388  
 Hoenig, S.A. 443  
 Hogge, C.B. 401, 402  
 Holland, L. 425  
 Höneß, H. 224  
 Hooke, R. 247, 283, 287, 289  
 Hopkins, H.H. 350  
 Hopkins, R.E. 51  
 Horn-d'Arturo, G. 175, 176  
 Houston, J.B. 51, 54  
 Howell, W.E. 276  
 Hu, N. 89  
 Huang, E.W. 193  
 Hufnagel, R.E. 376, 385, 394  
 Hügenell, H. 183  
 Humphries, C.M. 43, 172, 251,  
   272–274  
 Ichioka, Y. 57, 58, 68  
 Ingalls, A.G. 132  
 Inuiya, M. 57, 58, 68  
 Iye, M. 307, 322, 323, 328–333,  
   335–337, 339–344  
 Izumitani, T.S. 2  
 Jacobson, M.R. 425, 427, 433–438,  
   442  
 Jamin, J. 423  
 Johns, M. 192  
 Johnson, H.L. 231–233  
 Jones, R.A. 4–9, 12, 15, 56

- Kadakia, P.L. 56  
 Kadiri, S. 389, 390  
 Kaifu, N. 214  
 Kaufmann, H. 3, 46, 48, 55, 56  
 Keeler, J.E. 470  
 Keller, G. 395  
 Khinchin, A.Y. 376  
 Kingslake, R. 51, 52, 145  
 Kinnstaetter, K. 62, 65, 68  
 Knohl, E.D. 205, 255  
 Knop, K. 152  
 Kodaira, K. 211, 213  
 Koliopoulos, C.L. 65–68, 72  
 Kolmogorov, A.N. 320, 335, 353,  
     376–379, 392, 395, 396  
 Korhonen, T. 1, 18, 88, 89, 158, 160,  
     161, 167, 305  
 Kozicki, M. 442  
 Krasilnikov, V.A. 389  
 Küchel, M. 68–70, 72  
 Kurz, R. 175, 437, 439  
 Kutter, A. 111  
 Labeyrie, A. 411, 416, 422, 459  
 Lappalainen, T. 18  
 Lassell, W. 3, 257, 258, 275, 311, 470  
 Le Sueur, A. 470  
 Lee, R.W. 382  
 Lehmann, H. 145  
 Lemaître, G.R. 1, 23–27, 188, 237,  
     238, 306, 307  
 Lindgren, A.G. 276, 288  
 Liu, Y.M. 56, 74  
 Loibl, B. 153, 312  
 Loos, G.C. 401, 402  
 Lorentz, H.A. 427  
 Lowne, C.M. 316–318, 324, 328, 331,  
     332, 335, 337, 343  
 Lubliner, J. 19, 28, 29  
 Luks, T. 216  
 Lysyannyi, Y.K. 4  
 Lytle, J.D. 91  
 Mack, B. 255, 267, 268  
 Macleod, H.A. 433  
 Macy, W.W. 61  
 Mahajan, V.N. 363  
 Mahan, A.I. 374–376  
 Maksutov, D.D. 2, 3, 99, 101, 219, 225,  
     231, 236, 275  
 Malacara, D. 46–49, 51, 52, 74, 101  
 Malwick, A.J. 255, 266–268  
 Maréchal, A. 210, 350  
 Mariotti, J.M. 421  
 Markey, J.K. 406  
 Martin, H.M. 19, 21, 85  
 Massie, N.A. 64, 66  
 Mast, T.S. 31, 32, 354  
 Mayall, N.U. 146, 148  
 McCall, S.H.C.P. 466  
 McLeod, B.A. 114, 116, 119, 120  
 McNeill, J.R. 33  
 Meinel, A.B. 94, 100, 172, 213, 276,  
     278, 325, 388, 458  
 Meinel, M.P. 94, 100, 213  
 Meng, J.D. 309  
 Merkle, F. 397–402, 407–415  
 Mertz, L. 60, 61, 68, 176, 177  
 Mevers, G.E. 388, 395  
 Meyer, F. 258  
 Michelson, A.A. 49, 50  
 Miller, J. 76  
 Mischung, K.N. 220–222, 233, 236  
 Moore, P. 348  
 Moore, R. 66  
 Morbey, C.L. 241  
 Morian, H.F. 210, 224  
 Mottoni, G. de 232  
 Mountain, M. 175, 193, 437, 439  
 Müller, R. 224  
 Muller, R.A. 278  
 Musikant, S. 425  
 Nasmyth, J. 470  
 Nather, R.E. 226  
 Nelson, J.E. 19, 28–32, 181, 184, 278,  
     308, 318, 319, 354, 471  
 Newcomb, S. 376  
 Newton, I. 375  
 Nijboer, B.R.A. 351  
 Noethe, L. 232, 281, 288, 290, 297,  
     298, 300, 301, 303, 304, 335, 345,  
     458  
 Noll, R.J. 404  
 Norman, B.A. 93  
 Nugent, K.A. 62  
 O'Dell, C.R. 193  
 Obukhov, A.M. 376, 379–381  
 Offner, A. 77–79, 81–83, 96, 97  
 Osmer, P.S. 193  
 Parenti, R.R. 408  
 Parks, R.E. 1, 19, 86, 93, 94  
 Pausch, K. 215  
 Pearson, E.T. 255, 266–268  
 Perala, A. 184  
 Pfaender, H.G. 224

- Platt, B.C. 151  
 Pohl, R. 424  
 Poisson, S.D. 242  
 Pompea, S.M. 465, 466  
 Prescott, R. 462–464  
 Preston, F.W. 2, 4  
 Pringsheim, P. 424
- Racine, R. 319–325, 327, 328, 330,  
 332, 333, 335, 336, 344  
 Ramsey, L.W. 176–178  
 Randall, L. 308  
 Ray, F.B. 177, 313  
 Rayboult, K. 331, 332, 445  
 Rayleigh, J.W. Strutt, Lord 349, 350  
 Reed, M.A. 186  
 Reicher, D.W. 33  
 Reissner, E. 255  
 Richardson, E.H. 99, 172, 241, 459  
 Riekher, R. 219, 423, 424  
 Rigaut, F. 413  
 Ritchev, G.W. 101, 169, 216, 217, 219,  
 315, 470, 471  
 Robertson, H.J. 277  
 Robinson, T.R. 470  
 Roddier, C. 163–165, 167, 396  
 Roddier, F. 162–167, 376, 380–383,  
 385, 386, 388–395, 397, 398, 400–403,  
 418, 420, 421  
 Romig, H.W. 34  
 Ronchi, V. 167  
 Ross, F.E. 77, 78  
 Rosse, W. Parsons, Lord 169, 175,  
 258, 470  
 Rousset, G. 413, 415  
 Rozelot, J.-P. 238  
 Rubens, H. 427  
 Rule, B. 172
- Saint-Venant, A.B. de 247, 248, 251,  
 253, 254, 264, 280, 283, 284, 378, 385  
 Salinari, P. 190  
 Salmon, D. 355  
 Sarazin, M. 395  
 Sasiela, R.J. 408  
 Sauer, F. 460, 462, 464  
 Scheffler, H. 353  
 Schmadel, L.D. 93, 94, 100  
 Schmidt, B. 23  
 Schmidt, H. 460, 461, 464, 465  
 Schmidt-Kaler, T. 442  
 Schneermann, M. 208, 298, 299, 301  
 Schnur, G.F.O. 214–216  
 Schroeder, D.J. 114, 116, 194–196
- Schwarzschild, K. 376  
 Schwesinger, G. 43, 253–256, 260,  
 262–266, 268–272, 275, 278, 283, 284,  
 287, 288, 353, 354, 356, 362  
 Schwidler, J. 64, 65, 70  
 Sebring, T.A. 177  
 Selke, L.A. 255  
 Shack, R.V. 114, 115, 151–153  
 Shao, L.Z. 86, 93, 94  
 Shupmann, L. 81  
 Silvertooth, W. 95  
 Simpson, F.A. 96  
 Simpson, T. 375  
 Smartt, R.N. 166  
 Smith, G.M. 182  
 Smythe, R. 66  
 Snell, W. 374  
 Song, D.Y. 433  
 Stanford, J.L. 425, 437, 438  
 Stanley, N.R. 376, 385  
 Stenvers, K.-H. 215  
 Stock, J. 395  
 Strehl, K. 350, 356  
 Strittmatter, P.A. 189  
 Strong, J. 424, 429
- Takeda, M. 58–62, 68  
 Tarchi, D. 312  
 Tarenghi, M. 200, 205, 207  
 Tatarski, V.I. 376, 379–385, 389, 391,  
 392, 396, 397  
 Taylor, H.D. 132  
 Thompson, K. 114, 115  
 Thomson, E. 225  
 Timoshenko, S. 242–244, 246, 249–253  
 Tull, R.G. 302  
 Turner, A.F. 425  
 Twyman, F. 2, 49
- Väisälä, Y. 175  
 Vasilevskis, S. 146, 148  
 Vaughan, A.H. 465  
 Vaughan, W. 425  
 Villard, R. 194
- Walker, D.D. 238  
 Wallace, P.T. 450  
 Wang, J.Y. 404–406  
 Wang, S.-g. 191  
 Weaver, L.D. 458  
 Weigelt, G. 421, 422  
 Wenske, K. 23, 24  
 West, R. 292, 293  
 West, S.C. 187

- Wetherell, W. 357  
Wetthauer, A. 87  
Williams, J.T. 161, 186, 325  
Williams, W.E. 49, 50  
Wilson, R.N. 109, 113, 118, 120, 121,  
124, 151, 152, 156, 165, 169, 197, 200,  
220–222, 237, 275, 276, 279–281, 284,  
285, 288, 290, 291, 294–296, 302, 306,  
326, 339, 341, 345, 355, 365, 397, 398  
Wilson, S.R. 33  
Wilson, T.J. 35, 36  
Wizinowich, P. 20, 22  
Wojnowsky-Krieger, S. 242–244, 246,  
249–253  
Wolf, E. 427  
Womack, K.H. 61  
Wood, R.W. 240, 241  
Woolf, N.J. 327, 396  
Wyant, J.C. 57, 62, 65  
Yaglom, A.M. 380  
Yoder, P.R. 233, 258, 259  
Young, A.T. 325, 389, 393–395,  
461–464  
Young, T. 349  
Zago, L. 335–337, 339, 344, 345  
Zernike, F. 55, 284  
Zigmann, F. 233–235  
Zito, R.R. 443

# Subject index

- Aberration modes 200. *see also*  
Modes (aberration)
- Active optics 12, **26**, 27, **31**, 32, **37**,  
**39**, 41, **43**, 45, **80**, 84, 111, 120, **148**,  
149, 151, 181, 192, **199–202**, 205,  
**209–211**, 215, 219, 223, 224, 226, 228,  
231, **232**, 234, 236–240, 249, 250, **254**,  
256, 259, 261, 269, 272, **274–314**,  
**324**, 353, **364**, 397, 404, 407, 409,  
**415**, 450, 471
- active bandpass 215
  - adaptive bandpass 215
  - calibrations 256
  - closed-loop 216
  - correction cycle 202
  - dynamic range 194, 201
  - forced-based concept 215
  - position-based concept 215
  - Shack-Hartmann image analyser  
216
- Active optics control systems 274–314
- 1 m diameter test model mirror 290
  - 3 sectors and 6 sectors for VLT  
support 303
  - 8.2 m quartz primary 307
  - achievable optical quality with the  
NTT 294
  - active 3.5 m NTT 285
  - active centering 291
  - active concept for manufacture and  
operation 306
  - active correction cycle (VLT) 300
  - active mode 298
  - active optics 276–280, 283, 291, 293,  
294, 296, 305, 308, 311, 313, 314
  - active optics for space telescopes  
312, 314
  - active optics improvements (NOT)  
306
  - active optics in radio telescopes 312
- active optics system for the VLT 8 m  
primary 300
  - active optics system of the NTT  
297
  - active optics telescope 275
  - active optics upgrade 296
  - adaptive optics 274, 282, 311
  - adaptive optics bandpass C 281,  
311
  - adaptive optics correction 282
  - aluminium (blank) 306
  - ambient air 300
  - analytical theory (of flexure) 288
  - aspect ratios 298
  - astatic levers 289
  - astigmatism 275, 288, 293, 297, 302,  
303, 306
  - Astronomical First Light 292, 293
  - atmospheric turbulence (seeing)  
279 *see also* external seeing
  - auto-guiding 284
  - automatic correction cycle 290, 294,  
296–298
  - automatic guide star facility 297
  - axial support unit (VLT) 300, 301
  - bandpass 281, 282, 302
  - bandpass B 282 *see also* extended  
active optics bandpass B
  - bandpasses of errors 280
  - basic set-up and alignment 291
  - bending modes 313
  - bores in Subaru primary 307
  - BSC honeycomb (lightweighted)  
blank 308
  - calibration 286, 288, 299, 309
  - CCD detector 278, 292
  - centroiding of Shack-Hartmann  
images 289
  - Cerro Tololo 4 m primary mirror  
305

- Cerro Tololo 4 m telescope 297
- CFRP (carbon fibre reinforced plastic) 311
- classical Hartmann tests 285
- closed-loop active control 274, 277, 278, 280, 281
- closed-loop detection 282
- closed-loop support 310
- closed-loop, on-line system 304
- conversion from Nasmyth to Cassegrain (VLT) 300
- correction bandpass 281
- correction during operation 290
- costs of telescopes 279
- Couder Law 291, 311
- counterweights 290, 297
- dc active correction 289, 290, 292, 310
- decentering 278
- decentering coma 275, 278, 287, 289, 291, 293, 294, 310, 311
- defocus 278, 287, 289, 294, 297, 298, 310, 311
- detection problem (wind-buffetting) 301, 307, 310
- detector windows 280
- differential changes in radio telescopes 313
- differential correction system 300
- diffraction 279
- diffraction-limited performance 311
- diurnal correction 290 *see also* second level correction
- dynamic range 277, 287, 289, 292, 298–300, 308, 310, 312
- eigenfrequencies (VLT primary) 299
- eigenvalues 276
- eigenvectors 276
- elasticity 282
- enclosure design 301, 307, 310
- ESO 3.5 m NTT 276, 279, 285, 291, 293, 304, 313
- ESO 3.6 m telescope 285
- ESO 8 m VLT 276, 287, 298, 303, 310, 314
- ESO active optics system 277–279, 283, 284, 286, 305, 311
- extended active optics bandpass B 281, 301, 308, 310
- external force 303
- external seeing 274, 280, 281, 296 *see also* atmospheric turbulence (seeing)
- external-seeing monitors 279
- extremely stiff mirrors 310
- feedback loop 286
- field aberrations of a telescope 289
- field astigmatism 289
- first 25 natural modes for the VLT primary 299
- first level dc correction *see* dc active correction
- First Light of VLT 303
- first, astigmatic mode 300
- fixed points 303
- flat plate model 277
- flexibility of VLT primary 298, 299
- flexible scheduling 296
- flexure errors 275
- flexure mode 275, 283
- flushing speed 304
- force changes 286
- French 4 m IR spectroscopic telescope 278
- front detection method (wind-buffetting) 302
- full thermal control (honeycomb blanks) 308
- future potential of active optics in telescopes 313
- future space telescope 314
- Galileo (TNG) 3.5 m telescope 291, 298, 305, 314
- Gemini 2 × 8 m project 308, 314
- general active optics system 310
- globular cluster  $\omega$  Centauri (test object) 292
- hard supports 311
- hard, position-based support 287
- Hexapod 1.5 m Telescope (HPT) 311
- high spatial frequency residual errors 285, 294
- higher order modes 287
- highest quality active telescopes 296
- Hindle sphere geometry (wind-buffetting detection) 302
- Hooke's Law (of elasticity) 283, 287, 289
- HST guide star data base 297
- Hubble Space Telescope (HST) 2.4 m 276, 277, 308, 312, 314
- Hughes Danbury Optical Systems (HDOS) 277

- ill-conditioned solution matrix 287
- image analyser 278, 286, 289, 291, 292
- image analysis 290
- image quality comparison 295, 296
- inclined positions of primary 307
- independent point force (on mirrors) 311
- independent pressure (on mirrors) 311
- instruments of the NTT 298
- Intrinsic Quality (IQ) 285, 291, 306, 312
- isoplanatic angle 281
- Italian TNG telescope *see* Galileo (TNG) 3.5 m telescope
- Japanese Subaru telescope *see* Subaru 8.2 m telescope
- Keck 10 m telescope 181, 278, 304, 308–310, 313
- lateral support system 293
- LBT (Columbus) 2 × 8 m project 308
- lightweighted primaries 304, 308, 312
- linear superposition 283, 288
- local air effects 294, 303
- low frequency ambient air errors 310
- low frequency bandpass A 286
- Magellan 6.5 m project 308
- matching error 277, 278, 288, 291, 292, 297, 308, 312
- MATRA Espace 312
- measurement of wind-buffetting deformation 301
- mechanisms in space 314
- microwave holography 312
- mirror seeing 300, 308
- mirror supports 275
- mixed closed-loop and open-loop concepts 310
- MMT 4.4 m equivalent 278
- modal concept of flexure 311
- modal control 276, 277, 286, 287
- monolithic primaries 278
- movable counterweights 290
- natural flexure modes *see* natural modes
- natural mode correction 298
- natural modes 276, 277, 288
- natural ventilation 301, 310
- natural vibration modes *see* natural modes
- Nordic Optical Telescope (NOT) 2.5 m 305, 306, 314
- normal active optics bandpass A 281, 282, 289, 299, 301, 310
- normal active optics correction 280
- normal passive support 277
- NTT 279, 281, 284, 286–296, 298, 300, 310 *see also* ESO 3.5 m NTT
- NTT primary 288, 291, 298
- NTT upgrade 297
- null systems 288, 292
- offset guide star 278, 279, 281, 286
- open-loop active control 274, 275, 278, 310, 313
- open-loop controlled support 310
- open-loop detection 310
- open-loop prime mirror control (Keck) 304
- open-loop, laser alignment system of the MMT 278
- optical axis 289
- optical efficiency 296
- optical feedback telescope 275
- optical tolerances 310, 311
- original design goals of the NTT 298
- orthogonality (of aberration modes) 284
- orthogonality law 284
- partial solution of the wind-buffetting problem (VLT) 304
- passive ESO 3.6 m telescope 285
- passive mode 298
- passive specification 292
- passive support 289
- passive telescopes 274, 291
- physics of the atmosphere 282
- piston (phase) error 278
- positional active optics 310
- post-detection deconvolution 293
- precalibrated correction 293, 297, 298, 305
- prime mirror alone 278
- pupil 283
- purely push support 300
- push-pull axial supports 300, 311
- radio telescopes 304
- real-time image analyser 310
- relaxed low spatial frequency tolerances 308
- ripple 283
- Saint-Venant principle 277, 280, 283, 284, 299
- scaling law 303

- Schwersinger flexure theory 287
- Schwersinger Fourier definition 277
- second level correction 292 *see also* diurnal correction
- segmented primaries 278, 304, 308
- Shack-Hartmann type image analyser 286, 307
- SOAR 4 m project 305
- SOFIA 2.5 m IR telescope 313
- soft (astatic) axial support system 286
- space telescope applications 311, 312
- space telescopes 276, 304
- specification 310, 311
- spherical aberration 278, 287, 288, 292, 300, 308
- springs (for supports) 289, 290, 292, 297
- stainless steel blank 306
- statistical separation (of atmospheric errors) 281
- stiffness function 277
- stiffness matrix 287, 288
- stress polishing 306
- structure printthrough 308
- structured mirrors in borosilicate glass 308
- Subaru 8.2 m telescope 307, 310, 314
- Technical First Light 291
- telescope quality 279
- temperature sensors for Keck primary 310
- ten sources of error (telescope optics) 280
- tension springs 290 *see also* springs (for supports)
- thermal regime in space 311
- thin meniscus primaries 304, 306–308, 310
- thin meniscus projects 305
- thin meniscus technology (active) 302
- third level correction 290, 293, 294, 297
- tilt errors 278
- time frequency 274
- tracking quality 292
- uncontrolled modes 276
- vase-shaped mirrors 307
- very light, rigid, positional monolith 304
- VLT primaries 298
- warping 306
- wind deformation blockage in VLT 304
- wind-buffetting 282, 301, 302, 307, 308, 310
- wind-buffetting deformation 302
- wind-buffetting prevention 303
- wind-induced astigmatism 303
- wind-induced modes 303
- WIYN 3.5 m telescope 308
- Zernike polynomials 284, 298
- zero gravity regime 311
- Zerodur (blanks) 306
- Active telescopes 254, 354, 355, 473
- Actuators 211
- Adapters 449–458
  - *x-y* movements 451, 455, 456
  - AAT 3.9 m telescope 450
  - absolute tracking quality 452
  - active optics 450
  - alt-az mountings 450
  - ANTARES system 452
  - anti-collision measures 452
  - atmospheric seeing 454
  - autoguider integration time 454
  - background 449
  - Bowen class telescopes 449
  - calibration 450
  - calibration system (NTT) 453
  - CCD 452
  - center-field identification 450
  - CFHT 3.6 m telescope 450
  - dichroic mirror 452, 457
  - differential field effects 449
  - differential flexure problems 449
  - double rotation concept (VLT) 456
  - electronic detectors 450
  - equatorially-mounted telescopes 450
  - ESO 3.5 m NTT 450, 453
  - ESO 3.6 m telescope 449
  - ESO 8 m VLT 454
  - fast tracking 454
  - field center observation 449
  - field rotation 450
  - field rotation compensation 454
  - flange back focal distance 450
  - focus corrections 453
  - focus movement 450
  - Gascoigne plate corrector 449
  - GP sensor arm (VLT) 457
  - guide stars 452, 453
  - guide-probe (GP) 450

- guide-probes and image analysis (NTT) 450
- guiding camera 452
- guiding errors 454
- HST star catalogue 452
- image analyser 452
- image analysis 450
- independent rotations (VLT) 456
- instruments 450
- Keck 10 m telescope 450
- large pointing error 449
- NTT adapter 450, 457
- NTT adapter/rotator 450, 451, 454, 455
- oculars 449, 450
- offset guiding 449, 450
- offset-guider 450
- optical axis 455
- optical de-rotator 454
- photographic plates 450
- pointing models 450
- positioning accuracy of the GP 452
- prime focus 449
- reduction optics (NTT) 458
- rotation facility (NTT) 454
- Russian 6 m telescope 450
- scale of the NTT 452
- separate guiding telescope 449
- service of detectors (NTT) 453
- service of detectors (VLT) 457
- simplifications of VLT compared to NTT 456
- telescope "axis" 455
- telescope scale 457
- television 450
- tracking error 452, 454
- trombone 453, 457
- two-mirror trombone system 452
- VLT adapter/rotator 456
- VLT adapters 455-457
- Adaptive optics 189, **216, 274, 282**, 311, 373, 394, **396-420**
- active and adaptive optics 396, 397
- active bandpass A 396, 397
- active bandpass B 396, 397
- active optics 397, 404, 407, 409, 415
- active/adaptive correction system of the ESO 8 m VLT 414
- adaptive bandpass C 396, 397
- adaptive mirror 398, 399, 401, 403, 404, 406, 407, 409, 413, 416
- adaptive optics for military purposes 416
- adaptive optics for the ESO VLT 413
- adaptive optics improvement 416, 417 *see also* extent of adaptive correction
- adaptive optics in the visible 412
- adaptive optics parameters 402, 403
- angular seeing  $\omega$  403
- artificial reference star 409, 411, 412
- atmospheric absorption 396
- atmospheric scaling height 401
- atmospheric seeing 397
- bandwidth in adaptive optics correction 404, 417
- CCD detector 407
- CGE, Observatoire de Meudon and ONERA 404
- coherence area  $\sigma$  403
- COME-ON PLUS system 413, 415
- COME-ON system 407, 409, 413, 415
- conjugate plane 403
- continuous thin-plate mirrors 407, 409
- correction algorithm 404
- correction in the IR 415
- coudé optical train 413
- critical wavelength 413
- daytime function ( $C_n$ ) 400
- detection error 407
- detector (adaptive optics) 406, 407
- different types of deformable mirrors 408
- diffraction limit for  $\lambda \geq 2.2 \mu\text{m}$  413
- diffraction-limited performance 396, 404
- dynamic (correction) range  $\Delta z$  403
- dynamic range 397, 398, 401, 402
- efficiency of adaptive correction 405, 406
- elasticity theory 397
- entire bandpass 396
- ESO 3.6 m telescope 413, 415
- ESO 8 m VLT 401, 403, 404, 418
- ESO DISCO system 407
- extended active optics bandpass 396 *see also* active bandpass B
- extent of adaptive correction 410
- field derotator 413
- focus anisoplanatism 411, 417
- Fried parameter  $r_o$  399, 403
- fundamental limitation (of the isoplanatic patch) 409
- GEC Laboratories 407, 409

- ground-based telescope 396
- high-power laser 411
- higher temporal frequencies 397
- image analyser 398, 404, 406
- image-sharpening telescope 404
- IR 397, 402, 409, 411–413
- isoplanatic angle 397, 398, 401, 402, 409, 411–413, 418
- isoplanatic angle  $\Theta$  402, 403
- isoplanatic angle  $\theta_o$  399
- isoplanatic field 398
- isoplanatic patch 402, 403, 409, 410, 418
- Karhunen-Loeve (K-L) functions 406
- laser guide stars 416, 417 *see also* artificial reference star
- LIDAR system 411
- light loss in adaptive systems 415
- limitations of the isoplanatic patch 409
- long exposures 416
- maximum correction frequency 401
- membrane or pellicle mirrors 407
- mesospheric sodium layer 411, 418
- modal correction 399, 404, 406
- monolithic mirror 407
- MTF 416
- multi-conjugates adaptive optics (MCAO) 418
- natural stars 411
- Newton's law of conjugate shifts 403
- night-time function ( $C_n$ ) 400
- normal active optics bandpass A 413
- normal detector 407
- number of degrees of freedom  $N$  403
- number of speckles  $N_{sp}$  400, 403
- number of sub-apertures 400
- perspective elongation effect 418
- Phillips Laboratory Starfire Optical Range 416
- physics of the atmosphere 397
- piezoelectric actuators 409
- practical systems for adaptive optics 403
- prediction error 407
- principal planes 403
- principles of adaptive optics 398, 399
- pupil image position 403
- random apodisation 397
- Rayleigh backscatter 416
- real part correction 397
- refractive index structure constant  $C_n$  399, 400
- results achieved with COME-ON system 413
- scintillation 397, 402
- segmented actively-controlled primary 404
- segmented mirrors 407
- separate tilt compensation mirror 413
- separate tip-tilt mirror 407
- Shack-Hartmann image analyser 407, 412, 416
- shearing interferometer 407
- short exposures 416
- SOR 1.5 m telescope 416
- sources of error 396
- space telescope 397
- speckle interferometry 401
- speckle lifetime  $\tau$  401, 403
- Strehl ratio 396, 400, 401, 417
- telescope errors 396
- temporal bandpass 397
- temporal cut-off frequency 401
- theory of scintillation 397
- tilt anisoplanatism 418
- tilt correction 417
- total bandpass 413
- transferred pupil 398, 404
- visible wavelengths 397, 411, 418, 419
- wavefront fitting error 407
- Zernike polynomials 404, 406, 413
- zonal correction 399
- Airship-held platform 216, 419
- Alignment and adjustment of telescopes 111–131
  - Alignment of telescopes 105, 111–131
    - aberration field contributions 114
    - alignment of Schmidt telescopes 130
      - alignment operation 122
      - alignment procedure 125
      - aplanatic (RC) telescope 112
        - aspheric axis 122
        - aspheric surfaces 111
        - astigmatic field 120
        - astigmatic field center shift 117, 118
        - astigmatism 113, 114, 123
      - binodal decentering astigmatism 115

- binodal field astigmatism 114, 115
- Cassegrain telescope 111, 123
- CFS axis 114
- CFS *see* coma-free Schießspiegler (CFS)
- classical Cassegrain telescope 112, 119
- collimation error 120
- coma compensation 112
- coma point 129
- coma-free condition 119
- coma-free Schießspiegler (CFS) 111–113, 119–122, 124, 129–131
- corrector plate 130
- decentering aberration function 114
- decentering astigmatism 112, 114, 115
- decentering coma 111, 112, 122, 130
- effective lateral decenter  $\delta_{eff}$  118–121, 124
- effective optical axis (OPT) 122
- equivalent lateral decenter of Schmidt plate  $\delta_{Schm}$  131
- exit pupil 120
- field astigmatism 120, 121
- field center shift 118
- field coma 111
- field corrector 130
- field correctors at the Cassegrain focus 131
- Gregory telescope 111
- image analysis 123, 129
- inclination of the exit beam 120
- lateral decenter  $\delta$  114
- lateral decenter  $\delta_{corr}$  of field corrector 130
- nodal separation 117–119
- nodes 114, 115, 117, 118
- ovals of Cassini 115, 118
- pentaprism 124–126
- pointing correction 121
- preliminary adjustment with a laser 124
- prime focus 130
- pupil aberration 120
- pupil plates 129
- pure lateral decenter 113
- RC (aplanatic) telescopes 119
- Serrurier function 129
- sighting telescope (ST) 124
- spherical aberration 123
- spherical surfaces 111
- theoretical principles 111
- total decenter  $\delta$  114
- wide-field anastigmatic telescopes 119
- Alignment system (MMT)**
- open-loop laser active 187
- Aluminium** 28, **200**, 208, 209, **219–223**, **231–238**, 273, 306, 344, **423–425**, 428
- Aluminizing** 190
- Ambient air** 223, 227, 229, 300
- Array type** 173, **174**, 184, 199, **205**, **206**
- Aspect ratio (AR)** 43, 44, 173, 200, 260, **298**
- Astigmatism** **101–103**, **113**, **114**, **123**, **139**, **140**, **143**, **150**, **164**, **232**, **254**, **255**, **275**, **288**, **293**, **297**, **302**, **303**, **306**
- Atmospheric absorption** 216, 396
- Atmospheric optics** 373–396
  - 5/3 power law 390
  - $d_{80}$  (encircled energy criterion) 390
  - adaptive optics 394
  - Airy disk 386, 389, 390
  - angular seeing 389 *see also* atmospheric turbulence (seeing)
  - ASE blurred image 393 *see also* averaged short-exposure (ASE) images
  - astrometry 374
  - atmospheric dispersion 373, 374
  - atmospheric dispersion correctors 374
  - atmospheric refraction 373, 374, 376
  - atmospheric seeing *see* atmospheric turbulence (seeing)
  - atmospheric soundings 395
  - atmospheric turbulence (seeing) 373, 376, 384, 386, 389, 391
  - averaged short exposures (ASE) “far-field” 387
  - averaged short exposures (ASE) “near-field” 387
  - averaged short-exposure (ASE) images 387, 388, 391–393
  - Bessel empirical form for refraction 376
  - blurring 392–394
  - Cassini’s formula for refraction 374
  - Central Intensity Ratio (CIR) 386
  - coherence function 383, 385
  - complex amplitude calculations 382
  - concentric homogeneous atmosphere 374, 375

- concentric shell model 375
- conditions of astronomical observation (near vertical air path) 384
- conservative passive additives 380, 381
- daytime observation 382
- differential method (seeing measurement) 395
- diffraction 390, 394
- diffraction-limited telescope 386, 389
- DIMM (Differential Image Motion Monitor) 395
- energy transfer law 377
- equivalent uniform long-exposure seeing disk 389
- ESO VLT site-testing programm 395
- external seeing 373 *see also* atmospheric turbulence
- extinction 373
- far-field approximation 391
- fast automatic guiding 392
- first order velocity fluctuations 377
- frame selection 394
- Fried MTF treatment 391
- Fried parameter  $r_o$  385, 386, 388, 395
- Fried resolution  $R$  *see* resolution  $R$
- Fried's polynomial analysis 385
- Full Width Half Maximum (FWHM) 390
- fully developed turbulence 377
- gain in resolution in ASE case 392
- Gaussian distribution 390, 391
- general form of the structure function 379
- geometrical optics approximation 382
- horizontal propagation 384
- humidity 381
- humidity variations 381
- image analysis for active optics 384
- image motion 384, 385, 389, 391–395
- image motion monitor 396
- image motion removal 394
- image spectrum 374
- index structure function 383
- infinitely large telescope 387, 389
- “Infrared Myth” 389
- inner scale of turbulence 378–381, 384
- integrated seeing 384
- interferometric mode 380
- IR domain 394
- isoplanatic angle 389, 394
- Kolmogorov theory 378
- Kolmogorov-Obukhov “two-thirds law” 379, 380
- laminar flow of a fluid 377
- limiting resolution 387
- long-exposure atmospheric PSF 390, 391
- long-exposure images 384, 385, 387, 392
- long-exposure seeing disk 389
- MPIA 2.2 m telescope II 395
- near-field approximation 383, 391
- night-time observation 382
- normal limits of  $r_o$  388
- normalized resolution 387
- Obukhov “two-thirds law” 381–383, 385
- Obukhov law for temperature 381
- offset guider 394
- Optical Transfer Function (OTF) 385
- outer scale of turbulence 376, 378, 379, 381, 384, 394
- Palomar 5 m telescope 394
- phase structure function 383, 385
- plane parallel layer model 375
- probability of obtaining a “good” SE image 394
- random motion 384
- random system  $f(t)$  with stationary first increments 378
- reduced apertures 394
- refraction integral 375
- refraction *see* atmospheric refraction
- refractive index – height function 376
- refractive index fluctuations 381
- refractive index structure constant  $C_n$  376, 381, 388
- removal of image motion in long exposures 394
- resolution  $R$  386, 388, 389, 391
- Reynolds number  $Re$  377
- rms averaged image motion 392
- rotation interferometer 396
- Saint-Venant principle 378, 385
- scintillation measurements 396
- second order velocity fluctuations 377

- seeing disk 373
- seeing measurements with the DIMM 395
- seeing monitors 395
- short-exposure images (ASE) 385, 391, 392 *see also* averaged short exposure (ASE) images
- site selection 395
- small and smooth perturbation approximation 383
- SODAR 395
- solar astronomy 394
- speckle 384, 394
- speckle interferometry 394
- speckle structure 384
- spectral distribution 379, 382
- statistical properties 377
- Strehl ratio 386
- structure function 378, 379, 381
- structure function for  $\delta n$  381
- telescope vibrations 395
- temperature 380, 381
- temperature structure constant  $C_T$  381
- thermal sensors 396
- thin screen approximation 382, 383
- time frequencies of image motion 394
- time-averaged MTF 386
- total seeing 393
- viscous friction 377
- visual observation 392
- water vapour 380
- water vapour content (extinction) 373
- Atmospheric seeing 134, 201, **216**, 274, **279–281**, **296**, 314, 315, 320, **322**, 343, **349–351**, 356, 368, 370, 373, **376**, **384**, **386**, **389**, **391**, **397**, 422, 454
- Axial despace errors 105, 109
  - field coma 109, 110
  - focus movement 109
  - Gaussian (first order) errors 109
  - secondary mirror 109
  - spherical aberration 109, 110
  - third order aberrations 109
- Baffles 459–467
  - 2-baffle system for a Cassegrain telescope 461
  - 4-baffle system 464
  - accuracy of graphical procedure 464
  - angular fields 467
  - Apache Point 2.5 m wide-field telescope 465, 466
  - arbitrary parameter 461
  - baffling in the IR spectrograph (NTT) 465
  - BRDF (Bidirectional Reflectance Distribution Function) 466
  - CAD system 464
  - Cassegrain telescopes 460
  - central obstruction 461, 462, 464
  - classical solution for refractors 459, 460
  - complete generality of graphical procedure 462
  - conical tube above the primary 460
  - contrast loss from stray light 460
  - daylight use 460
  - effectiveness of baffling 461
  - entrance pupil 464
  - ESO 3.5 m NTT 462, 464
  - ESO 8 m VLT unit telescopes 464
  - exit pupil 460, 464, 465
  - extension of telescope tube 460, 463
  - field diameter 462
  - front ( $M_2$ ) baffle 461
  - general optimization of baffles 464
  - graphical procedure of Prescott 462–464
  - grazing incidence on vanes 466
  - instrument (baffling) 464
  - IR space telescope SIRTF 465
  - IR work (NTT) 464
  - iterative procedure 462, 464
  - large field diameter of  $1.5^\circ$  464
  - large fields 462
  - magnification  $m_2$  462
  - near grazing incidence 459
  - normal 2-baffle system 464
  - number of baffles 460
  - obstruction ratio 463
  - open enclosures 465
  - open structure tubes 460
  - paraxial (Gaussian) ray-trace data 462
  - Ramsden disk 460
  - RC telescope at the Hoher List observatory 464
  - real curvatures 464
  - real ray heights 464
  - rear ( $M_1$ ) baffle 461
  - refracting telescopes 459, 464
  - selection of paints for blank surfaces 466

- significant angular fields 463
- small fields 460, 462
- space telescopes 466
- stray light 465
- stray light analysis 466, 467
- stray light rejection performance 465
- surface scatter models 466
- systematic design of baffles for reflecting telescopes 460
- true optical design data 464
- two iterations of graphical procedure 462
- two tubular baffles 460
- vertical scale and horizontal scale 462
- wide field telescope 465
- Beam combination 174, 179, 186, 205, **207**
  - coherent (interferometric) 205–207
  - incoherent 205
- Beam combination aspects 458, 459
  - absence of mirror-imaging or inversions 458
  - beam combination system 458
  - beam combination system (VLT) 458
  - coudé focus (VLT) 458
  - equal azimuths 458
  - equal scales 458
  - ESO VLT Interferometer 458
  - focus 458
  - Gaussian conditions 458
  - instrument optics 459
  - interferometric mode 458
  - interferometry 458, 459
  - pupil geometry matching 458
  - pupil imagery 458
  - VLT adapters 458
- Beam diverger 51, 55, 76, 77
- Beam expander 51
- Beryllium 219, **220–222**, 223, **237–240**
- Bidirectional Reflectance Distribution Function (BRDF) 443, 466
- "Big dish" concept 205
- Blank
  - 5 m Pyrex (Palomar) 217
  - 6 m BSC (Russian) 224
  - 8.1 m ULE Gemini 227
  - 8.2 m Zerodur VLT 209, 210, 224
  - 8.3 m ULE Subaru 227
  - aluminium 200, 208, 209, 231–237
  - aluminium alloys 231, 232, 236
  - Angel lightweighted BSC 227, 228, 230, 231
  - austenitic stainless steels 236
  - beryllium 237–240
  - bores 211, 260
  - boules of fused silica 226, 227
  - breakthrough of Canigen coat 233
  - bubble and seed quality 226
  - build-up (BU) welding 233, 236
  - built-up (BU) welded aluminium blank 234
  - Canigen coat 232, 233, 238
  - carbon fibre reinforced plastic (CFRP) 240
  - cast iron 237
  - ceramization 209, 225
  - classical BSC 227
  - classical fused silica 226
  - classical passive 224
  - coat of enamel (flint glass) 237
  - compacted powder 238
  - compressive bulk stress 225
  - constant thickness 27
  - cost 237
  - critical zone 226
  - crown glass 217
  - cylindrical bores *see* bores
  - egg-crate 195
  - electrolytic coats 233
  - electron-beam (EB) welding 233, 236
  - ferritic stainless steels 236
  - fine-structured stainless steel 237
  - finely structured 237
  - first 8 m class (VLT) 209, 210, 224
  - flexible 210
  - flexure 173, 174
  - flexure problem 172
  - fused quartz (silica) 217, 225, 226
  - fused silica boules 226
  - glass 217, 218
  - glass ceramic 226
  - handling 225, 236
  - heat treatment 233
  - high density (for stainless steel) 236
  - homogeneity 233
  - honeycomb 22
  - honeycomb hexagonal structure 227, 228
  - invar 236
  - LAMA project 234, 236
  - lightweight composite materials 240
  - lightweighted 33, 174, 175, 187, 192, 193, 217, 225, 308

- lightweighted aluminium 237
- lightweighted fused silica 225
- lightweighted structure 217, 239, 260
- lightweighting 199, 219, 229, 237
- lightweighting Zerodur 224
- martensitic stainless steels 236
- massive 33
- meniscus 37
- metal 218, 231, 232
- metallurgical aspects of stainless steel 236
- modern meniscus 210
- psychological barriers to use of metal 238
- pure aluminium 231–233, 236
- pure iron 237
- Pyrex 224
- quilting 228
- replacement blank for the MMT 229, 230
- ribbed, lightweighted 219
- rotating furnace 229
- silicon carbide (SiC) 237–239
- sintered 238
- solid meniscus 228
- speculum metal 231
- spin-casting 224, 225
- stainless steel 233, 236, 237
- stainless steel meniscus 237
- strain measurements 225
- structure 222
- technology for primary mirrors 216
- tension stresses 225
- thermal cycling 234, 235, 237
- thermal cycling tests 232
- thermal equilibrium 228
- thermal problems 173, 174
- thermal properties 237, 240
- thick 6 m (Russian) 224
- thick fused quartz 226
- thickness 224
- thin 8 m 209
- thin meniscus 43, 193, 199, 209, 211, 214, 227
- thin, flexible 174, 175
- thin, solid stainless steel 237
- transparency 225
- transport 225
- ULE fused quartz 214, 226
- uncontrolled ceramization 224
- vapour-deposited materials 238
- vase-shaped 27, 232
- vertical sealing of quartz blanks 225, 226
- warping 232, 233, 237
- zero expansion glasses 237
- Zerodur 225, 226, 231, 233, 237, 240
- Blank production 216–242
- BSC (borosilicate) glass 227
- classical “thick” 227
- fused quartz 225
- glass ceramic 223
- metal 231
- Bowen-type telescopes **315, 318, 324, 350, 449**
- Bronze 219
- Canigen (nickel) coat 208, **219, 232, 233, 238**
- Carbon fibre reinforced plastic (CFRP) **214, 215, 219, 220–222, 240, 311**
- support/cell 214
- Carbon steel 219
- Cassegrain telescope 122, 170, 175
- Cast iron 218, **219, 237**
- Caustic **81, 134, 144, 159**
- CCD detector **46, 54, 55, 57, 67, 72, 133, 134, 151, 154, 156, 157, 159, 160, 165, 204, 278, 292, 407, 452**
- Chemical silvering 216, **423–425**
- Chromium coats 219
- CIR (Central Intensity Ratio) 41, 42, **356–358, 361–365, 369–371, 386, 423**
- Cleaning and maintenance of reflecting coats 370, **442–448**
  - *M*<sub>3</sub> mirrors of the VLT 448
  - μSCAN 443, 444
  - 8 m mirrors 445
  - aluminium coated mirror samples (laser cleaning) 446
  - bird droppings 442
  - BRDF (Bidirectional Reflectance Distribution Function) 443
  - clean environment 442
  - cleaning efficiency 443, 445, 447
  - CO<sub>2</sub> snow cleaning 443
  - CO<sub>2</sub> snowflakes 443–445, 448
  - Collodion (peeling) 445
  - Collodion films 444
  - damage threshold 446, 447
  - dust 442
  - effective diameter 444
  - enclosure 442
  - ESO 3.5 m NTT 442, 444
  - ESO 3.6 m telescope 448

- ESO 8 m VLT 444, 445, 447, 448
- frequent cleaning 445
- freshly deposited Al coats 442
- Gemini project 445
- greater efficiency of peeling 443
- hard protective coats 448
- jet of gas (CO<sub>2</sub> snow cleaning) 443
- La Silla observatory 444
- laser cleaning 445–448
- laser energy density (fluence) 446
- laser spot sizes 447
- laser wavelengths in the UV 445
- Laser-Laboratorium Göttingen 446
- loss of reflectivity of primaries 444
- oil 442
- OPTI-CLEAN peeling 443–445, 447
- optical efficiency 442
- PL-25 (peeling) 445
- plastic film peeling 443, 448
- primary mirror 442
- reflectivity enhancement 447
- REOSC 448
- risks of laser cleaning 447
- saturation 447
- scratching with “snow” 443
- silver coats 446
- snowflakes 443 *see also* CO<sub>2</sub> snowflakes
- STI Optronics 445
- tests of cleaning 443–445
- throughput 442
- TMA Technology 443
- washing 442
- Coatings *see also* Mirror reflecting coatings
  - silver reflecting coatings 193
- Coelostat feed 191
- Coherence 49, 205–207, 383, 385, 403
  - spatial 50
  - temporal 50
- Compensation (compensator) *see* Null (compensation) systems
- Compensator
  - reflecting Offner-type null system 196
  - refracting Offner-type null system 196
- Concave hyperboloids 95
- Conventional telescopes 172, 173
- Convex hyperboloids 86, 94 *see also* Testing convex (Cassegrain) secondary mirrors
- Copper 219, 425
- Corning (glass works) 193, 194, 211, 212, 214, 217, 223, 225–227, 308
- Corrector
  - ELT (Extremely Large Telescope) 178, 179
  - reflecting Schmidt plate 191
- Correctors 104
  - wide-field 241
- Cost of telescopes 172, 193, 196, 198, 213
- Cost scaling laws 172, 279
- COSTAR (HST) 197–199
- Couder Law of flexure 172, 173, 210, 242, 244, 245, 247, 249, 250, 252, 256, 291, 311
- Curvature sensing 75, 161–167
- Dall magnification parameter 78
- Decentering errors 105, 111, 112, 114, 115, 122, 130, 135, 150, 165, 278, 357
  - decentering astigmatism 106, 108
  - decentering coma 106
  - lateral (shear) decenter  $\delta$  105
  - parabolic primary 108
  - parabolic secondary 107, 108
  - rotation of the secondary 106
  - tangential coma 105
- Defocus 133, 134, 148, 202, 247, 254, 255, 264, 278, 287, 289, 294, 297, 298, 310, 311
- Density (blank materials) 220
- Detector *see also* CCD
  - CCD 241
- Diamond milling 39
- Diffraction limit 41, 349, 352, 353, 413
- Diffraction-limited quality 216, 311, 386, 389, 396, 404, 419, 422
- Diluted aperture 174, 176, 179, 185, 187, 188, 199, 206
- Diverger 77 *see also* Beam diverger
- Dome seeing 149, 158, 165, 181, 201, 314, 315, 319, 320, 322–324, 326, 335, 337, 338, 341, 343, 344
- Edge effect (thermal) 217
- Efficiency of telescopes 203, 213, 367–371, 471, 473
- Eigenfrequencies 216, 239, 252, 254, 299
- ELT (Extremely Large Telescope) corrector 178, 179
- Enamel 219

- Encircled energy concentrations 194, **351**, 352, 356
- Enclosure 212, 301, 307, 310, **318**, **335**, **344**, **442**, 459, 472
  - ESO NTT 187
  - ESO VLT 205, 208
  - ESO VLT final building 208
  - flushing cylindrical type 211
  - LBT (Large Binocular Telescope) 190
  - Magellan concept 192
  - MMT synchronously rotating 187
  - rotating building 200, 201, 203
  - size 171
- Error budget 211, **365**
- Extended active optics bandpass B 253, **281**, **301**, **308**, **310**, 335, 339, 345, **396**
- External (atmospheric) seeing *see* Atmospheric seeing
- Ferry-Capitain (stainless steel blank) 237
- Field coma **109–111**, 176
- Field rotation **172**, 413, **450**, **454**, **459**
- Figuring **1–45**, 210
- Filled aperture 174, 175
- Fizeau fringes 26, **46–49**
- Flats 76, **101–103**
  - Common-Ritchey test for plane mirrors 101, 102
  - large 101
- Focus **109**, **217**, **218**, 450, 453, 458
  - thermal change of focus 218
- Foucault knife-edge test 46, 56, **74**, **132**
- Fraunhofer diffraction theory 145
- Fried parameter 190, 211, 281, 295, 336, 353, **358**, **385**, 386, **388**, **395**, 399, **403**
- Fringe contrast 51, 66, 67, 84, **421**
*see also* Interferometer
- Fringe scanning **56**, 74, 75 *see also* Interferometer
  - passive 56, 63
- Fringe swamping 37, 44
- Gascoigne plate correctors **148–150**, 352, **449**
- Gay-Lussac linear expansion law 217, 223
- GEC **225**, 407, 409
- Glass **2**, 12, **216–223**, 238, **273**
  - borosilicate crown 24, 25
  - borosilicate glass (BSC) 173, 209, 217, 219, 227, 228
  - BSC (Pyrex, Duran, etc.) 227
  - ceramic 28
  - ceramic (Zerodur) *see* Zerodur
  - Cervit 223
  - classical crown 216
  - classical glasses 219
  - crown glass 218, 219
  - fused quartz 217, 218, 225, 227
  - fused quartz ULE (Corning) 193, 194
  - glass ceramic 174, 212, 217, 219, 223, 227
  - glass ceramic (Astro-Sitall) 223, 227
  - heavy flints 219
  - homogeneity 94
  - lightweighting fused silica 225
  - mass 224
  - plate glass 216
  - Pyrex (borosilicate glass) 217, 219, 225
  - quartz 26
  - ULE fused quartz 174, 211, 212, 217, 219, 225 *see also* fused quartz ULE (Corning)
  - Zerodur 179, 205, 208, 209, 214, 219, 223, 224
- Gregory telescopes 111, 122
- Grinding **1–45**
  - aspheric 44
- Ground-based telescope projects using new optical technology 345–347
- Hamilton Characteristic Function **55**, **148**, 253, 275
- Hardness (blank materials) 222
- Hardness (Knoop) (blank materials) 222
- Hartmann test **46**, **75**, 100, **144–150**, 152, 154, 160, 260
- Heat radiation 223
- Heterodyning 57
  - spatial 60, 62, 68, 69, 72
  - temporal 57, 59, 62, 68, 72
  - temporal (PSI) 66
- High resolution imaging apart from adaptive optics 420–422
  - adaptive optics 420
  - atmospheric seeing disk 422
  - auxiliary telescopes of the VLTI 421

- diffraction-limited reconstruction 422
- ESO 3.6 m telescope 422
- ESO 8 m VLT telescopes 422
- ESO VLTI (Very Large Telescope Interferometer) 421
- exposure time 421, 422
- fringe contrast 421
- high image quality 421, 422
- image reconstruction 420
- laser speckles 422
- limiting magnitude 422
- local air effects 422
- manufacturing tolerances 421
- Michelson interferometry 420–422
- optical bandwidth 420, 422
- outer scale of turbulence 420
- pathlength drift 421
- polarisation 421
- post-detection off-line procedures 420
- *S/N* ratio *see* signal/noise (*S/N*) ratio
- short-exposure stellar images 422
- signal/noise (*S/N*) ratio 420, 422
- speckle interferometry 420–422
- speckle masking 422
- telescope aberrations 422
- triple correlation method 422
- Hologram 84, 85, 153
  - computer generated (CGH) 85
  - synthetic 84
- HST Strategy Panel 196, 197, 474
- IBF *see* Ion beam figuring
- Image analyser 122, 123, 129, 150–158, 203, 216, 278, 286, 289–292, 316, 338, 371, 384, 398, 404, 406, 450, 452, 472
- Shack-Hartmann 150–158, 203
- Image quality specification 321, 349–367
  - $d_{80}$  354–356, 360, 367
  - $d_{FWHM}$  354, 355, 360, 367
  - $d_{rms}$  353, 362
  - $W_{rms}$  353, 362
  - active optics 353, 364
  - active optics bandpass A 365
  - active specification 355
  - active telescopes 354, 355
  - Airy disk 349, 351, 352
  - angular aberration 349, 350
  - angular aberration approach 350
  - atmospheric seeing 349–351, 356, 357
  - atmospheric turbulence theory 353, 362
  - automatic correction cycle (NTT) 356
  - axisymmetrical aberrations 358, 363
  - Bowen class telescopes 350
  - Central Intensity Ratio (CIR) 356–358, 361–365
  - CIR measurement 365
  - classical specification criteria 349–353, 356
  - decentering 357
  - Dierickx theory of CIR 358
  - diffraction 351, 352, 356
  - diffraction effects 351
  - diffraction limit 349, 352, 353
  - dynamic range 355
  - encircled energy including diffraction 352, 356
  - encircled energy percentages 351
  - equivalent Strehl ratio 360
  - Error Tree for the VLT 365
  - ESO 3.5 m NTT (active) 355, 356, 364
  - ESO 3.6 m telescope 351, 352
  - ESO 8 m VLT 353, 355, 356, 358, 364, 367
  - Fourier treatment 350
  - Fried parameter  $r_0$  353, 358
  - Gaussian distribution 353
  - general error budget 358
  - geometrical angular aberration 352
  - geometrical encircled energy 351, 352
  - high spatial frequency polishing errors 351
  - higher spatial frequencies 362
  - image motion 363
  - integrated atmospheric seeing 349, 350
  - Intrinsic Quality (IQ) 355, 356
  - IQ *see* Intrinsic Quality
  - Japanese Subaru 8 m telescope 367
  - Keck 10 m telescope 354
  - Keck 10 m telescope optical error budget 354
  - larger aberrations 350
  - laws of geometrical optics 351
  - local air seeing 355–357
  - long exposure MTF 358, 359
  - long exposure PSF 359

- lower spatial frequencies 362
- manufacture and test technology 353
- manufacturing errors 356, 357
- matching error 355
- Mauna Kea (Hawaii) 354
- MMT 4.4 m equiv. telescope 353
- Modulation Transfer Function (MTF) 350, 353, 356, 358
- MTF *see* Modulation Transfer Function
- natural units for diffraction 360
- natural units for seeing 360
- normalized MTF 356
- NTT *see* ESO 3.5 m NTT
- numerical calculations for CIR 364
- Optical Transfer Function (OTF) 350, 352
- OTF *see* Optical Transfer Function
- Palomar 5 m telescope 349, 351
- passive specification 355
- passive telescopes 352, 357
- photography 349
- point spread function (PSF) 350
- Rayleigh limit 349
- rms angular aberration criterion *see*  $d_{rms}$
- rms wavefront criterion *see*  $W_{rms}$
- Schwersinger Fourier modal approach 353
- Shack-Hartmann measures 364
- small aberrations 350
- space telescopes 352
- spatial frequency 356
- spatial frequency spectrum 351
- specifications for modern ground-based telescopes 353–367
- spot diagrams 351, 364
- Strehl criterion *see* Strehl Intensity Ratio
- Strehl Intensity Ratio (Strehl criterion) 350, 352, 353, 357, 360–363
- Subaru telescope Optical Error Budget 367
- support errors 357
- telescope errors 349
- thermal control 356
- third level of active control (NTT) 356
- visual observation 349
- VLT Optical Error Budget 364–366
- wavefront aberration approach 350
- wavefront phase error 349
- INNSE/TECNOL 234
- Interferogram
  - single *see* Single interferogram
- Interferograms 51
  - patterns 51–54
- Interferometer 46
  - air turbulence 66, 68, 72, 73
  - circular fringes 47
  - common path 66
  - DIRECT 100 (DMI) 68–73
  - DMI *see* DIRECT 100 (DMI)
  - dust 68
  - error sources 64, 70
  - Fizeau 46–49
  - FLIP (REOSC) 73, 75
  - fringe contrast 51, 66, 67
  - fringe scanning 56
  - Haidinger 46–48
  - Haidinger fringes 48
  - heterodyne 57
  - integrating bucket 62, 63
  - Laser Unequal Path (LUP) 46, 50, 51, 54, 55, 74–77
  - LUP *see* Laser Unequal Path (LUP)
  - Michelson 48, 50
  - Newton 46, 47
  - Newton's fringes 46
  - parallel channel phase shift 66
  - phase shift 56
  - phase shifting 57, 62
  - Phase Shifting (PSI) 66, 68
  - phase stepping 57, 62, 63
  - phase unwrapping 68, 73
  - point diffraction (Smartt) 66, 74
  - scattering effects 68
  - scatterplate 66
  - shearing *see* transverse wave-shearing
  - Simultaneous Phase Shift (SPSI) 66–68, 72
  - surface and coating errors 68
  - transverse wave-shearing 66, 74
  - Twyman-Green 46, 48–51, 55, 56, 66, 74
  - vibration 66–68, 72, 73, 75
  - vibration stabilization 69
  - Williams 49, 50, 55, 56
- Interferometric mode 206–208, 216, 380, 458
- Interferometry 86, 120, 174, 206–208, 419, 458, 459 *see also* Interferometer
- auxiliary telescopes (VLT) 206, 207

- digital phase-measuring 65
- fringe scanning 74, 75
- interferometric mode (VLTI) 206
- phase shifting (PSI) 66
- Intrinsic Quality (IQ) 18, 39, 41, 43, 45, 149, 154, 156, 160, 200, 201, 205, 285, 291, 306, 312, 338, 355, 356
- Ion beam figuring (IBF) 33–37, 41, 44, 179–182
- IQ** *see* Intrinsic Quality
- IR background 184, 199, 371, 430
- IR interferometry 74, 75, 84
- IR LUPI interferometry 75
- Isoplanatic angle 153, 216, 281, 314, 389, 394, 397–399, 401–403, 409, 411–413, 418, 419
- Kerber condition 25
- Kolmogorov turbulence 320, 378–380
- Krupp 214
- Lagrange differential equation (stress polishing) 25
- Lasers 46, 50, 51, 54, 55, 74–77, 152, 422, 445–448
  - multimode 51
  - single mode 51
  - stabilized single mode 51
- Lens surfaces 3
- Lightweight fibre composites 214, 240
- Lightweighting (telescopes) 216
- Linear temperature gradient 217
- Lissajous figures 65, 68
- Local air (of telescopes) 183, 201, 203, 208, 212, 294, 303, 314–316, 318, 324, 337–339, 343, 345, 355–357, 422, 472
- Local environmental aspects of telescopes 314–345
  - 2.2 m MPIA 324
  - 2.5 m INT (Isaac Newton Telescope) 316
  - 2.5 m Nordic Optical Telescope (NOT) 338, 344
  - 3.5 m ESO NTT 316, 319, 324–326, 331, 338, 339, 344
  - 3.6 m CFHT 315, 316, 319, 320, 322–325, 328, 336
  - 3.6 m ESO telescope 315, 320, 324, 338
  - 3.9 m AAT 315, 325
  - 4 m Cerro Tololo 324
  - 4.2 m WHT 325
  - 4.4 m MMT enclosure 324
  - 4.4 m MMT 319, 325, 344
  - 8 m ESO VLT 319, 328, 333, 335, 337, 339, 344, 345
  - 8 m VLT primaries 332, 334, 336, 337
  - 8 m thin meniscus blank 331
  - 10 m Keck telescope 319, 325, 345
  - AAT *see* 3.9 m AAT
  - active cooling 329
  - active cooling plate 335
  - active optics principles 324
  - active temperature control 327
  - active thermal adaptation 334
  - active thermal control 339, 344
  - adhesive Al foil 325
  - air flushing 338, 339
  - alt-az mount 325
  - alt-az mounted telescopes 344
  - aluminium (cooling plate) 334
  - aluminium enclosures 325
  - aluminium mirrors 344
  - automatic correction cycle 339
  - borosilicate glass (BSC) 327, 328
  - Bowen-type telescopes 318, 324
  - CFHT *see* 3.6 m CFHT
  - channels for coolant (blanks) 328
  - classical dome 326, 344
  - classical primaries 319
  - cold nodes 327
  - condensation risk 331
  - cooled radiation plate 329
  - cooled, lightweighted blanks 327
  - dewpoint problems 333, 335
  - differential dome seeing monitor (DDSM) 340, 342, 344
  - dome or tube seeing monitors 339
  - dome seeing 314, 315, 319, 320, 322–324, 326, 335, 337, 338, 341, 343, 344
  - dome seeing monitor 339
  - dome slit 323, 340
  - electronics (heat from) 315
  - elimination of air leaks and heat sources 324
  - enclosure ventilation 335
  - enclosures 318, 344
  - ESO 3.5 m NTT as a test bench 338
  - ESO 3.5 m NTT *see* 3.5 m ESO NTT
  - ESO 3.6 m telescope *see* 3.6 m ESO telescope
  - ESO 8 m VLT *see* 8 m ESO VLT

- experimental set-up with DDSM 340
- extended active optics bandpass B 335, 339, 345
- external (atmospheric) seeing 315, 320, 322, 343
- fast active optics control loop 339
- flushing 329
- flushing air 317
- flushing air flow 329, 344
- flushing air velocity 317, 330
- flushing efficiency 330
- flushing wind 329, 331, 336
- flushing windspeed 336, 337
- forced convective ventilation 327
- free convection case 335
- free natural ventilation 325
- Fried parameter 336
- functioning telescope using cooling plate 334
- functioning telescopes (experiments on) 344
- further laboratory experiments on mirror seeing (after Lowne) 329
- Gemini project 331, 335
- glass mirrors 344
- global optical concept 345
- good thermal conditions 339
- ground seeing 324
- heat sources 315
- high thermal diffusivity 329
- higher flushing windspeeds 345
- huge buildings and domes 315
- image analyser 316
- image analysis 338
- image motions 343
- image quality at the CFHT 321
- inclined mirror 317, 318
- inferior thermal conditions 338
- insulation 344, 345
- internal cooling in meniscus mirrors 328, 331, 334
- internal heat sources 343
- internal micro-climate 345
- Intrinsic Quality (IQ) 338
- Keck 10 m telescope *see* 10 m Keck telescope
- laminar air flushing 318
- laminar convective situation 339
- laminar flow 328
- laminar free convection 336
- last big refractors 318
- LBT (Large Binocular Telescope) 345
- lightweighted honeycomb blanks of borosilicate glass 327
- lightweighted primaries 345
- limit windspeed 335
- local air effects 314–316, 324, 339
- local air error measurements 318
- local air seeing 314, 337, 339, 343
- local air seeing and enclosures 343, 345
- local air variations 338
- low heat conductivity 328
- maximum flushing winds 337
- maximum windspeeds for wind-buffetting 337
- Melbourne 4-foot reflector 318
- meniscus mirrors in aluminium 328
- metal cooling plate 334, 344
- micro-climate 315
- microturbulence 325
- minimum flushing speed 344
- mirror seeing 314, 316, 319, 320, 322, 323, 326–329, 331, 332, 334–337, 343–345
- mirror seeing experiments 330, 331
- MMT upgrade 345
- MMT *see* 4.4 m MMT
- modal analysis 316, 344
- modal identification of local air seeing errors 338
- natural convection 318
- natural ventilation 318, 326
- natural wind flushing 344
- negative temperature difference (colder mirror) 317, 318, 323, 329, 330, 332, 336
- NTT building concept 318
- NTT *see* 3.5 m ESO NTT
- optical system errors 320, 322
- Palomar 5 m telescope 315, 318
- passive cooling 335
- passive telescopes 315
- passive thermal adaptation 332, 334
- positive temperature difference (warmer mirror) 317
- positive temperature overhang 334, 335
- pressure limitation (wind-buffetting) 335
- quadratic astigmatism 326
- quasi-zero expansion materials 315
- radiation cooling 325
- reduction of air volume (enclosures) 344

- refrigerated observing floor 324
- residual local air seeing 339
- Russian 6 m telescope 325
- scaling laws 335–337
- seeing monitor 316, 338
- segmentation 345
- segmented primaries 345
- sensor installation for temperature and wind 316
- site seeing 314, 326
- slit size 325
- specific local influence 314
- spherical aberration 326
- spiders 327
- stable micro-climate 344
- Strehl Intensity Ratio 329
- stronger laminar flushing 337
- Subaru 8.2 m telescope 328
- superb thermal conditions 338
- surface cooling of the ESO 8 m VLT primary 333
- systematic analysis and improvement (CFHT) 319
- telescope aerodynamics 337
- telescope enclosures 318, 324, 337, 344, 345
- telescope structure seeing 314, 326
- temperature and wind differences 338
- temperature and windspeed sensors 338
- temporal bandpass limitation 338
- thermal and wind sensors 320
- thermal control 315, 331, 345
- thermal control for a honeycomb blank 327
- thermal control of thin menisci 332
- thermal control system (with active optics) 339
- thermal environment 338, 344
- thermal printthrough 328
- thin meniscus primaries 328, 332, 339, 344
- tracking errors 344
- tube seeing monitor 340
- turbulent convective situation 339
- turbulent free convection 337
- turbulent motions 316
- turbulent natural convection 335
- typical cooling scenario 333
- typical telescope enlosures 319
- ULE fused quartz 328
- ventilation 315
- ventilation system 319
- VLT primaries at Paranal 333
- VLT *see* 8 m ESO VLT
- volume of local air 319
- wall gates (NOT) 338
- wavefront aberrations higher than “tilt” 341
- wavefront tilt 341, 342
- white enclosures 325
- wind 344
- wind flushing 316, 324, 343
- wind loading of telescopes 344
- wind-buffetting 315, 335, 337, 345
- wind-buffetting deformation 339, 345
- wind-buffetting detection 339, 345
- windscreening 342, 343
- Local seeing *see* Local air (of telescopes)
- LUPI (Laser Unequal Path Interferometer) *see* Interferometer
  
- Maintenance and operation of telescope optics 469–474
- active concept (for space telescopes) 474
- active optics control 471
- active telescope 473
- airports 469
- analogue maintenance situation 471
- astronomical first light (AFL) 471
- astronomical observation 472
- automation of optical maintenance 471
- cleanliness 473
- clear maintenance schedules 473
- coating plant of high quality 474
- committee design 470
- communication difficulty 470
- conferences 469
- costs 473
- Crossley 36-inch reflector 470
- development 469
- development end 472
- development of new equipment 469
- development of telescope optics 469
- development team 472
- development work 473
- development-maintenance relationship 472
- digital maintenance situation 471
- efficiency criterion  $E_O$  471, 473
- electronic systems engineer 473
- enclosure 472

- ESO 3.5 m NTT 474 *see also* NTT
- factor of cost for space projects 474
- flux throughput 473
- fully automatic active optics concept 472, 473
- ground-based telescopes 469–474
- high level of redundancy (for space telescopes) 474
- high optical quality 471
- HST 2.4 m 474
- HST spherical aberration error 474
- image analysis 472
- industrial contracts 469
- Keck 10 m telescope 471
- large, active, ground-based telescope 471
- Lick 36-inch refractor 470
- local air conditions 472
- maintenance 469
- maintenance of high quality 473
- maintenance situation for space telescopes 474
- Melbourne reflector 470
- mismatch between development and operation 469
- modern cleaning routines 474
- normal maintenance 472
- NTT 471, 472 *see also* ESO 3.5 m NTT
- observatory (on-site) 472
- off-line image analyser 473
- off-line mode 473
- oil refineries 469
- on-site maintenance team 472
- operation 469
- organisation 470–472
- organisational problem 471
- passive mode 471
- passive telescope 473
- reduced costs 474
- redundancy requirement for mechanisms 474
- reflecting coatings 473
- reflectivity measuring device 473, 474
- relaxed tolerances 474
- Ritchey telescopes 470
- security against error 474
- significance of photography 470
- site 472
- software 473
- space telescope standards 473
- space telescopes 474
- speculum mirror 470
- step function between development and maintenance 473, 474
- symbiosis between development and operation 470
- technical first light (TFL) 471
- technical time 471
- technically responsible person 472
- technically responsible person in the development team 473
- technically responsible person on-site 473
- thermal conditions 472
- thermal sensors 472
- top-quality maintenance engineers 469
- tracking and pointing 472
- very hard absolute tolerances (for space telescopes) 474
- VLT 471
- when will the telescope be finished? 472
- Yerkes 40-inch refractor 470
- MAN** 214
- Manufacture** 1–45, 353, 356, 357
  - aspherizing 9, 11
  - figuring 1–45
  - grinding 1–45
  - ion beam figuring 33–37
  - lapping 2, 3
  - microgrinding 14, 15
  - optical 1
  - polishing 1–45
- Manufacturing specifications** 148, 365, 366
- Manufacturing tolerances** 200, 421
- Mass problem** 173
- Mass reduction** 169–348
- Matching error** 80, 85, 88, 99, 100, 193, 196–199, 201, 277, 278, 288, 291, 292, 297, 308, 312, 355
- Mechanical stiffness** 222
- Mechanical tests (of mirror figure)** 86, 94
- Medial telescopes** 81
- Mercury pool flats** 87
- Mersenne afocal telescope** 108
- Milling**
  - diamond 1
- Mirror** 3
  - aspheric (hyperbolic) 76
  - aspheric concave 76
  - auxiliary concave reference 104
  - concave 86, 102

- convex 86
- convex Cassegrain secondary 86
- flexible 3
- plane 76, 101 *see also* Flats
- real image test problem 86
- spherical 6
- spherical test 76, 77
- Mirror blank materials
  - physical properties 220–222
- Mirror handling 272
  - aluminium 273
  - breakage 274
  - central hole 272
  - ESO VLT 8.2 m primaries 273, 274
  - glass mirrors 273
  - maximum induced stress 273
  - Pyrex 273
  - REOSC (VLT primaries) 274
  - safety factor 273
  - Schott (glass works) 274
  - tangential and radial stress 274
  - tensile strengths 273
  - thin plate theory 272
  - Zerodur 273
- Mirror reflecting coats 423–442
  - $\lambda/4$  stack enhancement 432, 433, 439
  - absorption 423
  - absorption band 428
  - Ag coats 434
  - Ag protection 433
  - Al coat with Ag overcoat 432, 433
  - Al coats 434, 437, 439
  - alloys of Ag and Al 434
  - basic coating design for the Gemini project 435
  - bound electrons 427
  - Brashear process 424
  - chemical silvering on glass 424
  - chemically deposited silver 423–425
  - CIR (Central Intensity Ratio) 423
  - cleaning 429
  - CO<sub>2</sub> “snow” 439
  - conventional Al coating 439
  - copper 425
  - deterioration of reflectivity 429
  - dewpoint 434
  - dielectric coat 426, 431
  - dielectric multilayer coatings 431
  - dielectric pair 430, 432
  - effective diameter 423
  - emitted power 434
  - enhanced Ag solution 431
  - enhancement 430
  - enhancement in the UV 433
  - ESO 8 m VLT 441
  - etchability 437
  - evaporated aluminium 423–425, 428
  - evaporated coats 437
  - evaporation 435, 437
  - extinction coefficient 425, 426
  - four reflections (throughput) 429
  - free electrons 425
  - Fresnel law 423, 426
  - Gemini 8 m primaries 435
  - Gemini project 425, 433, 434, 436, 437
  - Gemini update 437
  - gold 425
  - hafnium oxide 436
  - improved reflectivity 439
  - IR emissivity 430
  - large optics 429, 434
  - Leybold 441
  - light diffusion 429
  - loss of reflectivity 429
  - low emissivity 434
  - low-*E* architectural glass 434, 436
  - magnesium fluoride 428
  - magnetron sputtered coats 437, 441
  - magnetron sputtering plant for the Gemini primaries 435, 436
  - modern perspectives for reflecting coatings 430–448
  - multi-coat enhancement 430
  - need for protection (silver) 431
  - non-absorbing dielectric film 427
  - normal reflectivity 425, 427
  - optical efficiency 423
  - oxide layer 425
  - passivation 434
  - platinum 425
  - polarisation 428
  - primary mirrors 429
  - protected Ag coat 434, 437, 439, 441, 442
  - protection 434
  - protective coat 428, 430, 431
  - protective dielectric coating 436, 437
  - quarterwave stack principle 431
  - re-aluminization 429
  - reflecting coats for large optics 448
  - reflectivities of six evaporated metals 425–427
  - reflectivity 423–425, 427
  - reflectivity of “large” mirrors 423
  - refractive index 425

- relative throughput of Al and protected Ag 439
- removal of aluminium 428
- rhodium 425
- robustness 439
- Sample Reflectivity for Gemini coating 439
- secondary mirrors 429
- silicon monoxide 428
- silicon nitride 436
- silver 423, 425, 427, 431, 437
- silver reflecting coat with single protecting coat 434
- single dielectric pair 430
- speculum 423, 424
- sputtering 435, 437 *see also* magnetron sputtered coats
- sputtering facility for the VLT 8 m primaries 440, 442
- sputtering plant for the Gemini primaries 435, 436
- sputtering results for Ag 437
- tantalum oxide 436
- tarnishing 423, 424, 434
- thickness errors 432
- throughput 423
- unprotected aluminium 428, 429
- UV 431
- VLT primaries 441
- VLT sputtering facility *see* sputtering facility for the VLT 8 m primaries
- yttrium oxide 436
- Mirror seeing 174, 223, 229, 300, 308, 314, 316, 319, 320, 322, 323, 326–332, 334–337, 343–345
- Mirrors
  - aluminium 238
  - crown glass 217
  - glass 238
  - glass ceramic 240
  - lightweighted 260
  - liquid mirror telescopes (Hg) 240–242
  - metal 219, 231, 232, 236, 238
  - monolithic 254
  - paraboloidal primary 240
  - psychological barriers to use of metal 238
  - ripples on mercury 240, 241
  - secondary 237, 238
  - segmented primary 175
  - SiC secondary 240
  - speculum metal 216, 238
  - stainless steel 219, 238
  - vase-shaped 233
- MMT concept 174, 176, 184, 186, 189, 191, 278, 319, 325, 344, 353
- MMT square building 186, 187
- MMT upgrade 229, 345, 347
- MMT-type indirect segmentation 189
- Modern projects 175–216, 345–348
- Modes (aberration)
  - astigmatic 232
  - axisymmetrical 233
  - low spatial frequency 223, 232
  - natural flexure 210, 276, 277, 288, 298
- Monolithic primaries 174, 185, 199, 254, 278, 407
- Mount
  - alt-az 171, 187, 199, 238, 255
  - equatorial 171, 238
  - fixed telescopes 175
  - hexapod (HP) 214
  - movable telescopes 175
- Mountings and field rotation 459
  - alt-az mount 459
  - boule telescope 459
  - boule telescopes with mechanical supports 459
  - dead angle 459
  - enclosure 459
  - equatorial mount 459
  - field rotation 459
  - hydraulic support 459
  - pneumatic support 459
  - spherical mounts 459
- MTF (Modulation Transfer Function) 55, 350, 353, 356, 358, 416
- Natural ventilation 187, 301, 310, 318, 326
- Null (compensation) systems 51, 55, 70, 74–88, 93, 100, 104, 241, 288, 292
  - auto-compensation 84
  - compact 79, 80, 82
  - compensation 51
  - field lens 81, 82
  - independent test 85
  - magnification 80
  - matching error 85
  - Offner-type 70, 71, 79–82, 96
  - plano-convex lens 82
  - reflecting Offner-type 80, 82
  - reflection zones 70
  - refracting Offner-type 83, 84, 96
  - single mirror Offner-type 83

- stray light 80
- two lens Offner-type for IR 84
- two mirror Offner-type 83, 84
- zonal error 80, 82
- zonal wavefront error 79
- Null systems *see* Null (compensation) systems
- Null testing 77, 78, 81 *see also* Null (compensation) systems
- Ohara, Japan (glass works) 228
- Optical Arecibo concept 176, 178
- Optical efficiency 296, **367–371, 423, 442**
- Optical efficiency criteria 367–371
- approximate form of efficiency criterion 370
- atmospheric seeing image 370
- Central Intensity Ratio (CIR) 369–371
- cleanliness 370
- diameter-cost laws 369
- Dierickx criterion Optical Efficiency  $E_O$  369
- diffraction 370, 371
- diffusion of light 370
- direct imagery 368, 369
- effective diameter  $D_{eff}$  369
- effective light efficiency  $E$  368
- efficient coatings 370
- ESO 3.5 m NTT 369, 371
- ESO 3.6 m telescope 369
- external seeing 368, 370
- eye pupil 368
- functional performance of telescopes 371
- Herschel 48-inch reflector 368
- high image quality 369
- high spatial frequency error 369
- image analysers 371
- IR emission of the atmosphere 371
- “light buckets” of low quality 369
- limiting magnitude 369
- Lord Rosse 72-inch reflector 368
- minimum magnification 368
- modern electronic detectors 370
- on-line image analyser 371
- penetrating power into space 368
- photographic camera 368
- photometry 369
- photon-limited regime 368
- Point Spread Function (PSF) 368
- quantum efficiency of emulsions 368
- rms slope error of the wavefront 371
- signal/noise ratio  $S/N$  371
- sky background noise 371
- stellar photography 368
- technological optical efficiency  $E_t$  370
- throughput (transmission) 368, 370
- visual use 368
- wavelength dependence of CIR 370
- Owens-Illinois (glass works) 223
- Passive telescopes **149, 169, 200, 232, 254, 274, 291, 315, 352, 357, 473**
- Pentaprism 87, 88, 97, **100, 124–126**
- Performance (of telescopes) 194
- Phase map 55, 58, 68, 73, 97
- Phase shift **56, 57, 62, 66, 68** *see also* Heterodyning
- temporal 57
- Phase tracking 59
- Phase unwrapping **59, 68, 73**
- Plane mirrors 76, 104 *see also* Flats
- Plate
  - thick 29
  - thin 25, 29
- Poisson’s ratio 24, 26, **243, 262, 268**
- Polisher
  - conventional pitch 1, 2
  - membrane 44
  - strip 44
- Polishing 1–45
  - aspherization 17
  - CCOS 12–15, 31
  - CCST 9, 10, 39
  - computer controlled (CCP) 3–9, 11, 12, 15–17, 19, 33, 37, 44
  - dwell-time 4, 9, 11, 12, 15, 33
  - membrane 45
  - pressure 11, 12, 15, 17, 18, 44, 45
  - printthrough 16
  - relative velocity 15
  - ripple 12, 17
  - small tool 33
  - stress 8, 19, 23, 26, 27, 30–33, 37
  - stressed-lap 19–22
- Polynomials *see also* Hamilton, Zernike
  - Hamilton 55, 148
  - natural vibration 55, 276, 277, 288, 298
  - Zernike 55, 148, 253, 275, 284
- Preston constant **2, 74**
- Preston’s Law **2, 4, 15, 44**

- Primaries
  - monolithic 41
  - segmented 41
- Primary **278, 429, 442**
  - aluminium 232, 233
  - directly segmented 191
  - egg-crate 194
  - ESO NTT 3.5 m 210, 252, 270, 291
  - ESO VLT 8 m 210, 233, 249, 250, 252, 270
  - ESO VLT thin meniscus 252
  - fixed tessellated 176
  - flexible 201, 205
  - Galileo telescope (TNG) 205
  - LBT (Large Binocular Telescope) 229
  - lightweighted 193
  - metal (aluminium) 200
  - Pulkowa 0.7 m stainless steel 236
  - rigid 169
  - segmented 175
  - spherical 176, 179, 185, 188, 242
  - stationary, inclined, tessellated 178
  - stationary, segmented 179
  - thin meniscus 199, 205
  - vase-shaped 232
  - warping 232
  - Zerodur 232
- Primary f/no 169–172
- Primary weight 172
- Printthrough 16, 33, 34, 308, 328
- Profilometer 76, 86
- Properties (blank materials)
  - mechanical 217, 220–222
  - thermal 217, 220–222
- Pupil position 179, **283**, 403
- Pure aluminium **219, 231–233**, 236
- Radio astronomy 174
- Radio telescopes 172, 214, 304, **312**
- Rayleigh limit 50, 102, **349**
- Recursion formulae
  - general 106
- Reflecting coats **219, 423–442**, 448, 473 *see also* Mirror reflecting coats
  - dielectric multi-coats 175
  - evaporated aluminium 175, 219
  - protected silver 175
- Relative thermal insensitivity 221
- Ripple 12, 17, 73, **135, 161, 283**
- Ritchey-Chrétien (telescope form) 194
- Rotating Shoe concept **176, 177**, 191, 242
- Rotator 122, **454, 456**
- Rupture limit (glass) 25, 272–274
- Scaling law of flexure **172, 210, 249, 250**, 303
- Schmidt cameras 88
- Schmidt plate **20, 23, 25, 27, 191**
  - reflecting 27
- Schmidt telescope 24
- Schott (glass works) 193, **205**, 208, **209, 223–225**, 274
- Schwarzschild constant 19, **75, 79, 80, 82, 116, 170, 197**
- Secondaries 109, 237, 238, 429
  - Cassegrain 190
  - Gregory 190
- Seeing monitor 203, 316, 338, 395
- Segment **28–37**, 41, 160, 179–183, 185, 199
  - aspheric 34
  - circular 30, 31, 33, 176, 188
  - hexagonal 31, 32, 34, 178–180, 189
  - Keck primary mirror 35
  - non-circular 33
  - off-axis 28, 30, 34, 35
  - spherical 185
- Segmentation 169–348
  - dilute 188
  - direct 174, 175, 179, 185, 189, 199
  - indirect 174, 176, 179, 185, 187, 188, 199, 206
  - MMT-type indirect 186, 189
  - number of segments 174
- Segmented projects 185
- Sensitivities (decentering) 105–111
- Sensitivity of telescopes (photon flux) 212, 213
- Shack-Hartmann testing 75, 138, **150–158**, 160, **164–166**, 216, **286**, 307, 364, 407, 412, 416
- Single interferogram **57, 58, 61, 62, 68, 72**
- Site selection in height 395, **418, 472**
  - adaptive optics 419
  - airship-held base 419
  - diffraction-limited performance 419
  - hexapod-type telescopes 419
  - interferometry 419
  - ISLA proposal 419
  - isoplanatic angle 419
  - isoplanatic patch 419
  - Mauna Kea 419
  - rational site selection 418

- residual atmospheric seeing disk 419
- stratospheric platform 419
- visible spectral region 419
- Space optics 237, 276, 304, **352**, 397, 466, **474**
- Specific heat (blank materials) 220
- Specification (telescopes) 194, 211, **212**, 215, **310**, 311, **353–367**
- optical 122
- Speculum metal **216**, 231, **238**, **423**, **424**, **470**
- Spherical aberration 87, **88**, **109**, **110**, **123**, 134, **135**, 138, **140–145**, 149, 164, 175, **193**, **194**, **196**, 198, 218, **247–249**, **264**, 278, 287, **288**, **292**, 300, 308, 326
- autocompensation 86
- third order 80
- zonal 84
- Spherical aberration error (HST) 196, 197
- Spherical primary type telescope 176
- Spherometers 75
  - bar 75
  - curved bar 75
- Spherometry 75
- Spot-diagrams **146**, **351**, 364
- St. Gobain (glass works) 216
- Stainless steel 28, **219**, 233, **236–238**, 306
- Steel 218
- Stiff composites 199
- Stray light 80, **84**, **465–467**
- Strehl Intensity Ratio 42, 55, 194, **195**, **263**, **275**, 329, **350**, **352**, 353, 357, **360–363**, **386**, **396**, 400, 401, 417
- Stress polishing 4, 8, 19, **23**, 26, 27, **28–33**, 37, **179**, 306
- Structure (telescope)
  - rigid 169
- Submillimeter telescopes (SMT) 214
- Support systems for mirrors 3, 37, 43, **242–274**
  - 1-ring axial support 255
  - 3-point support 258, 259
  - 3-ring support 248, 249
  - 9-point support 258, 259
  - 18-point support 258, 259
  - 81-point support 258
  - active loading 249
  - alt-az mounted telescopes 266, 268
  - analytical theory 256, 259
- aspect ratio 260
- astatic lever 200, 249, 257, 259
- astaticity 259
- astigmatic errors 260
- astigmatic mode 252, 254, 264
- astigmatism 254, 255
- axial support theory 255
- axial supports 242, 254, 259, 260, 264
- axisymmetric mode 253
- axisymmetric support 248
- bands 255
- bending moments 262, 268
- boundary forces 261, 263
- cell flexure 258
- central hole 251, 266, 270
- classical thin plate theory 255
- coma 254
- compound lever 260
- constant pressure 243
- Couder scaling law 250
- Couder's Law of flexure 244, 245, 247, 249, 252, 256
- defocus 247, 254, 255, 264
- deformation from six edge supports 266
- dynamic relaxation 255, 266, 268
- edge support 260
- eigenfrequencies 252, 254
- equal slice approach 268
- equatorially mounted telescopes 266
- external point force 254
- external uniform pressure 244
- finite element analysis (FE) 253, 256, 259
- fixed points 248, 257
- flat belt or band 265
- flexibility 248
- flexure modes 253, 261, 275
- force-based support 257
- friction effects 242
- friction problem 260
- gravity field 249, 250
- Grubb whiffle-trees 258
- half compressive distribution 265
- handling of mirrors 250
- hard support 258
- Hooke's Law 247
- horizontal-axis mounted mirrors 260, 262
- hydraulic support 259
- ideal mirror radial edge support 264

- infinite thin flat plate 252, 256
- isolated load 249
- lapping tool pressure 242
- Lassell-Couder ring supports 258
- lateral (radial) supports for mirrors 259
- lateral edge support (push-pull) for the NTT primary 269
- lateral outer edge support for the ESO 8 m VLT primaries 271
- lateral pressure 251
- lateral supports 254, 255, 260, 266, 268
- lateral supports for alt-az mounted solid mirrors 270
- linear superposition 247
- linearity principle of Saint-Venant 247, 248, 250
- mechanical levers 260
- meniscus mirrors 266
- mercury bags 255, 265
- mirror supports during manufacture 242
- modal analysis 261, 264, 266, 270
- modal flexure function 254
- modern axial supports 256, 259
- modern theory of mirror supports 253
- optimum distribution of compressive edge forces 264
- optimum distribution of compressive forces along the lower half 265
- own weight of cylindrical plate 244
- Palomar internal mirror support 260
- passive axial 4-ring support 256
- passive mirror supports 249
- pneumatic support 259
- Poisson's ratio 262, 268
- polar coordinates 253
- principle of Saint-Venant 253, 264, 270
- pure bending 251
- push-pull radial support 256
- push-pull support 264, 268
- push-pull-shear edge support (Schwesinger) 270, 271
- radial and tangential forces 269
- radial force distributions 266
- Saint-Venant convergence 254
- Saint-Venant principle 253, 264, 270
- scaling laws 249, 250
- Schwesinger Fourier theory 261, 263
- shear deformations 255
- shear stresses 251, 266
- shell theory 268
- simple lever 260
- single edge support 266
- single ring axial support 247, 256
- single symmetrical point force 245
- SOAR primary 272
- soft support 258
- spherical aberration 247–249, 264
- structured mirrors 271
- support density 252
- tangential shearing forces 271
- thick circular plates 255
- thick plate theory 255
- thin circular plate 252
- thin cylindrical circular plates 242, 243
- three ring support 248, 249
- tilt (wavefront aberration) 254
- two flexible cables 265
- uni-directional tilt 267
- uniform flat sheet 251
- uniform force over thin annulus 245
- V-support 265
- vertical mirror 255
- vibrational mode 252
- VLT 8.2 m primary mirror 272
- weightless mirrors in space 250
- whiffle-tree 31, 258, 259
- wind-buffetting 250, 258
- Supports (mirrors)** *see* Support systems for mirrors
- Surface**
  - aspheric 3, 4, 7, 12, 15, 18–20, 23, 24, 27, 32, 39, 51, 74, 78
  - spherical 1, 3, 39, 51
- Systems**
  - active 12
  - compensation *see* Null (compensation) systems
  - null *see* Null (compensation) systems
  - passive 12
- TELAS** 234
- Telescope**
  - AAT 3.9 m 96, 315, 325, 450
  - Apache Point 3.5 m 229, 465, 466
  - central axis reflector 183
  - Cerro Tololo 4 m 165, 297, 324
  - CFHT 3.6 m 99, 278, 315, 316, 319, 320, 322–325, 328, 336, 450
  - Chinese spectroscopic survey telescope 191

- Columbus (now called LBT)  $2 \times 8$  m 169, 174, 228
- Crosley 36-inch reflector 470
- Danish 1.54 m 124, 142, 165, 294
- David Dunlap 74-inch 217
- DGT (German Large Telescope) 12 m project 174, 184, 185, 214
- ELT (Extremely Large Telescope) 178, 179
- ESO 1 m 143
- ESO 1 m Schmidt 131
- ESO 1.4 m CAT 255, 256
- ESO 3.5 m New Technology Telescope (NTT) 12, 17, 18, 20, 37, 43–45, 75, 80, 84, 105, 106, 109, 110, 113, 114, 116–121, 130, 148, 151, 154, 157, 160, 165, 169, 171, 185, 187, 194, 199–205, 208, 210, 211, 216, 223, 224, 227, 232, 233, 251, 252, 256, 268, 270, 276, 279, 281, 284–296, 298, 300, 304, 310, 313, 316, 319, 324–326, 331, 338, 339, 344, 346, 355, 356, 364, 369, 371, 442, 444, 450, 453, 462, 464, 471, 472, 474
- ESO 3.6 m 91, 95, 148–150, 154, 169, 171, 200, 225, 285, 294, 315, 320, 324, 338, 351, 352, 369, 413, 415, 422, 448, 449
- ESO 50 cm 161
- ESO VLT  $4 \times 8$  m 1, 9, 11, 18, 37–39, 41–43, 73–75, 84, 96, 100, 157, 169, 174, 185, 193, 199, 205–212, 224, 227, 233, 234, 237, 238, 249, 250, 252, 256, 270, 272, 276, 282, 287, 298, 303, 307, 308, 310, 314, 319, 328, 333, 335, 337, 339, 344, 345, 347, 353, 355, 356, 358, 364, 367, 401, 403, 404, 418, 422, 441, 444, 445, 447, 448, 456, 464, 471
- FIRST 214, 240
- French TEMOS project *see* TEMOS
- Galileo (TNG) 12, 44, 45, 201, 202, 204, 205, 224, 291, 298, 305, 314, 346
- Gemini  $2 \times 8$  m project 39, 174, 175, 193, 199, 236, 308, 314, 331, 335, 425, 433, 434, 436, 437, 445
- Gemini 1 (North) 193, 347
- Gemini 2 (South) 193, 347
- Geneva Observatory 1.2 m 89
- HET (Hobby-Eberly Telescope) 177–179, 242, 346
- Hoher List RC telescope 464
- HPT (Hexapod telescope) 1.5 m 214–216, 240, 258, 311
- Hubble Space Telescope (HST) 2.4 m 6, 80, 83, 85, 87, 89, 193–199, 201, 276, 277, 308, 312, 314, 474
- INT (Isaac Newton Telescope) 2.5 m 316
- ISLA project 216, 419
- Italian TNG *see* Galileo (TNG)
- Japanese Subaru (JNLT) 8.2 m 193, 199, 211–214, 303, 307, 308, 310, 314, 328, 347, 367
- Johnson 60-inch photometric telescopes 232
- Keck 10 m 1, 8, 28, 33–35, 86, 93, 94, 161, 174, 179–183, 185, 199, 224, 278, 304, 308–310, 313, 319, 325, 345, 346, 354, 450, 471
- Keck I 182–184, 346
- Keck II 182, 346
- KPNO 4 m 225, 255, 256, 264
- LAMOST project (China) 191, 192, 346
- Large Binocular Telescope (LBT)  $2 \times 8.4$  m 189–193, 228, 229, 308, 345, 347 *see also* Columbus
- Lick 36-inch refractor 470
- Lick 3 m 146, 147
- Lord Rosse 6-foot reflector 258, 368
- Macdonald 82-inch 217
- Magellan  $2 \times 6.5$  m project 192, 228, 229, 308
- Magellan 1 193, 347
- Magellan 2 347
- Melbourne (Grubb) 48-inch reflector 169, 216, 238, 318, 470
- Merate 1.37 m 232
- MMT (6.5 m conversion) *see* MMT (Upgrade)
- MMT (Original) 346
- MMT (Upgrade) 85, 188, 192, 230, 231, 347
- MMT 4.4 m equivalent 161, 172, 186–188, 199, 201, 225, 278, 319, 325, 344, 346, 353
- MPIA 2.2 m telescope I 155
- MPIA 2.2 m telescope II 132, 133, 152, 154–156, 264, 294, 324, 395
- MPIA 3.5 m 224, 264
- Mt. Hopkins 1.2 m RC 116
- Mt. Wilson (Ritchey) 60-inch 169
- Mt. Wilson 100-inch 216, 217, 248
- Multi-Mirror-Telescope (MMT) *see* MMT 4.4 m equivalent

- Next Generation Telescope (NGT) 176, 177, 184
- NNTT (National New Technology Telescope) 176
- Nordic (extremely large) 25 m 179, 185, 186
- Nordic Optical Telescope (NOT) 2.5 m 89, 159, 160, 192, 305, 306, 314, 338, 344
- North Carolina 3.5 m project 227
- NOT *see* Nordic Optical Telescope 2.5 m
- NTT (ESO) 3.5 m *see* ESO 3.5 m NTT
- NTT *see* ESO New Technology Telescope (NTT)
- OHP Schmidt 0.62 m 27
- Palomar 5 m 77, 78, 217, 225, 227, 256, 260, 307, 315, 318, 348, 349, 351, 394
- Penn State Spectroscopic Survey Telescope (PSSST) 8 m 176, 178
- Perkins 69-inch 217
- Phillips Lab 3.5 m 22
- Pulkowa 0.7 m 219, 236
- Russian 6 m 173, 209, 217, 224, 227, 238, 256, 325, 450
- Russian 10 m project 185
- SIRTF IR space telescope 465
- Smithsonian 48-inch RC 95
- SOAR 4 m project 272, 305
- SOFIA 12, 44, 45, 214, 240, 313
- Spanish 10 m project 185
- SST (Spectroscopic Survey Telescope) 177
- Stratoscope II 225
- Subaru 8.2 m *see* Japanese Subaru (JNLT) 8.2 m
- TEMOS 175, 188
- Texas 7.6 m telescope (proposed) 226
- TNG (Galileo) *see* Galileo
- University of Hawaii 88-inch 164
- University of Louvain 1.2 m 89
- Vatican (Lennon) 1.8 m 22
- VLT *see* ESO VLT 4 × 8 m
- W. Herschel 48-inch 169, 368
- William Herschel Telescope (WHT) 4.2 m 20, 217, 224, 255, 267, 325
- WIYN 3.5 m Telescope 308, 346
- Yerkes 40-inch refractor 470
- Telescope enclosure 318, 319, 324, 337, 344, 345 *see also* Enclosure
  - air volume 172
- Telescope evolution 169
- Telescope mechanics 171
- Telescope optics (development) 169, 171
  - evolution 169–175
  - revolution 169–175
- Telescope quality for interferometry 373, 420–422
- Telescopes *see also* Telescope
  - conventional 345
  - ESO VLT auxiliary (interferometric) 237
  - passive 200
  - Schmidt telescopes 23, 24, 191
- Terms *see also* Polynomials
  - Hamilton 55, 148
  - Zernike 55, 148, 253, 275, 284
- Test methods and image analysis of telescopes in function 131–167
  - $d_{80}$  energy concentration (quality) 148, 154, 155
  - 2-dimensional Hartmann test 145, 146
  - adaptive optics (curvature sensing) 162, 163
  - ANTARES I 157, 158
  - ANTARES II 157, 159
  - ANTARES image analysis system 133, 151
  - astigmatic circle at best mean focus 139
  - astigmatic lines 139
  - astigmatism 139, 140, 143, 150, 164
  - atmospheric seeing 134
  - axisymmetrical error 144
  - axisymmetrical zones 145
  - caustic 134, 144, 159
  - CCD detector 133, 134, 151, 154, 156, 157, 159, 160, 165
  - central obstruction ratio  $\epsilon$  136–141
  - chimney effects 149
  - classical qualitative methods 131
  - coma 140, 143, 164
  - coma axis 165
  - coma patch 136–138
  - coma point 136
  - coma point direction 138
  - coma vector 137
  - coma-free Schießspiegler (CFS) 136
  - concentric rings of Hartmann holes 146
  - concentric zones 143
  - contour map (plot) 147, 164

- curvature sensing (Roddier) 161–167
- decentering coma 135, 150, 165
- defocus 148
- defocused star images for pupil plates 133, 134
- dents or protuberances (pupil plates) 135, 143
- direct imaging 161
- disk of least confusion 141
- dome seeing 158, 165
- fifth order terms 154
- Foucault knife-edge 132
- Foucaultgram 132, 133
- Fourier transform process 134
- geometrical adjustment error 135
- guide stars 154
- guiding error 140
- Hartmann screen 136, 144–146, 150, 153, 157, 160
- Hartmann spots 144
- Hartmann test 144, 148–150, 152, 154, 160
- Hartmann test, classical axisymmetrical 144
- Hartmann test, generalisation of 146
- Hartmann-based procedures 133, 134, 144, 166, 167
- holographic gratings 153
- illumination 162
- image analysis 154
- image profile 156
- interference 167
- interference effect in Hartmann test 160
- interference spots (Hartmann) 160
- interferometric modification of the Hartmann test 158, 160
- irregular and high spatial frequency defects 142
- isoplanatism 153
- Laplace operator 162, 164
- laser etching (S-H lenslet rasters) 152
- local curvature 162
- measurement of spherical aberration 140
- measurement of the astigmatism vector 139
- measurement of the coma vector 136
- off-line testing 157
- photographic plates 157, 158
- photometric measurements 165
- photometric scanning principle 166
- photometric sensing 162
- point-diffraction interferometer 166
- polynomial analysis 148, 149, 154
- pupil plates 133, 135, 137–140, 142, 143, 161, 164–166
- “pupil plates” with defocused star images 133
- quadratic error 148
- radial grating interferometers 166
- rectangular raster of square lenslets 151
- rectangular, equal-step grid of Hartmann holes 146
- reduction in sampling 156
- reference beam (Shack-Hartmann) 153, 157
- ripple 135, 161
- Ronchi grating 167
- Ronchi test 167
- rotating Foucault knife-edge 166
- rotating knife techniques 167
- S-H test *see* Shack-Hartmann (S-H) test
- sampling 152, 154, 156, 157, 160, 163
- segmented mirrors 160
- Shack lenslet raster 152, 153, 157
- Shack-Hartmann (S-H) test 138, 150, 151, 154, 157, 160, 164–166
- Shack-Hartmann plate 152
- Shack-Hartmann test results 155
- software packages 158
- spherical aberration 134, 135, 138, 140–145, 149, 164
- spherical aberration sign 142
- star image with eyepiece 131, 133
- sub-aperture 144, 151
- support-induced astigmatism 135
- Technical Constant  $T$  145, 147
- testing of telescopes (curvature sensing) 163
- transferred exit pupil 154
- transferred pupil techniques 150
- triangular distortion (pupil plates) 143
- triangular error 148
- turned-down or turned-up edge 135, 143
- Twyman-Green interferometer 166
- vibration 166
- wave-shearing interferometer 166
- zones 135, 144, 161, 162

- Test procedures in function 105,  
**131–167** *see also* Test methods  
 and image analysis of telescopes in  
 function
- Testing 1, 37, **46–104**, 210
- Cassegrain secondaries *see* Testing convex (Cassegrain) secondary mirrors
  - Common-Ritchey test for plane mirrors 101, 102
  - concave primaries 51–56
  - correcting systems 104
  - field correctors 104
  - IR 45
  - large flats 101
- Testing convex (Cassegrain) secondary mirrors
- artificial star 89
  - autocollimation 87
  - autocompensation 93
  - auxiliary convex lens in front of the secondary 98
  - Cartesian lens 92
  - double pentaprism 87, 88
  - double reflection at the primary 90
  - double telescope 87
  - full-size plane mirror 87
  - Hindle sphere 94–96
  - interference test with a concave negative (matrix) 97, 100
  - Lytle test 91
  - Mach-Zehnder 89
  - natural stars 87
  - pentaprism test 87, 88, 97, 100
  - Prism Band 89
  - reduced size plane mirror 87
  - reflection through the back surface 93
  - refracting optics in front of the secondary 90
  - Richardson test 99
  - Silvertooth (inverse Hindle) test 95–97, 100
  - systematic errors 89
  - transmission meniscus Hindle sphere 96, 97, 100
  - Zenith mirror 89
- Thermal capacity 216, 218
- Thermal conductivity 218, 220, 231
- Thermal control 193, **315, 327**, 331, **332, 339, 345, 356**
- Thermal diffusivity 218, 220, 223, 231, 236
- Thermal expansion 216, 221
- Thermal insensitivity 221, 231
- Thermal problems 173, 174, **217, 218**
- Thermal quality criterion 218, 219
- Thermal stresses 218
- Thin meniscus technology **43, 193, 199, 205, 209, 211, 214, 227, 251, 302, 304–308**, 310, 328, 332, 339, 344
- Tool
- full aperture 4
  - full aperture pattern 4
  - membrane 4, 11, 12, 15–18, 44
  - strip 15, 18, 43
  - sub-aperture 4, 11
- Tracking errors 201, 292, **344, 452, 454, 472**
- Variable reflectivity (fixed primary concept) 176
- Ventilation **201, 223, 227, 315, 319**  
*see also* Natural ventilation
- VERTEX Antennentechnik 216
- Warping **31, 32, 200, 232, 233, 237, 306**
- Warping harness **31, 32, 34, 181**
- Weight of telescopes 172
- Weight-cost law 172
- Wind-buffetting 193, **250, 258, 282, 301–303, 307, 308, 310, 315, 335, 337, 339, 345**
- Wind-induced modes 303
- Workshop (optical)
- Carl Zeiss, Jena 12
  - Carl Zeiss, Oberkochen 1, **11, 12, 15–18, 37, 43–45, 68–74, 84, 89, 97, 98, 122, 200–202, 275, 291, 292, 355**
  - Contravez, Pittsburgh 214, 227
  - Eastman Kodak 1, 33–36
  - Grubb-Parsons 3, 96
  - Horst Kaufmann 1, 46, 56
  - ITEK 416
  - ITEK *see* Litton ITEK
  - Jobin-Yvon 153
  - Kodak *see* Eastman Kodak
  - KPNO 30
  - Litton ITEK 1, 9, 12–14, 31, 32, 416
  - OPTEON 305
  - optical 46
  - Perkin-Elmer (Hughes Danbury) (HDOS) 4–8, 277
  - Rayleigh Optical Corporation 95
  - REOSC 1, **9, 10, 37–42, 72, 75, 84, 88, 91, 96, 100, 209, 210, 225, 227, 235, 274, 448**

- REOSC/ONERA 234
  - small 3
  - Steward Observatory Mirror Laboratory 20–22, 80, 85, 229, 230
- X-ray telescope
- AXAF 224
  - ROSAT B 224
- Young's modulus 24, 26, 221, 243
  - Zernike polynomials 31, 32, 34, 55, 148, 253, 261, 275, 284, 298 *see also* Polynomials
  - Zonal masking 74
  - Zonal method
    - interferometric 74

## Acknowledgments for use of figure material

Acknowledgment and grateful thanks are due to the following publishers for permission to use figure material from their books. In most cases, the relevant figures were *line drawings* which have been redrawn, modified for notation and sometimes extended in content.

*John Wiley & Sons, Inc., New York:* Figures 1.38–1.40, 1.42–1.44, 1.55–1.58, 1.60, 1.61 adapted from Malacara, D., “Optical Shop Testing”, 1978, figures 1.16, 1.19, 1.33, 2.2, 2.21–2.29, 2.17–2.18, 14.1, 14.4–14.7, 14.9.

*Daniel J. Schroeder and Academic Press, Inc., San Diego:* Figures 3.22, 3.23 adapted from Schroeder, D.J., “Astronomical Optics”, 1987, figures 11.13–11.15.

*Birkhäuser Verlag AG, Basel, NASA and STScI:* Figure 3.25 adapted from Fischer, D., Duerbeck, H., “Hubble: ein neues Fenster zum All”, 1995, figures page 59 (source NASA) and page 60 (source STScI).

*McGraw-Hill Book Co., New York:* Figures 3.44, 3.45, 3.48 adapted from Timoshenko, S., Woinowsky-Krieger, S., “Theory of Plates and Shells”, re-issued 1987, figures 27, 37, 122.

*Marcel Dekker, Inc., New York:* Figure 3.51 adapted from Yoder, P.R., “Opto-Mechanical Systems Design”, 1986, figure 10.12.

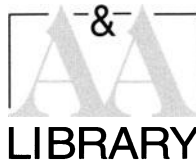
*The University of Chicago Press, Chicago:* Figure 3.52 adapted from Kuiper, G.P., Middlehurst, B.M., “Telescopes”, 1960, Plate III of Chap. 1.

*Dover Publications, Inc., New York:* Figure 5.2 adapted from Tatarski, V.I., “Wave Propagation in a Turbulent Medium”, 1961, figure 6.

*Emil Wolf (editor) and North Holland Publishing, Amsterdam:* Figure 5.4 adapted from Roddier, F., “Progress in Optics”, E. Wolf ed., Vol. XIX, 1981, figure 9 (page 340).

*Rolf Riekher and Verlag Technik GmbH, Berlin:* Figure 6.1 adapted from Riekher, R., “Fernrohre und ihre Meister”, 2. Auflage, 1990, figure 10.2.

*Editions Albert Blanchard, Paris:* Figure 7.6 adapted from Danjon, A., Couder, A., “Lunettes et Télescopes”, reprinted 1983 and 1990, figure 147.



# ASTRONOMY AND ASTROPHYSICS LIBRARY

---

**Series Editors:** I. Appenzeller · G. Börner · M. Harwit · R. Kippenhahn  
P. A. Srittmatter · V. Trimble

**Theory of Orbits** (2 volumes)

Volume 1: Integrable Systems and Non-perturbative Methods  
Volume 2: Perturbative and Geometrical Methods  
By D. Boccaletti and G. Pucacco

**Galaxies and Cosmology**

By F. Combes, P. Boissé, A. Mazure and A. Blanchard

**The Solar System** 2nd Edition By T. Encrenaz and J.-P. Bibring

**Nuclear and Particle Physics of Compact Stars**  
By N. K. Glendenning

**The Physics and Dynamics of Planetary Nebulae** By G. A. Gurzadyan

**Astrophysical Concepts** 2nd Edition By M. Harwit

**Stellar Structure and Evolution** By R. Kippenhahn and A. Weigert

**Modern Astrometry** By J. Kovalevsky

**Observational Astrophysics** 2nd Edition  
By P. Léna, F. Lebrun and F. Mignard

**Supernovae** Editor: A. Petschek

**General Relativity, Astrophysics, and Cosmology**  
By A. K. Raychaudhuri, S. Banerji and A. Banerjee

**Tools of Radio Astronomy** 2nd Edition  
By K. Rohlfs and T. L. Wilson

**Atoms in Strong Magnetic Fields**

Quantum Mechanical Treatment and Applications  
in Astrophysics and Quantum Chaos  
By H. Ruder, G. Wunner, H. Herold and F. Geyer

**The Stars** By E. L. Schatzman and F. Praderie

**Gravitational Lenses** By P. Schneider, J. Ehlers and E. E. Falco

**Relativity in Astrometry, Celestial Mechanics  
and Geodesy** By M. H. Soffel

**The Sun An Introduction** By M. Stix

**Galactic and Extragalactic Radio Astronomy** 2nd Edition  
Editors: G. L. Verschuur and K. I. Kellermann

**Reflecting Telescope Optics** (2 volumes)

Volume I: Basic Design Theory and its Historical Development  
Volume II: Manufacture, Testing, Alignment, Modern Techniques  
By R. N. Wilson

**Galaxy Formation** By M. S. Longair

---

R.N. Wilson

## **Reflecting Telescope Optics I**

**Basic Design Theory  
and its Historical Development**

1996. XIII, 543 pp. 233 figs.  
Hardcover DM 128,-  
ISBN 3-540-58964-3

This is the first volume of a monumental work giving a complete treatment of reflecting telescope optics.

It addresses the specialists in the field, both in the astronomical community and in industry. Consequently, subjects such as practical alignment, test techniques, and maintenance aspects occupy a significant part.

Whereas the second volume will concentrate on technical aspects and modern developments, this book is devoted to the theory of reflecting telescope optics, and with its historical development it should also be useful to students.



## **Astronomy and Astrophysics Library**

Errors and omissions excepted. Prices subject to change without notice. In EU countries the local VAT is effective. d&p BA 33640/SF - Gha



**Springer**